Institut d'Astrophysique

Faculté des Sciences

Multi-Wavelength Study of a Selected Sample of Massive Stars in NGC 6231 and Contribution to the Modelling of X-ray Emission in Colliding Winds Binaries

by

Hugues Sana

– June 2005 –

Dissertation présentée en vue
de l'obtention du grade de
Docteur en Sciences

Acknowledgments

As the reader will soon notice, this work relies on a large set of observations, which clearly forms the foundations on which this work has been built. It is thus naturally that my first thanks go to all those persons who, by their work, contributed to the access, the acquisition and/or the processing of the data. These three different steps, though often arduous and time-demanding, are crucial ones, without which no reliable scientific observational study could be performed. In this regard, I particularly would like to thank Drs. Eleanora Anthokina, Eric Gosset, Herman Hensberge, Jean Manfroid, Yaël Nazé, Gregor Rauw, Pierre Royer, Hawyung Sung, Jean-Pierre Swings and Jean-Marie Vreux for their essential contributions. "You've done a great job. Thanks!"

I am greatly indebted to all my teachers and masters who have contributed, in many different ways, to my education and to my current knowledge and abilities.

I warmly thank Dr. Jean-Pierre Franc, my physics teacher in secondary school, who has definitely triggered my interest for physics. I am also greatly indebted to Dr. Jean-Marie Vreux who, seven years ago, for my graduate dissertation, has launched me into the hot universe of massive stars. I am grateful to him for having, despite all the difficulties, always welcomed me with a smile and a word of encouragement.

I would also like to express my gratitude to Drs. Eric Gosset and Gregor Rauw, who, day after day, have shown me the way into research. May they be thanked for their constant quest for excellence and their taste for a 'well done job'. Although undoubtly each of them has his own way, both have truly been a source of inspiration.

My gratitude also goes to all those in the Institute who, by their enthusiasm and their good mood, behave so that coming to work was, and is (most of the time!), a real pleasure.

It is of course impossible to mention all my friends, but I can give it a try. I first wish to thank the peoples of Raymaldie, the companions from Saint-Michel and from the Lumière et l'Eclair. Thanks for enlarging my horizon and making it (much) broader than a computer screen. I also want to thank all my close friends, those I know since long, and those I know for not so long, thank you for being, at due times, just there at the right place. Finally, I should definitively not forget all the others, guys and girls from here and there, those I know well and those I do not know as well as they would have deserved: my greatest thanks for being just different, and open minded.

Last, but certainly not least, I would like to thank my family who supported me all along the way, all along my way. My thoughts also go to those that should have still been there, but could not. This work is also theirs.

Knowledge not only lies in books, laboratories, notes, but in and through friendship, the one of men, the one of beasts, the one of stars.
Claude Roy

The whole earth was my home, and the sun, the moon, and the stars belonged to me.
Morihei Ueshiba

Contents

Abstract

The present work is dedicated to a multi-wavelength study (in the optical and X-ray domains) of the massive star population of the young open cluster NGC 6231; it aims at providing a homogeneous set of observational constraints that could serve as guidelines for various theories related to O-type stars. This dissertation relies on a large set of observational material collected between 1996 and 2004, that combines intermediate- and high-resolution optical spectroscopy, narrow-band optical photometry and XMM-*Newton* X-ray observations.

Located at a distance of about 1.6 kpc from Earth and considered as the core of the Sco OB 1 association, NGC 6231 hosts a rich early-type star population of different subspectral types and luminosity classes. The present study is limited to a radius of about $15'$ around the cluster core, corresponding to the field of view (FOV) of the EPIC camera onboard XMM-*Newton*. In this area, one finds 15 O-type stars, a Wolf-Rayet binary, as well as about one hundred B-type stars. The present dissertation mainly focuses on the O-type star population of the cluster.

The first part of this work concentrates on the new X-ray view of NGC 6231 provided by the XMM-*Newton* satellite. Our observing campaign, of a nominal duration of 180 ks, reveals more than 600 X-ray emitters in the FOV. Most of them are probably pre-main sequence stars physically related to the cluster. Their study provides insight into the star formation history of the cluster. The X-ray images are however clearly dominated by the emission from the early-type stars and, indeed, all the O-type stars are detected in the X-rays. We probe the so-called *canonical* $L_{\rm X}$ vs. $L_{\rm bol}$ relation for O-type stars and find that the dispersion of their intrinsic X-ray emission around this relation, about 40%, is much more limited than previously admitted. Our investigations further suggest that X-ray emission produced by a wind interaction is the sole mechanism that, within our sample, seems to induce a significant deviation from this scheme. It is also the sole mechanism that, at our detection threshold, leads to a significant modulation of the observed X-ray emission from O-type stars.

The second part of this work more particularly concentrates on two close binaries, HD 152248 and CPD $-41°7742$. We indeed uncover the signature of an on-going wind interaction within both systems, although of a probably different kind each. For HD 152248, we probe the signature of the wind-wind interaction from the optical and X-ray domains; we also perform numerical hydrodynamical simulations that reproduce reasonably well the observed modulations of the system X-ray flux. For CPD $-41°7742$, we rather suggest that the dominant primary wind crushes on (or nearby) the secondary surface, leading to an extra X-ray emission mainly associated with the secondary inner face. As a strong support to our interpretation, we provide a geometrical model that reproduces the main features of the CPD $-41°7742$ X-ray light curve.

Finally, we also derive new SB2 orbital solutions for all the five O-type short period ($P < 6$ d) binaries located in the XMM-*Newton* FOV. We provide the analysis of the optical light curve of CPD $-41°7742$, the second known eclipsing binary in NGC 6231. In addition, we uncover the probable binary nature of four longer period systems and we propose a preliminary orbit for one of them. As a last step, we tightly constrain the binary fraction of the O-type star population in NGC 6231 and we probe the distribution of several orbital and physical parameters.

Résumé

Ce travail de thèse est dédié à l'étude multifréquentielle (dans les domaines optique et X) de la population d'étoiles massives du jeune amas ouvert NGC 6231; il vise à fournir un ensemble homogène de contraintes observationnelles qui pourraient servir de ligne de conduite à différentes théories reliées aux étoiles chaudes de type O. Notre étude repose sur un important ensemble d'observations, réalisées entre 1996 et 2004, et qui combine la spectroscopie optique à moyenne et haute résolution, la photométrie optique à bandes étroites et des observations X du satellite XMM-*Newton*.

Situé à environ 1.6 kpc de la Terre et considéré comme le noyau de l'association Sco OB 1, NGC 6231 abrite une large population d'étoiles chaudes de différents sous-types spectraux et de différentes classes de luminosité. Notre étude sera limitée à un rayon de $15'$ autour du centre de l'amas, ce qui correspond au champ de vision de la camera EPIC à bord de XMM-*Newton*. Dans cette zone se trouvent 15 étoiles de type O et une binaire Wolf-Rayet, ainsi qu'environ une centaine d'étoiles de type B. Nous nous focaliserons essentiellement sur la population d'étoiles O de l'amas.

La première partie de ce travail se concentre sur la nouvelle vision de NGC 6231 obtenue dans le domaine X grâce au satellite XMM-*Newton*. Notre campagne d'observations, d'une durée nominale de 180 ks, révèle plus de 600 émetteurs X dans le champ de vision. La plupart d'entre eux sont probablement des étoiles de la pré-séquence principale, liées physiquement à l'amas. Leur étude fournit un aperçu de l'historique de la formation stellaire dans l'amas. Les images X sont cependant dominées par l'émission des étoiles chaudes et, en effet, toutes les étoiles de type O sont détectées dans le domaine X. L'étude de la relation *canonique* $L_{\rm X}$ vs. $L_{\rm bol}$ pour ces étoiles révèle que la dispersion de leur émission intrinsèque autour de cette relation, de l'ordre de 40%, est beaucoup plus limitée que ce qui est généralement admis. Notre étude suggère de plus que l'émission X produite par une interaction de vent est le seul mécanisme qui, au sein de notre échantillon, semble induire une déviation significative de cette relation. C'est également le seul mécanisme qui, compte tenu de notre seuil de détection, produit une modulation significative de l'émission X observée pour les étoiles de type O.

La deuxième partie de ce travail se concentre plus particulièrement sur deux binaires serrées, HD 152248 et CPD $-41°7742$. Nous mettons en effet au jour la signature d'une interaction de vent dans ces deux systèmes. Pour HD 152248, nous étudions cette interaction à partir des domaines optique et X. Nous proposons aussi des simulations hydrodynamiques qui reproduisent raisonnablement les modulations observées dans le flux X du système. Pour CPD $-41°7742$, nous suggérons plutôt que le vent de l'étoile primaire, dominant dans le système, s'écrase sur (ou à proximité de) la surface de l'étoile secondaire. Cette interaction se traduit par la présence d'une émission X supplémentaire, essentiellement associée à la face intérieure de l'étoile secondaire. Comme argument principal à notre interprétation, nous fournissons un modèle géométrique qui reproduit les caractéristiques majeures de la courbe de lumière X de CPD $-41°7742$.

Enfin, nous déduisons également de nouvelles solutions orbitales (de type SB2) pour les cinq binaires O de courte période ($P < 6$ d) se trouvant dans le champ de vision de XMM-*Newton*. Nous fournissons aussi l'analyse de la courbe de lumière optique de CPD $-41°7742$, la deuxième binaire à éclipses connue dans NGC 6231. En plus de cela, nous indiquons la binarité probable de quatre systèmes à longue période et nous proposons une orbite préliminaire pour l'un d'entre eux. Pour conclure, nous contraignons fortement la fraction de binaires dans la population d'étoiles O de NGC 6231 et nous étudions la distribution de plusieurs paramètres orbitaux et physiques.

Introduction

What I know is not necessarily what you may find, says Merlin.
The best is to go and see.
René Barjavel

With typical luminosities in the range $10^5 - 10^6$ $L_\odot$ and effective temperatures of 30–40 000 K, massive stars of spectral-type O are found at the blue and bright end of the Hertzsprung-Russell (H-R) diagram. These are among the brightest and hottest objects of the Galaxy. As a consequence of their large masses ($M \gtrsim 10$ $M_\odot$), the rate of the nuclear reactions occurring in their core is strongly enhanced compared to lower mass stars, resulting in a shorter evolution time. O-type stars are indeed expected to evolve from the main-sequence through the different evolutionary phases and, ultimately, to the supernova stage, in less than 10 Myr. By comparison, the expected life-time of our Sun is about 10 Gyr, i.e. a factor 10^3 longer.

Beyond their initial masses, their rotation rates and their chemical compositions, their stellar winds are one of the key parameters that determine the evolution of these objects. Together with their evolved descendants, the Wolf-Rayet (WR) stars, the O-type stars indeed display powerful stellar winds characterized by terminal velocities (v_∞) between 1500 and 3000 $\mathrm{km\,s^{-1}}$ and by mass-loss rates ($\dot{M}$) ranging from 10^{-7} to 10^{-5} $M_\odot$ $\mathrm{yr^{-1}}$, or even larger for the most extreme objects. Again these values can be compared to those of the solar wind: $v_\infty \approx 400 - 700$ $\mathrm{km\,s^{-1}}$ and $\dot{M} \approx 10^{-14}$ $M_\odot$ $\mathrm{yr^{-1}}$. High-mass stars thus lose a sizeable fraction of their initial mass ($> 10\%$), even during their short life-time, which strongly affects their fate. The Wolf-Rayet stage is indeed thought to result from the *evaporation* of the original O-type star, that lost its outer hydrogen envelope through its wind. This process therefore reveals the inner layers of the star, which have been chemically enriched in products of the nucleosynthesis.

Because of their extreme properties, massive stars largely influence their surroundings. Their radiation peak being located in the UV, these stars are the first source of ionizing photons in the Universe, and are thought to be at the origin of the large-scale H II regions. Through their winds and their dramatic end as supernovae, their influence is also mechanical. For example, their winds are so powerful that they can shape the ambient medium, resulting in spectacular wind-blown bubbles. The massive stars are also the main cause of chemical enrichment of the interstellar medium (ISM) and, particularly, in heavy elements that are mostly produced during the last stages of their evolution and during the supernova phase. Beyond their influence on their host galaxy, high-mass stars are further important for a number of extragalactic and cosmological issues. Thanks to the *Wind-Momentum-Luminosity* relation, they have been thought to serve as cosmic candles. The first generation of massive stars may finally have reionised the early Universe and could have played a key role in the formation of supermassive black holes.

However, despite the progresses made over the last decades, many crucial issues are still lacking satisfactory answers. These *unsolved* questions range from the determination of the formation mechanism itself, to the upper-mass limit a massive star can have, and to their suspected link with the γ-ray burst phenomenon. The exact distribution of their physical and wind parameters, the existence and role of magnetic fields, the detailed understanding of their final stage as supernovae and the subsequent formation of neutron stars or black holes are further topics that still challenge our understanding. Even a detailed comprehension of the winds of the O and WR stars is still missing. In the following sections, we briefly summarize some selected aspects of the massive stars, focusing mainly on the issues related to the O-type star population, which is indeed the main concern of this work.

How massive is a massive star?

This question, though apparently simple, may still be controversial, which clearly illustrates the actual lack of understanding of some crucial aspects of massive stars. When defining the spectrum of masses of massive stars, one actually considers two distinct questions. The first one concerns the lower mass-limit of a star that is still being considered as *massive* while the second, of course, tackles the upper-mass limit of the interval and the maximum mass a star can have. We will restrain this brief overview to observational considerations.

The lower mass-limit

It is commonplace to consider the progenitors of neutron stars or of stellar-mass black holes as massive stars. *Massive* stars are thus stars initially large enough to ignite a carbon core-burning combustion phase in non-degenerate conditions, leading to type II/Ib,c supernovae. The cut-off line thus lies at initial masses of about 8 to 9 $M_{\odot}$. On the main-sequence, this commonly adopted definition includes objects of spectral-types B1 and earlier.

Zinnecker (2003) further indicates that this criterion also corresponds to the separation between stars which emit Lyman continuum radiation (above 8 $M_{\odot}$) or not (below). In addition, the H-burning stage for objects with initial masses on the main sequence of 8 $M_{\odot}$ or more already starts while the objects are still accreting material, at least if massive stars form through a scaled-up version of the low-mass star formation mechanism. As a result, the birthline joins the zero age main sequence (ZAMS) at ~ 8 $M_{\odot}$ and, therefore, massive stars do not have an observable classical pre-main sequence (PMS) phase.

Finally, we note that this cut-off line also corresponds to effective temperatures around 21 000 K, which is roughly the position of the so-called *first bi-stability jump* resulting of a change in the ionisation balance in the winds (Vink et al. 1999, 2000, 2001). This results in a different wind structure for stars above the limit (fast winds) and below (slow winds). The ratio between the wind velocities in these two regimes is about 2. Finally, the onset of a significant mass loss (i.e. significant enough to affect the stellar evolution) is considered to start at spectral-type B0, which is therefore the dividing line between O and B-type stars.

The upper mass-limit

Although the lower mass-limit for massive stars is relatively well constrained, the upper limit of the mass spectrum is still controversial. This partly results from the fact that the formation process of massive stars itself is still badly understood (see below). Additionally, the accurate weighing of a star can only be performed on a model independent basis for objects belonging to eclipsing binary systems (or at least, to systems that display ellipsoidal variations in their light curve). For stars not belonging to a binary, their masses have to be estimated from a putative extrapolation of the mass-luminosity relation. This method is however poorly accurate and has already shown its limitations. For example, R136a in 30 Doradus, was once thought to consist of a single star with a mass of $\sim$2500 $M_\odot$ (Cassinelli et al. 1981). It has, since then, been resolved into at least 12 components, the most massive one having an initial mass of 120 $M_\odot$ at maximum (Heydari-Malayeri 1996, and references therein). So far, the most massive stars with accurately measured masses are to be found in WR 20a (Rauw et al. 2005). This remarkable system indeed hosts two 80 $M_\odot$ objects that are probably at the transition between the O and WR evolutionary stages.

Massive stars are by nature quite rare objects. Indeed, adopting the usual IMF (initial mass function) shape $\mathrm{d}(\log N)/\mathrm{d}(\log m) = \Gamma$, where m is the initial stellar mass, N is the number of stars per logarithmic initial mass interval, and Γ is the index of the IMF, the expected number of stars of a given mass clearly decreases with the mass considered. In consequence, very massive stars are only expected to be formed from very massive initial molecular clouds. Commonly adopted IMF slopes ($\Gamma \sim -1.35$ – -0.9) usually indicate that only one very massive ($M > 150$ $M_\odot$) star is expected to be observed in most of the young open clusters in the Galaxy. Therefore, even the non detection of such a star in a given cluster remains in the *error bars* of the theory. On the observational point of view, statistical clues for the existence of an upper-mass limit were already pointed out by Oey & Clarke (2005). More recently, Figer (2005) observed the very massive Arches cluster and showed that no star more massive than 150 $M_\odot$ was observed while between 20 and 30 stars (according to the IMF slopes adopted) were expected. According to Figer's computations, this yields to the rejection of the null hypothesis that the mass distribution has no upper limit with a confidence level of 10^{-8}. In consequence, Figer's work puts on firmer ground the existence of some mechanism, other than the sole mass of the initial molecular cloud, that limits the maximum mass a Population I star can reach. We finally note that, even adopting the 150 $M_\odot$ upper limit suggested by Figer, there is still an appreciable gap with the most massive stars weighed in a binary system.

The present considerations hold at solar metallicities. It has been suggested that, at $Z = 0$ for example, super-massive Pop. III stars could have been formed in the primordial Universe with masses of several hundreds to 1000 $M_\odot$. However, as the formation mechanisms of the massive stars, whatever the value of Z, are still ill-understood, these results are, quantitatively at least, somewhat putative. Nonetheless, they suggest that, in its past history, the Universe could have at some stage contained stars significantly more massive than those actually observed. The present work addresses a less extreme sample of O-type stars. The most massive stars considered here have expected masses about 35 $M_\odot$ and we will thus largely avoid the *terra incognita* region that forms the upper end of the stellar mass spectrum. We conclude this note on the mass spectrum of the so-called *massive stars* by mentioning an additional convention used in this work: we will call *massive* a binary/multiple system that contains at least one high mass component ($M > 8$ $M_\odot$).

How do massive stars form?

As briefly mentioned in the previous section, the massive star formation is probably one of the most crucial astrophysical issues that still challenge our understanding in this early XXIst century. Because the core H-burning ignites before these stars have reached their final masses, radiative pressure could stop the gravitational contraction of the primordial molecular cloud while the mass of the protostar is only about 10 $M_{\odot}$. However massive stars are known to exist. Two main scenarios have then been proposed to overcome this problem but none has provided fully satisfying answers so far. The main observational facts that a *good* formation model should encounter are briefly recalled here below.

Massive stars form deeply embedded in their native clouds, and only emerge while already advanced in the core H-burning phase. This renders direct observational constraints on massive star formation processes rather tedious. However it is broadly admitted that massive stars **form within a few 10^5 yr**.

Because of their short life, massive stars are expected to be observed at or near their birth locus and, indeed, **most of them are found in young clusters**. Most of the isolated field stars are further considered as runaways, having been ejected from their birth place presumably as a result of close encountering and tidal interaction or after a supernova kick. de Wit et al. (2005) recently showed that only $4 \pm 2\%$ of all O-type stars with $V < 8^{\rm m}$ (the completeness limit of their sample) can be considered as formed outside a cluster environment. This however remains statistically in agreement with a *universal* richness (in terms of number of stars) distribution, including very poor clusters containing one single star (for more details see de Wit et al. 2005). This study clearly suggests that the formation of massive stars mostly (only?) occurs in a cluster environment.

Basic observational properties of the massive star population are also the relatively **large binary/multiple fraction** and, among these, the **large number of close binaries** and the predominant occurrence of systems formed by **two relatively similar components** (mass ratios smaller than a factor of a few). This could result from an observational bias because of the intrinsic difficulty to detect the signatures of two, relatively different components (large mass ratios). This would however mean that the binary fraction is even higher than the one actually observed. Still, the number of close high mass binaries with similar component will remains significant. This suggests that the formation of massive stars is tightly related to the formation of high mass binaries and that our understanding of both phenomena is probably inter-related. For this reason, we summarize here below the main mechanisms proposed to explain both high-mass star formation and binary/multiple system formation.

Massive (single) star formation

- **The accretion scenario:** As for low-mass stars, massive stars could be formed through the gravitational contraction of an initial molecular cloud and subsequent accretion onto a small-scale proto-stellar object. However massive star formation through accretion cannot be just a scaled-up version of the accretion scenario at work for lower-mass stars. Indeed, several difficulties arise. First the usually admitted accretion rate for low-mass stars ($\dot{M}_{\rm accr} \sim 10^{-5}$ $M_{\odot}$ yr^{-1}) is definitively too low to form a star of several tens of solar masses in less than 10^6 yr, i.e. within less than a sizeable fraction of the main sequence life-time. Second, the radiation pressure from

a high mass star can reverse the infall. This conclusion is somewhat confirmed by the fact that massive stars lose mass through their winds at a similar rate. Clearly higher accretion rates are needed for the accretion scenario to form a massive stellar object.

Norberg & Maeder (2000) have pointed out that there was actually observational evidence for such high accretion rates. The higher temperature and density conditions, as well as the turbulence of the gas in the molecular clouds (McKee & Tan 2003) that usually give birth to massive stars might indeed yield much higher accretion rates than usually adopted. As another example, Yorke & Sonnhalter (2002) also suggested that the limits imposed by the radiation pressure can be overcome by invoking a preferential accretion occurring through a disk in a rapidly rotating star.

- **The coalescence scenario:** Alternatively, Bonnell et al. (1998) proposed that, in dense stellar environments (i.e. in cluster cores), massive stars form by coalescence of lower mass proto-stars, themselves formed through the *classical* accretion scenario. By nature thus, this scenario overcomes the limitation induced by the radiation pressure. It however requires relatively high stellar density. It is also not yet proven whether a sufficient number of mergers can occur on the short time-scale implied.

- **Competitive accretion:** Interestingly enough, Bonnell et al. (2004) recently investigated in more details the formation of massive stars in the context of cluster formation. Among their main results, they found that the final mass of a star was independent of the initial mass of the original clump and that the bulk of the mass of a massive star is gained through competitive accretion. Finally, their results indicate a strong correlation between the maximum mass of a star and the number of stars in the final cluster. In consequence these authors stated that *"the formation of a massive star is a necessary byproduct of the formation of a cluster"*. It should however be pointed out that this study neglected both the radiative feedback of the stars and the details of the accretion process. They rather assumed that, somehow, accretion happens.

Massive binary star formation

- **Fragmentation:** Assuming that circumstellar disks exist around forming high mass stars, a binary system can arise from the fragmentation of the disk if the latter is gravitationally unstable. However, disk fragmentation will produce systems with a typical separation similar to the size of the disk, i.e. about several tens of AU (Yorke & Sonnhalter 2002), and with a relatively large mass-ratio ($q = M_1/M_2 \gtrsim 3$). This scenario thus has difficulty to explain the formation of close binary systems displaying two similar components.

- **Accretion:** In the framework of the above accretion model for single stars, Maeder & Behrend (2002) also proposed that Bondi-Hoyle accretion might favour high-mass binary formation by potentially giving them access to a larger gas reservoir.

- **Encounters and tidal capture:** The coalescence scenario of Bonnell et al. (1998) to form single stars might also lead to the formation of close binaries. These authors invoked the dissipation of the kinetic energy by tidal interaction, leaving the two objects gravitationally bound. Major difficulties with this scenario are similar to these in the coalescence scenario, namely the high star density required and the short time-scale for these interactions to happen.

- **N-body interactions:** Again, similarly to what was stated above, Bonnell (2005, and references therein) suggested that binary formation is a natural byproduct of the fragmentation of an initial molecular cloud. These stars are generally formed through three-body capture in the core of the cluster. Continuing accretion and/or subsequent interaction then contribute to harden the system (i.e. to reduce the separation between the components). The final products of this mechanism should be close binary systems with comparable masses, mainly located in the inner core of the cluster.

How large? How big? How hot?

The most fundamental parameters of a star are perhaps its mass and its size. However these parameters remain loosely constrained for a large number of early-type stars. The most accurate way to measure the mass and size of a star is the study of double eclipsing binary systems. These systems are unfortunately rather rare and, so far, only a few dozens have their orbital and physical parameters accurately determined (Gies 2003).

Beyond direct measurements, one can probe the parameters of massive stars via the use of stellar atmosphere models fitted to observed spectra. An alternative method consists in comparing the position of the star in the H-R diagram with predictions of evolutionary tracks. One long-standing problem however has been the so-called *mass discrepancy* (Herrero et al. 1992), i.e. the systematic discrepancy between the masses of early-type stars derived using either atmospheric codes or evolutionary models. The latter ones predicted masses systematically lower than the former ones. However recent works (Herrero et al. 2002; Crowther et al. 2002; Martins et al. 2002), that combine slightly lower temperatures for evolutionary models and a proper handling of the line blanketing using non-LTE spherically symmetric atmosphere codes, clearly improved the situation.

Very recently, Martins et al. (2005) published a fully revised temperature calibration for Galactic O stars of different luminosity classes. From their work, both categories of models give now very similar results, that differ only by a few % at maximum, while the agreement is often much better. While the *mass discrepancy* problem has not been relegated to astronomical history textbooks yet, significant improvements have been achieved in the last few years. One can now probably consider that, at least in its major lines, the *mass discrepancy* is mostly solved.

Powerful stellar winds?

Solar-type stars have a high temperature corona ($T \sim 10^6$ K) in which the high-gas pressure drives a net outflow of matter known as the stellar wind. High mass stars however do not possess the strong convective zone needed to heat a circumstellar corona. The thermal or *pressure-driven* mechanism is thus inefficient for driving a stellar wind. The stellar luminosity however scales with the fourth power of its effective temperature and high-mass stars thus display an enormous amount of radiative flux. It is their large luminosity, that, through line-scattering, is thought to be the main driving mechanism of the tremendous hot star winds.

Beyond the resonant nature of the line-scattering, which indeed increases by several orders of magnitude the matter-photon interaction cross-section compared to free-electron

scattering, the success of the line-driven winds comes from the Doppler effect. Indeed in a static envelope, the relatively rapid *saturation* of the lines will keep the overall line force quite small with respect to gravity. In the outward expanding region of the atmosphere, the Doppler effect however shifts the local-resonance. As a consequence, the atoms have now the opportunity to scatter photons at a slightly higher frequency, which in turn will increase the atom velocity allowing further *deshadowing* of the line.

Because the thermal sound speed of the gas, whatever the position in the wind, is much smaller than the outflow velocity, the spatial extent over which a photon of a given frequency can interact with a Doppler-shifted line is rather limited. This was first noted by Sobolev (1960) who proposed to consider the line-scattering region as infinitely narrow. This so-called *Sobolev approximation* implies that the line-scattering process can be described in terms of local conditions whatever the radius at which it happens. It further allows an analytical expression of the line force. Based on this approximation, Castor et al. (1975, CAK hereafter) developed a convenient formalism to handle radiatively-driven winds. It is based on the main assumptions that the (Doppler-shifted) scattering lines remain almost independent and that the line strengths follow a power-law distribution so that the cumulative line-force scales with a power of the local velocity gradient over density. The CAK formalism predicts a wind velocity law in the form

$$v(r) = v_\infty \left(1 - \frac{R_\star}{r}\right)^\beta$$

with $\beta = 0.5$. In the above equation, v_∞ is the terminal wind velocity, $R_\star$ is the stellar radius and r is the distance to the star centre. A more proper (numerical) handling of different approximations (corrections for finite-disk, radial ionisation balance, finite sound-speed) yields $\beta = 0.8 - 1.0$. Let us also mention that one of the major success of the CAK theory was to provide a theoretical framework to the observed *Wind-Momentum-Luminosity* relation.

We finally note that the line-driven mechanism is intrinsically unstable. In particular the Line-Deshadowing Instability (LDI) grows from a perturbation of the Doppler shift and causes the perturbed line force to increase proportionally to the perturbed velocity. Though the details of the process are beyond this brief overview, one can note that the LDI is expected to induce the strong shocks that are thought to be at the origin of the soft X-ray emission from O-type stars. We refer to the detailed book of Lamers & Cassinelli (1999) *"Introduction to Stellar Winds"* for a didactic review of the line-driven winds (see also the more recent summary by Owocki 2004).

What about two stellar winds in a binary system ?

In a binary system, the winds from the two massive stars are expected to collide, giving rise to a so-called *wind interaction region* (WIR), a density enhanced zone in which the shock material is heated to temperatures of about 10^7 K, thus yielding a significant thermal X-ray emission. For a solar-metallicity wind, an estimate of the post-shock temperature can be deduced from the strong shock limit of the Rankine-Hugoniot relations (e.g. Stevens et al. 1992):

$$T \approx 1.4 \times 10^7 \; v_{8,\perp}^2 \; \mathrm{K}$$

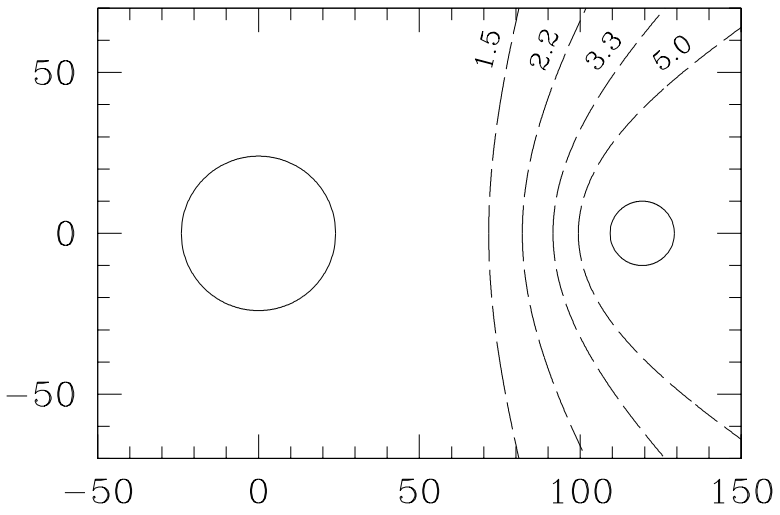

Figure 1: Position of the ram pressure equilibrium surface (dashed lines) computed for different values of the wind momentum ratio $\mathcal{R} = 1.5$, 2.2, 3.3 and 5.0. Axes are labelled in $R_\odot$units (sketch taken from Sana & Rauw 2003).

where $v_{8,\perp} = v_\perp/(10^8$ cm s$^{-1})$ and $v_\perp$ is the wind velocity component perpendicular to the interaction. Alternatively this can be expressed as

$$kT \approx 1.2\ v_{8,\perp}^2 \text{ keV}$$

This shows that, at typical terminal velocities of 2000 km s^{-1}, the gas is heated up to about 5 to 6×10^7 K, yielding a thermal X-ray emission with a typical energy of about 4 to 5 keV.

Initially proposed by Cherepashchuk (1976) and Prilutsky & Usov (1976), the theory of wind-wind collisions was brought to firmer grounds by Luo et al. (1990), Usov (1992) and Stevens et al. (1992). The WIR is delimited by two curved surfaces where the winds actually collide. Its location and shape mostly follow those of the ram pressure equilibrium surface. The latter is defined by the equation:

$$\rho_1\ v_{\perp,1}^2 = \rho_2\ v_{\perp,2}^2$$

where ρ_i is the density of the material that enters the shock and $v_{\perp,i}$ is the wind flow velocity component perpendicular to the surface. ρ_i can be obtained via the continuity equation for a spherically symmetric wind:

$$\rho_i = \frac{\dot{M}_i}{4\pi d_i^2 v_i}$$

where d_i is the distance from the star centre. One often defines the on-axis wind momentum ratio

$$\mathcal{R} = \sqrt{\frac{\dot{M}_1 v_{\infty,1}}{\dot{M}_2 v_{\infty,2}}} = \frac{d_1}{d_2}$$

with $v_{\infty,i}$ the terminal wind velocities, as the main parameter that governs the position and shape of the ram pressure equilibrium surface (see e.g. Fig. 1). Though this is true in first approximation, one has to account for the wind acceleration if the interaction occurs

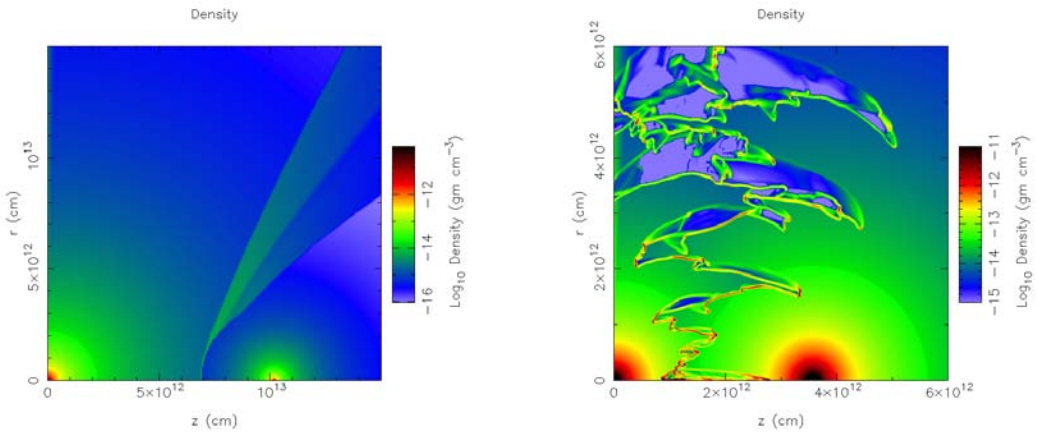

Figure 2: Density maps resulting from 2-D hydrodynamical simulations of the WIR in HD 93403 (left) and HD 152248 (right), carried out with the VH-1 hydrodynamical code (Stevens et al. 1992). These cartoons were adapted to reproduce the physical constraints of the two binary systems HD 93403 (O5.5I + O7V, P=15.09 d, Rauw et al. 2000, 2002) and HD 152248 (O7III + O7.5III, P=5.816 d, see Chap. 3).

within the wind acceleration zone. However $\mathcal{R}$ remains a good estimator of the relative wind strengths. As illustrated by Fig. 1, the WIR will wrap around the star that displays the weaker wind.

Not only the geometrical properties of the interaction region depend on the pre-shock velocities of the wind flow and on the amount of matter that enters the collision, but its cooling properties also do so. Stevens et al. (1992) defined the cooling parameter χ as the ratio of the typical cooling time over the escape time:

$$\chi = \frac{t_{\rm cool}}{t_{\rm esc}} = \frac{d_{12} v_8^4}{\dot{M}_{-7}}$$

where d_{12} is the distance from the star (in units 10^{12} cm), v_8^4 is the pre-shock velocity (in units 10^8 cm s^{-1}) and $\dot{M}_{-7}$ is the mass loss (in units 10^{-7} M$_\odot$ yr^{-1}). For $\chi < 1$, the WIR can be considered as radiative and, for $\chi > 1$, it displays a more adiabatic character.

While the mass-loss rate of a star can, at first order, be considered as mostly constant, the distance to the WIR may be varying along the orbit in an eccentric system. In close binaries, the shock often arises in the wind acceleration zone, thus well before the wind has reached its terminal velocity. This tends to reduce the shock strength, which yields a more radiative WIR.

Finally, the velocity law can also be altered because of the presence of the companion's radiation field. Stevens & Pollock (1994) investigated the effect of the radiation pressure of both stars on the material moving in-between them (*radiative inhibition*). They found that the presence of a luminous companion tends to reduce or inhibit the wind acceleration compared to an isolated star. In consequence the pre-shock wind velocity will be reduced. The shock is thus weaker, resulting in a fainter X-ray emission from the WIR.

In systems displaying two winds largely off balance, the stronger wind can be suddenly decelerated (*radiative braking*, Gayley et al. 1997) by the radiation field of the companion

as it approaches too close to the companion's surface. This can further alter the geometry and properties of the shock as well as its strength. While both phenomena have the same origin (i.e. the radiation pressure of a companion), they are significantly different. As the *radiative inhibition* only results in a flatter velocity law, the shock will still occur between two *a priori* supersonic winds. *Radiative braking* however actually decelerates the stronger wind and brings it to a stop, so that the weaker wind can expand further. The position of the interaction region therefore not only results from the ram pressure equilibrium equation but is also governed by the location at which the braking occurs.

As illustrated by Fig. 2, different system parameters might thus result in the formation of WIRs displaying rather different behaviours. As a consequence, it is important to investigate as wide a parameter space as possible, both observationally and using a theoretical approach.

Again it is not our purpose here to review the formalism of wind-wind collisions. An analytical approach is given by Usov (1992) for WR+O binaries but can easily be extended to O+O systems assuming a different chemical composition. In close binaries one has also to consider two accelerating winds. This makes the analytical treatment a bit more tedious but still accessible. Finally, beside the purely theoretical and observational views, numerical simulations have brought a third, complementary approach of the phenomenon. In the last years, one can mention, among other works, the contributions of Pittard & Stevens (1997) and more recently of Walder & Folini (2003).

The present dissertation

The present study is focused on NGC 6231, a young open cluster located at about 1.6 kpc and regarded as the core of the Sco OB 1 association. NGC 6231 is one of the richest open clusters of the Galaxy in terms of its early-type star content. It indeed offers a sample of about 15 O-type objects ranging from the late type O9.7 to O5.5/O6 and belonging to different luminosity classes. NGC 6231 has also been reported as one of the few clusters displaying an extremely large binary fraction ($\sim 80\,\%$, García & Mermilliod 2001). A detailed study of this rare sample was thus expected to enforce our understanding of the early-type stars in the Galaxy. A detailed review of the existing literature on NGC 6231 and on the Sco OB 1 association is given in the first pages of Chap. 2. We will henceforth not go into more details here and invite the reader to proceed to the corresponding pages.

The approach adopted in this work is definitively observational and aims at constraining the properties of the massive star population of the cluster. For this purpose, we will rely on a large set of data collected in the optical and X-ray domains (Chap. 1). The bulk of the optical observations is formed by high-resolution high signal-to-noise ratio spectra that allow, thanks to the photospheric lines, to probe the nature of the studied objects, their multiplicity, their physical and, possibly, their orbital properties. The X-ray data were collected with the European X-ray observatory XMM-*Newton* that was launched into space in December 1999. The data obtained are of an unprecedented quality and will allow to investigate the X-ray properties of this cluster, which offers a homogeneous sample of O-type stars in terms of age, distance, chemical composition and environment.

In parallel to the characterization of the orbital and X-ray properties of the O-type star population in NGC 6231, we will also search for the signature of ongoing wind interactions

in the binary systems of the cluster. Again the two data sets are complementary as evidences for this phenomenon can be found by studying the line profile variations of selected emission lines in the optical spectrum of the targets. The wind interaction phenomenon can also manifest itself through a modulation of the X-ray flux or by changing X-ray spectral properties. Even when no sign of the interaction is found from the optical, the latter data are of the utmost importance to constrain the orbital properties and provide the accurate ephemerides needed to correctly interpret the X-ray data, or to disentangle the phase-locked variations of some of the optical line profiles. To better investigate the nature of the wind interaction, we will also make use of hydrodynamic simulations as well as of a more phenomenological approach. This will allow a third, complementary, approach toward our understanding of this fascinating phenomenon.

This work is organised as follows. Chap. 1 presents an overview of the collected observational material on which this work relies. In Chap. 2, we investigate the X-ray properties of the NGC 6231 cluster and of its surroundings. In Chap. 3, we analyse two early-type binaries that both display a prominent wind-interaction, though of a different kind each. The properties of five other SB2 binaries are studied in Chap. 4. Chap. 5 focuses on the optical spectroscopy of the remaining early-type X-ray emitters in the XMM-*Newton* field of view. Finally, the last chapter (Chap. 6) presents a brief discussion of the distribution of the orbital and physical parameters of the present sample of stars. We conclude this dissertation by providing a summary of our work.

A large fraction of this dissertation (Chaps. 2 to 4) is presented in the form of a series of papers published in or recently submitted to the Astronomy & Astrophysics journal (A&A) or in the Monthly Notices of the Royal Astronomical Society (MNRAS). These three chapters all have the same structure. We first provide a brief introduction to the topics and briefly summarize the main results achieved. The related papers are then presented in the form under which they have been published or submitted. For papers recently submitted, we have chosen to keep the usual journal presentation for convenience. Their current status is clearly indicated in the introduction of each chapter. A list of the different publications related to this work is also given in Appendix C.

Chapter 1

The observational material

Telescope: instrument invented by the stars to look at our eye.
Hervé Basin

As an observational multiwavelength study, this work relies on a large set of data obtained during a series of observing campaigns spread over the last few years. Using different ground-based and spaceborne facilities, each of these campaigns clearly forms one of the pieces of a common puzzle: NGC 6231. The aim of the present chapter is to provide an overview of this observational material, highlighting the kind of information obtained. In addition, we briefly present the data reduction processes. Specific sub-sets of observations are thoroughly described in the "Observations and Data Reduction" sections of the different papers included in this work. In this chapter, we successively address the optical spectroscopic (Sect. 1.1) and photometric (Sect. 1.2) campaigns and the XMM-*Newton* observations (Sect. 1.3). Table 1.1 gives an overview of the NGC 6231 observations carried out for about 10 years. It also indicates the different persons, members of the Groupe d'AstroPhysique des Hautes Energies (GAPHE) in Liège, who have brought their contributions to this large observing program.

1.1 Optical spectroscopy

Since 1996, the GAPHE members carried out an extensive optical spectroscopic campaign towards NGC 6231. Performed mainly at the European Southern Observatory (ESO) at La Silla (Chile), the 14 observing runs described in Table 1.1 allowed to collect more than 400 optical spectra of 30 early-type stars of the cluster. The different objects did clearly not receive the same attention. Throughout the years, we mainly focused on the bright O-type stars and, particularly, on the known and probable massive binaries. As indicated by Table 1.1, the bulk of this spectroscopic data set comes from the FEROS instrument (Sect. 1.1.4), regularly used since 1999. The number of objects observed in the first years is very limited. With the move of the FEROS instrument to the ESO 2.2m telescope in October 2002, fainter objects became accessible and, in May 2004, we obtained snapshot spectra of selected members of the cluster for the purpose of spectral classification. Tables 1.2 and 1.3 provide a summary of the observation logs for the different spectroscopic runs since 1996. The detailed journal of the observations for specific objects can be found in the different devoted sections of the present work.

Table 1.1: List of the observational campaigns towards the young open cluster NGC 6231. The first two columns report the observational facility and the third column provides the observing dates. Cols. 4 to 7 list the programme ID, the Principal Investigator (PI) of the project and the persons who carried out the observations (Obs.) and handled the raw data (D.H.). Col. 8 indicates, for spectroscopic campaigns, the number of objects observed while, for the optical photometric and X-ray campaigns, it provides the size of the field of view. The number of exposures (images or spectra) obtained is given in Col. 9. Finally, the last column (Col. 10) lists the observed wavelength/energy domain.

Instr. [1]	Tel. [2]	Date [3]	ID [4]	PI[a] [5]	Obs.[a] [6]	D.H.[a] [7]	# Obj. [8]	# Exp. [9]	Domain [10]
				Optical spectroscopy					
B&C	ESO 1.5m	01/05–08/05/1996	057.D-0204	GR	GR	GR	1	11	$\lambda\lambda$3790-4765
B&C	ESO 1.5m	26/03–01/04/1997	058.D-0232	GR	GR	GR	1	6	$\lambda\lambda$3790-4765
CES	ESO CAT	23/03–29/03/1997	058.D-0329	EG	EG	EG	1	6	$\lambda\lambda$4450-4490
							1	4	$\lambda\lambda$4665-4705
CES	ESO CAT	19/06–27/06/1997	059.D-0145	GR	GR	GR/HS	2	10	$\lambda\lambda$4450-4490
							1	5	$\lambda\lambda$4610-4670
							2	12	$\lambda\lambda$4665-4705
CES	ESO CAT	29/06–06/07/1998	061.D-0502	GR	GR	HS	6	25	$\lambda\lambda$4460-4480
							1	6	$\lambda\lambda$4675-4695
FEROS	ESO 1.5m	30/04–05/05/1999	063.H-0061(A)	GR	GR	HS	9	39	$\lambda\lambda$3720-9200
FEROS	ESO 1.5m	23/05–29/05/1999	063.H-0093(A)	JMV	EG	HS	9	16	$\lambda\lambda$3720-9200
BME	CTIO 1.5m	29/05–03/06/1999	1999A.N0066	JMV	GR/EG	YN/JM	5	21	$\lambda\lambda$3850-5790
FEROS	ESO 1.5m	03/05–09/05/2000	065.H-0265(A)	JMV	HS	HS	11	52	$\lambda\lambda$3720-9200
FEROS	ESO 1.5m	06/05–12/05/2001	067.D-0059(A)	EG	HS	HS	9	26	$\lambda\lambda$3720-9200
FEROS	ESO 1.5m	01/03–06/03/2002	068.D-0095(A)	GR	HS	HS	9	30	$\lambda\lambda$3720-9200
FEROS	ESO 1.5m	16/04–19/04/2002	069.D-0381(A)	EG	EG	HS	10	23	$\lambda\lambda$3720-9200
FEROS	ESO 2.2m	20/05–25/05/2003	071.D-0369(A)	HS	HS	HS	7	24	$\lambda\lambda$3720-9200
FEROS	ESO 2.2m	04/05–10/05/2004	073.D-0609(A)	HS	HS	HS	28	109	$\lambda\lambda$3720-9200
				Optical photometry					
DLR-Cam.	Bochum 0.6m	22/03–19/04/1997	—	EG	PR/GR/JM	JM/EG	$3.2' \times 4.8'$	112	λ4686
								138	λ6051
				X-ray observations					
EPIC	XMM-*Newton*	05/09–10/09/2001	010949	JMV	—	HS	$\varnothing = 30'$	6×3	0.2-12.0 keV

a. EG: E. Gosset; JM: J. Manfroid; YN: Y. Nazé; GR: G. Rauw; PR: P. Royer; HS: H. Sana; JMV: J.-M. Vreux

Table 1.2: List of the NGC 6231 objects observed with the B&C, CES and BME instruments. The first column indicates the target name while the number of spectra obtained during the different observing runs are given in Cols. 2 to 7.

Instr.	B&C		CES	CES	CES	BME
Date	1996	1997	03/1997	05/1997	1998	1999
Domain			λ4471/λ4686	λ4471/λ4641/λ4686	λ4471/λ4686	
HD 152218	–	–	– / –	5 / – / 6	– / –	3
HD 152219	–	–	– / –	– / – / –	6 / –	–
HD 152233	–	–	– / –	– / – / –	– / –	3
HD 152234	–	–	– / –	– / – / –	– / –	5
HD 152248	11	6	6 / 4	5 / 5 / 6	1 / 6	5
HD 152249	–	–	– / –	– / – / –	– / –	5
HD 326331	–	–	– / –	– / – / –	5 / –	–
CPD −41°7733	–	–	– / –	– / – / –	5 / –	–
CPD −41°7735	–	–	– / –	– / – / –	2 / –	–
CPD −41°7742	–	–	– / –	– / – / –	6 / –	–

1.1.1 Boller & Chivens (B&C)

During two runs in May 1996 and March 1997, a set of medium resolution spectra of the colliding wind binary HD 152248 was obtained with the Boller & Chivens spectrograph (B&C) at the ESO 1.5m telescope. The detector was a 2k × 2k UV flooded Loral-Lesser CCD. The pixel size was 15 × 15μm. We used the holographic grating (ESO grating #32) with 2400 lines/mm, providing a spectral resolution of 1.2Å as measured from the FWHM of the lines of the HeAr comparison spectrum. The covered spectral range extends from λ3790 to λ4765Å.

The B&C observations were reduced in a standard way using the MIDAS package provided by ESO. The spectra were normalized by fitting a low order polynomial to the continuum.

1.1.2 Coudé Echelle Spectrograph (CES)

In 1997 and 1998, spectra of the brightest cluster members were acquired over different wavelength domains at the ESO 1.4m Coudé Auxiliary Telescope (CAT), using the Coudé Echelle Spectrograph (CES) equipped with the Long Camera (LC, before March 1998) or the Very Long Camera (VLC, after March 1998). The detector used was ESO CCD#38, a Loral 2688 × 512 pixel CCD with a pixel size of 15μm × 15μm. The slit width was chosen to achieve a nominal resolving power of 70 000–80 000. The effective resolving power as derived from the $FWHM$ of the lines of the ThAr calibration exposures is actually 65 000–75 000. Typical exposure times range from 20 to 40 min and the average S/N ratio is about 100. The wavelength domains observed are centered on the He I λ4471, N III λ4641 or He II λ4686 lines and they are $\sim$ 40 Å and $\sim$ 20 Å wide for spectra taken with the LC and the VLC respectively.

The CES observations were reduced in a standard way using the MIDAS package provided by ESO. The 2-D raw spectra were de-biased, flat-fielded and extracted to provide uni-dimensional spectra. Whenever possible, these were then rectified by means of an instrumental response curve built from the observations, obtained under similar conditions,

Table 1.3: List of the NGC 6231 objects observed with the FEROS instrument since 1999. The first column indicates the target name while the number of spectra obtained during the different observing runs are given in Cols. 2 to 7.

Object	1999	2000	2001	2002	2003	2004
HD 152076	– / –	–	–	– / –	–	1
HD 152200	1 / –	–	–	5 / 1	3	6
HD 152218	5 / 2	7	4	– / 3	3	5
HD 152219	5 / 2	7	5	6 / 5	–	12
HD 152233	– / 2	4	2	2 / 3	6	12
HD 152234	– / 2	5	2	2 / 1	5	6
HD 152235	– / –	–	–	– / –	–	6
HD 152247	– / 2	1	1	2 / 1	3	6
HD 152248	5 / 2	6	–	– / –	–	–
HD 152249	4 / 2	5	2	4 / 1	2	9
HD 152314	– / –	1	1	2 / –	2	10
HD 152437	– / –	–	–	– / –	–	1
HD 326320	– / –	–	–	– / –	–	2
HD 326329	– / –	2	–	– / –	–	6
HD 326331	5 / –	–	–	– / 2	–	6
HD 326343	– / –	–	–	– / –	–	1
CPD −41°7706	– / –	–	–	– / –	–	1
CPD −41°7712	– / –	–	–	– / –	–	1
CPD −41°7721p	– / –	–	–	– / –	–	1
CPD −41°7721s	– / –	–	–	– / –	–	1
CPD −41°7733	5 / 1	5	3	5 / 3	–	7
CPD −41°7737	– / –	–	–	– / –	–	2
CPD −41°7742	5 / 1	9	6	2 / 3	–	–
CPD −41°7744B	4 / –	–	–	– / –	–	1
CPD −41°7753	– / –	–	–	– / –	–	1
CPD −41°7755	– / –	–	–	– / –	–	1
CPD −41°7760A	– / –	–	–	– / –	–	1
CPD −41°7760B	– / –	–	–	– / –	–	1
Se 209	– / –	–	–	– / –	–	1
Se 259	– / –	–	–	– / –	–	1

of a metal-poor 'reference' star (HD 203608: F6V). Finally, the spectra were normalized by fitting a low order polynomial (a straight line or a parabola) to the continuum. When such a spectrum was not available the spectra were normalized by directly fitting a polynomial to the continuum of the science targets.

1.1.3 Bench-Mounted Echelle spectrograph (BME)

During a 5 night run in June 1999, another set of echelle spectra of five of the brightest cluster members was obtained with the Bench-Mounted Echelle Spectrograph (BME) attached to the CTIO 1.5 m Ritchey-Chrétien Telescope. Forty nine orders, covering the range $\lambda\lambda$3850–5790 Å, were observed using the KPGL2 316 lines mm^{-1} grating as a cross-disperser. The detector was a Tek 2048 CCD with 24 μm pixels. The slit width was set to 70 μm corresponding to a resolving power of 45 000. Exposure times were of the order of 45 minutes and the average S/N ratio in the continuum was about 100.

The BME data were reduced using the IRAF[1] package and following the recommendations of the BME User's Manual. The pixel to pixel variations were removed using flat field exposures taken with a very bright light source and a diffusing screen placed inside the spectrograph (so-called *milky flats*). A first rectifying of the extracted echelle orders was carried out with the projector flat exposures. The spectra were then normalized by fitting a low-order polynomial to the continuum of the targets.

1.1.4 Fiber-fed Extended Range Optical Spectrograph (FEROS)

During eight observing runs carried out since 1999, an extensive set of echelle spectra was taken with the Fiber-fed Extended Range Optical Spectrograph (FEROS) fed by the ESO 1.5 m or 2.2 m telescope at La Silla. Thirty-nine orders corresponding to a wavelength domain from about 3600 to 9200 Å were observed. The first three orders in the blue suffer from an important lack of signal, so that the blaze functions can usually not be defined. The effectively observed wavelength domain is thus 3750-9200 Å. The spectral resolving power of the FEROS instrument is 48 000. The detector used was an EEV CCD with 2048 $\times$ 4096 pixels of 15 $\times$ 15 μm. Exposure times ranged from a couple of minutes to 50 minutes according to the magnitude of the targets. The improving performances of the instrument and the variable weather conditions led to a wide spread in the obtained S/N ratios. However, thanks to the high efficiency of the instrument ($> 20\%$), the large majority of the obtained spectra have a S/N ratio above 150, while the average S/N ratio is probably around 200. With 319 high-resolution, high-quality spectra covering the whole optical domain, the FEROS spectrograph clearly provides the core of the present spectroscopic data set.

FEROS data were reduced using the FEROS context working under the MIDAS environment. With the experience acquired through the different observing runs, we found that the standard pipe-line reduction failed to provide satisfactory results (Hensberge 2002). With the help of Dr. H. Hensberge from the Royal Observatory of Belgium (Brussels), we locally implemented an improved reduction pipe-line that allows for a more accurate wavelength calibration, for a better correction for the diffuse background light and hence for an

[1] IRAF is distributed by the National Optical Astronomy Observatories.

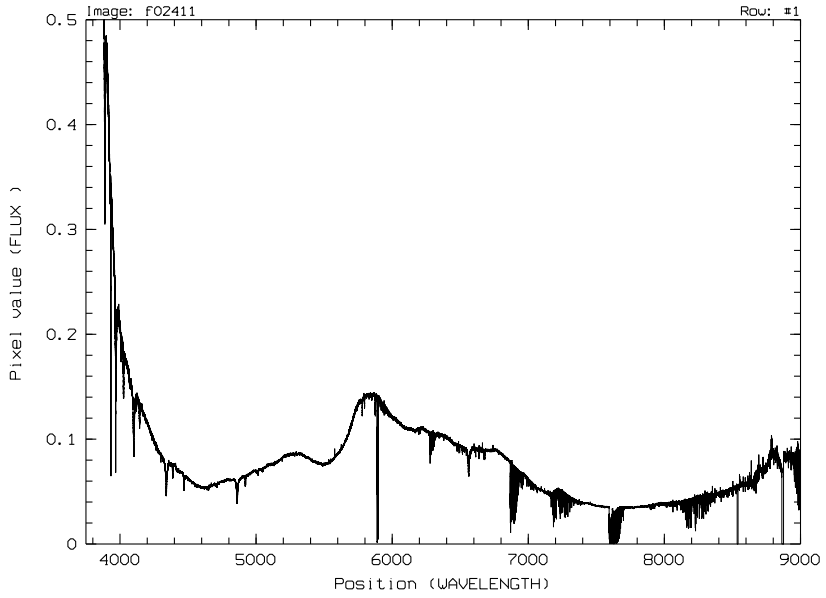

Figure 1.1: Raw 1-D FEROS spectrum of CPD −41°7744B obtained in May 2004. This figure illustrates the global shape of the response curve of the FEROS spectrograph.

improved determination of the blaze functions. In the earlier years of the campaign (until 2002), the latter displayed significant 'oscillations' due to the flat-field calibration lamps when extracted with the standard reduction pipe-line. These oscillations, not present in the stellar spectra, were therefore a major source of uncertainty in the determination of the continuum.

Within a night, slight sub-pixels variations in the positions of the different orders on the CCD also induced a modification of the effective response curve of the instrument with time. Finally, artefacts due to the merging of the echelle orders of the FEROS data are known to appear in a number of order reconnections. This problem, added to the complexity of the global shape of the spectrograph response curve (Fig. 1.1), renders the normalization step a non-trivial process. We usually adjusted polynomials over limited wavelength domains of the spectrum (either single orders or extracted regions from the merged spectrum) and we used the resulting empirical curve to normalize the considered region of the spectrum to the continuum.

1.2 Optical photometry

During a 'famous' one-month run at La Silla in 1997 (see description by Royer 2001, App. C), the core of NGC 6231 was intensively monitored through two narrow band filters (see below). The first aim of the campaign was to derive an accurate light curve of the eclipsing binary HD 152248 (chap. 3). Unfortunately, Mayer et al. (2001) published equivalent results prior to the completion of our analysis. In this work we thus mainly focus on the photometric observations of the late O-type system CPD −41°7742, another eclipsing binary in the cluster core that fell into the FOV of the CCD camera. The short period of

the system ($P \sim 2.4$ d) was intensively covered during the campaign and, thanks to the combined analysis of the spectroscopic and photometric data, we obtained the first measurements of the absolute parameters of the system (see Chap. 3). As a by-product, the present set of observations allow us to constrain the (non) variability of the other objects located in the central part of the cluster.

Between 1997 March 22 and April 19, we observed the core of the open cluster NGC 6231 with the 0.6-m Bochum telescope at La Silla, Chile. The Cassegrain focus of the telescope was equipped with a direct camera and a Thomson 7882 charge-coupled device (CCD) detector (384 × 576 pixels) subtending a full field of view of 3.2 by 4.8 arcmin. The photometric observations have been performed through two narrow band filters designed for the characterization of Wolf-Rayet stars: one called λ4686 covering the region of the He II line usually present in massive stars (centre: 4684 Å, FWHM: 30 Å) and another one labelled λ6051 addressing a region of the continuum free from strong lines in the spectra of WR stars (centre: 6051 Å, FWHM: 28 Å). More information on these filters can be found in Royer et al. (1998). The typical exposure times were 60s for both filters. Some 112 (resp. 138) useful frames were obtained with the λ4686 (resp. λ6051) filter.

All reductions were carried out with the National Optical Astronomy Observatories (NOAO) IRAF package. The debiased, flat-fielded frames were analyzed with the DAOPHOT software (Stetson 1987), using aperture radii between 2 and 5.5 arcsec. 'Absolute' photometry was obtained from the large aperture data, using a multi-night, multi-filter algorithm and a few standard stars (Manfroid 1993). This procedure yielded additional reference stars for each field. These secondary standards together with all non-variable stars were used to fix, through a global minimization procedure, the zero points for the individual frames and for each aperture radius, thus performing some kind of global differential photometry. Typically, the expected error on an 8th mag star corresponds to $\sigma = 0.007$ mag in differential photometry.

1.3 The XMM-*Newton* observing campaign

The X-ray observational campaign towards NGC 6231 was designed in the framework of the XMM-*Newton* guaranteed time of observation of the XMM-OM consortium. For a total duration of $\sim$ 180 ksec, six separate pointings of 30 ksec each were spread over five consecutive days. The observing plan aimed at covering the 5.8 d period of the colliding wind binary HD 152248 in order to monitor the expected phase-locked behaviour of its emission. As a direct consequence, the adopted schedule also allowed to study the phase-locked behaviour of the four other massive binaries with periods shorter than 6 days. The combination of the six exposures and of the three EPIC cameras provides the deepest X-ray view towards NGC 6231 so far. According to their brightness in the X-ray domain, the present data set further allows to probe the characteristics of the detected sources on typical time-scales ranging from a couple of minutes to several days.

In September 2001, the XMM-*Newton* satellite successfully performed the six observations within satellite revolutions 319 to 321. Two of the six data sets were unfortunately affected by soft proton flares which effectively reduced the observing time by about one third. Table 1.4 gives the journal of the X-ray campaign dedicated to the NGC 6231 cluster. The field of view was systematically centered on HD 152248 ($\alpha_{2000} = 16^{\rm h}54^{\rm m}10\overset{\rm s}{.}06$, $\delta_{2000} = -41°49'30\overset{''}{.}1$) in the core of the cluster. All three EPIC instruments were operated in the Full Frame mode together with the THICK filter to reject optical light. The

Table 1.4: Journal of the XMM-*Newton* observations of NGC 6231. Columns 2 and 3 give the spacecraft revolution number and the observation ID. The Julian Date (JD) at mid-exposure is reported in Col. 4. Cols. 5 to 7 (resp. Cols. 8 to 10) list the performed (resp. effective) exposure times (in ksec) for the EPIC MOS1, MOS2 and pn instruments. The total campaign duration is given in the last line of the table.

Obs.	Sat.	Exposure	Mean JD	Performed duration			Effective duration		
#	Rev.	ID	(−2 450 000)	MOS1	MOS2	pn	MOS1	MOS2	pn
1	319	0109490101	2158.214	33.3	33.3	30.7	33.1	33.2	30.6
2	319	0109490201	2158.931	22.1	22.1	20.2	19.8	19.8	16.5
3	320	0109490301	2159.796	34.4	34.4	31.8	33.7	33.9	30.1
4	320	0109490401	2160.925	31.4	31.4	29.1	26.0	24.3	11.7
5	321	0109490501	2161.774	31.1	31.1	28.5	30.9	31.0	28.4
6	321	0109490601	2162.726	32.9	32.9	30.3	32.9	32.8	30.3
Total duration (ksec)				185.2	185.2	170.6	176.5	175.0	147.5

RGS spectrographs were run in the Standard Spectroscopic mode. Due to the brightness of the NGC 6231 objects in the field of view (FOV), the Optical Monitor was switched off throughout the campaign.

The EPIC Observation Data Files (ODFs) were processed using the XMM-Science Analysis System (SAS) implemented on our computers in Liège. Since 2001, the raw data have been re-processed with different SAS versions in order to take advantage of the (sometimes crucial) improvements brought to the software along the time. The general philosophy of the reduction process remained however constant and is thoroughly described in Chaps. 2 and 3. In brief, we applied the *emproc* and *epproc* pipeline chains respectively to the MOS and pn raw data to generate proper event list files. No indication of pile-up was found in the data. We then only considered events with appropriate patterns and we applied the filtering criteria recommended by the Science Operation Centre (SOC). For each pointing, we rejected periods affected by soft proton flares. At energies above $\sim$ 10 keV, the integrated signal from the cameras is dominated by the background noise. We thus built light curves using only the events for which $PI > 10\,000$ (1PI $\approx$ 1 eV) and we discarded high background observing periods on the basis of an empirically derived threshold. The so-defined GTIs (Good Time Intervals) were finally used to produce adequate X-ray event lists from which we extracted the images and spectra that will be presented and analysed in the following chapters of this work.

Chapter 2

An X-ray view of the young open cluster NGC 6231

Tonight, looking at the sky, I came to the conclusion that there were many more stars than what we need.
Quino

The launch in 1999 of the two large X-ray observatories XMM-*Newton* and *Chandra*, that combine increased sensitivity and high angular and spectral resolution, has profoundly modified our view and understanding of the X-ray universe. In particular, it has provided unprecedented views of young open clusters and of their stellar content.

The present chapter is devoted to the X-ray observation campaign (Sect. 1.3) performed towards the young open cluster NGC 6231. It is organised along a series of papers (Sana et al. 2005c,g,h, hereafter Papers I to III) included in the following pages. Paper I (p. 23) presents the catalogue of the X-ray emitters in the XMM-*Newton* field of view (FOV) while Paper II (p. 43) and Paper III (p. 67) respectively investigate the properties of the early-type star population and of the optically faint X-ray sources. A review of recent X-ray observations of young open cluster is given in Paper I together with a summary of about 50 years of literature on the Sco OB 1 association and on NGC 6231. The remainder of this introduction briefly presents our new X-ray view of the young open cluster NGC 6231.

- **Paper I. The catalogue** (p. 23, accepted)

  This first paper of the series focuses on the source detection and identification and investigates the general distribution of the X-ray emitters. 610 X-ray sources are found in the XMM-*Newton* FOV. These are mostly point-like sources that cluster at the core of the cluster. We investigate the sensitivity limits of the present campaign and we estimate that the contamination by foreground and background sources is probably about 5%. This strongly suggests that most of the detected X-ray emitters are physically linked to NGC 6231 or to the wider Sco OB 1 association. We show that the radial distribution of these sources, once corrected for the difference in sensitivity of the different detector regions, is well reproduced by a King profile with a core radius of $3\farcm1$. This value is similar to the core radius obtained for the bright and intermediate ($V > 17$mag) stars. Finally, we note that the X-ray images of the cluster are dominated by the soft emission from the massive stars, while the remaining sources are fainter but harder and have an energy distribution that peaks above 1 keV.

- **Paper II. The early-type star population** (p. 43, submitted)

  In this second paper, we make a census of the OB-type stars in the XMM-*Newton* FOV. All O-type stars and about one quarter of the B-type stars can be associated with an X-ray source. The X-ray properties of the O- and B-type objects present clear-cut differences and we separately investigate these two populations. The O-type emitters are characterized by a strong but soft X-ray emission. They draw up a linear relation in the $L_{\rm X}$ vs. $L_{\rm bol}$ plane that is best represented by a scaling law

  $$\log L_{\rm X} - \log L_{\rm bol} = -6.912 \pm 0.153$$

  However, the two binary systems HD 152248 and CPD $-41°7742$ show an X-ray emission significantly larger than expected from this *canonical* relation. Both systems indeed display a strong signature of a wind interaction in the X-ray domain. They have thus been excluded from the above fit and will be studied in more details in the next chapter (Chap. 3). The present dispersion around the *canonical* relation is significantly reduced compared to previous works. Our sample is made of singles and binaries belonging to different luminosity classes and suggests that the dispersion of the intrinsic X-ray emission from O-type stars around the *canonical* relation is rather limited. In a complementary approach, we revisit recent results from Albacete Colombo et al. (2003) obtained from XMM-*Newton* observations of the Carina nebula and we reach very similar conclusions as those obtained from the NGC 6231 data.

  Regarding the B-type stars, we found that the detected X-ray emission is most probably due to a pre-main sequence physical (in a binary) or visual (on the light of sight) companion. We however note a significant correlation between the X-ray emission and the B stars bolometric luminosities. The exact origin of this observational relation is still not understood.

  Table 2 and Figs. 2 to 6 have been proposed for electronic publication only. This *online material* is presented in Appendix B.

- **Paper III. Optically faint X-ray sources** (p. 67, in preparation)

  This third paper in the series probes the properties of the X-ray sources with an optically faint counterpart and investigates the formation history of the stars in NGC 6231. Their location in the H-R diagram, their flaring behaviour and their X-ray spectra indicate that these objects are most probably pre-main sequence stars. The age spread among these objects is about 10 Myr and suggests that the star formation in NGC 6231 could have started more than 12 Myr ago at a relatively slow rate. From our results, this rate has then increased to culminate about $3 - 4$ Myr ago, a time at which the O-type stars were also formed. The star formation epoch finally ended rather abruptly about 1 Myr ago. Although Paper III has not been submitted yet, we have chosen to keep the usual A&A presentation for convenience.

Astronomy & Astrophysics manuscript no. ngc6231˙Xcat˙v5 May 21, 2005
(DOI: will be inserted by hand later)

An XMM-*Newton* view of the young open cluster NGC 6231⋆

I. The catalogue ⋆⋆

H. Sana[1,⋆⋆⋆], E. Gosset[1,†], G. Rauw[1,†], H. Sung[2] and J.-M. Vreux[1]

[1] Institut d'Astrophysique et de Géophysique, University of Liège, Allée du 6 Août 17, Bât. B5c, B-4000 Liège, Belgium
e-mail: sana@astro.ulg.ac.be, gosset@astro.ulg.ac.be, rauw@astro.ulg.ac.be, vreux@astro.ulg.ac.be
[2] Department of Astronomy and Space Science, Sejong University, Kunja-dong 98, Kwangjin-gu, Seoul 143-747, Korea
e-mail: sungh@sejong.ac.kr

Received October 15, 2004; accepted March 16, 2999

Abstract. This paper is the first of a series dedicated to the X-ray properties of the young open cluster NGC 6231. Our data set relies on an XMM-*Newton* campaign of a nominal duration of 180 ksec and reveals that NGC 6231 is very rich in the X-ray domain too. Indeed, 610 X-ray sources are detected in the present field of view, centered on the cluster core. The limiting sensitivity of our data is approximately 6×10^{-15}erg cm^{-2} s^{-1} but clearly depends on the location in the field of view and on the source spectrum. Using different existing catalogues, over 85% of the X-ray sources could be associated with an optical/infrared counterpart within a limited cross-correlation radius of 3″. The surface density distribution of the X-ray sources present a slight N-S extension. Once corrected for the spatial variation of the EPIC instruments sensitivity, the radial profile of the source surface density is well described by a King profile with a central density of about 8 sources per arcmin^2 and a core radius close to 3.1 arcmin. The distribution of the X-ray sources seems closely related to the optical source distribution. The expected number of foreground and background sources should not represent more than 6% of the detected sources, thus strongly suggesting that most of the detected X-ray emitters are physically belonging to NGC 6231. Finally, beside a few bright but soft objects – corresponding to the early-type stars of the cluster – most of the sources are relatively faint ($\sim 5 \times 10^{-15}$ erg cm^{-2} s^{-1}) with an energy distribution peaked around 1.0-2.0 keV.

Key words. Open clusters and associations: individual: NGC 6231 – X-rays: individuals: NGC 6231 – X-rays: stars – Stars: early-type – Catalogues

1. Introduction

Detailed studies of young clusters are powerful tools to probe crucial astrophysical issues. Because they *a priori* contain both early-type stars and pre-main sequence (PMS) stars, young clusters are privileged laboratories to test star formation and evolution theories. They indeed provide a homogeneous sample of stars in terms of distance, reddening, environment, chemical composition and age. With the currently available X-ray observatories, unprecedented investigations of young open clusters in the X-ray domain have been performed in the past few years. The increased sensitivity, spectral power and resolution of the XMM-*Newton* and *Chandra* observatories, compared to X-ray satellites of the previous generations, give now a much more complete view of the X-ray properties of the star populations in clusters.

For example a 76 ksec *Chandra* observation of the embedded young cluster NGC 2024 ($d \sim 410$ kpc; age = 0.3 – a few Myr) revealed 283 X-ray sources displaying heavily absorbed hard spectra with a mean temperature $kT \sim 3$ keV (Skinner et al. 2003). A significant fraction (25%) of the X-ray sources shows a wide range of variability within the exposure duration. In addition, *Chandra* detected at least 96% of the known classical T-Tauri stars in NGC 2024. Results for other clusters are very similar. Rauw et al. (2003) performed a 20 ksec observation of NGC 6383 ($d \sim 1.4$ kpc; age = 1.7 – 5 Myr) and found 77 sources, mostly centered on the cluster location. An important fraction of these sources are probable PMS objects. Using both XMM-*Newton* and *Chandra* facilities, Preibisch & Zinnecker (2004, and references therein) studied the very young stellar cluster IC 348 ($d \sim 310$ pc; age ~ 2 Myr) and found 286 X-ray sources among which over 50 classical T

Send offprint requests to: H. Sana

⋆ Based on observations collected with XMM-*Newton*, an ESA science mission with instruments and contributions directly funded by ESA Member States and the USA (NASA).

⋆⋆ Tables 3 and 6 are available via the CDS web site: http://www.u-strasbg.fr

⋆⋆⋆ FNRS Research Fellow (Belgium)

† FNRS Research Associate (Belgium)

Tauri stars. Comparison of *Chandra*- and XMM-*Newton*- based spectral properties suggested that the X-ray characteristics of T Tauri stars remain mostly constant over periods of years. NGC 6530 ($d \sim 1.8$ kpc; age $\sim$ 1.5–2.0 Myr) is a very rich open cluster containing several massive O-type stars as well as a large population of B-type stars. XMM-*Newton* observations by Rauw et al. (2002) revealed 119 sources, of which a large fraction are PMS candidates. Similarly to Skinner et al. results, the X-ray spectra of the PMS candidates are characterized by temperatures of a few keV. Using a 60 ksec *Chandra* observation centered on the same cluster, Damiani et al. (2004) revealed 884 X-ray sources, among which 90 to 95% are PMS stars.

From this review of the recent literature, there is an obvious body of observations showing that, besides the expected X-ray emission from massive stars, a large population of X-ray emitting low-mass PMS stars is to be found while observing young clusters. The present study of the very rich cluster NGC 6231 lies in the described framework. It aims at a better comprehension of both early-type stars and young open clusters by extending the previous sample of investigations to clusters with a large O-type star population. A severe limitation of several of the above cited works is the lack of detail studies on the concerned cluster at other wavelengths. Indeed, with *Chandra* and XMM-*Newton*, the X-ray observations are so deep that a deep photometry of the stars in the field of view is required. Such a data set is indeed essential to, for example, more clearly identify the evolutionary status of the different sub-populations of the cluster. Fortunately, as shown by the literature review of Sect. 2, the stars in NGC 6231 have been thoroughly studied. Together with the deepth of the present X-ray campaign, this is one of the strengths of the current work. Finally, the present work distinguishes itself from the previous investigations because of the particular planning of the X-ray observations. Indeed our XMM-*Newton* campaign towards NGC 6231 was actually split into six successive pointings, spread over a period of five days. This will allow us to probe the variability of the X-ray emission of the detected sources on different time-scales.

A detailed analysis of the central target of the field, the colliding wind binary HD 152248, has been presented recently in a dedicated paper (Sana et al. 2004). The source will therefore not be discussed in more details in this paper. Preliminary results from this campaign, mainly related to the early-type X-ray emitters, were also presented in Sana et al. (2005b). In this paper, we focus on the X-ray catalogue and we discuss some general properties of the detected sources. Other aspects of the X-ray properties of NGC 6231, such as the early-type and the pre-main sequence population characteristics, will be addressed in subsequent papers of this series.

This first paper is organized as follows. After a review of the abundant literature on NGC 6231 and on the Sco OB 1 association, Sect. 3 describes the campaign and the subsequent data reduction processes. In Sect. 4, we address the detection and identification of the sources in the XMM-*Newton* field of view, and we present the resulting X-ray catalogues. Finally, we probe the main properties of the cluster X-ray emitters (Sect. 5). Sect. 6 summarizes the results of the present work.

2. NGC 6231 and the Sco OB 1 association: a literature review

2.1. The Sco OB 1 association

Located in the Sagittarius-Carina spiral arm of our galaxy ($\alpha(2000) = 16^{\rm h}53^{\rm m}.6$, $\delta(2000) = -41^{\rm o}57'$; $l = 343^{\rm o}.3$, $b = 1^{\rm o}.2$, Perry et al. 1991), the Sco OB 1 association is an extremely rich and interesting region of the sky. 2° long by 1° wide, it extends from the gaseous nebula IC 4628 on its northern end to the young open cluster NGC 6231 towards its southern end. Its major axis is approximately parallel to the Galactic plane (Morgan et al. 1953a). A sparser group, Tr 24, is to be found near IC 4628 while two other clusters, NGC 6242 and NGC 6268, lie slightly north of the association. Finally the H II region IC 4878, centered on NGC 6231, extends by about 4° by 5° in the form of an elliptical ring and is probably triggered by the cluster. The emission nebula is faint within the ring but is very bright where the ring is crossed by the northern end of the association (Bok et al. 1966).

The interest in Sco OB 1 mainly originates from its extended early-type star content (Shobbrook 1983; Raboud et al. 1997). Beyond the numerous O- and B-type stars, the association also shelters two of the rare Wolf-Rayet (WR) stars, two Of stars displaying P Cygni profiles as well as several β Cephei variables (Balona & Engelbrecht 1985; Arentoft et al. 2001). Among the peculiar objects found within Sco OB 1 is the bright star ζ^1 Sco. With an absolute magnitude around $M_{\rm V}$=−8.3, ζ^1 Sco is one of the brightest star of the Milky Way. Many of the 'normal' early-type stars further present signs of variability and have a good chance to be binary systems (e.g. Raboud 1996; Arentoft et al. 2001).

2.2. The NGC 6231 cluster

Located near the southern end of the Sco OB 1 association, the young open cluster NGC 6231 ($\alpha(2000) = 16^{\rm h}54^{\rm m}09^{\rm s}$, $\delta(2000) = -41^{\rm o}59'36''$) contains an important number of bright early-type stars in its centre. Often considered as the nucleus of the association (Bok et al. 1966), its relationship to Sco OB 1 has been subject to different interpretation with time. Though Heske & Wendker (1984) presented evidence that Tr 24 and Sco OB 1 form a single aggregate, these authors proposed that NGC 6231 is actually a foreground cluster. Heske & Wendker also found a sub-cluster of PMS stars in the vicinity of Tr 24. Based on an extensive set of data (Perry et al. 1990, 1991) re-addressed these issues and carefully studied the interrelation between the three aggregates. They established that Sco OB 1, NGC 6231 and Tr 24 are located at the same distance and have the same age, thus demonstrating that NGC 6231 is not a foreground object but is clearly embedded in the Sco OB 1 association. NGC 6231 therefore retains its status as the nucleus of the association. Perry et al. could however not confirm the three stellar sub-aggregates found by Seggewiss (1968a) in Tr 24 and, as suggested by Heske & Wendker (1984), they casted further doubts on

the physical reality of the Tr 24 aggregate itself. Perry et al. finally confirmed the existence of a PMS sub-cluster near Tr 24.

The properties of NGC 6231 and of its stellar content have been thoroughly investigated during the past century. Three main streams of investigation were indeed designed, namely photometry, spectral classification and radial velocity measurements. The photometric approach is however predominant and was extensively performed using different photometric systems. The bulk of the available literature on the cluster relies on photographic, photoelectric or CCD campaigns: Brownlee & Cox (1953, PV), Houck (1956), Walraven & Walraven (1960, Walraven), Feast et al. (1961, UBV), Breckinridge & Kron (1963, PV), Bok et al. (1966, UBV Hβ), Feinstein & Ferrer (1968, UBV), Seggewiss (1968b, UBV), Schild et al. (1969, UBV), Crawford et al. (1971, uvby Hβ), Garrison & Schild (1979, UBV), Shobbrook (1983, uvby Hβ), Heske & Wendker (1984, UBV), van Genderen et al. (1984, Walraven), Perry et al. (1991, uvby), Meynet et al. (1993, UBV), Balona & Laney (1995, uvby Hβ), Raboud et al. (1997, Geneva), Sung et al. (1998, UBVRI Hα), Baume et al. (1999, UBVI). The more recent works (from ∼1990's) offer a much more complete view of the cluster both in terms of their angular extension and of the magnitude limit reached. An extensive still careful comparison of most (if not all) the works published prior to 1990 has been performed by Perry et al. (1991).

Spectral classification of the cluster objects has mainly been carried out by Morgan et al. (1953b), Houck (1956), Feast et al. (1961), Schild et al. (1969), Garrison & Schild (1979), Levato & Malaroda (1980), Conti & Alschuler (1971), Walborn (1972), Mathys (1988, 1989) and García & Mermilliod (2001). Radial velocity campaigns were led essentially by Struve (1944), Hill et al. (1974), Levato & Morrell (1983), Levato et al. (1988), Perry et al. (1990), Penny et al. (1994), Stickland & Lloyd (2001, IUE data), García & Mermilliod (2001) and Sana et al. (2002). Several authors also paid a special attention to particular objects, mainly binaries of which they performed a more detailed study. These objects are WR 79 (Lührs 1997), HD 152218 (Stickland et al. 1997), HD 152248 (Stickland et al. 1996; Penny et al. 1999; Sana et al. 2001; Sana et al. 2004), CPD −41°7742 (Sana et al. 2003, 2005a) and CPD−41°7733 (Sana et al. 2005c)

Aside these three main streams, several authors addressed specific aspects of the cluster that provide a useful complementary view. Among other topics, photometric variability of a few dozens of objects was investigated by Balona (1983), Balona & Engelbrecht (1985), Balona (1992) and more recently by Arentoft et al. (2001). These allowed to detect several β Cephei, a couple of δ Scuti and a few other variable stars, including a couple of eclipsing binaries. The binary fraction was estimated by Raboud (1996) and García & Mermilliod (2001). Raboud derived a minimum binary frequency of 52% in his sample of 53 B-type stars with spectral type between B1 and B9 while García & Mermilliod (2001) obtained an extremely high frequency of 82% for stars earlier than B1.5V and, in particular, of 79% for the O-type stars of the cluster. Raboud & Mermilliod (1998) showed evidence of mass segregation in NGC 6231, most probably related to the formation processes rather than to the dynamical evolution of the cluster. Proper motions were studied by Braes (1967) and Laval (1972) while most of the O-type stars of the clusters were included in the large ICCD Speckle campaign of Mason et al. (1998).

The distance modulus of the cluster reported in the earlier literature ranges from 10.7 (Mermilliod 1981) to 11.9 (Houck 1956, 2300pc – cited by Bok et al. 1966). In a more recent work, Perry et al. (1991) obtained $DM = 11.50$ and 11.55 for Sco OB 1 and NGC 6231 respectively, with an uncertainty of about 0.32. Balona & Laney (1995) derived $DM = 11.08 \pm 0.05$ for NGC 6231; Raboud et al. (1997), 11.2 ± 0.4; Sung et al. (1998), 11.0 ± 0.07 and Baume et al. (1999) 11.5 ± 0.25. The weighted mean of these five latter values gives $DM = 11.07 \pm 0.04$, corresponding to an actual distance of 1637 ± 30 pc. The same authors (but Sung et al.) respectively derived ages of 7.9 ± 0.9 Myr, 5 ± 1 Myr, 3.8 ± 0.6 Myr and 3 to 5 Myr. On the basis of the R-Hα index, Sung et al. (1998) found 12 PMS stars plus 7 PMS candidates.

A controversial question is the probable differential reddening across the cluster. Such a differential reddening was first suggested by Breckinridge & Kron (1963), outlining that the southern part of the cluster suffers a heavier reddening. Other authors (Shobbrook 1983; Perry et al. 1991; Balona & Laney 1995) rather proposed a uniform reddening across the field. More recently, Raboud et al. (1997) and Sung et al. (1998) results strongly support the first idea of Breckinridge & Kron (1963), and Sung et al. presented a map of the reddening distribution in NGC 6231. There seems to be an agreement in the early literature that most of the reddening occurs between a distance of 100 and 1300 pc. Based on FUSE observations, Marggraf et al. (2004) recently confirmed angular variations in the column density towards the core of the cluster. They reported that the absorption towards NGC 6231 occurs in several foreground clouds. The main absorption component lies in the Lupus cloud region at a distance of 150pc, while the second one is probably in the vicinity of the Sco OB 1 shell surrounding NGC 6231. Finally, Crawford (2001) probed the structure of the interstellar NaI and KI towards the cluster and reached conclusions similar to Marggraf et al. (2004). Crawford also outlined that no clues of active shocks in the shell components could be found. Polarimetric observations were performed by Feinstein et al. (2003) who found evidence for a past supernova explosion in the cluster. These authors however suggested that their observations could also be explained by a bubble triggered by winds from hot stars.

Finally, we note that the Hipparcos parallaxes derived for NGC 6231 were known to be problematic with a negative mean value of -0.8 ± 0.4 mas (Arenou & Luri 1999). These results were recently revised by Makarov (2003) who obtained 1.7 ± 0.4 mas, corresponding to a distance modulus of 8.9 ± 0.5, however still far from the mean value obtained from the photometric studies.

Table 1. Journal of the XMM-*Newton* observations of NGC 6231. Columns 2 and 3 give the spacecraft revolution number and the observation ID. The Julian Date (JD) at mid-exposure is reported in Col. 4. Cols. 5 to 7 (resp. Cols. 8 to 10) list the performed (resp. effective) exposure times for the EPIC MOS1, EPIC MOS2 and EPIC pn instruments. The last column provides the position angle (PA). The total campaign duration is given in the last line of the table.

Obs. #	Sat.	Exposure	JD	Performed duration (ksec)			Effective duration (ksec)			PA
	Rev.	ID	JD−2 450 000	MOS1	MOS2	pn	MOS1	MOS2	pn	DD:AM:AS.s
1	319	0109490101	2158.214	33.3	33.3	30.7	33.1	33.2	30.6	274:57:11.5
2	319	0109490201	2158.931	22.1	22.1	20.2	19.8	19.8	16.5	274:57:11.5
3	320	0109490301	2159.796	34.4	34.4	31.8	33.7	33.9	30.1	275:35:26.6
4	320	0109490401	2160.925	31.4	31.4	29.1	26.0	24.3	11.7	275:35:26.6
5	321	0109490501	2161.774	31.1	31.1	28.5	30.9	31.0	28.4	276:13:34.9
6	321	0109490601	2162.726	32.9	32.9	30.3	32.9	32.8	30.3	276:13:34.9
Total duration (ksec)				185.2	185.2	170.6	176.5	175.0	147.5	

Turning to the X-ray domain, NGC 6231 was observed by the ROentgen SATellite (ROSAT). Thirty-five objects were detected, mainly associated to the early-type stars of the cluster. Corcoran (1996, 1999) presented some results of this campaign as well as the X-ray light curve of three objects, namely HD 152218, HD 152248 and HD 152249. Only HD 152248 displayed clear variations of its flux. Finally a few objects were also observed at radio wavelength (Setia Gunawan et al. 2002, 2003) but only half of them were detected.

3. Observations and Data Reduction

3.1. The XMM-Newton campaign

The XMM-*Newton* campaign towards NGC 6231 has already been described in Sana et al. (2004). For the sake of completeness, we again give here a brief description of the X-ray observations. In September 2001, during satellite revolutions 319 to 321, the XMM-*Newton* observatory (Jansen et al. 2001) performed six successive exposures of an approximate duration of 30 ksec. The field of view (FOV) was centered on the O7.5 III+O7 III colliding wind binary HD 152248 (α_{2000} = $16^{\rm h}54^{\rm m}10\overset{\rm s}{.}06$, δ_{2000} = $-41°49'30\overset{''}{.}1$; Sana et al. 2001), in the core of the cluster. Position angles (PAs) were very similar through the six exposures, ranging approximatively from $274\overset{\circ}{.}95$ to $276\overset{\circ}{.}23$. All three EPIC instruments (Strüder et al. 2001; Turner et al. 2001) were operated in the Full Frame mode together with the Thick Filter to reject optical light. The RGS spectrographs (den Herder et al. 2001) were run in the Standard Spectroscopic mode. Due to the brightness of the cluster objects in the FOV, the Optical Monitor (Mason et al. 2001) was switched off throughout the campaign. Table 1 provides the journal of the X-ray observations.

3.2. Data Reduction

The EPIC Observation Data Files (ODFs) were processed using the XMM-Science Analysis System (SAS) v 5.4.1 implemented on our computers in Liège. We applied the *emproc* and *epproc* pipeline chains respectively to the MOS and pn raw data to generate proper event list files. No indication of pile-up was found in the data. We then only considered events with patterns 0-12 (resp. 0-4) for MOS (resp. pn) instruments and we applied the filtering criterion XMMEA_EM (resp. FLAG = 0) as recommended by the Science Operation Centre (SOC) technical note XMM-PS-TN-43 v3.0. For each pointing, we rejected periods affected by soft proton flares. For this purpose, we built light curves at energies above 10 keV[1] and discarded high background observing periods on the basis of an empirically derived threshold. The so-defined GTIs (Good Time Intervals) were used to produce adequate X-ray event lists for each pointing from which we extracted images using x- and y-image bin sizes of 50 virtual pixels [2].

We finally combined the event lists obtained for all six pointings to increase the statistics of faint sources. In this purpose, we use the SAS task *merge*. For each EPIC instrument, we included the event lists resulting from different pointings one by one. We also built merged event lists that combine the twelve MOS or the eighteen EPIC event lists. The Attitude Files generated by the pipeline were merged using the same approach and we adopted, for handling the merged event lists, the Calibration Index File (CIF) and the ODF corresponding to the first pointing (Obs. 1 in Table 1).

4. X-ray source detection and identification

In this section, we focus on the detection and identification of the X-ray sources in the XMM-*Newton* FOV. In this purpose we only used the merged event lists and images, accounting in this way for the six pointings at once. The total effective exposure times towards the cluster are, respectively for the MOS1, MOS2 and pn instruments, of 176.5, 175.0 and 147.5 ksec. Together with the high sensitivity of the XMM-*Newton* observatory, the combination of the six pointings and of the three instruments provides one of the deepest X-ray views of a young open cluster. Fig. 1 shows a three-colour image of NGC 6231

[1] Expressed in Pulse Invariant (PI) channel numbers and considering that 1 PI channel approximately corresponds to 1 eV, the adopted criterion is actually PI > 10 000.

[2] Though the physical pixels of the EPIC MOS and pn detectors have an extension on the sky of respectively 1.1″ and 4.1″, the virtual pixels of the three instruments correspond to an extension $0\overset{''}{.}05$. The obtained images have thus a pixel size of 2.5″.

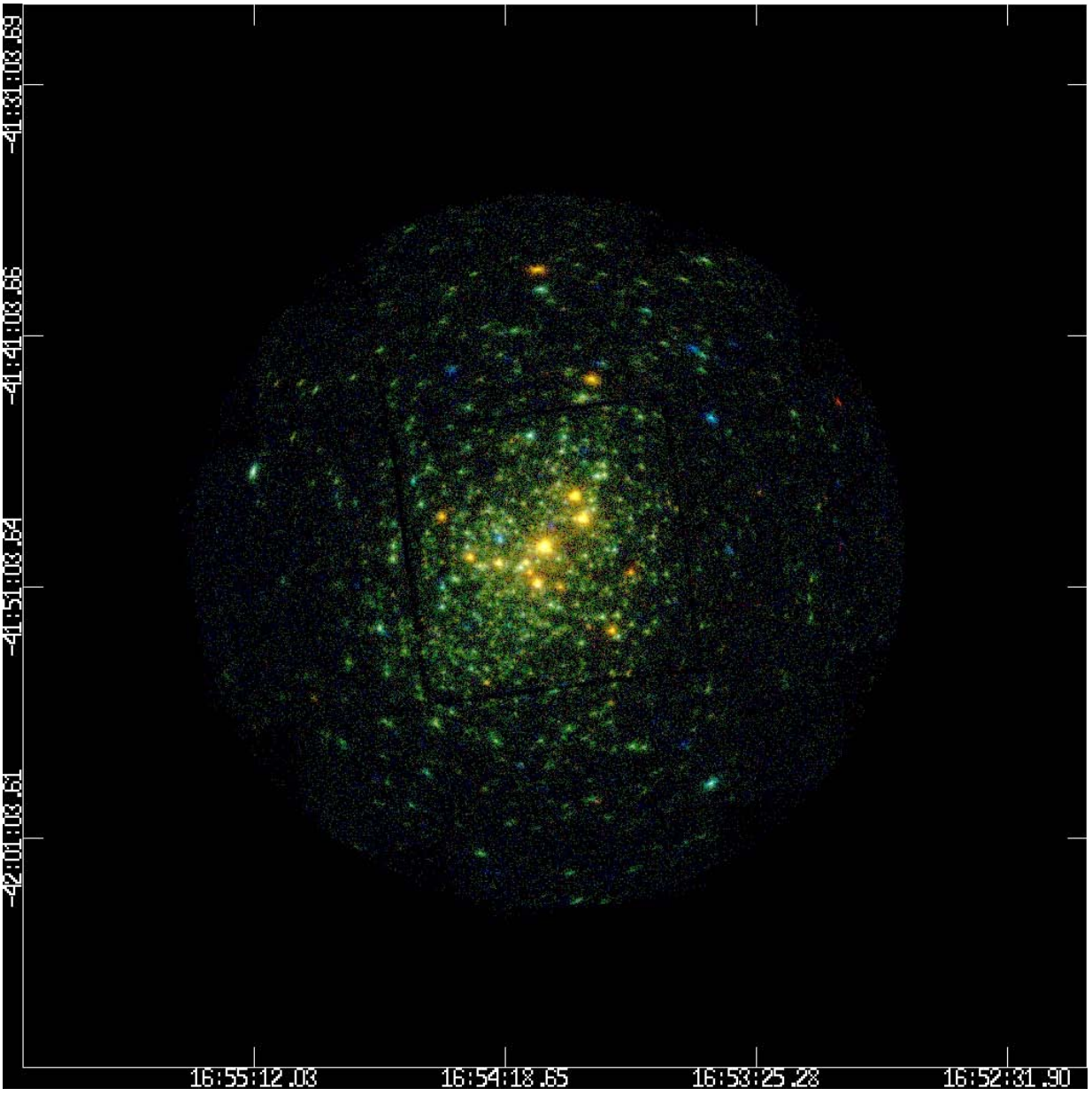

Fig. 1. EPIC MOS combined three-color X-ray image centered on the young open cluster NGC 6231. Red: 0.5-1.0 keV; Green : 1.0-2.5 keV; Blue : 2.5-10.0 keV.

and reveals a densely populated field with hundreds of point-like X-ray sources. This section therefore aims to provide a uniform catalogue of these sources. It is organised as follows. First we present the source detection procedure as well as a brief description of the obtained catalogues. As a next step, we focus on the identification of the X-ray sources and, finally, we investigate the detection limit of the present data set.

4.1. Source Detection

We based our source detection on the SAS detection chain *edetect_chain*. For this purpose, we selected three energy ranges: a soft (S_X) band (0.5-1.0 keV), a medium (M_X) band (1.0-2.5 keV) and a hard (H_X) band (2.5-10.0 keV) and we built the corresponding input images for the different instruments. The *edetect_chain* task is formed by the succession of the SAS tasks *eexpmap*, *emask*, *eboxdetect* run in local mode, *esplinemap*, again *eboxdetect* run in map mode and finally *emldetect*:

- *eexpmap* calculates the exposures maps corresponding to the input images;
- these exposure maps are used by *emask* to build masks which select the relevant image areas where the detection should take place;
- *eboxdetect*, run in local mode, uses a 5×5 pixel box and a surrounding background area to search for significant sources simultaneously in all input images;
- *esplinemap* uses the resulting source list to remove sources from the input images and creates smooth background maps by fitting a 2-D spline to the source-subtracted images;
- run in map mode, *eboxdetect* uses a 5×5 pixel box and the values from the background maps to search for significant sources simultaneously in all input images;
- *emldetect* finally uses the preliminary source list from *eboxdetect* and determines the sources parameters (e.g. coordinates, count rates, hardness ratios, etc.) by means of simultaneous maximum likelihood psf (point spread function) fitting to the source count distribution in all energy bands of each EPIC instrument. It also provides an equivalent logarithmic likelihood L_2 (Eq. A.1) commonly used as an indication of the *reality* of the corresponding source.

From our experience, the *eboxdetect* task run in map mode tended to eliminate some apparently real sources from the intermediate source list. We therefore preferred to use the preliminary source list obtained by *eboxdetect* in local mode as an input list for the psf fitting step performed by the *emldetect* task. This approach does not bias the result since, if the source is real, the psf fitting will provide a large logarithmic likelihood while, if instead the source is fake, the logarithmic likelihood will be low and the source will be rejected. Though more expensive in computation time, this approach results in a more complete source list. As it was known that the equivalent logarithmic likelihood values (L_2) computed by the *emldetect* task in the SAS v 5.4.1 (and earlier versions) were erroneous, we implemented a patch to recover the correct L_2 values. We give a brief description of this in Appendix A. The problem is now fixed from SAS version 6.0. We checked our corrected logarithmic likelihood values against SAS v 6.0 results and found them to be in close agreement.

We first performed single psf fit detection but, due to the crowdedness of the field, we also allowed for simultaneous fitting of up to four sources. In doing so, we adopt a value of 0.68 for the two parameters *scut* and *ecut*. This choice was led by the need to account for as large an energy fraction of the psf as possible while keeping the computation time down to reasonable limits. Due to the densely populated field, the wings of the source psf are often largely contaminated by emission from neighbouring sources. The adopted values therefore appeared as a reasonable compromise. On the axis, this corresponds to a physical radius of about 13″ at 1 keV for the two MOS and of about 7″ for the pn. Only a few tens of sources actually required multi-psf fitting, with three psf being adjusted simultaneously at the maximum. Finally, we re-run the *emldetect* task allowing for extended sources to be fitted. A careful comparison of the resulting lists shows that only a few sources increase significantly their detection likelihood while allowing for extended source fitting. An inspection of the X-ray images and of the optical catalogues reveals that these sources most probably correspond to unresolved point-like sources rather than physically extended sources.

Table 2. Adopted detection thresholds for the equivalent logarithmic likelihood L_2 for the different EPIC instruments (left column) or any combination of them (right column). Appendix B provides more details on how these values were adopted.

Instr.	L_2	Instr. Comb.	L_2
MOS1	11	MOS1 + MOS2	21
MOS2	11	MOS1 + pn	35
pn	25	MOS2 + pn	35
		MOS1 + MOS2 + pn	45

The described detection procedure was applied for each EPIC instrument as well as for any combination of them. The resulting source lists were generally consistent. The main difference comes from the presence of different gaps in the different data sets. We built our final source list adopting the following criteria.

(i) We selected the deepest combination of EPIC instruments, requiring that the detected source is distant by at least 13″ from any gap, bad column or detector edge.

(ii) By a visual inspection of each source in all images and subsequent combinations, we adopted an empirical equivalent logarithmic likelihood (L_2) threshold as the detection limit. This lead us to consider the best way to perform a consistent choice for the threshold values while dealing with different instrument combinations, and hence with different numbers of input images. Though it is stated otherwise in the SAS user guide, the equivalent logarithmic likelihood L_2 does not directly allow comparison between detection runs with different numbers of input images. A constant logarithmic likelihood threshold can therefore not account for different combinations of the EPIC instruments. This issue is presented into more details in Appendix B together with the adopted solution. Table 2 gives the logarithmic likelihood thresholds finally adopted. These values provide reasonably consistent (in terms of probability) logarithmic likelihood-based detection thresholds whatever the instrument combination used.

(iii) In the few cases for which multi-source fitting was relevant, we adopted the results obtained with the multi-source fitting. We however paid a special attention to fake multi-fitting sometimes induced by near-gap/edge effects or by multiple entries for a unique X-ray source in the preliminary source list.

(iv) We finally checked every sources in the final list by individually looking at the different image combinations. We eliminated the very few double entries in the list. Doing this, we notice a couple of presumably physical sources that were ignored by the detection algorithm. We decided to include those sources in the input source list of the *emldetect* task. Most of them were satisfyingly fitted, giving an equivalent logarithmic

Table 3. Sample of the NGC 6231 X-ray source catalogue. Each part of the table refers to a particular EPIC instrument. First column gives the source number. Second column provides the source position (J2000.0) following the format specified for XMM-*Newton* sources. Note that the coordinates are truncated, not rounded. The estimated error on the position (in ″) is listed in the third column ($\sigma_{\alpha\delta}$). The first three columns are reproduced at the beginning of the three parts of this table. Each sub-table concerns one of the three EPIC instruments and follows the same arrangement. Cols 4-16 (resp. 17-29 and 30-42) give the equivalent logarithmic likelihood L_2 for the given instrument, the total count rate *cr* in the whole energy band (0.5-10.0 keV) and its associated error (σ), the count rates in the different energy bands (S_X: [0.5-1.0 keV], M_X: [1.0-2.5 keV], H_X: [2.5-10.0 keV]) and their errors and, finally, the two hardness ratios HR_1 and HR_2 (Eqs. 1 and 2) as well as their related errors (σ_{HR1} and σ_{HR2}). The count-rates and the related uncertainties are all expressed in 10^{-3} cnt s^{-1}. Col. 43 provides the total equivalent logarithmic likelihood $L_2^{\rm EPIC}$ that has been compared to the adopted detection limit (see Table 2) according to the combination of instruments used (Col. 44). For those sources for which the fit is improved while adjusting an extended psf model, a note ('ext') is stated in Col. 45. Finally Col. 46 provides a warning for some sources for which no instrument combination were found to be far enough from gaps, instrument edges or detector bad columns. The full table can be consulted in the electronic version of the journal.

			EPIC pn instrument												
X#	XMMU J HHMMSS.s±DDAMAS	$\sigma_{\alpha\delta}$	$L_2^{\rm pn}$	$cr_{\rm pn}$	$\sigma_{\rm pn}$	$cr_{\rm pn}^{\rm S}$	$\sigma_{\rm pn}^{\rm S}$	$cr_{\rm pn}^{\rm M}$	$\sigma_{\rm pn}^{\rm M}$	$cr_{\rm pn}^{\rm H}$	$\sigma_{\rm pn}^{\rm H}$	$HR_1^{\rm pn}$	$\sigma_{HR1}^{\rm pn}$	$HR_2^{\rm pn}$	$\sigma_{HR2}^{\rm pn}$
[1]	[2]	[3]	[4]	[5]	[6]	[7]	[8]	[9]	[10]	[11]	[12]	[13]	[14]	[15]	[16]
1	165300.0-415444	1.20	—	—	—	—	—	—	—	—	—	—	—	—	—
2	165304.3-415334	1.38	—	—	—	—	—	—	—	—	—	—	—	—	—
3	165305.2-415204	1.11	—	—	—	—	—	—	—	—	—	—	—	—	—
4	165306.9-414930	1.24	—	—	—	—	—	—	—	—	—	—	—	—	—
5	165307.4-414659	1.03	—	—	—	—	—	—	—	—	—	—	—	—	—
6	165307.4-414345	0.54	—	—	—	—	—	—	—	—	—	—	—	—	—
7	165308.1-414533	0.89	—	—	—	—	—	—	—	—	—	—	—	—	—
8	165310.2-414733	1.08	—	—	—	—	—	—	—	—	—	—	—	—	—
9	165310.7-414451	1.04	—	—	—	—	—	—	—	—	—	—	—	—	—
10	165311.6-414755	0.60	348.9	7.427	0.492	2.271	0.247	3.871	0.301	1.285	0.301	0.261	0.062	−0.501	0.092
11	165313.0-415049	0.45	146.0	4.157	0.404	1.214	0.195	2.367	0.257	0.577	0.243	0.322	0.087	−0.608	0.137
12	165313.2-415222	0.43	295.3	6.215	0.438	1.623	0.211	3.538	0.279	1.054	0.264	0.371	0.065	−0.541	0.093
13	165313.5-415133	0.57	241.9	5.432	0.431	2.037	0.218	2.718	0.261	0.677	0.265	0.143	0.070	−0.601	0.129
14	165315.3-415011	0.84	65.5	2.567	0.344	0.787	0.157	1.319	0.198	0.462	0.234	0.253	0.117	−0.481	0.203
15	165315.7-414437	1.14	21.5	1.401	0.276	0.559	0.162	0.843	0.197	0.000	0.105	0.202	0.179	−1.000	0.249

			EPIC MOS1 instrument												
X#	XMMU J HHMMSS.s±DDAMAS	$\sigma_{\alpha\delta}$	$L_2^{\rm MOS1}$	$cr_{\rm MOS1}$	$\sigma_{\rm MOS1}$	$cr_{\rm MOS1}^{\rm S}$	$\sigma_{\rm MOS1}^{\rm S}$	$cr_{\rm MOS1}^{\rm M}$	$\sigma_{\rm MOS1}^{\rm M}$	$cr_{\rm MOS1}^{\rm H}$	$\sigma_{\rm MOS1}^{\rm H}$	$HR_1^{\rm MOS1}$	$\sigma_{HR1}^{\rm MOS1}$	$HR_2^{\rm MOS1}$	$\sigma_{HR2}^{\rm MOS1}$
[1]	[2]	[3]	[17]	[18]	[19]	[20]	[21]	[22]	[23]	[24]	[25]	[26]	[27]	[28]	[29]
1	165300.0-415444	1.20	33.0	1.079	0.199	0.318	0.081	0.636	0.120	0.125	0.136	0.334	0.140	−0.672	0.303
2	165304.3-415334	1.38	32.0	1.137	0.192	0.241	0.083	0.591	0.112	0.305	0.132	0.420	0.161	−0.319	0.213
3	165305.2-415204	1.11	18.8	0.911	0.191	0.189	0.073	0.400	0.110	0.322	0.138	0.357	0.206	−0.108	0.252
4	165306.9-414930	1.24	2.0	0.338	0.148	0.001	0.027	0.000	0.048	0.338	0.138	−1.000	120.824	1.000	0.283
5	165307.4-414659	1.03	28.9	1.048	0.178	0.000	0.035	0.287	0.092	0.761	0.148	1.000	0.246	0.453	0.149
6	165307.4-414345	0.54	172.8	1.957	0.192	1.627	0.159	0.330	0.099	0.000	0.043	−0.663	0.089	−1.000	0.259
7	165308.1-414533	0.89	28.2	0.921	0.179	0.199	0.063	0.566	0.119	0.157	0.118	0.481	0.146	−0.566	0.266
8	165310.2-414733	1.08	26.8	0.598	0.137	0.393	0.082	0.206	0.088	0.000	0.065	−0.312	0.215	−1.000	0.629
9	165310.7-414451	1.04	26.4	0.726	0.147	0.021	0.034	0.623	0.108	0.083	0.094	0.935	0.103	−0.766	0.237
10	165311.6-414755	0.60	—	—	—	—	—	—	—	—	—	—	—	—	—
11	165313.0-415049	0.45	116.4	1.735	0.187	0.419	0.079	1.219	0.147	0.097	0.085	0.488	0.085	−0.853	0.121
12	165313.2-415222	0.43	112.3	1.839	0.195	0.299	0.081	1.288	0.147	0.252	0.100	0.624	0.089	−0.672	0.113
13	165313.5-415133	0.57	71.7	1.465	0.185	0.294	0.073	0.898	0.132	0.273	0.107	0.506	0.107	−0.534	0.150
14	165315.3-415011	0.84	8.8	0.460	0.132	0.016	0.032	0.331	0.093	0.113	0.088	0.906	0.180	−0.489	0.314
15	165315.7-414437	1.14	11.7	0.522	0.142	0.065	0.047	0.391	0.101	0.066	0.087	0.713	0.188	−0.710	0.331

			EPIC MOS2 instrument																
X#	XMMU J HHMMSS.s±DDAMAS	$\sigma_{\alpha\delta}$	$L_2^{\rm MOS2}$	$cr_{\rm MOS2}$	$\sigma_{\rm MOS2}$	$cr_{\rm MOS2}^{\rm S}$	$\sigma_{\rm MOS2}^{\rm S}$	$cr_{\rm MOS2}^{\rm M}$	$\sigma_{\rm MOS2}^{\rm M}$	$cr_{\rm MOS2}^{\rm H}$	$\sigma_{\rm MOS2}^{\rm H}$	$HR_1^{\rm MOS2}$	$\sigma_{HR1}^{\rm MOS2}$	$HR_2^{\rm MOS2}$	$\sigma_{HR2}^{\rm MOS2}$	$L_2^{\rm EPIC}$	Instr.	Ext.	Comment
[1]	[2]	[3]	[30]	[31]	[32]	[33]	[34]	[35]	[36]	[37]	[38]	[39]	[40]	[41]	[42]	[43]	[44]	[45]	[46]
1	165300.0-415444	1.20	—	—	—	—	—	—	—	—	—	—	—	—	—	33.0	m1		
2	165304.3-415334	1.38	—	—	—	—	—	—	—	—	—	—	—	—	—	32.0	m1		
3	165305.2-415204	1.11	28.0	0.833	0.152	0.183	0.074	0.599	0.110	0.051	0.074	0.531	0.159	−0.844	0.212	45.9	mos		
4	165306.9-414930	1.24	127.2	1.400	0.194	1.156	0.124	0.072	0.077	0.172	0.128	−0.882	0.118	0.408	0.541	125.5	mos		
5	165307.4-414659	1.03	16.3	0.810	0.164	0.000	0.027	0.194	0.084	0.616	0.138	1.000	0.282	0.521	0.178	44.3	mos		
6	165307.4-414345	0.54	150.1	1.869	0.202	1.409	0.146	0.460	0.121	0.000	0.067	−0.508	0.105	−1.000	0.293	322.1	mos		
7	165308.1-414533	0.89	54.9	1.316	0.193	0.184	0.066	0.853	0.125	0.279	0.131	0.645	0.113	−0.507	0.183	82.2	mos		
8	165310.2-414733	1.08	14.3	0.586	0.143	0.241	0.064	0.213	0.082	0.131	0.098	−0.060	0.234	−0.238	0.397	40.2	mos		
9	165310.7-414451	1.04	34.5	0.989	0.173	0.296	0.075	0.567	0.117	0.126	0.103	0.315	0.148	−0.635	0.251	60.1	mos		
10	165311.6-414755	0.60	100.7	1.731	0.193	0.468	0.095	0.941	0.126	0.322	0.111	0.336	0.108	−0.491	0.141	448.3	m2pn		
11	165313.0-415049	0.45	83.1	1.280	0.160	0.263	0.068	0.983	0.130	0.034	0.065	0.578	0.097	−0.933	0.124	343.5	epic		
12	165313.2-415222	0.43	113.3	1.885	0.200	0.400	0.089	1.141	0.142	0.344	0.108	0.481	0.098	−0.537	0.121	518.6	epic		
13	165313.5-415133	0.57	112.7	1.832	0.198	0.326	0.079	1.187	0.139	0.320	0.117	0.569	0.091	−0.576	0.128	424.0	epic		
14	165315.3-415011	0.84	8.1	0.341	0.103	0.058	0.052	0.283	0.072	0.000	0.053	0.662	0.263	−1.000	0.373	79.0	epic		
15	165315.7-414437	1.14	15.7	0.777	0.160	0.147	0.065	0.348	0.098	0.283	0.108	0.406	0.219	−0.103	0.235	47.2	epic		

Table 4. Same as Table 3 but for the extended sources. $\sigma_{\rm psf}$ (Col. 4) gives, in arcsec, the σ extension of the adjusted Gaussian.

	XMMU J			EPIC pn instrument													
X#	HHMMSS.ss±DDAMAS	$\sigma_{\omega\delta}$	$\sigma_{\rm psf}$	$L_2^{\rm pn}$	$cr_{\rm pn}$	$\sigma_{\rm pn}$	$cr^{\rm S}_{\rm pn}$	$\sigma^{\rm S}_{\rm pn}$	$cr^{\rm M}_{\rm pn}$	$\sigma^{\rm M}_{\rm pn}$	$cr^{\rm H}_{\rm pn}$	$\sigma^{\rm H}_{\rm pn}$	$HR_1^{\rm pn}$	$\sigma^{\rm pn}_{HR1}$	$HR_2^{\rm pn}$	$\sigma^{\rm pn}_{HR2}$	
[1]	[2]	[3]	[4]	[5]	[6]	[7]	[8]	[9]	[10]	[11]	[12]	[13]	[14]	[15]	[16]	[17]	
125	165351.7-414850	0.76	2.3	307.6	5.585	0.337	2.457	0.206	2.761	0.218	0.367	0.154	0.058	0.057	–0.765	0.089	
133	165353.3-415101	1.42	3.1	—	—	—	—	—	—	—	—	—	—	—	—	—	
179	165359.3-415937	0.45	1.3	355.3	8.288	0.502	3.692	0.298	3.378	0.291	1.218	0.280	–0.045	0.059	–0.470	0.096	
204	165401.9-414335	0.51	1.4	—	—	—	—	—	—	—	—	—	—	—	—	—	
221	165404.0-415031	0.58	3.3	383.8	12.315	0.658	5.163	0.408	6.498	0.450	0.654	0.252	0.114	0.052	–0.817	0.065	
229	165405.0-414234	0.51	1.7	328.1	6.858	0.399	2.519	0.230	3.421	0.249	0.918	0.210	0.152	0.057	–0.577	0.080	
239	165405.6-414451	0.78	2.3	124.2	4.450	0.364	2.029	0.239	2.421	0.265	0.000	0.074	0.088	0.080	–1.000	0.061	
247	165406.4-414904	1.75	6.5	—	—	—	—	—	—	—	—	—	—	—	—	—	
265	165408.5-415021	0.75	4.9	540.7	20.183	0.954	11.738	0.637	8.077	0.629	0.368	0.329	–0.185	0.046	–0.913	0.075	
270	165409.0-415813	1.03	2.0	84.7	3.791	0.390	1.384	0.214	1.690	0.230	0.718	0.232	0.100	0.102	–0.404	0.147	
281	165410.3-414840	1.00	3.2	—	—	—	—	—	—	—	—	—	—	—	—	—	
289	165411.1-415233	0.61	2.9	520.0	10.391	0.461	4.518	0.286	5.270	0.307	0.604	0.190	0.077	0.043	–0.794	0.059	
344	165417.0-414540	0.54	1.9	385.5	6.539	0.354	2.457	0.209	3.041	0.225	1.041	0.175	0.106	0.056	–0.490	0.070	
377	165420.2-414849	0.56	2.1	—	—	—	—	—	—	—	—	—	—	—	—	—	
383	165421.1-415706	1.47	2.8	—	—	—	—	—	—	—	—	—	—	—	—	—	
411	165424.4-414935	0.76	3.2	356.6	10.426	0.537	3.783	0.331	5.623	0.354	1.019	0.232	0.196	0.052	–0.693	0.061	
417	165425.5-415424	0.71	1.5	—	—	—	—	—	—	—	—	—	—	—	—	—	
451	165429.6-414850	0.80	2.8	316.7	7.933	0.474	2.578	0.263	4.399	0.321	0.955	0.228	0.261	0.058	–0.643	0.073	
456	165429.9-413921	1.27	2.3	—	—	—	—	—	—	—	—	—	—	—	—	—	

	XMMU J			EPIC MOS1 instrument													
X#	HHMMSS.ss±DDAMAS	$\sigma_{\omega\delta}$	$\sigma_{\rm psf}$	$L_2^{\rm MOS1}$	$cr_{\rm MOS1}$	$\sigma_{\rm MOS1}$	$cr^{\rm S}_{\rm MOS1}$	$\sigma^{\rm S}_{\rm MOS1}$	$cr^{\rm M}_{\rm MOS1}$	$\sigma^{\rm M}_{\rm MOS1}$	$cr^{\rm H}_{\rm MOS1}$	$\sigma^{\rm H}_{\rm MOS1}$	$HR_1^{\rm MOS1}$	$\sigma^{\rm MOS1}_{HR1}$	$HR_2^{\rm MOS1}$	$\sigma^{\rm MOS1}_{HR2}$	
[1]	[2]	[3]	[4]	[18]	[19]	[20]	[21]	[22]	[23]	[24]	[25]	[26]	[27]	[28]	[29]	[30]	
125	165351.7-414850	0.76	2.3	72.7	1.397	0.155	0.468	0.082	0.824	0.110	0.105	0.071	0.276	0.102	–0.774	0.139	
133	165353.3-415101	1.42	3.1	61.4	1.483	0.181	0.458	0.092	0.930	0.131	0.096	0.086	0.340	0.108	–0.812	0.154	
179	165359.3-415937	0.45	1.3	168.5	2.799	0.241	0.900	0.121	1.398	0.157	0.501	0.138	0.217	0.083	–0.472	0.116	
204	165401.9-414335	0.51	1.4	961.2	6.975	0.383	1.679	0.202	4.103	0.281	1.193	0.166	0.419	0.057	–0.549	0.054	
221	165404.0-415031	0.58	3.3	135.1	3.762	0.316	1.065	0.167	2.275	0.230	0.421	0.137	0.362	0.081	–0.688	0.090	
229	165405.0-414234	0.51	1.7	136.3	2.204	0.196	0.629	0.099	1.317	0.138	0.258	0.098	0.354	0.083	–0.672	0.108	
239	165405.6-414451	0.78	2.3	36.8	1.355	0.192	0.334	0.094	0.888	0.139	0.134	0.094	0.454	0.128	–0.738	0.163	
247	165406.4-414904	1.75	6.5	48.0	5.111	0.876	2.860	0.763	2.250	0.415	0.000	0.111	–0.119	0.160	–1.000	0.099	
265	165408.5-415021	0.75	4.9	171.9	5.746	0.410	2.657	0.273	3.089	0.302	0.000	0.047	0.075	0.071	–1.000	0.030	
270	165409.0-415813	1.03	2.0	46.9	1.368	0.192	0.276	0.078	0.871	0.133	0.221	0.115	0.518	0.117	–0.595	0.174	
281	165410.3-414840	1.00	3.2	215.9	6.795	0.536	1.987	0.258	4.223	0.337	0.584	0.328	0.360	0.066	–0.757	0.121	
289	165411.1-415233	0.61	2.9	220.8	3.566	0.243	0.747	0.114	2.369	0.182	0.449	0.113	0.521	0.062	–0.681	0.071	
344	165417.0-414540	0.54	1.9	93.0	1.812	0.175	0.472	0.086	0.980	0.122	0.359	0.091	0.350	0.097	–0.464	0.111	
377	165420.2-414849	0.56	2.1	375.0	5.208	0.272	1.112	0.127	3.227	0.203	0.870	0.130	0.487	0.050	–0.575	0.054	
383	165421.1-415706	1.47	2.8	71.3	2.593	0.288	0.426	0.100	1.537	0.206	0.630	0.175	0.566	0.092	–0.419	0.127	
411	165424.4-414935	0.76	3.2	95.4	3.133	0.283	0.730	0.153	2.078	0.209	0.325	0.113	0.480	0.089	–0.730	0.085	
417	165425.5-415424	0.71	1.5	89.1	2.213	0.228	0.482	0.102	1.374	0.170	0.357	0.112	0.481	0.094	–0.588	0.110	
451	165429.6-414850	0.80	2.8	80.1	2.315	0.246	0.615	0.128	1.562	0.183	0.138	0.104	0.435	0.097	–0.837	0.114	
456	165429.9-413921	1.27	2.3	68.6	2.927	0.366	0.527	0.119	1.906	0.260	0.493	0.228	0.567	0.089	–0.589	0.157	

	XMMU J			EPIC MOS2 instrument														
X#	HHMMSS.ss±DDAMAS	$\sigma_{\omega\delta}$	$\sigma_{\rm psf}$	$L_2^{\rm MOS2}$	$cr_{\rm MOS2}$	$\sigma_{\rm MOS2}$	$cr^{\rm S}_{\rm MOS2}$	$\sigma^{\rm S}_{\rm MOS2}$	$cr^{\rm M}_{\rm MOS2}$	$\sigma^{\rm M}_{\rm MOS2}$	$cr^{\rm H}_{\rm MOS2}$	$\sigma^{\rm H}_{\rm MOS2}$	$HR_1^{\rm MOS2}$	$\sigma^{\rm MOS2}_{HR1}$	$HR_2^{\rm MOS2}$	$\sigma^{\rm MOS2}_{HR2}$	$L_2^{\rm EPIC}$	Instr.
[1]	[2]	[3]	[4]	[31]	[32]	[33]	[34]	[35]	[36]	[37]	[38]	[39]	[40]	[41]	[42]	[43]	[44]	[45]
125	165351.7-414850	0.76	2.3	111.1	1.775	0.162	0.539	0.086	1.025	0.111	0.211	0.081	0.311	0.087	–0.659	0.113	492.7	epic
133	165353.3-415101	1.42	3.1	127.0	2.256	0.211	0.801	0.120	1.311	0.147	0.144	0.093	0.241	0.088	–0.802	0.116	189.1	mos
179	165359.3-415937	0.45	1.3	135.8	2.387	0.225	0.908	0.118	1.033	0.140	0.446	0.130	0.064	0.094	–0.397	0.136	661.8	epic
204	165401.9-414335	0.51	1.4	—	—	—	—	—	—	—	—	—	—	—	—	—	961.2	m1
221	165404.0-415031	0.58	3.3	149.4	3.477	0.297	0.914	0.165	2.517	0.235	0.046	0.078	0.467	0.079	–0.964	0.060	670.4	epic
229	165405.0-414234	0.51	1.7	126.2	2.106	0.188	0.684	0.103	1.171	0.131	0.251	0.087	0.262	0.087	–0.647	0.106	592.5	epic
239	165405.6-414451	0.78	2.3	32.1	1.287	0.189	0.454	0.097	0.659	0.130	0.174	0.097	0.184	0.140	–0.583	0.195	193.7	epic
247	165406.4-414904	1.75	6.5	36.5	4.491	0.565	2.123	0.374	2.341	0.403	0.026	0.131	0.049	0.123	–0.978	0.109	85.1	mos
265	165408.5-415021	0.75	4.9	198.5	6.099	0.420	2.680	0.278	3.410	0.305	0.010	0.082	0.120	0.067	–0.994	0.048	913.3	epic
270	165409.0-415813	1.03	2.0	49.3	1.589	0.209	0.365	0.091	0.837	0.139	0.387	0.127	0.393	0.127	–0.368	0.159	182.2	epic
281	165410.3-414840	1.00	3.2	104.4	4.584	0.415	1.208	0.234	2.987	0.308	0.390	0.151	0.424	0.090	–0.769	0.082	321.3	mos
289	165411.1-415233	0.61	2.9	224.9	3.470	0.236	0.963	0.126	2.272	0.173	0.234	0.100	0.405	0.063	–0.813	0.074	968.4	epic
344	165417.0-414540	0.54	1.9	102.5	1.697	0.169	0.455	0.084	1.131	0.128	0.112	0.072	0.426	0.088	–0.820	0.107	582.4	epic
377	165420.2-414849	0.56	2.1	383.3	5.205	0.272	1.056	0.123	3.280	0.202	0.870	0.134	0.513	0.049	–0.581	0.055	760.0	mos
383	165421.1-415706	1.47	2.8	89.9	3.020	0.309	0.514	0.127	1.985	0.227	0.521	0.166	0.588	0.089	–0.584	0.111	162.1	mos
411	165424.4-414935	0.76	3.2	84.6	3.007	0.282	0.860	0.154	1.831	0.203	0.316	0.121	0.361	0.092	–0.706	0.100	537.7	epic
417	165425.5-415424	0.71	1.5	82.4	2.308	0.242	0.494	0.109	1.268	0.170	0.545	0.133	0.439	0.104	–0.399	0.117	172.4	mos
451	165429.6-414850	0.80	2.8	68.7	2.330	0.251	0.560	0.123	1.353	0.180	0.417	0.123	0.415	0.106	–0.529	0.117	466.5	epic
456	165429.9-413921	1.27	2.3	78.8	2.680	0.335	0.941	0.167	1.480	0.224	0.260	0.186	0.223	0.111	–0.701	0.186	148.3	mos

Table 5. Best fit parameters (Cols. 3-5) for the $\Phi(r)$ function (see text) for different optical/infrared catalogues. The adopted correlation radius (r_{corr}) is given in Col. 6. Col. 7 lists the actual number N_{corr} of identified X-ray sources (see Table 6) and the corresponding percentage related to the considered number of X-ray sources (N_X). Col. 8 gives the number of associated counterparts predicted by the distribution $\Phi(r)$ (Eq. 4) at a radius equals to r_{corr}. It also provides the corresponding percentage of theoretically identified X-ray sources. The next two columns provide, among the number of associated counterparts $\Phi(r_{corr})$, the number of true ($\Phi_{true}(r_{corr})$) and spurious ($\Phi_{spur.}(r_{corr})$) counterparts. The contribution of true and spurious counterparts to the total (theoretically) associated optical sources are also given in the corresponding columns.

N_X	Opt. Cat.	A	σ ($''$)	B $10^{-3}(''){}^{-2}$	r_{corr} ($''$)	N_{corr}	$\Phi(r_{corr})$	$\Phi_{true}(r_{corr})$	$\Phi_{spur.}(r_{corr})$
610	2MASS	481.1	1.12	8.52	3	492 (80.6%)	495.1 (81.2%)	467.5 (94.4%)	27.6 (5.6%)
610	GSC 2.2	406.2	1.31	2.50	3	372 (61.0%)	391.1 (64.1%)	377.2 (96.4%)	13.9 (3.6%)
610	USNO	317.8	1.05	3.30	3	344 (56.4%)	338.3 (55.5%)	312.3 (92.3%)	23.0 (7.7%)
609	SSB05	525.1	1.07	5.33	3	519 (85.2%)	526.5 (86.5%)	514.8 (96.4%)	11.7 (3.6%)

likelihood above the adopted detection threshold. These additional sources were included in the final catalogue.

(v) The main X-ray catalogue presented in Table 3 is based on the point-like source detection only. The sources for which the equivalent logarithmic likelihood L_2 is significantly improved while adjusting an extended source model are flagged and we provide a complementary extended source catalogue that gives, in addition to the results listed in the main catalogue, the *emldetect* extended-psf fit results for these sources.

The final catalogue (see Table 3) lists 610 sources in the XMM-*Newton* FOV, among which 16 are flagged as extended. Based on the *edetect_chain* results, it provides, among other information, the source position, the total count rates in the different instruments and the two hardness ratios :

$$HR_1 = \frac{M - S}{M + S} \quad (1)$$

$$HR_2 = \frac{H - M}{H + M} \quad (2)$$

A sample of the catalogue is provided in Table 3 while Table 4 gives the complementary catalogue for the 19 extended X-ray sources detected. In addition, source X#234 appears clearly double in the EPIC image though it is not detected as an extended object. Table 3 is available online via the Centre de Données astronomiques de Strasbourg (CDS, http://www.u-strasb.fr). Finding charts for the X-ray sources are provided by Figs. 2 and 3.

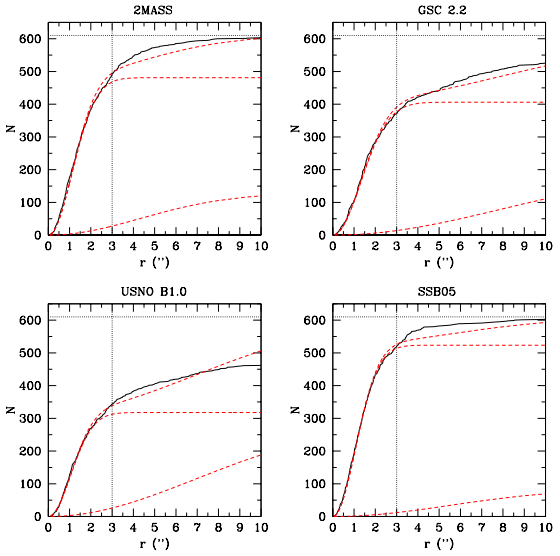

Fig. 4. Cumulative distributions (solid lines) of the number (N) of closest associated counterparts as a function of the correlation radius (r) for the different catalogues used. The horizontal dotted lines show the number N_X of X-ray sources in the catalogue field. The dashed lines, from top to bottom in each panels, correspond respectively to the best-fit $\Phi(r)$ function, the number of truly associated counterparts Φ_{true} and the number of spurious ones $\Phi_{spur.}$, as a function of the correlation radius r. Dotted vertical lines show the correlation radius for adopted the purpose of source identification.

4.2. Source Identification

To determine the optical counterparts of the detected X-ray sources, we cross-correlated our source list with several existing optical catalogues. We used the US Naval Observatory (Monet et al. 2003, USNO B1.0), the 2MASS All Sky Data Release (Cutri et al. 2003) and the Guide Star Catalogue-II (GSC 2.2 2001). We also make use of the optical catalogue of Sung et al. (1998, SBL98 hereafter). However, the star positions in the SBL98 catalogue as available from the Centre de Données astronomiques de Strasbourg (CDS) show systematic shifts compared to the true positions on the sky. This results from an excessive rounding of the star coordinates in the CDS database, that are given with a precision of respectively one second and one tenth of arcmin on the hour angle and declination. This is far insufficient in such a crowded field as NGC 6231. We therefore used the original SBL98 catalogue, that lists object coordinates a hundred times more accurately. Beyond the 860 objects with $V \leq 16$ listed in SBL98, this UBV(RI)$_C$ & Hα catalogue was completed with 7199 objects, extending the first version of the SBL98 catalogue down to $V = 21$. However, the SBL98 field of view was limited to a $20' \times 20'$ area and thus does not cover the whole EPIC FOV. More recently, one of us (H. Sung) acquired new UBV(RI)$_C$ observations covering a field of about $40' \times 40'$ around NGC 6231. 30866 stars were observed down to $V < 22$. These observations will be presented in a forthcoming paper (Sung et al. 2005, in preparation – Paper IV) and we only focused here on the re-

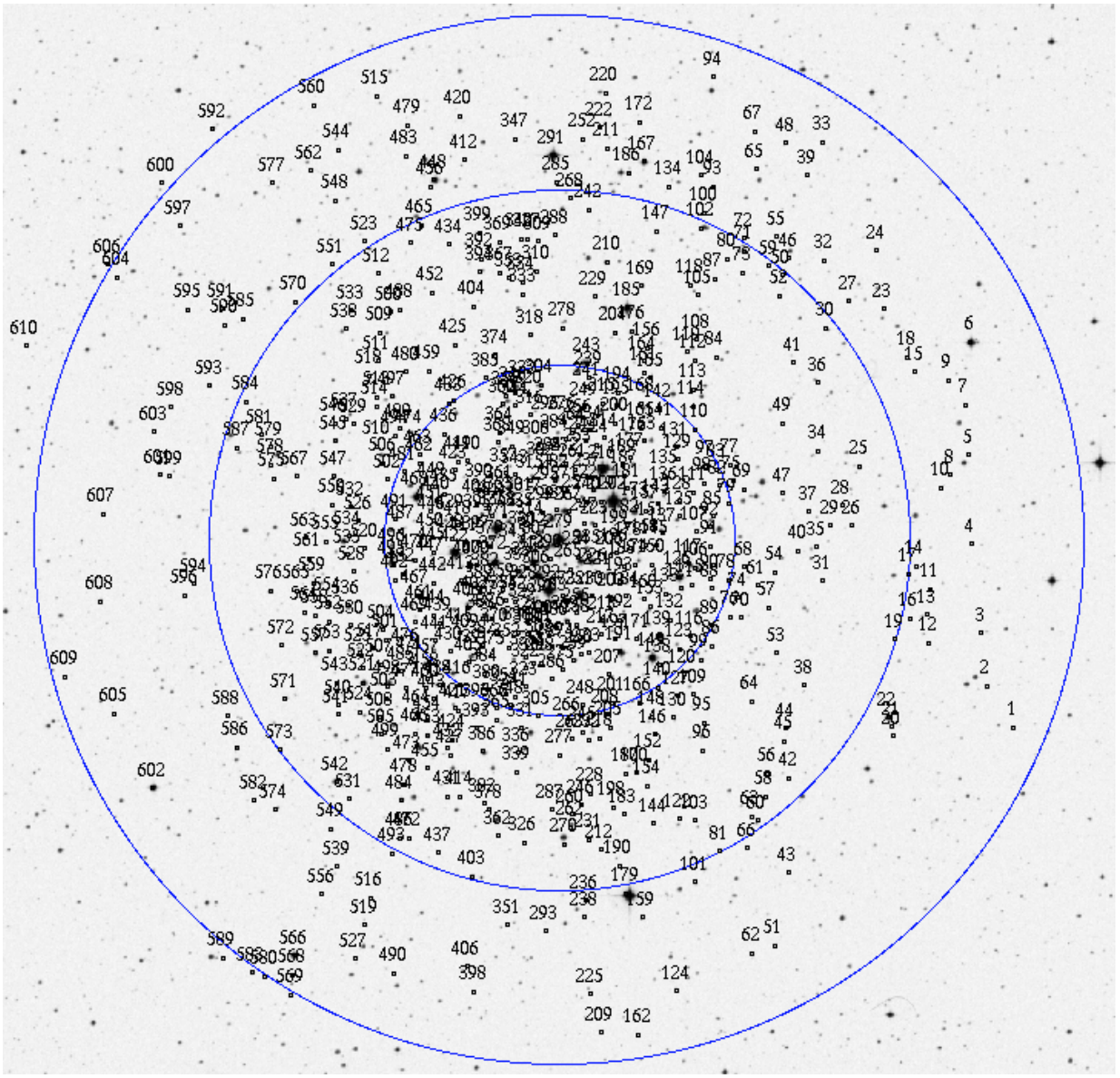

Fig. 2. Detected X-ray sources overlaid on a DSS image of the XMM-*Newton* FOV. The sources are indicated by black circles, with a radius of 3″, similar to the adopted cross-correlation radius. The numbers above these circles give the internal X-ray source identification as provided in the first column of Table 3. The three blue circles indicate regions of 5′, 10′ and 15′ radii around X# 279 (HD 152248). North is up and East to the left.

sulting catalogue. We will refer to this second version of the catalogue as SSB05. In the following, we exclusively use the SSB05 catalogue either for the purpose of source identification or while retrieving photometric information from Sung and coworkers work.

For each of the previously cited catalogues, we determine the closest optical counterpart of each X-ray source in the field of view. We then calculated the cumulative distribution ($\Phi(r)$) of the closest associated counterparts as a function of the correlation radius (see Jeffries et al. 1997). The generated diagrams are shown in Fig. 4. Following Jeffries et al. we assumed that $\Phi(r)$ is formed by two terms: the cumulative distribution of true correlations $\Phi_{\rm true}$ and the cumulative number of spurious associations $\Phi_{\rm spur.}$. This is expressed in the simple relation:

$$\Phi(r) = \Phi_{\rm true} + \Phi_{\rm spur.} \quad (3)$$

$$= A\left[1 - \exp\left(\frac{-r^2}{2\sigma^2}\right)\right] + (N_{\rm X} - A)\left[1 - \exp\left(-\pi r^2 B\right)\right] \quad (4)$$

that can be adjusted to the empirical distribution. In Eq. 4, $N_{\rm X}$ is the number of X-rays sources while A is the number of true correlations with the optical catalogue. B is the optical catalogue density and σ is related to the statistical uncertainty on

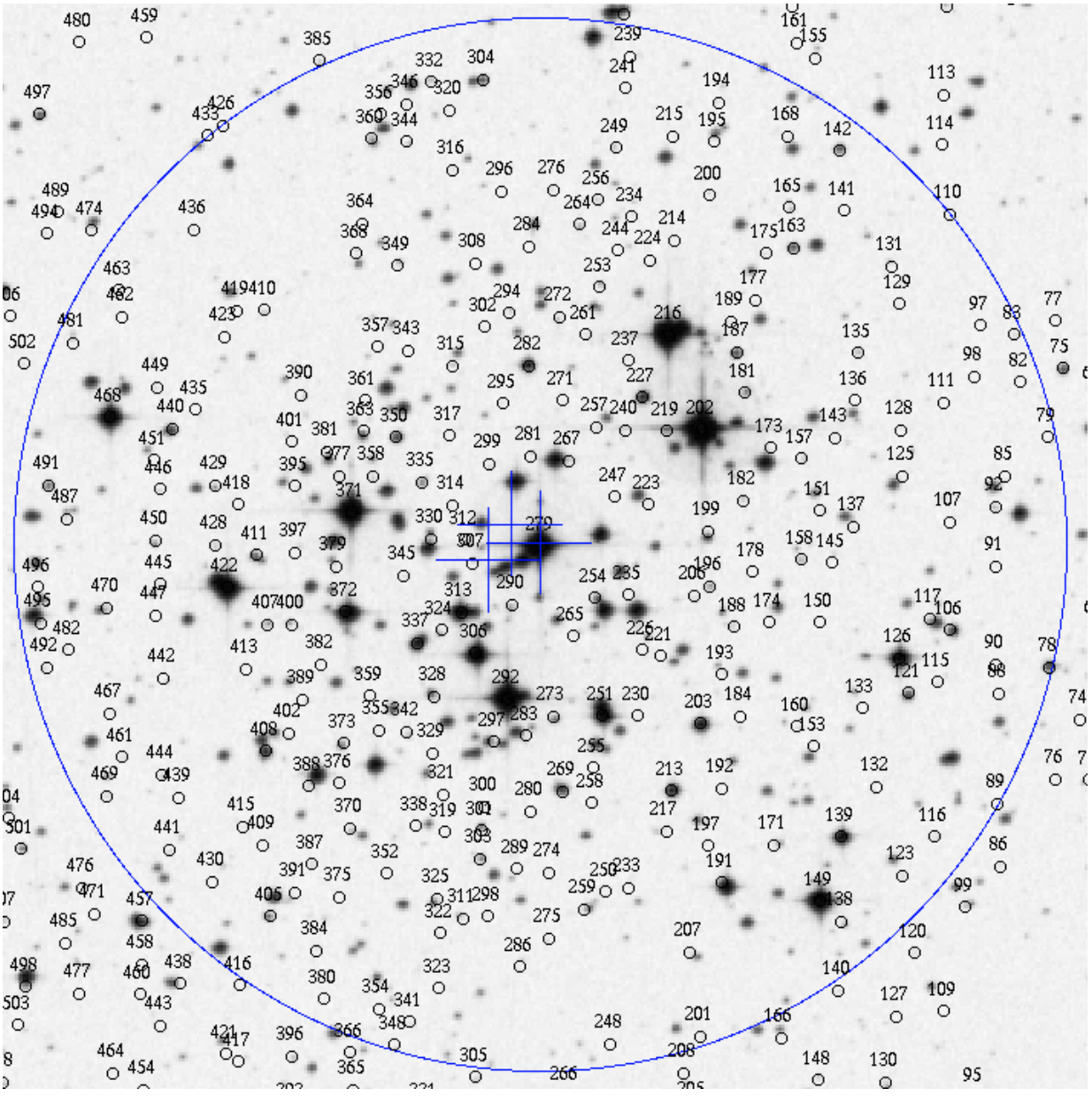

Fig. 3. Same as Fig. 2, zoomed on the inner part of the FOV. The circle radius is 5′. From left to right, the three crosses respectively give the position of the geometrical centre of the cluster, its X-ray emission centre (computed adopting the pn-equivalent count rates for each sources), and the position of HD 152248 (X# 279).

the X-ray source position. Preliminary results indicated B values about one order of magnitude larger than the true source density of the catalogues. We thus chose to hold the value of B fixed to the corresponding catalogue source density. The obtained results are much more coherent. For technical reasons, HD 152247 is not included in the SSB05 catalogue. As it is a known X-ray emitter, we did not account for the corresponding source correlation radius while computing the fit. We thus adopted $N_{\rm X}^{\rm SBL} = 609$. Though Eq. 4 is approximative and rests on the hypothesis of uniform optical catalogues (i.e. constant B through the FOV), it fits reasonably well the different curves plotted in Fig. 4. Table 5 gives the values of the A, B and σ parameters obtained.

From the cumulative distributions shown in Fig. 4 we adopted the cross-correlation radius corresponding to the knees in the distributions of true optical counterparts. The adopted radius is 3″ for all four catalogues. The percentage of identified sources ranges from 56 to 85 % according to the catalogue used. From Table 5, the results for the 2MASS and the SSB05 catalogues are clearly in contrast with the two other catalogues.

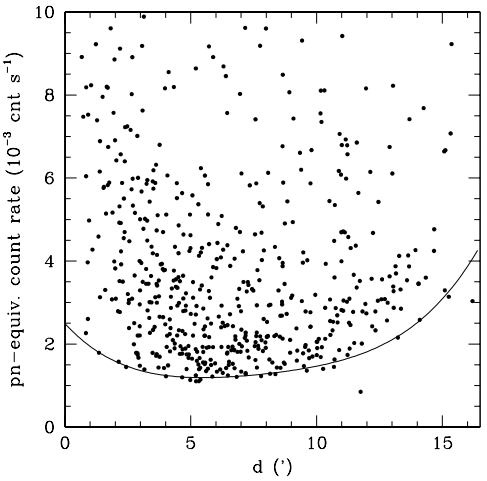

Fig. 5. Bottom part of the distribution of the *pn-equivalent* count rates as a function of the distance to HD 152248. The plain line shows the adopted lower limit given by Eq. 5.

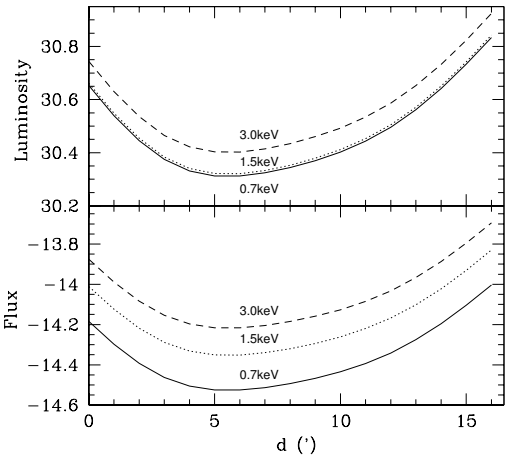

Fig. 6. Estimated detection limit expressed in flux (in $\log(\mathrm{erg\,cm^{-2}\,s^{-1}})$) and, adopting the distance of the NGC 6231 cluster ($DM = 11.07$), in luminosity (in $\log(\mathrm{erg\,s^{-1}})$). Different lines refer to different MEKAL model temperatures adopted in the conversion. The energy band considered is 0.5-10.0 keV.

With more than 85% of identified X-ray sources, among which only 4% statistically correspond to spurious associations, the SSB05 catalogue is obviously the most appropriate for our purposes. In the following, we thus adopt the SSB05 catalogue as the main reference in the identification of the sources and subsequent use of the photometric data. Table 6 provides the cross identifications between the X-ray source lists and the four optical catalogues. While carrying out this work, we noticed some confusion between the names of several sources reported in the widely consulted SIMBAD database. For this reason, Table 6 also gives other commonly adopted source denominations such as HD, CPD and Braes numbers. The Seggewiss numbering is also extensively used in the literature related to NGC 6231. We therefore used the original chart of Seggewiss (1968b) – subsequently completed by Raboud et al. (1997) – and we rederived the cross-correlation to avoid any previous misidentification.

4.3. The detection limit

This paragraph aims at the evaluation of the detection limit of the present X-ray catalogue. Though essential, this question is far from trivial because the detection limit is, *a priori*, not uniform throughout the field of view. Beside the areas where the detectors do not overlap and the presence of gaps between the detector CCDs, the XMM-*Newton* effective exposure duration is decreasing from the FOV centre towards its edges. In addition, both the crowdedness of the field in its central part and the numerous bright sources preferentially located in the core of the cluster also affect the detection limit in a non uniform way. As an approximation we neglect the effects of the gaps, mainly focusing on the three other effects.

The exposure maps computed for the three EPIC instruments and their different combinations display a smooth decrease from the centre of the detector to its edges by about a factor of three. In terms of the amount of signal collected for two similar sources – one located near the FOV axis, the other near one of its edges – the number of counts n received will be three times higher near the axis. Neglecting any background effect, the signal-to-noise ratio is approximately given by $S/N = \sqrt{n}$. For the outer source, it is therefore smaller by a factor of $\sqrt{3} \approx 1.7$. To the first order, the detection limit in the outer parts of the field is thus about a factor two higher than in the central part of the FOV. As a next step, we used the SAS task *esensmap* to build sensitivity maps corresponding to the current exposure maps and to the adopted logarithmic likelihood detection thresholds L_2. The sensitivity maps obtained actually provide the minimum number of counts for a source to be detected by the detection task *emldetect* according to the given equivalent logarithmic likelihood threshold. These maps indeed predict that the sensitivity of the EPIC camera is twice larger near the axis than in the outer parts of the detector whatever the instruments combination. This is in agreement with our previous estimate.

Accounting for the variation of the source density and the distribution of the bright sources in the FOV is a more tricky issue. We chose to adopt a completely empirical approach, taking advantage of the large number of X-ray sources in the field. We assumed that a very good indication of the detection limit in the different parts of the field is given by the brightness of the faintest sources detected in these selected areas. We adopted the following approach. Because of the presence of gaps, we computed an *equivalent* EPIC pn count rate for each sources. To the first order, the relation between the count rates measured in any of the two MOS detectors and in the pn detector is approximately linear. Using the count rates obtained for sources that were detected on several EPIC instruments, we derived an

Table 6. Cross-identification of the X-ray source catalogue of Table 3 and the different optical catalogues: 2MASS, GSC 2.2, USNO B1.0 and SBL v 2. d_{cc} is the distance (in ″) between the position of the X-ray source and its closest counterpart. Only the closest identification has been reported in this table. Cross-identification with commonly used denominations is given in the last columns (Col. 30 to 35) of the table.

	XMMU J	2MASS					GSC 2.2						USNO B1.0						
X #	HHMMSS.s±DDAMAS	d_{cc}	name	J	H	K	d_{cc}	name	R	B	V	cl	d_{cc}	name	R1	B1	R2	B2	I
[1]	[2]	[3]	[4]	[5]	[6]	[7]	[8]	[9]	[10]	[11]	[12]	[13]	[14]	[15]	[16]	[17]	[18]	[19]	[20]
1	165300.0−415444	1.231	16530004−4154458	14.597	13.942	13.766	1.355	S230322023799	16.58		17.48	3	1.375	0480−0520459		15.60	17.86	16.57	14.82
2	165304.3−415334						2.248	S230322024061	16.90		17.34	3	1.790	0481−0502790		15.92	17.73	16.91	14.95
3	165305.2−415204	1.664	16530516−4152052	15.310	14.353	13.998							1.322	0481−0502801		17.50	20.84	19.15	
4	165306.9−414931																		
5	165307.4−414659																		
6	165307.4−414345	1.310	16530729−4143454	7.933	7.926	7.894	1.322	S2303220656		8.71	8.50	0	1.326	0482−0494626	8.69	8.39	8.58	8.37	8.29
7	165308.1−414533	0.514	16530820−4145336	15.459	14.560	14.247													
8	165310.3−414733	1.281	16531017−4147340	13.148	12.553	12.271	1.131	S230322025106	15.97		16.68	3	1.142	0482−0494652		15.36	17.13	15.92	13.87
9	165310.8−414451	0.988	16531068−4144512	14.126	13.467	13.234	1.277	S230322025351	16.32		16.96	0	0.803	0482−0494657		15.59	17.33	16.49	14.87
10	165311.5−414755	2.937	16531161−4147582	15.438	14.490	14.349													
11	165312.9−415049	0.761	16531300−4150489	12.821	12.395	12.018	1.167	S230322024617	14.78		15.16	0	0.604	0481−0502869		14.40	15.71	14.28	13.17
12	165313.2−415222	0.964	16531315−4152218	13.426	12.709	12.393	1.555	S230322024317	15.87		16.36	0	1.117	0481−0502872		15.12	16.78	15.81	14.14
13	165313.6−415133	1.319	16531344−4151336	13.826	13.209	13.036	1.557	S230322024479	15.81		16.43	0	0.996	0481−0502879		15.20	16.75		14.29
14	165315.3−415011	1.033	16531528−4150113	14.925	14.070	13.681	1.254	S2303220106701	17.53			0	0.878	0481−0502898		16.93		17.92	15.75
15	165315.8−414436						0.632	S2303220108158	17.51			3	0.386	0482−0494707		16.55	19.18	17.80	15.62
16	165316.3−415139	2.479	16531618−4151423	14.891	14.169	13.907	2.251	S2303220106219	17.61			0	2.180	0481−0502907		16.83	19.16	17.66	15.72
17	165316.5−415024	2.343	16531643−4150266	15.897	15.118	14.763													
18	165317.0−414412	1.301	16531694−4144114	13.172	12.505	12.272	1.555	S230322025408	15.44		15.83	0	1.307	0482−0494722		14.81	16.75	15.32	14.00
19	165318.4−415215	1.285	16531851−4152161	15.297	14.335	14.006							1.676	0481−0502931				20.38	16.41
20	165318.7−415502	0.297	16531869−4155025	15.138	14.189	13.846							0.116	0480−0520711		17.47	21.34	19.45	16.63
21	165318.9−415446																		
22	165319.4−415431	1.167	16531939−4154299	9.650	9.546	9.478	0.699	S2300110209	10.27		10.58	0	0.675	0480−0520725		10.23	11.16	10.69	10.06
23	165320.6−414249						1.477	S230322025513	15.86		16.49	0	1.001	0482−0494765		15.05	17.99	15.69	14.02
24	165322.0−414109	0.443	16532192−4141093	14.806	13.970	13.719	0.713	S2303220108655	17.66			3	0.122	0483−0487362		17.04	21.08	17.94	15.36
25	165324.2−414720	1.659	16532414−4147222	11.989	11.567	11.458	1.608	S230322025129	13.49		13.86	0							

	XMMU J	SSB05								Other denominations					
X #	HHMMSS.s±DDAMAS	d_{cc}	name	V	V−I	B−V	U−B	R−Ha	Sp.Type	ID	HD/HDE	CD	CPD	Segg.	SBL98	Braes
[1]	[2]	[21]	[22]	[23]	[24]	[25]	[26]	[27]	[28]	[29]	[30]	[31]	[32]	[33]	[34]	[35]
1	165300.0−415444	1.231	928	17.515	1.699	1.336										
2	165304.3−415334	2.235	1065	17.960	2.047	1.541										
3	165305.2−415204	1.637	13015	19.757	2.755											
4	165306.9−414931															
5	165307.4−414659															
6	165307.4−414345	1.161	1147	8.471	0.358	0.240	−0.731									
7	165308.1−414533	0.458	13247	20.016	2.829											
8	165310.3−414733	1.157	1221	17.071	2.570	1.488										
9	165310.8−414451	0.919	1239	17.140	1.743	1.398	0.742									
10	165311.5−414755	2.744	13520	20.357	3.075											
11	165312.9−415049	0.871	1306	15.316	1.486	1.137	0.531									
12	165313.2−415222	1.555	1311	16.422	1.658	1.223	0.549									
13	165313.6−415133	1.465	1324	16.553	1.652	1.244	0.615									
14	165315.3−415011	1.078	13784	18.713	2.276	1.596										
15	165315.8−414436	0.389	13821	18.372	1.990	1.709										
16	165316.3−415139	2.362	13851	18.519	2.179	1.680										
17	165316.5−415024	2.317	13870	20.868	3.082											
18	165317.0−414412	1.373	1426	16.153	1.698	1.370	0.753								3021	
19	165318.4−415215	1.034	14024	20.390	3.195											
20	165318.7−415502	0.188	14041	19.530	2.547											
21	165318.9−415446															
22	165319.4−415431	1.367	1500	10.598	0.610	0.416	−0.437			HW331					19	
23	165320.6−414249	1.100	1535	16.870	1.894	1.496	0.926	−4.455							3075	
24	165322.0−414109	0.520	14282	18.967	2.472	1.707		−4.424							3119	
25	165324.2−414720	1.403	1615	13.892	1.132	0.876	0.259	−4.730							33	

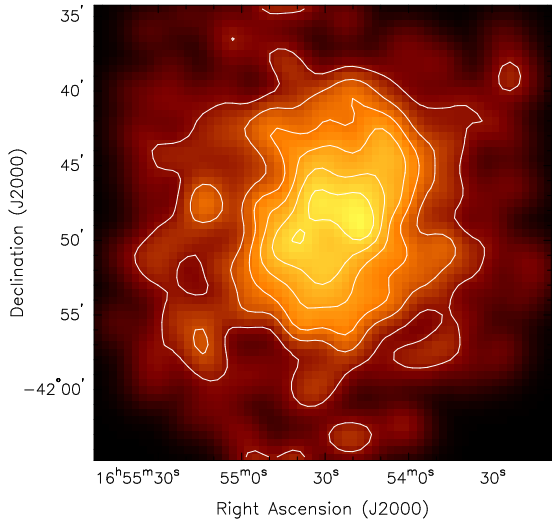

Fig. 7. 2-D distribution of the surface density of the X-ray sources. The image is centered on the location of HD 152248. The original source density chart was convolved with a Gaussian with $\sigma = 1'$. Overplotted contour levels are 1, 1.5, 2, 2.5, 3 and 3.5 sources per arcmin^2.

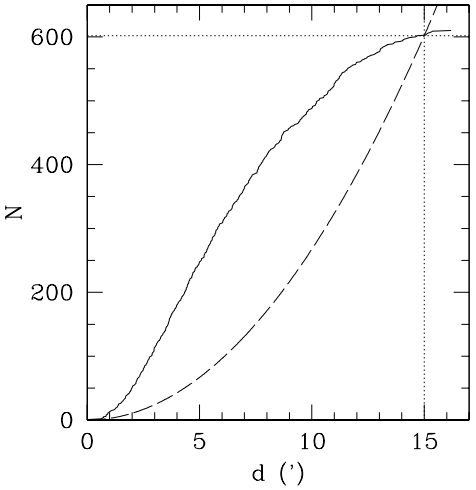

Fig. 8. Plain line: Cumulative distribution of the number of X-ray sources (N) with increasing distance (d) from HD 152248. **Dashed line:** idem, computed assuming a uniform distribution of the 602 sources (dotted horizontal line) within the inner 15′ (dotted vertical line) circle around HD 152248.

empirical conversion factor between the MOS1, MOS2 and pn count rates. These factors were then used to obtain *equivalent* pn count rates for sources that fall in the gaps of one or several instruments, yielding an approximately coherent source list whatever the position on the detectors. Figure 5 displays the source *pn-equivalent* count rates as a function of the distance from the central axis of the FOV – assumed to be the position of the binary HD 152248. A lower limit is clearly seen in the distribution. Selecting the faintest sources (i.e. the ones displaying the lowest *equivalent* count rates) in successive rings centered on HD 152248 provides an approximate sampling of this limit. We then adjusted a polynomial and derived an empirical detection limit in terms of *pn-equivalent* count rates ($cr_{\rm lim.}$) as a function of the distance (d) from the field axis. This limit (in units of 10^{-3} cnt s^{-1}) is described by the following relation:

$$cr_{\rm lim.}(d) = 2.49214 - 0.65577\,d + 0.11822\,d^2 - 0.00929\,d^3 + 0.00030\,d^4 \quad (5)$$

where d is the distance to HD 152248 expressed in arcmin. Eq. 5 is shown in Fig. 5. Clearly the detection limit is higher in the central part of the field ($d < 5'$), most probably because of the higher source density and because bright sources are preferentially located in the inner part. The sensitivity also decreases towards the CCD edges, as indicated both by the exposure maps and the sensitivity maps. Finally we used single temperature optically thin thermal plasma Raymond-Smith models to convert the *pn-equivalent* count rates given by Eq. 5 to fluxes and luminosities. For this purpose, we adopted the conversion computed by the WebPIMMS converter[3], assuming a density column of 0.26×10^{22} cm^{-2}, typical of the cluster interstellar absorbing column. Results are displayed in Fig. 6 for three different plasma temperatures. In conclusion, the flux detection limit is approximately located between about 3×10^{-15} and 1.5×10^{-14} erg cm^{-2} s^{-1}, depending on the distance from the detector axis and on the source spectrum.

[3] WebPIMMS is a NASA's HEASARC tool powered by PIMMS v3.6a. It is hosted at the following URL: http://heasarc.gsfc.nasa.gov/Tools/w3pimms.html

5. The X-ray sources in NGC 6231

This section presents an overview of the main properties of the X-ray sources in NGC 6231. No attempt will be made here to investigate the characteristics of the different sub-populations of the cluster. This work is postponed to devoted papers in preparation.

5.1. Spatial distribution

As seen from Figs. 1 to 3, there is an obvious clustering of the X-ray sources in the inner part of the FOV. Their spatial distribution projected on the sky presents, at first sight, an axi-symmetry around the centre of the field, i.e. the position of HD 152248. Considering the sources located at less than 15′ from HD 152248, we computed the geometrical centre of the source distribution. We also computed the *brightness* centre of the X-ray image. For this purpose, we adopted the pn-equivalent count rates for each source. The two centres are located slightly East from HD 152248, at no less than 30″ (see Fig. 3). From the two-dimensional map of the X-ray source density (Fig. 7), there is only a slight deviation from this scheme and the X-ray source distribution shows a slight N-S elongation. In the following, we however assume that the distance from the cluster centre, i.e. from HD 152248, remains the main parameter that shapes the source distribution. We also

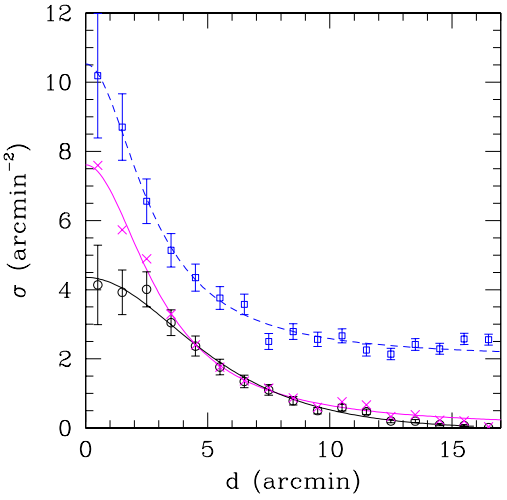

Fig. 9. Surface density profiles of the X-ray sources (open circles) and the optical sources (open squares) with $V < 17$. Crosses indicate the X-ray density profile corrected for the empirical EPIC sensitivity curve (see text). Best-fit King profiles are overplotted.

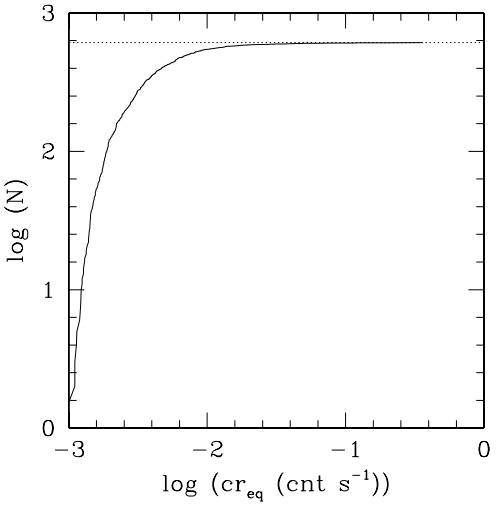

Fig. 10. Cumulative distribution of the number of sources with increasing *pn-equivalent* count rate. The horizontal dotted line indicates the total number of sources in the FOV.

adopted the HD 152248 position as the very centre of the cluster.

From Figs. 7 and 8, it is clear that the radial distribution of the sources is not uniform and that most of them lie within a 10′ radius around the cluster centre. We computed the radial density profile of the X-ray emitters and we adjusted a King empirical density profile (King 1962) for a spherically distributed source population :

$$f(d) = k\left[1/\sqrt{1+(d/d_{\rm c})^2} - 1/\sqrt{1+(d_{\rm t}/d_{\rm c})^2}\right]^2 \quad (6)$$

where k is the central density, $d_{\rm c}$ the core radius and $d_{\rm t}$ the limiting radius. The King profile is very sensitive to k and $d_{\rm c}$, but less sensitive to $d_{\rm t}$ which is indeed less meaningful for open clusters in the Galactic plane. The best fit parameters are $k = 8.9\,\mathrm{arcmin}^{-2}$, $d_{\rm c} = 6.5'$ and $d_{\rm t} = 20.5'$. As indicated by Figs. 5 and 6, our detection limit depends on the location of the source on the detector. In a second step, we thus applied a relative correction to the X-ray density profile, accounting for the sensibility difference as a function of the distance to the detector axis (crosses in Fig. 9). The profile is now sharper and is described by: $k = 7.6\,\mathrm{arcmin}^{-2}$, $d_{\rm c} = 3.1'$ and $d_{\rm t} = 1.5\times10^3$ arcmin. In Fig. 9, we also present the density profile of stars in SSB05, restrained to objects brighter than 17 in the V band. NGC 6231 is embedded in the Sco OB 1 association. As a consequence, the surface density does not drop to zero in the outer region of the field. We thus subtracted a threshold of $2\,\mathrm{arcmin}^{-2}$ prior to the adjustment. King best-fit values are this time $k = 8.6\,\mathrm{arcmin}^{-2}$, $d_{\rm c} = 2.7'$ and $d_{\rm t} = 1.4\times10^3$ arcmin. From Fig. 9, the correlation between the X-ray and optical surface density profile is obvious and yields similar core radii for NGC 6231. It further suggests that most of the detected X-ray emitters are physically belonging to NGC 6231.

As discussed in e.g. Sung et al. (2004), X-ray emission is probably one of the best membership criterion for young stars in open clusters and the present X-ray observations probably provide the best census of PMS stars in NGC 6231. However, the NGC 6231 X-ray sample might be contaminated by foreground (field stars) and background (AGNs) objects. As a last check, we thus roughly estimated the probable number of foreground and background X-ray sources detected in the present campaign. Starting with the foreground objects, we proceeded as explained below. Accounting for the different typical X-ray luminosities for field stars of spectral type O to M and for our flux detection limit, we estimated the maximum distance at which a star should be located and still be detected. Using the so-derived distance, we computed the volume projected onto the XMM-*Newton* FOV. As a last step, we adopted typical star densities in the solar neighbourhood as quoted by Allen (1973) for the different spectral types. We finally end up with about 20 foreground X-ray sources, most of which are expected to be G-type objects (12 stars) and F-type dwarves (4 or 5 stars).

We also obtain a rough estimate of the number of extragalactic background sources in our EPIC field. The Galactic coordinates of the cluster are $l_{\rm II} = 343.46°$, $b_{\rm II} = +1.19°$. Therefore, the total neutral hydrogen column density along this direction must be extremely large and should produce a substantial absorption of X-ray photons from extragalactic sources. Although they are in principle not suited for directions at $|b_{\rm II}| \leq 5°$, we used the *DIRBE/IRAS* extinction maps provided by Schlegel et al. (1998) to derive a first order estimate of the total column density. In this way, we find a total Galactic $E(B-V)$ of about 5.6 mag. Using the gas to dust ratio of Bohlin et al. (1978), we thus estimate a neutral hydrogen column density of $\sim 3.2\times10^{22}\,\mathrm{cm}^{-2}$. Assuming that extra-

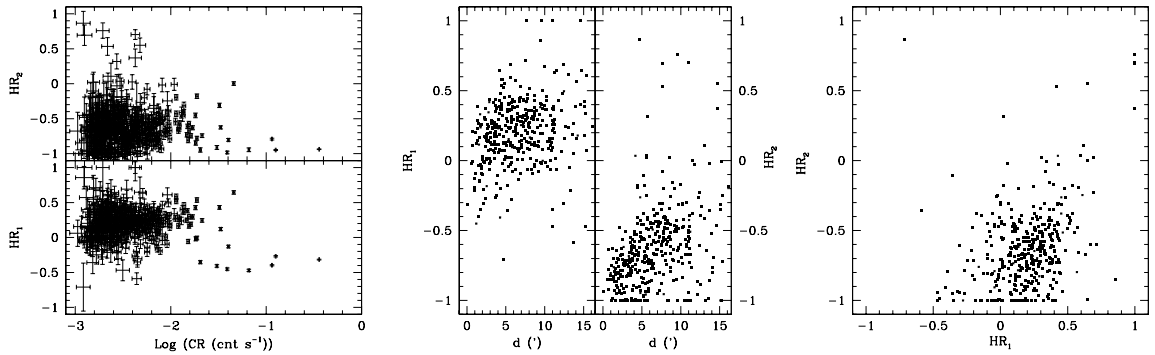

Fig. 11. Left panel: Hardness ratios versus count rate. **Middle panel:** Hardness ratios versus distance (d) from the FOV centre. **Right panel:** HR_2 versus HR_1. The three panels are plotted for the sources detected with the pn instrument. Results for the EPIC MOS instruments are similar.

galactic background sources have a power-law spectrum with a photon index of 1.4, and suffer a total interstellar absorption of 3.2×10^{22} cm^{-2}, the mean detection limit 1.9×10^{-3} cnt s^{-1} with the pn camera translates into unabsorbed fluxes of 1.2×10^{-14} and 3.5×10^{-13} erg cm^{-2} s^{-1} in the 0.5 – 2.0 keV and 2.0 – 10 keV band respectively. Using the $\log N - \log S$ relation from Giacconi et al. (2001), one expects thus about 13 – 16 extragalactic objects among the detected sources. Thus, about 2% of the total number of sources could be background AGNs. It should be emphasized that these background AGNs are expected to appear as rather hard (i.e. heavily absorbed) X-ray sources.

In summary, both the geometrical and X-ray brightness centres of the detected sources correspond to the cluster centre. The radial profile of the source density is well correlated with the optical source radial profile. Both indicate a cluster core radius close to 3′. Finally, we expect that only about 6% of the presently detected sources correspond to foreground or background objects. We thus propose that the large majority of the X-ray emitters revealed by the present XMM-*Newton* campaign are mostly belonging to NGC 6231. Some of them might alternatively belong to the Sco OB 1 association, in which NGC 6231 is embedded.

5.2. Emission distribution

While HD 152248, the brightest X-ray emitter in the FOV, displays an equivalent-pn count rate larger that 0.36 cnt s^{-1}, most of the other sources are much fainter with a count rate below 10^{-2} cnt s^{-1}(Fig. 10). It is clear from Fig. 1 that most of the brightest sources – associated with the O-type objects of the cluster – are relatively soft while the majority of the X-ray emitters have their maximum of emission in the medium band. Except for the brightest sources thus, there is no obvious correlation between the source intensity and the source hardness ratios. On average, the detected sources are moderately hard with $HR_1 > 0$ and $HR_2 < 0$ (Fig. 11). The hardness ratios might however show a slight increase towards the edge of the detectors, probably due to the relative dominance of low-mass stars in the outer regions of the FOV. The histograms of the detected sources count-rates in the S_X, M_X and H_X bands (Fig. 12) reveal clear peaks around 0.7, 1.0 and 0.2×10^{-3} cnt s^{-1} respectively. The count rate in the 0.5-10.0 keV band clusters at 2×10^{-3} cnt s^{-1} and the two hardness ratios around 0.2 and −0.6 respectively. Accounting for the cluster typical ISM absorbing column $n_{\rm H,ISM} = 0.26 \times 10^{22}$ cm^{-2}, these values are roughly described by a MEKAL model with a temperature of kT = 1.0 – 1.5. The corresponding observed flux is about 5×10^{-15} erg cm^{-2} s^{-1}. Adopting a distance modulus DM = 11.07, this yields a luminosity $\log(L_X) \sim 30.5$ (erg s^{-1}) for a typical X-ray emitter in the cluster.

6. Summary

We presented the first results of an XMM-*Newton* campaign on the young open cluster NGC 6231 in the Sco OB 1 association. For an effective duration of at least 170 ksec in the two EPIC MOS instruments and of about 150 ksec in the EPIC pn, the campaign was splitted into six successive observations performed within 5 days. The combined image, built from the data collected by the three EPIC instruments during the six pointings, reveals an extremely crowded field. Based on the SAS task *emldetect*, we detect 610 X-ray sources among which 19 are reported as extended sources. These latter are probably formed by non-resolved point-like sources rather than truly extended sources. We cross-correlate the present X-ray catalogue of the FOV with several optical/infrared catalogues and we find an optical/infrared counterpart for 536 X-ray sources within a 3″ cross-correlation radius. We estimate our detection limit to lie between about 3×10^{-15} and 1.5×10^{-14} erg cm^{-2} s^{-1} depending on the position on the detectors and on the source spectrum.

The source surface density distribution peaks at the centre of the cluster, which we find to be located very near HD 152248, and presents a slight N-S extension. Concerning the radial profile of the surface density distribution, over 50% of the sources are confined within a 5′ radius from the cluster centre and over 80% within 10′. The estimated contamination by foreground and background objects is about 6%. There is a good correlation with the distribution of stars brighter than

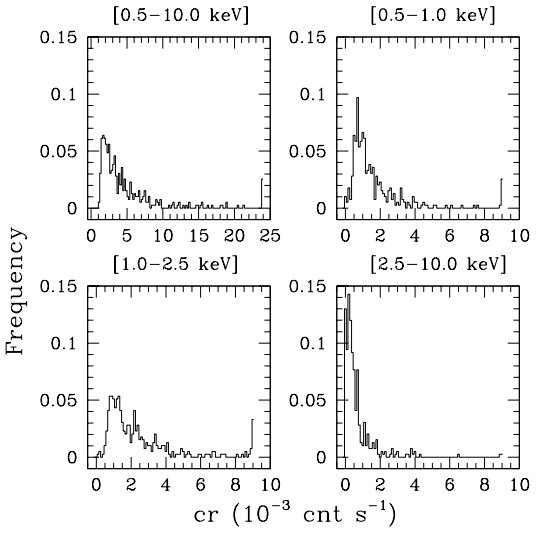

Fig. 12. X-ray emitters count-rates distribution in the different energy bands considered. The four panels were plotted using the 392 sources detected with the pn instrument only. Results for the EPIC MOS instruments are similar. The last bin indicates the contributions of the brightest X-ray sources.

$V = 17$, suggesting that most of the sources physically belong to NGC 6231. The radial surface density profile of the X-ray sources is well described by a King profile with a core radius of about 6′. Correcting the source density profile by the empirical spatial response of the present campaign yields a lower core radius of 3′, similar to the one indicated by the $V < 17$ optical sources density profile.

Finally, beside a few bright and soft objects correlated with the O-type stars of the cluster, the large majority of the X-ray population is relatively faint (pn-equivalent count rate below 10^{-2} cnt s^{-1}) and displays an intermediate spectrum of a typical energy probably around 1.0-2.0 keV. Typical count rates for the sources are 2.0, 0.7, 1.0 and 0.2×10^{-3} cnt s^{-1} respectively in the total energy band (0.5-10.0 keV), and in the three energy sub-ranges 0.5-1.0, 1.0-2.5 and 2.5-10.0 keV. At the NGC 6231 cluster distance, these values roughly correspond to an X-ray luminosity about $\log(L_X) \sim 30.5$ (erg s^{-1}).

More detailed investigations of the X-ray properties of the different sub-populations (early-type stars, PMS objects, ...) of the cluster will be presented in subsequent papers in this series. Finally, the X-ray data related to specific early-type systems of particular interest are presented in dedicated papers, together with the derivation of their orbital and physical parameters obtained on the basis of an extensive spectral monitoring campaign in the optical domain.

Acknowledgements. It is a pleasure to thank Dr. W. Seggewiss for providing a copy of his original paper on the cluster photometry (Seggewiss 1968b), our system manager, A. Detal, for essential assistance in installing and handling the successive SAS versions and Dr. J.-F. Claeskens for sharing numerical routines. This research is also supported in part by contract P5/36 "Pôle d'Attraction Interuniversitaire" (Belgian Federal Science Policy Office) and through the PRODEX XMM-OM and INTEGRAL projects. H. Sung acknowledges the support of the Korea Science and Engineering Foundation (KOSEF) to the Astrophysical Research Center for the Structure and Evolution of the Cosmos (ARCSEC″) at Sejong University.

This publication makes use of data products from USNO B1.0, the Two Micron All Sky Survey (2MASS) and the Guide Star catalogue (GSC) II. The 2MASS is a joint project of the University of Massachusetts and the Infrared Processing and Analysis Center/California Institute of Technology, funded by the NASA and the NSF. The GSC II is a joint project of the Space Telescope Science Institute and the Osservatorio Astronomico di Torino. Additional support is provided by the ESO, the Space Telescope European Coordinating Facility, the International GEMINI project and the ESA Astrophysics Division. The SIMBAD database and the Vizier catalogue access tool (CDS, Strasbourg, France) have been consulted for the bibliography and in the purpose of object cross-identification.

References

Allen, C. W. 1973, Astrophysical quantities (London: University of London, Athlone Press, 3rd ed.)
Arenou, F., & Luri, X. 1999, in ASP Conf. Ser., Vol. 167, Harmonizing Cosmic Distance Scales in a Post-HIPPARCOS Era, ed. D. Egret & A. Heck, 13
Arentoft, T., Sterken, C., Knudsen, M. R., et al. 2001, A&A, 380, 599
Balona, L. A. 1983, MNRAS, 203, 1041
Balona, L. A. 1992, MNRAS, 254, 404
Balona, L. A., & Engelbrecht, C. A. 1985, MNRAS, 212, 889
Balona, L. A., & Laney, C. D. 1995, MNRAS, 276, 627
Baume, G., Vázquez, R. A., & Feinstein, A. 1999, A&AS, 137, 233
Bohlin, R. C., Savage, B. D., & Drake, J. F. 1978, ApJ, 224, 132
Bok, B. J., Bok, P. F., & Graham, J. A. 1966, MNRAS, 131, 247
Braes, L. L. E. 1967, Bulletin of the Astronomical Institute of the Netherlands Supplement Series, 2, 1
Breckinridge, J. B., & Kron, G. E. 1963, PASP, 75, 248
Brownlee, R. R., & Cox, A. N. 1953, ApJ, 118, 165
Cash, W. 1979, ApJ, 228, 939
Conti, P. S., & Alschuler, W. R. 1971, ApJ, 170, 325
Corcoran, M. F. 1996, in Revista Mexicana de Astronomia y Astrofisica Conference Series, Vol. 5, 54
Corcoran, M. F. 1999, in Revista Mexicana de Astronomia y Astrofisica Conference Series, Vol. 8, 131
Crawford, I. A. 2001, MNRAS, 328, 1115
Crawford, D. L., Barnes, J. V., Hill, G., & Perry, C. L. 1971, AJ, 76, 1048
Cutri, R. M., Skrutskie, M. F., Van Dyk, S., et al. 2003, University of Massachusetts and Infrared Processing and Analysis Center (IPAC/California Institute of Technology)
Damiani, F., Flaccomio, E., Micela, G., et al. 2004, ApJ, 608, 781
den Herder, J. W., Brinkman, A. C., Kahn, S. M., et al. 2001, A&A, 365, L7
Feast, M. W., Stoy, R. H., Thackeray, A. D., & Wesselink, A. J. 1961, MNRAS, 122, 239

Feinstein, A., & Ferrer, O. E. 1968, PASP, 80, 410
Feinstein, C., Martínez, R., Vergne, M. M., Baume, G., & Vázquez, R. 2003, ApJ, 598, 349
García, B., & Mermilliod, J. C. 2001, A&A, 368, 122
Garrison, R. F., & Schild, R. E. 1979, AJ, 84, 1020
Giacconi, R., Rosati, P., Tozzi, P., et al. 2001, ApJ, 551, 624
GSC 2.2. 2001, Space Telescope Science Institute (STScI) and Osservatorio Astronomico di Torino
Heske, A., & Wendker, H. J. 1984, A&AS, 57, 205
Hill, G., Crawford, D. L., & Barnes, J. V. 1974, AJ, 79, 1271
Houck, T. E. 1956, Ph.D. Thesis
Jansen, F., Lumb, D., Altieri, B., et al. 2001, A&A, 365, L1
Jeffries, R. D., Thurston, M. R., & Pye, J. P. 1997, MNRAS, 287, 350
King, I. 1962, AJ, 67, 471
Laval, A. 1972, A&A, 21, 271
Levato, H., & Malaroda, S. 1980, PASP, 92, 323
Levato, H., & Morrell, N. 1983, Astrophys. Lett., 23, 183
Levato, H., Morrell, N., Garcia, B., & Malaroda, S. 1988, ApJS, 68, 319
Lührs, S. 1997, PASP, 109, 504
Makarov, V. V. 2003, AJ, 126, 2408
Marggraf, O., Bluhm, H., & de Boer, K. S. 2004, A&A, 416, 251
Mason, B. D., Gies, D. R., Hartkopf, W. I., et al. 1998, AJ, 115, 821
Mason, K. O., Breeveld, A., Much, R., et al. 2001, A&A, 365, L36
Mathys, G. 1988, A&AS, 76, 427
Mathys, G. 1989, A&AS, 81, 237
Mermilliod, J. C. 1981, A&A, 97, 235
Meynet, G., Mermilliod, J.-C., & Maeder, A. 1993, A&AS, 98, 477
Monet, D. G., Levine, S. E., Canzian, B., et al. 2003, AJ, 125, 984
Morgan, W. W., González, G., & González, G. 1953a, ApJ, 118, 345
Morgan, W. W., Whitford, A. E., & Code, A. D. 1953b, ApJ, 118, 318
Penny, L. J., Bagnuolo, W. G., & Gies, D. R. 1994, Space Science Reviews, 66, 323
Penny, L. R., Gies, D. R., & Bagnuolo, W. G. 1999, ApJ, 518, 450
Perry, C. L., Hill, G., Younger, P. F., & Barnes, J. V. 1990, A&AS, 86, 415
Perry, C. L., Hill, G., & Christodoulou, D. M. 1991, A&AS, 90, 195
Preibisch, T., & Zinnecker, H. 2004, A&A, 422, 1001
Raboud, D. 1996, A&A, 315, 384
Raboud, D., & Mermilliod, J.-C. 1998, A&A, 333, 897
Raboud, D., Cramer, N., & Bernasconi, P. A. 1997, A&A, 325, 167
Rauw, G., Nazé, Y., Gosset, E., et al. 2002, A&A, 395, 499
Rauw, G., De Becker, M., Gosset, E., Pittard, J. M., & Stevens, I. R. 2003, A&A, 407, 925
Sana, H., Rauw, G., & Gosset, E. 2001, A&A, 370, 121
Sana, H., Rauw, G., Gosset, E., & Vreux, J.-M. 2002, in ASP Conf. Ser., Vol. 260, Interacting Winds from Massive Stars, ed. A. Moffat & N. St-Louis, 431
Sana, H., Hensberge, H., Rauw, G., & Gosset, E. 2003, A&A, 405, 1063
Sana, H., Stevens, I. R., Gosset, E., Rauw, G., & Vreux, J.-M. 2004, MNRAS, 350, 809
Sana, H., Antokhina, E., Royer, P., et al. 2005a, A&A, in press
Sana, H., Nazé, Y., Gosset, E., et al. 2005b, in Massive Stars in Interacting Binaries, ed. A. Moffat & N. St-Louis, ASP Conf. Ser., 5p., in press
Sana, H., Rauw, G., & Gosset, E. 2005c, A&A, submitted
Schild, R. E., Hiltner, W. A., & Sanduleak, N. 1969, ApJ, 156, 609
Schlegel, D. J., Finkbeiner, D. P., & Davis, M. 1998, ApJ, 500, 525
Seggewiss, W. 1968a, Zeitschrift fur Astrophysics, 68, 142
Seggewiss, W. 1968b, Veroeffentlichungen des Astronomisches Institute der Universitaet Bonn, 79
Setia Gunawan, D. Y. A., Chapman, J. M., Stevens, I. R., Rauw, G., & Leitherer, C. 2002, private communication
Setia Gunawan, D. Y. A., Chapman, J. M., Stevens, I. R., Rauw, G., & Leitherer, C. 2003, in IAU Symposium, Vol. 212, A Massive Star Odyssey: from main sequence to supernova, ed. K. van der Hucht, A. Herrero, & C. Esteban, 230
Shobbrook, R. R. 1983, MNRAS, 205, 1229
Skinner, S., Gagné, M., & Belzer, E. 2003, ApJ, 598, 375
Stickland, D. J., & Lloyd, C. 2001, The Observatory, 121, 1
Stickland, D. J., Lloyd, C., Penny, L. R., Gies, D. R., & Bagnuolo, W. G. 1996, The Observatory, 116, 226
Stickland, D. J., Lloyd, C., & Penny, L. R. 1997, The Observatory, 117, 213
Strüder, L., Briel, U., Dennerl, K., et al. 2001, A&A, 365, L18
Struve, O. 1944, ApJ, 100, 189
Sung, H., Bessell, M. S., & Lee, S. 1998, AJ, 115, 734
Sung, H., Bessell, M. S., & Chun, M. 2004, AJ, 128, 1684
Turner, M. J. L., Abbey, A., Arnaud, M., et al. 2001, A&A, 365, L27
van Genderen, A. M., Bijleveld, W., & van Groningen, E. 1984, A&AS, 58, 537
Walborn, N. R. 1972, AJ, 77, 312
Walraven, T., & Walraven, J. H. 1960, Bull. Astron. Inst. Netherlands, 15, 67

Appendix A: On correcting the L_2 values in SAS v 5.4.1

The equivalent (or transformed) logarithmic likelihood L_2 associated with each source detected by the SAS task *emldetect* (column DET_ML in the output file) is given by:

$$L_2 = -\ln\left(1 - P\left(\frac{\nu}{2}, L'\right)\right) \tag{A.1}$$

with

$$L' = \sum_{i=1}^{i=n} L_i, \tag{A.2}$$

where P is the incomplete Gamma function, ν is the number of degrees of freedom (d.o.f.) of the fit, n is the number of input

images (i.e. the number of energy bands times the number of instruments considered), and $L_i = C_i/2$ with C_i being the Cash statistics for image i, specially designed by Cash (1979) for photon counting experiments. More insight into the physical meaning of Eq. A.1 will be given in the next section. In this section we focus on the implemented patch for correcting L_2 values.

Indeed the logarithmic likelihood L_2 is known to be erroneous in SAS version v 5.4.1 and earlier versions (XMM-*Newton* News #29 – 11-Mar-2003). According to SAS Observation Report SASv5.4/8665[4], the factor 2 in equation $L_i = C_i/2$ has been forgotten, leading to erroneous L' and hence L_2. Knowing the number of degrees of freedom ν, it is a simple exercise to invert Eq. A.1 and to obtain values for L'. From Eq. A.2, it is obvious that the corrected value for L' is $L'_{\rm corr} = L'/2$, to be used in Eq. A.1 to recover the corrected $L_2^{\rm corr}$ value that can then be used for scientific analyses.

For large values of L_2 ($L_2 \gtrsim 10\,000$) the numerical limits of classical compilers are however exceeded. Fortunately Eq. A.1 tends to a linear relation between L' and L_2 for large values and for a given ν. The correction is therefore straightforward with $L_2^{\rm corr} = L_2/2$. Though this bug was present at the time we analysed the data, this issue has been fixed later in SAS version v 6.1. We checked our corrected $L_2^{\rm corr}$ values against SAS v 6.1 and found them in close agreement.

Appendix B: On the choice of coherent detection thresholds using the transformed likelihood L_2

As it can be deduced from the previous section (App. A), the logarithmic likelihood L_2 is related to the probability that a detected source is due to background fluctuations (large L_2). Computed for each sources of the input list, it uses a combination of the Cash statistics C_i obtained for the different input images i. The Cash statistics C_i actually obeys a χ^2 distribution (Cash 1979) with 3 or 4 degrees of freedom (i.e. the intensity, the X- and Y-coordinates of the source and, eventually, the extension of the source if allowed). Therefore any linear combination of n C_i, and hence any computed $2L'$, also follows a χ^2 statistics with $n+2$ or $n+3$ d.o.f. In this sense, the transformed logarithmic likelihood L_2 is indeed linked, through the simple relationship

$$L_2 = -\ln(Q), \tag{B.1}$$

where

$$Q = Q\left(\frac{\nu}{2}, L'\right) = 1 - P\left(\frac{\nu}{2}, L'\right), \tag{B.2}$$

to the probability Q for a random Poissonian fluctuation of the expected background to have caused such a high value of $2L' = \sum_{i=1}^{i=n} C_i$ as the one observed. The equivalent logarithmic likelihood L_2 will therefore be large if the observed source is likely not produced by a statistical fluctuation, and small otherwise.

As a consequence, a threshold in L_2 can in principle be adopted as a detection limit. However, as we show below, while the expression given in Eq. B.2 indeed takes into account the number ν of d.o.f. to compute the Q probability and the subsequent value of L_2, it does not allow a direct comparison between L_2 obtained with different numbers of input images. This statement is illustrated in the following due consideration

[4] http://xmm.vilspa.esa.es/xmmhelp/

Table B.1. Illustration of consistently determined L_2 thresholds (Col. 2) for the different instruments and instrument combinations reported in Col. 1. The number of input images (n) and corresponding degrees of freedom (ν) are given in Cols. 3 and 4. L' (Col. 5) is linked to L_2 through Eq. A.1. A given L' is also linked to other L' of this table through Eq. A.2 (see text). We emphasize that adopting any of the L_2 or L' presented in this table automatically determines the other values of L' and L_2 reported here below.

Instr. Comb.	L_2	n	ν	L'
MOS1	10.00	3	5	13.75
MOS2	10.00	3	5	13.75
pn	22.77	3	5	27.51
MOS1+MOS2	19.25	6	8	27.51
MOS1+pn	31.70	6	8	41.26
MOS2+pn	31.70	6	8	41.26
MOS1+MOS2+pn	40.86	9	11	55.02

Let us assume that we are dealing, for example, with 3 energy bands and let us only consider point-like source fitting (parameter *withextendedsource*='no'). For the purpose of the demonstration, let us adopt a uniform detection threshold, for any instrument or instrument combination, of $L_2 = 10$.

As a first step, let us deal with the source detection on the EPIC MOS1 images. In this particular configuration, there are three input images ($n = 3$) that correspond to the three energy bands. From the inversion of Eq. A.1 with $L_2^{\rm MOS1} = 10$ and $\nu = 5$, we obtain $L'_{\rm MOS1} = 13.75$; where $L'_{\rm MOS1}$ is the sum of the $L_i^{\rm MOS1}$ for each of the three input images as given by Eq. A.2, i.e.

$$L'_{\rm MOS1} = \sum_{i=1}^{i=3} L_i^{\rm MOS1}.$$

Now assuming that the two instruments MOS1 and MOS2 are exactly identical, a detection threshold $L_2^{\rm MOS2} = 10$ similarly corresponds to $L'_{\rm MOS2} = \sum_{i=1}^{i=3} L_i^{\rm MOS2} = 13.75$.

In a next step, let us work with a combination of the two EPIC MOS instruments. Equation A.2 allows us to easily build the combined $L'_{\rm MOS1+MOS2}$ as the sum of the L_i for each instrument and energy band :

$$L'_{\rm MOS1+MOS2} = \sum_{i=1}^{i=3} L_i^{\rm MOS1} + \sum_{i=1}^{i=3} L_i^{\rm MOS2} = 27.5.$$

With two instruments and hence 6 images, $L'_{\rm MOS1+MOS2}$ follows a χ^2 distribution with 8 d.o.f. ($\nu = 8$). Equation A.1 then gives $L_2^{\rm MOS1+MOS2} = 19.25$ quite differenr from the value $L_2^{\rm MOS1+MOS2} = 10$ obtained with the adopted constant threshold limit $L_2 = 10$. The situation is even worse while dealing with the EPIC pn detector. Indeed, making the reasonable assumption that $L'_{pn} \approx 2L'_{\rm MOS}$, a similar reasoning would gives $L_2^{\rm pn} = 22.77$, $L_2^{\rm MOS1+pn} = L_2^{\rm MOS2+pn} = 31.70$ and $L_2^{\rm MOS1+MOS2+pn} = 40.86$ far from the value of 10.0 initially adopted. Basically, when combining several instruments

together, we improve the Poissonian statistics. Consequently, the fact that we adopt a constant value for L_2 implies a cut-off in fluxes or count rates that is dependent on the number of instruments considered. Instead, if we prefer to stabilize the cut-off in absolute values rather independently of the instruments considered, we have to adapt the L_2 value to the situation. The intermediate results and number of d.o.f. used in establishing these values are given in Table B.1.

One of the main results of the present discussion is that one can not adopt a constant threshold limit in L_2 for different instrument combinations. We similarly established that one can not use arbitrarily fixed L_2 thresholds either. Indeed we have shown that the L_2 thresholds in different combinations are linked through Eqs. A.1 and A.2 and through the detectors physical characteristics that condition the C_i values. In consequence adopting a particular value as a threshold for a specific instrument or instrument combination implicitly assigns related values to the L_2 thresholds for any other instrument or combination considered. Therefore, if one wants to adopt a consistent detection threshold whatever the considered instrument or combination, the previous reasoning becomes a forced step. This issue is particularly relevant to consistently deal with sources that fall on gaps or on specific detector areas where the different instruments do not overlap.

We finally remind the reader that the above presented method to determine self-consistent L_2 thresholds rests on two simplifying, but reasonable, assumptions. The first is that the two EPIC MOS instruments are identical. The second is that the EPIC pn gives approximately twice as much counts as the MOS instruments, which is expressed by $L'_{\rm pn} \approx 2L'_{\rm MOS}$. Any refinement of these two assumptions (i.e. any relation giving the L' of one instrument as a more realistic function of the L' of the other instruments) can be easily included in the method. This is however beyond the scope of the present discussion.

Astronomy & Astrophysics manuscript no. ob˙v2 May 22, 2005
(DOI: will be inserted by hand later)

An XMM-*Newton* view of the young open cluster NGC 6231⋆

II. The early-type star population⋆⋆

H. Sana ⋆⋆⋆, G. Rauw†, Y. Nazé, E. Gosset†, and J.-M. Vreux

Institut d'Astrophysique et de Géophysique, University of Liège, Allée du 6 Août 17, Bât. B5c, B-4000 Liège, Belgium
e-mail: sana@astro.ulg.ac.be, rauw@astro.ulg.ac.be, naze@astro.ulg.ac.be, gosset@astro.ulg.ac.be, vreux@astro.ulg.ac.be

Received September 15, 1996; accepted March 16, 1997

Abstract. In this second paper of the series, we pursue the analysis of the 180 ksec XMM-*Newton* campaign (see Paper I) towards the young open cluster NGC 6231 and we focus on its rich early-type star population. We present a literature-based census of the OB-stars in the monitored field of view and we report more than one hundred objects, among which one third can be associated with an X-ray source.

All the O-type stars are detected in the X-ray domain as soft and reasonably strong emitters. Their spectra are usually well reproduced by two- or three-temperature `mekal` models. The main two `mekal` components have kT about 0.3 and 0.7 keV. In the 0.5-10.0 keV band, the X-ray luminosities of the O-type stars scale with their bolometric luminosities as $\log L_{\rm X} - \log L_{\rm bol} = -6.912 \pm 0.153$. Such a scaling-law holds in the soft (0.5-1.0 keV) and intermediate (1.0-2.5 keV) bands but breaks down in the hard band. The two colliding wind binaries in our sample clearly deviate from this scheme. However, the remaining objects shows a very limited dispersion (40% or 20% according to whether 'cold' dwarfs are included or not), much smaller thus than obtained from previous studies. A new analysis of the Carina data sample of Albacete Colombo et al. (2003) confirms much of these conclusions. At our detection threshold and with our sample, the sole identified mechanism that produces significant modulations in the O star X-ray emission is related to wind interaction. We thus conclude that the intrinsic X-ray emission of O-type stars has a mostly constant level for a given star, and that this level is tightly related to the intrinsic stellar properties of the object.

Among B-type stars, the detection rate is only about 25% and remains mostly uniform throughout the different sub-populations of B stars. The associated X-ray spectra are harder than those of O-type stars, with a second temperature usually above 1.5 keV. The spectral and time analyses point towards the detected emission to be associated with a visual (on the line of sight) or physical (in a multiple system) PMS companion. However, we still observe a significant correlation between the bolometric luminosity of the B star and the measured X-ray luminosity. The best fit power-law in the 0.5-10.0 keV band yields $\log L_{\rm X} = 0.22(\pm0.06) \log L_{\rm bol} + 22.8(\pm2.4)$. The origin of this relation remains a puzzle. The demarcation line between these two behaviours and the extent of the *canonical* O-star relation towards lower luminosities remains poorly constrained and, indeed, the transition zone is poorly mapped by the present studied sample. It should however occur at about $L_{\rm bol} \approx 10^{38}$ erg s^{-1} as previously suggested by Berghöfer et al. (1997).

Key words. Stars: fundamental parameters – Stars: early-type – X-rays: individuals: NGC 6231 – X-rays: stars – Open clusters and associations: individual: NGC 6231

1. Introduction

X-ray emission from early-type stars of spectral type O was, in December 1978, one of the earliest findings of the EINSTEIN satellite (Harnden et al. 1979; Seward et al. 1979). It was soon realized that all O-type stars were X-ray emitters. Most of them were characterized as soft (kT < 1 keV) and reasonably strong ($10^{31} \lesssim L_{\rm X} \lesssim 10^{33}$ erg s^{-1}) X-ray emitters. Harnden et al. (1979) already suggested that the X-ray luminosity was directly linked to the characteristic luminosity of the emitter, though at the time the authors proposed a scaling law between $L_{\rm X}$ and the visual luminosity. However as the stars of their sample had mostly the same colors, it is equivalent to assert that $L_{\rm X}$ scales with $L_{\rm bol}$. Using various samples of stars observed with EINSTEIN, different authors (Long & White 1980; Pallavicini et al. 1981; Cassinelli et al. 1981;

Send offprint requests to: H. Sana

⋆ Based on observations collected with XMM-*Newton*, an ESA science mission with instruments and contributions directly funded by ESA Member States and the USA (NASA).

⋆⋆ Table 2 and Figs. 2 to 6 are only available in the electronic version of the paper.

⋆⋆⋆ FNRS Research Fellow (Belgium)

† FNRS Research Associate (Belgium)

Vaiana et al. 1981; Seward & Chlebowski 1982) confirmed the so-called *canonical* relation $L_X \approx 10^{-7}\ L_{bol}$. Based on the EINSTEIN *X-ray Observatory catalog of O-type stars* (Chlebowski et al. 1989), Sciortino et al. (1990) performed a more comprehensive study of the *relationship between the optical and X-ray properties of O-type stars*. They confirmed the existence of a *canonical* $L_X - L_{bol}$ relation, though with a rather large dispersion. They were unable to find any significant correlation with the rotation rate ($v \sin i$), the wind terminal velocity (v_∞) or the mass-loss rate ($\dot{M}$), but observed a strong correlation with the wind momentum ($\dot{M}v_\infty$) and with the wind luminosity ($0.5\dot{M}v_\infty^2$). More recently, Berghöfer et al. (1997) investigated the properties of the bright OB-type stars detected in the ROSAT all-sky survey (Berghöfer et al. 1996) and found that the *canonical* relation extends down to spectral type B1-B1.5. They established the separation line between the O-star relation and a less constrained relation for B-stars to lie at a bolometric luminosity $L_{bol} \approx 10^{38}$ erg s^{-1}.

Historically, two physically different models have been proposed to explain the hot-star X-ray emission. Cassinelli & Olson (1979) suggested a scaled-up version of a solar-type *coronal emission* model that yielded a roughly correct prediction for the X-ray flux but could not render the softness of the observed spectrum. Indeed in the coronal emission model, the X-rays are produced near the photosphere and are thus expected to suffer absorption by the overlying dense wind. Such an absorption is however not seen in the X-ray spectrum of hot stars. This suggests that the X-ray emission is rather produced throughout a significant fraction of the wind volume, which has been a strong argument in favor of the *embedded wind-shock* model. In this second model, the X-ray emission is supposed to arise from shocks occurring in the denser layers of the winds and that grow from small-scale instabilities of the line-driven winds. Since the phenomenological model of Lucy (1982), hydrodynamical simulations (e.g. Owocki et al. 1988; Feldmeier et al. 1997) have brought further support to this interpretation.

However, recent high resolution spectral observations of early-type stars are bringing the wind shock model to its limits. Indeed the unprecedented spectral resolution reached by the XMM-*Newton* and *Chandra* observatories (corresponding to about 300 km s^{-1} in velocity space) allows now to probe the widths and profiles of the X-ray emission lines seen in the spectra of hot stars. These contribute to put constraints on the velocity (Doppler broadening) and location (*f/r* line ratio, Porquet et al. 2001) of the emitting plasma, yielding thus an unprecedented characterization of its localization in the expanding winds. Kramer et al. (2003) reported that the O-type supergiant ζ Puppis (O4 Ief) displays broad, blue-shifted and asymmetric line profiles that are generally consistent with the wind-shock model. However, observations of other early-type stars suggest different pictures and hybrid magnetic wind models have been proposed. For example, the X-ray emission lines in the spectrum of τ Scorpii (B0.2 V) are significantly narrower than what would be expected from the *standard* wind-shock model (Cohen et al. 2003). These authors rather suggested *magnetically confined* wind shocks (ud-Doula & Owocki 2002), eventually coupled with the *clump infall* model (Howk et al. 2000), as the prime origin for the observed X-ray emission. A similar model was also successfully applied to the magnetic rotator θ^1 Ori C (O5.5 V) (Gagné et al. 2005). Finally Schulz et al. (2003) have suggested that young massive stars could enter the main sequence carrying a significant residual magnetic field. Therefore, massive ZAMS stars could generate their X-ray luminosities via the *standard* model and magnetic confinement may provide an additional source of X-rays.

Compared to single stars of the same spectral type, close massive binaries are also known to display an extra X-ray emission (Chlebowski & Garmany 1991) which is generally attributed to a wind-wind collision. In a binary system, the winds from the two stars are indeed expected to interact through an hydrodynamical shock, leading to the formation of a shock region whose position is roughly determined by the wind ram pressure equilibrium. The so-called interaction region is delimited by two curved shock surfaces where the winds actually collide. Within the interaction region, the shock gas is expected to be heated to temperatures of a few 10^7 K and to generate a substantial amount of X-rays, which are thus produced in addition to the intrinsic emission by each of the components. This extra-emission can be further modulated because e.g. of a variation of the optical depth along the line of sight towards the system due to the orbital motion. It could also reflect the changing properties of the shocks due, for example, to a variation of the distance between the two stars in an eccentric binary system.

Though the exact mechanism has not been clearly identified (possibly because several mechanisms are actually at work) the X-ray emission from O- and early B-type stars has been the subject of numerous investigations. The X-ray emission from later B stars is however more controversial. Because these stars do not have the convective zones required to sustain a magnetic dynamo, coronal emission is not supposed to occur. Their stellar winds are also much weaker than those of their hotter sisters, and are therefore not supposed to provide a sizeable amount of X-rays.

While the earliest works based on EINSTEIN data suggested the *canonical* relation to extend down to A5 stars (e.g. Pallavicini et al. 1981), Schmitt et al. (1985) showed that the latter law does not hold for A-type stars. Later works (Rosner et al. 1985; Cassinelli et al. 1994) further suggested that the X-ray emission from B-stars of spectral-type B2 or later was indeed not following the same scheme as O-type stars. Indeed, Berghöfer et al. (1997) reported that, for stars of spectral type B2 or later, the detection rate drops below 10%. Actually the intrinsic emission from B-type stars could, comparatively, be much lower than from O-type stars, with $\log(L_X/L_{bol}) \sim -8.5$ (Cohen et al. 1997). This suggests that most of the detected X-ray emission for B-stars in distant cluster is actually associated with unresolved companions, either in a binary system or located by coincidence on the same line of sight. The question of the intrinsic B-type X-ray

emission has however not yet received a satisfactory answer. One of the difficulties is the intrinsic lack of homogeneity of the B-type population that contains different kinds of objects (β Cep, Be stars, shell stars, ...). This diversity might render even more difficult the identification of the physical parameters that govern the X-ray emission. An additional difficulty is their lower emission level (if any), which thus limits the number of detections on shorter duration exposures or in distant fields. It was hoped that the advent of the 'large' X-ray observatories, which combine improved sensitivity and spatial resolution, would help to solve this question. A scan of the recent literature (e.g. Stelzer et al. 2003, and references therein) indeed favours the 'companion' option but provides by no mean a definitive answer to this question.

The young open cluster NGC 6231 is considered as the core of the Sco OB 1 association and contains a large OB-star population. It offers thus an excellent opportunity to probe a homogeneous sample of early-type stars in terms of e.g. distance, age, reddening, environment and chemical composition. In Sana et al. (2005c, hereafter Paper I), we have given a description of our XMM-*Newton* campaign towards NGC 6231 that had revealed hundreds of point-like sources in the 15′ radius field of view (FOV) of the satellite. In the present paper, we focus on the O- and B-type star population in the FOV. The analysis of the sources associated with optically faint counterparts is postponed to a forthcoming paper in this series (Sana et al. 2005g, Paper III). Preliminary results of this work were presented in Sana et al. (2005d) but should be considered as supplanted by the present analysis. The remaining of this paper is organised as follows. The next section provides a brief overview of the X-ray data set and data reduction processes. Sect. 3 makes a census of the early-type star population in the core of NGC 6231 and identifies the early-type X-ray emitters. Sect. 4 investigates the X-ray properties of the detected O and B-type stars and the appropriate $L_{\rm X} - L_{\rm bol}$ relations are derived in Sect. 4.2. Sect. 5 presents the properties of the individual early-type sources while Sect. 6 discusses the results of our study. Finally Sect. 7 provides a summary of this work and presents our conclusions.

2. Observations and Data Reduction

In September 2001, we have acquired six 30 ks X-ray observations of the young open cluster NGC 6231 using the XMM-*Newton* facility. These data were obtained in the framework of the Liège program for the exploitation of the Optical Monitor consortium guaranteed time. The campaign, spread over 5 days, is described in the first paper of this series (Paper I) and we only provide a brief summary here. All three EPIC instruments (Strüder et al. 2001; Turner et al. 2001) were operated in the Full Frame mode together with the Thick Filter to reject UV/optical light. Due to the brightness of the objects in the FOV, the Optical Monitor was switched off throughout the campaign.

In Paper I, using the combination of the six exposures and of the three EPIC instruments, we identified 610 X-ray sources in the XMM-*Newton* FOV. About 85% of these X-ray sources

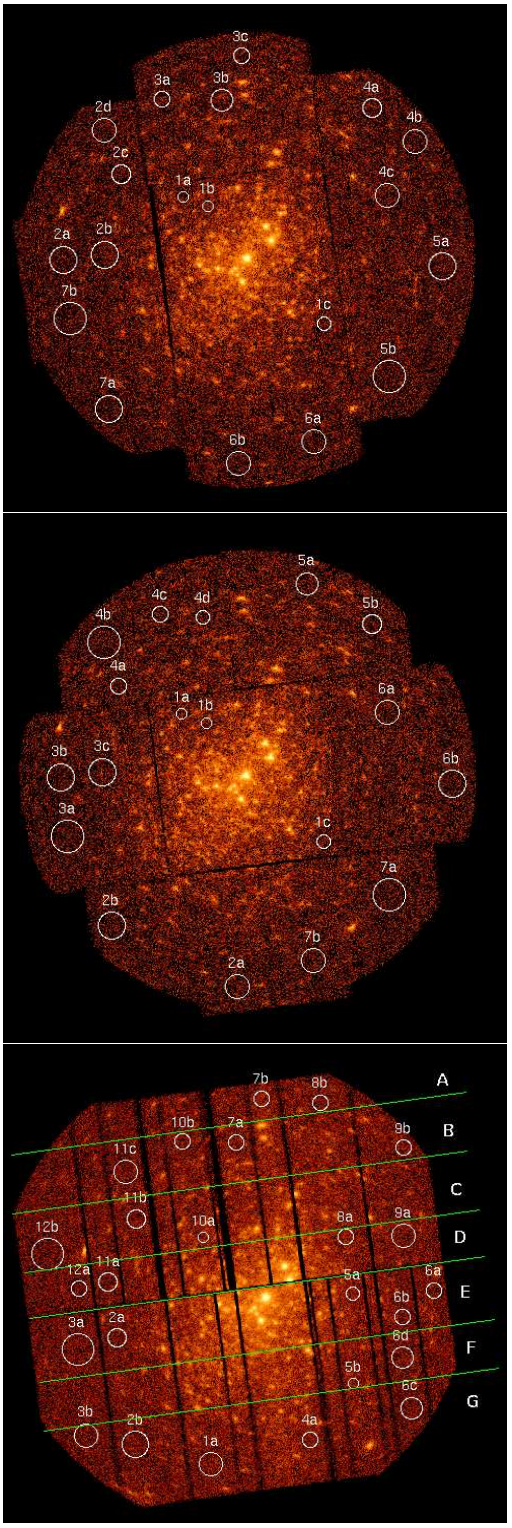

Fig. 1. From top to bottom, combined EPIC MOS1, MOS2 and pn images in the range 0.5-10.0 keV. The background extraction regions adopted according to the different positions of the sources on the detectors have been overplotted. North is up, East to the left. A colour version of these figures is available in the electronic version of the paper.

Table 1. Positions and sizes ($r_{\rm extr.}$) of the adopted background extraction regions in the FOV of the different EPIC instruments.

Bkg.	Label	α (J2000.0)	δ (J2000.0)	$r_{\rm extr.}$
		MOS1		
CCD 1	1a	16h54m31$^{\rm s}$.43	−41°45′42.″2	20″
	1b	16h54m23$^{\rm s}$.28	−41°46′14.″7	20″
	1c	16h53m44$^{\rm s}$.12	−41°53′34.″6	25″
CCD 2	2a	16h55m12$^{\rm s}$.05	−41°49′34.″0	50″
	2b	16h54m57$^{\rm s}$.95	−41°49′16.″7	50″
	2c	16h54m52$^{\rm s}$.31	−41°44′13.″0	35″
	2d	16h54m58$^{\rm s}$.19	−41°41′29.″2	45″
CCD 3	3a	16h54m38$^{\rm s}$.42	−41°39′33.″3	30″
	3b	16h54m18$^{\rm s}$.46	−41°39′36.″0	40″
	3c	16h54m11$^{\rm s}$.88	−41°36′51.″0	30″
CCD 4	4a	16h53m28$^{\rm s}$.04	−41°40′06.″8	35″
	4b	16h53m13$^{\rm s}$.61	−41°42′10.″2	45″
	4c	16h53m22$^{\rm s}$.95	−41°45′35.″4	45″
CCD 5	5a	16h53m04$^{\rm s}$.39	−41°49′59.″9	50″
	5b	16h53m21$^{\rm s}$.91	−41°56′55.″4	60″
CCD 6	6a	16h53m47$^{\rm s}$.44	−42°01′00.″9	45″
	6b	16h54m12$^{\rm s}$.79	−42°02′23.″5	45″
CCD 7	7a	16h54m56$^{\rm s}$.95	−41°58′55.″4	50″
	7b	16h55m09$^{\rm s}$.87	−41°53′17.″6	60″
		MOS2		
CCD 1	1a	16h54m31$^{\rm s}$.43	−41°45′42.″2	20″
	1b	16h54m23$^{\rm s}$.28	−41°46′14.″7	20″
	1c	16h53m44$^{\rm s}$.12	−41°53′34.″6	25″
CCD 2	2a	16h54m12$^{\rm s}$.79	−42°02′38.″5	45″
	2b	16h54m55$^{\rm s}$.16	−41°58′50.″5	50″
CCD 3	3a	16h55m09$^{\rm s}$.87	−41°53′17.″6	60″
	3b	16h55m12$^{\rm s}$.05	−41°49′35.″0	50″
	3c	16h54m57$^{\rm s}$.95	−41°49′16.″7	50″
CCD 4	4a	16h54m52$^{\rm s}$.53	−41°43′55.″5	30″
	4b	16h54m57$^{\rm s}$.29	−41°41′14.″2	60″
	4c	16h54m38$^{\rm s}$.53	−41°39′29.″6	30″
	4d	16h54m24$^{\rm s}$.48	−41°39′38.″5	25″
CCD 5	5a	16h53m49$^{\rm s}$.69	−41°37′34.″7	40″
	5b	16h53m28$^{\rm s}$.04	−41°40′06.″8	35″
CCD 6	6a	16h53m22$^{\rm s}$.95	−41°45′35.″4	45″
	6b	16h53m01$^{\rm s}$.20	−41°49′59.″8	50″
CCD 7	7a	16h53m21$^{\rm s}$.91	−41°56′55.″4	60″
	7b	16h53m47$^{\rm s}$.44	−42°01′00.″9	45″

Table 1. Continued.

Bkg.	Label	α (J2000.0)	δ (J2000.0)	$r_{\rm extr.}$
		pn		
A	8b	16h53m51$^{\rm s}$.25	−41°37′04.″7	30″
	7b	16h54m11$^{\rm s}$.43	−41°36′48.″5	30″
B	9b	16h53m22$^{\rm s}$.96	−41°39′56.″7	30″
	7a	16h54m20$^{\rm s}$.24	−41°39′36.″0	30″
	10b	16h54m38$^{\rm s}$.42	−41°39′33.″3	30″
	11c	16h54m58$^{\rm s}$.19	−41°41′29.″2	45″
C	10a	16h54m31$^{\rm s}$.43	−41°45′42.″2	20″
	11b	16h54m54$^{\rm s}$.54	−41°44′28.″0	35″
	12b	16h55m24$^{\rm s}$.85	−41°46′43.″3	60″
D	9a	16h53m22$^{\rm s}$.95	−41°45′35.″4	45″
	8a	16h53m42$^{\rm s}$.61	−41°45′38.″3	30″
	11a	16h55m04$^{\rm s}$.20	−41°48′31.″5	35″
	12a	16h55m14$^{\rm s}$.27	−41°48′57.″4	30″
E	6a	16h53m12$^{\rm s}$.40	−41°49′02.″6	30″
	6b	16h53m23$^{\rm s}$.00	−41°50′44.″2	30″
	5a	16h53m40$^{\rm s}$.35	−41°49′14.″5	25″
	2a	16h55m01$^{\rm s}$.01	−41°52′06.″6	35″
	3a	16h55m14$^{\rm s}$.79	−41°52′49.″9	60″
F	6d	16h53m23$^{\rm s}$.29	−41°53′21.″2	40″
	5b	16h53m39$^{\rm s}$.86	−41°55′02.″0	20″
G	6c	16h53m20$^{\rm s}$.12	−41°56′32.″9	40″
	4a	16h53m54$^{\rm s}$.85	−41°58′36.″0	30″
	1a	16h54m28$^{\rm s}$.93	−42°00′10.″9	45″
	2b	16h54m54$^{\rm s}$.93	−41°58′53.″0	50″
	3b	16h55m11$^{\rm s}$.85	−41°58′18.″7	45″

can be associated with an optical/near-IR counterpart within a cross-correlation radius of 3″. Using a census of the OB population in the FOV (see Sect. 3), we have now identified the early-type X-ray emitters. For the latter ones, we adopted the X-ray source positions given in the NGC 6231 X-ray catalogue of Paper I and we extracted, using the SAS v6.0 software, the X-ray spectra from the merged event lists, i.e. from the event lists built using the combination of the six pointings.

The source and background extraction regions were chosen as follows. For each early-type source, we adopted a circular extraction region with a radius corresponding to half the distance to the nearest neighbouring X-ray source. Due to the crowded nature of the cluster core in the X-rays (see Fig. 1 in Paper I) and the limited spatial resolution of the EPIC detectors, the background could not be evaluated in the immediate vicinity of the stars, but had to be taken from the very few source free regions. We adopted several circular background regions spread throughout the FOV. For the two EPIC MOS instruments, as the background can be considered uniform on a particular CCD, we associated, to each X-ray emitter, source-free background regions located on the same CCD detector. Regarding the pn instrument, the background is rather considered to depend on the distance to the detector read-out nodes. We therefore selected source-free regions approximately situated at the same distance from the read-out nodes as the target of interest. The adopted background extraction regions for MOS and pn instruments are displayed in Fig. 1. Their respective positions and sizes are given in Table 1. We used the appropriate redistribution matrix files (rmf) provided by the Science Operations Centre (SOC), according to the position of the considered source on the detectors. We built the corresponding ancillary response files (arf) using the ARFGEN command of the SAS software. The spectra were finally binned to have at least 10 counts per bin. The analysis of these spectra is presented in Sect. 4.

Finally, using the source positions given in Paper I, we ran the SAS task *emldetect* on the individual pointings to obtain the background-subtracted, vignetting- and exposure-corrected count rates of the objects during each observation. Similarly, we used the extraction regions described above to build X-ray good time interval corrected and background subtracted light curves in the different energy bands considered in Paper I. These were computed for a series of time-bin sizes ranging from a few hundred seconds to 5 ks. These temporal information allow to probe the variability of the early-type X-ray emit-

Table 3. List of the early-type X-ray emitters in the XMM-*Newton* FOV. The first five columns give the source identifiers. Col. 6 indicates the separation d_{cc} between the associated optical and X-ray sources. Cols. 7 and 8 respectively provide the adopted instrument combination and the radius of the source extraction region. The adopted background regions are indicated in Cols. 9 to 11 for each EPIC instrument (see Table 1). The last three columns provide the bolometric luminosity (L_{bol}), the ISM-corrected X-ray luminosity (L_X) and the L_X/L_{bol} ratio respectively. The objects are ordered by decreasing L_{bol}.

Object IDs.					d_{cc}	Instr.	$r_{extr.}$	Background regions			$\log L_{bol}$	$\log L_X$	$\log \frac{L_X}{L_{bol}}$
X#	HD	CPD−41°	Se68	SBL98	(″)		(″)	MOS1	MOS2	pn	(erg s^{-1})	(erg s^{-1})	
[1]	[2]	[3]	[4]	[5]	[6]	[7]	[8]	[9]	[10]	[11]	[12]	[13]	[14]
279	152248	7728	291	856	0.8	EPIC	19.0	1	1	E	39.49	32.87	−6.62
202	152234	7716	290	855	1.2	MOS	10.0	1	1	–	39.45	32.42	−7.03
216	152233	7718	306	858	1.2	EPIC	14.0	1	1	D	39.30	32.40	−6.90
292	152249	7731	293	857	1.4	EPIC	11.5	1	1	E	39.22	32.30	−6.92
371	152270	7741	220	854	1.0	MOS	11.0	1	1	–	39.12[a]	31.83	−7.29
291	152247	7732	321	–	0.5	EPIC	23.0	3	5	B	38.99	32.09	−6.90
422	326331	7744	338	571	0.7	MOS	12.0	1	1	–	38.92	31.96	−6.96
468	152314	7749	161	615	0.8	EPIC	15.5	1	1	D	38.90	31.80	−7.10
185	152218	7713	2	853	1.2	MOS	20.0	3	5	–	38.77	31.87	−6.90
149	152219	7707	254	234	1.3	EPIC	08.0	1	1	F	38.68	31.80	−6.88
306	–	7733	297	862	1.4	EPIC	11.5	1	1	E	38.62	31.83	−6.79
372	–	7742	224	505	1.3	MOS	13.0	1	1	–	38.48	31.94	−6.54
126	152200	7702	266	206	1.1	EPIC	10.0	1	1	E	38.44	31.29	−7.15
6	152076	7684	–	–	1.8	MOS	37.5	4	6	–	38.44	31.04	−7.40
566	–	7760AB	810	–	1.9	pn	17.0	–	–	G	38.44	30.19	−8.25
313	326329	7735	292	434	0.7	EPIC	07.5	1	1	E	38.33	31.78	−6.55
251	–	7721	309	350	1.6	EPIC	10.0	1	1	E	38.31	31.44	−6.87
448	–	7746	769	–	2.3	MOS	07.0	3	4	–	38.06	30.79	−7.27
139	–	7706	253	226	1.7	MOS	17.0	1	1	–	37.74	31.17	−6.57
521	–	7755	112	684	2.0	MOS	13.0	7	3	–	37.59	31.08	−6.51
167	326320	7710	745	–	0.5	EPIC	16.0	3	5	B	37.57	30.60	−6.97
203	–	7715	261	303	1.5	EPIC	11.0	1	1	E	37.36	30.87	−6.49
337	–	7737	294	461	0.5	EPIC	07.5	1	1	E	37.19	31.20	−5.99
213	–	–	259	317	2.0	EPIC	11.0	1	1	E	37.15	30.97	−6.18
282	–	–	209	394	1.5	EPIC	13.0	1	1	D	37.14	31.12	−6.02
22	326343	7688	616	19	0.9	EPIC	08.0	5	7	F	37.13	30.26	−6.87
602	152437	7766	798	–	2.5	MOS1+pn	40.0	7	–	F	36.66	30.18	−6.48
440	–	–	160	593	1.2	EPIC	08.0	1	1	D	36.48	30.67	−5.81
559	–	–	142	748	1.1	MOS2+pn	15.0	–	3	E	36.39	30.66	−5.73
78	–	–	41	149	1.4	EPIC	15.0	1	1	E	36.28	30.85	−5.43
557	–	–	127	746	0.6	EPIC	11.0	7	3	E	36.08	30.73	−5.35
121	–	–	265	200	1.4	EPIC	09.0	1	1	E	35.64	30.81	−4.83

[a] The bolometric luminosity for HD 152270 (≡ WR 79) was adopted from Nugis & Lamers (2000)

ters on the different time-scales covered by the present data set (see Sect. 5).

3. Early-type stars in NGC 6231

Prior to our scientific analysis, we first went through a deep overview of the existing literature and databases on NGC 6231 and we made a census of the early-type star population in the observed FOV. Our census mainly relies on selected published works (see references in Paper I), on the Catalog of Galactic OB Stars (Reed 2003) and on the WEBDA[1] and SIMBAD[2] databases. We first selected all stars for which at least one of the previous references quoted a spectral type O, B or Wolf-Rayet (WR), regardless of their sub-spectral type, their luminosity classification or their single/multiple status. This resulted in 108 objects among which 92 B-stars, 15 O-stars and one WR system (WR 79). These are listed in Table 2[3]. Together with various cross-identifications (Cols. 1 to 7), Table 2 provides the adopted positions (Col. 8) and the V and $B-V$ magnitudes (Cols. 9 and 10) obtained from the SSB05 catalogue (Sung et al. 2005, in preparation; see also Paper I for a brief description). The visual (M_V) and bolometric (M_{bol}) absolute magnitudes (Cols. 11 and 12) were computed using a distance modulus $DM = 11.07$ (see Sect. 4), the intrinsic colours and bolometric correction scale of Schmidt-Kaler (1982) and a reddening law $A_V = R \times E(B-V)$ with $R = 3.3$ (Sung et al. 1998). A_V was computed for each object to account for the differential reddening existing across

[1] http://obswww.unige.ch/webda/

[2] http://simbad.u-strasbg.fr/Simbad/

[3] Table 2 is available in the electronic version of the present paper or on request from the author.

Table 4. Best-fit single temperature models of the form: $\texttt{wabs}_{\rm ISM}$ `* wabs * mekal`. The first and second columns give the X-ray and optical identifiers. Col. 3 provides the adopted interstellar column ($n_{\rm H}^{\rm ISM}$, in 10^{22} cm^{-2}). The next three columns (Cols. 4 to 6) list the best-fit absorbing column ($n_{\rm H}$, in 10^{22} cm^{-2}), temperature (kT, in keV) and normalisation factor (in cm^{-5}, $norm = \frac{10^{-14}}{4\pi d^2}\int n_{\rm e} n_{\rm H} dV$ with d, the distance to the source – in cm –, $n_{\rm e}$ and $n_{\rm H}$, the electron and hydrogen number densities – in cm^{-3}). The quoted upper and lower values indicate the limits of the 90% confidence interval. The obtained reduced chi-square and the number of degrees of freedom (dof) of the fit are given in Col. 7. Cols. 8 and 9 provide the observed ($f_{\rm X}$) and the ISM absorption-corrected ($f_{\rm X}^{\rm corr.}$) fluxes (in 10^{-14} erg cm^{-2} s^{-1}) in the range 0.5-10.0 keV. The horizontal lines separate the O-type objects (upper part of the table) from the B-type stars (middle part of the table). HD 152437 is presented in the bottom part of the table because, altough previously reported as B9 III, we preferred an A0 III classification.

X #	ID	$n_{\rm H}^{\rm ISM}$	$n_{\rm H}$	kT	*norm*	χ^2_ν (dof)	$f_{\rm X}$	$f_{\rm X}^{\rm corr.}$
[1]	[2]	[3]	[4]	[5]	[6]	[7]	[8]	[9]
6	152076	0.29	< 0.12	$0.28^{0.36}_{0.23}$	$1.85^{4.20}_{1.20} \times 10^{-5}$	1.08 (92)	0.92	3.42
22	326343	0.36	$0.43^{0.87}_{0.09}$	$0.56^{0.84}_{0.28}$	$< 4.73 \times 10^{-5}$	1.08 (13)	0.25	0.57
167	326320	0.24	$0.61^{0.73}_{0.47}$	$0.61^{0.82}_{0.50}$	$2.50^{3.85}_{1.39} \times 10^{-5}$	0.94 (70)	0.79	1.24
448	7746	0.30	$0.48^{0.67}_{0.27}$	$0.58^{0.75}_{0.43}$	$2.99^{6.00}_{0.00} \times 10^{-5}$	1.12 (11)	1.01	1.92
566	7760	0.42	$0.79^{1.69}_{0.00}$	$0.28^{1.74}_{0.08}$	< 1.71	0.76 (23)	0.18	0.48
602	152437	0.11	n.	$0.48^{0.70}_{0.24}$	$< 1.83 \times 10^{-5}$	1.13 (72)	0.31	0.47

the cluster (Sung et al. 1998). The adopted spectral types and the corresponding reference are quoted in Cols. 13 and 14. For binary systems, the quoted visual and bolometric magnitudes are given for the system as a whole. To compute the latter ones, we used the respective visual brightness ratio of the system components and derived a reddening correction that accounts for the component spectral types and for their relative contribution to the total light from the system. Doing so, we deduced the $M_{\rm V}$ for the system. We then derived the individual visual and bolometric magnitudes. Finally, we combined the latter values to obtain the total bolometric magnitude for the system. The last column (Col. 15) of Table 2 provides miscellaneous notes about the objects, together with the related references. Compared to the previous results presented in Sana et al. (2005d), some spectral types have been revised thanks to recent FEROS observations (Sana 2005). The distribution of the selected stars among the different spectral sub-types and luminosity classes given in Sana et al. (2005d) still provides a good overview of the early-type population in NGC 6231.

As a next step, we cross-correlated the X-ray catalogue of Paper I with the obtained list of early-type stars in the FOV. We first built the distribution of the number of associated OB counterparts as a function of the cross-correlation radius. The curve reveals 32 associations within a cross-correlation distance ($d_{\rm cc}$) of 2.″5. Six additional sources are found with $d_{\rm cc}$ between 3.″0 and 3.″6. The remaining associations require $d_{\rm cc} > 4.''8$. For consistency with the results of Paper I, we adopted a cut-off radius of 3″, thus resulting in 32 early-type X-ray emitters. After a visual inspection of the X-ray images at the position of the remaining OB stars in the FOV, we completed this list by two additional objects, for which we have good reasons to think that the above procedure has been biased. This probably results from a poor determination of the positions for these objects on the EPIC images because of the crowdedness of the field in these particular regions. The spectra of these sources could of course not be securely extracted because of the probable contamination by X-ray neighbours. These two sources are thus not included in the discussions of Sect. 4. Inspecting the X-ray images, we also observed larger residuals than expected for source-free regions at the positions of seven B-type stars. These might be X-ray sources below the detection threshold of our catalogue (see details in Paper I). The early-type X-ray emitters in the XMM-*Newton* FOV are identified in Table 2 (Col. 6). The two additional sources for which the X-ray position is probably biased are identified with a cross (+) added to the number of the X-ray source. For these two sources, we emphasize that the corresponding X-ray source in the catalogue of Paper I is probably constituted by different unresolved components. In Table 2, we also identified the B-type stars for which larger residuals are seen. Finally, for the sake of completeness, we also analysed the X-ray spectra of the sources with $3.''0 < d_{\rm cc} < 3.''6$. These are identified with an asterisk (*) added to the number of the X-ray source in Table 2. The results of the spectral analysis are given in Table 7 but they will not be included in the following discussions.

As a first result, we note that the WR and the 15 O-type objects in the FOV are all detected in the X-rays. They account for about half of the identified early-type X-ray emitters. The situation is clearly different for the B-type stars. Only ∼25% (15 out of 63) of the early B stars (sp. type B0–B4) are detected, a percentage that remains almost constant within the subtypes B0 to B4. This percentage reaches 50% among the giants and supergiants (4 out of 8), but clearly the situation is much different than for O-type stars. Except for the respectively known (CPD −41°7737) and suspected (Se 209) slow pulsating B-type stars (SPB) in the FOV, that are both detected in the X-ray domain, no particular correlation is found for the different sub-populations. Three out of the six (resp. eight) known (resp. known or suspected) β Cep are detected. Five (resp. six) out of the 16 (resp. 26) known (resp. known or suspected) binaries are also detected. For the later B-type stars (subtypes B5 and later), only four of them are detected, which seems to be a slightly smaller detection ratio, although it is based on a small number of objects. In summary, we can already conclude that, among

Table 5. Same as Table 4 for two-temperature models of the form: $\mathtt{wabs}_{\rm ISM}$ * ($\mathtt{wabs}_1$ * $\mathtt{mekal}_1$ + $\mathtt{wabs}_2$ * $\mathtt{mekal}_2$).

X # [1]	ID [2]	$n_{\rm H}^{\rm ISM}$ [3]	$n_{\rm H,1}$ [4]	kT_1 [5]	$norm_1$ [6]	$n_{\rm H,2}$ [7]	kT_2 [8]	$norm_2$ [9]	χ^2_ν (dof) [10]	$f_{\rm X}$ [11]	$f_{\rm X}^{\rm corr.}$ [12]
126	152200	0.23	< 0.06	$0.36^{0.40}_{0.32}$	$1.94^{2.41}_{1.58} \times 10^{-5}$	$0.23^{0.38}_{0.10}$	$0.71^{0.78}_{0.65}$	$1.51^{1.93}_{1.11} \times 10^{-5}$	1.35 (157)	2.80	6.13
149	152219	0.26	n.	$0.26^{0.29}_{0.22}$	$7.5^{8.2}_{6.5} \times 10^{-5}$	$0.22^{0.35}_{0.11}$	$0.67^{0.72}_{0.63}$	$5.0^{5.4}_{4.2} \times 10^{-5}$	1.09 (268)	6.90	19.50
185	152218	0.26	$0.01^{0.17}_{0.00}$	$0.31^{0.34}_{0.27}$	$8.82^{24.70}_{7.37} \times 10^{-5}$	$0.40^{0.52}_{0.30}$	$0.71^{0.76}_{0.65}$	$7.99^{9.63}_{6.65} \times 10^{-5}$	0.95 (159)	9.49	23.24
202	152234	0.22	$0.22^{0.29}_{0.12}$	$0.27^{0.29}_{0.25}$	$1.05^{1.66}_{0.57} \times 10^{-3}$	$0.67^{0.81}_{0.58}$	$0.76^{0.80}_{0.72}$	$3.56^{3.98}_{3.12} \times 10^{-4}$	1.47 (234)	39.74	82.23
251	7721	0.24	$0.41^{0.48}_{0.31}$	$0.24^{0.28}_{0.22}$	$3.45^{5.42}_{3.02} \times 10^{-4}$	$1.38^{1.89}_{0.46}$	$1.33^{1.90}_{1.03}$	$2.48^{4.50}_{1.44} \times 10^{-5}$	0.92 (204)	4.07	8.56
291	152247	0.28	< 0.06	$0.25^{0.28}_{0.21}$	$1.49^{3.63}_{1.30} \times 10^{-4}$	$0.12^{0.24}_{0.03}$	$0.63^{0.69}_{0.59}$	$7.41^{8.67}_{5.89} \times 10^{-5}$	1.26 (351)	12.20	37.90
292	152249	0.27	$0.25^{0.30}_{0.21}$	$0.23^{0.24}_{0.22}$	$1.45^{2.02}_{1.09} \times 10^{-3}$	$1.18^{1.70}_{0.86}$	$0.81^{0.93}_{0.73}$	$1.23^{1.66}_{0.94} \times 10^{-4}$	1.40 (389)	21.39	61.85
372	7742	0.28	n.	$0.59^{0.62}_{0.50}$	$0.74^{0.80}_{0.62} \times 10^{-4}$	$0.73^{0.86}_{0.62}$	$1.05^{1.26}_{0.97}$	$1.39^{1.59}_{1.29} \times 10^{-4}$	1.09 (209)	14.0	27.2
422	326331	0.28	$0.29^{0.42}_{0.19}$	$0.23^{0.25}_{0.20}$	$7.78^{17.3}_{3.97} \times 10^{-4}$	$1.23^{1.85}_{0.88}$	$0.88^{1.02}_{0.76}$	$1.06^{1.58}_{0.79} \times 10^{-4}$	1.19 (157)	10.70	28.74
78	Se 41	0.21	$0.65^{0.79}_{0.38}$	$0.21^{0.29}_{0.19}$	$2.16^{6.64}_{0.81} \times 10^{-4}$	$0.76^{1.86}_{0.06}$	$1.66^{2.56}_{1.20}$	$1.18^{1.86}_{0.77} \times 10^{-5}$	1.11 (74)	1.31	2.02
121	Se 265	0.26	$0.52^{0.69}_{0.26}$	$0.19^{0.23}_{0.14}$	$1.87^{7.67}_{0.35} \times 10^{-4}$	$0.49^{1.03}_{0.24}$	$1.83^{2.47}_{1.43}$	$1.37^{1.88}_{0.77} \times 10^{-5}$	1.37 (105)	1.34	2.22
139	7706	0.25	$0.62^{0.84}_{0.37}$	$0.26^{0.38}_{0.19}$	$1.32^{6.97}_{0.28} \times 10^{-4}$	< 0.51	$2.56^{3.25}_{1.82}$	$1.98^{2.84}_{1.64} \times 10^{-5}$	0.99 (92)	3.02	4.62
203	7715	0.25	$0.58^{0.79}_{0.29}$	$0.23^{0.27}_{0.18}$	$1.28^{6.32}_{0.53} \times 10^{-4}$	$1.00^{2.15}_{0.60}$	$1.32^{1.82}_{1.08}$	$1.87^{2.89}_{1.29} \times 10^{-5}$	1.29 (94)	1.42	2.32
213	Se 259	0.26	$0.75^{0.87}_{0.61}$	$0.15^{0.16}_{0.14}$	$1.85^{3.83}_{1.21} \times 10^{-3}$	< 1.77	$2.00^{3.33}_{1.26}$	$1.60^{3.03}_{1.06} \times 10^{-5}$	1.10 (100)	1.75	2.88
282	Se 209	0.24	$0.76^{0.83}_{0.64}$	$0.16^{0.17}_{0.14}$	$1.69^{2.80}_{0.72} \times 10^{-3}$	$0.71^{1.05}_{0.32}$	$1.65^{2.20}_{1.45}$	$3.04^{3.81}_{2.30} \times 10^{-5}$	1.02 (168)	2.66	4.06
337	7737	0.26	$0.57^{0.70}_{0.39}$	$0.24^{0.37}_{0.22}$	$2.17^{3.69}_{1.05} \times 10^{-4}$	$0.52^{0.92}_{0.00}$	$1.76^{2.55}_{1.50}$	$2.93^{3.59}_{1.96} \times 10^{-5}$	0.91 (122)	3.09	4.95
440	Se 160	0.29	$0.85^{1.13}_{0.00}$	$0.23^{0.42}_{0.08}$	$1.61^{7.98}_{0.09} \times 10^{-4}$	$0.18^{6.06}_{0.00}$	$3.10^{13.93}_{1.84}$	$5.73^{14.12}_{3.34} \times 10^{-6}$	0.82 (35)	0.96	1.45
521	7755	0.27	n.	$0.63^{0.75}_{0.47}$	$5.40^{7.04}_{3.97} \times 10^{-6}$	< 0.39	$2.28^{2.86}_{1.74}$	$1.66^{2.08}_{1.39} \times 10^{-5}$	1.02 (43)	2.31	3.72
557	Se 127	0.33	$0.19^{0.81}_{0.00}$	$0.27^{0.69}_{0.19}$	$1.05^{13.44}_{0.33} \times 10^{-5}$	$0.92^{1.87}_{0.47}$	$1.11^{1.56}_{0.90}$	$1.92^{3.49}_{1.26} \times 10^{-5}$	0.88 (42)	0.91	1.66
559	Se 142	0.29	< 0.85	$0.68^{0.88}_{0.38}$	$2.18^{12.99}_{1.19} \times 10^{-6}$	< 2.32	$3.16^{n.}_{1.70}$	$6.18^{13.03}_{1.75} \times 10^{-6}$	0.87 (43)	0.93	1.42

B stars with a similar sub-type, only one quarter are seen in the X-rays. Regarding the luminosity classes, 50% of the B-type giants are detected while, considering only the main sequence stars, this percentage drops to about 20%.

4. X-ray properties

4.1. X-ray spectrum

Using the list of identified early-type X-ray emitters built in the previous section, we extracted their merged X-ray spectra in the different EPIC instruments using the procedure described in Sect. 2. We selected the deepest instrument combination (see Table 3), requiring that the source is not located too close to a gap or a detector edge. The radius of the source extraction region and the identification of the associated background regions in the different instruments are also given in Table 3. Except for WR 79, the obtained spectra are relatively soft and peak at an energy well below 1.5 keV. These X-ray spectra are presented in Figs. 2 to 6, available in the electronic version of the present work. Beyond the different emission levels, the O- and B-type spectra show different characteristics. The former ones reach their maximum at energies about 0.8–0.9 keV and drop quite rapidly towards higher energies. Compared to the observed maximum, their emission level is about one and a half order of magnitude lower at 2 keV and about 4 orders of magnitude lower at 5 keV. The count rate beyond 5 keV is usually very low ($< 10^{-4}$ cnt s^{-1} keV^{-1}). We remind the reader that a count rate of 10^{-5} cnt s^{-1} in a particular energy bin corresponds to about 2 photons being detected in the bin during the whole campaign. On the contrary, the B-type spectra peak at about 1 keV. Although they are fainter X-ray emitters, they present a much flatter energy distribution. Their hard energy tail displays an emission level which, relatively to the emission maximum, is lower by about one order of magnitude at 2 keV and by only two orders of magnitude at 5 keV. The X-ray emission associated with B-type stars is thus intrinsically harder than that from O-type stars.

To quantify the physical properties of the X-ray emission, we adjusted a series of optically thin thermal plasma MEKAL models (Mewe et al. 1985; Kaastra 1992) to the obtained spectra. For the purpose of scientific analysis, we limited the considered energy range to the 0.5-10.0 keV band and we simultaneously fitted the different EPIC spectra using the XSPEC software v.11.2.0[4] (Arnaud 1996). In the spectral fits, we requested an equivalent column density of neutral hydrogen larger or equal to the interstellar (ISM) column density $n_{\rm H}^{\rm ISM}$. The latter was estimated from the color excess using the relation of Bohlin et al. (1978): $n_{\rm H} = E(B-V) \times 5.8 \times 10^{21}$ cm^{-2}. As previously mentioned in Sect. 3, the interstellar columns were inferred for each source from the data of Table 2, to reflect the differential reddening across the cluster. Good spectral fits are generally obtained using two-temperature (2-T) `mekal` models with two independent absorbing columns. However, the brightest sources may require an additional, higher temperature component (3-T models) while the spectra of a few very

[4] http://xspec.gsfc.nasa.gov/

Table 6. Same as Table 4 for three-temperature models of the form: $\texttt{wabs}_{\rm ISM}$ * $\sum_i$ ($\texttt{wabs}_i$*$\texttt{mekal}_i$), with $i = 1, 3$. The fourth column gives the number i of the considered component in the model.

X # [1]	Object ID. [2]	$n_{\rm H}^{\rm ISM}$ [3]	i [4]	$n_{{\rm H},i}$ [5]	kT_i [6]	$norm_i$ [7]	χ^2_ν (dof) [8]	$f_{\rm X}$ [9]	$f_{\rm X}^{\rm corr.}$ [10]
216	152233	0.25	1	$0.53^{0.60}_{0.48}$	$0.15^{0.16}_{0.14}$	$1.47^{2.46}_{1.10}\times10^{-2}$			
			2	<0.05	$0.48^{0.51}_{0.44}$	$1.17^{1.43}_{1.07}\times10^{-4}$			
			3	$0.89^{1.10}_{0.78}$	$0.64^{0.69}_{0.61}$	$4.10^{4.72}_{3.53}\times10^{-4}$	1.74 (544)	33.16	78.20
279	152248	0.26	1	n.	$0.29^{0.39}_{0.19}$	$7.41^{7.86}_{6.96}\times10^{-4}$			
			2	$0.44^{0.47}_{0.41}$	$0.64^{0.79}_{0.49}$	$1.20^{1.33}_{1.07}\times10^{-3}$			
			3	n.	$4.75^{1.50}_{8.00}$	$2.38^{4.31}_{0.46}\times10^{-5}$	2.40 (783)	98.1	232.
306	7733	0.26	1	n.	$0.26^{0.28}_{0.25}$	$0.99^{1.03}_{0.93}\times10^{-4}$			
			2	$0.45^{0.56}_{0.35}$	$0.65^{0.70}_{0.61}$	$6.42^{7.20}_{5.13}\times10^{-5}$			
			3	$6.00^{15.7}_{1.14}$	$2.36^{9.25}_{1.18}$	$0.16^{1.02}_{0.00}\times10^{-4}$	1.29 (311)	8.12	22.4
313	326329	0.22	1	<0.34	$0.30^{0.34}_{0.19}$	$3.51^{28.64}_{2.69}\times10^{-5}$			
			2	$0.33^{0.43}_{0.20}$	$0.66^{0.75}_{0.60}$	$7.78^{10.40}_{5.07}\times10^{-5}$			
			3	<0.19	$2.62^{3.25}_{2.21}$	$2.93^{3.54}_{2.32}\times10^{-5}$	1.24 (323)	9.96	18.58
468	152314	0.30	1	$0.11^{0.17}_{0.00}$	$0.24^{0.26}_{0.19}$	$1.64^{5.46}_{0.74}\times10^{-4}$			
			2	$0.21^{0.39}_{0.06}$	$0.68^{0.78}_{0.60}$	$3.11^{4.59}_{1.81}\times10^{-5}$			
			3	<4.89	$4.70^{63.0}_{2.18}$	$5.65^{10.60}_{3.48}\times10^{-6}$	1.07 (296)	6.53	19.85
371	152270	0.27	1	$1.19^{0.98}_{1.49}$	$0.08^{0.12}_{0.08}$	$4.82^{11.44}_{0.02}\times10^{-1}$			
			2	$0.23^{0.39}_{0.03}$	$4.81^{7.39}_{3.44}$	$5.62^{6.63}_{4.86}\times10^{-5}$			
			3	$30.3^{41.0}_{22.9}$	>31.9	$2.32^{2.97}_{1.78}\times10^{-4}$	1.16 (157)	19.44	21.17

faint sources are satisfactorily described by a single temperature (1-T) component. The observed emission is generally soft (k$T \leq 2.0$ keV) and slightly absorbed ($n_{\rm H} \leq 10^{22}$ cm^{-2}). Best fit results are given in Tables 4 to 6 together with the observed and ISM-absorbtion corrected fluxes in the range 0.5-10.0 keV.

It is difficult to compare the spectral properties obtained with models composed by a different number of MEKAL components. For this reason, the different resulting tables were organised according to the number of MEKAL components used in the model. Table 5 probably provides the best illustration of the clearly distinct X-ray spectral characteristics of the O- and B-type stars.

With the temperatures of the two MEKAL components mostly below 1 keV, the X-ray emission from O-type stars is particularly soft. The first temperature is about 0.3 keV, except for CPD $-41°7742$. However, Sana et al. (2005a) showed that the intrinsic X-ray emission from this system is generally contaminated by an extra-component resulting from an ongoing wind interaction process, except when the interaction region is occulted. At these particular phases at which we probably only detect the intrinsic emission from the O-type primary, it is interesting to note that the temperature of the 'cold' component drops to about 0.35 keV (Sana et al. 2005a), thus quite close to the average 'cold' temperature of the other O-type objects.

The absorbing column associated to the lower temperature component is generally very low. The best-fit value might drop to zero so that only an upper limit can be provided. It is known from past experience, that suppressing the local absorbing column of the soft component can lead a better fit and more stable results (Sana et al. 2004, 2005a,b,e,f). When appropriate this is indicated by a 'n.' in Tables 4, 5 and 6. The temperature of the second component is usually about 0.7 keV and the associated column of absorbing matter remains moderate, with a mean value about 0.5×10^{22} cm^{-2}. We note that the described pattern for the X-ray emission from O-type stars as predicted by the 2-T models is also seen in the results of the 3-T models (Table 6). The first two components are indeed almost unchanged. An additional high temperature component (with k$T > 2$ keV) however describes the higher energy part of the spectrum. This third component has generally an emission measure at least five times lower than the less energetic components and is probably only seen because the corresponding sources are bright X-ray emitters, which allow us to probe the higher energy tail of their spectrum. Alternatively, the high energy components could come from an unresolved PMS companion located along the same line of sight. These objects have indeed X-ray spectra typically harder than O-type stars (see Paper III), but should not bias the measured X-ray flux of the O-stars as the latter is at least one order of magnitude brighter.

From Table 5, the X-ray spectra of the B-type stars show quite different properties (see also Fig. 2 to 6). Compared to the O stars, the low energy component has a slightly lower temperature but a much larger absorbing column. The main difference however is seen for the high temperature component which is systematically larger than 1 keV. Beyond this spectral scheme, it is obvious that B-type X-ray emitters are fainter than O-type emitters and, probably for this reason, we do not require more than 2-T models to satisfyingly reproduce their spectrum.

Table 7. Same as Table 5 for the six X-ray sources with an identified B-type counterparts within $3\farcs0 < d_{cc} < 3\farcs6$.

X # [1]	ID [2]	$n_{\rm H}^{\rm ISM}$ [3]	$n_{\rm H,1}$ [4]	kT_1 [5]	$norm_1$ [6]	$n_{\rm H,2}$ [7]	kT_2 [8]	$norm_2$ [9]	χ^2_ν (dof) [10]	$f_{\rm X}$ [11]	$f_{\rm X}^{\rm corr.}$ [12]
191	7712	0.25	$0.52^{0.62}_{0.33}$	$0.19^{0.26}_{0.18}$	$2.21^{4.99}_{0.45}\times10^{-4}$	<1.10	$3.57^{6.20}_{2.17}$	$0.59^{1.01}_{0.46}\times10^{-5}$	0.85 (81)	1.43	2.64
199	Se 276	0.23	$0.37^{0.60}_{0.25}$	$0.28^{0.53}_{0.22}$	$4.07^{18.54}_{2.29}\times10^{-5}$	$0.80^{1.62}_{0.50}$	$1.29^{1.88}_{0.95}$	$1.12^{1.77}_{0.67}\times10^{-5}$	1.35 (100)	1.18	2.08
328	Se 235	0.26	$0.54^{0.70}_{0.34}$	$0.20^{0.22}_{0.18}$	$3.80^{11.31}_{0.83}\times10^{-4}$	$0.90^{1.55}_{0.67}$	$1.30^{1.94}_{1.18}$	$3.66^{4.56}_{2.61}\times10^{-5}$	1.11 (178)	2.76	4.86
386	Se 89	0.32	$0.63^{0.87}_{0.25}$	$0.24^{0.52}_{0.18}$	$1.20^{6.53}_{0.28}\times10^{-4}$	$2.51^{4.55}_{0.42}$	$1.07^{2.23}_{0.47}$	$3.32^{55.30}_{0.97}\times10^{-5}$	1.53 (57)	1.06	1.86
542	Se 121	0.29	$0.22^{0.72}_{0.11}$	$0.65^{0.90}_{0.25}$	$6.12^{46.49}_{1.49}\times10^{-6}$	$0.14^{1.08}_{0.00}$	$2.31^{3.82}_{1.57}$	$1.81^{2.80}_{1.10}\times10^{-5}$	0.75 (49)	2.05	2.93
545	Se 172	0.27	$0.32^{0.87}_{0.00}$	$0.18^{0.65}_{0.08}$	$9.38^{70.88}_{0.22}\times10^{-5}$	$0.00^{41.10}_{0.00}$	$3.37^{79.9}_{0.87}$	$5.05^{14.67}_{2.40}\times10^{-6}$	0.76 (21)	1.01	2.21

4.2. $L_{\rm X} - L_{\rm bol}$ relationship

To infer the intrinsic X-ray luminosities, we corrected the observed fluxes quoted in Table 4 to 6 from the interstellar reddening and we computed the corresponding *unabsorbed* fluxes. Since the early 1990's, several studies attempted to derive the distance to the NGC 6231 cluster. Different authors obtained a distance modulus (DM) of 11.56 ± 0.32 (Perry et al. 1991), 11.08 ± 0.05 (Balona & Laney 1995), 11.2 ± 0.4 (Raboud et al. 1997), 11.00 ± 0.07 (Sung et al. 1998) and 11.50 ± 0.25 (Baume et al. 1999). The weighted mean of these values yields $DM = 11.07 \pm 0.04$ which we adopted to infer the intrinsic X-ray luminosities of the considered objects (Table 3).

Fig. 7 presents the X-ray luminosities in the 0.5-10.0 keV energy range plotted versus the bolometric luminosities. The different properties of the X-ray emitters (spectral type, luminosity class, multiplicity) are indicated in the upper panel of the figure. The lower panel gives, in addition, the upper detection limit for the undetected B-type stars, computed according to their respective position on the detector (see Paper I). These were estimated using Eq. 5 and Fig. 6 from Paper I and correspond to a source with a temperature about 0.7-1.5 keV and a typical ISM reddening corresponding to an equivalent column of neutral hydrogen of 0.26×10^{22} cm^{-2}. We emphasize that no additional (local) absorption column is considered in this typical model.

Clearly the O- and B-type stars show a different behaviour. The former ones are brighter (as expected) and seem to present a steeper $L_{\rm X} - L_{\rm bol}$ relation than the latter. The B-type stars and the late O-type stars also seem to present a larger dispersion around the observed trends. Fig. 7 clearly identifies the location of each object in the $L_{\rm X} - L_{\rm bol}$ plane and indicates their main properties. We actually note that the impression of dispersion towards lower $L_{\rm X}$ comes mainly from five points, namely HD 152076 for the O-type stars and CPD −41°7760, CPD −41°7746, HD 326320 and HD 326343 for the B-type sample. These sources correspond to five out of the eight OB sources with an off-axis distance over 10′. The other three sources are HD 152437, whose classification has recently been revised to A0 III (Sana 2005) and is thus not plotted in the current diagram, HD 152235, a B1 Ia star whose X-ray emission could not be disentangled from a brighter neighbour (and which is thus not plotted either), and HD 152247, an X-ray bright O9.5 III star. We note that the position of HD 152247 in the $L_{\rm X} - L_{\rm bol}$ diagram fits very well the expected linear relation. Further inspection of the results of Tables 4 to 6 reveals that the X-ray fluxes from these five sources were all obtained with single temperature models. These were characterized by kT about 0.25 keV for the O star and about 0.5-0.6 keV for the four other B stars. Comparing these single temperature fits with the results of the 2-T models, we note that the obtained kT corresponds to the lower temperature component of the 2-T models. We caution that, because these sources are located in the outer parts of the detector, where the sensitivity significantly decreases, only the softest part of the spectrum produces a significant number of photons. The harder part of the spectrum provides too faint a contribution for a 2-T model being used, which probably biased the computation of the observed flux in the 0.5-10.0 keV band. HD 152247 is about one order of magnitude brighter in the X-rays. It is probable that, thanks to its large X-ray luminosity, the higher energy part of the spectrum remains relatively well constrained. The obtained spectrum is indeed of good quality and a 2-T model is definitively required to properly reproduce it.

To preserve an early-type sample as homogeneous as possible, both in terms of location in the cluster and in terms of the hypotheses that underlie the analysis, the following discussion will be restrained to the results obtained with the 2-T and 3-T models. In addition, we will not consider the WR star which, by definition, belongs to a different class of objects than the O- and B-type stars.

As previously indicated by Berghöfer et al. (1997), the separation between the different behaviours in the observed emission occurs at about $\log L_{\rm bol} \approx 38$ (erg s^{-1}). We note however that none of the B-stars in our selected sample has $L_{\rm bol}$ larger than 10^{38} erg s^{-1}. This value thus naturally separates the O- and B-type stars. In the remainder of this section, we address separately the two categories of objects.

Before deriving the $L_{\rm X} - L_{\rm bol}$ relationships for our sample, we would like to draw the attention of the reader to the following point. In the rest of this paper, we will make a difference between a scaling law (SL):

$$L_{\rm X} = K\, L_{\rm bol},$$

where K is the scaling constant, and a power law (PL):

$$L_{\rm X} = K\, L_{\rm bol}^{\Gamma},$$

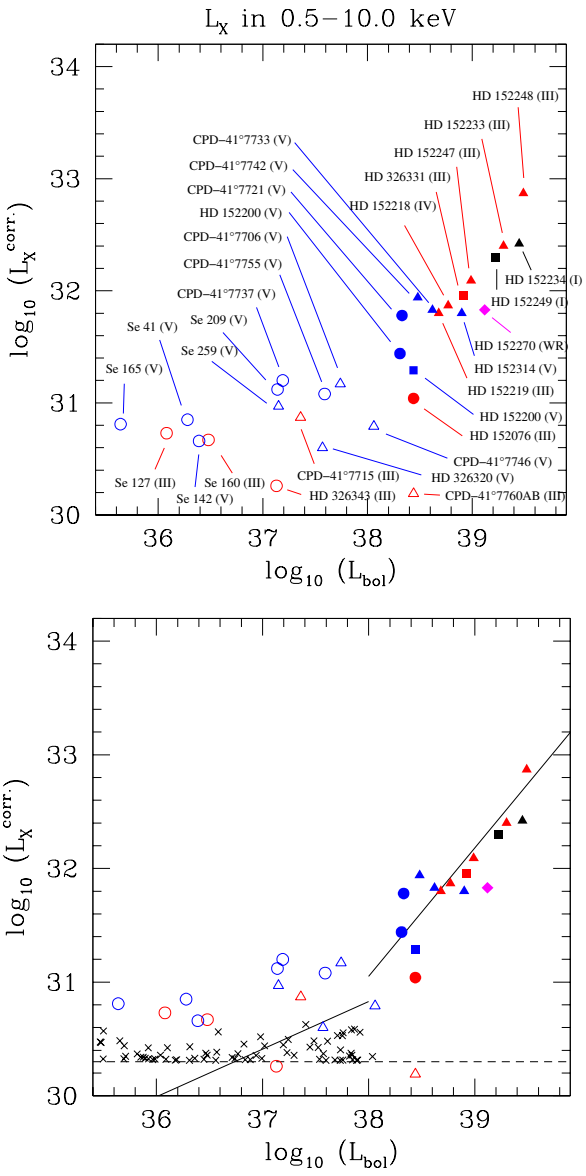

Fig. 7. Top panel: ISM-absorption corrected X-ray luminosities in the 0.5-10.0 keV band plotted vs. bolometric luminosities. The different symbols indicate the different properties of the sources. Spectral type: O (filled symbols), B (open symbols). Luminosity class: supergiant (I or black), giant (III or red), main sequence (V or blue). Multiplicity: binary (triangles), radial velocity variable (squares), presumably single star (circles). The magenta diamond indicates the WR6+O6 system WR 79 (≡ HD 152270). **Bottom panel**: same as the upper panel, the plain lines give in addition the Berghöfer et al. (1997) relations obtained in the 0.1-2.0 keV band, respectively for objects with $\log L_X > 38$ (erg s^{-1}) and for those below. The dashed line indicates our typical detection limit at a distance of about 5′ from the axis for a source with a temperature kT around 0.7-1.5 keV and an ISM column of absorbing hydrogen of $n_H^{ISM} = 0.26 \times 10^{22}$ cm^{-2} (see Paper I). The crosses indicate the upper limits for the undetected B-type stars (see text).

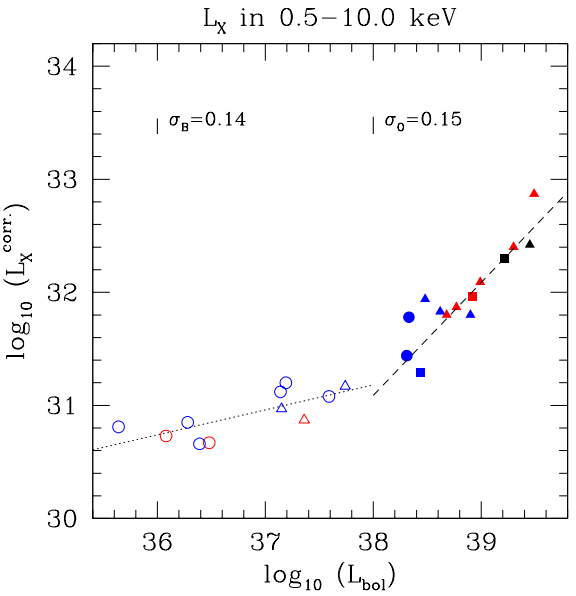

Fig. 8. ISM-absorption corrected X-ray luminosities in the 0.5-10.0 keV energy band plotted vs. bolometric luminosities. The symbols have the same meanings as in Fig. 7. Best-fit linear relations in the log – log plane for O (Eq. 2) and B (Eq. 7) stars are indicated by the dashed and the dotted lines respectively. The two vertical bars in the upper part of the graph give the expected 1-σ deviation for B (σ_B) and O (σ_O) type stars.

where Γ is the power law index. In the log – log plane, both relations yield a straight line:

$$\log L_X = \log L_{bol} + \log K$$

for the scaling law, and

$$\log L_X = \Gamma \log L_{bol} + \log K$$

for the power-law. We emphasize that the former expression has a slope equal to unity in the log – log plane and is equivalent to the statement $\log(L_X/L_{bol}) = cst$, with $cst = \log K$. The earliest works on the *canonical* relation mostly used scaling relations while, later on, power-laws were used to provide an additional degree of freedom to the fitted model. Some confusion between these two fundamentally different kinds of relations was apparent in some works and a word of caution was thus necessary to clarify the notation and vocabulary used in the present paper. In the following, both kinds of models will be tested and their results will be compared.

4.2.1. X-ray emission from O-type stars ($L_{bol} > 10^{38}$ erg s^{-1})

As seen in Figs. 7 and 8, the O-type stars mostly concentrate in a line in the $L_X - L_{bol}$ plane. As a first step in the analysis, we computed the linear-correlation coefficient r (Table 8). We then estimated the probability for an uncorrelated parent distribution to yield a value of r equal or larger than the observed value (see e.g. Bevington 1969). For all the considered O-star

Table 8. Comparison between best-fit $L_X - L_{bol}$ scaling-law (SL) and power-law (PL) models, computed in the 0.5-10.0 keV energy bands (upper part of the table) and in the soft (S_X) and intermediate (M_X) energy ranges (bottom part). The first two columns specify the O-star sample used (see text) and the number N of stars in the sample. The third column provides the $\log L_X - \log L_{bol}$ correlation coefficient r. The next two columns indicate the best-fit scaling laws, the reduced χ^2 and the number of degree of freedom (dof) of the fit. Cols. 6 and 7 yield the same information for the best-fit power laws. Note that, in Cols. 5 and 7, the χ^2 statistics do not have been normalized by the intrinsic variance of the data. The last column gives the values of the statistics F_χ.

Sample	N	r	SL (Eq. #)	χ^2_ν (dof)	PL	χ^2_ν (dof)	F_χ
A	14	0.89	Eq. 1	3.46×10^{-2} (13)	$\log L_X = 0.91(\pm0.13) \log L_{bol} - 3.6(\pm5.1)$	3.62×10^{-2} (12)	0.4
B	12	0.91	Eq. 2	2.34×10^{-2} (11)	$\log L_X = 0.85(\pm0.12) \log L_{bol} - 1.2(\pm4.7)$	2.24×10^{-2} (10)	1.5
C	10	0.97	Eq. 3	7.56×10^{-3} (9)	$\log L_X = 0.88(\pm0.08) \log L_{bol} - 2.2(\pm3.1)$	6.58×10^{-3} (8)	2.3
B	12	0.86	Eq. 4	3.75×10^{-2} (11)	$\log L_{X,S} = 0.80(\pm0.15) \log L_{bol} + 0.6(\pm5.9)$	3.53×10^{-2} (10)	1.7
B	12	0.85	Eq. 5	4.22×10^{-2} (11)	$\log L_{X,M} = 0.75(\pm0.16) \log L_{bol} + 0.6(\pm6.2)$	3.95×10^{-2} (10)	1.8

samples (see below), we could reject this hypothesis at a significance level of 0.001. Assuming first that $L_X/L_{bol} = cst$, a least-square fit performed on the 14 objects (sample A) yields:

$$\log (L_X/L_{bol})_A = -6.865 \pm 0.186 \quad (1)$$

with a typical dispersion of the X-ray luminosity of about 55% around Eq. 1. However, we note that most of the dispersion comes from four points. Among them, HD 152248 and CPD −41°7742 are known to display a significant extra-emission associated with a wind interaction phenomenon occurring in both systems (Sana et al. 2004, 2005a). This extra emission, averaged over the orbital cycle may account for at least one third of the observed flux (see individual notes for more details). Rejecting these two binary systems from the fit (sample B), we now obtain:

$$\log (L_X/L_{bol})_B = -6.912 \pm 0.153 \quad (2)$$

with a typical 1-σ deviation corresponding to about 40% on L_X (see Fig. 8). Beyond these two colliding wind systems, the remaining dispersion is mainly due to HD 152200 and HD 326329. It is interesting to note that, with a respective spectral type of O9.5 and O9.7, these two presumably single stars are the two coldest O-type main sequence stars of our sample. Excluding these two main sequence stars with a sub-spectral type later than O9 (sample C), the best fit values are almost unchanged:

$$\log (L_X/L_{bol})_C = -6.925 \pm 0.087 \quad (3)$$

However the residuals drop this time to 20%. Except for the late O-type main sequence and the two identified systems with strong wind interaction effects, the X-ray luminosity of the other objects of our sample displays thus a very limited dispersion around the newly derived *canonical* relation. Among these ten stars, dwarfs, giants and supergiants are found, as well as presumably single stars and binaries. In Sect. 5, we pay a more particular attention to each of these objects.

As a next step, we also computed the X-ray luminosities of the sample stars in different energy bands. Plotted against the bolometric luminosities (Fig. 9), we again observed linear relations in the log – log plane in the soft (S_X: 0.5-1.0 keV) and medium (M_X: 1.0-2.5 keV) bands, while a large dispersion is seen at higher energies (H_X: 2.5-10.0 keV). We note that in the S_X and M_X bands, the relative position of the stars is very similar. The two colliding wind systems display a larger deviation in the intermediate band than in the soft band. This is to be expected as the X-ray emission produced in the wind-interaction region is typically harder than the intrinsic emission from O-type stars, which drops significantly beyond 1-1.5 keV. Best-fit relations in the soft (0.5-1.0 keV) and intermediate (1.0-2.5 keV) energy ranges are respectively:

$$\log (L_{X,S}/L_{bol})_B = -7.011 \pm 0.195 \quad (4)$$

and

$$\log (L_{X,M}/L_{bol})_B = -7.578 \pm 0.203 \quad (5)$$

with a typical dispersion on L_X of about 55% and 60% respectively. The hard band shows a much larger dispersion and further suggests a slightly different behaviour for main-sequence stars compared to more evolved objects. The former ones are about at least one order of magnitude brighter than the giants of a similar spectral type. There also seems to be a steep trend in the giant and supergiant population and their fluxes in the hard band indeed increase by more than one order of magnitude towards larger bolometric luminosities. We caution however that the measured X-ray flux above 2.5 keV is probably little constrained, except for the brightest X-ray emitters, and that the present results for the hard band probably require confirmation using a larger sample of stars.

As mentioned earlier, we also adjusted power-laws to the data by means of a linear regression performed in the log – log plane. The best-fit relations are quoted in Table 8 for the different samples and energy bands considered. These only yield a marginal improvement of the residuals and the dispersion of the data around the power-law relations is virtually unchanged. To test the judiciousness of including this additional degree of freedom in the model, we used a F_χ-test as described in e.g. Bevington (1969). The F_χ statistics is given in Table 8 and was obtained from the equation:

$$F_\chi = \frac{\chi^2_{SL} - \chi^2_{PL}}{\chi^2_{PL}/(N-2)} \quad (6)$$

where N is the number of points in the considered sample. None of the quoted power-laws successfully passed the test,

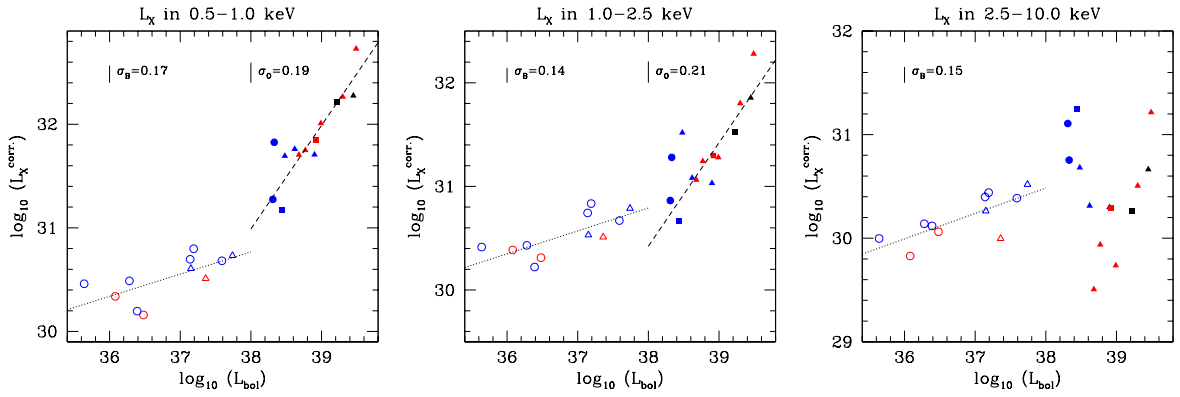

Fig. 9. ISM-absorption corrected X-ray luminosities in different energy bands plotted vs. bolometric luminosities. The symbols have the same meanings as in Fig. 7. Best-fit linear relations in the log – log plane are indicated by dotted and dashed lines respectively for B- and O-type stars.

even adopting a loose significance level of 0.1. In consequence we consider that the power-law model does not provide any significant improvement compared to the simpler scaling law. In the following, we have adopted the *canonical* $L_{\rm X} - L_{\rm bol}$ relation given by Eq. 2.

Sect. 6 provides a more detailed discussion of the $L_{\rm X} - L_{\rm bol}$ relation and comparison with earlier works. In a first approach, we might however note than the observed dispersion around the best-fit relation is much more limited than in the previous studies. Indeed, accounting for all O-type stars in our sample, the X-ray luminosity displays a dispersion of 55% (compared to the factor 2.5 of Berghöfer et al. 1997). Excluding the identified systems with strong wind interaction effects, the dispersion is limited to about 40% while it drops to 20% when excluding the late O-type dwarfs. The present sample of stars suggests thus that the natural dispersion of the intrinsic X-ray emission from O-type stars is very limited.

We however note that the present sample of stars does not extend towards spectral types earlier than O6, nor to bolometric luminosities larger than $\log L_{\rm bol} = 39.5$. Because of the limited range in $L_{\rm bol}$ (less than 1.5 order of magnitude), extrapolation towards earlier types should be considered with caution. We however note that no systematic deviation is observed for stars belonging to different luminosity classes. Their X-ray luminosity seems to follow the same relation and scales with their bolometric luminosity in a similar way, suggesting thus a common underlying physical mechanism to generate the observed X-ray emission.

4.3. X-ray emission from B-type stars ($L_{\rm bol} < 10^{38}$ *erg s*$^{-1}$)

As mentioned in sect. 4.1, the B-type stars have a quite harder emission ($kT_2 > 1.0$ keV) compared to the O-type stars. They are however much more luminous in the 0.5-10.0 keV band than predicted by the Berghöfer et al. (1997) relation (Fig. 7). This probably results from the fact that the higher energy part of the B-type spectrum falls outside the observable energy range of the ROSAT satellite. Like the O-type stars, their X-ray and bolometric logarithmic luminosities are apparently still linked by a linear relation. The computed linear-correlation coefficients r are about 0.75, which rejects the null hypothesis of such a high value occurring by chance from an uncorrelated distribution at a significance level of 0.01. Only the r value computed for the $S_{\rm X}$ band is slightly lower ($r = 0.68$) and yields the rejection of the null hypothesis only if we adopt a looser significance level of 0.05.

It is obvious from Figs. 7 to 9, that the slope of a putative relation is significantly different from unity and indeed the F_χ test described above indicates that the power-law provides a very significant improvement of the quality of the fit compared to a simple scaling law. From our selected sample of 11 B-type stars, we obtain:

$$\log L_{\rm X} = 0.22(\pm0.06) \log L_{\rm bol} + 22.8(\pm2.4) \quad (7)$$

with a typical dispersion around Eq. 7 of 0.14 in the log – log plane, thus corresponding to about 37% in the X-ray luminosities.

From Fig. 9, the emission of the B-type stars in the log – log plane also follows a linear relation in the different energy bands considered. By opposition to the behaviour of O-type stars, this linear behaviour also holds in the harder band. However, we note that the softest part (< 5 keV) of the hard band is responsible for most of the flux. The latter remains indeed very limited above this value (see e.g. Fig. 4). From linear regressions, we obtain:

$$\log L_{\rm X,S} = 0.21(\pm0.08) \log L_{\rm bol} + 22.6(\pm2.8) \quad (8)$$

$$\log L_{\rm X,M} = 0.22(\pm0.07) \log L_{\rm bol} + 22.4(\pm2.5) \quad (9)$$

$$\log L_{\rm X,H} = 0.24(\pm0.07) \log L_{\rm bol} + 21.1(\pm2.6) \quad (10)$$

with typical dispersions of respectively 0.17 (47%), 0.26 (84%) and 0.15 (42%) around these relations.

5. Individual objects

This section aims at providing specific information on the different early-type X-ray emitters detected in the XMM-*Newton* FOV. In particular, we have investigated their variability on the different time-scales allowed by our data set. Using the *emldetect* count rates obtained in Sect. 2, we performed a χ^2 test of hypothesis with a significance level of 0.01 and we actually tested the null hypothesis of a constant count rate throughout the six pointings of the XMM-*Newton* campaign. Ten sources displayed consistent indications for variability in all the EPIC instruments. These are noted 'var.' after their name in the individual sections here below. In addition, CPD −41°7715 and CPD −41°7737 displayed consistent results in all the EPIC instruments with a significance level of 0.1 only. They are noted 'var?'. Finally, HD 326329 presents significant variations at the 0.01 level but is probably contaminated by a neighbouring strong source (X#324). The latter displayed a strong flare that is also seen in the HD 326329 count rates. It is thus difficult to determine whether, in addition to the contaminating component, the HD 326329 source displays intrinsic variation of its flux or not.

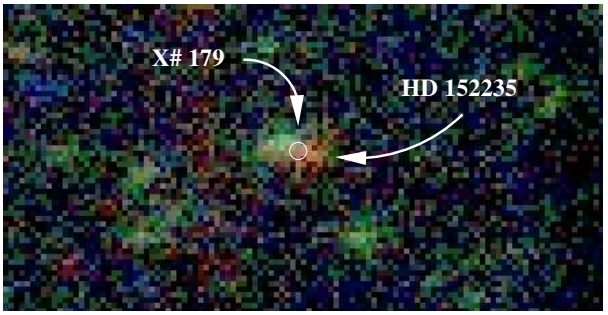

Fig. 10. HD 152235: EPIC three-colour image: red, S_X band; green, M_X band; blue, H_X band. The location of X#179 is clearly biased by the presence of two close, unresolved sources that can only be distinguished in this image thanks to their different spectral properties. The supergiant B-star HD 152235 is clearly associated with the soft emission. The image appears in colour in the electronic edition of the paper.

5.1. O-type stars

- **HD 152076** is located at 13′ N-NW of the cluster core. It lies outside the pn detector FOV and is thus only seen in the two MOS instruments. It presents a constant flux throughout the campaign. The quality of the obtained spectra is definitively too low to constrain an hypothetic 2-T model. We suspect the adopted single temperature model to bias the computed flux in the 0.5-10.0 keV band. This source was thus not included in the derivation of the $L_X - L_{bol}$ relationship.

- **HD 152200** is the latest O-type star of our sample. It is reasonably bright and well isolated in the X-ray images and its X-ray flux remains constant. We considered it to be reasonably well constrained. HD 152200 is however one of the O-type stars that deviate the most from the derived $L_X - L_{bol}$ relation. We have not been able to identify a cause that could possibly bias the determination of its flux and we consider the observed deviation to be significant.

- **HD 152218** displays a slight modulation of its flux by about 20% but its X-ray spectral properties remain almost unchanged (Sana et al. 2005e). The observed modulations could be linked to a possible wind-wind collision occurring in this O+O system, but the latter authors note that second order effects, such as radiative inhibition, might actually govern the wind interaction properties in this system. However, the HD 152218 X-ray flux remains probably dominated by the intrinsic emission from the stars.

- **HD 152219** presents a slight modulation of its flux (Sana et al. 2005b) which could be related to a similar wind interaction as in CPD −41°7742. Except for the longer orbital period of HD 152219, the two systems are indeed very similar. The amplitude of the variation seems however much more limited than in CPD −41°7742. This probably results from the longer period of the system, yielding thus a larger separation between the components and a subsequent dilution of the wind material that enters the interaction.

- **HD 152233** is most probably a long period ($P \sim$ months) binary (Sana 2005), but its orbital properties are still not constrained. We are currently monitoring the system to constrain its period and to provide a reliable orbital solution. The HD 152233 X-ray flux presents an apparently constant level throughout the campaign.

- **HD 152234** (var.) is reminiscent of HD 152233. The system is most probably a long period ($P \sim$ months) binary (Sana 2005), but its orbital properties are poorly constrained so far. Its X-ray flux slightly decreased throughout the XMM-*Newton* campaign with an average slope of about -4.3×10^{-3} cnt s^{-1} per day. This corresponds to a reduction from about 75×10^{-3} to about 55×10^{-3} cnt s^{-1} between the first and sixth observations. This could be due to a wind interaction between the two components, whose strength is varying because e.g. of the changing separation between the stars. However, a more precise analysis requires first to constrain the orbital properties of the system. An ongoing monitoring campaign should soon provide this missing piece of the puzzle.

- **HD 152235** (not resolved) is a B1Ia star in the southern part of the field. The cross-correlation did not associate this object with an X-ray source. An inspection of the three-colour image (Fig. 10) however clearly reveals that HD 152235 is a soft X-ray emitter. The source detection has actually been biased because of a close, harder emitter, companion. Due to this close neighbour, the HD 152235 spectrum can unfortunately not be reliably extracted and

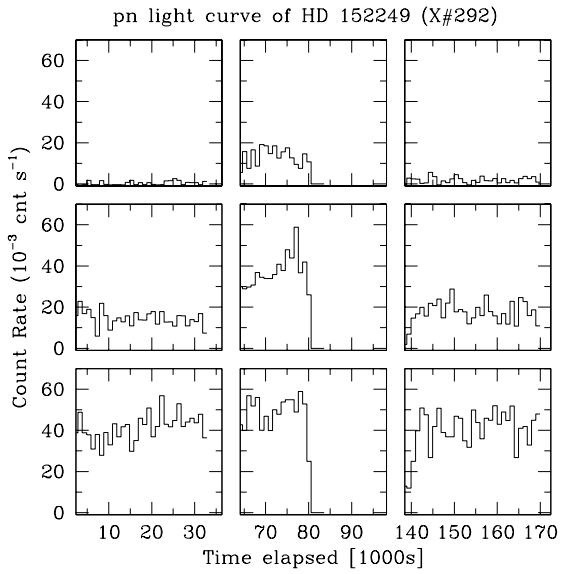

Fig. 11. HD 152249: EPIC pn light curves in the three energy bands: 0.5-1.0 keV (lower panels), 1.0-2.5 keV (middle panels) and 2.5-10.0 keV (upper panels) during XMM-*Newton* Obs. 1 to 3. The time is given in ks since the beginning of Obs. 1. The bin size is 1 ks. The effective duration of Obs. 2 has been reduced because of a high background event. The contamination by the stellar flaring source is clearly seen. Its relative influence increases towards harder energies.

the source was thus not included in the present analysis.

- **HD 152247** is located in the outer region of the field. It is most probably an SB1 binary (Sana 2005), but its period is largely undetermined. It could however be of the order of one year. The X-ray flux seems to remain constant from one pointing to the other.

- **HD 152248** (var.): the colliding wind binary HD 152248 is the brightest X-ray source in the FOV (Sana et al. 2004) and presents phase-locked modulations of its X-ray fluxes because of the varying strength of the shock in this eccentric system. The X-ray data have been thoroughly analysed in Sana et al. (2004). To provide averaged properties for this peculiar system, we adjusted a 3-T model to its spectrum. Unfortunately, we could not get χ^2_ν values better than 2.4. This might reflect the changing spectral properties of the system and the impossibility for MEKAL models to reproduce, in this case, an averaged emission level. Because of the $\chi^2_\nu > 2$, the XSPEC software did not allow to explore the parameter space to search for a better local minimum. For the same reason, we could not directly compute the limits of the 90% confidence intervals. In Table 6, the quoted intervals were estimated from the 1-σ error bars that were converted into 90% confidence intervals assuming a Gaussian distribution of the uncertainties. We note however that the obtained flux in the 0.5-10.0 keV band is very similar to the average value of the six fluxes observed during the six individual pointings (Sana et al. 2004). This indicates that the present result is quite consistent with the previous analysis. Using the newly derived $L_X - L_{bol}$ relation of Eq. 2 and the individual luminosities, we expect $\log L_X = 32.58$. We observed, on average, $\log L_X = 32.87$, which is about twice larger.
In Sana et al. (2004), we have modelled the X-ray emission expected from the wind-wind interaction using hydrodynamical simulations. Once diluted by the intrinsic emission from the two stars, the modelling qualitatively reproduced the observed modulations. However, the predicted X-ray flux was about a factor two too faint compared to the observed emission level of the system. At the time, we attributed this difference to the observed dispersion around the Berghöfer et al. (1997)'s *canonical* relation. The intrinsic emission from the O-type stars in NGC 6231 is now much better constrained and, in particular, the dispersion around the $L_X - L_{bol}$ relation is presumably much more limited than previously expected. By comparison with the observed L_X for the system, one can now probably better estimate, from the observational point of view, the *exact* amount of X-ray emission produced in the wind interaction. Therefore, the HD 152248 system probably deserves further theoretical work to quantitatively explain the observed modulations and the *exact shape* of its light curve.

- **HD 152249** presents a strong increase of the measured flux during Obs. 2. This increase is seen in the three energy bands, but is most prominent in the intermediate (M_X) and, especially, in the hard (H_X) bands (Fig. 11). An inspection of the corresponding images reveals a nearby flaring source, located at about 6″ S-W of HD 152249, thus well within the extraction region. The contaminating source is still slightly seen in the hard band during Obs. 3 while is has vanished during the remainder of the campaign. The contamination by the flaring source is also seen in the extracted spectra for HD 152249 with the apparition of a hard component during Obs. 2. The count rates obtained during the other four pointings remain however in acceptable agreement. The spectral fit given in Table 5 and the derived values for the fluxes and luminosities were thus obtained considering only the four pointings with no contamination.

- **HD 152314** is a relatively isolated bright X-ray emitter whose X-ray flux seems to remain constant.

- **HD 326329** (contaminated?) is located in a relatively crowded region of the cluster. The count rates obtained via the SAS task *emldetect* are clearly affected by the bright X-ray source X#324 that displays a flare during Obs. 4 (see Paper III). We re-derived the count rates in a limited extraction region of 7.″6 but obtained mitigated results. Clearly the derived fluxes for this object should be regarded with cautioun. It is interesting to note that, after the two wind interaction systems, HD 326329 presents the largest deviation from Eq. 2. From the above remark, this dispersion is probably artificial and might not be

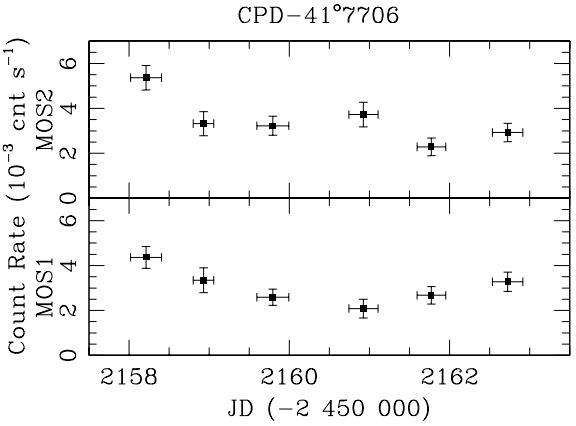

Fig. 12. CPD −41°7706 background corrected EPIC MOS light curves (in the range 0.5–10.0 keV) during the XMM-*Newton* campaign. The average count rates during each pointing are given. The vertical bars are the 1-σ deviations while the horizontal bars give the duration of each pointing.

linked to any physical process. This supports the idea that wind-interaction is the only identified mechanism that, in favorable configuration, can produce a significant deviation from the canonical relation.

- **HD 326331** optical spectrum reveals particularly broad lines displaying slight profile variations. Some authors (Hill et al. 1974; Levato & Morrell 1983; García & Mermilliod 2001) have suggested that it could actually be a binary system. From our work (Sana 2005), we believe that the binarity is far from being confirmed and that the profile variations are probably not due to the presence of a companion. The X-ray flux of HD 326331 remains constant over the duration of the campaign.

- **CPD −41°7721** is a visual double star with components, labelled 'p' and 's' respectively, separated by $\sim 5.8''$. Other denominations for these components are SBL 350 and 351 or BVF 12 and 27. The X-ray source X#251 is clearly associated with the O-type 'p' component. Larger residuals are seen at the position of SBL 358 ($V = 15.89$), but there seems to be no detected X-ray emission associated with the B-type star CPD −41°7721s. The *emldetect* count rates show some deviating points, especially at Obs. 2 for the MOS2 instrument and at Obs. 4 for the pn. These deviating points are however not confirmed by the other instruments. We re-derived the count rates using the same extraction region as the one adopted for the spectra and we found that the X-ray flux from CPD −41°7721p is probably constant throughout the campaign. We note that the extracted spectra might be contaminated by the residual X-ray emission located at $\sim 8''$ from CPD −41°7721p and probably associated with SBL 358. We however caution that the contamination is probably very low and limited to the soft part of the spectrum, thus in the energy range where CPD −41°7721p displays the strongest X-ray emission.

- **CPD −41°7733** presents an approximatively constant X-ray flux throughout its orbit (Sana et al. 2005c) and indeed, no significant X-ray overluminosity from a possible wind interaction is expected at our detection threshold.

- **CPD −41°7742** (var.) is the second known SB2 eclipsing early-type binary in NGC 6231 and has a period close to 2.4 d (Sana et al. 2003). It is about 3 times brighter in the X-rays than expected from Eq. 2. Sana et al. (2005a) presented the MOS X-ray light-curve of the system, almost fully covering the orbital cycle with a time bin of 1 ks. We showed that an extra-emission component is associated with the inner face of the secondary. When the orientation of the line of sight is favourable, this component could be responsible for an increase of the X-ray flux by about a factor of 2. These features were interprated as the primary wind crushing on (or nearby) the secondary surface. Alternatively, the wind-photosphere interaction could be altered leading to a wind-wind interaction region located close to the secondary surface. Even at its lowest flux level, the logarithmic X-ray luminosity is still about 0.3 above the one expected for the intrinsic emission of this O+B binary.

5.2. B-type stars

Before reviewing the individual B-type emitters, we note that only about 25% of the B-type stars are associated with an X-ray source in the catalogue of Paper I. Among these, four sources are apparently single and, at our detection threshold, do not display significant variations of their flux. These are Se 127 (≡ SBL 746, B8III/IV), Se 142 (≡ SBL 748, B4V), Se 160 (≡ SBL 593, B3III), and HD 326343 (B3III). These stars will not be discussed any further.

- **HD 152437** is probably a foreground star reported as B9 III/IV (Houk 1978). From our data however (Sana 2005), we prefer to adopt the slightly later type A0III. According to its visual magnitude $V = 9.145$ and to $B - V = 0.15$, we obtained $m_V \approx 8.6$, indicating that the star is probably located at about 500 pc from the Sun. Its X-ray flux is seen as constant. As a newly classified A-type star, the object was not considered in the discussion.

- **HD 326320** is an SB2 binary located in the outer regions of the FOV. At our detection threshold, we do not detect any significant variations but the count rates are quite low. Its spectrum is well described by a single temperature model.

- **CPD −41°7706** (var.) is a B1+B1 binary (Levato & Malaroda 1980; García & Mermilliod 2001). Sana (2005) reported that the Hα and all the He I lines from λ4920 to λ7100 display mixed absorption plus emission. All these lines have the same profile with a narrow absorption

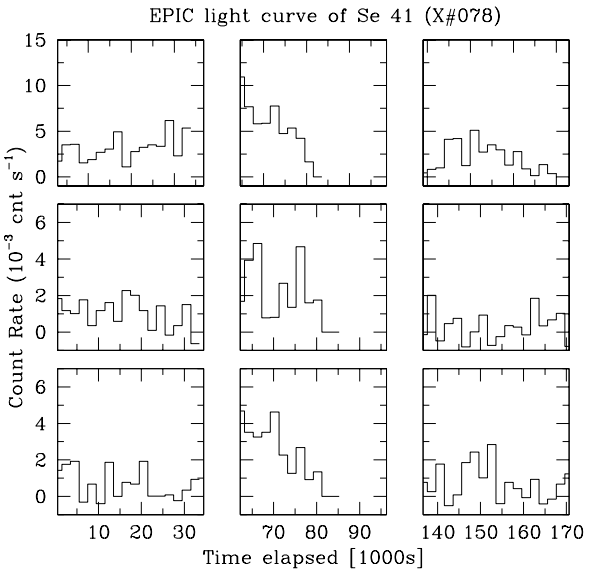

Fig. 13. Se 41/SBL 149 EPIC pn (top panels), MOS2 (middle panels) and MOS1 (lower panels) light curves (for PI in the range 500 to 10 000) during XMM-*Newton* Obs. 1 to 3. The time is given in ks since the beginning of Obs. 1. The bin size is 1 ks. The effective duration of Obs. 2 has been reduced because of a high background event.

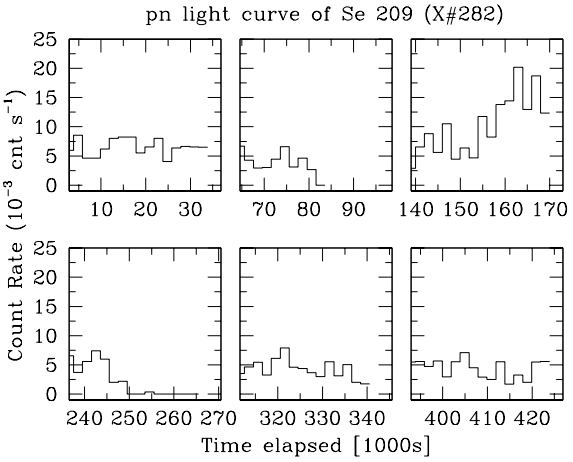

Fig. 14. Se 209 / SBL 394 EPIC pn light curve (for PI in the range 500 to 10 000) during XMM-*Newton* Obs. 1 to 6. The time is given in ks since the beginning of Obs. 1. The bin size is 2 ks. The effective durations of Obs. 2 and 4 have been reduced because of a high background event.

superposed on a broader emission which results in line profiles reminiscent of the Be spectral signature. Because the component signatures are blended, it is not possible to decide if both components or just one of them is actually a B1Ve star. The source presents a smooth variation of its X-ray flux (Fig. 12), but no sign of flaring activities could be found for this system.

- **CPD −41°7715** (var?) is reported as a spectroscopic binary by Raboud (1996) and as a β Cep-type star by Arentoft et al. (2001). There might be an increase of the detected flux during Obs. 2 but a χ^2 test with a significance level of 0.01 did not allow to reject the null hypothesis of constant count rate throughout the six pointings.

- **CPD −41°7737** (var?) is a slowly pulsating B2V star (Arentoft et al. 2001). There is a slight increase (∼40%) of the count rate during Obs. 5, but because of the large error-bars, it might not be significant. A χ^2 test with a significance level of 0.01 did not allow to reject the null hypothesis of constant count rate throughout the six pointings.

- **CPD −41°7746** was reported as an SB1 system by García & Mermilliod (2001). Located in the outer part of the FOV, it falls on a gap of the pn instrument. The MOS count rates are too low to investigate the intra-pointing variability. However, no sign of flaring activities is seen. The spectrum is very poor and the star was not considered in the present analysis.

- **CPD −41°7755** (var.) is an apparently single B1V star. The X-ray flux seems in a higher state during the last three observations than at the beginning of the campaign. An inspection of the images does not reveal any contaminating source. The maximum emission is seen during Obs. 5 and is about a factor 3 to 4 higher than during the first three pointings. We caution however that the count rates are low (between 1 and 4×10^{-4} cnt s^{-1} in the two MOS instruments).

- **CPD −41°7760** is a visual binary with separation of about 2″. The two components have a probable spectral type B0.5III and B1V respectively. CPD −41°7760 lies in the outer region of the field, outside the MOS detection area. It is thus only seen in the pn instrument. Its X-ray emission is close to our detection limit, but seems to remain constant throughout the six pointings. The obtained spectrum is of poor quality (Fig. 5) and was not considered in the derivation of the $L_X - L_{bol}$ relations.

- **Se 41 / SBL 149** (var.) is a B4V according to SIMBAD. With an average pn vignetting and exposure-time corrected count rate of about 5×10^{-3} cnt s^{-1}, it is a relatively bright X-ray source. Its count rate is higher by a factor 2 to 3 during Obs. 2, whereas it is almost constant during the 5 other exposures. This increase is also seen in the three energy bands. Inspection of the images indicates no sign of a contamination by a nearby flaring source within the extraction region. We therefore consider the flare to be associated with Se 41. We built light curves with a temporal resolution of 1, 2 and 5 ks for all three instruments. They consistently indicate that the emission is decreasing from the beginning of Obs. 2 and reaches a similar emission level as during the other pointings at the

end of Obs. 2 (Fig. 13).

- **Se 209 / SBL 394** (var.) has been proposed either as a binary candidate (Raboud 1996) or a slowly pulsating B star (Arentoft et al. 2001). It presents an increase of its emission during Obs. 3 (Fig. 14), which yields an average count rate higher by about a factor 2.5 compared to other pointings.

- **Se 259 / SBL 317** is suspected to display radial velocity variations (Raboud 1996) possibly related to an SB2 nature (Sana 2005). This source seems to present a constant, though faint, count rate throughout the campaign.

- **Se 265 / SBL 200** (var.) is a late B-type main sequence (B8.5V according to SIMBAD) and was quoted as a cluster non-member by Baume et al. (1999). Its average count rate during Obs. 4 is about a factor two larger than during other the pointings while, actually, its emission level seems to decrease throughout Obs. 4. However, the count rates are quite low (4×10^{-3} cnt s^{-1} in the pn and 10^{-3} cnt s^{-1} in the MOS, on average during the low emission state) and caution should be the rule.

6. Discussion

As demonstrated here above, the X-ray sources associated with O- and B-type counterparts have well-defined properties, both in terms of emission levels and of spectral shapes. In the present section, we discuss the obtained results for both category of objects.

6.1. The O-type X-ray emitters

In Sect. 4, we derived various $L_X - L_{bol}$ relations corresponding to the O-type stars of our sample. The favoured relation is the scaling law $\log(L_X/L_{bol}) = -6.912 \pm 0.153$. Previous works however proposed power law $L_X - L_{bol}$ relations and we can use the relations quoted in Table 8 for comparison. The latter ones are indeed formally equivalent to the scaling relations derived in Eqs. 1 to 5. Working in the 0.2-4.0 keV band, Sciortino et al. (1990) proposed

$$\log L_X = 1.08(+0.06/-0.22) \log L_{bol} - 9.38(+2.32/-0.83).$$

In the 0.1-2.0 keV band, Berghöfer et al. (1997) obtained

$$\log L_X = 1.13(\pm0.10) \log L_{bol} - 11.89(\pm0.38),$$

while in the 0.3-12.0 keV band, Albacete Colombo et al. (2003) reported

$$\log L_X = 1.07(\pm0.04) \log L_{bol} - 6.2(\pm0.1)$$

(though see Sect. 6.1.2). Our adopted slope for a power-law $L_X - L_{bol}$ relation in the log – log plane is 0.85 ± 0.12 which is thus significantly lower than values from Berghöfer et al. (1997) and from Albacete Colombo et al. (2003). We note that, even our scaling relation, with a slope equal to unity, is still at more than 1-σ from the values quoted in the two latter works. The identification of the strong CWB systems in our sample and their rejection from the fit can explain part of the observed difference. Indeed including the CWB systems in the fit yields a larger value for the slope (see Table 8).

6.1.1. The natural dispersion around the *canonical* $L_X - L_{bol}$ relation

Working on the Rosat All-Sky survey data (Berghöfer et al. 1996), Berghöfer et al. (1997) obtained a natural dispersion of about 0.40 around their log – log relation (thus a factor of about 2.5 on the X-ray luminosity). It is unlikely that such a high dispersion is only due to the non-discrimination of the CWB systems. It could rather reflect the instrumental limitations of this previous work. Although Berghöfer et al. (1997) dispersion was already much reduced compared to Sciortino et al. (1990) work, the results of the present study suggest that the natural dispersion of the intrinsic emission from O-type star could be even more limited. We also emphasize that, the present sample is much more homogeneous in terms of age and chemical composition, wich might also play a role in preserving a low level of dispersion. In the present analysis, we have considered the bolometric luminosities as the independent variable and performed the linear fit accounting only for errors on the X-ray luminosities. It is however probable that part of the residual dispersion comes from the computation of the bolometric luminosities, via the usual error measurements on the determination of the spectral types and luminosity classes, but also via the bolometric correction scale.

The direct comparison of the present results with previous works should further be considered with caution, because of the different energy bands considered and, in particular, of the lower energy cut-off adopted for the analysis. As we are engaged in the hunt for the intrinsic properties of the stars, the observed fluxes need to be corrected for the ISM absorption. The exact influence of the latter is however difficult to constrain and its role increases dramatically towards lower energy. For example, assuming an ISM absorption column of 0.26×10^{22} cm^{-2}, which is typical for NGC 6231, the correction factor is 39.3, 2.68, 1.43 and 1.04 respectively in the 0.2-0.5, 0.5-1.0, 1.0-2.5 and 2.5-10.0 keV bands[5]. Clearly a slight uncertainty on the measured fluxes at low energy will have a large influence on the intrinsic fluxes computed. The very low energy edge (0.1 keV) adopted by Berghöfer et al. (1997) could be one of the reasons for the large dispersion observed in their sample. Another reason is probably the fact that, as explained in Berghöfer et al. (1996), these auhors computed the X-ray fluxes by using the count rates together with an energy conversion factor adopted on the basis of the

[5] These values were computed using the HEASARC's W3PIMMS tool available at `http://heasarc.gsfc.nasa.gov/Tools/w3pimms.html`. We used a Raymond-Smith model with a temperature of 1.0 keV, but the latter parameter has only a limited influence on the quoted results.

hardness ratio. Though this method is certainly what can be done best when the number of counts is low, it is certainly less accurate than the present approach. From Fig. 7, we however note that the Berghöfer et al. (1997) relation obtained in the 0.1-2.0 keV band for O-type stars remains qualitatively valid in the 0.5-10.0 keV band. Given the previous consideration, this agreement is probably a stroke of good fortune.

As mentioned earlier, we have adopted a quite large value (0.5 keV) for the low energy cut-off of our analysis. This should indeed limit the influence of the correction for the ISM absorption which, at low energy, can significantly amplify small uncertainties on the observed flux. Indeed the observed dispersion of our sample around the *canonical* relation is extremely limited (∼ 40% for the whole sample, ∼ 20% excluding the two dwarfs of subtype later than O9). We note that our sample contains both single stars and binaries, and contains objects from different luminosity classes. All of them seem to follow the same *canonical* relation, suggesting thus a common mechanism for the X-ray emission. Finally, beyond possible observational artifacts (e.g. contamination by neighbouring sources, see Sect. 5), the sole cause for the observed deviation from the *canonical* relation is X-ray emission from a wind interaction zone. This extra-emission however does not seem to significantly affect all the O-type binaries of the present sample. It is also the sole mechanism that, at our detection limit, yields a modulation of the X-ray flux in our star sample. In consequence, from the present analysis, we conclude that, at our detection threshold, the intrinsic X-ray emission from O-type stars does not show any significant variability and can be considered as constant for a given star.

6.1.2. Constraints from the Carina region

Albacete Colombo et al. (2003) have recently analysed a 44 ks XMM-*Newton* observation of the Carina nebula. In the FOV there are about 13 O-type stars for which they derived the X-ray luminosities in the 0.3-12 keV and 3.0-12.0 keV bands. Their sample is mainly formed by main-sequence single stars and binaries, presenting a range of spectral types from O3 to O9. From their data, they reported to have derived the relation $\log L_{\rm X} = 1.07(\pm0.04)\log L_{\rm bol} - 6.2(\pm0.1)$. However drawing this relation on their Fig. 9, one can notice that the plotted line actually lies over two orders of magnitude above their data (see Fig. 15). Their statement that "*in the $L_{\rm X} - L_{\rm bol}$ plane, this function becomes a constant relation:* $L_{\rm X} \approx 6.0^{7.5}_{4.8} \times 10^{-7} L_{\rm bol}$" is rather a crude conversion from a power law to a scaling law. Indeed the latter ratio corresponds to an independent term of -6.2 ± 0.1 in the log – log plane. However the authors completely ignored the index (1.07 ± 0.04) of their quoted power-law, which indeed dramatically modify the relation, both quantitatively and qualitatively.

Using the data quoted in their Table 6 and considering the same objects as they did (thus 11 stars, among which 10 dwarfs), an unweighted linear regression yields

$$\log L_{\rm X} = 1.02(\pm0.15)\log L_{\rm bol} - 6.9(\pm5.8) \quad (11)$$

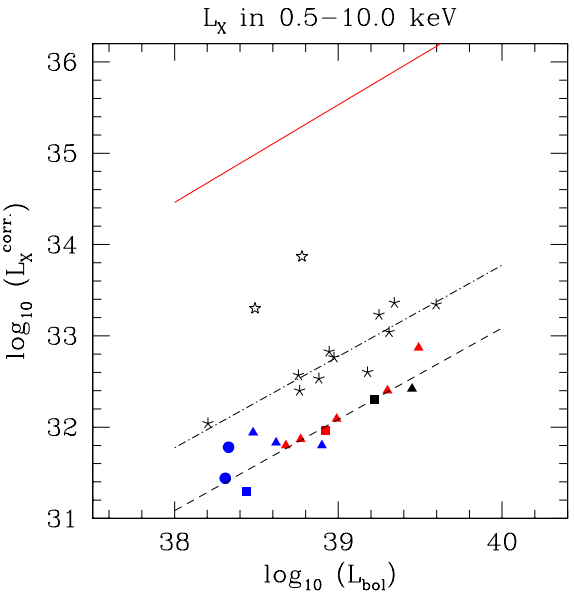

Fig. 15. Same as Fig. 8 for O-type stars. The asterisks give in addition the Albacete Colombo et al. (2003) data while the dashed-dotted line indicates our corresponding best-fit scaling law to these data (Eq. 13). The open star symbols show two points that, following Albacete Colombo et al., were not included in the fit. The plain line on top of the panel displays the power-law by quoted by Albacete Colombo et al..

The typical dispersion around the relation is about 0.18 in the log – log plane, thus very similar to the dispersion obtained from our data set. Performing a weighted fit using the absolute error on the fluxes quoted in their Table 6 yields

$$\log L_{\rm X} = 1.04(\pm0.03)\log L_{\rm bol} - 7.9(\pm1.2) \quad (12)$$

whose best-fit parameters are very similar to the above Eq. 11. The explanation of the large difference in the obtained errors is found in the reduced chi-square value: $\chi^2_\nu = 30.2$. This extremely large value for the reduced chi-square indicates that either the error bars have been underestimated or that the observed dispersion of the points around the best-fit relation can not be explained by the instrumental errors. As a consequence, we did not consider their quoted error bars iin the remaining of this work.

As a last step, we performed an unweighted fit of a scaling relation, we would have obtained

$$\log (L_{\rm X}/L_{\rm bol}) = -6.23 \pm 0.17 \quad (13)$$

The latter relation is plotted in Fig. 15 together with the data of Albacete Colombo et al. (2003). Finally, comparing the present residuals with those obtained from the unweighted power law fit (Eq. 11), we computed $F_\chi = 0.01$, which clearly indicates that the power-law does not provide any significant improvement of the fit compared to the scaling law.

This new analysis of the Albacete Colombo et al. (2003) data put into light two important points. First, as in our case, the preferred $\log L_{\rm x} - \log L_{\rm bol}$ relation takes the form of a

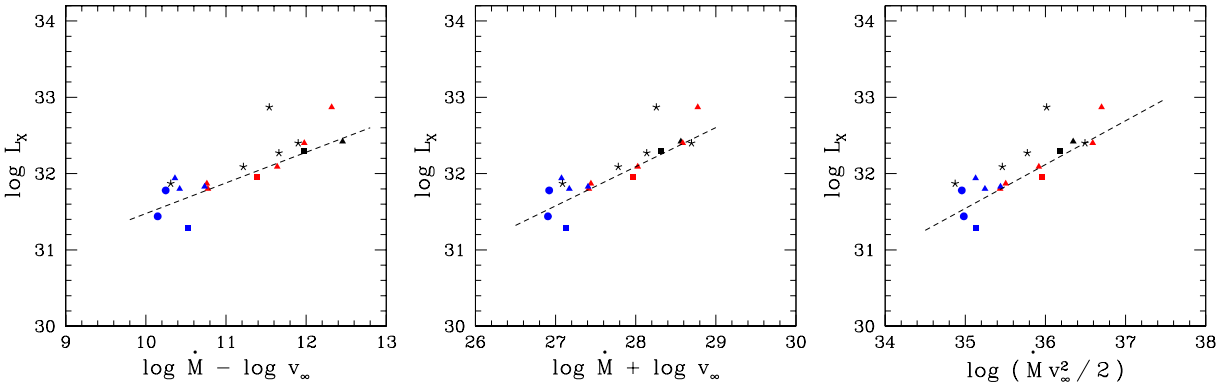

Fig. 16. $\log L_X$ plotted versus different wind parameters. The filled symbols have the same meanings as in Fig. 7. The abscissa were computed using the recipes of Vink et al. (2000, 2001). Dashed lines show the obtained best-fit relations (Eqs. 14 to 16). The asterisks were computed using the $\dot{M}$ and v_∞ measurements of Howarth & Prinja (1989) for the available objects.

scaling law. This clearly contrasts with the latter studies (e.g. Chlebowski & Garmany 1991; Berghöfer et al. 1997) which probably used the power law to provide an extra degree of freedom to the fit. The second point relies on the different nature of the considered samples. Our sample contains O6–O9 stars belonging to different luminosity classes whereas Albacete Colombo et al. (2003) data set is almost uniformly formed by main-sequence stars ranging from O8.5 to O3. However, in both cases, the scaling law is preferred and both samples displayed a limited dispersion around the best-fit relation. We suggest that the slightly larger dispersion observed in Albacete Colombo et al. (2003) data could come from a less uniform analysis and, in particular, of their handling of the correction for the ISM absorption. Accounting for the difference in the analysis (different spectral models used) and in the considered energy ranges, the two relations can be regarded as being in mutual agreement if about one fifth of the X-ray flux is actually emitted in the 0.3-0.5 keV range.

6.1.3. On the origin of the $L_X - L_{bol}$ scaling

As pointed out by different authors already, the scaling between L_X and L_{bol} could be an indirect effect. Indeed, in the framework of the embedded wind shock model, it is expected that the X-ray luminosity rather scales with the wind parameters or with some physically meaningful combination of them. Sciortino et al. (1990) indeed observed a correlation with the wind momentum ($\dot{M}v_\infty$) and the wind kinetic luminosity ($0.5\dot{M}v_\infty^2$) but did not find direct correlation with the sole mass-loss rate ($\dot{M}$) nor with the terminal velocity (v_∞). It is only through the scaling of the properties of the radiatively driven winds with the star luminosity that the dependence between L_X and L_{bol} is supposed to occur. Kudritzki et al. (1996) and Owocki & Cohen (1999) later suggested that an important parameter could be the mean wind density, which is related to $\dot{M}/v_\infty$. Indeed, from the exospheric approximation, Owocki & Cohen (1999) established that the X-ray luminosity is expected to scale with the wind density parameter $\dot{M}/v_\infty$ in the form $L_X \sim (\dot{M}/v_\infty)^2$ for optically thin winds and $L_X \sim (\dot{M}/v_\infty)^{(1+s)}$ for optically thick winds, with s being the index of the radial power law dependence of the X-ray filling factor $f \sim r^s$.

These considerations clearly contrast with the observed tight dependence between L_X and L_{bol}. Using the Vink et al. (2000, 2001) recipes, we estimated the density parameter ($\dot{M}/v_\infty$), the wind momentum ($\dot{M}v_\infty$) and the wind kinetic luminosity ($0.5\dot{M}v_\infty^2$) for the different O-type objects in our sample. We assumed $v_\infty = 2.6\, v_{esc}$. Masses and temperatures were taken from the new calibration for O star parameters of Martins et al. (2005) while the L_{bol} were obtained in Sect. 3. Fig. 16 shows the resulting diagrams. Using the same sample of stars as for Eq. 2, we obtained:

$$\log L_X = (0.402 \pm 0.064) \log\left(\dot{M}/v_\infty\right) + (27.46 \pm 0.71) \quad (14)$$

$$\log L_X = (0.513 \pm 0.075) \log\left(\dot{M}v_\infty\right) + (17.74 \pm 2.07) \quad (15)$$

$$\log L_X = (0.574 \pm 0.084) \log\left(0.5\dot{M}v_\infty^2\right) + (11.45 \pm 3.01) \quad (16)$$

with a typical residual dispersion of 0.16. Eq. 14 indicates a filling factor index s of ~ -0.6. Compared to Eq. 2, Eqs. 14 to 16 could however not be considered as independent. Indeed we used the mass-loss recipes of Vink et al. which analytically express $\dot{M}$ in terms of L_{bol}, T_{eff} and the stellar mass M. Using Eq. 2 to express L_{bol} in terms of L_X in the mass loss recipes, we indeed re-derived analytically very similar slopes as those quoted in Eqs. 14 to 16. For example, subtracting $\log v_\infty$ from $\log \dot{M}$ almost removes the first order dependency in T_{eff}. The remaining relation is dominated by the L_{bol} term.

Wind terminal velocities and star mass-loss rates were measured by Howarth & Prinja (1989) for five of the brightest stars of our sample. The corresponding observational wind parameters are displayed in Fig. 16. The agreement is rather acceptable although slight systematic upward shifts are observed. Only HD 152248 shows strong deviations from these relations, but the derivations of $\dot{M}$ and v_∞ have probably been biased by the ongoing wind-wind interaction.

Clearly, these observational data are not sufficient to provide further constraints on the link between the observed X-ray

luminosity and the star (and stellar winds) properties. It is beyond the scope of this paper to pursue the quest of the physical origin for the scaling between the X-ray and the bolometric luminosities. Though the physical processes responsible of the X-ray emission in hot stars might not be directly related to $L_{\rm bol}$, the scaling between these two parameters is an observational fact. The dispersion around the best-fit relation is extremely limited for stars of spectral-type O9 or earlier. A limited dispersion is also obtained from the Albacete Colombo et al. (2003) data. Indeed, compared to parameters such as $\dot{M}$ and v_∞, or any combination of these, the bolometric luminosity of an object is probably much easier to measure and can be estimated to a better accuracy. We note that this relation is now tightly constrained and still awaits to be explained on firm theoretical grounds.

6.2. The B-type X-ray emitters

Among the ∼90 B-type stars in the XMM-*Newton* FOV of the present campaign, about 25% of them can be associated an X-ray counterpart displaying $\log L_{\rm X} \sim 31$ (erg s^{-1}). However, except for the earliest sub-types, the B stars are not supposed to emit in the X-ray domain. Indeed their stellar winds are much weaker than those of O-type stars and should thus not contribute to the X-ray emission. In addition, no coronal emission is expected as these stars are not supposed to have the convective zones required. From our data thus, either the B-type stars are intrinsic X-ray emitters, which would imply a revision of the related theories, or the detected X-ray emission is actually associated with a later-type or PMS object along the same line of sight or physically linked with the B star.

The detected dependency between the B-star bolometric luminosities and the associated X-ray luminosities, with a linear-correlation coefficient of ∼0.75 (thus significant at the 0.01 level) is in favour of the first hypothesis. On the other hand, the fact that we only detect a fraction of the B stars at a given spectral type is clearly against. Indeed, if the X-ray luminosity was actually an intrinsic property of the star, it should be expected that similar stars would display similar $L_{\rm X}$.

In regard of these two hypotheses, the study of the variability of the individual objects presented in Sect. 5 is particularly relevant. It indicates that, among the 11 B-type stars used to derived the $L_{\rm X} - L_{\rm bol}$ relations, four are displaying a flaring activity, which is clearly in favour of the emission coming from a PMS companion, either in a binary system or located along the line of sight. Two others display long term variations whose origin is less clear. Comparing the best-fit spectral parameters of Table 5 for the X-ray emission associated with B-type stars with the spectral parameters derived for PMS emitters (see Paper III), there is at first sight a clear difference. The former display kT of 0.2 and 1.5 keV while the latter ones have temperatures of 0.7 and 2.5 keV. However, we note that two different kinds of models were used. Actually, the two models are degenerated and, using the Paper III models to fit the X-ray spectra associated with the B-type stars, we derived strikingly similar parameters as those obtained for PMS stars. As shown in Paper I, only about 20 sources over the 600 are expected to be foreground objects. The chance for such an object to be located by chance on the same line of sight of a B-type stars is thus very limited and can not explained the number of association between an X-ray source and a B-type stars.

Finally, about 50% of the B-type stars are expected to be actually in binary or multiple systems. However, typical X-ray emission from a late-type companion is probably too faint to be detected at the distance of NGC 6231. In consequence, only X-ray emission from PMS companions is expected. This could explain the difference between the expected fraction of binaries and the observed detection ratio among B stars.

Though the above discussion is clearly in favour of the X-ray emission associated with some of the B-type stars to be rather produced by a companion, the observed correlation, at a significance level of 0.01, between the bolometric luminosity of the B-star and the associated X-ray luminosity is intriguing. A possible scenario could imply some connection between the B-type star and its PMS companion. Though highly putative, such a mechanism could justify the observed link between the B-type properties ($L_{\rm bol}$) and the observed X-ray emission from the PMS companion. However, we note that the observed relation might also result from a border effect. Indeed, if the real distribution of the emission 'associated' with B-stars has about the form of a cluster of points and assuming that we only observe the upper part of the distribution, one might potentially detect an apparent relation between the two considered variables although, actually, it results from an observational bias.

6.3. The demarcation line

In this paper, we have voluntarily restrained our analysis to objects whose spectra were of sufficient quality to be fitted with 2-T models. This actually led to the rejection of the early B-type stars that were only marginally detected. It is not impossible that some of these actually form the low luminosity tail of the $L_{\rm X} - L_{\rm bol}$ relationship derived for O-type stars. Another possibility is that, in this tail, the stellar winds are becoming so weak that only weak shocks are produced, yielding thus a possibly softer emission (see e.g. the case of HD 152235 in Sect. 5). Our approach was clearly not designed to investigate the location of the demarcation line. Actually we have preferred to preserve the homogeneity of our sample, thinking that it was a higher priority to put strong constraints on the nature and shape of the $L_{\rm X} - L_{\rm bol}$ relationship prior to worry about its extent towards lower luminosities. Most of the transition objects (with $L_{\rm bol} \approx 10^{38}$ erg s^{-1}) were further not ideally positioned in the XMM-*Newton* FOV. We suggest that a dedicated study, eventually targeting transition objects located closer to the Earth (to more easily reach good S/N ratios) could help to clarify the position of this demarcation line.

7. Summary and conclusions

In this second paper of the series, we have pursued the analysis of the X-ray data of the young open cluster NGC 6231. While Paper I focused mainly on the detection and identification of the numerous X-ray sources in the XMM-*Newton* FOV, this paper was devoted to the properties of the rich early-type

star population monitored throughout the 5-day campaign. A detailed census of the OB-type stars within the FOV resulted in more than one hundred objects identified. Using a limited cross-correlation radius of 3″, about one third of them could be associated with an X-ray counterpart. Among these, the 15 O-type stars as well as the Wolf-Rayet system WR 79 are all detected in the X-rays. On the other hand, the B-type stars detection rate only amounts to about 25% and is mostly constant from spectral sub-types B0 to B4 while it slightly drops beyond that. The detection rates among B giants is about 50% while it is only of 20% for main sequence stars. Apart from the two probable SPB stars in the FOV, no other B sub-population (β Cep stars, binaries) deviates from this scheme.

The combined spectra of the identified early-type X-ray emitters were extracted in all the EPIC instruments. Their background-subtracted, vignetting and exposure-corrected count rates during each of the six pointings of our campaign were obtained using the SAS task *emldetect*. The properties of the emitting plasma were constrained using up to three temperature MEKAL models. Focusing on the objects fitted with 2 and 3-T models, a clear dichotomy between the O-type and B-type X-ray emitters was observed. The former ones are soft and usually bright sources characterized by temperatures of kT = 0.3 and 0.7 keV. The latter have a similar low energy component but their second temperature is well above 1 keV. The B-type X-ray emitters are thus significantly harder than the O-type sources. This difference is also seen in their spectra, which present a much more flattened profile compared to the O-type star spectra.

As a next step, we have investigated the $L_{\rm X} - L_{\rm bol}$ relationships of the X-ray emitters of our sample. O- and B-type emitters clearly present a different behaviour in the $\log L_{\rm X} - \log L_{\rm bol}$ diagram, though both types draw up a linear relation in the log–log plane. The separation between the two sub-sets is located at about $\log L_{\rm bol} = 38$ (erg s^{-1}), as previously suggested by Berghöfer et al. (1997). The dispersion around the expected linear relation is apparently quite small. In the O-type stars sample, the two objects that show the largest deviations are known to display an extra-emission component due to a wind interaction (HD 152248, Sana et al. 2004; CPD −41°7742, Sana et al. 2005a). These were thus excluded from the subsequent discussion. We showed that, for the O-type stars, the X-ray luminosities are scaling with the bolometric luminosities. In the 0.5-10.0 keV energy range, we obtained:

$$\log L_{\rm X} - \log L_{\rm bol} = -6.912 \pm 0.153.$$

We also found that a power-law relation did not provide any significant improvement to the quality of the fit. The obtained dispersion around this new *canonical* relation is very limited. It becomes even smaller while excluding the 'cooler' O dwarfs (later than spectral-type O9) from the fit. It this case, the typical dispersion drops to about 0.08 in the log – log plane, thus corresponding to only 20% on the X-ray luminosities. We finally note that the only identified mechanism that provides a significant deviation from this relation is extra-emission produced in a wind interaction region. It is also the sole mechanism that, at our detection threshold, produced a significant variability in the observed fluxes in our O-type star sample (see Sect. 5). Though relatively limited, the present sample suggests that the intrinsic X-ray emission from O-type stars is very tightly correlated with their bolometric luminosity. Beyond the two strong CWB systems, our sample is formed by single stars and binaries belonging to different luminosity class. Though not extending towards sub-types earlier than O6, they all seem to follow the *canonical* relation, suggesting thus a common mechanism for X-ray production in these objects.

We emphasize that this apparent scaling might indirectly results from a scaling of the X-ray luminosity with the wind properties, themselves scaling with the bolometric luminosities for these stars with radiatively driven winds. Nonetheless the $L_{\rm X} - L_{\rm bol}$ relation remains one of the best observational constraints deduced so far that links the intrinsic X-ray emission of the O-type stars with the fundamental properties of the emitter.

We also provides a new analysis of recent flux measurements obtained in the Carina region (Albacete Colombo et al. 2003). This sample is mainly formed by main sequence stars ranging from O8.5 to O3. We note that this new analysis confirms much of our present conclusions. The best $L_{\rm X} - L_{\rm bol}$ relation is indeed in the form of a scaling law rather than a power law. The dispersion around the obtained relation is very limited and the difference with our own relation might possibly be accounted for by the different energy ranges considered.

Turning to B-type stars, the fact that only about one quarter of the stars of a given spectral sub-type is actually associated with an X-ray source argues strongly against X-ray emission being an intrinsic property of these stars. We however note that we still observed a linear relation that links $\log L_{\rm X}$ and $\log L_{\rm bol}$:

$$\log L_{\rm X} = (0.22 \pm 0.06) \log L_{\rm bol} + 22.8(\pm 2.4)$$

The dispersion around this relation is quite limited (∼0.14) and the linear pattern is also seen in the different energy sub-ranges considered. The time analysis reveals that, among the 11 objects considered in our sample, four were displaying flares while two others were presenting smooth variations of their X-ray fluxes. Finally, adopting a similar model for the spectral analysis as the one used in Paper III for pre-main sequence (PMS) stars, we noticed that the different results were almost indiscernible. This, in addition to the flaring activities seen in about one third of the sample and to the low detection rate among the B-star population in the FOV, clearly points towards the X-ray emission to originate from a low mass PMS visual or physical companion. The observed relation between $L_{\rm X}$ and $L_{\rm bol}$ is however not understood and could result from an observational bias. Alternatively it could be linked to some particularities of the B-type stars in NGC 6231 or to a putative interaction between the PMS object and its B-type companion, yielding to an X-ray emission partly governed by the intrinsic properties of the B-type primary.

Finally, we note that the separation line between the O- and "B-type" behaviours (around $L_{\rm bol} = 10^{38}$ erg s^{-1}) is poorly mapped by our present sample. The adopted criterion to preserve the homogeneity of the spectral analysis (requiring at least 2-T models) have further led to the rejection of the objects

in the transition zone from our sample. The extent of the *canonical* relation towards lower luminosities probably deserves a more particular attention. Dedicated observations, combined with the already observed fields, could help to increase the number of objects in this zone, which is probably a necessary condition for a dedicated study to provide a more detailed answer to this still open question.

Acknowledgements. The authors are greatly indebted towards the 'Fonds National de la Recherche Scientifique' (FNRS), Belgium, for multiple supports. This research is supported in part by contract P5/36 "Pôle d'Attraction Interuniversitaire" (Belgian Federal Science Policy Office) and through the PRODEX XMM-OM and INTEGRAL projects. The SIMBAD and WEBDA database and the Vizier catalogue access tool (CDS, Strasbourg, France) have been consulted for the bibliography and in the purpose of object cross-identification.

References

Albacete Colombo, J. F., Méndez, M., & Morrell, N. I. 2003, MNRAS, 346, 704
Arentoft, T., Sterken, C., Knudsen, M. R., et al. 2001, A&A, 380, 599
Arnaud, K. A. 1996, in ASP Conf. Ser., Vol. 101, Astronomical Data Analysis Software and Systems V, ed. G. Jacoby & J. Barnes, 17
Balona, L. A. 1983, MNRAS, 203, 1041
Balona, L. A., & Shobbrook, R. R. 1983, MNRAS, 205, 309
Balona, L. A., & Engelbrecht, C. A. 1985, MNRAS, 212, 889
Balona, L. A., & Laney, C. D. 1995, MNRAS, 276, 627
Baume, G., Vázquez, R. A., & Feinstein, A. 1999, A&AS, 137, 233
Berghöfer, T. W., Schmitt, J. H. M. M., & Cassinelli, J. P. 1996, A&AS, 118, 481
Berghöfer, T. W., Schmitt, J. H. M. M., Danner, R., & Cassinelli, J. P. 1997, A&A, 322, 167
Bevington, P. 1969, Data Reduction and Error Analysis for the Physical Sciences (USA: McGraw-Hill Book Company, Inc.)
Bohlin, R. C., Savage, B. D., & Drake, J. F. 1978, ApJ, 224, 132
Braes, L. L. E. 1967, Bulletin of the Astronomical Institute of the Netherlands Supplement Series, 2, 1
Cassinelli, J. P., & Olson, G. L. 1979, ApJ, 229, 304
Cassinelli, J. P., Waldron, W. L., Sanders, W. T., et al. 1981, ApJ, 250, 677
Cassinelli, J. P., Cohen, D. H., Macfarlane, J. J., Sanders, W. T., & Welsh, B. Y. 1994, ApJ, 421, 705
Chlebowski, T., & Garmany, C. D. 1991, ApJ, 368, 241
Chlebowski, T., Harnden, F. R., & Sciortino, S. 1989, ApJ, 341, 427
Cohen, D. H., Cassinelli, J. P., & Macfarlane, J. J. 1997, ApJ, 487, 867
Cohen, D. H., de Messières, G. E., MacFarlane, J. J., et al. 2003, ApJ, 586, 495
Feldmeier, A., Puls, J., & Pauldrach, A. W. A. 1997, A&A, 322, 878
Gagné, M., Oksala, M. E., Cohen, D. H., et al. 2005, ArXiv Astrophysics e-prints
García, B., & Mermilliod, J. C. 2001, A&A, 368, 122
Garrison, R. F., & Schild, R. E. 1979, AJ, 84, 1020
Harnden, F. R., Branduardi, G., Gorenstein, P., et al. 1979, ApJ, 234, L51
Hill, G., Crawford, D. L., & Barnes, J. V. 1974, AJ, 79, 1271
Houk, N. 1978, Michigan catalogue of two-dimensional spectral types for the HD stars (Ann Arbor : Dept. of Astronomy, University of Michigan : distributed by University Microfilms International, 1978-)
Howarth, I. D., & Prinja, R. K. 1989, ApJS, 69, 527
Howk, J. C., Cassinelli, J. P., Bjorkman, J. E., & Lamers, H. J. G. L. M. 2000, ApJ, 534, 348
Kaastra, J. 1992, An X-Ray Spectral Code for Optically Thin Plasmas, (Internal SRON-Leiden Report, updated version 2.0)
Kramer, R. H., Cohen, D. H., & Owocki, S. P. 2003, ApJ, 592, 532
Kudritzki, R. P., Palsa, R., Feldmeier, A., Puls, J., & Pauldrach, A. W. A. 1996, in Roentgenstrahlung from the Universe, 9–12
Laval, A. 1972, A&A, 21, 271
Levato, H., & Malaroda, S. 1980, PASP, 92, 323
Levato, H., & Morrell, N. 1983, Astrophys. Lett., 23, 183
Long, K. S., & White, R. L. 1980, ApJ, 239, L65
Lucy, L. B. 1982, ApJ, 255, 286
Luehrs, S. 1997, PASP, 109, 504
Martins, F., Schaerer, D., & Hillier, D. 2005, A&A, in press
Mayer, P., Harmanec, P., Lorenz, R., et al. 2001, in ASSL Vol. 264: The Influence of Binaries on Stellar Population Studies, 567
Mewe, R., Gronenschild, E. H. B. M., & van den Oord, G. H. J. 1985, A&AS, 62, 197
Nugis, T., & Lamers, H. J. G. L. M. 2000, A&A, 360, 227
Owocki, S. P., & Cohen, D. H. 1999, ApJ, 520, 833
Owocki, S. P., Castor, J. I., & Rybicki, G. B. 1988, ApJ, 335, 914
Pallavicini, R., Golub, L., Rosner, R., et al. 1981, ApJ, 248, 279
Perry, C. L., Hill, G., Younger, P. F., & Barnes, J. V. 1990, A&AS, 86, 415
Perry, C. L., Hill, G., & Christodoulou, D. M. 1991, A&AS, 90, 195
Porquet, D., Mewe, R., Dubau, J., Raassen, A. J. J., & Kaastra, J. S. 2001, A&A, 376, 1113
Raboud, D. 1996, A&A, 315, 384
Raboud, D., Cramer, N., & Bernasconi, P. A. 1997, A&A, 325, 167
Reed, B. C. 2003, AJ, 125, 2531
Rosner, R., Golub, L., & Vaiana, G. S. 1985, ARA&A, 23, 413
Rufener, F., & Bartholdi, P. 1982, A&AS, 48, 503
Sana, H. 2005, PhD thesis, Liège University
Sana, H., Rauw, G., & Gosset, E. 2001, A&A, 370, 121
Sana, H., Hensberge, H., Rauw, G., & Gosset, E. 2003, A&A, 405, 1063
Sana, H., Stevens, I. R., Gosset, E., Rauw, G., & Vreux, J.-M. 2004, MNRAS, 350, 809
Sana, H., Antokhina, E., Royer, P., et al. 2005a, A&A, in press
Sana, H., Gosset, E., & Rauw, G. 2005b, A&A, submitted
Sana, H., Gosset, E., Rauw, G., Sung, H., & Vreux, J.-M.

2005c, A&A, accepted
Sana, H., Nazé, Y., Gosset, E., et al. 2005d, in Massive Stars in Interacting Binaries, ed. A. Moffat & N. St-Louis, ASP Conf. Ser., 5p., in press
Sana, H., Nazé, Y., O'Donnell, B., Rauw, G., & Gosset, E. 2005e, A&A, submitted
Sana, H., Rauw, G., & Gosset, E. 2005f, A&A, submitted
Sana, H., Rauw, G., Sung, H., Gosset, E., & Vreux, J.-M. 2005g, A&A, in preparation
Schild, R. E., Neugebauer, G., & Westphal, J. A. 1971, AJ, 76, 237
Schmidt-Kaler, T. 1982, Landolt-Börnstein, Numerical Data and Functional Relationships in Science and Technology, New Series, Group VI, Vol. 2b, Physical Parameters of the Stars (Berlin: Springer-Verlag)
Schmitt, J. H. M. M., Golub, L., Harnden, F. R., et al. 1985, ApJ, 290, 307
Schulz, N. S., Canizares, C., Huenemoerder, D., & Tibbets, K. 2003, ApJ, 595, 365
Sciortino, S., Vaiana, G. S., Harnden, F. R., et al. 1990, ApJ, 361, 621
Seward, F. D., & Chlebowski, T. 1982, ApJ, 256, 530
Seward, F. D., Forman, W. R., Giacconi, R., et al. 1979, ApJ, 234, L55
Stelzer, B., Huélamo, N., Hubrig, S., Zinnecker, H., & Micela, G. 2003, A&A, 407, 1067
Stickland, D. J., Lloyd, C., & Penny, L. R. 1997, The Observatory, 117, 213
Strüder, L., Briel, U., Dennerl, K., et al. 2001, A&A, 365, L18
Sung, H., Bessell, M. S., & Lee, S. 1998, AJ, 115, 734
Turner, M. J. L., Abbey, A., Arnaud, M., et al. 2001, A&A, 365, L27
ud-Doula, A., & Owocki, S. P. 2002, ApJ, 576, 413
Vaiana, G. S., Cassinelli, J. P., Fabbiano, G., et al. 1981, ApJ, 245, 163
Vink, J. S., de Koter, A., & Lamers, H. J. G. L. M. 2000, A&A, 362, 295
Vink, J. S., de Koter, A., & Lamers, H. J. G. L. M. 2001, A&A, 369, 574

Astronomy & Astrophysics manuscript no. pms˙v2 May 21, 2005
(DOI: will be inserted by hand later)

An *XMM-Newton* view of the young open cluster NGC 6231⋆

III. Optically faint X-ray sources

H. Sana[1,⋆⋆], G. Rauw[1,⋆⋆⋆], H. Sung[2], E. Gosset[1,⋆⋆⋆] and J.-M. Vreux[1]

[1] Institut d'Astrophysique et de Géophysique, University of Liège, Allée du 6 Août 17, Bât. B5c, B-4000 Liège, Belgium
e-mail: sana@astro.ulg.ac.be, rauw@astro.ulg.ac.be, gosset@astro.ulg.ac.be, vreux@astro.ulg.ac.be
[2] Department of Astronomy and Space Science, Sejong University, Kunja-dong 98, Kwangjin-gu, Seoul 143-747, Korea
e-mail: sungh@sejong.ac.kr

Received date / Accepted date

Abstract. We discuss the properties of the X-ray sources with faint optical counterparts in the very young open cluster NGC 6231. From their position in the H-R diagram, we find that the bulk of these objects are probably low-mass pre-main sequence stars with masses in the range 0.3 to 3.0 $M_\odot$. The age distribution of these objects indicates that low-mass star formation in NGC 6231 started more than 10 Myr ago and culminated in a starburst-like event about 2 – 3 Myr ago when the bulk of the low-mass PMS stars as well as the massive cluster members formed. We find no evidence for a spatial age gradient that could point towards a sequential star formation process. Only a few X-ray sources have counterparts with a reddening exceeding the average value of the cluster or with infrared colours indicating the presence of a moderate near-IR excess. The X-ray spectra of the brightest PMS sources are best fitted by rather hard thermal plasma models and a significant fraction of these sources displays flares in their light curve. The X-ray brightest flaring sources have decay times between 2 and 16 ks. The X-ray selected PMS stars in NGC 6231 have $\log L_{\rm X}/L_{\rm bol}$ values that increase strongly with decreasing bolometric luminosity and can reach a saturation level ($\log L_{\rm X}/L_{\rm bol} \sim -2.4$) for non-flaring sources and even extremer values during flares.

Key words. Stars: pre-main sequence – X-rays: individuals: NGC 6231 – X-rays: stars – Open clusters and associations: individual: NGC 6231

1. Introduction

The formation of massive stars is currently one of the key questions in stellar astrophysics. Various scenarios have been proposed; accretion from a circumstellar envelope (e.g. Shu et al. 1987, Behrend & Maeder 2001), accretion from a turbulent molecular core (McKee & Tan 2003) or a mixture of competitive accretion and collisions of lower mass protostars in the core of dense stellar clusters (e.g. Bonnell et al. 1998, Bonnell & Bate 2002) being the most popular ones. Since the bulk of the massive stars are found in open clusters, some clues on this question can probably be obtained from a study of the star formation processes within young open clusters. Beside their massive star population, such clusters usually harbour a wealth of lower mass objects with the least massive ones that have not yet reached the zero age main sequence. An important issue is the relationship between the high-mass cluster members and these low-mass objects. While it has sometimes been suggested that the massive stars trigger the formation of the lower mass objects, in several cases, the lower mass pre-main sequence stars are found to be significantly older than the massive cluster members. Herbig (1962) accordingly suggested that the formation of early-type stars could stop the formation process of lower mass stars in a cluster by dispersing the ambient gas. Other authors (e.g. Sung et al. 1997) however suggested that the observed age discrepancy might result from the fact that the PMS evolutionary tracks actually overestimate the *real* age of the protostars. Obviously, investigating the properties of lower mass pre-main sequence (PMS) stars in very young open clusters can help us understand the feedback of massive stars on their environment and can thereby shed light on the way the most massive objects have formed.

Classical T Tauri PMS stars display emission in the Balmer lines and can thus be identified through photometric observations with an Hα narrow band filter. Most classical T Tauri stars (cTTs) also display near-infrared excesses that are attributed to heated dust in a disk-like accretion structure (e.g. Meyer et al. 1997). However, another category of PMS objects, the so-

Send offprint requests to: H. Sana

⋆ Based on observations with *XMM-Newton*, an ESA science mission with instruments and contributions directly funded by ESA member states and the USA (NASA).

⋆⋆ Research Fellow FNRS (Belgium)

⋆⋆⋆ Research Associate FNRS (Belgium)

called weak-line T Tauri stars (wTTs) do not display significant near-IR excesses nor optical line emission. An interesting property that can help us identifying these PMS stars is their relatively strong X-ray emission with $\log L_{\rm X}/L_{\rm bol}$ reaching values as large as -3 (e.g. Neuhäuser 1997, Feigelson & Montmerle 1999). X-ray observations can therefore enable the selection of PMS stars, such as wTTs, that would neither be detected through Hα nor near-IR photometry (e.g. Damiani et al. 2004). The high sensitivity of *XMM-Newton* and the exceptional spatial resolution of *Chandra* have already been used to study some rich young open clusters in the X-ray domain. For instance, NGC 6530 at the core of the Lagoon Nebula was found to harbour both classical and weak-line T Tauri stars with masses between 0.5 and 2.0 $M_\odot$, but only a few of the X-ray selected PMS candidates were found to be cTTs (Rauw et al. 2002, Damiani et al. 2004).[1] NGC 6383 on the other hand, does not contain any known cTTs, but our *XMM-Newton* observations releaved a number of weak X-ray sources in this cluster that are most likely associated with wTTs (Rauw et al. 2003). A preliminary analysis of the optical properties of these sources suggested that they are in fact older than the massive binary HD 159176 (O7 V + O7 V) in the centre of the cluster.

NGC 6231 - at the core of the Sco OB1 association - is another very young open cluster, rich in massive O-type stars. The early-type star population of this cluster contains an amazing fraction of binary or multiple systems, most of which are concentrated in its core. Using $UBV(RI)_C H\alpha$ photometry, Sung et al. (1998, hereafter SBL) inferred a mean cluster reddening of $\overline{E(B-V)} = 0.466 \pm 0.054$ and a distance modulus of 11.0 ± 0.07. These authors noted that the reddening law towards NGC 6231 could be somewhat peculiar with $R_V = 2.45\,E(V-I_C)/E(B-V) = 3.3 \pm 0.1$. Sung et al. found only 12 PMS objects (and 7 PMS candidates) brighter than $V = 17$ displaying Hα emission. However, as pointed out above, there could be a number of PMS stars without Hα emission; but with optical photometry only, these would be very difficult to distinguish from field stars lying to the right of the cluster main-sequence. In this paper, we use the catalogue of *XMM-Newton* sources in NGC 6231 presented by Sana et al. (2005a, hereafter Paper I) to investigate the properties of X-ray sources with faint optical counterparts in this cluster. The X-ray properties of the early-type stars in NGC 6231 are discussed in a separate paper (Sana et al. 2005b, Paper II).

2. Optical counterparts

449 of the X-ray sources in the NGC 6231 field have an optical counterpart in the catalogue of Sung et al. (1998) extended down to $V = 21$. We note that our combined EPIC field of view extends over a wider area than the actual field investigated by SBL and some sources outside the SBL area actually have counterparts in the USNO, GSC or SSB05 catalogues (see Paper I). Nevertheless, throughout this paper, we will restrict ourselves to the sources with counterparts in the SBL catalogue. The reasons are, on the one hand, that the USNO and GSC photometry is less accurate than the results of SBL. On the other hand, the new photometry acquired by one of us (H. Sung) over a larger field than initially investigated by SBL (referred to as SSB05 in Paper I) does not include observations with the R filter.

The V vs. $B-V$ and V vs. $V-I_C$ colour-magnitude diagrams of the optical counterparts are shown in Fig. 1. The bulk of the objects in this diagram are indeed found to be rather faint stars mostly located to the right of the main-sequence. At $V = 18$, the photometric error of most colours reaches about 0.1 mag.

To identify Hα emitting stars among the X-ray selected objects, we compare the $R - H\alpha$ index to its value for main sequence stars. For the latter, we use the relation between the $R - H\alpha$ and $V - I_C$ indices for main sequence stars proposed by Sung et al. (1997) and we account for the effect of cluster reddening on the $V - I_C$ colour. Following Sung et al. (1997), we consider that a star displays Hα emission if $\Delta(R - H\alpha) = (R - H\alpha) - (R - H\alpha)_{\rm MS} \geq 0.21$ mag, whereas a star will be considered a Hα emission candidate if $0.12 \leq \Delta(R - H\alpha) \leq 0.21$. In this way, we find that about one quarter of the X-ray selected objects are either confirmed or potential Hα emission objects (Fig. 2, upper panel). This large number of Hα emission candidates compared to the original results of SBL is mainly due to the fact that the photometry used here extends down to much fainter magnitudes (Fig. 2, lower panel).

Although a small fraction (≤ 6%, see Paper I) of the X-ray selected objects might in fact be field stars (either foreground or background) unrelated to NGC 6231, we have assumed that all stars are located at the distance of the cluster (DM = 11.0) and are all subject to the same reddening ($A_V = 1.538$, Sung et al. 1998). We have then built the Hertzsprung-Russell diagram of these EPIC sources using effective temperatures and bolometric corrections interpolated from the dereddened $V - I_C$ colour indices for main sequence stars of spectral types B0 to M6 tabulated by Kenyon & Hartmann (1995). Figure 3 compares the location of the X-ray selected objects to the pre-main sequence evolutionary tracks of Siess et al. (2000) for $Z = 0.02$ and without overshooting (note that these evolutionary models include neither rotation nor accretion).

We find that most of the X-ray selected, optically faint objects ($V \geq 14$) fall between the PMS evolutionary tracks for stars of masses in the range 0.3 to 3.0 $M_\odot$.

A comparison with the isochrones (see Fig. 4) indicates that the majority of these objects should have ages ranging from 1 to 10 Myr. The distribution of ages peaks around $\sim 3-4$ Myr and decreases towards lower ages. Note that Sung et al. (1998) compared the H-R diagram of NGC 6231 to PMS tracks of Bernasconi & Maeder (1996) finding an age spread of about 11 Myr for the low mass objects. While this is similar to the age spread found here, we caution however that a direct comparison of age determinations of PMS stars made with different evolutionary models and different calibrations might be biased (see e.g. the discussion in Siess et al. 2000). As for NGC 6530, we

[1] We note here that the luminosities derived by Rauw et al. (2002) for the PMS objects in NGC 6530 are too low, leading to an overestimate of their ages. The reason for this error is that the $V - I_C$ colours quoted by Sung et al. (2000) are given in the Cousin photometric system while the `Vizier` database indicates that these are expressed in the Johnson system.

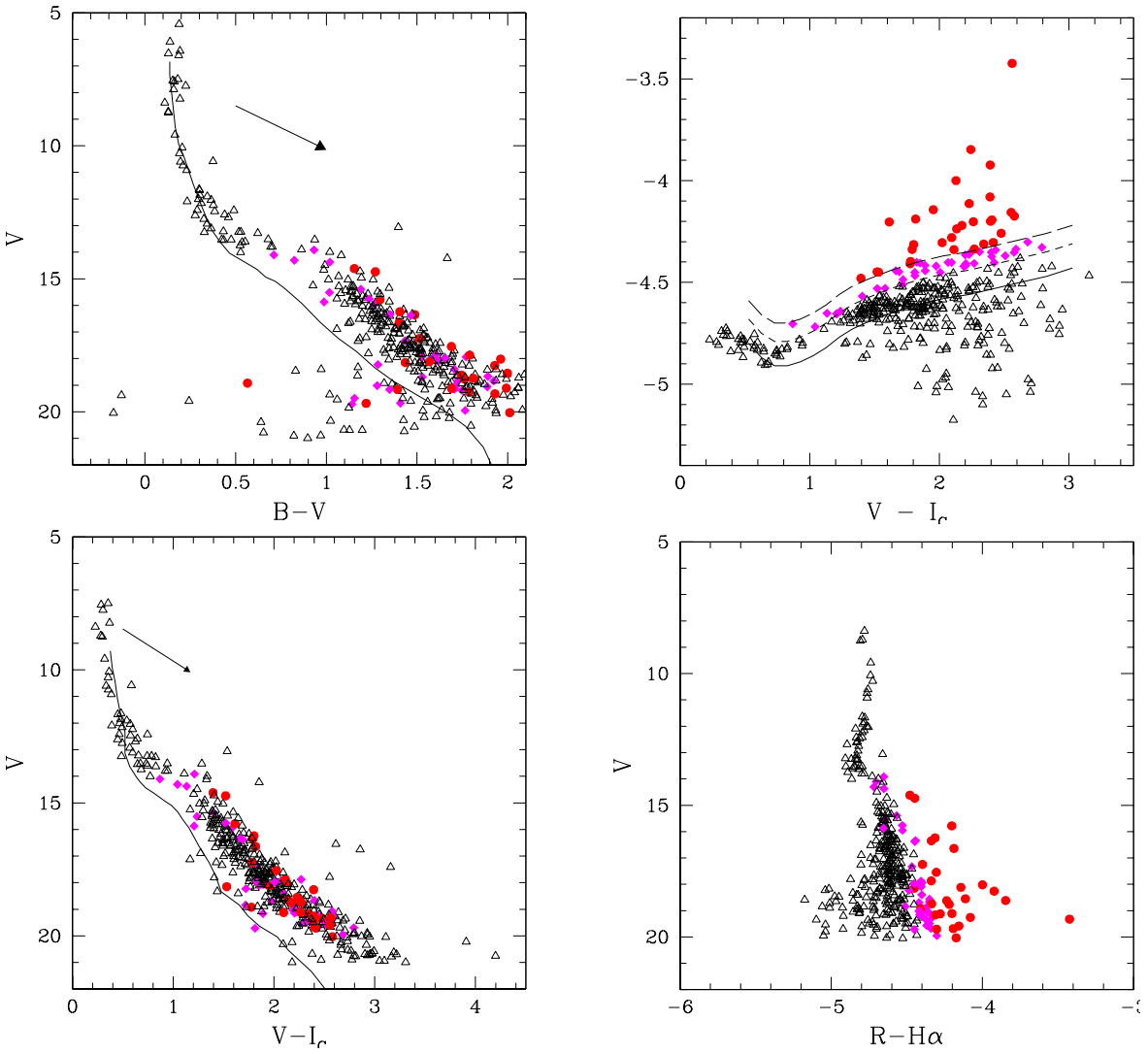

Fig. 1. Colour-magnitude diagrams of the X-ray sources with an optical counterpart in the SBL catalogue. Filled dots, filled diamonds and open triangles indicate respectively Hα emitting stars, Hα candidates and stars with no evidence for emission (see Fig. 2). The reddening vector with $R_V = 3.3$ and $E(V - I_C)/E(B - V) = 1.365$ (Sung et al. 1998) is indicated and the solid line shows the ZAMS relation taken from Schmidt-Kaler (1982) shifted by a distance modulus DM = 11.0 and reddened with $E(B - V) = 0.466$ (Sung et al. 1998).

Fig. 2. Top panel: $R - H\alpha$ as a function of $V - I_C$. The symbols have the same meaning as in Fig. 1. The solid line yields the $R - H\alpha$ versus $V - I_C$ relation for main sequence stars taken from Sung et al. (1997) and reddened with the average reddening of NGC 6231. The short- and long-dashed lines yield respectively the thresholds for Hα emission candidates and Hα emitters (see text). **Bottom panel:** V-magnitude as a function of $R - H\alpha$ for the SBL optical counterparts of our EPIC sources.

do not find a large age difference between those stars displaying Hα emission (on average 4.4 Myr) and those without (4.9 Myr). What we do see, is that Hα emission seems restricted to X-ray selected stars with masses below about 2.5 $M_\odot$. This is again reminiscent of the situation in NGC 6530.

Zinnecker (2002) noted that the binary frequency among pre-main sequence stars is at least as high as among main sequence stars. Binarity affects the distribution of a coeval population of PMS stars in the H-R diagram by introducing a band shifted upwards from the true isochrone (Siess et al. 1997) leading to an underestimate of the actual age. Palla (2002) evaluated the average age discrepancy for a realistic distribution of binary mass ratios, finding that age estimates that do not account for binarity can be off by a factor ~ 1.5. Therefore, binarity should not have too large an impact on our age estimates above. In any case, binarity cannot explain the tail of the age distributions towards older ages (see Fig. 4).

A total of 384 EPIC sources in the field of view of NGC 6231 have a counterpart in the Two Micron All Sky

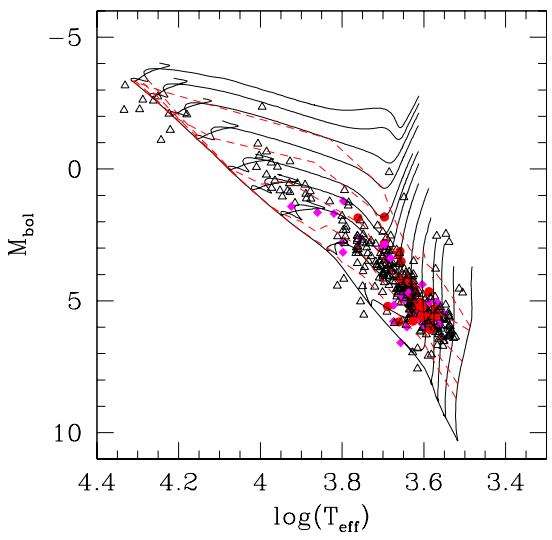

Fig. 3. Hertzsprung-Russell diagram of the EPIC sources with optical counterparts in the SBL catalogue (see text). Evolutionary tracks from Siess et al. (2000) for masses of 0.2, 0.3, 0.4, 0.5, 0.7, 1.0, 1.5, 2.0, 2.5, 3.0, 4.0, 5.0, 6.0 and 7.0 $M_\odot$ are overplotted. The symbols have the same meaning as in Fig. 1. The thick solid line shows the ZAMS, while the dashed lines correspond to isochrones for ages of 0.5, 1.5, 4.0, 10.0 and 20.0 Myr.

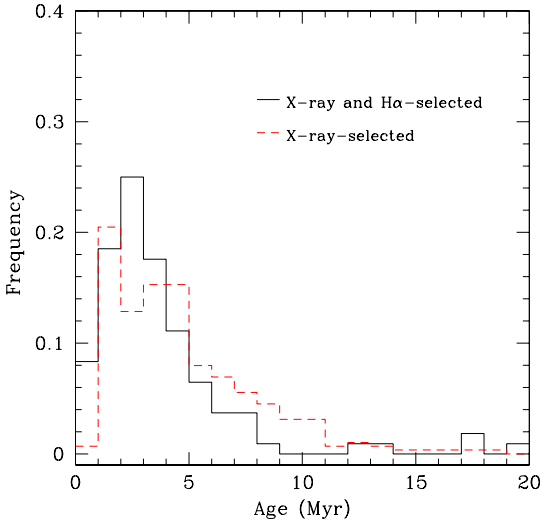

Fig. 4. Distribution of the ages of X-ray selected PMS objects as interpolated from the isochrones derived from the Siess et al. (2000) evolutionary tracks. PMS candidates with $\Delta(R-H\alpha) \geq 0.12$ are indicated by the solid line, whilst those with $\Delta(R-H\alpha) < 0.12$ are indicated by the dashed line. The total numbers of objects with $\Delta(R-H\alpha) \geq 0.12$ and $\Delta(R-H\alpha) < 0.12$ are respectively 93 and 303.

Survey point source catalogue (2MASS, Cutri et al. 2003). Among these, 333 sources have also a counterpart in the SBL catalogue. We used the March 2003 update of the colour transformations, initially derived by Carpenter (2001) and available on the 2MASS website[2], to convert the $J-H$ and $H-K_s$ colours to the homogenized JHK photometric system introduced by Bessell & Brett (1988).

Assuming that the 2MASS and SBL magnitudes are not affected by photometric variability, we tried to establish the effective temperature and bolometric correction using a dereddened $V-K$ colour index[3]. Comparing the results with those obtained from the $V-I_C$ index, we find that, for the vast majority of the stars, the former technique yields systematically lower temperatures (sometimes by more than 1000 K) than the latter method. For objects surrounded by circumstellar material, such a discrepancy could reflect the presence of a near-IR excess (that would mimic a lower temperature in the $V-K$ colour). However, for the bulk of the objects, the most likely explanation for this effect is probably the rather large errors in the 2MASS magnitudes. Note also that the reddening correction over such a wide wavelength range using the extinction law of Rieke & Lebofsky (1985) might simply not be adequate for stars in NGC 6231 (perhaps as a result of the peculiarities of the extinction law discussed by Sung et al. 1998). In addition, the 2MASS colours and magnitudes of some objects are either subject to large uncertainties or are only upper limits due to non-detections. In total, we find that only 295 out of the 384 2MASS counterparts have quality flags A, B, C or D for the measurements of all three individual near-IR magnitudes. Restricting the JHK colour-colour diagram to these objects, we find that their location is consistent with slightly reddened main-sequence or giant stars (see Fig. 5). Only a couple of sources show evidence for a moderate IR excess and only about ten objects display strongly reddened IR colours.

3. X-ray properties of the faint sources

3.1. X-ray spectra

Spectra were extracted for each source, for each instrument and each observation using the procedure described in Paper II. Briefly we adopted circular extraction regions with a radius corresponding to half the distance to the nearest neighbouring X-ray source. For each source, the background spectrum was obtained over source-free regions chosen according to the source location. A thorough description of these background extraction regions is given in paper II. We adopted the redistribution matrix files provided by the *XMM-Newton* SOC, whereas the ancillary response files were built with the appropriate SAS tasks. The spectra were binned to have at least 10 counts per energy channel. In the following, we discuss only the spectra of those sources that have an average, vignetting and exposure-corrected count rate[4] above 5×10^{-3} or 10^{-2} cts s^{-1} for EPIC-MOS or pn respectively and are not associated with

[2] `http://www.ipac.caltech.edu/2mass/index.html`

[3] For this purpose we use the reddening law of Rieke & Lebofsky (1985).

[4] We note that the actual (uncorrected) count rates are substantially lower for sources near the edge of the field of view.

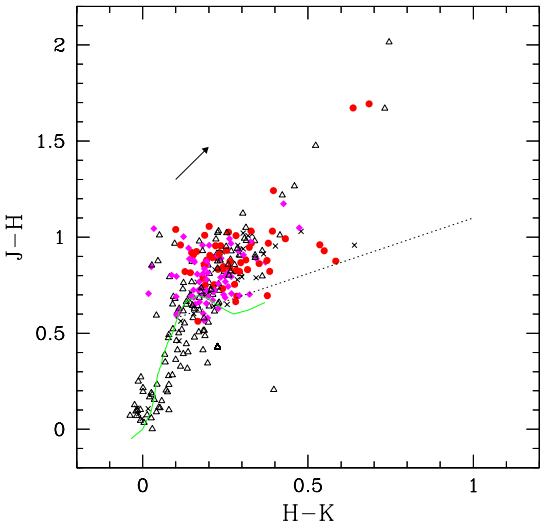

Fig. 5. JHK colour-colour diagram of the 2MASS counterparts with good quality near-IR photometry of the X-ray sources in the EPIC field of view around NGC 6231. The heavy solid line yields the intrinsic colours of main sequence stars following Bessell & Brett (1988), whereas the reddening vector is illustrated for $A_V = 1.538$ and adopting the reddening law of Rieke & Lebofsky (1985). The crosses stand for 2MASS sources having no counterpart in the SBL catalogue (mainly because they fall outside the field of view investigated by Sung et al. 1998). The other symbols have the same meaning as in Fig. 1. The dotted straight line yields the locus of dereddened colours of classical T Tauri stars according to Meyer et al. (1997).

OB stars. The X-ray spectra of the OB stars are discussed in a separate paper (Paper II). We use the numbering scheme of the sources as introduced in Paper I.

For sources that display no significant variability, we have analysed the merged spectra of all observations, while for those sources that experience a flare in their light curve, we rather analyse the spectra of the observation when the flare occured. The spectra were then modelled by means of rather simple models (absorbed `mekal` optically thin thermal plasma model (Mewe et al. 1985; Kaastra 1992) with one or two temperatures, absorbed power-law, absorbed bremsstrahlung model or absorbed blackbody energy distribution).

Most of the flaring sources display a spectrum that is best represented by a single temperature `mekal` model with best fit temperatures of $kT \geq 3.4$ keV. For the majority of the non-flaring bright X-ray sources, a second temperature is needed to model the spectra. In these cases, we find that most objects (except sources #478 and #535) have moderate hydrogen column densities ($N_{\rm H} \leq 0.36 \times 10^{22}$ cm^{-2}, in reasonable agreement with the average $N_{\rm H}$ estimated from the cluster reddening, see below) and temperatures of order 0.7 and 2.5 – 3.5 keV for the soft and hard component respectively. The flaring sources thus appear to have significantly harder spectra than the non-flaring objects. Finally, some of the objects have spectra that are best modelled by a power-law spectral energy distribution. Three out of five sources in this group have no optical counterpart (not even in the deeper extension of the SSB05 catalogue).

3.2. X-ray light curves

Light curves were extracted for each source over the same area as for the spectra. They were background subtracted and corrected for the effect of the good time intervals. We used different energy bands and different time bins from 10 s to 5 ks and we applied various tests to search for variability.

Considering the typical count rates of the sources studied here, the most useful time bin to investigate variability is 1 ks and we thus focus on the light curves obtained for this binning.

3.2.1. Comments on individual sources

In this section, we discuss the light curves and spectra of X-ray sources that are either variable or have ambiguous spectral fits. Sources #181, 228, 251, 269, 290, 297, 350, 407, 478, 535, 568 and 603 display no significant variability in their light curve and are not discussed here.

#41 This source displays little variability. The spectrum is best fitted by an absorbed power law model (Table 2), although a blackbody model (with $kT = 1.50$ keV and $N_{\rm H} \leq 0.08 \times 10^{22}$ cm^{-2}) yields a fit that is only slightly poorer ($\chi^2_\nu = 0.96$).

#43 The merged spectrum of this source displays a clear Fe K line. The best quality fit is achieved for a single temperature `mekal` model (see Table 1). A power law fit yields $\chi^2_\nu = 1.08$ for $N_{\rm H} = 0.39 \times 10^{22}$ cm^{-2} and $\Gamma = 1.65$. The source is somewhat brighter and the spectrum somewhat softer during revolution #6.

#48 This object displays a flare during revolution 4.

#100 While no X-ray emission is detected during observations 1, 2, 4 and 6, the source undergoes a strong flare during observation 3 (see Fig. 6) and is also clearly detected (though with a much lower count rate) during observation 5. The spectra obtained during observation 3 display a moderate Fe K line and are best fitted with a $kT \sim 4.3$ keV `mekal` model (see Table 1), though a power law model with a photon index of 2.2 also yields a χ^2_ν of 0.90. The spectrum from observation 5 is of much lower quality, but still suggests that the source was much softer ($kT \sim 0.9$ keV) and about 50 times fainter compared to observation 3.

#138 The X-ray flux is about 3 times larger during observation 5, though the light curve exhibits no clear flaring behaviour.

#171 No significant variability is found for this source. The spectrum cannot be fitted by a single temperature `mekal` model, though a 2-T model ($N_{\rm H} = 0.79 \times 10^{22}$ cm^{-2}, $kT_1 =$

Table 1. Best fit parameters of the absorbed single temperature `mekal` models (`wabs*mekal`) fitted to the EPIC spectra of faint X-ray sources in NGC 6231. The source numbering scheme is adopted from Paper I. The second and third columns indicate the combinations of observations and instruments used in the spectral analysis. Columns [8] and [9] yield the observed and absorption-corrected X-ray flux respectively. The fluxes are expressed in 10^{-14} erg cm^{-2} s^{-1} and are evaluated over the 0.5 – 10.0 keV energy band. Numbers between brackets are taken from the most recent extension of the SSB05 catalogue (see Paper I).

Source	Obs.	Inst.	$N_{\rm H}$ (10^{22} cm^{-2})	kT (keV)	χ^2_ν	d.o.f.	$f_{\rm X}^{\rm obs}$	$f_{\rm X}^{\rm corr}$	SBL	V	$V-I_C$
[1]	[2]	[3]	[4]	[5]	[6]	[7]	[8]	[9]	[10]	[11]	[12]
#43	all	M2 + pn	$0.32^{+.04}_{-.04}$	$8.96^{+2.22}_{-1.48}$	1.05	440	22.4	26.6			
#48	#4	M2	$0.16^{+.20}_{-.07}$	$3.43^{+2.83}_{-1.20}$	1.62	19	22.4	26.5	[1987]	[15.89]	[1.47]
#100	#3	M2 + pn	$0.19^{+.06}_{-.05}$	$4.32^{+0.89}_{-0.69}$	0.87	79	24.2	28.6	4664	20.69	2.90
#175	#4	M1 + M2	$0.15^{+.07}_{-.06}$	$4.26^{+1.08}_{-0.73}$	1.01	66	37.9	43.5	5433	18.27	2.08
#285	#1	EPIC	$0.23^{+.04}_{-.05}$	$4.44^{+0.78}_{-0.55}$	1.19	153	34.2	41.1	[3321]	[17.36]	[2.04]
#442	#1	EPIC	$0.17^{+.05}_{-.05}$	$4.04^{+0.62}_{-0.54}$	1.29	118	13.9	16.2	7554	20.24	2.18
#467	#3	EPIC	$0.27^{+.06}_{-.06}$	$5.70^{+1.80}_{-0.95}$	1.09	129	21.8	26.2	7757	18.12	1.95
#469	#6	EPIC	$0.27^{+.06}_{-.06}$	$4.17^{+0.76}_{-0.59}$	1.20	105	18.1	22.6	7772	17.46	1.87
#583	all	pn	$0.11^{+.15}_{-.11}$	$5.58^{+10.61}_{-2.23}$	0.89	27	3.2	3.4	[25121]	[18.08]	[2.21]

Table 2. Same as Table 1, but for the absorbed power law models (`wabs*power`).

Source	Obs.	Inst.	$N_{\rm H}$ (10^{22} cm^{-2})	Γ	χ^2_ν	d.o.f.	$f_{\rm X}^{\rm obs}$	$f_{\rm X}^{\rm corr}$	SBL	V	$V-I_C$
[1]	[2]	[3]	[4]	[5]	[6]	[7]	[8]	[9]	[10]	[11]	[12]
#41	all	M1 + M2	$0.62^{+.23}_{-.23}$	$0.89^{+.16}_{-.13}$	0.94	179	19.1	21.5			
#171	all	EPIC	$0.47^{+.03}_{-.03}$	$3.42^{+.17}_{-.15}$	1.45	284	4.3	13.7			
#228	all	M1 + pn	$0.38^{+.07}_{-.06}$	$3.16^{+.30}_{-.19}$	0.97	100	3.0	7.3	332	15.71	1.49
#241	#5	EPIC	$0.37^{+.09}_{-.07}$	$2.25^{+.19}_{-.16}$	0.76	80	16.1	24.8			
#568	all	pn	$0.59^{+.21}_{-.15}$	$3.45^{+.80}_{-.45}$	0.87	49	2.7	10.1	[4893]	[16.17]	[2.00]

0.27 keV and k$T_2 = 1.61$ keV) yields $\chi^2_\nu = 1.30$, slightly better than the power-law model quoted in Table 2.

#175 This source is clearly detected in all our observations. During the first three pointings, the average MOS count rate is about 6×10^{-4} cts s^{-1}. At some point between observation 3 and 4, the X-ray flux of the source has increased by at least a factor 30 (see Fig. 7). Indeed, during the fourth pointing, the count rate slowly decreases from $\sim 2.0 \times 10^{-2}$ to $\sim 0.6 \times 10^{-2}$ cts s^{-1}. During the last two observations, the source is still brighter than at the beginning of our campaign though the average MOS count rate decreases slowly from $\sim 5.1 \times 10^{-3}$ to $\sim 2.6 \times 10^{-3}$ cts s^{-1}. The spectrum of observation 4 indicates a rather hot (k$T = 4.3$ keV, see Table 1) plasma, though a power law fit ($\Gamma \sim 2.0$) is only marginally poorer ($\chi^2_\nu = 1.05$). During observations 5 and 6, the spectrum is slightly softer (kT decreases to 3.4 keV or Γ increases to 2.6).

#204 A flare is seen in the MOS 1 count rate towards the end of observation 4. However, no pn or MOS 2 data are available for this source to confirm this result.

#241 The count rate of this source is about a factor 15 (respectively 6) larger during observation 5 (resp. 6) than during observations 1 to 4. It is likely that the source has undergone a flare at some time between the end of the fourth and the beginning of the fifth pointing, and that our data actually cover the decreasing tail of this flare.

#249 No significant variability is found for this source during the different pointings, although the EPIC count rates are somewhat larger during the last observation.

#254 During observation 5, the source exhibits a small flare with an increase of the count rate by a factor 5 to 6 which is consistently seen in all three EPIC instruments.

#258 The X-ray flux is largest during observation 1 and decreases slowly afterwards.

#285 This source experiences a strong flare during the first observation and a subsequent decrease of the count rate during the second observation (see Fig. 8). A small flare is seen

Table 3. Same as Table 1, but for the absorbed 2-T `mekal` models (`wabs*(mekal`$_1$`+mekal`$_2$`)`).

Source	Obs.	Inst.	$N_{\rm H}$ (10^{22} cm^{-2})	kT_1 (keV)	kT_2 (keV)	χ^2_ν	d.o.f.	$f_{\rm X}^{\rm obs}$	$f_{\rm X}^{\rm corr}$	SBL	V	$V-I_C$
[1]	[2]	[3]	[4]	[5]	[6]	[7]	[8]	[9]	[10]	[11]	[12]	[13]
#138	all	M1 + M2	$0.20^{+.06}_{-.11}$	$0.70^{+0.17}_{-0.10}$	$2.54^{+0.93}_{-0.46}$	0.96	62	3.6	5.1			
#181	all	EPIC	$0.20^{+.04}_{-.03}$	$0.63^{+0.05}_{-0.05}$	$2.48^{+0.27}_{-0.24}$	1.23	254	5.2	7.4	[2843]	14.77	1.43
#187	all	EPIC	$0.19^{+.03}_{-.04}$	$0.81^{+0.05}_{-0.07}$	$2.25^{+0.27}_{-0.22}$	0.91	173	4.2	5.8	285	12.94	0.57
#204	all	M1	$0.36^{+.17}_{-.08}$	$0.75^{+0.11}_{-0.09}$	$3.64^{+1.57}_{-0.83}$	0.92	56	6.7	11.3	304	15.64	1.45
#249	all	EPIC	$0.14^{+.06}_{-.02}$	$0.87^{+0.10}_{-0.07}$	$3.39^{+0.69}_{-0.44}$	0.92	214	4.3	5.3	5980	16.65	1.79
#254	#5	EPIC	$0.13^{+.13}_{-.06}$	$0.82^{+0.13}_{-0.13}$	$3.69^{+0.53}_{-0.80}$	0.87	69	9.6	11.6	356	13.29	0.82
#258	all	EPIC	$0.20^{+.08}_{-.05}$	$0.76^{+0.09}_{-0.12}$	$2.58^{+0.38}_{-0.36}$	1.05	124	3.0	4.1			
#269	all	EPIC	$0.14^{+.07}_{-.05}$	$0.74^{+0.10}_{-0.10}$	$2.82^{+0.33}_{-0.33}$	1.11	192	4.8	6.0	370	12.24	0.60
#290	all	EPIC	$0.08^{+.02}_{-.02}$	$0.68^{+0.07}_{-0.02}$	$2.29^{+0.25}_{-0.14}$	1.11	334	6.0	7.1	405	15.51	1.24
#297	all	EPIC	$0.21^{+.04}_{-.04}$	$0.64^{+0.05}_{-0.05}$	$2.42^{+0.40}_{-0.29}$	1.05	131	2.7	4.0	413	12.75	0.49
#304	#2	EPIC	$0.23^{+.03}_{-.03}$	$1.31^{+3.12}_{-0.56}$	$8.2^{+22.5}_{-2.10}$	0.99	265	90.1	105.4	423	13.25	0.49
#324	all	EPIC	$0.20^{+.03}_{-.03}$	$0.67^{+0.08}_{-0.05}$	$2.55^{+0.19}_{-0.20}$	1.00	281	9.0	12.3	448	15.57	1.48
#350	all	EPIC	$0.19^{+.05}_{-.05}$	$0.82^{+0.05}_{-0.07}$	$2.33^{+0.32}_{-0.19}$	0.81	168	3.7	5.1	472	12.42	0.75
#407	all	EPIC	$0.20^{+.06}_{-.03}$	$0.80^{+0.06}_{-0.10}$	$2.37^{+0.30}_{-0.27}$	1.30	158	4.8	6.8	550	15.32	1.39
#478	all	M2 + pn	$0.64^{+.13}_{-.04}$	$0.63^{+0.08}_{-0.05}$	$2.37^{+0.50}_{-0.32}$	0.91	137	4.9	15.3	628	15.03	1.50
#535	all	M1 + M2	$0.69^{+.11}_{-.16}$	$0.62^{+0.19}_{-0.05}$	$2.78^{+0.83}_{-0.58}$	1.08	92	4.9	16.3	8459	16.64	1.62
#553	#2	EPIC	$0.32^{+.09}_{-.09}$	$0.91^{+0.30}_{-0.11}$	$4.54^{+0.94}_{-0.69}$	0.86	110	43.7	57.3	729	13.63	0.83
#603	all	M1 + M2	$0.35^{+.07}_{-.04}$	$0.59^{+0.11}_{-0.10}$	$5.10^{+1.17}_{-0.77}$	0.97	198	25.4	35.7	[27130]	[20.65]	[1.36]

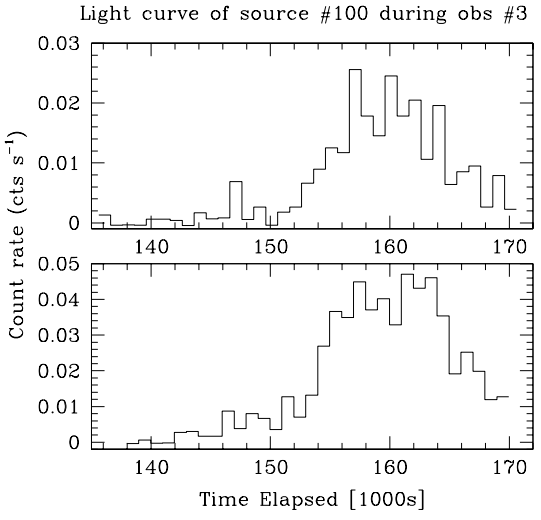

Fig. 6. X-ray flare of source #100 as observed during observation 3 with EPIC-MOS 2 (top panel) and EPIC-pn (lower panel). The light curve was extracted for pulse invariant channels 500 to 10000 (i.e. for energies approximately in the range 0.5 – 10 keV). The time is given in ks from the beginning of the first observation.

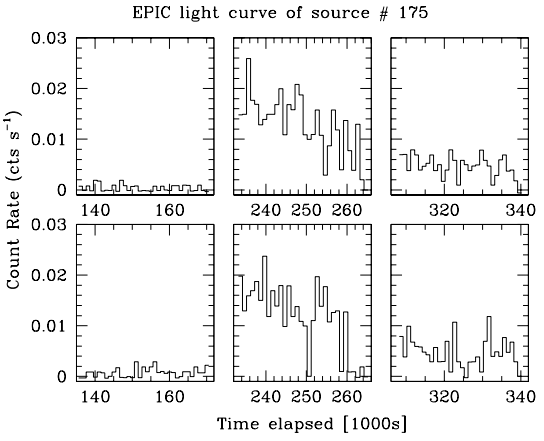

Fig. 7. EPIC-MOS 1 (top panels) and MOS 2 (lower panels) light curve (for PI in the range 500 to 10000) of source #175 during *XMM* observations 3, 4 and 5 (from left to right). The time is given in ks from the beginning of observation 1.

in all EPIC instruments during the fifth pointing. The spectrum obtained during the flare of the first observation can be fitted by a 1-T `mekal` model (see Table 1), although a fit of equal quality can be obtained for a power law model with $N_{\rm H} = 0.37 \times 10^{22}$ cm^{-2} and $\Gamma = 2.10$.

#304 A strong flare is seen during the second observation where the count rates increase by about a factor 100 (Fig. 9). The spectrum during the flare exhibits a prominent Fe K line.

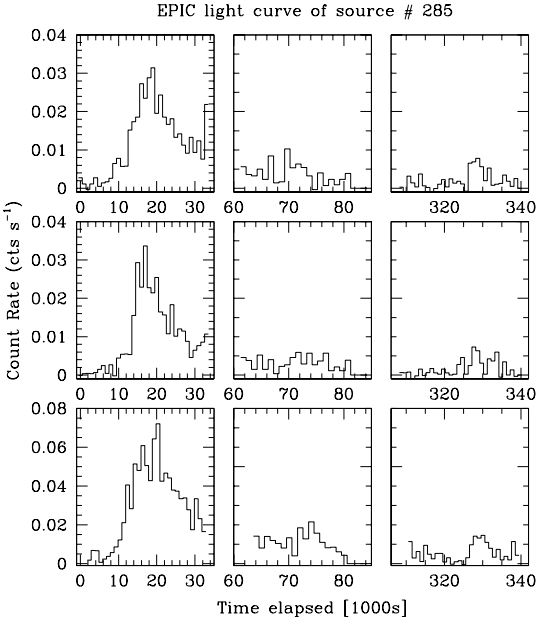

Fig. 8. EPIC-MOS 1 (top panels), MOS 2 (middle panels) and pn (lower panels) light curve (for PI in the range 500 to 10000) of source #285 during observations 1, 2 and 5 (from left to right). The time is given in ks from the beginning of observation 1.

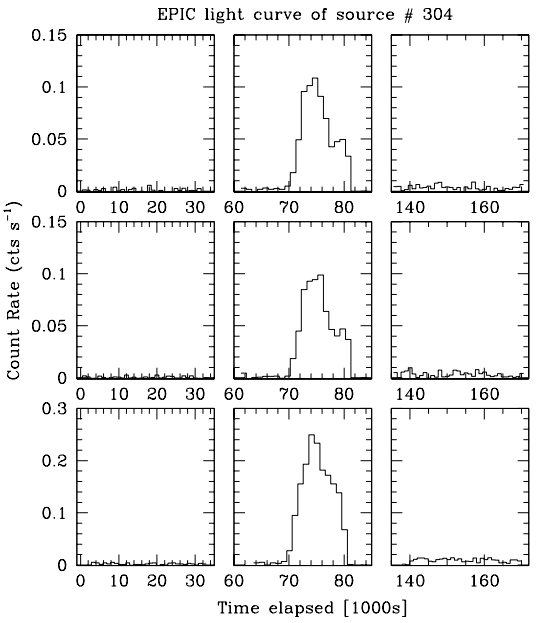

Fig. 9. Same as Fig. 8 but for source #304 during observations 1, 2 and 3 (from left to right).

#324 The source is about a factor 2 brighter during the fourth observation, whilst the count rates of the different instruments during the other observations exhibit no coherent significant variability.

#442 A flare with an increase of the count rate by a factor 10 occurs during the first observation. During the subsequent observations, the count rate slowly decreases (Fig. 10).

#467 The source exhibits a flare during the third observation (Fig. 11). During the flare, the spectrum is equally well described by a k$T = 5.7$ keV single temperature `mekal` model (see Table 1) or a power law model with $\Gamma = 1.81$ and $N_{\rm H} = 0.34 \times 10^{22}$ cm^{-2}.

#469 Another flaring source with an increase of the count rate by a factor ~ 60 during the last observation (Fig. 12). During the flare, the spectrum is again equally well described by a single temperature `mekal` model (see Table 1) or a power law model with $\Gamma = 2.09$ and $N_{\rm H} = 0.38 \times 10^{22}$ cm^{-2}.

#553 This source displays a steady increase of its count rate over the duration of the second observation (Fig. 13). The light curve is truncated at the end of the observation due to the rejection of a soft proton flare from our data (see Paper I). During the remaining observations, little variability is seen. While we adopt the 2-T `mekal` model (see Table 3), which fits the Fe K line better, we note that a power law model with $\Gamma = 2.27$ and $N_{\rm H} = 0.42 \times 10^{22}$ cm^{-2} yields a fit of formally equal quality.

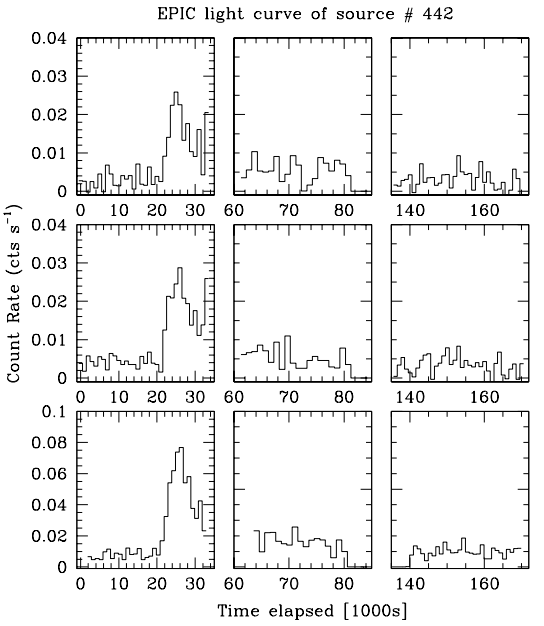

Fig. 10. Same as Fig. 8 but for source #442 during observations 1, 2 and 3 (from left to right).

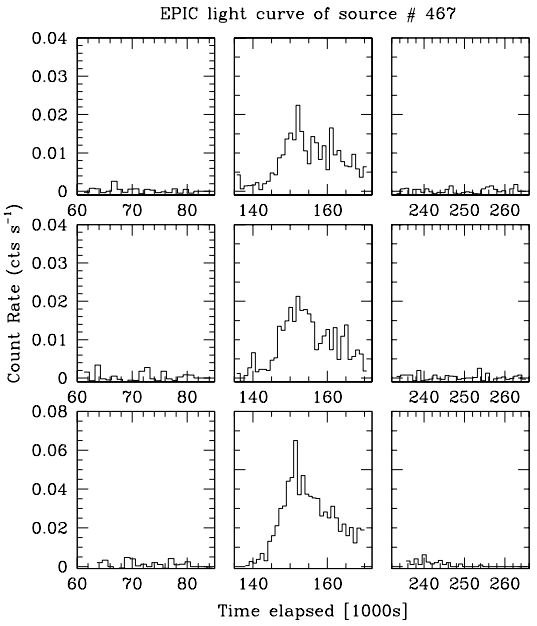

Fig. 11. Same as Fig. 8 but for source #467 during observations 2, 3 and 4 (from left to right).

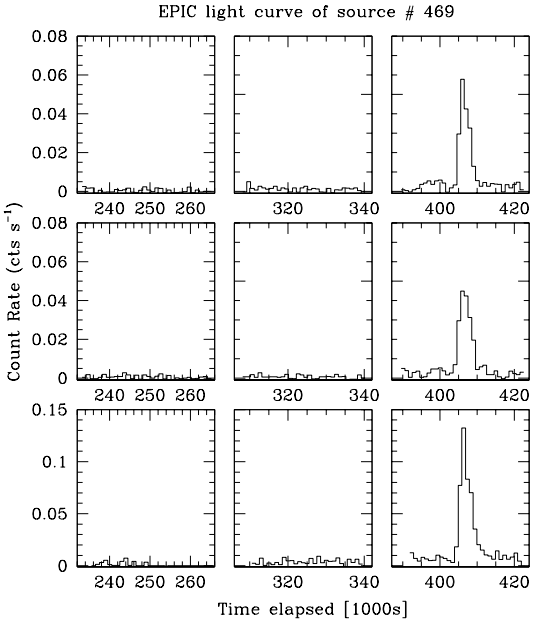

Fig. 12. Same as Fig. 8 but for source #469 during observations 4, 5 and 6 (from left to right).

#583 A flare is seen during the fourth observation (Fig. 14). The spectrum has a rather low quality because of a low actual count rate.

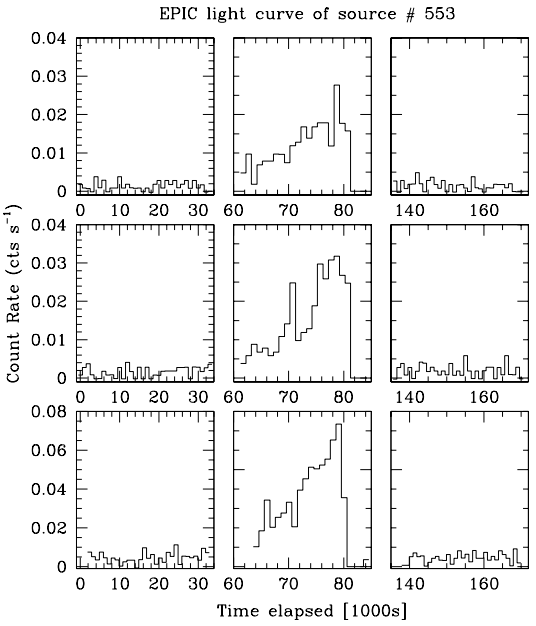

Fig. 13. Same as Fig. 8 but for source #553 during observations 1, 2 and 3 (from left to right).

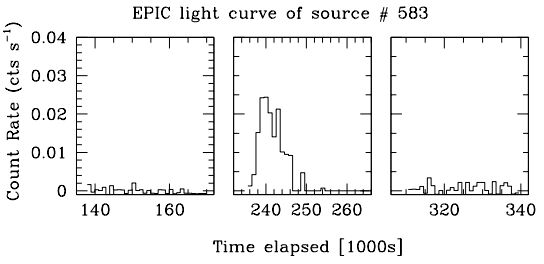

Fig. 14. EPIC-pn light curve (for PI in the range 500 to 10000) of source #583 during observations 3, 4 and 5 (from left to right). The time is given in ks from the beginning of observation 1.

3.2.2. X-ray flares

Most of the flares displayed in Figs. 6-14 exhibit an impulsive rise of the source X-ray luminosity within a few ks followed by a slower decay. The exceptions are sources #100 and probably #553 that display a much slower rise on timescales of 10 ks and ≥ 20 ks respectively.

Some quantitative insight into the flare events can be obtained assuming that the flaring plasma is confined in a closed coronal loop as is the case for solar flares. For these situations, Serio et al. (1991) have established a simple analytical relation between the loop half-length l, the maximum temperature at the top of the loop $T_{\rm max}$ and the thermodynamic decay time τ.

$$l \sim 0.129\,\tau\,\sqrt{{\rm k}T_{\rm max}}$$

where l is expressed in $R_\odot$, kT in keV and τ in ks. This relation is valid for the initial decay phase during which the emission

Table 4. Properties of the flaring sources: τ yields the $1/e$ decay time, k$T_{\rm obs}$ is the best fit plasma temperature during the flare (a value between brackets correspond to the hottest component of a 2-T fit) and l is the loop half-length. For comparison the stellar radii computed from the effective temperatures and bolometric magnitudes derived in Sect. 2 are provided in the sixth column. Column 7 indicates the value of the $R-H\alpha$ index compared to the value of this index for main sequence stars with the same intrinsic $V-I_C$ (whenever available). Finally, the last two entries correspond to the JHK colours derived from the 2MASS measurements.

Source	Obs	τ (ks)	k$T_{\rm obs}$ (keV)	l R$_\odot$	R_* R$_\odot$	$\Delta(R-H\alpha)$	$J-H$	$H-K$
#48	4	8.8	3.43	1.0			0.641	0.215
#100	3	5.3	4.32	0.7	1.3			
#204	4		(3.64)		2.6	0.03	0.620	0.171
#254	5	7.3	(3.69)		3.7	0.08	0.388	0.067
#285	1	9.4	4.44	1.2			0.788	0.343
#304	2	5.5	(8.2)		1.6		0.204	0.071
#442	1	7.6	4.04	0.9	0.8			
#467	3	16.0	5.70	2.4	1.7	0.45	0.991	0.432
#469	6	2.1	4.17	0.3	2.1	-0.04		
#583	4	5.2	5.58	0.8			0.460	0.110

measure decay is roughly exponential and has been applied to flares in a variety of active stars (e.g. Briggs & Pye 2003, Giardino et al. 2004 and Favata 2005). When the temperatures are determined from spectral fits of EPIC data, a correction has to be applied to the observed temperature to derive the maximum temperature at the top of the loop (see Giardino et al. 2004, Briggs & Pye 2003).

Whenever possible, we have determined the $1/e$ decay times of the flares by a least square fit of an exponential decay to the decay phase of the observed light curves. Usually, the results for the different EPIC instruments are in good agreement (to better than 10% of τ), except for sources #254, #285, #442 for which we have a larger dispersion of $\sim$ 20% between the values determined from the three light curves. For source #175 and #241 our data do not cover the maximum of the flare and are hence not suited to constrain the decay time, although we note that the light curve of #241 during observations 5 and 6 is well fitted with a single exponential decay suggesting a rather large decay time ($\geq$ 30 ks).

Table 4 yields the properties of the flaring X-ray sources with a sufficiently large count rate to study their spectrum and light curve. All flaring sources have rather large temperatures during the flare. For those spectra that were fitted with a 2-T model, Table 4 indicates the temperature of the hotter model component between brackets. The decay times range from about 2 ks to 16 ks and the loop half-lengths are in the range 0.3 to 2.4 R$_\odot$. Most loops appear rather compact ($l \leq R_*$) except perhaps for source #467.

Favata (2005) note that while most flaring structures are indeed relatively compact, extremely slowly decaying flares have been detected in some young stellar objects (with $\tau \sim 40$ ks) which correspond to rather large loops ($l \sim 14$ R$_\odot$). Favata (2005) accordingly suggests that the magnetic structures that produce these large loops link the star to the circumstellar disk. We note that our dataset is not suited to clearly identify slowly decaying flares (although the decay seen for source #241 might be a candidate for such an event).

In this context, it is also interesting to note that among the five objects in Table 4 for which a $\Delta(R-H\alpha)$ value can be computed, only source #467 shows a strong Hα emission. Further evidence for circumstellar material around this source comes from its near-IR excess. From Table 4 it appears that #467 is also the source with the largest loop half-length ($l \sim 1.4\,R_*$) in our sample.

3.3. X-ray fluxes

Using the bolometric magnitudes derived above from the SBL photometry and the vignetting and background corrected EPIC count rates determined by the source detection algorithm, we can build an empirical $L_{\rm X}/L_{\rm bol}$ relation for the sources in the NGC 6231 field. In order to convert the EPIC count rates into X-ray luminosities in the 0.5 – 10 keV range, we took the average of the available count rates of the pn, MOS1 and MOS2 instruments assuming a conversion factor 2 between the MOS and pn count rates. Next, we computed a flux/pn count rate conversion factor assuming that the sources have an absorbed optically thin thermal plasma spectrum with a temperature of 1 keV and $N_{\rm H} = 5.8\times10^{21}\times E(B-V) = 2.7\times10^{21}$ cm^{-2} (Bohlin et al. 1978). Note that adopting a temperature of 2 keV (more typical of the spectra of the brightest sources) would only slightly increase this conversion factor (by 14%). Finally, we converted the unabsorbed fluxes into luminosities, assuming that all sources are members of NGC 6231 ($DM = 11.0$). Figure 15 displays the resulting $\log L_{\rm X}/L_{\rm bol}$ as a function of $M_{\rm bol}$. This value increases from about -7 for B0 stars (the hottest objects plotted in this figure) to almost -2 for the lower mass objects. A similar trend was already observed in NGC 6530 (Rauw et al. 2002).

Of course the results in Fig. 15 could be somewhat biased by the fact that some of the sources are detected only during their flaring activity. We have repeated the same procedure for the brighter sources discussed hereabove. In the bottom panel of Fig. 15, we distinguish between the flaring and non flaring sources. We find that the average luminosity during a flare can

reach up to 3×10^{32} erg s^{-1} (source #304) and $\log L_{\rm X}/L_{\rm bol}$ can temporarily increase to values as large as -1.00 (source #100). On the other hand, the brighter steady sources also display rather large X-ray luminosities, up to $\sim 4 \times 10^{31}$ erg s^{-1}, as well as large $\log L_{\rm X}/L_{\rm bol}$, up to ~ -2.4. Therefore, we conclude that even non-flaring PMS sources in NGC 6231 can be rather X-ray bright.

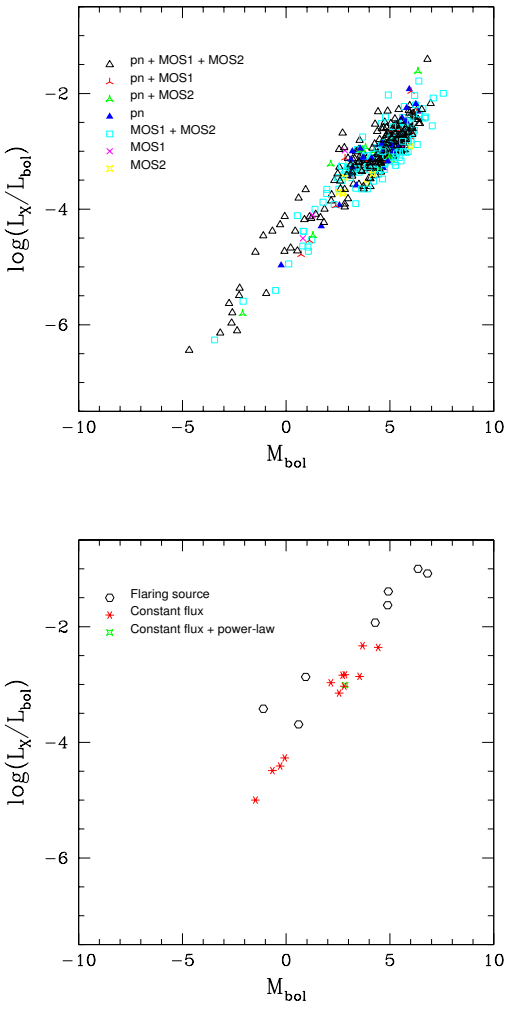

Fig. 15. Top panel: logarithm of $L_{\rm X}/L_{\rm bol}$ as a function of the bolometric magnitude for the EPIC sources with optical counterparts in the SBL catalogue (see text). $L_{\rm X}$ refers to the X-ray luminosity in the energy range 0.5 to 10 keV. The various symbols correspond to different combinations of EPIC instruments used in the determination of the X-ray luminosity (see the insert in the upper left corner). **Bottom panel**: $\log L_{\rm X}/L_{\rm bol}$ as a function of the bolometric magnitude for those EPIC sources with optical counterparts in the SBL catalogue and for which a detailed modelling of the spectra was possible (see Tables 1, 2 and 3). Asterisks correspond to sources that have a rather constant flux during our six observations, whereas hexagons stand for flaring sources.

4. Discussion

Our *XMM-Newton* campaign provides the deepest X-ray view ever of NGC 6231. While the X-ray images of the cluster are dominated by its high-mass members (see Paper I), we detect a substantial number of sources that have faint optical counterparts. The typical spectra of these sources, their flaring behaviour, their X-ray luminosities as well as the location of their optical counterparts in the H-R diagram indicate that these sources form a population of PMS stars. Compared to previous optical investigations of the cluster (Sung et al. 1998), the number of PMS stars is increased by a factor 20 at least.

An interesting feature is the age spread among the low-mass PMS objects ($\sim$ 11 Myr) that exceeds the main sequence lifetime of the massive O stars in the cluster. This feature was already noted by previous authors. Raboud et al. (1997) obtained photometry of NGC 6231 in the Geneva system. Fitting isochrones to the main sequence and post-main sequence stars believed to be single, these authors derived an age between 3.2 and 4.5 Myr for the more massive stars, whilst they noted that the PMS stars detected in their observation were mostly older than 3.2 Myr and had ages up to 10 Myr. A similar situation was found by Sung et al. (1998) who derived an age of 2.5 – 4 Myr for the massive stars in the cluster, while they found an age spread of 11 Myr in the PMS objects. Raboud et al. (1997) accordingly suggested that there was a continuous low-mass star formation activity in NGC 6231 at previous times, which came to an end about 3.2 – 4.5 Myr ago when the massive O stars of the cluster formed during a nearly coeval burst. Our results confirm this picture. The age distribution of X-ray selected low-mass stars peaks around 3 – 4 Myr, i.e. at the time of the formation of the early-type cluster members. However, the formation of low mass stars in NGC 6231 started already more than 12 – 15 Myr ago at a rather slow rate. The star formation rate subsequently increased, culminating in a starburst event during which most of the PMS as well as the more massive objects formed. Then, about 1 Myr ago, the formation of stars in NGC 6231 came to end rather abruptly.

In the case of NGC 6530, Damiani et al. (2004) report on a spatial age gradient, suggesting a sequence of star formation events. To check whether a similar situation holds for NGC 6231, we have plotted the spatial distribution of X-ray selected PMS stars of different ages in Fig. 16. It can be seen that in the case of NGC 6231 there exists no clear separation between the different groups. While this could be a projection effect (if star formation were progressing along our line of sight towards the cluster), we nevertheless conclude that there is no evidence in our data for a spatial age gradient in NGC 6231.

The star formation history of NGC 6231 provides constraints on future modelling of massive star formation in open clusters. Several properties of the NGC 6231 cluster could be explained by a massive star formation scenario involving physical collisions in a dense cluster core (Bonnell et al. 1998). These features are the large binary fraction among the massive stars in this cluster, the spatial concentration of PMS stars around the massive cluster members and last but not least, the age difference between the PMS objects and the more massive stars. Indeed, N-body simulations of compact cluster cores in-

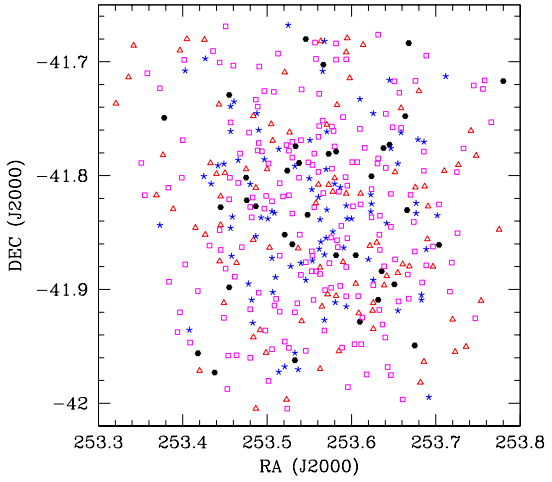

Fig. 16. Spatial distribution of the X-ray selected low-mass stars in NGC 6231. The triangles, squares, stars and filled hexagons indicate stars with ages of less than 2 Myr, between 2 and 5 Myr, between 5 and 9 Myr and more than 9 Myr respectively.

cluding the effects of stellar evolution and physical collisions (Portegies Zwart et al. 1999) show that, because of mass segregation, physical collisions between stars are frequent in the cluster core. The resulting mergers could lead to the formation of very massive ($\geq 100\,M_\odot$) stars within 3 – 4 Myr. The stars are rejuvenated by each new collision, therefore considerably extending their lifetime. The products of such a process would thus appear as some sort of 'blue stragglers' in the H-R diagram of the cluster.

Alternatively, a moderate age difference could also result if massive star formation proceeds through accretion as proposed by Norberg & Maeder (2000) and Behrend & Maeder (1996). These authors assumed that the PMS objects accrete a constant fraction of the observed outflow rates, which in turn increase with the stellar luminosity and hence the stellar mass. In their models, the stars become visible on the birthline once a significant part of the surrounding cocoon has been dispersed. For instance, in the models of Norberg & Maeder (2000), an accreting protostar that will eventually form a $120\,M_\odot$ star would spent half of the accretion time below a mass of about $2\,M_\odot$. The time needed for an accreting protostar to increase its mass from 2 to $120\,M_\odot$ would then be about 1 Myr. These models require rather high accretion rates (of order $8 \times 10^{-3}\,M_\odot\,yr^{-1}$ to form an $85\,M_\odot$ star, Behrend & Maeder 1996). Though this value seems high, it is apparently not forbidden by the results of Wolfire & Cassinelli (1987). The models of Behrend & Maeder (1996) accordingly predict that low mass stars form first and high mass stars form slightly later. However, the duration for the formation of an $80\,M_\odot$ star is only about 10% larger than that of an $8\,M_\odot$ star.

Acknowledgements. The Liège team is greatly indebted to the Fonds National de la Recherche Scientifique (Belgium) for multiple assistance. This research is also supported in part by contract P5/36 "Pôle d'Attraction Interuniversitaire" (Belgian Federal Science Policy Office) and through the PRODEX XMM-OM and INTEGRAL projects. H. Sung acknowledges the support of the Korea Science and Engineering Foundation (KOSEF) to the Astrophysical Research Center for the Structure and Evolution of the Cosmos (ARCSEC″) at Sejong University. The SIMBAD database has been consulted for the bibliography.

References

Behrend, R., & Maeder, A. 2001, A&A, 373, 190
Bernasconi, P.A., & Maeder, A. 1996, A&A, 307, 829
Bessell, M.S., & Brett, J.M. 1988, PASP, 100, 1134
Bohlin, R.C., Savage, B.D., & Drake, J.F. 1978, ApJ, 224, 132
Bonnell, I.A., & Bate, M.R. 2002, MNRAS, 336, 659
Bonnell, I.A., Bate, M.R., & Zinnecker, H. 1998, MNRAS, 298, 93
Briggs, K.R., & Pye, J.P. 2003, MNRAS, 345, 714
Carpenter, J.M. 2001, AJ, 121, 2851
Cutri, R.M., Skrutskie, M.F., Van Dyk, S., et al. 2003, The 2MASS All-Sky Catalog of Point Sources, University of Massachusetts and Infrared Processing and Analysis Center (IPAC/California Institute of Technology)
Damiani, F., Flaccomio, E., Micela, G., Sciortino, S., Harnden, F.R.Jr., & Murray, S.S. 2004, ApJ 608, 781
Favata, F. 2005, Mem. S. A. It., in press, [astro-ph/0412511]
Feigelson, E.D., & Montmerle, T. 1999, ARA&A, 37, 363
Giardino, G., Favata, F., Micela, G., & Reale, F. 2004, A&A, 413, 669
Herbig, G.H. 1962, ApJ, 135, 736
Kaastra, J.S. 1992, *An X-ray spectral code for optically thin plasmas*, Internal SRON-Leiden Report
Kenyon, S.J., & Hartmann, L. 1995, ApJS, 101, 117
McKee, C.F., & Tan, J.C. 2003, ApJ, 585, 850
Mewe, R., Gronenschild, E.H.B.M., & van den Oord, G.H.J. 1985, A&AS, 62, 197
Meyer, M.R., Calvet, N., & Hillenbrand, L.A. 1997, AJ, 114, 288
Neuhäuser, R. 1997, Science, 276, 1363
Norberg, P., & Maeder, A. 2000, A&A, 359, 1025
Palla, F. 2002, in *Physics of Star Formation in Galaxies*, Saas-Fee Advanced Course 29, eds. A. Maeder & G. Meynet, 9
Portegies Zwart, S.F., Makino, J., McMillan, S.L.W., & Hut, P. 1999, A&A, 348, 117
Raboud, D., Cramer, N., & Bernasconi, P.A. 1997, A&A, 325, 167
Rauw, G., Nazé, Y., Gosset, E., et al. 2002, A&A, 395, 499
Rauw, G., De Becker, M., Gosset, E., Pittard, J.M., & Stevens, I.R. 2003, A&A, 407, 925
Rieke, G.H., & Lebofsky, M.J. 1985, ApJ, 288, 618
Sana, H., Gosset, E., Rauw, G., Sung, H., & Vreux, J.-M. 2005a, A&A, submitted (Paper I)
Sana, H., et al. 2005b, A&A, submitted (Paper II)
Schmidt-Kaler, T. 1982, in *Physical Parameters of the Stars, Landolt-Börnstein Numerical Data and Functional Relationships in Science and Technology*, Group VI, Vol. 2b
Serio, S., Reale, F., Jakimiec, J., Sylwester, B., & Sylwester, J. 1991, A&A, 241, 197
Shu, F.H., Adams, F.C., & Lizano, S. 1987, ARA&A, 25, 23
Siess, L., Forestini, M., & Dougados, C. 1997, A&A, 324, 556
Siess, L., Dufour, E., & Forestini, M. 2000, A&A, 358, 593
Sung, H., Bessell, M.S., & Lee, S.-W. 1997, AJ, 114, 2644
Sung, H., Bessell, M.S., & Lee, S.-W. 1998, AJ, 115, 734 (SBL)
Sung, H., Chun, M.-Y., & Bessell, M.S. 2000, AJ, 120, 333
Wolfire, M.G., Cassinelli, J.P. 1987, ApJ, 319, 850
Zinnecker, H. 2002, in *Physics of Star Formation in Galaxies*, Saas-Fee Advanced Course 29, eds. A. Maeder & G. Meynet, 135

Chapter 3

Two colliding wind binaries

The sciences do not try to explain, they hardly even try to interpret, they mainly make models. By a model is meant a mathematical construct which, with the addition of certain verbal interpretations, describes observed phenomena. The justification of such a mathematical construct is solely and precisely that it is expected to work.
Johann von Neumann

It has long been known that massive early-type binaries display an enhanced X-ray emission compared to single stars of the same spectral types and luminosity classes (Chlebowski & Garmany 1991). This extra emission is usually thought to originate from a so-called *wind interaction region* (WIR) heated up by the collision of the supersonic stellar winds between the two stars. Alternatively, if the strengths of the two winds are strongly off balance, the dominant wind can crush on the companion surface, thus leading to an interaction of a quite different nature. Initially proposed by Cherepashchuk (1976) and Prilutsky & Usov (1976), the theory of wind-wind collision was brought to firmer grounds by Luo et al. (1990), Usov (1992) and Stevens et al. (1992). Subsequent physical effects were then proposed (Stevens & Pollock 1994; Gayley et al. 1997) that modify the wind properties of a star because of the presence of a companion. These have been reviewed in the introduction of this work.

Beside the X-ray domain, a wind interaction can also be disclosed from other wavelength ranges. In the UV and optical, the interaction region can contribute to the formation of emission lines through the recombination process. At radio wavelengths, systems with a large separation can also display a non-thermal radio emission due to synchrotron radiation of a relativistic electron population that has been accelerated in the wind-wind shock. The most striking example probably comes from the Wolf-Rayet system WR 140 (WC7+O4-5I) for which Dougherty et al. (2005) have recently performed milli-arcsec observations at the Very Long Baseline Array (VLBA). These authors clearly resolved the WIR as a bow-shaped arc that rotates as the orbit progresses. They further indicated that the properties of the shock were mainly controlled by the separation between the two components in this highly eccentric binary ($e \approx 0.88$).

The present chapter focuses on the two stronger colliding wind binary (CWB) systems in NGC 6231: HD 152248 and CPD $-41°7742$. Both systems indeed show a significant X-ray emission excess compared to the *canonical* $L_{\rm X} - L_{\rm bol}$ relation (see Chap. 2). The nature of the ongoing wind interaction is however rather different, as can be expected from the quite different characteristics of HD 152248 and CPD $-41°7742$. The study

of the optical and X-ray properties of the other individual massive stars in the FOV is postponed to the following chapters (Chap. 4 and 5). Some of these also present moderate evidence of a wind interaction. However, the two systems addressed in this chapter are particularly relevant for probing the details of the wind-interaction phenomenon. Indeed both systems are eclipsing binaries so that their sizes and the orbital inclination can be tightly constrained. The results of the present investigations have been reported in a number of papers published since 2001. We provide first a brief summary. The related papers are then included in the following pages.

- **HD 152248** is the brightest X-ray source in the FOV and is often considered as the central star of the NGC 6231 cluster. In Sana et al. (2001, see p. 81), we derive a new more accurate SB2 orbital solution of the system and revise the spectral classification of the two components as O7.5III(f)+O7III(f). We also study the profile variations of the He IIλ4686 and H α lines and show that they are constituted of three components. Two absorption components, associated with the two stars in the system, are superimposed on a broader emission which is most probably produced in a WIR. Finally, we provide observational constraints on the Struve-Sahade effect which was known to affect this system (Howarth et al. 1997). Its origin is still not understood but one of the promising ideas is that the Struve-Sahade effect is due to surface flows produced by the companion's radiation field.

  In a second paper (Sana et al. 2004, see p. 97), we analyse the X-ray observations of the system and show that the flux increases by about 50% at apastron compared to periastron. We interpret this as the signature of a wind interaction that, in HD 152248, happens in the wind acceleration region. The wind pre-shock velocities are thus larger at apastron compared to periastron, yielding a stronger shock and a correspondingly larger X-ray emission. We also present 2-D hydrodynamical simulations of the wind-wind interaction performed using the VH-1 code of Stevens et al. (1992). The emerging X-ray emission was then computed in the 3-D space, accounting in this way for both the orientation of the system and for its orbital inclination. The computed model predicts an enhanced X-ray flux at apastron compared to periastron. While diluting the expected modulation of the X-ray emission from the interaction region by the intrinsic emission from the two stars of the system, we qualitatively reproduce the observed emission level. This confirms that X-ray emission from the wind-wind interaction is probably the cause of the observed flux modulations though indeed, more detailed 3-D physics might be required to explain the details of the variations.

- **CPD -41°7742** is a short period ($P \sim 2.44$ d) eclipsing binary. In Sana et al. (2003, see p. 117), we derive the very first reliable SB2 solution of the system and find strong evidences that the system is actually an eclipsing binary. This was confirmed by our archive Bochum photometric data that were obtained a few years ago (see Sect. 1.2).

  In the second paper of the series (Sana et al. 2005a, see p. 129), we analyse the optical light curve of the system. We also present an unprecedented set of X-ray observations. Indeed thanks to the short period of the system, our XMM-*Newton* campaign provides an almost complete coverage of the orbital period. The measured X-ray flux is clearly variable. We also provide a phenomenological wind-interaction model that reproduces relatively well the main features of the X-ray light-curve. In this model, the overwhelmingly dominant primary wind crushes on the secondary star surface, yielding an extra X-ray emission associated to the secondary star surface, emission which is thus only seen at specific phases in this eclipsing binary.

A&A 370, 121–135 (2001)
DOI: 10.1051/0004-6361:20010221

Astronomy & Astrophysics

HD 152248: Evidence for a colliding wind interaction⋆

H. Sana, G. Rauw⋆⋆,†, and E. Gosset⋆⋆⋆,†

Institut d'Astrophysique et de Géophysique, Université de Liège, 5 avenue de Cointe, 4000 Liège, Belgium

Received 18 December 2000 / Accepted 7 February 2001

Abstract. We present the results of a four year spectroscopic campaign on the early-type binary system HD 152248. Our analysis yields a new classification as O7.5III(f) + O7III(f), in contradiction with previous classifications of the components as supergiants. We derive improved orbital elements and the corresponding masses ($M_1 = 29.6\,M_\odot$ and $M_2 = 29.9\,M_\odot$) are somewhat larger than previously reported in the literature, although they are still significantly lower than the ones expected from evolutionary tracks. Both components of the system are close to filling their Roche lobe at periastron passage. We also investigate the equivalent width variations of the lines of the two components and we discuss their relation to the *Struve-Sahade* effect. Finally, we show that the line profile variability of the He II λ4686 and H α lines is consistent with a strong wind interaction between the two stars, quite as predicted by current colliding wind models.

Key words. binaries: close – binaries: spectroscopic – stars: early-type – stars: fundamental parameters – stars: individual: HD 152248 – stars: winds, outflows

1. Introduction

Early-type stars of spectral-type O or Wolf-Rayet (WR) undergo a considerable mass loss through their powerful winds. Within a binary system, we expect that the winds from both stars collide, forming a wind interaction region that can manifest as enhanced X-ray emission. This X-ray emission from the shock can display a phase-locked modulation due to the variation of the line-of-sight opacity or due to a changing separation between the stars in eccentric binaries (Pittard & Stevens 1997). The wind-wind collision can also contribute to the formation of optical emission lines through the recombination process (e.g. Thaller 1997).

Over the last twenty years, the interest in wind interaction has grown, and numerous studies both from theoretical (e.g. Stevens et al. 1992; Walder 1998; Pittard 2000) and observational (e.g. Corcoran 1996; Rauw et al. 1999; Hill et al. 2000) points of view have been undertaken. These studies demonstrate that considerable insight into the mass loss process can be gained from a detailed investigation of the wind interaction phenomenon. In addition, binary systems provide precious astrophysical laboratories allowing a direct determination of the fundamental parameters of the stars that are crucial in order to test evolutionary models and to probe the impact of binarity on the evolution of the components of the system.

HD 152248 is an O+O binary system that belongs to the young open cluster NGC 6231 which is considered to be the nucleus of the rich Sco OB1 association. Situated at a distance of 1.99 kpc (Baume et al. 1999), this cluster contains a number of interesting single O stars as well as O binaries and a WR+O system (WR79). Not only is the HD 152248 system one of the brightest objects of the cluster ($V = 6.06$, Baume et al. 1999) but it also appears from ROSAT X-ray observations to be the brightest X-ray source in NGC 6231. Corcoran (1996) has further shown that the ROSAT X-ray flux from HD 152248 displays phase-locked variations, though the poor phase coverage of the ROSAT data did not allow elucidation of their origin. On these grounds, NGC 6231 has been selected as a target for the XMM X-ray observatory as part of the Liège project for guaranteed time. The pointings will be centered on HD 152248 for a total duration of 180 ksec, consisting of six 30 ksec exposures in order to adequately sample the orbital variations.

In this context, we have undertaken a spectroscopic campaign to monitor the optical counterpart of most of

Send offprint requests to: H. Sana,
e-mail: sana@astro.ulg.ac.be

⋆ Based on data collected at the European Southern Observatory (La Silla, Chile) and at the Cerro Tololo Inter-American Observatory (Cerro Tololo, Chile).

⋆⋆ Chargé de Recherches FNRS (Belgium).

⋆⋆⋆ Chercheur Qualifié FNRS (Belgium).

† Visiting Astronomer, CTIO, National Optical Astronomy Observatories (NOAO). NOAO is operated by the Association of Universities for Research in Astronomy, Inc. under contract with the National Science Foundation.

the ROSAT X-ray sources of the NGC 6231 cluster. Some preliminary results have already been presented by Sana et al. (2001). The present paper is the first of a series devoted to the O stars in NGC 6231. We present here a complete and detailed spectroscopic study of the HD 152248 system (the main target of our campaign) in the optical domain. One aim is to derive accurate, contemporaneous ephemerides required to correctly interpret the forthcoming XMM data and to clarify the evolutionary status of both components of the system. Another objective of this study is the search for the optical signature of a wind interaction which is suspected to exist within the system because of its high and variable X-ray luminosity.

This paper is organised as follows. The next section is devoted to a review of the main results already published about this object in the literature. In the third section, we describe our spectroscopic observing campaign, the data we collected and the data reduction techniques we applied. The determination of the orbital parameters is presented in the fourth section. The fifth one is devoted to the study of the variations of the equivalent widths of the absorption lines and their link to the Struve-Sahade effect (S-S effect). We next turn to the emission lines displayed by the spectrum of this system. Particular attention is paid to the He II λ4686 and H α lines and to their phase-locked variability. Section 7 is devoted to the discussion of the evolutionary status of the system, and, among other things, we re-investigate its spectral and luminosity classification. Finally, we present a wind-wind interaction model that is consistent with most of the observational features of the emission lines. The last section is devoted to a brief summary of our main results.

2. Overview

HD 152248 is a double line O+O spectroscopic binary with a period close to six days. It was first reported to be a binary by Struve (1944), although he suggested an orbital period of 3 days. Walborn (1972) quoted a spectral type of O7.5I(n)(f)p for the composite spectrum. Hill et al. (1974, HCB hereafter) managed to separate the primary and secondary components and derived a period of 5.97 days, assuming a zero eccentricity. Levato & Morrell (1983) confirmed the 6 day period and derived a non-zero eccentricity ($e = 0.18 \pm 0.02$) for the system. A polarimetric study by Luna (1988) constrained the inclination of the orbit between 60° and 76°, with a preferred value of 71°. The study of the light curve of HD 152248 by Mayer et al. (1992) revealed that the system displays two eclipses of unequal depth and that both minima are not separated by a 0.5 cycle, suggesting a non-zero eccentricity. Based on IUE observations and using a cross-correlation technique, Stickland et al. (1996, ST96 hereafter) derived a period of 5.816083 days, an eccentricity of 0.124 and a mass ratio of 0.941. The deepest eclipse corresponds to the occultation of the less-massive component. In order to avoid confusion, we choose to adopt the convention of ST96 for the primary and secondary. In the following, we will thus refer to the component occulted during the deepest (i.e. primary) eclipse as the primary star of the system.

Based on the same set of IUE data and using a tomographic reconstruction algorithm to separate primary and secondary spectra, Penny et al. (1999, PGB hereafter) derived a spectral type of O7I+O7I. They also re-analysed the light curve of the system, complementing the Mayer et al. (1992) data set with Hipparcos observations. PGB showed that the system displays ellipsoidal light variations due to tidal deformations. They derived an inclination of $72° \pm 3°$ for the orbit of the system and polar radii of $R_1 = 13.4 \pm 2.0\,R_\odot$ and $R_2 = 12.9 \pm 2.0\,R_\odot$ for the primary and secondary respectively. Combining spectroscopic and photometric results, they computed masses of $M_1 = 24.2 \pm 2.0\,M_\odot$ and $M_2 = 25.8 \pm 2.0\,M_\odot$. Howarth et al. (1997) reported that HD 152248 is displaying the *Struve-Sahade* effect, i.e. that the secondary lines seem to be stronger when the secondary is approaching. However, this result was not confirmed by PGB, who found no evidence for this effect in the strength of the cross-correlation function of the IUE spectra of HD 152248 with their standard star, HD 34078.

3. Observations and data reduction

3.1. Observations

We have been monitoring the HD 152248 binary for four years (from May 1996 until May 2000), collecting a number of spectra with various instruments at the European Southern Observatory (ESO) and at the Cerro Tololo Inter-American Observatory (CTIO). In this section, we present the general features of the instrumental configuration and data reduction. The campaign we have undertaken represents a total of 69 useful spectra obtained during 49 nights spread over nine separate runs. The main journal of the observations is given in Table 1.

During two runs in May 1996 and March 1997, a set of medium resolution spectra was obtained with the Boller & Chivens spectrograph (B&C) fed by the ESO 1.5 m telescope. The detector was a 2k × 2k UV flooded Loral-Lesser CCD. The pixel size is 15 × 15 μm. We used the holographic grating (ESO grating #32) with 2400 lines/mm, providing a spectral resolution of 1.2 Å as measured from the $FWHM$ of the lines of the HeAr comparison spectrum. The covered spectral range extends from λ3790 to λ4765 Å.

High resolution spectra of the He I λ4471, N III $\lambda\lambda$4634-4641 and He II λ4686 lines were obtained with ESO's 1.4 m Coudé Auxiliary Telescope (CAT) at La Silla, using the Coudé Echelle Spectrometer (CES) equipped with the Long Camera (LC, before March 1998) or the Very Long Camera (VLC, after March 1998). The detector used was ESO CCD#38, a Loral 2688 × 512 pixel CCD with a pixel size of 15 × 15 μm. The slit width was chosen to achieve a nominal resolving power of 70 000–80 000. The effective resolving power as derived from the $FWHM$ of the lines of the ThAr calibration exposures is 65 000–75 000. Typical

Table 1. Main journal of the spectroscopic observations of the HD 152248 system. The first column lists the heliocentric Julian date (HJD). The second gives the observational phase as computed from our He I λ4471 RV orbital solution (cf. Table 3). Columns 3 and 4 (resp. 5 and 6) provide the He I λ4471 line RV (resp. the mean RV) for the primary and secondary stars, in the "zero systemic velocity" reference frame (cf. text). The number of lines used to compute the mean RV is given in Col. 7 and the last column provides information about the instrumentation used

HJD	ϕ	He I λ 4471$-\overline{\gamma_{4471}}$		$\overline{RV_\lambda - \gamma_\lambda}$		n	Instrument.
$-2\,450\,000$		RV_1	RV_2	RV_1	RV_2		
205.859	0.851	207.4	−208.0	212.7	−214.0	6	ESO 1.5 m + B&C
206.852	0.022	−11.6	−11.6	−56.3	38.1	6	ESO 1.5 m + B&C
207.816	0.188	−207.2	203.6	−200.8	204.2	6	ESO 1.5 m + B&C
208.795	0.356	−156.1	155.8	−166.8	164.4	6	ESO 1.5 m + B&C
208.879	0.370	−150.4	136.7	−148.9	164.1	6	ESO 1.5 m + B&C
209.789	0.527	−7.5	−7.5	1.7	1.7	6	ESO 1.5 m + B&C
209.903	0.546	−7.0	−7.0	−10.4	−8.6	6	ESO 1.5 m + B&C
210.782	0.698	167.3	−173.9	184.7	−167.2	6	ESO 1.5 m + B&C
210.910	0.720	187.2	−196.4	183.8	−199.2	6	ESO 1.5 m + B&C
211.777	0.869	186.7	−187.8	203.2	−180.6	6	ESO 1.5 m + B&C
211.912	0.892	175.0	−177.9	194.8	−178.9	6	ESO 1.5 m + B&C
534.902	0.426	−75.7	129.5	−110.3	95.9	6	ESO 1.5 m + B&C
535.904	0.599	70.7	−110.5	91.1	−114.9	6	ESO 1.5 m + B&C
536.888	0.768	213.2	−208.9	209.1	−210.1	6	ESO 1.5 m + B&C
537.897	0.941	98.7	−73.8	116.9	−121.8	6	ESO 1.5 m + B&C
538.889	0.112	−165.6	135.6	−163.5	156.3	6	ESO 1.5 m + B&C
539.907	0.287	−201.4	191.8	−200.0	191.5	6	ESO 1.5 m + B&C
531.908	0.912	160.2	−155.2	160.2	−155.2	1	CAT + CES + LC
532.881	0.079	−97.9	122.7	−97.9	122.7	1	CAT + CES + LC
533.859	0.247	−206.7	219.7	−206.7	219.7	1	CAT + CES + LC
534.844	0.416	−99.7	108.2	−99.7	108.2	1	CAT + CES + LC
535.859	0.591	48.7	−85.6	48.7	−85.6	1	CAT + CES + LC
536.856	0.762	219.0	−201.2	219.0	−201.2	1	CAT + CES + LC
622.604	0.506	−4.9	1.9	−4.9	1.9	1	CAT + CES + LC
623.628	0.682	154.2	−170.8	154.2	−170.8	1	CAT + CES + LC
624.554	0.841	215.8	−211.1	215.8	−211.1	1	CAT + CES + LC
625.607	0.022	−2.2	−2.2	−2.2	−2.2	1	CAT + CES + LC
626.571	0.188	−202.0	214.9	−202.0	214.9	1	CAT + CES + LC
1000.668	0.509	0.3	3.1	0.3	3.1	1	CAT + CES + VLC
1299.817	0.945	136.7	−91.8	130.4	−103.7	11	ESO 1.5 m + FEROS
1300.809	0.115	−147.8	163.4	−150.5	166.8	11	ESO 1.5 m + FEROS
1301.815	0.288	−204.3	202.5	−202.4	194.7	11	ESO 1.5 m + FEROS
1302.808	0.459	−12.9	−12.9	−50.1	42.6	11	ESO 1.5 m + FEROS
1304.889	0.817	223.2	−213.0	213.0	−210.3	11	ESO 1.5 m + FEROS
1323.740	0.058	−88.6	49.4	−86.8	76.5	11	ESO 1.5 m + FEROS
1327.780	0.753	199.2	−202.4	200.7	−202.9	11	ESO 1.5 m + FEROS
1328.734	0.917	151.8	−150.2	158.2	−144.5	6	CTIO 1.5 m + BME
1329.738	0.089	−130.2	117.9	−122.6	136.2	6	CTIO 1.5 m + BME
1330.739	0.261	−215.9	194.0	−212.9	184.1	6	CTIO 1.5 m + BME
1331.771	0.439	−81.4	36.7	−91.5	60.6	6	CTIO 1.5 m + BME
1332.798	0.615	84.8	−108.4	94.7	−107.2	6	CTIO 1.5 m + BME
1668.832	0.393	−108.1	131.5	−120.5	125.2	11	ESO 1.5 m + FEROS
1669.853	0.568	36.0	−42.3	37.2	−51.4	11	ESO 1.5 m + FEROS
1670.836	0.737	206.7	−190.0	204.2	−188.4	11	ESO 1.5 m + FEROS
1671.839	0.910	157.9	−158.6	163.2	−159.3	11	ESO 1.5 m + FEROS
1672.828	0.080	−122.7	102.1	−120.9	111.4	11	ESO 1.5 m + FEROS
1673.809	0.248	−203.6	217.2	−206.4	207.6	11	ESO 1.5 m + FEROS

exposure times were of the order of 20 min and the average S/N ratio is above 150. The wavelength domain is centered on the He I λ4471, N III λ4641 or He II λ4686 lines and is ∼40 Å and ∼20 Å wide for spectra taken with the LC and the VLC respectively.

During three observing runs in April – May 1999, end of May 1999 and May 2000, a set of echelle spectra was taken with the Fiber-fed Extended Range Optical Spectrograph (FEROS) attached to the ESO 1.5 m telescope at La Silla. Thirty seven orders corresponding to a

wavelength domain from 3650 to 9200 Å were observed. Typical exposure times were of the order of 6 min and the average S/N ratio is about 100, 220 and 150 at 4050, 6000 and 7500 Å respectively. The spectral resolving power of the FEROS instrument is 48 000. The detector was an EEV CCD with 2048×4096 pixels of $15 \times 15\,\mu$m.

Finally, another set of echelle spectra over the range 3850 to 5790 Å was obtained with the Bench-Mounted Echelle Spectrograph (BME) attached to the 1.5 m CTIO Ritchey-Chrétien Telescope, during a 5 night run in June 1999. Forty nine orders were observed using the KPGL2 316 lines mm^{-1} grating as a cross-disperser. The detector was a Tek 2048 CCD with $24\,\mu$m pixels. The slit width was set to 70 μm corresponding to a resolving power of 45 000. Exposure times were of the order of 45 min and the average S/N ratio in the continuum is about 100.

3.2. Data reduction

The B&C and CAT observations were reduced in a standard way using the MIDAS package provided by ESO. Whenever possible, the spectra were rectified using a reference star observed under the same conditions. When such a spectrum was not available the spectra were normalized by fitting a polynomial to the continuum.

We used the FEROS context working under the MIDAS environment to reduce the FEROS echelle spectra. The reduction was performed using the *standard* option. Most of the unavoidable strong fringes that affect the red part of the spectrum (above 6600 Å) are simply corrected by flat-fielding. There are however a few residual fringes near 6670, 7140, 7385 and 7930 Å. Finally, the spectra were normalized over a range of a few hundred Å at once by fitting a polynomial of degree 4 or 5 to the continuum. Whenever doubt existed about the quality of the automatic merging between the different orders, we checked our results using the unmerged spectrum. Good agreement between both methods was generally observed.

The BME data were reduced using the IRAF[1] package and following the recommendations of the BME User's Manual. The pixel to pixel variations were removed using flat field exposures taken with a very bright light source and a diffusing screen placed inside the spectrograph (so-called *milky flats*). A first rectification of the extracted echelle orders was carried out with the projector flat exposures. The spectra were then normalized by fitting a low-order polynomial to the continuum.

4. *RV* measurements and orbital solutions

The inspection of our data reveals that the spectra of the primary and secondary are very similar and that every absorption line detected is present in both spectra. Several lines are further present in emission and we will discuss them later in this paper.

[1] IRAF is distributed by the National Optical Astronomy Observatories.

4.1. RV measurements

We selected eleven pure absorption lines in the spectrum of HD 152248 to compute the orbital elements of the system. These lines were chosen according to the following criteria: the intensity of the line, the fact that they do not suffer a heavy blend with another neighbouring line at large *RV* separation phases (e.g. H δ, C IV $\lambda\lambda$5801-12) and the requirement that they should be free from pollution by any ISM lines (e.g. H ϵ) or telluric lines (e.g. He I λ7065). The selected lines are listed in Table 2. We measured the Doppler shifts by fitting two Gaussians at phases where the separation between the lines of both stars was sufficient. We then used the cross-correlation like method described in Rauw et al. (2000) to attempt to disentangle the blended lines. As HD 152248 is an eclipsing binary, we used the light curve of PGB to achieve a rough first order correction of the relative line intensity at eclipsing phases. The observed lines are further affected by slight intensity and/or profile variations; we assumed, from our experience, that the errors on Doppler shifts measured in this way are about 2.5 times larger than the errors on the two-Gaussian fit results. For those phases where the lines were too heavily blended for the latter method to give reliable results, we adopted the *RV* obtained with a single Gaussian fit. We estimated, from the $FWHM$ of the blend, that the accuracy on the line position in this latter case could be ten times lower than the one reached at large separation phases (i.e. with the two-Gaussian fit method). While computing the orbital solution, we thus attributed a relative weight of 1.0, 0.15 and 0.01 to the *RV*s respectively measured with the two-Gaussian fit, the cross-correlation like and the single Gaussian fit methods. Ruling out the single Gaussian fit points provides orbital parameters that are only marginally different.

We adopted the effective wavelengths for O stars listed in Table 2 to compute the barycentric *RV*s. These effective wavelengths are from Conti et al. (1977) below 5000 Å, and from Underhill (1994) above. As our spectra taken with different instruments cover different wavelength ranges, the number of *RV* points associated with the different lines is variable. We report this number in Col. 6 of Table 2. The He I λ4471 line provides the largest data set with 47 *RV* points. These measurements are listed in Table 1.

4.2. Orbital solutions

4.2.1. The code

Our orbital solution computation code is based on a modified version of the Wolfe, Horak & Storer algorithm (see Wolfe et al. 1967, for the method; and Rauw et al. 2000, for the modifications implemented) and requires a previous knowledge of the orbital period to be run.

Table 2. List of the absorption lines used to compute the orbital solution together with the adopted effective wavelengths. Column 3 gives the best-fit period value as deduced from the different *RV* data sets. The errors quoted were computed using the Wolfe, Horak & Storer algorithm. The primary and secondary *apparent* systemic velocities derived are respectively listed in Cols. 4 and 5. The last column provides the number of *RV* points associated with each line data set

Line	Effective wavelength (Å)	Period (days)	$\gamma_{\lambda,1}$ ($\mathrm{km\,s^{-1}}$)	$\gamma_{\lambda,2}$ ($\mathrm{km\,s^{-1}}$)	n
He I λ4026	4026.072	5.816072 ± 0.000196	-34.1 ± 3.7	-36.0 ± 8.1	30
He II λ4200	4199.830	5.815943 ± 0.000187	-7.9 ± 3.1	-14.7 ± 6.4	35
H γ	4340.468	5.816123 ± 0.000222	-43.6 ± 3.9	-36.3 ± 8.8	35
He I λ4471	4471.512	5.816045 ± 0.000092	-30.5 ± 1.5	-28.5 ± 4.3	47
He II λ4542	4541.590	5.816022 ± 0.000116	-24.4 ± 2.0	-18.8 ± 4.9	35
He I λ4713	4713.200	5.815972 ± 0.000224	-29.1 ± 4.3	-20.7 ± 9.6	30
H β	4861.190	5.816508 ± 0.000849	-37.2 ± 5.0	-37.7 ± 11.7	18
He I λ4922	4921.929	5.815834 ± 0.000487	-26.8 ± 2.7	-23.5 ± 7.1	13
He I λ5016	5015.680	5.816139 ± 0.000965	-19.9 ± 6.3	-12.6 ± 14.4	13
He II λ5411	5411.520	5.815877 ± 0.000515	-19.0 ± 3.1	-15.3 ± 8.0	13
O III λ5592	5592.370	5.816510 ± 0.000864	-18.8 ± 4.3	-22.2 ± 11.5	18

4.2.2. The period

The best (i.e. with the smallest rms error) estimate of the period from the literature is $P = 5.816083 \pm 0.000019$ days as given by ST96. As the He I λ4471 *RV*s are the most numerous among our *RV* data, we first used this set to investigate the period value. For this purpose we applied the Lafler & Kinman method (Lafler & Kinman 1965) and the generalized spectrogramme Fourier technique (Heck et al. 1985). The results obtained with both methods lie within 5 10^{-4} days of the value of ST96, which is one order of magnitude smaller than the error estimated from the width of the peak in the periodogramme. We then iteratively ran our code, allowing for a differential correction of the orbital period. The convergence was reached in each case after a few iterations at most. This provides us with the period value which yields the orbital solution that best matches the observations (i.e. with the lowest rms residual) of the considered data set. Column 3 of Table 2 lists the period values obtained. Their weighted mean is $P = 5.816032 \pm 0.000058$ days, which is very close to the He I λ4471 value and contains both ST96 and Mayer et al. (1992) values within a $\pm 1\sigma$ interval. The very small uncertainty of the ST96 period determination results from the large time base of their IUE data set (∼5860 days) which is almost exactly four times ours. However, the HD 152248 system is most probably undergoing an apsidal motion of a few degrees per year (see below and Mayer et al. 2001) and the large time base of ST96 could actually bias their period determination. In the following, we choose to adopt our mean value $P = 5.816032$ days for the orbital period.

4.2.3. The orbital solutions

As a first step, we computed an orbital solution for each of the 11 absorption line data sets. Accounting for the error bars, the computed orbital elements do agree with each other, except for the *apparent* systemic velocities γ_1 and γ_2 (respectively associated with the primary and secondary star). Though the γ_1 and γ_2 values are in acceptable agreement with each other for the same line (see Table 2), their values as deduced from the different lines are indeed significantly different. This illustrates the well-known effect that different lines might reflect different systemic velocities. This might stem from the fact that these lines are formed at different depths in the atmosphere and thus at different outward velocities, resulting in slightly different apparent systemic velocities.

In order to combine the *RV*s obtained from the different lines, we had to refer all the *RV* measurements to a "zero systemic velocity" reference frame. For this purpose, we simply subtracted the corresponding weighted mean between γ_1 and γ_2 from the individual *RV*s of the considered line. We then computed a weighted *RV* mean from all the *RV* data obtained at the same observing date. These mean *RV*s in the *zero systemic velocity* reference frame are listed in Cols. 5 and 6 of Table 1.

The computed orbital solutions from the He I λ4471 *RV* and the mean *RV* sets are both presented in Table 3. These two solutions are in excellent agreement with each other. Our way of combining the *RV*s from the different lines is further justified by the fact that the *apparent* systemic velocities computed from the mean data lie well within 1σ of the zero velocity. We also tested the value of the period found by ST96. This does not affect the rms residual by more than a few tenths of $\mathrm{km\,s^{-1}}$ and the difference between the computed orbital elements is not significant.

4.3. Physical parameters

The He I λ4471 velocity curve is plotted in Fig. 1. This solution deduced from the optical wavelength domain is in good general agreement with the previous determination by ST96 from the UV domain. Our apparent systemic velocity is however $12\,\mathrm{km\,s^{-1}}$ more positive than theirs. This difference might result from the zero velocity point in their cross-correlation method, but it is probable too that the optical and the UV domains reflect different

Table 3. Computed orbital solution for HD 152248 using the *RV*s of the He I λ4471 absorption lines (left) or the mean *RV*s (right). T_0 is the time of the periastron passage

	He I λ4471 common solution		Mean *RV*s common solution	
P(days)	5.816032 (fixed)			
e	0.127	$\pm$ 0.007	0.134	$\pm$ 0.006
$\omega(^\circ)$	84.8	$\pm$ 4.7	81.8	$\pm$ 4.3
T_0(HJD $-2\,450\,000$)	2003.879	$\pm$ 0.072	2003.841	$\pm$ 0.066
γ_1 (km s^{-1})	-30.3	$\pm$ 1.5	0.2	$\pm$ 1.4
K_1 (km s^{-1})	216.0	$\pm$ 1.5	216.6	$\pm$ 1.3
$a_1 \sin i$ ($R_\odot$)	24.59	$\pm$ 0.17	24.66	$\pm$ 0.15
γ_2 (km s^{-1})	-28.7	$\pm$ 4.3	2.6	$\pm$ 3.4
K_2 (km s^{-1})	213.7	$\pm$ 5.2	214.3	$\pm$ 4.2
$a_2 \sin i$ ($R_\odot$)	24.35	$\pm$ 0.62	24.40	$\pm$ 0.50
rms residual (km s^{-1})	9.5		8.2	
q ($= m_1/m_2$)	0.990	$\pm$ 0.023	0.990	$\pm$ 0.018
$m_1 \sin^3 i$ ($M_\odot$)	23.19	$\pm$ 1.19	23.34	$\pm$ 0.96
$m_2 \sin^3 i$ ($M_\odot$)	23.44	$\pm$ 0.73	23.58	$\pm$ 0.61

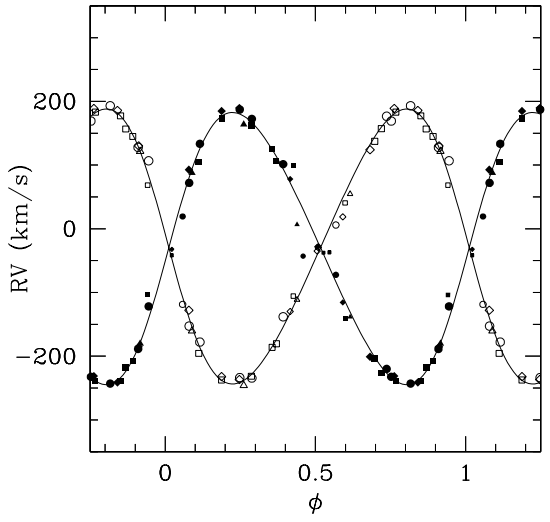

Fig. 1. Radial velocity curve of the HD 152248 binary system as computed from the He I λ4471 line plotted against the phase (ϕ). Different symbols refer to different instruments: triangle = BME, square = B&C, diamond = CES, circle = FEROS. Different sizes indicate different weights assigned to the data points in the computation of the orbital solution. Open symbols stand for the primary, while filled symbols indicate the secondary's *RV*s

apparent systemic velocities. Though the primary parameters from both our and their solution are very close, a more intriguing discrepancy is the difference between the mass ratios deduced. Indeed, our mass ratio ($q = 0.990$) is much closer to unity than the ST96 value ($q = 0.941$), and this manifests in the fact that our secondary component parameters K_2 and $a_2 \sin i$ are larger. The minimal masses we derive are also larger than the values inferred by ST96 and PGB. Adopting the PGB value for the inclination $i = 72^\circ$ yields absolute masses of $M_1 = 27.0\,M_\odot$ and $M_2 = 27.2\,M_\odot$ for the primary and the secondary respectively. We used Eggleton's formula (Eggleton 1983) to estimate the radii of the Roche lobe (*RRL*) for both components. Again assuming $i = 72^\circ$ yields respectively $RRL_1 = 19.45\,R_\odot$ and $RRL_2 = 19.55\,R_\odot$ if we neglect the effect of the eccentricity (however see below). Thus if we adopt $R_1 = 13.4\,R_\odot$ and $R_2 = 12.9\,R_\odot$, this result confirms the assertion of PGB that the system should not be undergoing a Roche lobe overflow (RLOF) mass transfer. However, Mayer et al. (2001) reported a lower value for the inclination ($i = 67.2^\circ$) and larger radii ($R_1 = 15.6\,R_\odot$ and $R_2 = 17.1\,R_\odot$). In this latter case, the primary and secondary are respectively filling 72 and 91% of their Roche lobe volume at periastron. If these preliminary results of Mayer et al. (2001) for the radii are confirmed, we then expect the system to be very unstable near periastron passage and important mass transfer or mass loss could be initiated.

4.4. Apsidal motion

While recomputing the orbital solution from previously published *RV* data at different epochs in order to check the consistency of our method, we were led to suspect the presence of an apsidal motion within the binary system HD 152248. In the following investigation, we considered three sets of data that are summarized in Table 4. We decided to ignore the complementary data obtained by HCB near JD $\sim 2\,440\,000$ because their very poor phase coverage did not allow us to derive any significant constraint on the longitude of periastron. Keeping the value of the orbital period and the eccentricity fixed at our new value, we have fitted the *RV* data from the literature. Table 4 lists the ω values that provide the best fit to the various data sets. From these results, it is clear that the system is undergoing an apsidal motion. A simple linear regression yields a rate for the apsidal motion of about $3.4^\circ\,\mathrm{yr}^{-1}$. A more detailed study by Mayer et al. (2001) based on new recent photometric results is currently underway. These authors independently discovered the presence of an apsidal motion in HD 152248 and they estimate a period of 132 years, in acceptable agreement with our value.

5. Equivalent widths and S-S effect

Using a two-Gaussian fit, we measured the *EW*s of the primary and secondary absorption lines listed in Table 2, except near conjunction. Particular attention has been paid to the normalization process to avoid systematic deviations. We estimate that our continuum determination is self-consistent with an accuracy better than 0.5%. For the strongest lines, this corresponds to a maximum contribution to the error on the *EW* measurements of about 0.05 Å. We further estimate that the mean contribution of the continuum determination to the error is about 0.02 Å

Table 4. Summary of the investigation we undertook to estimate the apsidal motion of the HD 152248 system. Second to fourth columns list respectively the approximative mean JD in format JD −2 400 000, the time interval (expressed in days) and the number of *RV* points in the set. Column 5 reports the values of the angle of periastron passage (ω) which provide the best fit. The last column lists the rms residual between the best fit and the data

Data set	$\overline{\text{JD}}$	Time base	n	ω (°)	rms (km s^{-1})
Struve[1]	∼31 200	14	22	−95	27.5
ST96	∼48 500	5861	26	76	12.1
This work	∼51 000	1468	47	85	9.2

1. Struve (1944); also described in HCB.

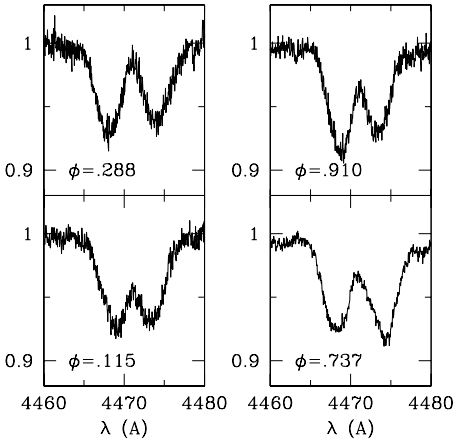

Fig. 2. Illustration of the variation of the He I λ4471 line strength. Note that the primary is on the blue side of the spectra at phases $\phi = 0.115$ and 0.288 while it is on the red side of the spectra at the phases shown in the right panel. The depletion in the red wing of the spectrum at $\phi = 0.737$ is the blue shifted secondary Mg II λ4481 line

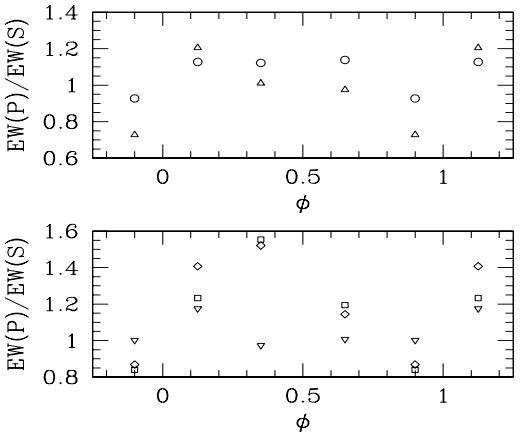

Fig. 3. Primary to secondary ratios of the mean *EW*s of the He I lines in each quadrant. Downwards triangles = He I λ4026, circles = He I λ4471, diamonds = He I λ4713, squares = He I λ4922, upright triangles = He I λ5016

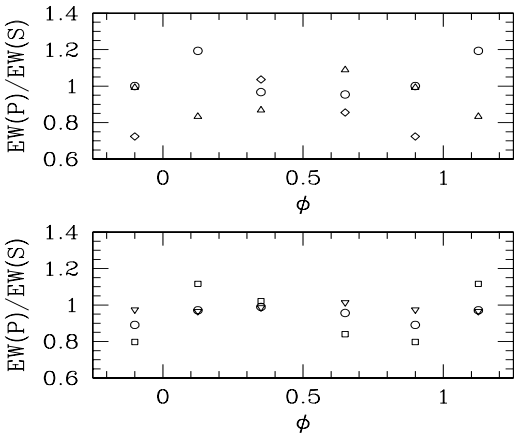

Fig. 4. Primary to secondary ratios of the mean *EW*s of the Balmer and the O III (upper panel) lines and of the He II (lower panel) lines in each quadrant. Upper panel: circles = Hγ, diamonds = Hβ, upright triangles = O III λ5592. Lower panel: squares = He II λ4200, circles = He II λ4542, downwards triangles = He II λ5411

and that the intrinsic error related to the measurement process is of the same order of magnitude.

Several clear tendencies appear from these measurements and are presented below. First of all, let us divide the orbital cycle into four parts which we call quadrants, each of them corresponding to an interval of 90° in true anomaly. The first quadrant ranges then from the primary eclipse to the first quadrature; the second, from the first quadrature to the secondary eclipse and so on for the third and fourth quadrants. Due to the blend near conjunction, the effective corresponding phase intervals are, respectively for 1st to 4th interval, [0.06–0.22], [0.22–0.40], [0.66–0.80] and [0.80–0.95]. To limit the uncertainties and outline the observed trends, we computed the mean *EW*s over each of the quadrants. These are listed in Table 5. The primary to secondary ratios of the mean *EW*s in each quadrant are further plotted in Figs. 3 and 4.

From these figures, we can identify the following trends:

1. The He I lines: a very intriguing variation is observed for the He I λ4471 line and is also present in other He I lines. The primary to secondary *EW* ratio is reversed in the fourth quadrant. Indeed, during the first three quadrants, the lines associated with the primary are slightly more intense than the secondary ones. In the fourth quadrant (i.e. $\phi = 0.8$–1.0) however the situation is exactly the opposite, with the primary's lines being fainter. Thus the secondary lines seem stronger between phases 0.8 and 1.0, when the star is approaching. However, we have to mention that this effect is not detected for the He I λ4026 line, but this line is actually a blend with the He II λ4026 transition;
2. The He II lines: a clear enhancement of the secondary lines compared to the primary ones is observed for the He II $\lambda\lambda$4200 and 4542 lines during the 3rd and

Table 5. List of the mean equivalent widths (expressed in Å) over each of the four quadrants (see text). The P and S stand for Primary and Secondary respectively

Line	Quadrant 1		Quadrant 2		Quadrant 3		Quadrant 4	
	P	S	P	S	P	S	P	S
He I λ4026	0.281	0.239	0.242	0.248	0.258	0.256	0.265	0.264
He I λ4471	0.299	0.265	0.296	0.264	0.302	0.265	0.266	0.287
He I λ4713	0.095	0.068	0.094	0.062	0.086	0.075	0.063	0.073
He I λ4922	0.101	0.082	0.116	0.075	0.107	0.090	0.087	0.104
He I λ5016	0.106	0.088	0.097	0.096	0.098	0.101	0.083	0.114
He II λ4200	0.188	0.168	0.173	0.169	0.195	0.233	0.185	0.232
He II λ4542	0.280	0.288	0.283	0.286	0.283	0.296	0.268	0.301
He II λ5411	0.421	0.436	0.425	0.431	0.439	0.433	0.418	0.429
H γ	0.914	0.766	0.804	0.832	0.812	0.851	0.837	0.836
H β	n.	n.	0.758	0.732	0.740	0.865	0.603	0.833
O III λ5592	0.195	0.234	0.260	0.299	0.203	0.186	0.191	0.193

4th quadrants, while the secondary is approaching. However the He II λ5411 line does not seem to display any significant variation of the *EW* ratio (Fig. 4);

3. The Balmer lines: these lines do not seem to display such a clear general trend as the He I or He II lines. Indeed, although the four Balmer absorptions (i.e. Hβ, Hγ, H δ and Hϵ) most often exhibit the blueshifted component with the largest *EW*, this probably results, for the H δ and H ϵ lines, from a blend with neighbouring lines on the blue side. The H γ line displays an inversion of the primary and secondary *EW* ratio between the 1st and 2nd quadrants. Finally, though none of the H β spectra could be separated in the 1st quadrant, the secondary line is clearly strengthened when this star is approaching (i.e. quadrants 3 and 4). The primary line also seems fainter at those phases;
4. The O III λ5592 line: this line displays a behaviour opposite to the ones of the lines previously discussed. In this case, the secondary line is fainter in the 3rd and 4th quadrants, while the secondary star is approaching.

As suggested by Howarth et al. (1997), these variations might be related to the so-called Struve-Sahade effect (S-S effect) though the origin of this effect is still not fully understood. First reported by Struve (1937), the *Struve-Sahade effect is the apparent strengthening of the secondary spectrum of a hot binary when the secondary is approaching and the corresponding weakening of the lines when it is receding* (Bagnuolo et al. 1999). We refer to the paper of Bagnuolo et al. for a recent review of the problem. In their paper, Bagnuolo et al. re-analysed three systems previously reported to display this effect and concluded that these "*three classical massive binaries* [...] *have a different tale*": localized heating by colliding winds for AO Cas, no Struve-Sahade effect for Plaskett's Star and a probable RLOF scenario for 29 CMa. So the Struve-Sahade effect is thus probably a similar manifestation of different physical phenomena and must then be investigated one case at a time.

Strictly speaking, only H β and two of the three studied He II lines display the S-S effect. Indeed, the variation of the He I line intensity does not match the "classical" definition of the S-S effect, as the strengthening of the secondary lines and the corresponding weakening of the primary ones occur between the 3rd and the 4th quadrants. A detailed investigation of the intrinsic variations of the *EW*s related to each star would further require correcting them for the relative contribution of the primary and secondary fluxes to the continuum. However, we have to defer this task to future works as we do not have at our disposal, at this stage, the appropriate photometric information required to properly carry out this study.

Finally, Gayley (2001) has recently suggested that the S-S effect might be due to surface flows generated by the irradiation of the stellar surface by the companion. This could modify the rotational broadening of the lines and might break down the approaching/receding symmetry, resulting in shallower or deeper absorption lines according to the line of sight. However, no influence on the intensity of the line is expected due to surface flows. The maximum projected velocity of such surface flows predicted in the case of the components of HD 152248 lies near 110 km s^{-1}. The measured *FWHM*s of the absorption lines in the spectrum of HD 152248 present a scatter of about 0.3–0.4 Å around the mean value, though no clear correlation with the phase is observed. This corresponds to a variation of the broadening velocity of about 25 km s^{-1}. The exact contribution of surface flows induced by irradiation to these slight profile variations is unknown. Clearly, detailed numerical modelling as well as more observations combining very high S/N and high resolution are needed to clarify this question.

6. The emission lines

As mentioned earlier in this paper, the HD 152248 spectrum presents several emission features. These include the He II λ4686 and H α lines that consist of a mixture of absorption and emission lines, the heavily blended N III $\lambda\lambda$4634-4641 features, the C III λ5696 line and the faint unidentified of emissions at λ4486 and λ4504.

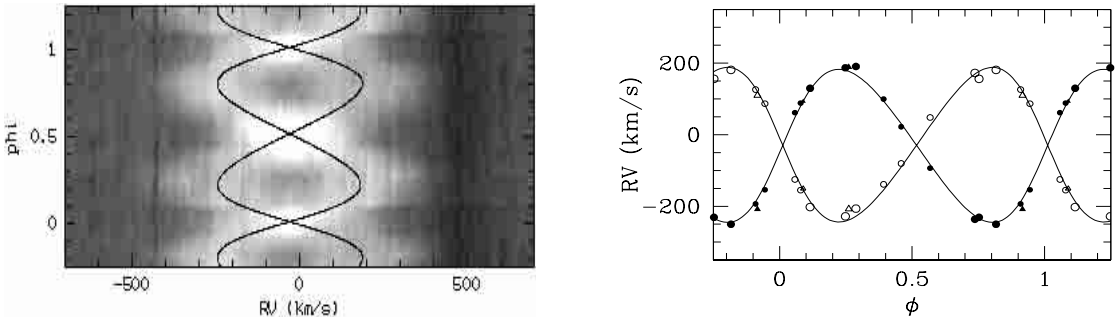

Fig. 5. Left: dynamical spectrum of the C III λ5696 emission line. The cuts are set to [0.97–1.08]. The He I λ4471 line *RV* curve has been overplotted. Right: *RV*s of the C III λ5696 line overplotted on the He I λ4471 line *RV* curve. The symbols used have the same signification as in Fig. 1

6.1. The C III λ5696 line

As it clearly appears from Fig. 5, the C III λ5696 emission line turns out to be double peaked around quadrature and the peaks seem to move in phase with the *RV* curves of the absorption lines. In order to measure the *RV*s associated with these peaks, we first modelled the diffuse interstellar band (DIB) at $\lambda = 5704.97$ Å ($EW \approx 0.064$ Å) on a spectrum where it was well separated from the C III line (HJD 2451669.853). We then subtracted the modelled DIB from all spectra and fitted two Gaussians to the C III emission line whenever the separation between the components was large enough; at other phases, we used the cross-correlation like method. The measured *RV*s are plotted together with the He I λ4471 *RV* curve on the right panel of Fig. 5. The left panel presents a grey scale image around the C III line; the He I λ4471 line orbital solution has been overplotted. It is clear from the two panels of Fig. 5 that the C III λ5696 lines closely follow the orbital motion. As we already pointed out in the case of HD 93403 (Rauw et al. 2000), this is a strong argument in favour of a photospheric origin of the C III λ5696 line as suggested by Nussbaumer (1971) and Cardona-Núñez (1978). Finally, unlike the case of HD 93403 (see Rauw et al. 2001), the C III λ5696 line in the spectrum of HD 152248 does not seem to display a reversal of the intensity ratio due to the Struve-Sahade effect.

6.2. The N III λλ4634-4641 structure

The HD 152248 spectrum presents a highly complex emission structure between about $\lambda = 4625$ Å and $\lambda = 4645$ Å, which displays important phase-locked profile variations. In this region of the spectrum, the N III $\lambda\lambda$4634 and 4641 lines are heavily blended with each other as well as with the neighbouring Si IV λ4631 and C III $\lambda\lambda$4647-4650 lines at all phases. Due to their lower resolution, we excluded the B&C spectra from our study. Similarly we did not consider the CTIO spectra because of their relatively lower S/N ratio. A complementary journal of the CAT N III $\lambda\lambda$4634-4641 observations is given in Table 6. A careful comparison of the CAT and FEROS N III $\lambda\lambda$4634-4641 spectra with the predicted line positions computed from our ephemerides and our orbital solution allows us to identify the components of the blend. Both stars of the HD 152248 system present the N III $\lambda\lambda$4634-4641 lines in emission in their spectra. Following e.g. Mathys (1988), an (f) tag should then be added to their spectral classification. The Si IV λ4631 and C III $\lambda\lambda$4647-4650 lines are in absorption in both spectra.

6.3. The unidentified λλ4486, 4504 lines

The two $\lambda\lambda$4486, 4504 emission lines are related to the Of phenomenon and still remain unidentified, although they have been known for several decades now. These two lines are rather faint in the spectra of HD 152248 and their peak intensities reach maxima of respectively 2.5% and 2% of the continuum level at conjunction phases. The stellar Mg II λ4481 lines, the DIB near λ4502 and the probable presence of the N III $\lambda\lambda$4510-4514 absorption lines render this region of the spectrum very crowded and prevent us from performing a detailed analysis. It seems however clear that the λ4486 line is double peaked with the two components closely following the orbital motion. The situation is less clear concerning the λ4504 line, because of the DIB that affects the blue side of the line. A careful inspection of the spectra however suggests that the λ4504 line might also be double peaked according to the orbital motion.

6.4. The He II λ4686 and H α lines

We have a total of 51 He II λ4686 line spectra (17 B&C, 16 CES, 5 BME and 13 FEROS) at our disposal that provide a very good phase coverage. The journal of the CAT observations of He II λ4686 is given in Table 6. Our H α line data set is much more limited and consists of only 13 FEROS spectra. The normalization of the FEROS spectra around these two lines turned out to be a rather difficult task. Indeed, both lines are situated at the junction of two echelle orders and we had to normalize the spectra locally. To compare the B&C spectra with the echelle spectra, we

Table 6. Complementary journal of the CAT observations of the N III $\lambda\lambda$4634-4641 and He II λ4686 lines. The notations used are identical to those of Table 1

Line	HJD −2 450 000	ϕ	Instrument.
N III $\lambda\lambda$4634-41	621.781	0.364	CAT + CES + LC
	622.802	0.540	CAT + CES + LC
	623.805	0.712	CAT + CES + LC
	624.771	0.878	CAT + CES + LC
	625.785	0.053	CAT + CES + LC
	626.762	0.220	CAT + CES + LC
He II λ4686	532.911	0.084	CAT + CES + LC
	533.902	0.254	CAT + CES + LC
	534.897	0.425	CAT + CES + LC
	535.895	0.597	CAT + CES + LC
	621.707	0.351	CAT + CES + LC
	622.735	0.528	CAT + CES + LC
	623.741	0.701	CAT + CES + LC
	624.700	0.866	CAT + CES + LC
	625.714	0.040	CAT + CES + LC
	626.696	0.209	CAT + CES + LC
	995.821	0.676	CAT + CES + VLC
	996.782	0.841	CAT + CES + VLC
	997.767	0.011	CAT + CES + VLC
	998.753	0.180	CAT + CES + VLC
	999.760	0.353	CAT + CES + VLC
	1000.727	0.520	CAT + CES + VLC

Table 7. Measured equivalent widths of the three components of the He II λ4686 and H α lines as measured on the spectrum taken on HJD 2451673.809 ($\phi = 0.248$)

Line component	*EW* (He II λ4686) (Å)	*EW* (H α) (Å)
Primary absorption	0.245	0.590
Secondary absorption	0.178	0.400
Emission	−0.630	−2.588

also had to apply a local normalization around He II λ4686 on the B&C spectra, in order to account for the broad underlying emission extending from 4600 to 4720 Å.

Both the He II λ4686 and H α lines consist of a mixture of absorptions and emissions. Dynamical spectra of these two lines are displayed as a function of orbital phase on the grey-scale images in Fig. 7. These were built by direct linear interpolation along the time axis of the observed spectra.

It is clear from these two diagrams and from Fig. 6 that the He II λ4686 and H α line profiles are strongly variable. For both lines, we can identify two absorption components at *RV*s that closely match the orbital motion. These absorptions are thus most probably formed in the atmosphere of the stars of the system. These two absorption features are superimposed on a broader emission component. The width of this latter emission varies with orbital phase (see e.g. Fig. 6).

To quantify these variations, we first measured the total *EW* of the lines. The results for both lines are plotted against the phase in Fig. 8. Concerning the He II λ4686

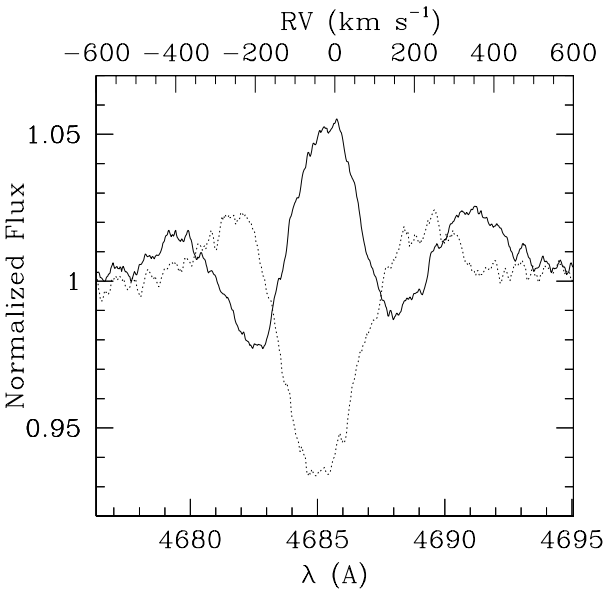

Fig. 6. Two superimposed spectra of the He II λ4686 line: the full line corresponds to $\phi = 0.910$; the dashed line, to $\phi = 0.568$

line, we notice that the absorption is clearly dominating near phase $\phi = 0.5$ and in a less prominent way near $\phi = 0.0$. On the other side, the emission is overwhelming at phase $\phi \approx 0.8$ (and to some extent at $\phi \approx 0.25$).

We next attempted to restore the emission component. To this aim, in order to model the three line components, we fitted three Gaussians to the line profile on a spectrum where the two absorption contributions are well separated. The *EW*s of all three components as obtained from the fit are reported in Table 7. These results should however be considered with caution since the *EW*s of the three components are most probably undergoing some variation with phase. For each observed spectrum, we then shifted the template of the absorption components according to our He I λ4471 orbital solution and the observation phase, and we subtracted the shifted fake lines from the observed profile. This "restoration" process is a very crude method. In fact, the apparent systemic velocities of the He II λ4686 and H α absorption components are unknown and could be different from that of the He I λ4471 line, though Fig. 7 suggests that this difference should be small. In addition, HD 152248 displays both ellipsoidal variations and photometric eclipses. As a consequence, the *EW*s of the lines are most probably varying with phase, and it is almost impossible to correctly account for this effect without the exact knowledge of the amount of light originating from the primary and from the secondary at each orbital phase. However, we used the eclipse depths from PGB to derive a first order correction for the line intensities of the absorbing components. We then measured the full width at the base of the restored emission components. To this aim, we defined the limits of the emission at a normalized intensity of 1.01, i.e. we considered the emission above 1% of

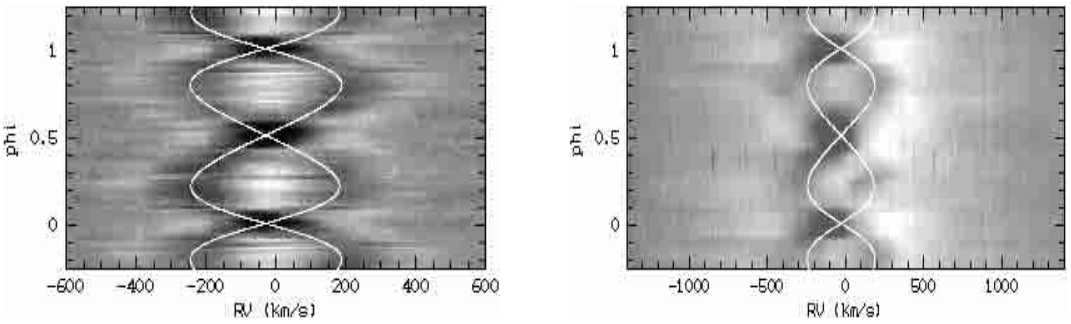

Fig. 7. Dynamical spectra of the He II λ4686 (left) and H α (right) lines. The cuts are respectively set to [0.95–1.05] and [0.95–1.1]. The He I λ4471 *RV* curve has been overplotted on both panels

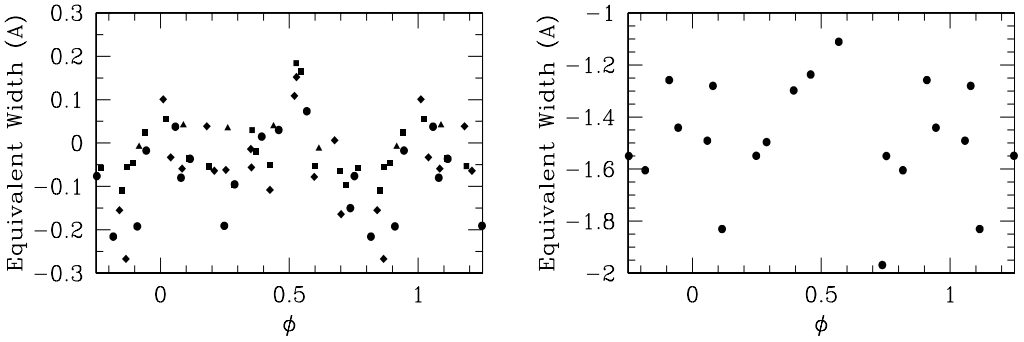

Fig. 8. Equivalent widths of the He II λ4686 (left) and H α (right) lines. Different symbols refer to different instruments: triangle = BME, square = B&C, diamond = CES, circle = FEROS

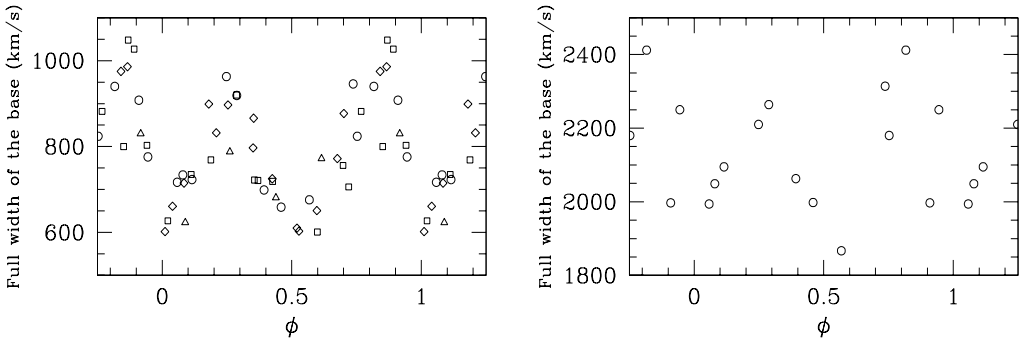

Fig. 9. Full widths of the base of the emission component of the He II λ4686 (left) and H α (right) lines. Different symbols refer to different instruments: triangle = BME, square = B&C, diamond = CES, circle = FEROS

the continuum. Results are displayed in Fig. 9 and show a strong phase-locked variation of the full width at the base of the emission components. Similar measurements have been carried out on the raw observed spectra to check that our restoration method does not bias the results. Only slight differences of the order of 20 km s^{-1} for the start and end positions of the He II λ4686 emission component were detected. The H α emission component being much more intense, no significant difference could be detected for this line.

In summary, the He II λ4686 and H α lines behave similarly in many points. A common interpretation of the observed phase-locked modulation of both lines will be provided in Sect. 8, within the framework of a colliding wind model. However, we first need to discuss the evolutionary status of the components of HD 152248.

7. Evolutionary status

7.1. Spectral types and luminosity classes

Following the criterion of Conti (1973), we use the logarithm of the EW ratio of He I λ4471 and He II λ4542 to determine the spectral types of both components of the system. We get for the mean ratio:

$$\log W'_{\rm prim}(\lambda4471/\lambda4542) = 0.013\ [-0.035, 0.056]$$
$$\log W'_{\rm sec}(\lambda4471/\lambda4542) = -0.044\ [-0.101, 0.006].$$

This gives a spectral type of O7.5 and O7 for the primary and secondary stars respectively. The values between brackets correspond to a 1σ dispersion on the mean value of the EW ratios. The agreement with the previous determination by PGB using IUE data (O7 + O7) is quite good.

Walborn (1972) quoted a supergiant luminosity class for the composite spectrum of HD 152248 though he noted that his classification could be vitiated because of the peculiar He II λ4686 profile. PGB also adopted a supergiant luminosity class for both components of the system. However, the presence of He II λ4686 and H α in absorption in the spectrum of both stars argues against such a classification. In fact, PGB's assertion was based on the following UV criteria: a very strong emission in the Si IV $\lambda\lambda$1394-1403 lines in all the IUE composite spectra and a blue asymmetry and red emission in the N IV λ1718 line in both primary and secondary spectra. However, as these authors mentioned in Penny et al. (1996), the Si IV $\lambda\lambda$1394-1403 doublet is a *wind feature* that might not be associated with the photosphere. Furthermore, the dependence of the N IV λ1718 line on wind strength might lead to a more luminous classification in the case of a star with an unusually strong wind. We believe that previous confusion about the luminosity class of this system arises mainly from the fact that the lines adopted as luminosity classification criteria are probably affected by a wind interaction process occurring within the HD 152248 system (see below).

Based on the presence of He II λ4686 and H α in absorption in the spectrum of both components, we follow Mathys (1988) recommendation and, according to a rough determination of the EW of the He II λ4686 absorption components (from Table 7), we adopt a giant luminosity class for both stars of the HD 152248 system. Morrell et al. (1991) further showed that the unidentified $\lambda\lambda$4486, 4504 lines display a clear luminosity dependence. An estimate of the intensity of the λ4486 line in the spectrum of HD 152248 also suggests that the stars of HD 152248 are giants.

Finally both stars present N III $\lambda\lambda$4634-4641 in emission so that, associated with weak He II λ4686 absorption, an (f) tag should be added to the spectral classification. The new classification for this system is thus: O7.5III(f) + O7III(f).

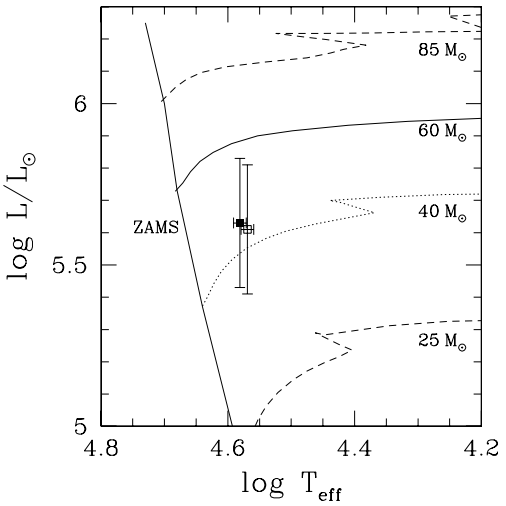

Fig. 10. Hertzsprung-Russell diagram of the HD 152248 system. The open and filled symbols stand for the primary and secondary respectively. Evolutionary tracks are from Schaller et al. (1992) for $Z = 0.020$ and adopting 'standard' mass loss rates

7.2. Location in the H-R diagram

Adopting the effective temperature calibration of Chlebowski & Garmany (1991), the spectral types derived above yield $T_{\rm eff} = 37100 \pm 1000$ K and $T_{\rm eff} = 38\,100 \pm 1000$ K for the primary and the secondary respectively. The quoted uncertainty corresponds to half a spectral subtype.

Howarth et al. (1997) and Penny et al. (1999) quote a luminosity ratio in the UV and in the visible of $I_{\rm sec}/I_{\rm prim} \simeq 0.98$. Raboud et al. (1997) reported $V = 6.09$ and $E(B-V) = 0.46$ for HD 152248. The photometry of HD 152248 is affected by the presence of a nearby visual companion that is about 2.0 mag fainter than the close binary (Mason et al. 1998). The values of the distance modulus of the NGC 6231 cluster range from 10.7 to 11.6. In the following, we will adopt the value $DM = 11.2$ derived by Raboud et al. (1997). We thus obtain $\log(L^{\rm prim}_{\rm bol}/L_\odot) = 5.61 \pm 0.2$ and $\log(L^{\rm sec}_{\rm bol}/L_\odot) = 5.63 \pm 0.2$ for the primary and secondary respectively. The uncertainties on the quoted luminosities correspond to the sole uncertainty (0.5 dex) on the distance modulus of NGC 6231.

The locations of the components of HD 152248 are plotted in a H-R diagram in Fig. 10 together with the evolutionary tracks of Schaller et al. (1992). From the above results, we can infer radii of $R_1 = 15.4^{+3.9}_{-3.1}\,R_\odot$ and $R_2 = 14.9^{+3.9}_{-3.1}\,R_\odot$. These radii overlap within the errors with the values derived by PGB (13.4 and 12.9 $R_\odot$ for the primary and secondary respectively) and Mayer et al. (15.6 and 17.1 $R_\odot$ for the primary and secondary respectively). Our values of the radii are slightly larger than the typical radii of O7–O7.5 giants as listed by Howarth & Prinja (1989), but they are definitely smaller than the radii of luminosity class I stars of same spectral type

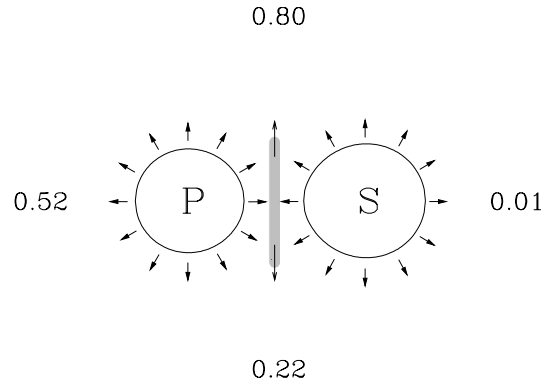

Fig. 11. Schematic view of the wind-wind interaction process occurring within the HD 152248 system. The shaded area represents the high density, emitting region. The P and S letters refer respectively to the primary and secondary components of the system. Conjunction and quadrature phases have been indicated. The adopted value for the separation between the two components is 53.1 $R_\odot$, corresponding to $i = 67.2°$, and the shapes of the stars have been computed assuming mean radii $R_1 = 15.6\ R_\odot$ and $R_2 = 17.1\ R_\odot$ (Mayer et al. 2001) respectively

(Howarth & Prinja 1989) lending further support to our assertion that the components in HD 152248 are giants rather than supergiants.

From a crude interpolation between the evolutionary tracks of Schaller et al. (1992), we derive "theoretical" masses of $M_1 = 41.7^{+10.3}_{-6.1}\,M_\odot$ and $M_2 = 43.7^{+10.1}_{-6.1}\,M_\odot$. If we adopt the inclination of 67.2° as determined by Mayer et al. (2001), the minimal masses reported in Table 3 yield observed masses of 29.6 and 29.9 $M_\odot$ for the primary and the secondary respectively. These latter values are significantly smaller than the masses predicted from the theoretical models for stars at the same location in the HR diagram. This problem was already pointed out by PGB. Improved stellar evolution models including the effects of rotation (Meynet & Maeder 2000) might provide a solution for this mass discrepancy. In fact, the new models discussed by Meynet & Maeder (2000) predict a large scatter in the mass-luminosity relation that can amount to a difference of 30% in mass. However, we caution that the components of HD 152248 do not show an exceptionally large projected equatorial rotational velocity (see Howarth et al. 1997).

Another way to account for this mass discrepancy consists to postulate a Roche lobe overflow scenario that could have altered the evolution of the components. Indeed the stars are close to their stability limit near periastron passage and mass loss could be initiated at that time. However, we did not find any evidence that such a process is currently taking place in HD 152248. The stars might, however, have been transferring mass through the L_1 point in the past, though the amount of transferred mass as well as the reason why this process came to a stop are unclear. Finally, we also mention Gayley's suggestion (Gayley 2001) that non-conservative mass transfer prior to the RLOF phase might exist in highly eccentric close binaries. As this is still a "working idea", we refer to his paper for more details.

8. Wind-wind interaction

We now attempt to provide a consistent explanation to all our observations. It is obvious, from the results presented above, that both components of the HD 152248 system are very similar. They indeed have similar polar radii, masses, luminosities and spectral types. Therefore, we can expect that the stars also have similar wind properties (mass loss rates and asymptotic velocities). Howarth et al. (1997) derived terminal velocities of $v_{\infty,1} = 2420\,\mathrm{km\,s^{-1}}$ and $v_{\infty,2} = 2010\,\mathrm{km\,s^{-1}}$ for the primary and secondary respectively. We can use the stellar parameters derived above in conjunction with the theoretical mass loss recipe of Vink et al. (2000) to estimate the mass-loss rates of the two components. In this way, we obtain $\log \dot{M}_1 = -5.53$ and $\log \dot{M}_2 = -5.48$ ($M_\odot\,\mathrm{yr^{-1}}$) yielding a wind momentum ratio (Stevens et al. 1992) of

$$\mathcal{R} = \left(\frac{\dot{M}_1\,v_{\infty,1}}{\dot{M}_2\,v_{\infty,2}}\right)^{1/2} \simeq 1.03 \qquad (1)$$

From these simple arguments, we expect therefore that the stagnation point of a wind-wind collision should be located near the center of mass of the HD 152248 system. Adopting a "standard" β velocity law (with $\beta = 1$), we find that, depending on the orbital separation, the winds of both stars should reach between about 0.34 and $0.50 \times v_\infty$ before they collide. Using these pre-shock velocities, we obtain rather low values of the cooling parameter $\chi \leq 0.02$–0.15 (see Stevens et al. 1992 for the definition of χ). Radiative cooling could therefore play an important role in the interaction region and cool the shock-heated material to temperatures where the recombination process can efficiently contribute to the formation of the H α and He II λ4686 emission lines.

A very simple model that can match most of the observations consists therefore in assuming the existence of a wind-wind interaction region located mid-way between both stars and limited by two roughly planar hydrodynamic shocks. This high density region, where the He II λ4686 and H α emission components are assumed to be produced, would (partly) be occulted at conjunction phases ($\phi = 0.01$ and 0.52) which explains why the absorption is overwhelming near these phases. Similarly, this simple scenario also accounts for the phase-locked variations of the width of the emission component. Indeed, we expect from our model that the inner shock region would be almost perpendicular to the axis of the system, so that the distribution of the radial velocities of the particles escaping from the wind interaction region should be broader when our line of sight is aligned with the interaction zone (i.e. around $\phi = 0.22$ and 0.80). On the other hand, this velocity distribution should be narrower at conjunction

phases when our line of sight is forming an angle of about $i \approx 70°$ with the interaction region. Near conjunction, we thus expect to observe a narrower emission line than around quadrature.

Part of the difference of the relative strengthening of the emission near quadrature phases might be explained by assuming that the emission process is depending of the separation D between the two stars following some power of 1/D. Indeed this distance is slightly larger at $\phi = 0.22$ than at $\phi = 0.80$. The difference between the two *absorption peaks* at conjunction phases might also result from a difference in the separation between the two stars since the phases $\phi = 0.0$ and $\phi = 0.5$ respectively coincide with the periastron and the apastron passage. The unequal depths of the primary and secondary eclipses might also account for part of this difference, as the continuum level is lower at primary eclipse and the dilution of the emission is thus weaker. We might expect that the forthcoming X-ray observations will help to address those questions and will further allow us to refine the wind-wind interaction model of the HD 152248 system.

9. Conclusion

We presented the results of an optical spectroscopic campaign on the HD 152248 O+O binary system. Based on a large set of medium and high resolution spectra which provides a very good phase coverage, we derived improved orbital parameters. Combining literature data with our observations, we detected the presence of an apsidal motion with a rate of about $3.4° \, \mathrm{yr}^{-1}$. As this system is going to be observed with the XMM X-ray observatory, the new contemporaneous ephemerides we derived are of major importance to correctly interpret the X-ray observation of the HD 152248 binary.

We found that the previous classification of both components as supergiants is most probably erroneous and we provide a new classification as O7.5III(f) + O7III(f) for the system. This leads to a better agreement between the observed radii and masses of the components and the typical values for O7–O7.5 giants. The masses we derived are, however, still significantly lower than the ones predicted by the evolutionary tracks.

Finally, we demonstrated that the He II λ4686 and H α line profiles result from a blend of two absorption components, associated with the stars of the system, with a broader and more intense emission component. We further showed that their profile and intensity variations are consistent with a wind-wind collision process within the system, assuming that the He II λ4686 and H α emissions are produced within the interaction region through the recombination process.

The probable existence of a wind-wind interaction within the HD 152248 system makes this object an even more attractive target for XMM X-ray observations. The XMM pointings are scheduled to properly cover the orbital cycle and will further allow to investigate the different time scales of the wind interaction process. Detailed comparison of these data with recent theoretical hydrodynamical simulations (e.g. Stevens et al. 1992; Pittard 2000) will provide an important test for these models. It will further help to improve our understanding of the wind-wind collision process, and more widely of the winds of hot stars in general.

Acknowledgements. We wish to thank Dr. O. Stahl and Dr. A. Kaufer for their efficient help in adapting the FEROS reduction package to our data and the referee Dr. Stahl for his suggestions that improve our manuscript. We are grateful to Y. Nazé and Dr. J. Manfroid for their help in the reduction of the BME data. We thank Dr. J.-M. Vreux for many helpful comments and stimulating discussions. We are also grateful to Drs. P. Harmanec and P. Eenens for discussion about HD 152248 and for communicating their results prior to publication. We are greatly indebted to the Fonds National de la Recherche Scientifique (Belgium) for multiple support. This research is also supported in part by contract P4/05 "Pôle d'Attraction Interuniversitaire" (SSTC-Belgium). Partial support through the PRODEX XMM-OM and INTEGRAL Projects is also gratefully acknowledged. The SIMBAD database was consulted for the bibliography.

References

Bagnuolo, W. G. Jr., Gies, D. R., Riddle, R., & Penny, L. R. 1999, ApJ, 527, 353
Baume, G., Vázquez, R. A., & Feinstein, A. 1999, A&AS, 137, 233
Cardona-Núñez, O. 1978, Ph.D. Thesis, University of Colorado, Boulder
Chlebowski, T., & Garmany, C. D. 1991, ApJ, 368, 241
Conti, P. S. 1973, ApJ, 179, 181
Conti, P. S., Leep, E. M., & Lorre, J. J. 1977, ApJ, 214, 759
Corcoran, M. F. 1996, Rev. Mex. A. A. Conf., 5, 54
Eggleton, P. P. 1983, ApJ, 268, 368
Gayley, K. G. 2001, in Interacting Winds from Massive Stars, ASP Conf. Ser., ed. A. F. J. Moffat, & N. St.-Louis, in press
Heck, A., Manfroid, J., & Mersch, G. 1985, A&AS, 59, 63
Hill, G., Crawford, D. L., & Barnes, J. V. 1974, AJ, 79, 1271
Hill, G. M., Moffat, A. F. J., St.-Louis, N., & Bartzakos, P. 2000, MNRAS, 318, 402
Howarth, I. D., & Prinja, R. K. 1989, ApJS, 69, 527
Howarth, I. D., Siebert, K. W., Hussain, G. A. J., & Prinja, R. K. 1997, MNRAS, 284, 265
Lafler, J., & Kinman, T. D. 1965, ApJS, 11, 216
Levato, H., & Morrell, N. 1983, ApL, 23, 183
Luna, H. G. 1988, A&AS, 74, 427
Mason, B. D., Gies, D. R., Hartkopf, W. I., et al. 1998, AJ, 115, 821
Mathys, G. 1988, A&AS, 76, 427
Mayer, P., Lorenz, R., & Drechsel, H. 1992, IBVS, 3765, 1
Mayer, P., Harmanec, P., Lorenz, R., et al. 2001, in The Influence of Binaries on Stellar Population Studies, ed. D. Vanbeveren (Kluwer Academic Publisher), in press
Meynet, G., & Maeder, A. 2000, A&A, 361, 101
Morrell, N. I., Walborn, N. R., & Fitzpatrick, E. L. 1991, PASP, 103, 341
Nussbaumer, H. 1971, ApJ, 170, 93
Penny, L. R., Gies, D. R., & Bagnuolo, W. G. Jr. 1996, ApJ, 460, 906

Penny, L. R., Gies, D. R., & Bagnuolo, W. G. Jr. 1999, ApJ, 518, 450
Pittard, J. M. 2000, Ph.D. Thesis, University of Birmingham (UK)
Pittard, J. M., & Stevens, I. R. 1997, MNRAS, 292, 298
Raboud, D., Cramer, N., & Bernasconi, P. A. 1997, A&A, 325, 167
Rauw, G., Vreux, J.-M., & Bohannan, B. 1999, ApJ, 517, 416
Rauw, G., Sana, H., Gosset, E., et al. 2000, A&A, 360, 1003
Rauw, G., Sana, H., Vreux, J.-M., Gosset, E., & Stevens, I. R. 2001, in Interacting Winds from Massive Stars, ASP Conf. Ser., ed. A. F. J. Moffat, & N. St.-Louis, in press
Sana, H., Rauw, G., Gosset, E., & Vreux, J.-M. 2001, in Interacting Winds from Massive Stars, ASP Conf. Ser., ed. A. F. J. Moffat, & N. St.-Louis, in press
Schaller, G., Schaerer, D., Meynet, G., & Maeder, A. 1992, A&AS, 96, 269
Stevens, I. R., Blondin, J. M., & Pollock, A. M. T. 1992, ApJ, 386, 265
Stickland, D. J., Lloyd, C., Penny, L. R., Gies, D. R., & Bagnuolo, W. G. Jr. 1996, Observatory, 116, 226
Struve, O. 1937, ApJ, 85, 41
Struve, O. 1944, ApJ, 100, 189
Thaller, M. L. 1997, ApJ, 487, 380
Underhill, A. B. 1994, ApJ, 420, 869
Vink, J. S., de Koter, A., & Lamers, H. J. G. L. M. 2000, A&A, 362, 295
Walborn, N. R. 1972, AJ, 77, 312
Walder, R. 1998, Ap&SS, 260, 243
Wolfe, R. H. Jr., Horak, H. G., & Storer, N. W. 1967, in Modern Astrophysics, ed. M. Hack (Gordon & Breach, New York), 251

Mon. Not. R. Astron. Soc. **350,** 809–828 (2004) doi:10.1111/j.1365-2966.2004.07719.x

A phase-resolved *XMM–Newton* campaign on the colliding-wind binary HD 152248

H. Sana,[1⋆] I. R. Stevens,[2] E. Gosset,[1] G. Rauw[1] and J.-M. Vreux[1]
[1]*Institut d'Astrophysique et de Géophysique, Université de Liège, Bat. B5c, Allée du VI Août 17, B-4000 Liège, Belgium*
[2]*School of Physics & Astronomy, University of Birmingham, Edgbaston, Birmingham B15 2TT*

Accepted 2004 February 10. Received 2004 February 6; in original form 2003 October 21

ABSTRACT

We report the first results of an *XMM–Newton* monitoring campaign of the open cluster NGC 6231 in the Sco OB 1 association. This first paper focuses on the massive colliding-wind binary HD 152248, which is the brightest X-ray source of the cluster. The campaign, with a total duration of 180 ks, was split into six separate observations, following the orbital motion of HD 152248. The X-ray flux from this system presents a clear, asymmetric modulation with the phase and ranges from 0.73 to 1.18×10^{-12} erg s^{-1} cm^{-2} in the 0.5–10.0 keV energy band. The maximum of the emission is reached slightly after apastron. The EPIC spectra are quite soft, and peak around 0.8–0.9 keV. We characterize their shape using several combinations of MEKAL models and power-law spectra and we detect significant spectral variability in the 0.5–2.5 keV energy band.

We also perform 2D hydrodynamical simulations using different sets of parameters that closely reproduce the physical and orbital configuration of the HD 152248 system at the time of the six *XMM–Newton* pointings. This allows a direct confrontation of the model predictions with the constraints deduced from the X-ray observations of the system. We show that the observed variation of the flux can be explained by a variation of the X-ray emission from the colliding-wind zone, diluted by the softer X-ray contribution of the two O-type stars of the system. Our simulations also reveal that the interaction region of HD 152248 should be highly unstable, giving rise to shells of dense gas that are separated by low-density regions.

Finally, we perform a search for short-term variability in the light curves of the system and we show that trends are present within several of the 30-ks exposures of our campaign. Further, most of these trends are in good agreement with the orbital motion and provide a direct constraint on the first-order derivative of the flux. In the same context, we also search for long-range correlations in the X-ray data of the system, but we only marginally detect them in the high-energy tail of the signal.

Key words: binaries: close – stars: early-type – stars: individual: HD 152248 – stars: winds, outflows – X-rays: individual: HD 152248 – X-rays: stars.

1 INTRODUCTION

Early-type stars of spectral type O and their evolved descendants, the Wolf–Rayet stars, are among the most luminous and hottest objects of the Milky Way. Characterized by their strong and powerful winds, and their huge mass-loss rates, they have also been known to be X-ray emitters since the late 1970s and the advent of the X-ray observatories equipped with Wolter focusing mirrors. Though with some dispersion, the X-ray emission from single O and early B stars approximately scales with their bolometric luminosity: $L_{\rm X} \sim 10^{-7} L_{\rm bol}$ (Berghöfer et al. 1997) and displays a soft thermal spectrum ($kT \sim 0.2$–1.0 keV). The exact mechanism of this X-ray emission, however, is still not fully understood but it is generally thought that, in the lower layers of the winds, the plasma is heated in shocks that arise from small-scale wind structures that grow out from line-driven wind instabilities (Feldmeier, Puls & Pauldrach 1997; Dessart & Owocki 2003).

Beyond this general scheme, it is now established that massive binaries often display an additional X-ray luminosity compared to single stars of the same spectral types and luminosity classes (Chlebowski & Garmany 1991). The extra X-ray component is usually attributed to emission from a hot plasma that results from the hydrodynamical collision of the winds of the two stars. The

⋆E-mail: sana@astro.ulg.ac.be

standard collision model predicts the interaction region to be limited by two curved shock surfaces between which the gas is heated up to temperatures of a few 10^8 K. From the observational point of view, this phenomenon can manifest itself (i) as a modulation of the X-ray emission due to the variation of the line-of-sight opacity with the orbital motion, (ii) in an eccentric binary, as a variation of the intrinsic emission due to a variation of the separation between the two components, as the densities of the colliding material and, in close binaries, the pre-shock wind velocities depend on the distance to the originating star. Though the X-ray domain is probably the most adequate to study the wind interaction region in close binary systems, the observational signature of the collision is not restricted to high energies. From the ultraviolet (UV) and optical domains, for example, the interaction may be traced in emission lines that are produced by recombination of the cooling gas that escapes the interaction region after the shocks (see, e.g. Sana, Rauw & Gosset 2001; Rauw et al. 2002b).

In addition to the improvements in observational capabilities, another tool for probing the physics of wind–wind collisions has undergone important development in the past 10–15 years. Namely, computational fluid dynamics (CFD) applied to the hydrodynamical problem of wind–wind collision holds out promise of insight into the physics of the phenomenon (Stevens, Blondin & Pollock 1992; Pittard & Stevens 1997; Henley, Stevens & Pittard 2003; De Becker et al. 2004a). For example, from the work of Stevens et al. (1992, SBP92 hereafter), it is obvious that the shocks and the interaction zone properties are strongly dependent on the characteristics of the fluids upstream of the shock. In a first step to classify the shocks, SBP92 introduced a parameter $\chi = t_{\rm cool}/t_{\rm flow}$ that represents the ratio of the characteristic cooling time of the fluid downstream of the shock ($t_{\rm cool}$) to the characteristic flow time ($t_{\rm flow}$). Based on this simple criterion, two forms of extreme behaviour might be distinguished. On the one hand, the gas escapes the interaction region with almost no significant cooling ($\chi \gg 1$) and the phenomenon is mostly adiabatic. On the other hand, whenever $\chi \lesssim 1$, the radiative cooling then plays a crucial role. In the adiabatic case, the escaping flow is expected to be relatively smooth and the region in between the shocks is quite large. When the flow is dominated by radiative cooling, however, the shock region collapses and the steady state is disrupted by Kelvin–Helmholtz and thermal instabilities (SBP92).

However, until recently, very few X-ray observations of O+O colliding-wind binaries (CWBs) had sufficient quality (counts, time resolution, etc.) to allow for a detailed comparison with predictions from CFD calculations. With the advent of the *XMM–Newton* and *Chandra* X-ray observatories, the hot-star community was offered, for the first time, the possibility of acquiring high-quality data that would provide a strong test of the latest models. This should therefore noticeably contribute to improving our understanding of X-ray emission from early-type stars, and more specifically of the winds of these particular objects. However, despite their interest, still very few O+O binaries have been the target of such X-ray monitoring to detect the expected phase-locked behaviour of the emission.

HD 93403 is an O5.5I + O7V binary with an orbital period close to 15.1 d and an eccentricity of 0.234 (Rauw et al. 2000). An *XMM–Newton* campaign revealed a phase-locked behaviour of the X-ray flux that is mostly consistent with a $1/D_{\rm sep}$ dependence, where $D_{\rm sep}$ is the separation between the two stars, as expected for an adiabatic wind–wind interaction (Rauw et al. 2002b).

Similar behaviour is observed in the case of HD 93205, an eccentric system ($e = 0.37$, $P_{\rm orb} = 6.08$ d) consisting of an O3 V primary and an O8 V secondary, in the Tr 16 cluster near η Car. Antokhin et al. (2004) analyse five *XMM–Newton* observations of the region around η Car. They report a clear phase-locked modulation of the flux, with maximum emission occurring at periastron and minimum around apastron.

In the case of the O7 V + O7 V binary HD 159176 ($P_{\rm orb} = 3.367$ d), De Becker et al. (2004a) obtained a single observation with *XMM–Newton*. The system was found to display a rather modest X-ray overluminosity attributed to a wind collision. The authors further find that only part of the wind kinetic power is actually emitted in the X-ray domain as a result of the wind interaction.

In this context, we undertook a phase-resolved *XMM–Newton* campaign targeting the early-type binary HD 152248. This system lies at the centre of the young open cluster NGC 6231 in the core of the Sco OB 1 association. It is a close SB2 eclipsing binary consisting of two almost identical O-type giants with a period close to 5.8 d. The orbital and physical properties of the system were established by Sana et al. (2001, Paper I) from medium- and high-resolution optical spectroscopy. In Paper I, we showed that HD 152248 is an O7.5(f) III + O7(f) III system with the O7.5 III primary being slightly less massive than the secondary. The convention that refers to the less massive component as the primary star historically results from the light curve of the system that displays a deeper minimum during the occultation of the O7.5 star. Table 1 provides the physical and orbital parameters of the system. Though HD 152248 could not be resolved with the *Einstein* observatory due to the limited spatial resolution of the satellite and the crowded nature of the field, HD 152248 was observed by the Röntgen Satellite (*ROSAT*) and clear variations of the flux with the orbital phase could be identified (Corcoran 1996). Paper I also presents strong clues that HD 152248 harbours a colliding-wind phenomenon that could be tracked in the

Table 1. Orbital and physical parameters of the HD 152248 binary. The usual notation has been adopted. T_0 is the time of periastron passage and is adopted as phase $\phi = 0.0$. Most of the quoted values are from Paper I. Whenever this is not the case, reference to the original paper is provided.

$P_{\rm orb}$ (d)	5.816 032	±	0.000 058
e	0.127	±	0.007
ω (°)	84.8	±	4.7
i (°)	67.2[a]		
T_0(HJD −2450 000)	2003.879	±	0.072
γ_1 (km s^{-1})	−30.3	±	1.5
K_1 (km s^{-1})	216.0	±	1.5
$a_1 \sin i$ ($R_\odot$)	24.59	±	0.17
γ_2 (km s^{-1})	−28.7	±	4.3
K_2 (km s^{-1})	213.7	±	5.2
$a_2 \sin i$ ($R_\odot$)	24.35	±	0.62
q ($=M_1/M_2$)	0.990	±	0.023
$M_1 \sin^3 i$ ($M_\odot$)	23.19	±	1.19
$M_2 \sin^3 i$ ($M_\odot$)	23.44	±	0.73
R_1 ($R_\odot$)	15.4	±	3.5
R_2 ($R_\odot$)	14.9	±	3.5
v_∞ (km s^{-1})	2420[b,d]		
log $\dot{M}_1$ ($M_\odot$ yr^{-1})	−5.53		
log $\dot{M}_2$ ($M_\odot$ yr^{-1})	−5.48		
d (pc)	1757	±	370[c]

[a]Mayer et al. (2001). [b]Howarth et al. (1997). [c]Raboud et al. (1997). [d]see Section 4.1.

optical domain through the phase-locked profile variations of the He II λ4686 and H α emissions.

It therefore appeared extremely promising to compare the latest X-ray observations of this object with the predictions of recent hydrodynamical models. Indeed the quality of the HD 152248 *XMM–Newton* data combined with the very good knowledge of the system and the high level of constraints on its physical and geometrical parameters (including the usually rather tricky determination of the inclination) provide the opportunity to:

(i) perform numerical simulations corresponding to a well-constrained configuration, and consequently very representative of the HD 152248 geometry;
(ii) provide predictions that are suitable for a direct confrontation with observational results;
(iii) test the state-of-the-art CWB models;
(iv) gain insight into the physics of wind–wind collisions;
(v) uncover new routes to improve hydrodynamical simulations of close binary systems.

In this paper, we thus discuss the X-ray emission from the HD 152248 system both from the observational point of view and by means of hydrodynamical calculations of wind–wind collisions. The analysis of the other X-ray sources of the field will be addressed in subsequent papers. We further focus on the EPIC observations of the system and on a detailed comparison with corresponding numerical simulations. We do not tackle here the analysis of the RGS data. Indeed, as the field around HD 152248 is relatively crowded, the RGS spectra are contaminated by rather bright neighbouring sources and a simultaneous analysis of the EPIC data of the contaminants as well as specific techniques to estimate the level of the contamination are required. This is beyond the scope of this study and will be deferred to future work.

The present paper is organized as follows. The next section presents a description of the *XMM–Newton* campaign and the data reduction. Section 3 is focused on *XMM–Newton* EPIC spectra analysis and, in Section 4, we describe the performed hydrodynamical simulations. We also provide a detailed comparison between observation and simulation results. The next section (Section 5) investigates the short-term variability of the observed X-ray emission. Finally, Section 6 presents a summary of the main results of this paper as well as the conclusions of the present work.

2 OBSERVATIONS AND DATA REDUCTION

2.1 The *XMM–Newton* observing campaign

The X-ray observational campaign was designed in the framework of the *XMM–Newton* guaranteed time of observation of the *XMM*–OM consortium. It initially consisted of six 30-ks pointings towards the young open cluster NGC 6231 that shelters the HD 152248 binary. These six observations were spread over the 5.816-d period of the system (see Fig. 1) to monitor the expected phase-locked behaviour of the emission. In 2001 September, the *XMM–Newton* satellite successfully performed the six observations within satellite revolutions 319–321, i.e. within a single orbital cycle of HD 152248. Two of the six data sets were unfortunately affected by soft proton flares which effectively reduced the observing time by about one-third. Table 2 gives the journal of the X-ray campaign dedicated to the cluster NGC 6231. All three EPIC instruments were operated in the Full-Frame mode together with the Thick filter to reject optical light. The RGS spectrographs were run in the Standard Spectroscopic mode. Due to the brightness of the objects in the field of view (FOV) of NGC 6231, the Optical Monitor was switched off throughout the campaign.

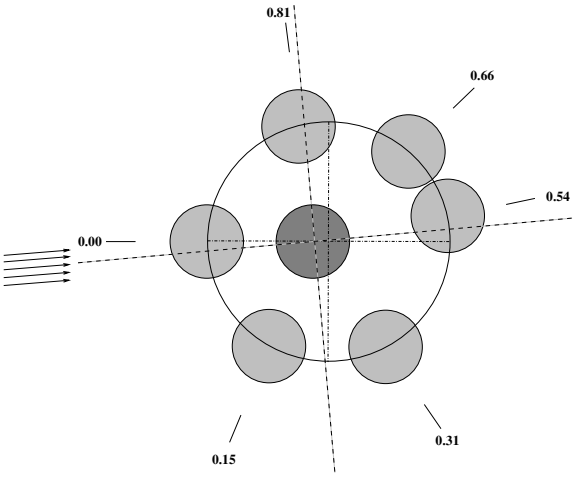

Figure 1. Scale sketch, in the orbital plane of the system, representing the configuration of the HD 152248 binary at the time of the six *XMM–Newton* pointings. The primary star is in dark grey while the secondary is represented in light grey. Arrows at left-hand indicate the projection, on to the orbital plane, of the line of sight of the satellite towards the system.

2.2 *XMM–Newton* EPIC data reduction

The EPIC Observation Data Files (ODFs) were processed using the *XMM* Science Analysis System (SAS) v5.2 implemented on our computers in Liège. We applied the EMPROC and EPPROC pipeline chains respectively to the MOS and pn raw data to generate proper event list files. No indication of pile-up was found in the data. We then only considered events with patterns 0–12 (resp. 0) for MOS (resp. pn) instruments and we applied the filtering criteria XMMEA_EM and XMMEA_EP as recommended by the Science Operation Centre (SOC) technical note XMM-PS-TN-43 v2.0. For each pointing, we rejected periods affected by soft proton flares. For this purpose, we built light curves at energies above 10 keV[1] and discarded high-background observing periods on the basis of an empirically derived threshold. The so-defined good time intervals (GTIs) were used to produce adequate X-ray event lists from which we extracted images and spectra.

For the purpose of spectral analysis, we adopted a circular extraction region centred on HD 152248. However, the NGC 6231 cluster around this object is relatively crowded (see Fig. 2) and we could not adopt an extraction radius larger than about 40 arcsec, which corresponds to a fractional encircled energy of about 85 per cent. This extraction region was used for the three EPIC instruments throughout the data treatment of the observing campaign. For the same reason, we could not adopt an annular region around the source to estimate the background level. After several tests, we selected a circular region located outside the crowded part of the cluster (see Fig. 2). As a complementary test, we also determined the background level using the BLANKSKY files created from deep-field observations. These

[1] Expressed in pulse-invariant (PI) channel numbers and considering that one PI channel approximately corresponds to 1 eV, the adopted criterion is actually PI $>$ 10 000.

Table 2. Journal of the *XMM–Newton* observations of HD 152248. Columns 2 and 3 give the spacecraft revolution number and the observation ID. The mean Julian Day (JD) is reported in Col. 4. The next three columns list the performed exposure times for the EPIC MOS, EPIC pn and RGS instruments. The last column provides the orbital phase of HD 152248 for each *XMM–Newton* observation at mid-exposure, according to the ephemerides given in Table 1. The quoted uncertainties stand for the phase intervals that correspond to the durations of each observation.

Obs. #	Sat. Rev.	Exposure ID	Mean JD JD−2450 000	Performed duration (ks) MOS	pn	RGS	Phase of HD 152248
1	319	0109490101	2158.214	33.3	30.7	33.8	0.54 ± 0.03
2	319	0109490201	2158.931	22.1	20.2	22.4	0.66 ± 0.02
3	320	0109490301	2159.796	34.4	31.8	35.0	0.81 ± 0.03
4	320	0109490401	2160.925	31.4	29.1	31.5	0.00 ± 0.03
5	321	0109490501	2161.774	31.1	28.5	31.6	0.15 ± 0.03
6	321	0109490601	2162.726	32.9	30.3	33.5	0.31 ± 0.03

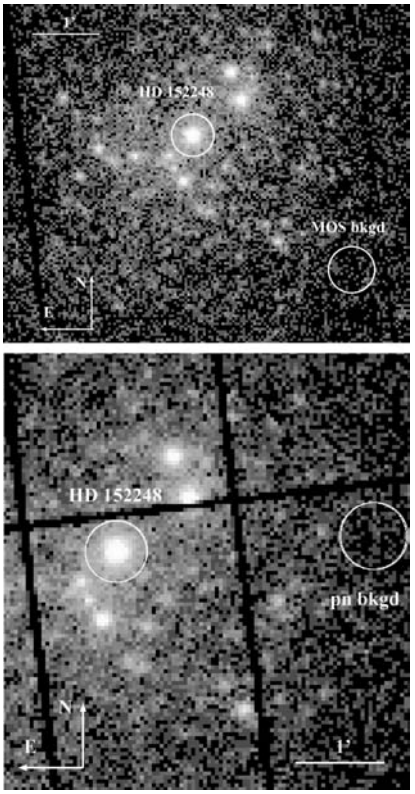

Figure 2. MOS1 (upper panel) and pn (lower panel) images of the central part of the NGC 6231 cluster in the energy band 0.5–2.0 keV. Adopted extraction regions for HD 152248 and for the background are also indicated.

are described in the SOC technical note CAL-TN-0016-1-1, v2.0. However, these observations were performed with the Thin filter whereas our data were obtained with the Thick one. As the background sky level may be dependent on this factor, we tried to account for it: we extracted the Thin background spectra from the BLANKSKY files using a region identical to the extraction area adopted for the HD 152248 binary. We then adjusted an empirical model to the Thin background and generated an equivalent Thick background using the FAKEIT XSPEC command. For this operation, we used the ARF+RMF response file provided by the SOC. This latter approach was limited to the EPIC MOS data sets as a proper corresponding pn BLANKSKY file was unavailable. However, the two background techniques give consistent results, well within the mutual error bars. This supports the a priori idea that, due to the brightness of HD 152248, the background determination is not a critical issue for this object. In the following, we adopt the background as determined from our observations. We generated adequate RMF and ARF files using the RMFGEN and ARFGEN commands. We also used the matrices provided by the SOC. Again no difference was found between the spectra obtained in both ways. Finally, background-corrected spectra were produced using the GRPPHA command of the FTOOLS package.

3 *XMM–NEWTON* EPIC OBSERVATIONS

3.1 Light curves

As a major aim of this project is to monitor the X-ray variability of the HD 152248 system, we first extracted broad-band light curves from the EPIC data. Plots of the count rates against the phase (see Fig. 3) clearly reveal an important enhancement of the global emission by about 60 per cent at the apastron passage. The maximum is

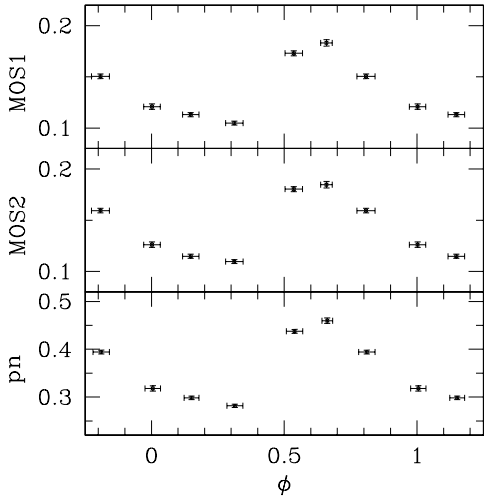

Figure 3. EPIC MOS and pn light curves (in cnt s^{-1}) of the HD 152248 system in the 0.5–10.0 keV energy band. Horizontal bars represent the effective duration of the exposure while vertical bars are the 1σ uncertainties in the count rates.

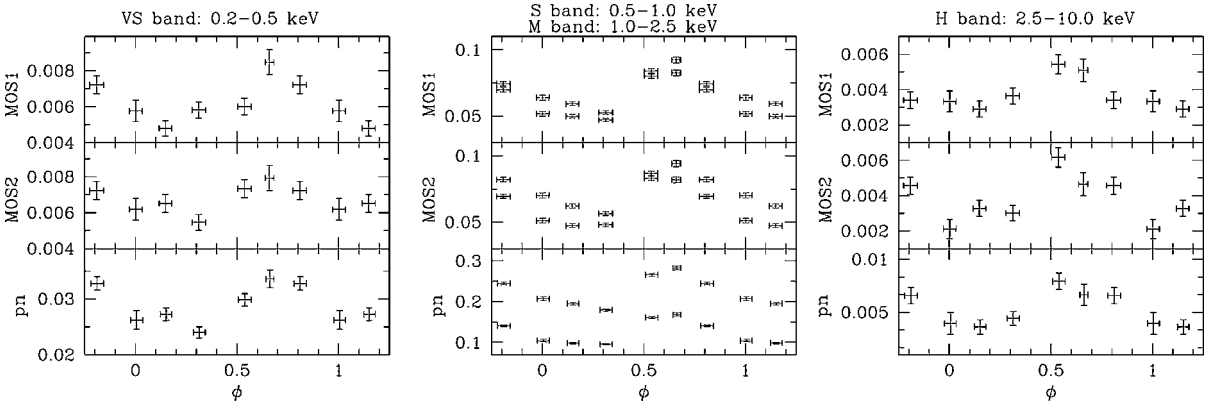

Figure 4. EPIC MOS and pn light curves (in cnt s^{-1}) of the HD 152248 system in different energy bands. Left panel: 0.2–0.5 keV, Middle panel: 0.5–1.0 keV (upper curves) and 1.0–2.5 keV (lower curves). Right panel: 2.5–10.0 keV. Horizontal bars represent the effective duration of the exposure while vertical bars are the 1σ uncertainties in the count rates.

reached at $\phi = 0.66$, slightly after apastron, and is followed by a rapid decrease that slows down after periastron passage. To refine our analysis, we selected four energy bands: very soft (VS) 0.2–0.5 keV; soft (S) 0.5–1.0 keV; medium (M) 1.0–2.5 keV; and hard (H) 2.5–10.0 keV. Fig. 4 presents the background-corrected light curves and reveals that the increase around apastron occurs throughout the different energy ranges. However, we outline that (i) the shape of the curves in the H energy band is more symmetric around apastron, with an increase that is already present at $\phi = 0.31$ and with the maximum at $\phi = 0.54$; and (ii) the relative increase is larger for the harder energy bands. The observed enhancement indeed corresponds, respectively, in the S, M and H bands, to about 50, 70 and over 100 per cent of the minimal flux level. Such an enhancement of the X-ray emission around apastron passage is definitely not compatible with a $1/D_{\rm sep}$ dependence of the flux, as is observed in other colliding-wind binaries (e.g. HD 93403; Rauw et al. 2002b). The corresponding hardness ratios show that the emitted X-ray flux is harder around apastron than around periastron. Finally, we emphasize that the S band accounts for about 50–55 per cent of the total detected counts in the 0.5–10.0 keV band. Spectra of HD 152248 are therefore presumably rather soft.

3.2 Spectra and spectral fits

As described in Section 2.2, the X-ray spectra of HD 152248 were consistently extracted for the three instruments from each of the six data sets and they were binned to reach at least 25 counts per bin.[2] As shown in Fig. 5, the obtained spectra are relatively soft with their maximum located between 0.8 and 0.9 keV. At first sight they reveal little variability but a general increase of the emission level after apastron passage. In order to characterize the X-ray spectral properties of HD 152248, and search for any modification with time, we investigated several spectral models using the XSPEC v.11.0 software. In the following, we limit our study to energies above 0.5 keV. We fixed the interstellar column of absorbing matter to a value of $n_{\rm H,ISM} = 0.311 \times 10^{22}$ cm^{-2}, obtained from the Ryter (1996) formula with $A_{\rm V} = 1.4$ (Baume, Vázquez & Feinstein 1999). The fitted models are a combination of thermal MEKAL models and power-law spectra and we allow a specific circumstellar column of absorbing matter for each component. For each observation, the models were adjusted to the individual EPIC MOS and pn spectra. We performed simultaneous fits to all three EPIC spectra as well. Resulting parameters are reasonably consistent and Table 3 gives the sole results of the EPIC simultaneous fitting.

It became rapidly obvious that a single-temperature (1T) model was insufficient to reproduce the observed spectra ($\chi^2_\nu > 4$). As a second step, we adopted two-component models (Fig. 6). We either combined a 1T MEKAL model with a power law (PL) or we adjusted two-temperature (2T) MEKAL models. Though 1T+PL models clearly give a better agreement with the data (lower χ^2_ν), they fail to reproduce the emission lines in EPIC spectra (see, e.g. the Si XIII multiplet at ∼1.85 keV in Fig. 6). Restraining the fit to the spectral region below 2.5 keV considerably improves the quality of the 2T models with respect to the 1T+PL models. Actually the power-law component helps to reproduce the flux at high energy that is not explained by 2T models in some of the spectra that show enough signal above 3 keV. Adding a PL as a third component to the 2T models again increased the quality of the fit for those particular spectra (Fig. 7). The high-energy tail could also be reproduced by a high-temperature ($kT_3 \sim 4$ keV) MEKAL component. However, except for Obs. 1 ($\phi = 0.54$), a slightly better χ^2 is reached using 3T models for which the three components are soft ($kT < 1$ keV). In this latter case, however, the hard-energy tail might sometimes not be adequately reproduced. Though 2T+PL models provide slightly better fits, it is, however, tricky to choose definitely among all these types of models. If the high-energy tail does actually correspond to a PL component, this latter is then characterized by a photon index $\Gamma \simeq 3.7$. This component has a much steeper slope than the value $\Gamma = 1.5$ that is expected from inverse Compton scattering emission produced by a relativistic population of electrons accelerated in strong shocks (Chen & White 1991). Table 4 provides the observed and dereddened fluxes as deduced from the best-fitting 2T+PL models.

Though the X-ray flux from HD 152248 definitely shows a clear variation by about a factor 1.6 between its lower and higher value, the spectra reveal very little variability at first sight. To detect and to quantify the evolution of the fitted spectral parameters in the

[2] We also performed the complete analysis using spectra binned with at least 10 counts per bin. This does not alter either the qualitative conclusion, nor the quantitative values of the resulting spectral parameters of the fitted models. However, the obtained χ^2_ν were systematically lower than those obtained with 25 counts per bin spectra.

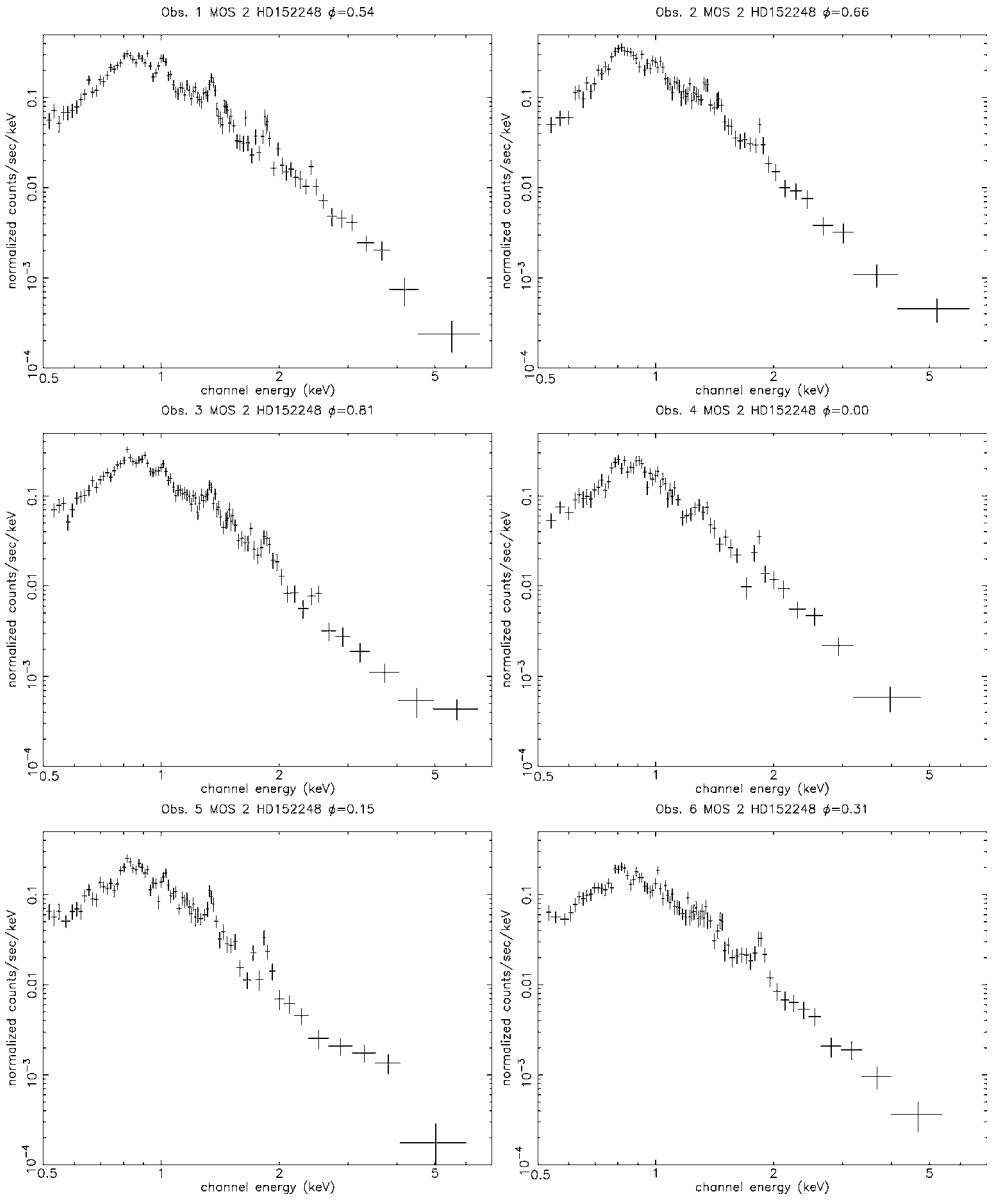

Figure 5. EPIC MOS2 spectra of HD 152248 for the different pointings of the *XMM–Newton* satellite.

different pointings is not straightforward, as different models, and also different solutions of the same model, fit the data with similar quality. This latter aspect can be seen from Table 3 in which the values of the spectral parameters may vary discontinuously from one phase to another. This indeterminacy probably results from too large a number of free parameters and from the lack of physical constraints imposed on the model parameters. We therefore choose to limit the fitted interval to the range 0.5–2.5 keV which is reasonably well reproduced using a 2T MEKAL model. This approach offers the advantage of avoiding the uncertainty about the nature of the hard-energy tail. Though this helps to improve the situation, some of the fits still present local minima of similar depth. Best-fitted values for the column of absorbing matter of the first component ($n_{\rm H,1}$) usually tend to be very small, if not equal to zero. Adopting 2T models where this parameter is neglected ($n_{\rm H,1} = 0\,{\rm cm}^{-2}$) improves slightly but systematically the quality of the different fits. It also solves the degeneracy between the local minima of the fit, resulting in a coherent fit for the six *XMM–Newton* pointings. Results of these fits are presented in Table 5. The fact that the column of absorbing matter of the cold component of the model is ill-constrained could be due to the fact that the fitted parameter $n_{\rm H}$ stands for an equivalent hydrogen column density of neutral gas. The material that is responsible for the local absorption of the X-ray flux in the HD 152248 system, however, is ionized due to the amount of UV photons emitted by the two O-type stars. A neutral absorbing column can then probably not properly reproduce the local circumstellar absorption. The resulting

Table 3. Spectral parameters of HD 152248 as obtained from three-component models simultaneously fitted to the three EPIC spectra. The upper part of this table gives the best-fitting 3T models (WABS$_{\rm ISM}$*(WABS$_1$*MEKAL$_1$+WABS$_2$*MEKAL$_2$+WABS$_3$*MEKAL$_3$)). The lower part reports the best-fitting 2T+PL models (WABS$_{\rm ISM}$*(WABS$_1$*MEKAL$_1$+WABS$_2$*MEKAL$_2$+WABS$_3$*POWER)). $n_{\rm H}$ gives the equivalent hydrogen column of absorbing matter (in 10^{22} cm^{-2}), kT is the temperature of the MEKAL component (in keV) and Γ is the spectral index of the power-law component. The normalization coefficient of the MEKAL component N (in cm^{-5}) equals $(10^{-14}/4\pi d^2)\int n_{\rm e} n_{\rm H}\,{\rm d}V$ where d is the distance to the source (in cm), and $n_{\rm e}$ and $n_{\rm H}$ are the electron and hydrogen number densities (in cm^{-3}), whereas N equals the photon flux at 1 keV for the PL models. The upper and lower numbers quote the 90 per cent confidence intervals.

(a) Three-temperature models

ϕ	$n_{\rm H,1}$	kT_1	N_1 (10^{-4})	$n_{\rm H,2}$	kT_2	N_2 (10^{-4})	$n_{\rm H,3}$	kT_3	N_3 (10^{-4})	χ^2_ν	dof
0.536	<0.03	$0.31^{0.32}_{0.30}$	$9.93^{11.8}_{9.62}$	$0.48^{0.53}_{0.45}$	$0.71^{0.72}_{0.70}$	$11.6^{12.5}_{10.9}$	<1.09	$4.50^{8.28}_{2.63}$	$0.78^{1.26}_{0.56}$	1.68	419
0.659	$0.31^{0.47}_{0.13}$	$0.18^{0.21}_{0.14}$	$74.5^{19.9}_{205.}$	<0.02	$0.53^{0.57}_{0.48}$	$5.30^{6.50}_{4.18}$	$0.81^{0.95}_{0.67}$	$0.77^{0.84}_{0.72}$	$10.7^{12.3}_{9.19}$	1.49	314
0.808	$0.42^{1.62}_{0.38}$	$0.14^{0.15}_{0.14}$	$284.^{307.}_{223.}$	<0.02	$0.41^{0.43}_{0.39}$	$5.57^{5.92}_{5.23}$	$0.85^{0.89}_{0.75}$	$0.80^{0.83}_{0.78}$	$10.6^{11.4}_{10.2}$	1.39	386
0.002	$0.29^{0.42}_{0.16}$	$0.15^{0.17}_{0.14}$	$105.^{285.}_{33.5}$	<0.04	$0.50^{0.53}_{0.46}$	$4.48^{8.67}_{3.96}$	$0.87^{1.07}_{0.72}$	$0.89^{0.98}_{0.79}$	$5.40^{6.94}_{4.53}$	1.34	223
0.148	$0.29^{0.39}_{0.18}$	$0.15^{0.17}_{0.14}$	$104.^{241.}_{53.0}$	<0.03	$0.47^{0.50}_{0.41}$	$4.05^{4.57}_{3.69}$	$0.78^{0.92}_{0.66}$	$0.78^{0.86}_{0.72}$	$5.86^{6.93}_{4.97}$	1.43	318
0.312	$0.38^{0.47}_{0.31}$	$0.15^{0.16}_{0.14}$	$182.^{375.}_{99.2}$	<0.02	$0.48^{0.50}_{0.43}$	$3.59^{3.99}_{3.19}$	$1.08^{1.25}_{0.97}$	$0.83^{0.90}_{0.78}$	$8.08^{9.45}_{6.95}$	1.46	335

(b) Two-temperature + power-law models

ϕ	$n_{\rm H,1}$	kT_1	N_1 (10^{-4})	$n_{\rm H,2}$	kT_2	N_2 (10^{-4})	$n_{\rm H,3}$	Γ	N_3 (10^{-4})	χ^2_ν	dof
0.536	<0.02	$0.33^{0.34}_{0.32}$	$7.73^{9.20}_{7.01}$	$0.33^{0.40}_{0.26}$	$0.71^{0.72}_{0.69}$	$6.59^{7.93}_{5.43}$	<0.03	$3.3^{3.5}_{3.1}$	$2.38^{2.87}_{1.81}$	1.56	419
0.659	<0.15	$0.22^{0.27}_{0.20}$	$5.54^{17.3}_{3.65}$	<0.08	$0.59^{0.61}_{0.58}$	$6.06^{7.29}_{5.17}$	$0.25^{0.63}_{0.08}$	$4.1^{4.6}_{3.8}$	$6.12^{10.1}_{4.18}$	1.38	314
0.808	<0.06	$0.32^{0.33}_{0.30}$	$7.80^{11.5}_{7.09}$	$0.43^{0.52}_{0.35}$	$0.71^{0.73}_{0.67}$	$5.88^{7.12}_{4.78}$	<0.03	$3.7^{3.9}_{3.5}$	$2.57^{3.03}_{2.10}$	1.26	386
0.002	<0.07	$0.20^{0.24}_{0.17}$	$5.26^{12.1}_{4.18}$	<0.04	$0.57^{0.59}_{0.53}$	$4.04^{4.73}_{3.55}$	<0.15	$3.6^{3.8}_{3.3}$	$2.28^{3.01}_{1.79}$	1.27	223
0.148	<0.33	$0.21^{0.26}_{0.14}$	$5.49^{61.4}_{3.78}$	<0.10	$0.57^{0.59}_{0.50}$	$4.01^{5.14}_{3.19}$	<0.09	$3.6^{3.8}_{3.3}$	$2.00^{2.58}_{1.54}$	1.34	318
0.312	<5.33	$0.20^{0.23}_{0.19}$	$5.35^{34.4}_{4.56}$	<0.61	$0.57^{0.58}_{0.54}$	$3.07^{5.04}_{2.80}$	$0.10^{0.35}_{0.00}$	$3.7^{3.7}_{3.4}$	$2.93^{3.78}_{2.57}$	1.32	335

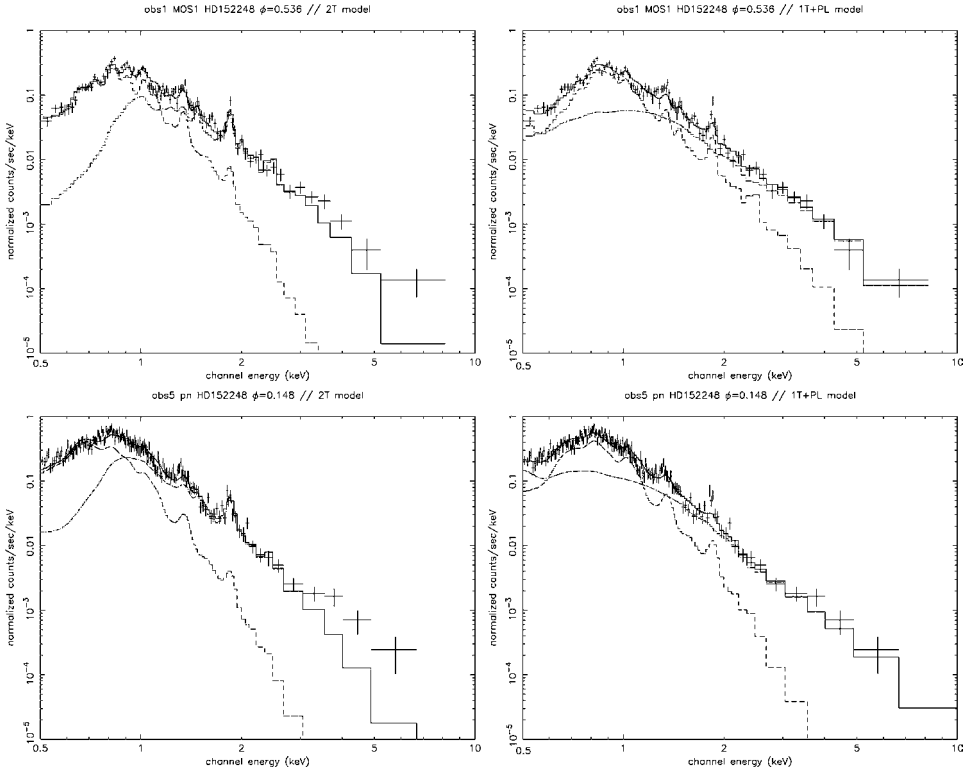

Figure 6. EPIC MOS1 and pn spectra at $\phi = 0.54$ (upper panels) and $\phi = 0.15$ (lower panels). The spectra were fitted either with 2T MEKAL models (left-hand column) or 1T+PL models (right-hand column). The model components are drawn with dashed or dashed-dotted lines while the solid lines represent the resulting models. Note how the PL component compensates the flux above 3 keV, resulting in a fitted model that does not provide a satisfying fit to the emission lines.

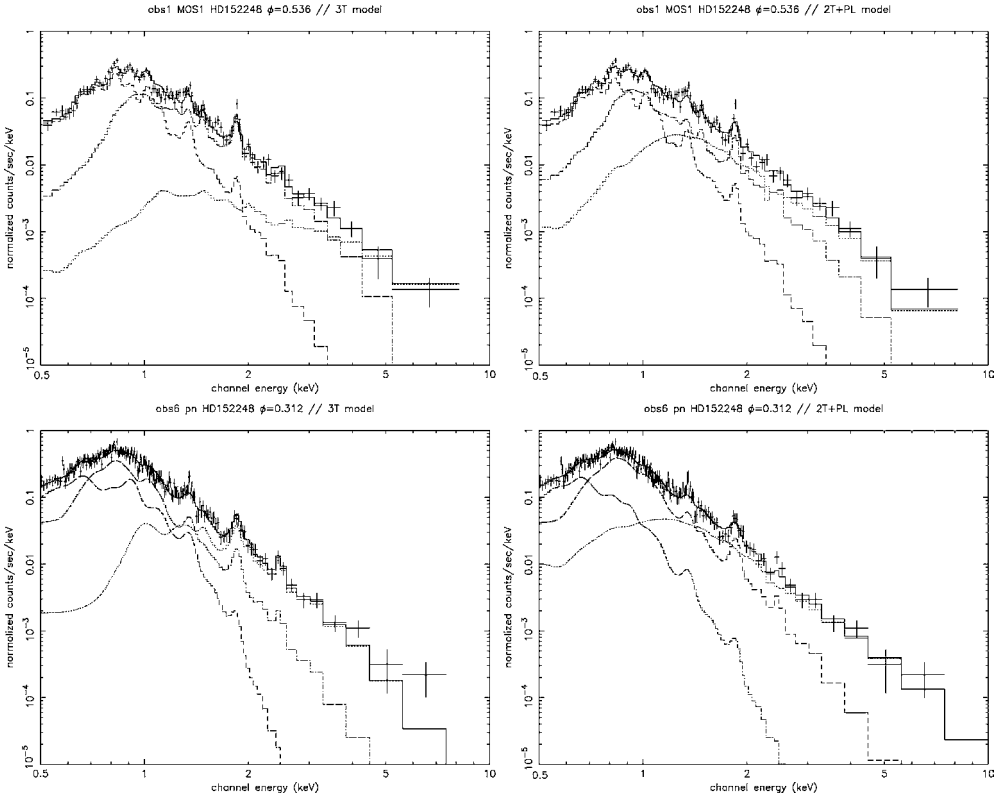

Figure 7. EPIC MOS1 and pn spectra at $\phi = 0.54$ (upper panels) and $\phi = 0.31$ (lower panels). The spectra were fitted either with 3T MEKAL models (left-hand column) or 2T+PL models (right-hand column). The model components are drawn with dashed, dashed-dotted or dotted lines while the solid lines represent the resulting models. Note the improvement compared to two-component models.

Table 4. Observed (Obs.) and dereddened (Dered.) X-ray fluxes of HD 152248 in the energy band 0.5–10.0 keV corresponding to the best-fitted 2T+PL models (see Table 3). The dereddened fluxes were corrected for the ISM absorption only. The corresponding luminosities were computed assuming a distance modulus DM = 11.2.

ϕ	Flux (erg s $^{-1}$ cm^{-2})		Luminosity (erg s $^{-1}$)
	Obs.	Dered.	Dered.
0.536	1.16 10^{-12}	3.11 10^{-12}	1.12 10^{33}
0.659	1.18 10^{-12}	3.33 10^{-12}	1.20 10^{33}
0.808	1.02 10^{-12}	2.96 10^{-12}	1.07 10^{33}
0.002	8.28 10^{-13}	2.58 10^{-12}	9.32 10^{32}
0.148	7.52 10^{-13}	2.36 10^{-12}	8.53 10^{32}
0.312	7.33 10^{-13}	2.23 10^{-12}	8.06 10^{32}

discrepancies will mainly manifest themselves at lower energies where the absorption is the most efficient.

Fig. 8 shows the evolution, with the phase, of the best-fitting values of the 2T MEKAL parameters in the range 0.5–2.5 keV. The temperatures and normalization coefficients of the two components present clear variations. These are in fair agreement with the observed modulations of the broad-band light curves (see Fig. 4). Variations of the equivalent column of absorbing matter of the higher-temperature component are less clear-cut. However, there might exist two increases at phases $\phi = 0.3$ and $\phi = 0.8$ which roughly correspond to the quadrature phases of the HD 152248 system. Though the confidence intervals are quite large, this could indicate an enhancement of the local absorption while the line of sight is almost perpendicular to the binary axis and therefore crosses the radial structure of the interaction region (see Section 4).

3.3 Phase-locked variability

Though the observations clearly show a decrease of the emitted flux from Obs. 1–2 to Obs. 6, our *XMM–Newton* campaign alone can, however, neither establish the phase-locked behaviour of the observed variations, nor whether this behaviour is stable on longer time-scales. Indeed, as seen from Table 2, the *XMM–Newton* observations of HD 152248 extended over about 5 d and therefore did not cover more than a single orbital cycle of the binary. In order to investigate this question, we retrieved previous *ROSAT* Position-Sensitive Proportional Counter (PSPC) observations of the NGC 6231 cluster (Corcoran 1996) and we re-analysed the data adopting the ephemerides from Table 1, that are much better constrained than those Corcoran used at the time. We extracted light curves and spectra in the *ROSAT* energy band. Due to the modest sensitivity and energy coverage of the satellite, the PSPC spectra are well reproduced by a single-temperature component at $kT = 0.24$ keV and no significant spectral variability could be observed in the PSPC data. With the help of the XSPEC software, we then combined the 2T+PL models that best reproduced the *XMM–Newton* observations with

Table 5. Spectral parameters of HD 152248 as obtained from 2T MEKAL models simultaneously fitted to the three EPIC spectra in the range 0.5–2.5 keV. Details of the models are: $\mathrm{WABS_{ISM}}$*($\mathrm{WABS_1}$*$\mathrm{MEKAL_1}$+$\mathrm{WABS_2}$*$\mathrm{MEKAL_2}$) in which the value of $n_{\mathrm{H},1}$ has been fixed to zero (see text). The same notation as in Table 3 has been used.

ϕ	$n_{\mathrm{H},1}$ ($\mathrm{cm^{-2}}$)	kT_1 (keV)	N_1 (10^{-4} $\mathrm{cm^{-5}}$)	$n_{\mathrm{H},2}$ (10^{22} $\mathrm{cm^{-2}}$)	kT_2 (keV)	N_2 (10^{-4} $\mathrm{cm^{-5}}$)	χ^2_ν	dof
0.536	0	$0.310^{0.317}_{0.303}$	$10.12^{10.44}_{9.797}$	$0.54^{0.58}_{0.51}$	$0.712^{0.726}_{0.699}$	$13.61^{14.24}_{12.97}$	1.73	390
0.659	0	$0.304^{0.316}_{0.289}$	$10.62^{11.11}_{10.08}$	$0.48^{0.53}_{0.43}$	$0.694^{0.716}_{0.657}$	$13.57^{15.05}_{12.43}$	1.51	302
0.808	0	$0.293^{0.302}_{0.284}$	$10.51^{10.87}_{10.17}$	$0.59^{0.63}_{0.45}$	$0.694^{0.731}_{0.663}$	$12.56^{13.71}_{11.40}$	1.46	363
0.002	0	$0.257^{0.271}_{0.239}$	$9.057^{9.639}_{8.431}$	$0.41^{0.47}_{0.34}$	$0.623^{0.648}_{0.595}$	$9.303^{10.30}_{8.385}$	1.47	216
0.148	0	$0.256^{0.268}_{0.243}$	$8.734^{9.151}_{8.287}$	$0.42^{0.48}_{0.36}$	$0.621^{0.648}_{0.599}$	$8.769^{9.511}_{8.085}$	1.45	308
0.312	0	$0.272^{0.290}_{0.258}$	$8.127^{8.584}_{7.748}$	$0.60^{0.65}_{0.53}$	$0.656^{0.709}_{0.625}$	$9.183^{10.71}_{8.620}$	1.53	317

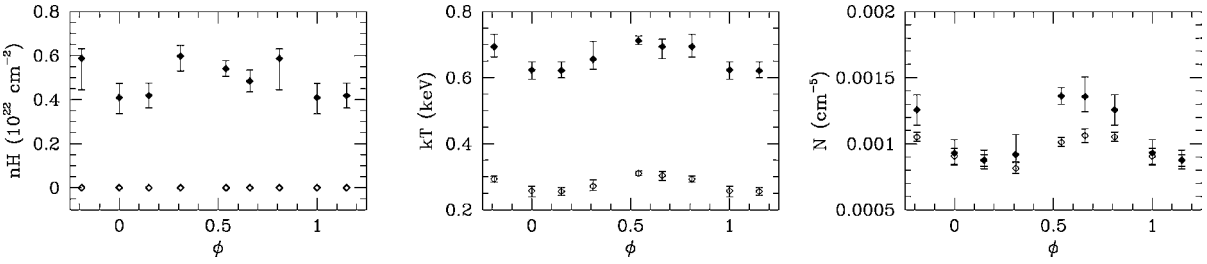

Figure 8. Best-fitting spectral parameters of the 2T MEKAL models ($\mathrm{WABS_{ISM}}$*($\mathrm{WABS_1}$*$\mathrm{MEKAL_1}$+$\mathrm{WABS_2}$*$\mathrm{MEKAL_2}$)) in the range 0.5–2.5 keV plotted versus the phase. Open diamonds refer to the first, low-temperature, component parameters while filled diamonds stand for the second temperature component (see Table 5). Left: equivalent column of neutral hydrogen n_{H}. Centre: temperature kT. Right: normalization coefficient N.

the PSPC response file to estimate the equivalent PSPC count rates of our *XMM–Newton* data. Fig. 9 gives a direct comparison of the equivalent PSPC rates with the actual *ROSAT* observations in the same energy range. In view of the difficulty of accurately comparing the count rates measured from two such different satellites, the current agreement between *XMM–Newton* and *ROSAT* observations is quite reasonable and gives strong support for phase-locked behaviour of the observed variability. It also suggests the relative stability, on longer time-scales, of the dominant phenomenon that produces the observed variation in the light curves of HD 152248. Indeed, the *ROSAT* PSPC observations were obtained between 1991 March and 1993 February, i.e. about 10 years prior to our *XMM–Newton* monitoring campaign.

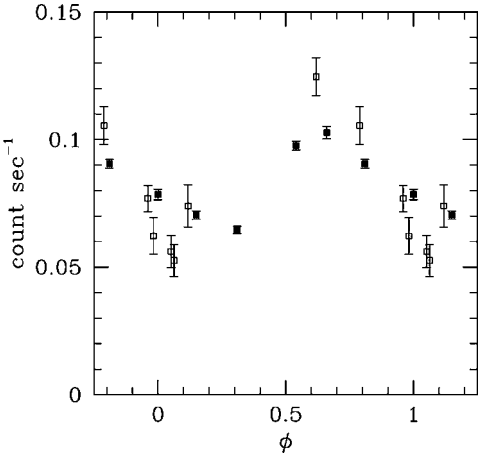

Figure 9. Comparison of observed *ROSAT* PSPC count rates (open symbols) and equivalent *XMM–Newton* count rates (filled symbols) of HD 152248 in the range 0.2–2.4 keV. Phases of the *ROSAT* observations have been computed adopting the ephemerides reported in Table 1.

4 HYDRODYNAMICAL SIMULATIONS

As suggested by Pittard & Stevens (1997), comparisons of X-ray observations of CWBs with detailed hydrodynamic simulations may help to better understand and constrain the physics of the phenomenon. Indeed our *XMM–Newton* campaign reveals precious information about the global flux emitted by the system that a priori results from the X-rays produced in the interaction area as well as within the denser layers of the winds of the two O-type components. However, without further analysis they provide little understanding of the local physics of the interaction region. Indeed, the 'inversion' of the X-ray data to recover the details of the local emission processes as well as the various parameters that affect them is certainly a very ill-posed problem. In this regard, computational fluid dynamics (CFD) has proved to open a new window on the physics of the X-ray emission from the winds themselves (Feldmeier et al. 1997; Dessart & Owocki 2003) and from the wind–wind collision zone (Pittard & Stevens 1997, 2002).

This section is organized as follows. First, we give a general description of the code used to solve the hydrodynamic problem and we describe the performed computational runs (Section 4.1). Section 4.2 presents the model used to estimate the fluxes that are predicted by the hydrodynamical grids. We then report the predictions of the present model (Section 4.3) and we compare them to the *XMM–Newton* observations (Section 4.4). Finally, we conclude by discussing some of the obvious limitations of this work (Section 4.5).

4.1 The hydrodynamical code

In this section, we limit ourselves to a brief overview of the hydrodynamical code. A more complete description is given by SBP92 and references therein. The VH-1 hydrodynamic code aims at the resolution of the set of Euler differential equations for inviscid fluids. It is based on the piecewise parabolic method (Colella & Woodward 1984), a third-order accurate time-marching algorithm that is proved to be shock-capturing and therefore naturally takes care of the shocks. Very briefly, this method is a generalization of the Gudonov scheme that handles each cell interface as a shock-tube problem. In this regard, it builds the global solution of the equations by solving the local behaviour of the fluid (see Anderson 1995, for a general introduction to CFD techniques).

In this work, we adopt the simplified configuration of two spherically symmetric winds of constant velocities. We therefore neglect both the orbital motion and the wind acceleration. We assume that the wind material is fully ionized ($\gamma = 5/3$) and behaves as a perfect gas. Our computations account neither for the viscosity, nor for a possible magnetic field. These approximations result in an axisymmetric geometry around the line of centres and allow us to reduce the hydrodynamical problem to a two-dimensional flow. For that reason, all the hydrodynamical runs presented in this paper are performed on 2D grids. We adopt a typical grid size of 300×600 cells, corresponding to a physical size of $(6 \times 10^{12}) \times 10^{13}$ cm^2, and we let the flow evolve with time from an initial situation where both winds have not yet collided. We let the interaction grow while the time elapses and we follow the process for at least 4000 steps, long enough so that a *steady state* may be reached. However, the HD 152248 CWB harbours a highly radiative collision zone and the post-shock flow is dominated by instabilities. Therefore no 'true' steady state may be reached. Nevertheless the chosen evolution time of the simulations is long enough for the flow to relax from the initial condition dependencies. The time elapsed between two iterations is a free parameter that is adjusted at each step according to numerical stability considerations, but a typical time interval between two steps is about 70–120 s. We performed test runs with higher- as well as lower-resolution grids to check that the observed behaviour of the flow is not, within the tested configurations, resolution-dependent (see, however, Section 4.5). Energy-loss due to radiation is computed after each hydrodynamical iteration and is the only source term accounted for in the adopted version of the code. Reflective boundary conditions were imposed along the line of star centres while we let the gas flow freely out of the grid at the other three boundaries.

As our aim is to compare observations and model predictions, the hydrodynamical runs were performed adopting a system configuration and wind parameters that closely reproduced the configuration of the HD 152248 system at the time of the six *XMM–Newton* observations. Table 6 reports the adopted values for the physical parameters. The separations between the stars were computed using the orbital parameters and ephemerides tabulated in Table 1. Mass losses are deduced from the formula of Vink, de Koter & Lamers (2000) with terminal wind velocities $v_\infty = 2420$ km s^{-1} (Howarth et al. 1997) as quoted in Paper I.[3] HD 152248 being a close binary, the winds collide well before reaching their terminal velocities. As wind acceleration is neglected, we circumvent this problem and adopt the wind velocities reached at the position of the ram pressure equilibrium surface on the binary axis. This is obtained by solving the on-axis ram pressure equilibrium equation:

$$\frac{\dot{M}_1 v_1}{d_1^2} = \frac{\dot{M}_2 v_2}{d_2^2} \quad (1)$$

where d_1 and d_2 are the distances from the equilibrium surface to either star centre; $d_1 + d_2$ is the separation between the centres. Both wind velocities v_1 and v_2 are computed from a standard β-law with $\beta = 0.8$. Equation (1) usually provides three solutions, two of which correspond to unstable equilibria. The third one gives the position of the stable equilibrium that we then use to derive the constant wind velocities reported in Table 6. Though this is a rather crude method, it allows us to bypass the problem of non-terminal wind velocities. This provides a reasonable approximation to the fact that, as the system is rather eccentric, the orbital separation is variable and the winds therefore reach quite different velocities at the shock surfaces for the different orbital phases that we are studying.

Table 6. Effective separation and wind velocities at the ram pressure equilibrium surface on the axis of the system (see text) as a function of the HD 152248 orbital phase ϕ at the time of the six *XMM–Newton* observations. The last column provides the logarithm of the total theoretical X-ray luminosity computed for an idealized planar collision region (see text).

Obs. #	ϕ	Separation		Wind vel. (km s^{-1})		log L_X^{th}
		$R_\odot$	10^{12} cm	O7 III	O7.5 III	erg s^{-1}
1	0.54	59.8	4.16	1240	1330	35.73
2	0.66	57.4	3.98	1180	1280	35.70
3	0.81	51.5	3.58	990	1160	35.58
4	0.00	46.4	3.22	950	1150	35.56
5	0.15	49.9	3.46	910	1160	35.55
6	0.31	56.4	3.92	1160	1260	35.68

The hydrodynamical runs performed adopting these six sets of parameters finally provide the evolution of the values of the gas density, gas pressure and the radial and axial velocity components at each grid cell, from which other hydrodynamical variables (such as temperature, internal energy, entropy, etc.) and radiative properties (see Section 4.2) can be inferred. Fig. 10 gives typical density and temperature maps provided by the simulations of the HD 152248 CWB system.

4.2 X-ray emission

From the results of the simulations described in the previous section, we extracted maps of the hydrodynamical configuration (i.e. density, pressure, temperature, *r*- and *z*-velocity component maps, etc.) once every 10 time-steps. Depending on the initial configuration, it takes about 2100–2600 iterations for the system to relax from the initial conditions, which corresponds to an elapsed time ranging from about 1.5×10^5 to 2.0×10^5 s. Once the dynamical flow has relaxed, we obtained a snapshot approximately every 700–750 s. From the succession of these snapshots, we thus follow the evolution of the hydrodynamical variables with time, and therefore of the wind–wind interaction phenomenon, in the *frozen* configuration of the HD 152248 system that corresponds to one of the six *XMM–Newton* observations. By themselves, the hydrodynamical simulations are very instructive and it is worth monitoring the flow structure of the collision area. However, to compare these simulations with observational results, we need to deduce observable variables from the hydrodynamical grids. For this purpose we then solve the radiative problem corresponding to the different hydrodynamical configurations.

[3] In Paper I, we reported a slightly erroneous value for the terminal velocity of the secondary component. The present value (see Table 1) is therefore corrected accordingly. Fortunately, this does not alter the mass-loss rate computation. Our previous conclusions therefore remain unchanged except that, using the present corrected values, the on-axis wind momentum ratio is now slightly in favour of the secondary star.

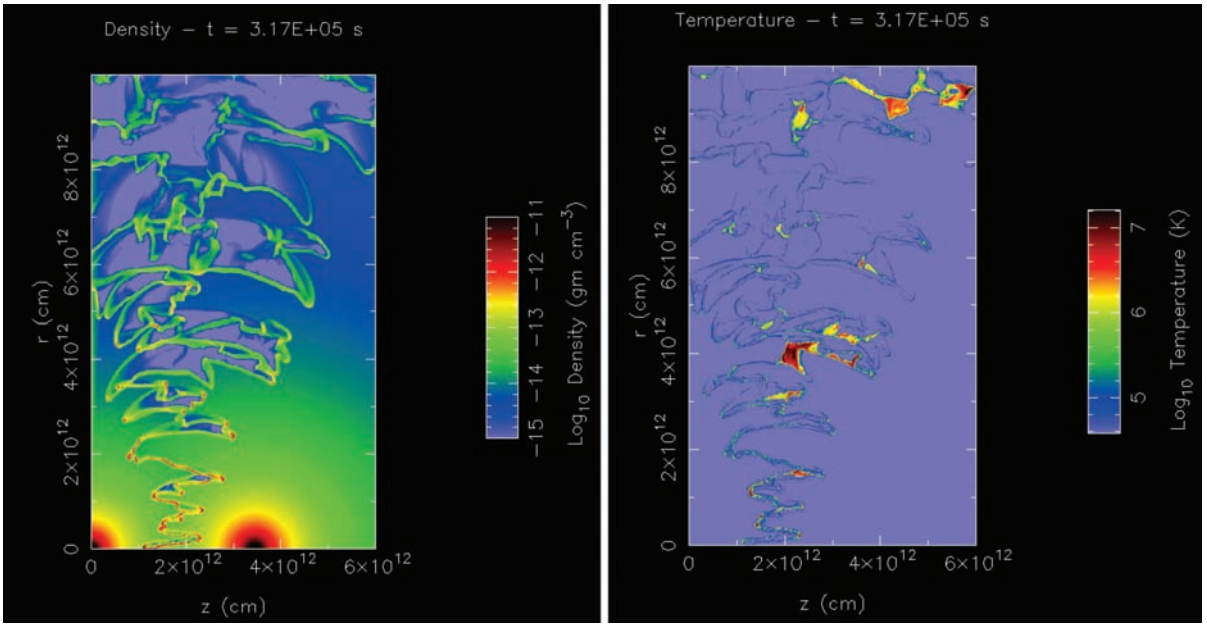

Figure 10. Density (left) and temperature (right) maps as computed from our hydrodynamical simulations. The adopted parameters (see text) reproduce the HD 152248 configuration at phase $\phi = 0.15$.

The X-ray emission from the system was evaluated by summing up the emissivity of each cell, accounting for proper extinction (see details in SBP92). The computation of the column of absorbing matter along the line of sight required a three-dimensional geometry as we have to account both for the inclination of the system and for the variable line of sight of the observer. A 3D grid was thus generated by a rotation of the 2D hydrodynamical grid around the line of centres. The adopted angular resolution of the constructed 3D cells is 2°. The chemical composition of both winds was supposed to be solar. For each cell, we computed the emissivity as a function of the mean cell temperature. The contribution of grid cells with a temperature lower than 10^6 K was neglected. For the emitting cells, the corresponding column of circumstellar absorbing matter towards the observer was computed and we used proper absorbing coefficients to derive the intrinsic attenuated spectra. Cells with temperature higher than 10^9 K were considered not to give a significant contribution to the absorption. Eclipses were accounted for, assuming stellar radii of 15 $R_\odot$. Interstellar absorption was taken into account assuming a column of absorbing matter of $n_{\rm H,ISM} = 0.311 \times 10^{22}$ cm^{-2}. We finally obtained predicted X-ray fluxes and spectra that are suitable for a direct comparison with the *XMM–Newton* observations.

4.3 Predictions of the simulations

As can be seen from Fig. 10, the collision zone turns out to be highly unstable. The wind–wind interaction region appears to be extremely thin and to develop filaments that form smoke-like structures while time elapses. Similar patterns are found for the six configurations in which we performed the simulations. The thinness of the collision zone is expected due to the highly radiative behaviour of the collision ($\chi = 0.02$–0.15). The interaction region appears to be so narrow in our simulations that its inner structure could not be resolved with our mesh size. Increasing the resolution by a factor two does not solve the problem. This failure to resolve the collision area constitutes an obvious limitation of our work that will be discussed in Section 4.5.

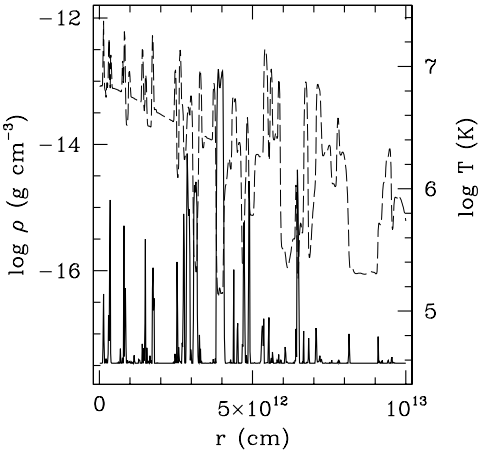

Figure 11. Cross-section at $z = 2\ 10^{12}$ cm in the density (dashed line) and temperature (solid line) maps presented in Fig. 10. Both variables are plotted using logarithmic scales.

The filaments that form the interaction region slowly evolve to produce thin but dense shells that are separated by low-density regions (Fig. 11). In addition to this general pattern, some pockets of high-temperature gas seem to undergo an adiabatic expansion with typical cooling time-scale larger than a couple of weeks. It is probable that some of these pockets might survive till far from the axis but, due to their very low density, it is unlikely that they provide a significant contribution to the total emission from the wind–wind interaction.

To investigate the collision zone luminosity, we computed the expected emission for each of the extracted snapshots. One of the surprising results of these simulations is that the luminosity from the wind collision can vary by a factor of a few on time-scales of a

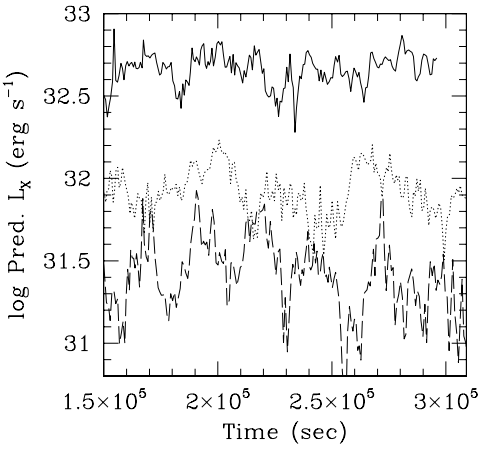

Figure 12. Evolution with the time of the logarithm of the absorbed X-ray luminosity emerging from the interaction region in the range 0.5–10.0 keV, as predicted by the models. Different lines refer to different configurations of the system. Solid line: $\phi = 0.54$. Dashed line: $\phi = 0.00$. Dotted line: $\phi = 0.15$.

couple of hours (see Fig. 12). As the time resolution of our simulations is about 750 s, we also performed a run in a particular configuration, extracting snapshots after each hydrodynamical iteration. This provides a light curve with a time step of about 75 s. The latter almost exactly matches the previous light curve that has a resolution ten times lower. We can therefore reasonably assume that all the temporal information concerning the variability of the luminosity is already contained in the light curves presented in Fig. 12. To estimate the expected luminosity at a given phase of HD 152248, we therefore computed the average and dispersion of the luminosity of the selected snapshots. This is presented in Fig. 13 where the

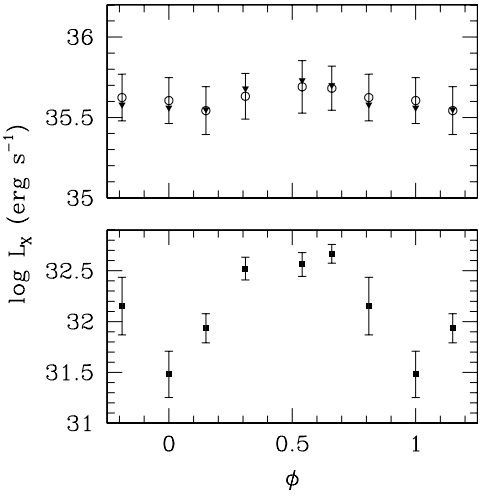

Figure 13. Simulated X-ray luminosity from the collision zone in the range 0.5–10.0 keV as predicted by the models at the different phases of HD 152248. Upper panel: Open circles: Intrinsic emission of the collision zone. Filled triangles: theoretical X-ray luminosities from the collision of two identical winds (see Table 6). Lower panel: Emerging luminosity accounting for (i) eclipses, (ii) local absorption, (iii) ISM absorption. The vertical bars represent the 1σ dispersion on the emerging fluxes.

vertical bars should be considered as the model envelope rather than as 'classical' error bars. The upper panel gives the variation of the intrinsic emission produced in the collision of the winds. The latter displays a variation of about 40 per cent between periastron and apastron. However, accounting for the eclipses and the absorption by the circum- and interstellar medium drastically changes the relative amplitude of the variation. From the lower panel of Fig. 13, it is obvious that the performed hydrodynamical simulations predict a phase-locked variation of the outgoing flux by about one order of magnitude. The maximum of the flux is reached around apastron, while the emitted flux is minimum at periastron.

In order to check the quality of our model, we also computed the theoretical luminosity emitted by the collision of two winds of equal strength that would form an idealized planar interaction region. In this simple model, we further assumed that the kinetic energy of the flow component radial to the shock surface is fully converted into X-rays. For each wind, this is given by (Luo, McCray & Mac Low 1990):

$$L_{X,i}^{th} = \frac{L_{w,i}}{6} = \frac{\dot{M}_i v_i^2}{12} \quad (2)$$

where $L_{w,i} = \frac{1}{2}\dot{M}_i v_i^2$ is the equivalent wind luminosity of star i, characterized by a mass-loss rate $\dot{M}_i$ and a pre-shock velocity v_i. Typical values for the kinetic energy are of the order of 10^{36}–10^{37} erg s^{-1} for single O stars with terminal wind velocities. Values reported in Table 6 for the HD 152248 system result from the sum of the X-ray luminosities from the two shocked winds: $L_X^{th} = L_{X,1}^{th} + L_{X,2}^{th}$. These values are in excellent agreement with the averaged intrinsic luminosities predicted by the hydrodynamical simulations (see Fig. 13) and lend further support to the consistency of our numerical results.

4.4 Comparison with the *XMM–Newton* observations and discussion

The hydrodynamical simulations of wind–wind collisions performed in configurations as close as possible to those of the HD 152248 system at the different phases of interest predict an increase of the emitted fluxes from the interaction region by about one order of magnitude around apastron. Though the observed EPIC light curves indeed reveal an enhancement of the emission at this particular phase, the increase is limited to a factor of about 1.6 and further shows a clear asymmetry between the phase interval, 0.5–1.0 and 0.0–0.5. Due to the 2D nature of the simulations, the predicted light curve is naturally symmetric around apastron and, in this regard, does not render the observations. This might suggest that the observed asymmetry could partly find an explanation in the orbital motion and the resulting deflection of the colliding-wind zone.

Assuming a distance modulus DM = 11.2 (Raboud, Cramer & Bernasconi 1997) as the one we used to infer the bolometric luminosities and subsequent mass-loss rates reported in Paper I and Table 1, the predicted model luminosity clearly underestimates the 'true' luminosity of the system (see Table 4). However, the luminosities computed from the hydrodynamical simulations only account for the emission coming from the wind–wind collision itself. Until now, the intrinsic X-ray emission of the two O stars has indeed been neglected. From Paper I, we know that $\log(L_{bol}^{prim}/L_\odot)$ and $\log(L_{bol}^{sec}/L_\odot)$ equal 5.61 and 5.63, respectively, for the primary and secondary component. Using the relation of Berghöfer et al. (1997) for stars with $L_{bol} > 10^{38}$ erg s^{-1}:

$$\log(L_X) = 1.13 \log(L_{bol}) - 11.89 \quad (3)$$

we find that the intrinsic X-ray luminosities of the components of HD 152248 should be about $\log(L_{\rm X}^{\rm prim}) = 32.39$ and $\log(L_{\rm X}^{\rm sec}) = 32.42$ (erg s^{-1}), respectively. Adding the dereddened flux originating from the interaction region therefore provides a total X-ray luminosity suitable for comparison with the observed values. We outline that the Berghöfer et al. relation is based on observed X-ray emissions from O stars and so includes the effect of intrinsic wind absorption. The resulting luminosities of the components of HD 152248 are, however, not corrected for the additional absorption associated with the colliding-wind region nor for the eclipses that occur in the system. Fig. 14 presents a direct comparison of the dereddened observational X-ray luminosities with the luminosities predicted by the simulations. The latter are obtained by summing up the emission from the interaction region with the expected intrinsic contributions from both stars of the system. Though there is still a difference of about a factor 2 between the observations and the model for some of the pointings, the agreement is now much better. The intrinsic dispersion of the Berghöfer et al. relation and the resulting uncertainty on the intrinsic $L_{\rm X}$ can, by itself, be responsible for such a discrepancy. The amplitude of the variation between apastron and periastron in the model and in the observed light curve differs by about 50 per cent. Given the approximations inherent to our simulations, the agreement can be considered as quite good.

Though the quality of our model is limited (see Section 4.5), these results suggest that the observed phase-locked behaviour of the X-ray flux of HD 152248 may indeed be reasonably explained by a variation of the X-ray emission produced in the interaction region. While the intrinsic colliding-wind flux increases at apastron due to larger pre-shock wind velocities, the major effect is to be attributed to the variation of the absorption properties. The predicted modulation, if diluted by the intrinsic emission of the two components of the system, indeed reasonably reproduced the observed amplitude of the fluxes deduced from the *XMM–Newton* EPIC spectra.

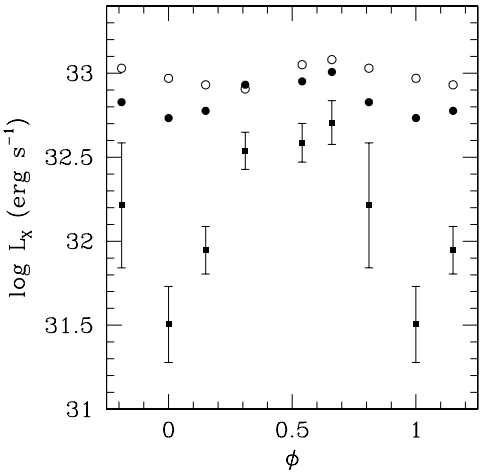

Figure 14. Comparison between the computed dereddened luminosities as resulting from our simulation runs and the observational dereddened luminosities. Filled squares: dereddened luminosities of the interaction region as predicted by the model. The vertical bars have the same meaning as in Fig. 13. Filled circles: total predicted luminosities, i.e. resulting from the predicted emission of the interaction region plus the expected contribution from the two components of HD 152248 (see text). Open circles: observational dereddened luminosities as deduced from the fitting of the *XMM–Newton* EPIC spectra (see Table 4).

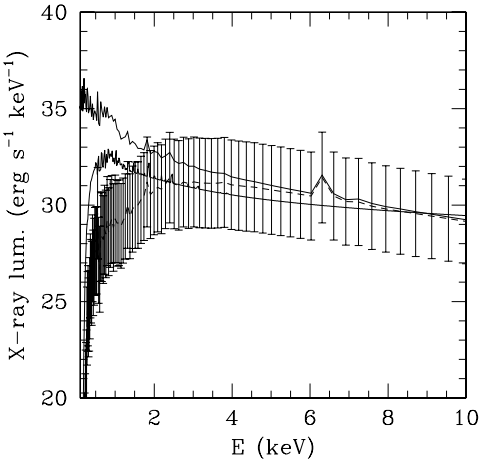

Figure 15. Comparison between the computed spectra as resulting from our simulation runs and the observational best-fitting model for the configuration of the HD 152248 system at $\phi = 0.31$. Plain thin line: intrinsic predicted spectrum. Dashed line: absorbed predicted spectrum. Vertical bars stand for the model envelope due to fluctuations in the predicted spectrum. Thick line: best-fitting 2T+PL model at $\phi = 0.31$ (see Table 3).

The energy distribution of the predicted X-ray emission presents its maximum around 3 keV. Fig. 15 provides a direct comparison with the best-fitting model 2T+PL that reproduces the observational spectral properties of the HD 152248 system. Similar patterns are found in the six configurations. It is seen that the predicted spectra are much harder than the observed ones and, on average, underestimate the flux at low energy (below 2 keV) while the flux is overestimated at higher energies. However, as previously emphasized, the predicted spectra only account for the wind–wind collision emission and the X-ray fluxes from the two stars are neglected. The X-ray emission from individual stars is expected to be relatively soft, with its maximum peak being reached around 1 keV. This can therefore account for the observed discrepancy at low energy. On the other hand, the disagreement of the high-energy tail might come from an excessive strength of the shocks in the model, possibly resulting from too large pre-shock wind velocities being assumed. Wind acceleration might indeed be slowed down by specific effects such as radiative inhibition (Stevens & Pollock 1994). However, the boundaries of the spectra predicted by the hydrodynamical models still overlap the observational best-fitting model at high energy.

Finally, a moderately strong 6.7-keV Fe line is clearly predicted by the simulations while its presence is not so obvious in the data presented until now. The observational model plotted in Fig. 15 is a 2T+PL model in which the PL component accounts for the high-energy tail and could intrinsically not reproduce the Fe XXV line at 6.7 keV. Determining whether this line is present or not in the spectrum of HD 152248 might help to clarify the nature of the hard-energy tail. For this purpose, we combined the EPIC data of the six *XMM–Newton* pointings to increase the signal-to-noise ratio at high energy. We built merged event lists and created combined MOS and pn ARF using the FTOOLS command ADDARF. The merged pn spectrum of HD 152248 is presented in Fig. 16 and corresponds to a total exposure time of around 130 ks. We then adjusted an empirical model (POWER + GAUSS) in the range 4.0–10.0 keV. This

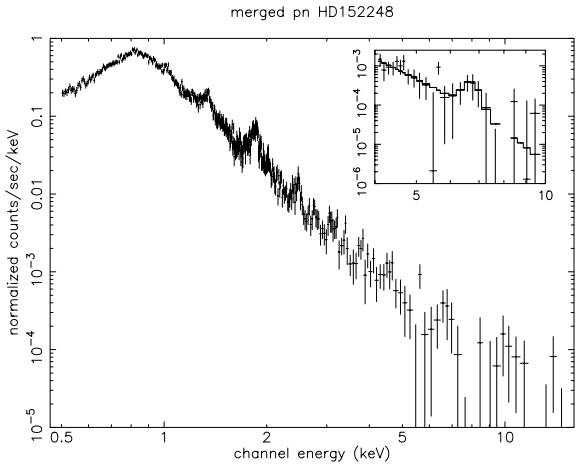

Figure 16. Merged EPIC pn spectrum of the HD 152248 binary. The spectrum is plotted using 17 counts per bin for the sake of clarity. The inset presents the result of a PL + Gaussian model adjusted in the vicinity of the 6.7-keV Fe line (see text).

model is made of a PL component, that reproduces the continuum, and of a Gaussian component

$$\frac{K}{\sqrt{2\pi}\sigma_{\rm G}} \exp\left[-\left(\frac{E-E_{\rm G}}{\sigma_{\rm G}}\right)^2\right]$$

that fits the Fe line (see Fig. 16). Best-fitting values for the Gaussian parameters give $E_{\rm G} = 6.70 \pm 0.14$ keV, $\sigma_{\rm G} = 0.24 \pm 0.14$ keV and $K = 4.3 \pm 2.6\ 10^{-7}$ cnt s^{-1} cm^{-2}, yielding an equivalent width of about 2.3 keV. From the merged data, we can infer that the 6.7-keV Fe line is most probably present in the HD 152248 spectrum and that, therefore, at least part of the high-energy tail has a thermal origin. Finally, we mention that De Becker et al. (2004b) recently noted that non-thermal phenomena could also contribute to the Fe XXV emission at 6.7 keV. The above diagnostic seems, however, to remain quite robust as these authors mentioned that the relative contribution of the non-thermal and thermal processes to the emission is directly proportional to the fraction of the free-electron population that reaches relativistic energies. It is therefore to be expected that a non-thermal contribution to the Fe XXV line remains marginal.

4.5 Limitations of the model

A first obvious limitation of these simulations is the use of constant wind velocities in a geometry for which we definitively know that the collision occurs in the acceleration region of the winds. Adopting the velocities reached at the ram pressure equilibrium surface nevertheless offers the advantage of a quite straightforward solution. This approach probably provides a good approximation close to the line of centres. However, our simulations reveal that the structure of the interaction extends far from the binary axis and the hypothesis of constant wind velocity is definitely too simplistic there. One of the ways to account for the line-driven acceleration would be to include an extra source term that would express a radiative force on the wind material. Due to the wind acceleration, the pre-shock wind velocities away from the axis would definitely be larger and the shocks stronger. Under the influence of an increased ram pressure, and of its component normal to the shock surface, the interaction region could be more confined along the radial direction. However, such an effect is difficult to estimate and, furthermore, would probably be disrupted by the orbital motion in the system.

Moreover, as seen from Fig. 10, our grid is too coarse to resolve the inner structure of the interaction region. Though a thin interaction is expected due to the importance of the radiative cooling, a linear increase of the resolution would, however, not have helped to solve the problem. Indeed we are facing the need to resolve small-scale structures simultaneously around and inside the interaction region, but also to follow the evolution of large-scale structures such as the shells. However, computation time prevents us from increasing both the resolution of the mesh and simultaneously maintaining a good coverage of the collision far from the axis. From the density and temperature conditions of the interaction region inferred from our simulations, we estimate the typical cooling length of the shock-heated plasma to be around 10^7–10^8 cm. On axis, however, extreme values of a few 10^6 cm can be found. Our grid resolution along the axis is 2×10^{10} cm and is definitely not designed to resolve the inner structure of the collision zone. Increasing our resolution by a factor of 10^4 is probably required to overcome that problem. This is unfortunately not realistic with the present hardware resources. In such a situation, the need to adopt non-linear metrics that would increase the resolution towards the central axis of the systems is obvious. An adaptive grid that automatically clusters grid points in the region of high flow-field gradients (see, e.g. Anderson 1995) certainly offers another powerful way to overcome this problem. Due to the instability of the region and the complex structure that results from it, the mesh should also ideally be readjusted after each iteration. Therefore, to adequately perform hydrodynamical simulations of wind–wind collisions in close binary systems, an adaptive mesh algorithm, able to identify the regions where an increased resolution is needed, can provide an adequate description using reasonable time and resources. The implementation of such techniques is not trivial, but remains one of the most promising ways to increase significantly the quality of numerical simulations of close highly radiative CWBs. Nevertheless, as seen from Fig. 13 and Table 6, the macroscopic properties, and more specifically the intrinsic emission, of the interaction region in our simulation are in fair agreement with what is expected from purely theoretical considerations. This lends good support to our results, even if it is clear that a linear grid such as the one we used is certainly not the most optimized approach to the current problem.

Other limitations are related to the 2D nature of the simulations that inherently neglects the orbital motion of the binary. In a system such as HD 152248, the orbital velocities of a few hundred km s^{-1} compete with the pre-shock wind velocities that are only 2–4 times larger. Under such circumstances, the hypothesis of isotropic winds might also break down. Furthermore, in our simulations, the shell structure has radial progression velocity of only 100 km s^{-1}, much slower than the orbital motion. It is therefore very likely that the orbital motion might have a considerable influence on the geometry of the interaction region. One of the most obvious effects is the deflection of the interaction region. Due to the competition between the orbital motion and the radial velocities of the shell structure, we expect the interaction zone to be rather tilted. Another problem inherent to the 2D nature of the simulation is that we let the flow evolve in a *frozen* orbital configuration. Therefore the X-ray emission obtained is definitely independent of the history of the system. The winds, escape flow and orbital motion of the HD 152248 system seem to evolve on similar time-scales. In the real world, one can therefore reasonably expect that these phenomena compete or combine and that the resulting X-ray emission is correlated to the history of the different phenomena. We also note that tidal

distortions of the stars in an eccentric binary may induce an asymmetric behaviour of their interaction with respect to periastron (Moreno & Koenigsberger 1999).

To conclude this section, the physics of the model itself can still be improved, notably by including in the simulations other physical phenomena such as radiative braking (Gayley, Owocki & Cranmer 1997) and/or inhibition (Stevens & Pollock 1994). In the particular case of the binary HD 152248, sudden radiative braking is unlikely to play a major role as both stars of the system are of a broadly similar nature and therefore display similar luminosities and have winds of similar mass-loss rates and velocities. These winds will thus have similar radiative driving efficiencies (that is, similar CAK-type wind constants k and α). All these factors work against sudden radiative braking being important in this system and we can safely ignore it as a major effect for the studied object. A potentially more significant problem is the inhibition effect. Since the stars are quite close, the radiation of both stars will play an important role and could alter the geometry of the wind–wind collision, both in terms of slowing and obliquely deflecting the colliding-wind stream. Finally, the influence of the X-rays emitted by the collision on the winds of the stars and tidal distortions of the star surfaces that probably affect the structure of the winds are further effects that should also be addressed in CWB simulations. Properly accounting for all the above-mentioned physical phenomena within the code is, however, far beyond our present purposes and remains part of long-term developments of CWB hydrodynamical models.

5 SHORT-TERM VARIABILITY

As suggested by the hydrodynamical simulations, the X-ray light curves of HD 152248 might display evidence of short-term variability, i.e. variations on characteristic time-scales ranging from a couple of minutes to a couple of hours and that are therefore much shorter than the orbital period. This section summarizes the results of the different methods implemented to search for short-term variability within the collected *XMM–Newton* data. For each pointing, we applied the following variability tests:

(i) we fitted polynomials of degree n, with $n = 0$, 1 or 2, and we estimated both the quality Q of the fit and the merit F_χ of including an additional term;

(ii) we applied the Kolmogorov–Smirnov test to check the uniformity of the distribution function;

(iii) we used a corrected version of the *probability of variability* test suggested by Preibisch & Zinnecker (2002, see Appendix A);

(iv) finally, we also performed a *detrended fluctuation analysis* (DFA), a method that aims at searching for long-range correlation within time series.

The last three methods were applied on the series formed by photon arrival times. Though it was therefore not possible to account for a background correction, we restrain our analysis to PI events larger than 500 to minimize the impact of background events. Indeed, in the [500–10 000] PI energy band, the background level only accounts for about 2 per cent of the detected counts and should therefore not be a critical issue for these tests.

5.1 Polynomial fits

For each pointing, we first extracted background-corrected light curves from the filtered event list using time bin sizes ranging from 10 to 5000 s in order to investigate the different time-scales. We then fitted polynomials of degree $n = 0$, 1 and 2 to the light curves. In doing so, we only consider here the detection of trends within a single 30-ks observation. The following criteria were used to estimate the adequacy of the fitted model. First, we computed the merit F_χ of adding a supplementary term to a polynomial of degree n. This is given by:

$$F_\chi = \frac{\chi_n^2 - \chi_{n+1}^2}{\chi_{n+1}^2/(N-n-2)} \tag{4}$$

where N is the number of bins in the light curve (see, e.g. Bevington 1969). As the ratio of two χ^2 distributions, the statistic F_χ follows the Snedecor F-distribution with $\nu_1 = 1$ and $\nu_2 = N - n - 2$. We then required that F_χ exceeds a threshold value $F_\chi \geqslant f$, corresponding to the probability $P_F(f;\, \nu_1,\, \nu_2) = 0.95$. Secondly, the model should reasonably fit the light curve, i.e. the quality Q of the fit – which is given by

$$Q\left(\frac{\nu}{2}, \frac{\chi^2}{2}\right) = 1 - P\left(\frac{\nu}{2}, \frac{\chi^2}{2}\right), \tag{5}$$

where P is the incomplete gamma function and ν is the number of degrees of freedom – should yield a reasonable value (see, e.g. Press et al. 1989). Table 7 reports the values of the trends whenever a linear model was the most appropriate to describe the data. Though these values seem to be quite small in terms of count rate, they might account for a 10–20 per cent variation over a 30-ks exposure and are therefore significant. The inclusion of an additional square term turns out to be unnecessary in most of the cases and only marginally improves the quality of the fit in the very few cases where an additional term could have been relevant. These constraints on the values of the first-order derivative of the flux might be useful in testing more evolved models where, for example, the orbital evolution of the system with time is accounted for.

Table 7. Best-fitting values of the slope whenever a linear model is the most appropriate to describe the light curve. The adopted bin size is 1000 sec and the energy ranges approximately from 0.5 to 10 keV (PI ∈ [500–10 000]). All the values are expressed in 10^{-7} cnt s^{-2}.

EPIC	Obs. 1	Obs. 3	Obs. 4	Obs. 5
MOS1	9.6 ± 2.4	-5.4 ± 2.1	-4.5 ± 2.1	4.7 ± 2.2
MOS2	5.3 ± 2.4	-8.4 ± 2.1	-2.5 ± 2.2	7.6 ± 2.2
pn	11.0 ± 4.0	-19.5 ± 3.6	1.2 ± 3.8	11.6 ± 3.7

We note that the slopes observed for the two MOS instruments are in reasonable agreement, whereas the pn best-fitting slope is usually steeper. This might be explained by the different response of the MOS and pn and, indeed, the slopes observed in the S and M energy bands are often significantly different. This is further in agreement with the fact that the global variation of the flux goes along with a modification of the spectral properties of HD 152248 (see Section 3.2). Fig. 17 displays the background-corrected light curve of Fig. 3 on which the detected local trends have been represented. It is clear from this figure that most of the detected trends are indeed in line with expectations from the longer time-scale orbital variation, but for Obs. 5 at $\phi = 0.15$. Indeed the steep trend detected in Obs. 5 count rates seems to initiate a rising of the flux towards apastron, as seen in the model predictions. However, Obs. 6 at $\phi = 0.31$ clearly does not follow that trend and shows a further decrease of the flux. The exact reason of the limitation of the flux increase towards apastron remains at this stage largely unexplained. However, the simulations of the previous section indicate that part of the answer might be linked to the orbital motion of the system.

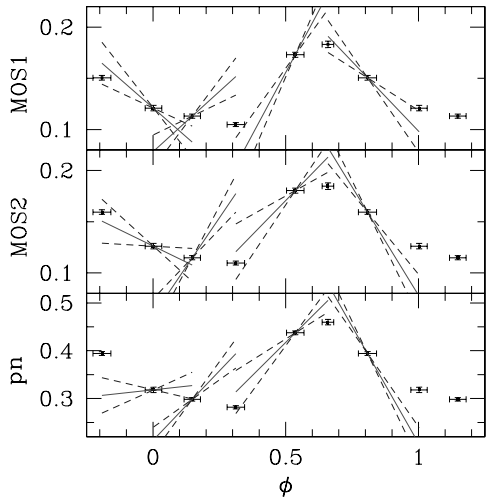

Figure 17. Background-corrected light curve (in cnt s^{-1}) of the HD 152248 system in the range PI ∈ [500–10 000] as presented in Fig. 3. Detected local trends within the different sets of observation (see Table 7) have been overplotted (plain lines). Dashed lines were computed assuming a 1σ difference from the best-fitting slope values. The fitted local trends of Obs. 2 and 6 (at respectively $\phi = 0.66$ and 0.31) are not significantly different from a constant level and are therefore not plotted on this figure.

5.2 Kolmogorov–Smirnov test

To check for constancy, the Kolmogorov–Smirnov test was applied to the series formed by the time difference between two photon arrivals. We accounted for the bad time intervals (BTIs) within a single pointing by subtracting the respective BTI durations from the arrival time of the photons that were chronologically following the BTIs. This is equivalent to assuming that the detector is switched off during the BTIs. Such a procedure might actually favour the rejection of the null hypothesis of a uniform distribution if and only if the underlying distribution is not uniform. In this sense, we might therefore consider that the adopted elimination of the BTIs does not bias the Kolmogorov–Smirnov test.

The Kolmogorov–Smirnov test reveals significant variability (>95 per cent) for those pointings that display trends, as shown in the previous paragraph (Section 5.1). Inspection of the time series further allows us to assert that the Kolmogorov–Smirnov test actually detects the local trends within the relevant pointings, in agreement with the results of the polynomial fits (Section 5.1).

5.3 Probability of variability

We applied a modified version of the Preibisch & Zinnecker (2002) probability of variability (*pov*) test (see Appendix A) to the HD 152248 and background event lists for which the PI events are in the range 500–10 000. One of the advantages of this method is to directly account for the Poissonian distribution of low count-rate observations and it is therefore particularly designed to investigate any background variability. As the values of the adopted binning depend upon the expected number of counts $\langle N \rangle$, we choose $\langle N \rangle$ to range from two to a few thousands in order to investigate different time-scales. Indeed a larger value for $\langle N \rangle$, and hence for the time bin size, favours the detection of long-range variation. On the other hand, small values of $\langle N \rangle$ will tend to enhance small-scale variations that could be diluted or averaged out in the first case. The choice for $\langle N \rangle$ could thus enhance or hide variability within a particular characteristic time-scale. We adopt a confidence level of $pov > 0.99$ for the rejection of the null hypothesis of a uniform distribution of the counts throughout the exposure.

Concerning the HD 152248 binary system, clear-cut positive results occur for Obs. 3 ($\phi = 0.81$) for the EPIC MOS2 and pn instruments while variability in the MOS1 is only marginally detected ($0.90 < pov < 0.99$). The variability seems to occur on time-scales above 1000 s and might be related to the detection of a 'steep' trend in the related data. The background of Obs. 4 ($\phi = 0.00$) is also variable, especially for the EPIC pn instrument though the corresponding HD 152248 event list for Obs. 4 gives a negative result under the *pov* test. Finally marginal variability ($0.90 < pov < 0.99$) is also detected for Obs. 1 ($\phi = 0.54$) and might again be related to the detected trend.

In conclusion, the three methods described in Sections 5.1–5.3 give fully consistent results and prove that local trends, presumably linked to the orbital variability, are clearly present within four out of the six pointings. However, shorter time-scale variability such as that seen in the results of the models described in Section 4 has not been found. We might wonder if the local trends do not alter the properties of the time series and therefore obscure the possible intrinsic variability of the wind–wind collision. One of the recently developed methods that allows us to characterize a signal intrinsic variability regardless of possible local trends is the *detrended fluctuation analysis*. This will be the focus of the next section.

5.4 Detrended fluctuation analysis

The *detrended fluctuation analysis* (DFA) is a method that aims at searching for long-range correlations in noisy signals (Peng et al. 1994, 1995) and is based on the variance analysis of the fluctuations around the local trend. Assuming a self-similar sequence $\{y(i)\}$ of N elements, we divide the series into N_w non-overlapping windows of $k = N/N_\mathrm{w}$ elements. We then compute the mean square fluctuation around the local trend y_l in the considered window:

$$F_k^2(l) = \frac{1}{k} \sum_{i=lk+1}^{(l+1)k} (y(i) - y_l(i))^2 \qquad (6)$$

where y_l is the least-square linear fit function in the window l ($l = 0$, 1, 2, ..., $N_\mathrm{w} - 1$). We then average $F_k^2(l)$ over the N_w windows of size k. Repeating the operation for different k values yields a power-law relation between the root mean square fluctuation function F and the window size k (see, e.g. Kantelhardt et al. 2001):

$$F(k) = \sqrt{\left\langle F_k^2 \right\rangle} \sim k^\alpha \qquad (7)$$

where α is the Hurst exponent, also called the long-range correlation exponent, which is typical of the series behaviour. For a purely random walk (e.g. Brownian motion), $\alpha = \frac{1}{2}$. For $\alpha < \frac{1}{2}$, the signal harbours *antipersistent* correlations while for $\alpha > \frac{1}{2}$, *persistent* correlations are present (see, e.g. Feder 1989). This method has proved its worth in a wide variety of domains such as physiology (Ashkenazy et al. 2001), biophysics (Stanley et al. 1993) and econophysics (Vandewalle & Ausloos 1997). Stanley et al. (1993) also compared its performance to other more widespread techniques (correlation function, power spectrum, rescaled range (R/S) analysis) and report that the performances of the DFA method merely rest on its increased ability to reduce the noise in the determination of the correlation exponent α and to the fact that the method is mostly insensitive to both local and global trends. Some authors

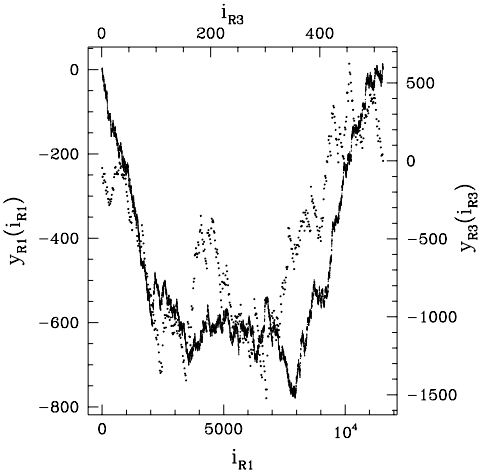

Figure 18. Integrated time series $y(i) = \sum_{j=1}^{i} \left(\Delta t_j - \overline{\Delta t}\right)$ built from the EPIC pn observation at $\phi = 0.81$ in two energy ranges. R1: PI ∈ [500–10 000] (solid line) and R3: PI ∈ 2000–10 000 (dotted line). Left and bottom scales refer to R1 while right and top scales refer to R3.

(e.g. Hu et al. 2001) suggest the use of polynomials of degree n (DFA-n analysis), with n larger than one, instead of the linear local trend y_l. We, however, already showed (Section 5.1) that linear models are the most successful in describing the trend within a single pointing. We therefore limit our DFA analysis to the so-called DFA-1 approach.

As the extension of the method over several decades of the window size k is crucial to estimate the correlation exponent properly, we construct our time series using the time intervals Δt_i that separate the arrivals of two successive photons in the adopted region for HD 152248 (see Section 2.2). The constructed time series are then mapped on to a self-similar process by integration:

$$y(i) = \sum_{j=1}^{i} \left(\Delta t_j - \overline{\Delta t}\right) \tag{8}$$

where $\overline{\Delta t}$ is the average of the time intervals Δt over the whole time series. Fig. 18 shows an example of such a series corresponding to the EPIC pn observation of HD 152248 at $\phi = 0.81$. For a window size ranging approximately from $k = 4$ to $k = N/4$, we then compute the average $F(k)$ values. As can be seen from Fig. 19, this yields a power-law relation $F(k) \sim k^{\alpha}$. We then adjust a linear relation on a log–log scale to estimate the value of the power-law parameter α. Fig. 19 presents a typical evolution of $F(k)$ with the number k of elements in a window and Table 8 gives the values of the Hurst exponent α as obtained from a least-square linear fit. We performed a similar analysis in different energy bands. While, in the range PI ∈ [500–10 000], α takes values around 0.5, and it appears that the self-similarity parameter α tends to reach somewhat higher values when restricting the data set to higher energies. This suggests that persistent long-range correlation might be present in the higher-energy tail of the flux. As indicated by our simulations, this hard tail above 2 keV might find its origin in the interaction region.

Sreenivasan & Meneveau (1986) showed that several facets of turbulence could be related to fractals. In particular, Meneveau & Sreenivasan (1987) reported that energy dissipation in turbulent processes displays long-range correlations with $\alpha < 0.5$. Their best model yields $\alpha \approx 0.45$. The apparent increase of the self-similarity coefficient with the energy in our *XMM–Newton* time series tends

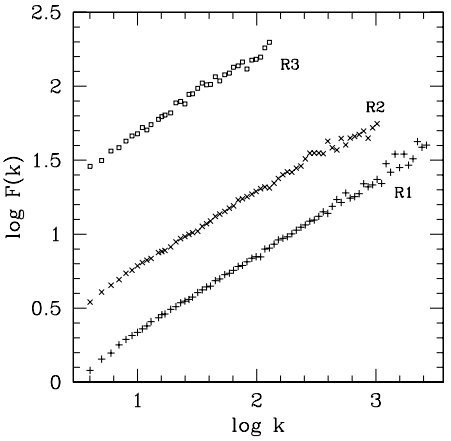

Figure 19. Evolution of $F(k)$ with the window size k plotted on a log–log scale diagram. The data set is built from EPIC pn events at $\phi = 0.81$. Different symbols refer to different energy ranges. Notation R1–R3 has the same meaning as in Fig. 18 and in Table 8.

Table 8. Values of the Hurst exponent (or long-range correlation exponent) α as obtained from a least-square linear fit on a log–log scale for the three EPIC instruments and for different energy ranges. R1: PI ∈ [500–10 000]; R2: PI ∈ [1000–10 000]; R3: PI ∈ [2000–10 000].

Obs. #	PI	MOS1	MOS2	pn
1	R1	0.540 ± 0.006	0.540 ± 0.004	0.512 ± 0.004
	R2	0.532 ± 0.009	0.547 ± 0.006	0.519 ± 0.006
	R3	0.555 ± 0.016	0.535 ± 0.016	0.537 ± 0.008
2	R1	0.496 ± 0.008	0.495 ± 0.009	0.506 ± 0.006
	R2	0.494 ± 0.008	0.510 ± 0.007	0.515 ± 0.006
	R3	0.470 ± 0.021	0.681 ± 0.056	0.674 ± 0.019
3	R1	0.502 ± 0.009	0.500 ± 0.007	0.514 ± 0.007
	R2	0.479 ± 0.014	0.518 ± 0.012	0.503 ± 0.006
	R3	0.563 ± 0.021	0.589 ± 0.025	0.568 ± 0.014
4	R1	0.521 ± 0.009	0.496 ± 0.009	0.546 ± 0.005
	R2	0.496 ± 0.011	0.503 ± 0.012	0.514 ± 0.013
	R3	0.549 ± 0.021	0.583 ± 0.025	0.517 ± 0.022
5	R1	0.553 ± 0.011	0.521 ± 0.009	0.502 ± 0.004
	R2	0.497 ± 0.011	0.495 ± 0.011	0.461 ± 0.007
	R3	0.535 ± 0.021	0.687 ± 0.027	0.496 ± 0.017
6	R1	0.548 ± 0.007	0.477 ± 0.008	0.500 ± 0.005
	R2	0.521 ± 0.013	0.475 ± 0.010	0.508 ± 0.007
	R3	0.547 ± 0.019	0.494 ± 0.022	0.514 ± 0.015

to yield α values slightly larger than 0.5 and might therefore not be directly related to turbulence occurring within the wind–wind interaction region. Though the results of the DFA method presented in this paper are not clear cut, they do, however, constitute an encouragement to apply this kind of technique to a wide variety of astrophysical time series analyses.

5 SUMMARY AND CONCLUSIONS

In this paper, we presented the results of an *XMM–Newton* campaign on the massive CWB binary HD 152248 that was performed as part

of the GT observation time of the OM-consortium. The campaign was split into six separate pointings, for a total duration of 180 ks and the phase resolution of the observations is probably one of the best ever performed on an O+O colliding-wind binary. We showed that the X-ray flux emitted by HD 152248 presents a clear enhancement of about 50 per cent culminating slightly after apastron passage and that the relative amplitude of this increase is also dependent on the considered energy range. Comparison with previous *ROSAT* PSPC data provides good support for phase-locked behaviour of the observed modulations that further remains stable on time-scales of at least 10 yr. The *XMM–Newton* EPIC spectra are relatively soft and present their maximum peak between 0.8 and 0.9 keV. They are reasonably well described by a two-temperature MEKAL model in the range 0.5–2.5 keV. The temperature of the low-energy component is located between 0.26 and 0.31 keV while the second component has a temperature ranging from 0.62 to 0.71 keV (see Table 5). A third component of higher energy is clearly seen in several spectra, though its nature could not be unambiguously established. It could indeed correspond to a power-law tail characterized by a photon index $\Gamma \sim 3.7$ or, though with a slightly lower confidence, to a thermal component with a temperature of a few keV. If the existence of the non-thermal component is indeed confirmed, then its spectral index is much larger than the 1.5 value expected for a strong shock. Indeed, Chen & White (1991) expect such a component to be produced by inverse Compton scattering radiation emitted by a population of relativistic electrons that would have been accelerated in shocks through the first-order Fermi process. This result is similar to what has been observed for other early type O stars such as 9 Sgr and HD 93403 (Rauw et al. 2002a; Rauw et al. 2002b) and the problem definitely deserves further attention. Combining the data from all six pointings, however, reveals that the Fe line at 6.7 keV is most probably present. This implies that at least part of the high-energy tail is likely to have a thermal origin.

We also performed numerical hydrodynamical simulations that closely reproduce the geometrical and orbital configuration of the HD 152248 system at the six phases corresponding to the different *XMM–Newton* pointings. The resulting hydrodynamical maps reveal that the interaction region is highly unstable and, as we progress away from the binary axis, it develops a filamentary structure that alternates thin but dense shells with larger low-density regions. The computed averaged intrinsic flux produced by such a configuration is in excellent agreement with the analytical estimate for the X-ray emission resulting from the interaction region of two identical winds. For a given configuration, the absorbed X-ray luminosity predicted by the model further presents clear variations on time-scales of a couple of hours. Finally, the predicted luminosities show a clear enhancement by about one order of magnitude around apastron. Adding the expected intrinsic contribution of the two O-type stars of the system, the total X-ray luminosity reasonably well reproduces both the observed luminosities and the amplitude and phase of their variation. Due to the 2D nature of the simulations and the fact that we neglect the orbital motion, the predicted light curve is symmetric around apastron and could therefore not properly render the observed decrease of the flux beyond periastron phase. Part of the answer to this problem may probably be found in the deflection of the interaction region due to the orbital motion and subsequent absorption.

The energy distributions predicted by the hydrodynamical simulations are peaked around 3 keV and are therefore much harder than the observed EPIC spectra. The models under-predict the flux at low energy, which is most probably due to the fact that the X-ray contribution of the two O stars has been neglected. Similarly, the hard-energy tail seems to be overestimated in the model prediction, though the observed energy distribution still remains within the boundaries of the model. We are conscious that our simulations rest on several oversimplified hypotheses such as constant wind velocities and *frozen* orbital configurations, whose effects may influence the output of our models. We are, however, confident that our results provide a good approximation to 'reality'. Another limitation that we are facing is the extremely thin interaction region that could not be resolved with the adopted numerical mesh. One significant improvement for hydrodynamical simulations of highly radiative colliding-wind interactions could therefore be the use of adaptive meshes.

Using different techniques, we also investigated the X-ray variability of the source on short time-scales. Linear trends are definitely present in several data sets and helped to constrain the first-order derivative of the flux. We also applied detrended fluctuation analysis, a method that has proved its merits in other domains of science. Its application to the EPIC data suggests that long-range correlations might be present in the series formed by the photon arrival times, especially while restricting the analysis to the hard-energy tail of the data. This, however, does not seem to be directly related to possible turbulent processes occurring within the interaction region. Short-time variability with time-scales of a couple of hours as seen in the predictions of the simulations could not finally be brought into light. On one hand, it is possible that these variations are diluted by the additional flux from the two stars or perturbed by some physical phenomenon not accounted for in the simulations, such as the orbital motion. On the other hand, the predicted variability might be an artefact resulting from the 2D nature of the simulations in which the symmetry might lead to an overestimate of the variability. Again 3D simulations are required to clarify this question.

Finally, we emphasize that this campaign on the massive binary HD 152248 is one of the most complete phase-resolved X-ray studies of a colliding-wind O+O binary ever performed. It further outlines the insight in the physics of the phenomenon that can be gained from a detailed comparison of the observations with hydrodynamical models. It also emphasizes that more detailed hydrodynamical models, possibly using a 3D configuration and accounting for the orbital motion, are needed to achieve a better understanding of the local physics that governs the X-ray emission of colliding-wind binaries. The need to extend this kind of study to a growing number of CWB systems, either O+O or WR+O binaries, is obvious to achieve a detailed understanding both of the hot star winds and of their interaction within CWB systems.

ACKNOWLEDGMENTS

This work was based on observations collected with *XMM–Newton*, an ESA Science Mission with instruments and contributions directly funded by ESA Member States and the USA (NASA). HS is a Research Fellow FNRS (Belgium); EG and GR are Research Associates FNRS (Belgium). The authors wish to thank the referee, Dr Ken Gayley, for careful reading of the manuscript. HS would like to express his thanks to David B. Henley for very helpful discussions on the hydrodynamical simulations. He is also grateful to Dr Nicolas Vandewalle for his assistance in handling the DFA method and to Michaël De Becker and Yaël Nazé for comments on the variability analysis techniques. The Liège team acknowledges support from the Fonds National de la Recherche Scientifique (Belgium) and through the PRODEX XMM–OM and Integral projects. This research is also partly supported by contracts P4/05 and P5/36 'Pôle d'Attraction Interuniversitaire' (Belgian Federal

Science Policy Office). IRS acknowledges funding from PPARC. HS's thanks also go to the Communauté Française de Belgique for travel support ('Bourse de Voyage'), to PPARC for funding a visit to Birmingham and to the University of Liège for taking care of his integration and for *generously* providing heat and electricity.

REFERENCES

Anderson J. D., Jr, 1995, Computational Fluid Dynamics. McGraw-Hill, Singapore
Antokhin I. I., Rauw G., Vreux J.-M., van der Hucht K. A., Brown J., 2004, in preparation
Ashkenazy Y., Ivanov P. Ch., Havlin S., Peng C.-K., Goldberger A. L., Stanley H. E., 2001, Phys. Rev. Lett., 86, 1900
Baume G., Vázquez R. A., Feinstein A., 1999, A&AS, 137, 233
Berghöfer T. W., Schmitt J. H. M. M., Danner R., Cassinelli J. P., 1997, A&A, 322, 167
Bevington P. R., 1969, Data Reduction and Error Analysis for the Physical Sciences. McGraw-Hill, New York, Chap. x
Chen W., White R. L., 1991, ApJ, 366, 512
Chlebowski T., Garmany C. D., 1991, ApJ, 368, 241
Colella P., Woodward P. R., 1984, J. Comput. Phys., 54, 174
Corcoran M. F., 1996, Rev. Mex. A. A. Conf., 5, 54
De Becker M., Rauw G., Pittard J. M., Antokhin I. I., Stevens I. R., Gosset E., Owocki S. P., 2004a, A&A, 416, 221
De Becker M., Rauw G., Blomme R., Waldron W. L., Sana H., Pittard J. M., Eenens P., Stevens I. R. et al., 2004b, A&A, in press
Dessart L., Owocki S. P., 2003, A&A, 406, L1
Feder J., 1989, Fractals. Plenum, New York
Feldmeier A., Puls J., Pauldrach A. W. A., 1997, A&A, 322, 878
Gayley K. G., Owocki S. P., Cranmer S. R., 1997, ApJ, 475, 786
Henley D. B., Stevens I. R., Pittard J. M., 2003, MNRAS, 346, 773
Howarth I. D., Siebert K. W., Hussain G. A. J., Prinja R. K., 1997, MNRAS, 284, 265
Hu K., Ivanov P. C., Chen Z., Carpena P., Stanley H. E., 2001, Phys. Rev. E, 64, 011114
Kantelhardt J. W., Koscielny-Bunde E., Rego H. H. A., Havlin S., Bunde A., 2001, Physica A, 295, 441
Luo D., McCray R., Mac Low M. -M., 1990, ApJ, 362, 267
Mayer P., Harmanec P., Lorenz R., Drechsel H., Eenens P., Corral L. J., Morrell N., 2001, in Vanbeveren D., ed., Astrophysics and Space Science Library (ASSL) 264, The Influence of Binaries on Stellar Population Studies. Kluwer, Dordrecht, p. 567
Meneveau C., Sreenivasan K. R., 1987, Phys. Rev. Lett., 59, 1424
Moreno E., Koenigsberger G., 1999, Rev. Mex. A. A. Conf, 35, 157
Peng C.-K., Buldyrev S. V., Havlin S., Simons M., Stanley H. E., Goldberger A. L., 1994, Phys. Rev. E, 49, 1685
Peng C.-K., Havlin S., Stanley H. E., Goldberger A. L., 1995, Chaos, 5, 82
Pittard J. M., Stevens I. R., 1997, MNRAS, 292, 298
Pittard J. M., Stevens I. R., 2002, A&A, 388, L20
Preibisch T., Zinnecker H., 2002, AJ, 123, 1613
Press W. H., Flannery B. P., Teukolsky S. A., Vetterling W. T., 1989, Numerical Recipes, The Art of Scientific Computing (Fortran Version), Cambridge Univ. Press, Cambridge, Chap. xiv
Raboud D., Cramer N., Bernasconi P. A., 1997, A&A, 325, 167
Rauw G., Sana H., Gosset E., Vreux J.-M., Jehin E., Parmentier G., 2000, A&A, 360, 1003
Rauw G., Blomme R., Waldron W. L. et al., 2002a, A&A, 394, 993
Rauw G., Vreux J.-M., Stevens I. R., Gosset E., Sana H., Jamar C., Mason K. O., 2002b, A&A, 388, 552
Ryter C. E., 1996, Ap&SS, 236, 285
Sana H., Rauw G., Gosset E., 2001, A&A, 370, 121
Sreenivasan K. R., Meneveau C., 1986, J. Fluid Mech., 173, 357
Stanley H. E., Buldyrev S. V., Goldberger A. L., Havlin S., Peng C.-K., Simons M., 1993, Physica A, 200, 4
Stevens I. R., Pollock A. M. T., 1994, MNRAS, 269, 226
Stevens I. R., Blondin J. M., Pollock A. M. T., 1992, ApJ, 386, 265
Vandewalle N., Ausloos M., 1997, Physica A, 246, 454
Vink J. S., de Koter A., Lamers H. J. G. L. M., 2000, A&A, 362, 295

APPENDIX A: THE *PROBABILITY OF VARIABILITY* TEST REVISITED

A1 The Preibisch & Zinnecker probability of variability test

The *probability of variability* (*pov*) test suggested by Preibisch & Zinnecker (2002) basically gives the confidence level – called the *probability of variability* (*pov*) – to reject the null hypothesis of a constant count rate for the considered source. To do so, given the mean count rate, they first estimate the mean time interval Δt during which two photons are expected to be detected by the instrument. Then, using a sliding window, they determine the maximum number of counts $N_{\max}$ received during such a period Δt. Finally, they estimate the probability p that a Poissonian distribution of mean *2* gives at least $N_{\max}$ counts in an interval Δt. This is simply given by the formula :

$$p = 1 - q = 1 - \sum_{k=0}^{N_{\max}-1} \mathrm{e}^{-2} \frac{2^k}{k!}. \quad \text{(A1)}$$

The *probability of variability*, given by $pov = 1 - p$, estimates whether such a high number of counts $N_{\max}$ as observed is rather improbable, which is expressed by a large value of the *pov* and suggests a significant variability in the data.

However, in their method, Preibisch & Zinnecker do not account for the fact that, actually, they are not performing a single experiment (i.e. observing a single interval) but rather $n_{\rm int}$ of them, where the value for $n_{\rm int}$ can be quite large (a few thousand in the case of our present observations). Indeed, repeating a counting experiment increases the probability of observing a number of counts that seems to deviate significantly from the expected values but is still in fair agreement with the statistical theory. Preibisch & Zinnecker also failed to consider a more subtle aspect: the fact that their 'sliding window' approach implies that the observed intervals are overlapping and thus that the counting of photons in the different windows is not independent. In its current form, the *pov* confidence level used by Preibisch & Zinnecker is biased towards larger values (see Table A1 for an example) and clearly favours the rejection of the null hypothesis of non-variability, which might lead to a dramatic increase of type I error occurrences.

Table A1. Example of the dependence of the *pov* estimator with the number of observed intervals $n_{\rm int}$. The first column gives the values of $n_{\rm int}$. The second to fourth columns provide the *pov* confidence level for maximum observed counts $N_{\max}$, respectively, of 5, 6 and 8 as computed following our revised version with $\langle N \rangle = 2$ (see Section A2). Preibisch & Zinnecker would have obtained values corresponding to $n_{\rm int} = 1$ for each case.

$n_{\rm int}$	probability of variability		
	$N_{\max} = 5$	$N_{\max} = 6$	$N_{\max} = 8$
1	0.9473	0.9834	0.9989
2	0.8975	0.9671	0.9978
5	0.7630	0.9197	0.9945
10	0.5822	0.8458	0.9891
20	0.3390	0.7154	0.9783
100	0.0045	0.1882	0.8961
1000	0.0000	0.0000	0.3338

A2 The *pov* revisited

Let Δt be the time period during which the expected number of counts is $\langle N \rangle$ ($\langle N \rangle = 2$ in the original method of Preibisch & Zinnecker). Let $n_{\rm int}$ be the number of non-overlapping intervals of size Δt among which we distributed our data. Finally, let $N_{\rm max}$ be the maximum number of counts found in a single interval among the $n_{\rm int}$ intervals. Therefore, as the $n_{\rm int}$ countings might reasonably be considered as independent, and neglecting the fact that Δt has been estimated from the time series, the probability of finding by chance (i.e. due to statistical fluctuations) at least $N_{\rm max}$ counts in one or more intervals among the $n_{\rm int}$ observed ones is now given by:

$$P = 1 - q^{n_{\rm int}} = 1 - \left(\sum_{k=0}^{N_{\rm max}-1} {\rm e}^{-\langle N \rangle} \frac{\langle N \rangle^k}{k!} \right)^{n_{\rm int}} \quad \text{(A2)}$$

while the *probability of variability*, i.e. the probability that such a high number of counts $N_{\rm max}$ is not due to statistical fluctuations, is given by $pov = 1 - P$. As, of course $q < 1$, P increases with the number of intervals $n_{\rm int}$ and the pov might thus be drastically reduced (see Table A1).

With respect to the present considerations, the pov levels found by Preibisch & Zinnecker (2002) in their section 7 on the variability of the studied objects are therefore overestimated or, at least, could not be compared to a unique rejection criterion as larger values of their pov confidence level are naturally expected for data displaying a larger number of counts. This is especially true concerning the objects with the higher number of counts (N-045-02 and L-312) for which the large values of their pov confidence level found ($pov = 0.95$) are most probably due to statistical fluctuations rather than reflecting any intrinsic variability of the sources.

This paper has been typeset from a TEX/LATEX file prepared by the author.

A&A 405, 1063–1074 (2003)
DOI: 10.1051/0004-6361:20030643

Astronomy & Astrophysics

The massive binary CPD – 41° 7742 I. High-resolution optical spectroscopy⋆

H. Sana[1,⋆⋆], H. Hensberge[2], G. Rauw[1,⋆⋆⋆], and E. Gosset[1,⋆⋆⋆]

[1] Institut d'Astrophysique et de Géophysique, Université de Liège, Allée du 6 Août 17, Bât. B5c, 4000 Liège, Belgium
e-mail: sana@astro.ulg.ac.be
[2] Royal Observatory of Belgium, Ringlaan 3, 1180 Brussels, Belgium
e-mail: Herman.Hensberge@oma.be

Received 28 February 2003 / Accepted 23 April 2003

Abstract. We present the results of a spectroscopic campaign on the early-type binary CPD – 41° 7742. For the first time, we unambiguously detect the secondary's spectral signature and derive an accurate orbital solution for both components of the system. We confirm that the orbit displays a slight but definite eccentricity ($e = 0.027 \pm 0.006$) despite the short period ($P = 2.44070 \pm 0.00043$ days). Previous radial velocity measurements available in the literature constitute together with our new observations a data set that spans more than 30 years. The combined primary orbital solution inferred is in excellent agreement with our solution and gives a period $P = 2.44062 \pm 0.00005$ days. Based on spectroscopic criteria, we derive a spectral and luminosity classification of O9 III + B1 III. However, the luminosities and radii inferred from the membership of NGC 6231 rather indicate lower luminosity classes. We show that the equivalent widths of well isolated primary lines display variations that suggest that CPD – 41° 7742 is an eclipsing binary. This makes CPD – 41° 7742 the second known SB2 eclipsing early-type binary of the NGC 6231 cluster. We approximately constrain the inclination of the system $i_{\rm min} \approx 60°$. This may indicate that the system does not offer enough room for two stars with radii typical of giant stars and lends further support to a less evolved luminosity classification for at least one of the objects.

Key words. stars: individual: CPD – 41° 7742 – stars: binaries: close – stars: binaries: spectroscopic – stars: early-type – stars: fundamental parameters

1. Introduction

Early-type stars of spectral type O and Wolf-Rayet are among the hottest and most luminous objects of our Galaxy and play a crucial role in numerous galactic issues such as the galactic evolution. Massive stars are essential sources of ultraviolet and ionizing radiation. Their influence on their surroundings is also mechanical and results from their huge stellar winds associating large terminal velocities with enormous mass-loss rates. They can even trigger giant star formation events (Maeder & Meynet 1995; Deharveng et al. 2003). However, despite their importance, our understanding of these objects is still far from satisfactory and more accurate observational data are needed to constrain the theoretical models. Indeed parameters as essential as the mass and the mass-loss rates are still poorly constrained, not to mention the rotation (Maeder & Meynet 2000). The studies of binaries in open stellar clusters is of special relevance for our understanding of star formation processes, dynamical interaction in clusters and stellar evolution in general (Gimenez 1996). In this context, we undertook a multiwavelength observing campaign on several stars of the NGC 6231 cluster in the core of the Sco OB 1 association. The project combines optical and XMM X-ray data and aims at providing a homogeneous set of observational constraints on the physical parameters of a sample of O-type stars. This first paper about CPD – 41° 7742 is devoted to the spectroscopic analysis of the system. One aim is to obtain contemporaneous accurate ephemerides that are needed to correctly interpret the X-ray data. Another is to derive reliable physical and orbital parameters of the system.

CPD – 41° 7742 ($V = 8.32$, Baume et al. 1999) is an early-type spectroscopic binary that belongs to the young open cluster NGC 6231. Commonly used alternative names are CD–41°11042, Braes 945 (Braes 1967), Seggewiss 224 (alternatively S 224, Seggewiss 1968), V1034 Sco (Kukarkin et al. 1971), Sung 505 (alternatively SBL 505, Sung et al. 1998) and Baume 11 (alternatively BVF 11, Baume et al. 1999). This object was first suspected to be a binary by Struve (1944) on the

Send offprint requests to: H. Sana, e-mail: sana@astro.ulg.ac.be
⋆ Based on observations collected at the European Southern Observatory (La Silla, Chile).
⋆⋆ Research Fellow FNRS (Belgium).
⋆⋆⋆ Research Associate FNRS (Belgium).

Table 1. Journal of the spectroscopic observations of CPD – 41° 7742. Column 1 reports the heliocentric Julian Date at mid-exposure. The next three columns give the phases as calculated from the He I λ4471 orbital solution as well as the radial velocities (RVs) of the primary (Col. 3) and secondary (Col. 4) as measured from the Doppler shifts of the He I λ4471 line. A similar structure is adopted for the last three columns. $\phi_{\overline{\text{He I}}}$ reports the phases computed from the average He I solution (see Sect. 3.3). $\overline{RV_1 - \gamma_{\lambda,1}}$ and $\overline{RV_2 - \gamma_{\lambda,2}}$ present the values obtained by averaging the RVs of He I lines measured on the FEROS spectra. Prior to averaging, the RVs have been corrected for the systemic velocities of the individual lines (see Table 3). The phase $\phi = 0.0$ corresponds to the time of periastron passage as given in the corresponding orbital solutions of Table 4.

Hel. Jul. Date (−2 450 000)	$\phi_{\text{He I }\lambda4471}$	RV_1 (km s^{-1})	RV_2 (km s^{-1})	$\phi_{\overline{\text{He I}}}$	$\overline{RV_1 - \gamma_{\lambda,1}}$ (km s^{-1})	$\overline{RV_2 - \gamma_{\lambda,2}}$ (km s^{-1})
995.723	0.549	119.4	−271.8			
996.654	0.931	−82.6	−82.6			
997.669	0.347	−79.7	26.7			
998.657	0.751	84.4	−226.8			
999.664	0.164	−185.9	231.2			
1000.642	0.565	126.4	−278.2			
1299.843	0.154	−188.4	283.6	0.129	−163.9	289.1
1300.841	0.563	131.5	−275.4	0.538	155.0	−273.9
1301.847	0.975	−137.3	173.4	0.950	−108.9	198.5
1302.847	0.385	5.4	−113.6	0.360	23.8	−40.5
1304.841	0.202	−163.5	218.1	0.177	−137.1	255.8
1327.863	0.635	142.8	−308.4	0.609	167.6	−296.9
1668.928	0.377	3.4	−101.5	0.350	22.3	−37.3
1669.791	0.730	99.6	−257.2	0.703	125.1	−230.7
1669.923	0.784	64.3	−187.3	0.758	79.8	−154.4
1670.787	0.138	−192.3	281.0	0.112	−169.3	293.3
1670.901	0.185	−173.3	221.7	0.158	−152.1	265.4
1671.800	0.553	123.5	−274.9	0.527	147.6	−268.6
1671.926	0.605	142.0	−295.9	0.578	162.4	−295.1
1672.782	0.956	−122.7	164.5	0.929	−92.7	185.8
1672.925	0.014	−167.1	206.9	0.988	−138.9	244.1
2037.792	0.509	102.1	−254.7	0.480	128.3	−232.9
2037.887	0.547	123.1	−278.6	0.519	146.2	−272.6
2039.783	0.324	−65.5	n.	0.296	−56.3	54.4
2039.907	0.375	−23.2	−23.2	0.347	2.6	13.1
2040.788	0.736	100.3	−243.5	0.708	121.3	−220.3
2040.908	0.785	71.7	−146.5	0.757	87.9	−138.7
2337.860	0.453	69.9	−194.6	0.424	91.6	−167.8
2338.794	0.836	21.6	−114.2	0.806	49.2	−72.2
2381.723	0.425	46.7	−116.8	0.395	64.1	−103.4
2382.741	0.842	15.6	−104.2	0.812	40.9	−64.9
2383.738	0.250	−131.4	180.2	0.221	−105.6	204.9

basis of only two spectra. A few decades later, from a set of sixteen observations, Hill et al. (1974, HCB74 hereafter) determined a period of $P = 2.446 \pm 0.005$ days and a low eccentricity of $e = 0.07 \pm 0.04$. Only the primary component was detected and the semi-amplitude of the radial velocity curve was found to be $K_1 = 162.5 \pm 8.2\,\mathrm{km\,s^{-1}}$. These authors also reported a photometric variability of $\Delta V = 0.45$ mag. Levato & Malaroda (1980) assigned a spectral type of O9 IV and, with four more observations, Levato & Morrell (1983, hereafter LM83) determined $P = 2.430155 \pm 0.00001$ days, $e = 0.08 \pm 0.03$, $K_1 = 160 \pm 5\,\mathrm{km\,s^{-1}}$, $v \sin i = 130\,\mathrm{km\,s^{-1}}$. In 1990, Perry et al. (1990, PHYB90 hereafter) published three more radial velocity (RV) points obtained in the late 1960s, but no new orbital solution. Finally, García & Mermilliod (2001, GM01 hereafter) recently claimed to have detected the secondary spectral signature on three out of their eight new medium resolution spectra. Combining these new data with the previous measurements reported in the literature, they proposed a first SB2 solution for the system. They adopted a longer period $P = 2.453087 \pm 0.000012$ days and, contrasting with previous papers, derived a quite large eccentricity ($e = 0.205$) for such a short period. However, we will show in Sect. 4 that this option

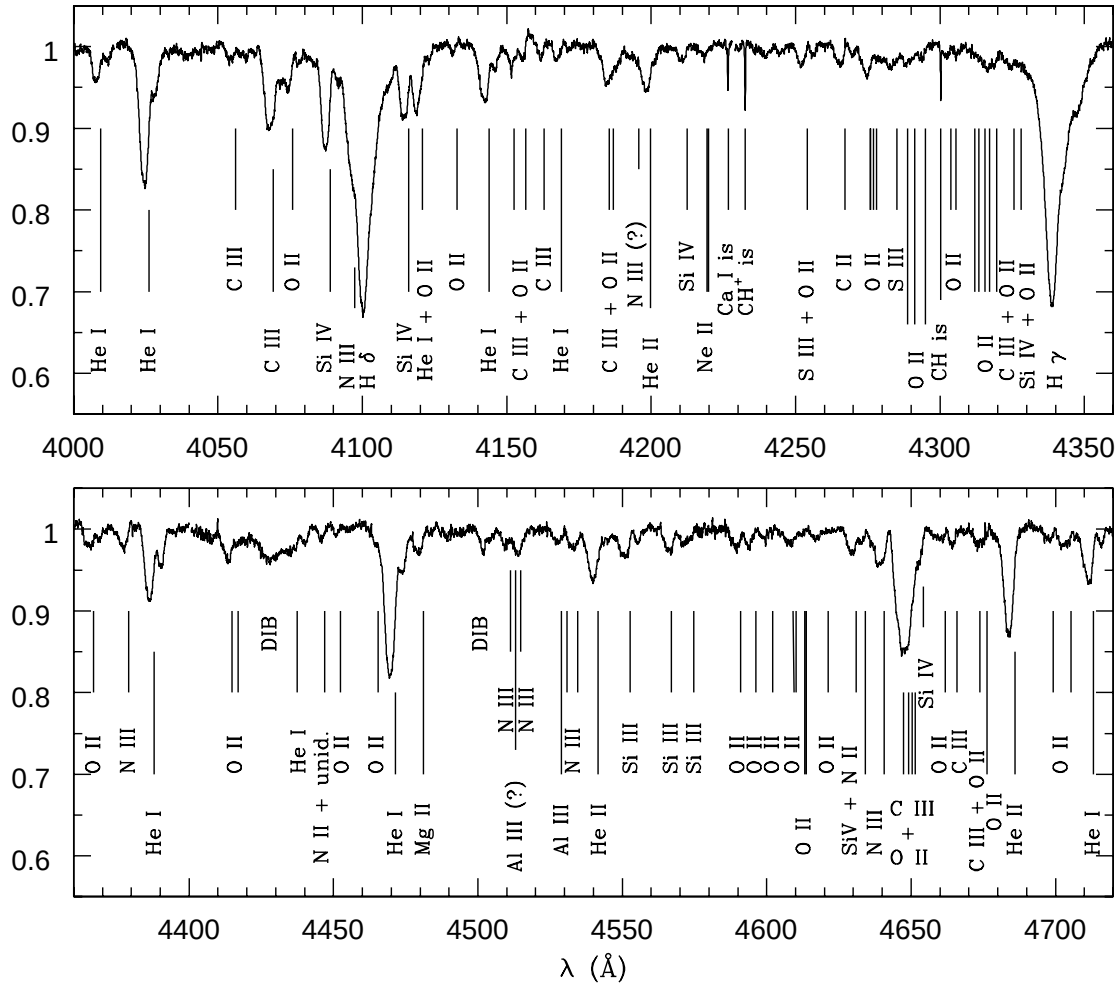

Fig. 1. Blue spectrum of CPD – 41° 7742 as obtained on HJD = 2 452 383.738 ($\phi_{\overline{\text{He I}}} = 0.221$). The identification of the main lines has been indicated. He I lines display a clear SB2 signature, with the blue-shifted primary and the red-shifted secondary components. The identification ticks refer to the rest wavelengths.

is erroneous and we will provide an alternative global orbital solution for the system.

This paper is organized as follows. In the next section, we first describe both our data set and the reduction processes that we applied. Section 3 is devoted to the determination of the orbital motion of the system. In Sect. 4, we combine our data with previous observations reported in the literature. We pay particular attention to the discrepancies between GM01 results and ours. In Sect. 5, we discuss the physical parameters and the evolutionary status of the binary components. The last section summarizes our main conclusions.

2. Observations and data reduction

2.1. Observations

The present work is based on 32 high-resolution spectra of CPD – 41° 7742 obtained at the European Southern Observatory (ESO, La Silla, Chile). These were acquired during 25 nights distributed over 7 runs between July 1998 and April 2002. The journal of the observations is presented in Table 1.

In July 1998, six spectra in the range 4460–4480 Å (He I λ4471) were obtained at the ESO 1.4 m Coudé Auxiliary Telescope (CAT), with the Coudé Echelle Spectrograph (CES) equipped with the Very Long Camera (VLC). The detector used was ESO CCD#38, a Loral 2688 × 512 pixel CCD with a pixel size of 15 μm × 15 μm. The slit width was chosen to achieve a nominal resolving power of 70 000–80 000. The effective resolving power as derived from the $FWHM$ of the lines of the ThAr calibration exposures is 65 000–75 000. Typical exposure times were 40 min and the average S/N ratio is about 100.

Between April 1999 and April 2002, we collected 26 spectra covering the whole optical range (3800–9200 Å) using the FEROS echelle spectrograph mounted at the ESO 1.5 m telescope at La Silla. The detector was a 2k×4k EEV CCD with

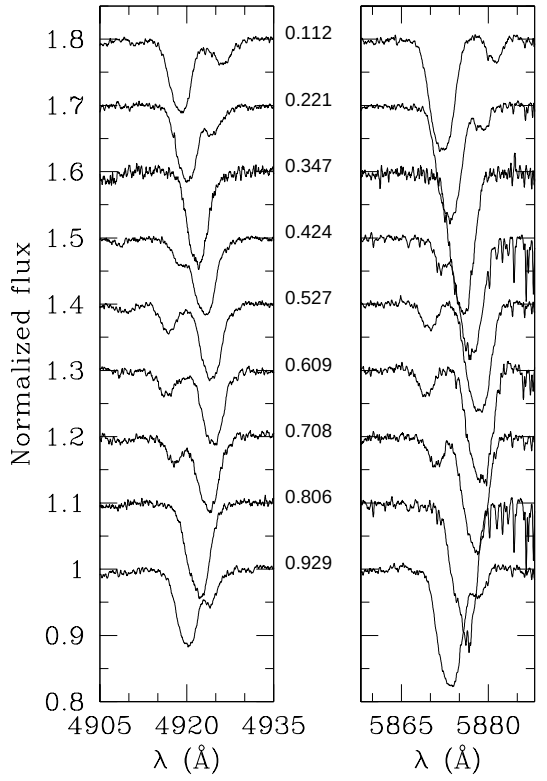

Fig. 2. He I λ4922 (left) and He I λ5875 (right) lines at various phases. The numbers in between the two panels give the phases $\phi_{\overline{\text{He I}}}$ at mid-exposure. The spectra were shifted along the vertical axis for the sake of clarity. The secondary spectral signature is clearly identified on most spectra but the blended ones.

a pixel size of 15 μm × 15 μm. The spectral resolving power of FEROS is 48 000. Typical exposure times were 30 min, resulting in typical S/N of about 150 and 180 at 4200 Å and 6000 Å respectively. During the two runs of May 2000 and 2001, we obtained two spectra per night, separated by a few hours (typically 3 to 4 h), in order to solve the period aliasing that a preliminary analysis of the data had revealed.

2.2. Data reduction

CES data were reduced in a standard way using the MIDAS package supported by ESO. The spectra were then rectified by means of an instrumental response curve built from the observations, obtained under similar conditions, of a metal-poor "reference" star (HD 203608: F6V). Finally, the spectra were normalized by fitting a low order polynomial (a straight line or a parabola) to the continuum.

FEROS data were reduced using the FEROS context working under MIDAS environment. We found that the standard pipe-line reduction failed to provide satisfactory results (Hensberge 2002). Based on the expertise of one of the authors (HH), we locally implemented an improved reduction pipe-line that allows a more accurate wavelength calibration (with rms residuals down to 3.0×10^{-3} Å), a better correction for the diffused background light and hence an improved determination of the blaze functions that, in the basic reduction case, displayed "oscillations" due to the flat-field calibration lamps. These oscillations, not present in the stellar spectra, were therefore a major source of uncertainty in the determination of the continuum. Finally, artefacts due to the merging of the echelle orders of the FEROS data are known to appear in a number of order reconnections. This problem, added to the complexity of the global shape of the spectrograph response curve, renders the normalization step a non-trivial process. For these reasons, we performed the normalization both on the merged spectra and on the individual orders separately, and we carefully compared both resulting normalized spectra to avoid any anomaly due to the automatic FEROS merging. In some cases, we also used a reference star with few metallic lines (either HD 152248 or 9 Sgr), observed and reduced under similar conditions, to build an instrumental response curve. This allowed us to perform an additional check of the normalization process.

Table 2. Period search carried out with the Lafler & Kinman (L&K) and Fourier (HMM, see text) techniques and based on the *RV*s associated with the He I λ4471 (upper part of the table) and O III λ5592 (lower part) lines. The last column gives the value either of the normalized L&K statistic or of the Fourier semi-amplitude at the given optimum period.

Data set	Method	Period (d)	Θ_1 / $A_{\max}$
He I λ4471: RV_1	L&K	2.44084	0.036
RV_2		2.44067	0.060
RV_1–RV_2		2.44067	0.055
RV_1	HMM	2.44065	164
RV_2		2.44076	291
RV_1–RV_2		2.44075	460
O III λ5592: RV_1	L&K	2.44052	0.084
RV_1	HMM	2.44064	162

3. CPD – 41° 7742 spectrum and orbital solution

3.1. The spectrum of CPD – 41° 7742

The spectrum of CPD – 41° 7742 (see Fig. 1) is clearly dominated by the Balmer lines and by the He I and He II absorption lines. Numerous metallic lines (C, N, O, Si and Mg ions) can also be identified. The Balmer lines and all the He I lines in the observed wavelength range present a clear SB2 signature with the primary lines being several times stronger than the associated secondary lines (see e.g. Fig. 2). No emission line is detected in the CPD – 41° 7742 spectrum.

We first measured the line positions, and thus the Doppler shifts, and we computed the radial velocities (*RV*s) associated with the main lines of the spectra. We then used them to deduce a new SB2 orbital solution for the system. For this purpose, we selected well isolated lines and measured the line positions by fitting Gaussians to the studied profiles. Depending on the separation of the double (SB2) lines, one or two Gaussians were simultaneously adjusted. Whenever possible, we attempted to separate blended lines using templates of both primary and secondary lines built on the basis of the large *RV*-separation spectra. The method has been described in Rauw et al. (2000).

Table 3. Orbital solutions deduced from different *RV* data sets. The usual notations for the orbital elements have been used. s_y/s_x is the ratio of the relative uncertainties associated to secondary and primary *RV*s respectively. ω is the primary longitude of periastron. A "n" indicates that the related element has no relevance as a better agreement with the data has been reached assuming a circular orbit. Quoted uncertainties are the 1-σ error bars.

Lines	P (d)	s_y/s_x	e	ω (°)	K_1 (km s^{-1})	K_2 (km s^{-1})	γ_1 (km s^{-1})	γ_2 (km s^{-1})	rms (km s^{-1})
He I λ4009	2.44066	1.7	n.	n.	157.7 ± 2.5	302.1 ± 4.7	−2.8 ± 2.6	−13.1 ± 4.3	10.1
He I λ4026	2.44065	2.1	0.022 ± 0.011	112 ± 34	165.2 ± 2.2	295.5 ± 4.0	−14.9 ± 2.1	−14.7 ± 3.0	8.4
He I λ4471	2.44068	2.3	0.046 ± 0.009	139 ± 14	168.5 ± 1.7	291.9 ± 2.9	−23.8 ± 1.6	−22.6 ± 2.1	8.4
He I λ4922	2.44075	2.1	0.042 ± 0.008	167 ± 8	169.8 ± 1.5	296.6 ± 2.6	−11.0 ± 1.3	−34.0 ± 1.7	6.9
He I λ5016	2.44067	2.2	0.026 ± 0.005	99 ± 16	169.4 ± 1.2	306.5 ± 2.2	−16.4 ± 1.1	−29.7 ± 1.6	5.2
He I λ5048	2.44070	2.3	0.027 ± 0.015	190 ± 21	169.9 ± 2.3	310.3 ± 4.1	−17.3 ± 2.2	−35.4 ± 3.1	9.8
He I λ5875	2.44069	2.4	0.026 ± 0.005	122 ± 12	168.4 ± 1.0	304.0 ± 1.7	−15.3 ± 0.9	−23.4 ± 1.2	4.2

Due to the presence of numerous metallic lines, some interesting lines are usually blended with neighbouring ones. In those cases where the line profiles are effectively affected by the surrounding lines, we carried out simultaneous multi-Gaussian fits. To compute the *RV*s associated with the measured Doppler shifts, we mostly adopted the effective wavelengths for O-stars from Conti et al. (1977) below 4800 Å and from Underhill (1994) above. For the metallic lines that are typically not present in O-star spectra, we used rest wavelengths from Moore (1959). A selection of He I *RV* measurements is presented in Table 1.

3.2. Period determination

As a next step, we searched for the period P of the orbital motion. For this purpose, we applied both the method of Lafler & Kinman (1965, L&K hereafter) and the Fourier analysis of Heck et al. (1985, HMM hereafter; see also Gosset et al. 2001 for comments). The period search algorithms were applied on the data sets associated with the He I λ4471 and O III λ5592 lines. The first set is the most extensive with 32 observations and offers thus the largest time base. However, the He I λ4471 lines are most of the time blended with the O II λ4465 and Mg II λ4481 lines. Primary and secondary lines are also heavily blended near conjunction phases. On the other hand, the O III λ5592 is a single line that is associated with the primary component. It is also well isolated in the spectrum of CPD – 41° 7742. Consequently, though it is a fainter line ($EW \approx 0.16$ Å), its position can be well determined at all phases. Period values, obtained with Lafler & Kinman and Fourier analyses, based on different *RV* sets are reproduced in Table 2. The He I λ4471 time base is $T = 1388$ d, leading to a natural width of the peak in the power spectrum of $\Delta\nu = 1/T = 0.00072$ d^{-1} and a corresponding resolution on the quoted period value $\Delta P = 0.0043$ d. The full width at half maximum in the periodogram gives $\Delta P = 0.0039$ d, as expected from the theoretical value. Adopting a final uncertainty of one tenth of the peak width, we obtain $\sigma_P = 4\,10^{-4}$ d. Following a similar reasoning, the uncertainty on the O III λ5592 associated period is 5×10^{-4} d. Period values given in Table 2 do well agree within their uncertainties.

3.3. Orbital solutions

We used a modified version of the Wolfe et al. (1967) algorithm to compute new orbital solutions based on various lines. Beyond the general philosophy of the modifications implemented and described in Rauw et al. (2000), new considerations hold in the case of a binary with two components that have quite different luminosities. Indeed in such a situation where the primary and secondary lines could not be adjusted with a similar accuracy (e.g. due to a significant brightness difference), it is necessary to attribute a different relative weighting to the primary and secondary *RV*s. In our derived solutions, we adopted a period value and a relative primary to secondary weight ratio that yield the lowest residuals. Table 3 displays the deduced orbital parameters depending on the selected lines. These are in a quite acceptable agreement from one line to the other.

Finally, we computed the average *RV*s of all the quoted He I lines by shifting the individual *RV*s to a common centre, taking into account the systemic velocities deduced from the individual orbital solutions. This combined curve gives a better accuracy and the fit will be adopted as our final SB2 solution for the physical and orbital parameters, and for the ephemerides. The values of the corresponding variables are given in Table 4. Figure 3 illustrates this average He I line solution. In the following, we briefly compare our results with previously published solutions.

1. Period: The period values deduced from our different data sets are in excellent agreement. Their mean value is $P = 2.44069 \pm 0.00003$ d, with a standard deviation one order of magnitude below the period uncertainty deduced from the power spectrum peak width. This period is considered as equivalent to the adopted value $P = 2.44070$ d reported in Table 4. Our period is therefore situated between the two extreme values of LM83 (2.430155 d) and of GM01 (2.45087 d), but is closer to a previous determination by HCB74 (2.446 d). Periods around 2.430 and 2.450 days are incompatible with our data set.

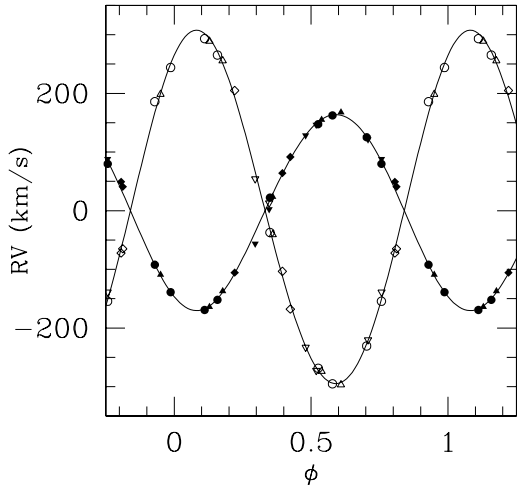

Fig. 3. Phase diagram giving the *RV* curves corresponding to the average He I line solution in the *zero systemic velocity* reference frame. Measured *RV* points associated with the primary (filled symbols) and secondary (open symbols) components are overplotted. Different symbols refer to different observation periods: upward triangles = CES 1998; squares = FEROS 1999; circles = FEROS 2000; downward triangles = FEROS 2001; diamonds = FEROS 2002.

Table 4. Orbital and physical parameters of CPD – 41° 7742 as deduced from different data sets: our data on He I λ4471, on the average over selected He I lines (see Sect. 3) and a data set extended by primary *RV*s found in the literature (see Sect. 4).

	He I λ4471	He I lines	Lit.
P (d)	2.44068	2.44070	2.44062
s_y/s_x	2.3	2.1	n.
m_1/m_2	1.728 ± 0.024	1.803 ± 0.015	n.
e	0.046 ± 0.009	0.027 ± 0.006	0.030 ± 0.017
ω (°)	139 ± 14	149 ± 10	27 ± 31
T_0 (HJD	2400.212	2400.284	2399.444
−2 450 000)	±0.092	±0.067	±0.208
K_1 (km s^{-1})	168.5 ± 1.7	167.1 ± 0.9	161.2 ± 2.5
K_2 (km s^{-1})	291.9 ± 2.9	301.3 ± 1.8	n.
γ_1 (km s^{-1})	−23.8± 1.6	0.7 ± 0.9	−16.0 ± 1.8
γ_2 (km s^{-1})	−22.6 ± 2.1	−0.6 ± 1.3	n.
$a_1 \sin i$ ($R_\odot$)	8.13 ± 0.08	8.05 ± 0.05	7.77 ± 0.12
$a_2 \sin i$ ($R_\odot$)	14.05 ± 0.14	14.52 ± 0.09	n.
$m_1 \sin^3 i$ ($M_\odot$)	15.61 ± 0.37	16.69 ± 0.25	n.
$m_2 \sin^3 i$ ($M_\odot$)	9.03 ± 0.19	9.25 ± 0.12	n.
rms (km s^{-1})	8.4	4.8	13.1

2. Eccentricity: Values for the eccentricity (resp. the longitude of periastron passage ω) from the different data sets show some dispersion that might be related to the difficulty to accurately determine a low eccentricity along with corresponding time of periastron passage in such a system. However, if we except the case of the He I λ4009 line, a better agreement between the *RV* curves and the observations is obtained adopting a slightly eccentric orbit rather than a circular one. Primary individual *RV* solutions from O III λ5592 and He II λ4686 confirm a moderate eccentricity. Though HCB74 and LM83 already suggested a low eccentricity for the system, GM01 proposed a much larger eccentricity $e = 0.205$, clearly in disagreement with our independently derived orbital solution. We will discuss this discrepancy more into details in the next section.

3. Systemic velocities: Weighted average values for *apparent* systemic velocities are -15.3 ± 0.5 and -26.3 ± 0.7 km s^{-1} for the primary and secondary respectively. The quoted errors give the uncertainties on the mean values, while the actual scatter (standard deviation) of the present sample of systemic velocities is about 4.5 and 6.4 km s^{-1} for γ_1 and γ_2 respectively. Comparing these values with the mean error on the individual systemic velocities may suggest that either the latter are underestimated or that our measurements suffer from some source of systematic error. Mainly, such non-random errors may originate from non-Gaussian profiles of the studied lines or from slightly different effective rest wavelengths than those we used. For these reasons, we choose to refer the measured *RV*s to a *zero systemic velocity* reference frame prior to averaging. Finally, primary *apparent* systemic velocities are on average 10 km s^{-1} more positive than secondary ones. These mean values will be taken into account when comparing our average He I solution and *RV* points with other "uncorrected" data.

4. An orbital solution combining (new and) published data

This section presents a combined study of the CPD – 41° 7742 *RV* measurements adding those reported in the literature. The journal of the published observations is presented in Table 5. We excluded however Struve's (1944) data from our survey because of their much poorer quality. As the reader may have noticed at this point, there are some major discrepancies between our orbital solution and the one of García & Mermilliod (GM01). Before attempting to combine all the data available, we first need to clarify this point.

4.1. GM01's data and their orbital solution

GM01 data result from CASLEO optical observations with the REOSC-SEL[1] echelle spectrograph. They observed the spectral range between 3750 and 4861 Å. The REOSC-SEL resolving power is about ∼14 000. The S/N ratio was between 50 and 80 for a typical exposure time of 30 min. Concerning CPD – 41° 7742, they reported to have carried out *RV* measurements, on average, on 15 lines for the primary component, whereas they worked with 10, 11 and 2 lines for the three secondary observations. This might correspond to Balmer and He I lines for the secondary, adding He II lines for the

[1] Spectrograph Echelle Liège – jointly built by REOSC and Liège observatory and on long-term loan from the latter.

Table 5. Journal of the observations of CPD – 41° 7742 reported in the literature. Column 1 gives the heliocentric Julian Date. Column 2 gives the phases as calculated from the average He I orbital solution (see Sect. 3). Columns 3 and 4 report the radial velocities (*RV*s), respectively associated with the primary (Col. 3) and secondary (Col. 4) components. Column 5 indicates the origin of the data. cGM01 stands for corrected GM01 data (see text).

Hel. Jul. Date (−2 400 000)	$\phi_{\overline{\text{He I}}}$	RV_1 (km s^{-1})	RV_2 (km s^{-1})	Source
39959.792	0.900	47.0		PHYB90
40018.810	0.081	−92.0		
40019.833	0.500	0.0		
40807.734	0.318	−114.0		HCB74
40808.632	0.685	166.4		
40809.479	0.032	−55.5		
40809.568	0.069	−98.8		
40809.690	0.119	−132.2		
40810.532	0.464	−40.6		
40812.486	0.265	−166.2		
40812.642	0.328	−142.9		
40813.481	0.672	145.8		
40813.587	0.716	145.0		
40813.703	0.763	151.0		
40814.510	0.094	−129.5		
40815.500	0.499	−9.4		
40815.595	0.538	21.3		
40817.479	0.310	−150.4		
40817.677	0.391	−71.3		
43647.711	0.909	13.3		LM83
43648.775	0.345	−125.0		
43649.765	0.750	144.0		
43650.789	0.170	−164.0		
49912.743	0.808	36.5		cGM01
49914.521	0.537	127.5		
49915.538	0.954	−127.8	145.5	
49967.537	0.258	−94.8		
50593.680	0.801	6.6		
50594.726	0.229	−129.2	193.0	
50596.827	0.090	−162.8	195.9	
50597.811	0.493	115.8		

primary. Excluding the point where the secondary is only detected in 2 lines does not solve the observed discrepancies.

First of all, we tried to reproduce the GM01 solution, which is presented in their Fig. 1 (labelled 505). However, the number of *RV* points presented in their orbital solution seems to be much smaller than what they claimed to have used. Our Fig. 4 (left panel) presents what should be an equivalent figure. It is clear that several *RV* points have been discarded when GM01 plotted their figure, i.e. one secondary *RV* point (out of three) and other HCB74 points around GM01 phase 0.7 are missing. PHYB90 *RV* points are not plotted on their figure either. The latter points clearly disagree with GM01 orbital solution (see Fig. 4, left panel). Finally, it is clear from Fig. 4 (right panel) that our *RV* points are incompatible with GM01 period and orbital solution.

According to Mermilliod (2003), some of the Julian Dates reported in GM01 are wrong by one day and should be corrected by subtracting one day to the published dates. Their

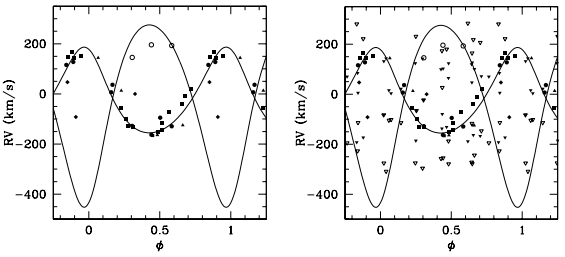

Fig. 4. Phase diagrams based on the ephemerides of GM01 (P = 2.453087 d). Different observational points are also plotted along with the orbital solution suggested by GM01. *Left*: Published primary (filled symbols) and secondary (open symbols) *RV* points: diamonds = PHYB90, squares = HCB74, triangles = LM83, circles = GM01. *Right*: idem but our He I λ4471 *RV* points have been added (downward triangles). The latter ones do obviously not match the orbital solution proposed by GM01.

proposed solution is therefore spurious, as is the high eccentricity found. Once the one-day shift is applied to the last four observations reported by GM01, the corrected GM01 data (cGM01) reach a good agreement with previous and new observations. The Julian Dates quoted in Table 5 have therefore been corrected accordingly to prevent further erroneous use of these data.

4.2. Combined period determination

As a next step, we tested our period and solution against published *RV* values. This is presented in Fig. 5. A small shift is visible between our solution and the position of PHYB90, HCB74 and LM83 measurements. This shift might result either from a small uncertainty on the period or from the ill-constrained time of periastron passage that we adopted as phase zero. Note that a similar shift could also arise from an apsidal motion of a slightly eccentric orbit. However all these data points seem in acceptable agreement with a shifted version of our *RV* curve. The cGM01 data are almost contemporaneous with ours and the primary *RV*s present a better agreement with our orbital solution. However we observe a large amplitude difference between cGM01 secondary points and our solution. This probably comes from the poorer resolution and S/N ratio of their spectra which prevent accurate *RV* measurements for the fainter component.

In addition, we applied the L&K method and the HMM Fourier analysis on different data sets, combining our *RV*s with published measurements, in order to find a common value for the period. For this purpose, we only used primary *RV* points. As the primary lines are much more intense than the secondary ones, the bias resulting from the blending of primary and secondary lines on lower resolution spectra should not too strongly affect primary *RV* measurements. Results are summarized in Table 6. We observe that the values for the period deduced either from the combined data set (P = 2.44062 d) or from our different sets (cf. Tables 3 and 4) are in very good agreement.

The next paragraph presents a primary orbital solution as computed by combining our new data with all previous

Table 6. Period searches carried out with the L&K and HMM methods and based on published primary *RV* points combined with our new measurements. The first column indicates the data set used. The second gives the number of *RV* points in the set. Columns 3 and 4 provide the period found and the relevant normalized statistic of the L&K method. The next two columns report similar values obtained from the HMM Fourier analysis. $A_{\rm max}$ is the semi-amplitude of the Fourier term. The last two columns present the time base of the set and the uncertainty on the L&K period as supposed to correspond to one tenth of the natural width of the peak. The uncertainties on the HMM values are of the same order of magnitude. cGM01 stands for corrected GM01 data as quoted in Table 5.

		L&K		HMM			
Data set	n	P (d)	Θ_1	P (d)	$A_{\rm max}$	Time base (d)	σ_P (d)
cGM01	8	2.440634	0.404	2.440586	152	686	8.7×10^{-4}
PHYB90+HCB74+LM83	23	2.440611	0.077	2.440646	156	3691	1.6×10^{-4}
PHYB90+HCB74+LM83+cGM01	31	2.440619	0.049	2.440615	155	10639	4.2×10^{-5}
cGM01+this work	40	2.440709	0.033	2.440683	161	2471	2.4×10^{-4}
PHYB90+HCB74+LM83+this work	55	2.440620	0.023	2.440627	161	12424	4.8×10^{-5}
All the available data	63	2.440619	0.019	2.440626	160	12424	4.8×10^{-5}

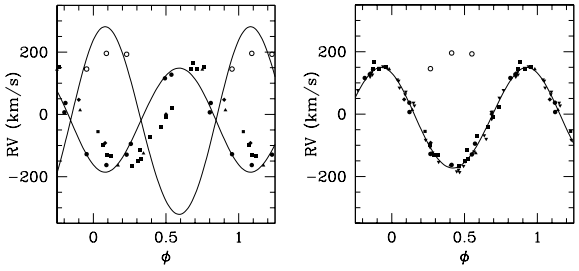

Fig. 5. Phase diagrams based on our ephemerides and orbital solutions as given in Table 4. *Left*: Published primary (filled symbols) and secondary (open symbols) *RV* points overplotted on our average He I line *RV* curves. Phases have been calculated from the average He I line ephemerides (P = 2.44070 d). *Right*: combined primary orbital solution. Corresponding orbital elements are presented in Table 4 in the column labelled "Lit." (P = 2.44062 d). In both panels the symbols have the same meaning: diamonds = PHYB90, squares = HCB74, triangles = LM83, circles = corrected GM01, downward triangles = this work.

RV measurements that we were able to find in the literature, except those from Struve (1944).

4.3. A global orbital solution for the primary

A *RV* curve that combines published data with those of the present work is presented in Fig. 5 (right panel) and the corresponding orbital solution is given in Table 4. A very good agreement is found with our derived solution. We emphasize that the literature *RV* points combined with ours provide a time base T of 12 424 days. This corresponds to a theoretical peak width in the power spectrum of $\Delta\nu = 1/T = 8.0\times10^{-5}\,{\rm d}^{-1}$, giving $\Delta P = 4.8\times10^{-4}$ d. The observed width of the peak is in good agreement with that value. Finally, the combined data set gives a period of $P = 2.44062 \pm 0.00005$ d.

In conclusion, we showed that the reported GM01 data were problematic and incompatible with previous and new observations of CPD – 41° 7742. This results from the use of erroneous Julian Dates. The period and eccentricity that GM01 derived using their set of data is therefore not correct. Shifting some of the reported HJD by one day as suggested by Mermilliod (2003) solves the observed discrepancies and allows us to include the corrected GM01 data in the combined solution. Finally, the other *RV* measurements found in the literature are in excellent agreement with our results and therefore reinforce the confidence that we have in our newly derived SB2 solution.

5. Physical parameters ofCPD – 41° 7742

5.1. Spectral types and luminosity classes

5.1.1. Primary component

The spectral signature of the primary component is easily discernible in the spectrum of CPD – 41° 7742. We adopted the classification criteria from Conti (1973) as adapted to late O-stars by Mathys (1988); they are based on the equivalent width (EW) ratio of the He I λ4471 and He II λ4542 lines. He I λ4471 EWs were only measured on spectra obtained at large *RV* separation phases. We obtain a mean $\log W'(\frac{W_{\lambda4471}}{W_{\lambda4542}}) = 0.42\pm0.04$ which corresponds to a spectral type O9, with spectral type O9.5 within $1\,\sigma$.

To determine the luminosity class, we adopted the criterion from Conti & Alschuler (1971) based on the EW ratio of the Si IV λ4089 and He I λ4144 lines. We obtain $\log W''(\frac{W_{\lambda4089}}{W_{\lambda4144}}) = 0.24\pm0.04$, which leads to a giant luminosity class. We are also aware of Mathys criterion based on $\log W''' = \log(W_{\lambda4388}) + \log(W_{\lambda4686})$. However, as it is based on the product of absolute EWs and not on their relative ratio, we first need to estimate the optical brightness of both components of the system (see Sect. 5.2).

5.1.2. Secondary component

The main spectral signatures of the secondary star in CPD – 41° 7742 are the Balmer and He I lines for which we were able to measure the positions and EWs with a good confidence. We also note the absence of He II lines, as well as of the O III λ5592 line, at the positions predicted by the orbital solution (see e.g. Fig. 6). The absence of He II lines definitively excludes an O spectral type and, at our detection threshold, most probably indicates a spectral subtype later than B0.7 (Walborn & Fitzpatrick 1990, WF90 hereafter).

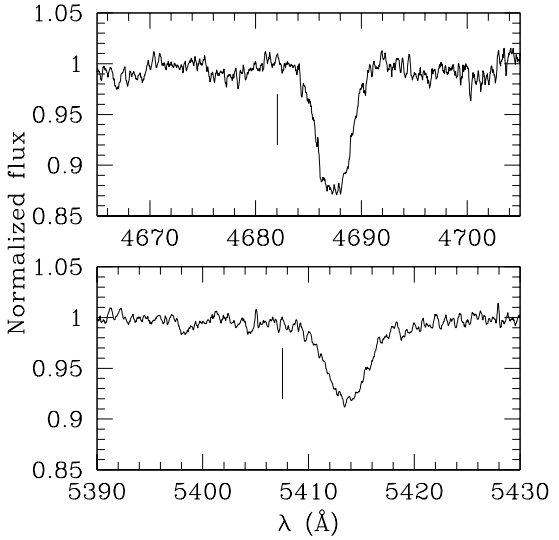

Fig. 6. He II λ4686 (upper panel) and He II λ5412 (lower panel) lines in the spectra obtained respectively at $\phi_{\overline{\text{He I}}} = 0.48$ and $\phi_{\overline{\text{He I}}} = 0.71$. The vertical marks indicate the expected position of the secondary line according to our orbital solution.

Table 7. Identified metallic lines associated to the secondary component of CPD – 41° 7742. First column gives the identified ion. The second and third columns respectively report the mean equivalent width (*EW*) of the line and the rest wavelength adopted for *RV* computations. The uncertainties quoted in Col. 2 are the 1 σ dispersions of our measurements.

Line	*EW* (Å)	Rest wavelength (Å)
Si IV λ4089	0.067 ± 0.012	4088.863
Si III λ4253[a]	0.022 ± 0.009	4253.593
C II λ4267	0.030 ± 0.012	4267.02
O II λ4367	0.029 ± 0.011	4366.896
N III λ4379	0.020 ± 0.011	4379.09
Mg II λ4481	0.028 ± 0.014	4481.228
Si III λ4552	0.051 ± 0.021	4552.654

[a] Most probably blended with the O II $\lambda\lambda$4253.74-53.98 lines.

To refine our subtype classification, we carefully searched for the presence of secondary metallic lines in our FEROS spectra. This led us to consider low intensity lines, with *EW*s down to ∼0.02 Å, and we therefore excluded spectra with too low S/N. Numerous metallic lines associated with the primary (and thus statistically more intense than the relevant secondary lines) render this task even more delicate. The results that we present in Table 7 only concern the lines that could unambiguously be associated with the secondary orbital motion (see e.g. Figs. 7 and 8) and do not pretend to be exhaustive.

WF90 suggest to use the Si III λ4552/He I λ4388 (resp. Si III λ4552/Si IV λ4089) ratio for the luminosity (resp. spectral type) classification of B0-3 stars. From our measurements, we obtained 0.44 ± 0.20 (resp. 0.76 ± 0.34). Comparing the CPD – 41° 7742 secondary spectrum to the OB atlas of WF90, the first criterion definitively excludes a supergiant luminosity class. This is reinforced by the low intensity of the secondary O II spectrum. The same criterion, though with a lower confidence, also seems to indicate a giant luminosity class rather than classes V or IV. Finally the ratio Si III λ4552/Si IV λ4089 tends to favor spectral type B1 compared to B2. We are then left with a O9 III + B1 III classification for the CPD – 41° 7742 system.

5.2. Optical brightness ratio

We roughly estimated the optical brightness ratio based on the dilution of the primary lines in the spectrum of CPD – 41° 7742. For this purpose, we compared mean *EW*s of primary lines with typical (averaged) *EW*s of O9 III stars (Conti & Alschuler 1971; Conti 1973). Based on the He I $\lambda\lambda$4026, 4388, 4471 and He II λ4542 lines, we respectively obtained a brightness ratio of $l_1 = \frac{L_1}{L_{\rm tot}} = 0.97, 0.98, 0.87$ and 0.86. Mean value is then $l_1 = 0.92 \pm 0.06$. Note that He II λ4686 is even more intense in CPD – 41° 7742 global spectrum than on average O9 III spectra and may thus rather indicate a class V for the primary star. Comparing secondary intrinsic *EW*s with typical *EW*s for B star (Didelon 1982) gives $l_2 \sim 0.1$, at the B1-B3 peak, for the He I lines. Together with C II, Mg II and Balmer lines, the same test implies $l_2 \leq 0.14$ and confirms a B1-3 V-III class for the secondary.

Adopting $l_1 = 0.92 \pm 0.06$, $W^{\rm obs}_{\lambda 4388} = 351 \pm 25$ mÅ and $W^{\rm obs}_{\lambda 4686} = 526 \pm 27$ mÅ[2], Mathys criterion gives $\log W'''_{\rm prim} = \log W(\lambda 4388) + \log W(\lambda 4686) = 5.34 \pm 0.06$, which corresponds to a giant luminosity class for the primary. One needs $l_1 \leq 0.86$ to derive a class V. The reverse criterion may also be used: a class III for the primary implies $l_1 \geq 0.86$ or $l_2 \leq 0.14$, compatible with constraints previously deduced.

In the previous paragraph, we compared observed primary *EW*s with typical *EW*s of O9 giants and deduced that the primary was probably a giant. On the other hand, we may wonder what classification would be found if we compared the observed *EW*s with typical class V *EW*s. Indeed this would yield a larger dilution ratio for the primary and might then affect Mathys criterion. We get $l_1 = 0.80 \pm 0.06$ and therefore $\log W''''_{\rm prim} = 5.46 \pm 0.07$. The criterion gives, in this case, a main sequence class, in agreement with the hypothesis made. In consequence, Mathys criterion does not provide any further constraint as the obtained classification depends on the a priori hypothesis made to estimate the brightness ratio. Finally, we mention that the Si IV λ4089 line is much more intense in CPD – 41° 7742 primary spectrum than in typical O9 V spectra.

Typical $M_{\rm V}$ for O9 stars given by Howarth & Prinja (1989) are −5.1 and −4.2 for class III and V respectively. We adopted $M_{\rm V} = -4.54 \pm 0.26$ for CPD – 41° 7742. This results from an average of the photometry of NGC 6231 and

[2] These averaged *EW*s only take into consideration spectra that were not obtained at conjunction phases (see Sect. 5.4).

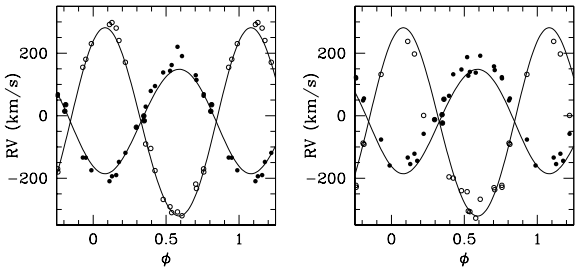

Fig. 7. Phase diagrams with C II λ4267 (left) and O II λ4367 (right) *RV* points associated to the primary (filled dots) and the secondary (open dots). The *RV* curves associated with the average He I line solution have been overplotted in both panels.

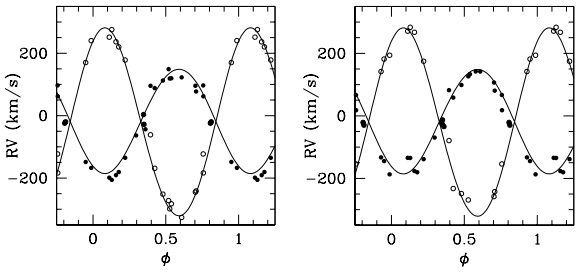

Fig. 8. Phase diagrams with Si III λ4552 (left) and Mg II λ4481 (right) *RV* points associated to the primary (filled dots) and the secondary (open dots). The *RV* curves associated with the average He I line solution have been overplotted in both panels.

of CPD – 41° 7742 published in the last ten years (Perry et al. 1991; Raboud et al. 1997; Sung et al. 1998; Baume et al. 1999). This value gives the total magnitude of the system and should therefore be considered as a lower limit for the primary component magnitude. Adopting $l_1 = 0.92 \pm 0.06$, we obtain $M_{V,1} = -4.45 \pm 0.27$. This is clearly far from a typical O9 III magnitude. If we assume that the CPD – 41° 7742 primary is indeed a main sequence star, and hence $l_1 = 0.80 \pm 0.06$, we derive $M_{V,1} = -4.30 \pm 0.27$. In this regard, the CPD – 41° 7742 primary component is thus more consistent with a main sequence classification, though all the spectral criteria indicate a giant class. At this stage it is worth to mention that the luminosity criteria based on lines that are sensitive to the surface gravity and were established for presumably single O stars may not be adapted for close binary systems.

Finally, with $V = 8.32$ and $U - B = -0.67$ (Baume et al. 1999), CPD – 41° 7742 lies at the bottom of the O9-O9.5 III clump in the colour-magnitude diagram (CMD) of NGC 6231 (see e.g. WEBDA data base: `http://obswww.unige.ch/webda/`). Its position above the main sequence is consistent with the fact that it is an SB2 binary. The previously derived combined spectral type for CPD – 41° 7742 is indeed O9 IV (Levato & Malaroda 1980). From CPD – 41° 7742's position in the CMD and from the previous discussion, we conclude that both stars belong most probably to luminosity class IV or V.

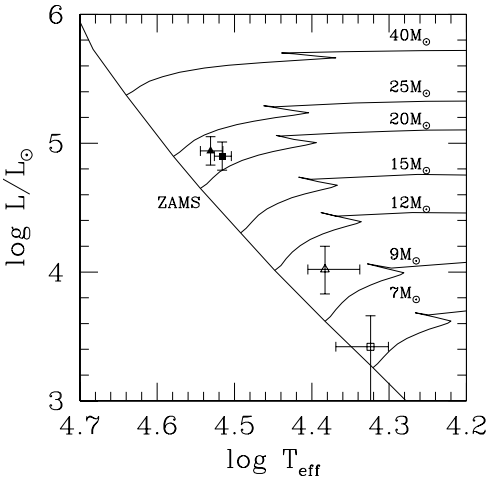

Fig. 9. Position of the primary (filled symbols) and secondary (open symbols) components of CPD – 41° 7742 in the H–R diagram. The squares (resp. triangles) refer to the positions computed by assuming giant (resp. main sequence) luminosity classes. We refer to the text for a description of the quoted error bars.

5.3. Location in the H–R diagram

Adopting the effective temperature calibration of Humphreys & McElroy (1984), the spectral types derived above (O9 III + B1 III) yield $T_{\rm eff} = 32.8\,^{33.6}_{31.9}$ kK for the primary component and $T_{\rm eff} = 21.1\,^{23.4}_{20.0}$ kK for the secondary. The quoted intervals correspond to the effective temperatures of the neighbouring subtypes. The locations of the components are plotted in the H–R diagram in Fig. 9 together with the evolutionary tracks of Schaller et al. (1992). For this purpose, we assigned $M_V = -4.54 \pm 0.26$ and we assumed that the quoted uncertainty contains both the errors on the distance modulus of the cluster and on the light variability of the system (see Sect. 5.4).

Using $l_1 = 0.92 \pm 0.06$, we finally get $\log\left(\frac{L_1^{\rm bol}}{L_\odot}\right) = 4.90\,^{5.01}_{4.79}$ and $\log\left(\frac{L_2^{\rm bol}}{L_\odot}\right) = 3.42\,^{3.66}_{2.82}$ for the bolometric luminosity of both components. The major source of uncertainty for the primary star comes from the absolute magnitude adopted. For the secondary component, it results from the uncertainty on the brightness ratio. Due to the crude method used, the above results should be taken with caution taking properly into consideration the quoted intervals especially for the secondary component. However, we can still use the information to infer constraints on the stellar radii. We obtain $R_1 = 8.7\,^{10.5}_{7.3}\,R_\odot$ and $R_2 = 3.8\,^{5.6}_{1.6}\,R_\odot$. These values are to be compared to "typical" O9–B1 giant radii of about $12-12.5\,R_\odot$. Our values are thus significantly smaller, suggesting that we are indeed dealing with luminosity class V or IV objects.

Therefore, if we assume that CPD – 41° 7742 components are indeed main sequence objects, the same reasoning with $l_1 = 0.80 \pm 0.06$ yields $\log\left(\frac{L_1^{\rm bol}}{L_\odot}\right) = 4.94\,^{5.05}_{4.83}$, $\log\left(\frac{L_2^{\rm bol}}{L_\odot}\right) = 4.02\,^{4.20}_{3.83}$ and therefore $R_1 = 8.5\,^{10.4}_{7.1}\,R_\odot$ and $R_2 = 5.8\,^{8.9}_{4.3}\,R_\odot$. Corresponding typical radii are in this case of 9.3 and 7.0 $R_\odot$ for O9 and B1 main sequence stars.

A rough interpolation of the masses from the tracks of Schaller et al. (1992) shows that the position of the giant secondary component is incompatible with the minimal mass obtained in Table 4. Adopting main sequence classifications, the relevant minimal stellar masses would yield an inclination i of about 65 to 75°.

5.4. CPD – 41° 7742, an eclipsing binary

Several authors reported a variable luminosity for the CPD – 41° 7742 system. Arentoft et al. (2001), who searched for new variable stars in NGC 6231, briefly discussed CPD – 41° 7742 and claimed to have observed incomplete eclipses but were unable to determine the times of mid-eclipses. We measured the *EW*s of two well isolated single primary lines (He II λ4686 and O III λ5592) and plotted these data versus the phase (see Fig. 10). A clear increase could be detected around $\phi \approx 0.35$, when the primary star is expected to be in front of the secondary. On the other hand, a slight dip at the other conjunction phase (i.e. around $\phi = 0.85$) may also be present while the primary is behind.

Assuming that the CPD – 41° 7742 light curve displays two eclipses as suggested above, constraints on the radii deduced in the previous section imply $i \geq 61 \pm 5°$ or $i \geq 57 \pm 5°$ according to either a giant or a main sequence class hypothesis. The quoted extreme values approximately correspond to the extreme values on the radii. $i = 61 \pm 5°$ would yield absolute masses of $24.9 \pm 3.6\,M_\odot$ and $13.8 \pm 2.0\,M_\odot$ for the primary and the secondary components respectively. The primary mass contains within its error bars typical masses of O9 III and O9 V stars as given by Howarth & Prinja (1989). We can therefore reasonably assume $i_{\rm min} \approx 60°$, in good agreement with the constraints deduced from the location of the objects in the H–R diagram.

5.5. CPD – 41° 7742, a close binary system

With a minimal orbital separation $a \sin i = (a_1 + a_2) \sin i = 22.57 \pm 0.10\,R_\odot$ and a quite high inclination as required by the presence of eclipses, CPD – 41° 7742 may be considered as a close binary system. Indeed the separation between the stellar surfaces is most probably only half of the total orbital separation. The orbital parameters given in Table 4 yield (Eggleton 1983) minimal Roche lobe (RL) radii of $R_{\rm RL} \sin i = 9.72 \pm 0.05\,R_\odot$ and $7.43 \pm 0.04\,R_\odot$ for the primary and the secondary respectively. Adopting an inclination of $i \geq 60°$ and stellar radii obtained in Sect. 5.3, we find that the filling ratio of the Roche lobes of the stars are at minimum(maximum) of about 49(72)% and 9(13)% respectively if giant classes are assumed and of 43(67)% and 31(49)% otherwise. Typical radii of giant stars of the same spectral type would require $i \leq 45°$ to avoid a Roche lobe overflow phenomenon whereas eclipses would then require $i \geq 43°$.

6. Conclusions

Using high resolution spectra, we have clearly identified the secondary orbital signature, and for the first time, we derived an accurate orbital solution for both components of CPD – 41° 7742. We showed that the orbit is slightly eccentric and obtained a period of $P = 2.44070 \pm 0.00043$ days. We further combined our data with data from the literature in order to compute a global solution for the primary. The latter turns out to be in excellent agreement with our SB2 solution. While doing this, we noticed that the data reported by García & Mermilliod (2001, GM01) were partly erroneous and should be corrected before being used. The details of this issue are explained in Sect. 4. The final set of data for the primary star covers a time range of more than 30 years. This combined analysis then suggests a period $P = 2.44062 \pm 0.00005$ days in excellent agreement with our independently derived value.

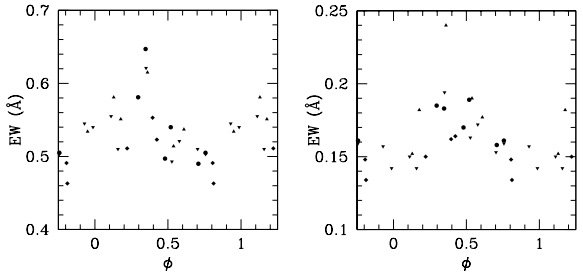

Fig. 10. He II λ4686 and O III λ5592 *EW*s plotted against the phase (as computed from the average He I line solution). Different symbols refer to different observing runs (see caption of Fig. 3).

The spectroscopic classification criteria that we applied suggest that the system is composed of a primary O9 III star and of a secondary B1 III. However, luminosity and radii obtained for the stars clearly disagree with typical values of giant stars of the same spectral types. Adopting instead a main sequence luminosity class for both objects solves much of the discrepancy. Furthermore the system is most probably too close to offer enough space for two giant stars, with typical radii, without displaying a Roche lobe overflow phenomenon.

Equivalent widths of well isolated primary lines display variations suggesting that CPD – 41° 7742 is an eclipsing binary, in agreement with incomplete observations of eclipses by Arentoft et al. (2001). Preliminary results from a photometric campaign partly dedicated to the core of NGC 6231 also confirm this idea; the results will be presented in a subsequent paper along with an X-ray lightcurve of the system. In fact, this recent discovery makes CPD – 41° 7742 an even more interesting object. Combining these new constraints with the results of the present paper will provide crucial information about the physical parameters of the system.

Finally, we emphasize that CPD – 41° 7742 is the second known SB2 eclipsing early-type binary system of the NGC 6231 cluster (the first being HD 152248, Sana et al. 2001). The results of these papers together with other papers in preparation on the early-type objects of NGC 6231 will help to constrain both early-type evolutionary models as well as binary formation theories of these objects.

Acknowledgements. We are grateful to the referee, Dr. J. C. Mermilliod, for his helpful comments and suggestions. We thank Jean Manfroid and Pierre Royer for communicating preliminary results of

their photometric campaign. We also acknowledge support from the PRODEX XMM-OM and Integral Projects, contracts P4/05 and P5/36 "Pôle d'Attraction Interuniversitaire" (Belgium).

References

Arentoft, T., Sterken, C., Knudsen, M. R., et al. 2001, A&A, 380, 599
Baume, G., Vázquez, R. A., & Feinstein, A. 1999, A&AS, 137, 233
Braes, L. L. E. 1967, Bulletin of the Astronomical Institute of the Netherlands, Supp. Ser., 2, 1
Conti, P. S. 1973, ApJ, 179, 181
Conti, P. S., & Alschuler, W. R. 1971, ApJ, 170, 325
Conti, P. S., Leep, E. M., & Lorre, J. J. 1977, ApJ, 214, 759
Deharveng, L., Zavagno, A., Salas, L., et al. 2003, A&A, 399, 1135
Didelon, P. 1982, A&AS, 50, 199
Eggleton, P. P. 1983, ApJ, 268, 368
García, B., & Mermilliod, J. C. 2001, A&A, 368, 122 (GM01)
Gimenez, A. 1996, in The origins, evolution, and destinies of binary stars in clusters, ed. E. F. Milone, & J. C. Mermilliod, ASP Conf. Ser., 90, 109
Gosset, E., Royer, P., Rauw, G., Manfroid, J., & Vreux, J.-M. 2001, MNRAS, 327, 435
Heck, A., Manfroid, J., & Mersch, G. 1985, A&AS, 59, 63 (HMM)
Hensberge, H. 2002, Evaluation of FEROS Pipeline, `http://www.ls.eso.org/lasilla/Telescopes/2p2T/E1p5M/FEROS/Reports/index.html`
Hill, G., Crawford, D. L., & Barnes, J. V. 1974, AJ, 79, 1271 (HCB74)
Howarth, I. D., & Prinja, R. K. 1989, ApJS, 69, 527
Humphreys, R. M., & McElroy, D. B. 1984, ApJ, 284, 565
Kukarkin, B. V., Kholopov, P. N., Pskovsky, Y. P., et al. 1971, General Catalogue of Variable Stars, 3rd ed.
Lafler, J., & Kinman, T. D. 1965, ApJS, 11, 216 (L&K)
Levato, H., & Malaroda, S. 1980, PASP, 92, 323
Levato, H., & Morrell, N. 1983, ApL, 23, 183 (LM83)
Mathys, G. 1988, A&AS, 76, 427
Maeder, A., & Meynet, G. 1995, Msngr, 80, 19
Maeder, A., & Meynet, G. 2000, A&A, 361, 159
Mermilliod, J. C. 2003, private communication
Moore, C. E. 1959, in A Multiplet Table of Astrophysical Interest, Technical Note 36, National Bureau of Standards (Washington: U. S. Department of Commerce)
Perry, C. L., Hill, G., Younger, P. F., & Barnes, J. V. 1990, A&AS, 86, 415 (PHYB90)
Perry, C. L., Hill, G., & Christodoulou, D. M. 1991, A&AS, 90, 195
Raboud, D., Cramer, N., & Bernasconi, P. A. 1997, A&A, 325, 167
Rauw, G., Sana, H., Gosset, E., et al. 2000, A&A, 360, 1003
Sana, H., Rauw, G., & Gosset, E. 2001, A&A, 370, 121
Schaller, G., Schaerer, D., Meynet, G., & Maeder, A. 1992, A&AS, 96, 269
Seggewiss, W. 1968, Veroeff. Astron. Inst. Bonn, 79, 1
Struve, O. 1944, ApJ, 100, 189
Sung, H., Bessell, M. S., & Lee, S.-W. 1998, AJ, 115, 734
Underhill, A. B. 1994, ApJ, 420, 869
Walborn, N. R., & Fitzpatrick, E. L. 1990, PASP, 102, 379 (WF90)
Wolfe, R. H. Jr., Horak, H. G., & Storer, N. W. 1967, in Modern Astrophysics, ed. M. Hack, Gordon, & Breach (New York), 251

Astronomy & Astrophysics manuscript no. cpd7742b˙v4 May 23, 2005
(DOI: will be inserted by hand later)

The massive binary CPD – 41° 7742 :

II. Optical light curve and X-ray observations ⋆

H. Sana[1,⋆⋆], E. Antokhina[2], P. Royer[3], J. Manfroid[1,⋆⋆⋆], E. Gosset[1,†], G. Rauw[1,†], and J.-M. Vreux[1]

[1] Institut d'Astrophysique et de Géophysique, Université de Liège, Allée du 6 Août 17, Bât. B5c, B-4000 Liège, Belgium
e-mail: sana@astro.ulg.ac.be, manfroid@astro.ulg.ac.be, gosset@astro.ulg.ac.be, rauw@astro.ulg.ac.be, vreux@astro.ulg.ac.be
[2] Sternberg Astronomical Institute, Moscow State University, Universitetskii pr., 13, 119899 Moscow, Russia e-mail: elant@sai.msu.ru
[3] Instituut voor Sterrenkunde, Katholieke Universiteit Leuven, Celestijnenlaan 200 B, B-3001 Leuven, Belgium
e-mail: pierre@ster.kuleuven.ac.be

Received September 15, 2000; accepted September 15, 2000

Abstract. In the first paper of this series, we have presented a detailed high-resolution spectroscopic study of CPD – 41° 7742, deriving for the first time an orbital solution for both components of the system. In this second paper, we focus on the analysis of the optical light curve and on recent XMM-*Newton* X-ray observations. In the optical, the system presents two eclipses, yielding an inclination $i \sim 77°$. Combining the constraints from the photometry with the results of our previous work, we derive the absolute parameters of the system. We confirm that the two components of CPD – 41° 7742 are main sequence stars (O9 V + B1-1.5 V) with masses ($M_1 \sim 18$ M$_\odot$ and $M_2 \sim 10$ M$_\odot$) and respective radii ($R_1 \sim 7.5$ R$_\odot$ and $R_2 \sim 5.4$ R$_\odot$) close to the typical values expected for such stars.
We also report an unprecedented set of X-ray observations that almost uniformly cover the 2.44-day orbital cycle. The X-ray emission from CPD – 41° 7742 is well described by a two-temperature thermal plasma model with energies close to 0.6 and 1.0 keV, thus slightly harder than typical early-type emission. The X-ray light curve shows clear signs of variability. The emission level is higher when the primary is in front of the secondary. During the high emission state, the system shows a drop of its X-ray emission that almost exactly matches the optical eclipse. We interpret the main features of the X-ray light curve as the signature of a wind-photosphere interaction, in which the overwhelming primary O9 star wind crushes on the secondary surface. Alternatively the light-curve could result from a wind-wind interaction zone located near the secondary star surface. We finally provide a phenomenological geometric model that qualitatively reproduces the observed modulations of the X-ray emission.

Key words. stars: individual: CPD – 41° 7742 – binaries: close – binaries: eclipsing – stars: early-type – stars: fundamental parameters – X-rays: stars

1. Introduction

In the quest for accurate measurements of the fundamental stellar parameters, eclipsing spectroscopic binaries are unique physical laboratories all over the Hertzsprung-Russell diagram. The combined spectroscopic and photometric study indeed provides a direct determination of the masses and sizes of their stellar components. This is of a particular interest in the upper left part of the diagram. Though few in number, the massive early-type stars have a large influence on their surroundings through their mechanical and radiative energy input. A detailed knowledge of both their evolution and wind properties is thus crucial in many different contexts. For example, these objects seem to play a key role in the formation of the less massive stars in starburst regions or within the core of OB associations. However, our understanding of massive stars is clearly still fragmentary. Only a few tens of objects have their orbital and physical parameters determined with a reasonable accuracy (Gies 2003). The problem of their exact formation mechanism is largely unsolved (Zinnecker 2003) and, from the theoretical point of view, their physical parameters (effective temperatures, radii, masses, ...) significantly differ from one study to another (Humphreys & McElroy 1984; Howarth & Prinja 1989;

Send offprint requests to: H. Sana

⋆ Based on observations collected at the European Southern Observatory (La Silla, Chile) and with XMM-*Newton*, an ESA Science Mission with instruments and contributions directly funded by ESA Member States and the USA (NASA).

⋆⋆ Research Fellow FNRS (Belgium)

⋆⋆⋆ Research Director FNRS (Belgium)

† Research Associate FNRS (Belgium)

Table 1. Orbital and physical parameters of CPD – 41° 7742 as derived from the He I lines orbital solution presented in Paper I. The usual notations have been adopted. T_0 is the time of periastron passage and is adopted as phase $\psi = 0.0$. The column to the right provides the revised estimate of the errors, obtained with Monte-Carlo simulation techniques (see Sect. 4).

$P_{\rm orb}$ (days)	2.44070	±	0.00050	
e	0.027	±	0.006	0.008
ω (°)	149	±	10	17
T_0(HJD −2 450 000)	2400.284	±	0.067	0.113
γ_1 (km s^{-1})	−15.3	±	0.5	1.2
K_1 (km s^{-1})	167.1	±	0.9	1.4
$a_1 \sin i$ ($R_\odot$)	8.05	±	0.05	0.07
γ_2 (km s^{-1})	−26.3	±	0.7	2.4
K_2 (km s^{-1})	301.3	±	1.8	3.0
$a_2 \sin i$ ($R_\odot$)	14.52	±	0.09	0.14
q (= M_1/M_2)	1.803	±	0.015	0.023
$M_1 \sin^3 i$ ($M_\odot$)	16.69	±	0.25	0.39
$M_2 \sin^3 i$ ($M_\odot$)	9.25	±	0.12	0.18

Vacca et al. 1996). The observational masses deduced from atmosphere models are systematically lower than the predicted masses using evolutionary models (the so-called *mass discrepancy* problem, Herrero et al. 1992; Herrero 2003). Fortunately, recent works (Crowther et al. 2002; Herrero et al. 2002; Bianchi & Garcia 2002; Martins et al. 2002) using line-blanketed atmosphere models and accounting both for the spherical stellar atmosphere and for the stellar winds yielded new effective temperature scales for early-type stars and, simultaneously, led to a better agreement between the spectroscopic and evolutionary masses. In this context, the accurate determination of the massive star fundamental parameters, over the whole spectral type and luminosity class range covered by these objects, provides thus the basic material to strengthen our understanding of this particularly important stellar population.

The early-type binary systems are also crucial for the mapping of X-ray emitting plasmas. So far, the most reliable way to constrain the geometry of the hot plasma around stars of various spectral types is through the study of the temporal changes of the X-ray fluxes of eclipsing binaries or rotating stars; the latter only in cases of non-uniform surface distributions of X-ray plasma. A good time coverage of the orbital or rotation cycle is of course critical to provide as complete a description as possible. While late-type stars often experience flaring activities which may considerably complicate the task of mapping their coronae, the situation should, in principle, be much easier in early-type stars. In fact, single early-type objects usually do not display a strong X-ray variability (Berghöfer & Schmitt 1994). In early-type binaries, a significant fraction of the X-ray emission may however arise in a wind interaction zone. The orbital modulation of their X-ray flux is thus quite common, either because of the changing opacity along the line of sight towards the shock region, or as a consequence of the changing properties of the wind interaction zone in an eccentric binary.

In this context, we have undertaken a detailed study of CPD – 41° 7742, a double line spectroscopic binary located in the core of the young open cluster NGC 6231. In Sana et al. (2003, Paper I hereafter), we presented a first accurate orbital solution for the two components of the system. We derived a short period $P = 2.44070$ days and a slight but definite eccentricity $e = 0.027$. Based on spectroscopic criteria, we proposed a spectral type and a luminosity class of O9 III + B1 III for the two components of the system. However we outlined the strong ambiguity concerning the quoted luminosity classification. Indeed the luminosities and radii inferred from the membership in NGC 6231 rather indicate a class V or IV for both components. The analysis of the light curve of the system will allow to elucidate this question.

We refer to Paper I for a review of the previous works on the object. In Paper I, we dit not mention the work of Balona & Laney (1995) in which the authors present a first light curve of CPD – 41° 7742, showing a clearly-marked eclipse. We also refer to Paper I for details on the spectroscopic analysis of the system. Table 1 summarizes the computed orbital solution and the constraints obtained on its physical parameters. This second paper will complete our current view of the system by providing the analysis of the photometric light curve and of XMM-*Newton* X-ray observations. It is organised as follows. After a description of the optical and X-ray data sets and data handling (Sect. 2), we present the analysis of the system light curve (Sect. 3). In Sect. 4, we combine the newly obtained information with results from Paper I and we derive the absolute parameters of the system. The X-ray properties of CPD – 41° 7742 are described in Sect. 5. In Sect. 6, we investigate the wind properties and we propose to interpret the X-ray light curve as the signature of a wind interaction. We also present a simple phenomenological model that reproduces reasonably well the observed modulations. Final considerations and conclusions of this work are summarised in Sect. 7.

2. Observations and data reduction

2.1. Photometry

Between 1997 March 22 and April 19, we observed the core of the open cluster NGC 6231 with the 0.6-m Bochum telescope at La Silla, Chile. The Cassegrain focus of the telescope was equipped with a direct camera and a Thomson 7882 charge-coupled device (CCD) detector (384 × 576 pixels) subtending a full field of view of 3.2 by 4.8 arcmin. The photometric observations have been performed through two narrow band filters: one called λ4686 addressing the region of the He II line usually present in massive stars (centre: 4684 Å, FWHM: 30 Å) and another one labelled λ6051 addressing a region of the continuum free from strong lines (centre: 6051 Å, FWHM: 28 Å). More information on these filters can be found in Royer et al. (1998). The typical exposure times were 60s for both filters. Some 112 (resp. 138) useful frames were obtained with the λ4686 (resp. λ6051) filter. Flat field calibrations were obtained daily on the floodlit dome. No twilight flat could be acquired due to the narrowness of the filters. Several biases were cautiously acquired all along the different nights. The frames

Table 2. Journal of the photometric observations of CPD – 41° 7742 in the two filters λ6051 and λ4686 (see text). Odd columns give the heliocentric julian dates (in format HJD − 2 450 000). Even columns provide the observed magnitudes in the selected filter.

λ6051						λ4686					
HJD	mag	HJD	mag	HJD	mag	HJD	mag	HJD	mag	HJD	mag
530.8192	8.103	540.8836	8.103	549.9225	8.417	534.8722	8.540	545.8333	8.533	554.8312	8.777
530.8203	8.098	540.9142	8.088	550.7756	8.129	534.8968	8.533	545.8758	8.525	554.8680	8.678
531.8341	8.130	540.9223	8.098	550.8198	8.132	535.7976	8.520	545.9226	8.546	554.9149	8.594
531.8354	8.123	540.9286	8.101	550.8595	8.129	535.8262	8.526	546.7415	8.521	555.7662	8.569
533.8018	8.123	541.7697	8.106	550.8872	8.125	535.8670	8.534	546.7979	8.516	555.8110	8.574
533.8033	8.127	541.7939	8.105	550.9163	8.139	535.9103	8.530	546.8556	8.522	555.8573	8.643
533.8041	8.126	541.8431	8.108	550.9216	8.148	537.7754	8.690	546.9197	8.527	555.9148	8.726
533.8291	8.138	541.8689	8.091	551.7497	8.105	537.8168	8.607	547.7870	8.541	555.9303	8.756
533.8299	8.147	541.8974	8.112	551.7937	8.115	537.8576	8.568	547.8468	8.542	556.7881	8.535
533.8307	8.146	542.7511	8.127	551.8060	8.124	537.8590	8.571	547.8905	8.517	556.8690	8.558
533.8571	8.161	542.7896	8.128	551.8631	8.124	537.9009	8.552	547.9242	8.510	557.7451	8.517
533.8579	8.160	542.8192	8.141	551.9181	8.100	538.7595	8.614	548.7645	8.692	557.7899	8.525
533.8587	8.151	542.8482	8.118	552.7605	8.113	538.8022	8.674	548.8095	8.614	557.8334	8.525
533.8823	8.198	542.8906	8.126	552.8081	8.117	538.8615	8.755	548.8509	8.565	557.8599	8.509
533.8831	8.188	543.7525	8.342	552.8566	8.105	538.9045	8.772	548.8781	8.544	557.9078	8.506
533.8839	8.194	543.8084	8.356	552.8789	8.093	539.7730	8.560	548.9168	8.538	557.9249	8.511
533.9053	8.234	543.8701	8.292	552.8798	8.093	539.8246	8.552	548.9212	8.538	558.6961	8.545
533.9063	8.236	543.8955	8.242	552.9189	8.090	539.8655	8.560	549.7466	8.710	558.7425	8.543
533.9270	8.273	543.9226	8.199	553.7507	8.118	539.8983	8.569	549.8067	8.858	558.7897	8.521
533.9278	8.263	544.7848	8.159	553.7947	8.124	540.7890	8.514	549.8637	8.902	558.8082	8.543
533.9286	8.267	544.8474	8.255	553.8328	8.116	540.8306	8.516	549.9214	8.824		
533.9294	8.266	544.8936	8.374	553.8736	8.114	540.8815	8.523	550.7748	8.534		
533.9302	8.274	544.9210	8.442	553.9195	8.111	540.9135	8.531	550.8190	8.531		
534.7974	8.123	544.9281	8.457	554.7069	8.470	540.9217	8.547	550.8586	8.537		
534.8227	8.129	545.7752	8.112	554.7540	8.485	540.9280	8.542	550.8864	8.524		
534.8456	8.130	545.8341	8.119	554.7937	8.430	541.7689	8.523	550.9155	8.546		
534.8730	8.142	545.8766	8.123	554.8319	8.343	541.7931	8.534	550.9208	8.561		
534.8976	8.132	545.9234	8.128	554.8686	8.253	541.8423	8.532	551.7489	8.528		
535.7984	8.118	546.7423	8.100	554.9156	8.168	541.8681	8.523	551.7930	8.535		
535.8270	8.118	546.7987	8.097	555.7669	8.148	541.8966	8.538	551.8052	8.528		
535.8678	8.124	546.8564	8.095	555.8117	8.168	542.7503	8.546	551.8623	8.535		
535.9111	8.110	546.9205	8.109	555.8581	8.228	542.7888	8.542	551.9173	8.519		
537.7762	8.275	547.7881	8.108	555.9156	8.310	542.8183	8.569	552.7569	8.542		
537.8176	8.195	547.8476	8.109	555.9311	8.342	542.8474	8.535	552.7614	8.540		
537.8601	8.157	547.8913	8.086	556.7887	8.135	542.8898	8.546	552.8074	8.528		
537.9021	8.145	547.9250	8.092	556.8698	8.138	543.7516	8.769	552.8551	8.530		
538.7603	8.186	548.7674	8.255	557.7458	8.106	543.8076	8.765	552.8782	8.521		
538.8030	8.258	548.8105	8.184	557.7907	8.095	543.8693	8.701	552.9174	8.522		
538.8623	8.328	548.8519	8.140	557.8342	8.087	543.8947	8.657	553.7500	8.557		
538.9053	8.342	548.8789	8.115	557.8607	8.082	543.9218	8.623	553.7941	8.556		
539.7738	8.137	548.9179	8.115	557.9094	8.079	544.7840	8.560	553.8321	8.540		
539.8254	8.132	548.9200	8.119	557.9257	8.087	544.8465	8.672	553.8729	8.554		
539.8663	8.140	548.9223	8.113	558.6969	8.127	544.8928	8.784	553.9188	8.550		
539.8991	8.142	549.7474	8.302	558.7433	8.103	544.9202	8.858	554.7062	8.887		
540.7898	8.096	549.8075	8.449	558.7910	8.099	544.9272	8.863	554.7533	8.914		
540.8314	8.101	549.8645	8.490	558.8091	8.113	545.7744	8.530	554.7928	8.840		

were debiased using a master zero frame and, in the absence of overscan, a level value interpolated between the various bias frames taken during the same night. The optical elements close to the CCD proved to be frequently contaminated by dust. Hence, the pixel-to-pixel (high spatial frequency) part of the flat-field calibration had to be carefully extracted from the calibration frames obtained daily. The large scale component of the dome flat fields varied slightly from day to day. This was found to be due to minor changes in the instrumental setup. Night sky superflats proved to be more stable, but yielded a strong systematic vignetting as shown by Manfroid et al. (2001). Consequently, the illumination correction was entirely obtained from the 'photometric superflats' based on stellar measurements (see e.g. Manfroid 1995). All reductions were carried out with the National Optical Astronomy Observatories (NOAO) IRAF package. The debiased, flat-fielded frames were analyzed with the DAOPHOT software (Stetson 1987), using aperture radii between 2 and 5.5 arcsec. 'Absolute' photometry was derived

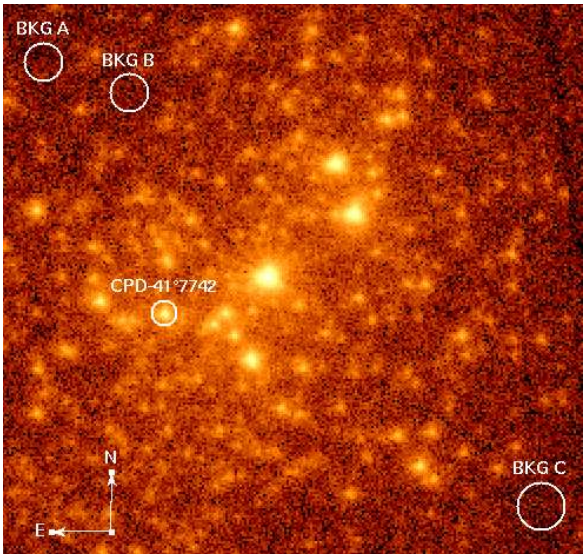

Fig. 1. Broad-band [0.5 - 10.0 keV] image of the NGC 6231 core. This EPIC MOS1+MOS2 image combines the two instruments and the six pointings of the campaign for a cumulated effective exposure time of 351.5 ks. The source and background extraction regions are shown.

from the large aperture data, using a multi-night, multi-filter algorithm and a few standard stars (Manfroid 1993). This procedure yielded additional reference stars for each field. These secondary standards together with all non-variable stars were used to fix, through a global minimization procedure, the zero points for the individual frames and for each aperture radius, thus performing some kind of global differential photometry.

Comparing the photometry performed through the different apertures, we noted that a faint companion visible at 3-4″ to the W-SW of CPD – 41° 7742 has actually no influence on the differential photometry. The final magnitudes are given in Table 2 and correspond to a 2.″5 radius aperture. The expected error on a star of similar brightness as CPD – 41° 7742 corresponds to σ = 0.007 mag in differential photometry.

2.2. X-ray observation

CPD – 41° 7742 was observed with XMM-*Newton* (Jansen et al. 2001) during the six pointings of the campaign towards NGC 6231 (Sana et al. 2004, 2005a) performed within the guaranteed time programme of the Optical Monitor consortium. The MOS cameras (Turner et al. 2001) were operated in the full frame mode and using the thick filter to avoid contamination by UV/optical light. No EPIC pn data were collected for CPD – 41° 7742 since the star fell on a gap of the pn detector. Due to the brightness of the objects in the field of view (FOV), the Optical Monitor was switched off throughout the campaign. The raw data were processed with the Scientific Analysis System (SAS) version 5.4.1. For details on the XMM-*Newton* observations and on the data processing, we refer to the previous work on HD 152248 – the central target of the FOV – by Sana et al. (2004).

For the purpose of scientific analysis, we adopted a circular extraction region with a radius of 13.2 arcsec and centered on CPD – 41° 7742. This radius corresponds to half the distance to the nearest neighbouring X-ray source. Using the SAS task CALVIEW, we estimated that, at the position of CPD – 41° 7742, the adopted extraction region corresponds to an encircled energy fraction of about 64% and 63% respectively for the MOS1 and MOS2 instruments. Unfortunately, due to the crowded nature of the NGC 6231 cluster core in the X-rays (see Fig. 1), the background could not be evaluated in the immediate vicinity of CPD – 41° 7742, but had to be taken from the very few source free regions in the cluster core. We adopted three circular background regions – labelled A, B and C on Fig. 1 – centered on (α, δ) = ($16^h54^m31^s.43$, $-41°45'42''.2$), ($16^h54^m23^s.28$, $-41°46'14''.7$) and ($16^h53^m44^s.12$, $-41°53'34''.6$), and with respective radii of 20, 20 and 25 arcsec. These regions are somewhat offset from the source region but all three are located on the same CCD detector (CCD #1) as CPD – 41° 7742.

Using the average count rates in each pointing, we built raw and background-corrected broad-band light curves in the range [0.5-10.0 keV][1]. We also extracted light curves in three different energy bands: a soft (S_X) band [0.5 - 1.0 keV], a medium (M_X) band [1.0 - 2.5 keV] and a hard (H_X) band [2.5 - 10.0 keV]. For comparison, we used the background corrected count rates in each pointing as given in the cluster X-ray source catalogue. These latter values were obtained by means of a psf-model fit to the source using the SAS task *emldetect* and a spline background function (see details in Sana et al. 2005a). While the catalogue count rates turn out to be about 50% larger than the extracted count rates, both are in excellent agreement when these latter are corrected for the encircled energy fraction. The obtained X-ray light curves show clear variability. To increase our time resolution, we extracted light curves with temporal bins of 5 ks, over the same energy ranges as stated above. These latter curves were corrected for the various good time intervals that result from the data processing; they will be discussed in Sect. 5.

Finally, adopting the same source and background regions, we extracted X-ray spectra for each observation and for each of the two MOS instruments. For this purpose, we used the redistribution matrix files (*rmf*) provided by the XMM-*Newton* instrument teams and we built the appropriate ancillary response files (*arf*) with the help of the SAS software. The spectra were binned in such a way as to have at least 10 counts per energy bin. Using the BLANKSKY files for the MOS instruments, we extracted the spectra corresponding to the adopted source and background regions. The impact of the offset in the background regions on the background spectrum, and on the instrumental emission lines in particular, was found to be negligible.

[1] Expressed in pulse-invariant (PI) channel numbers and considering that one PI approximately corresponds to 1 eV, the adopted range is actually PI$\in$ [500-10 000].

Table 3. Time and orbital phase (according to the ephemeris of Table 1) at mid-exposure for each XMM-*Newton* observation of CPD – 41° 7742. The other columns yield the count rates (in units of 10^{-3} cnt s^{-1}) over different energy bands (expressed in keV) for the two MOS instruments, as obtained using the SAS task *emldetect* (see details in Sana et al. 2005a). The observations lasted on average for 30 ks (corresponding to a phase interval of 0.14). Note that due to background flares, part of some observations had to be discarded.

Obs.	JD	ψ	MOS1				MOS2			
#	−2 450 000		[0.5-10.0]	[0.5-1.0]	[1.0-2.5]	[2.5-10.0]	[0.5-10.0]	[0.5-1.0]	[1.0-2.5]	[2.5-10.0]
1	2158.214	0.819	16.5 ± 0.9	7.7 ± 0.6	8.7 ± 0.6	0.1 ± 0.1	14.3 ± 0.8	7.7 ± 0.6	6.2 ± 0.5	0.4 ± 0.2
2	2158.931	0.113	29.7 ± 1.5	9.8 ± 0.8	17.0 ± 0.9	2.9 ± 0.5	29.0 ± 1.5	10.1 ± 0.9	16.6 ± 1.1	2.2 ± 0.5
3	2159.796	0.468	22.8 ± 1.0	9.0 ± 0.6	12.2 ± 0.6	1.6 ± 0.3	23.6 ± 1.0	9.2 ± 0.6	13.1 ± 0.8	1.3 ± 0.3
4	2160.925	0.930	19.0 ± 1.0	8.4 ± 0.7	9.5 ± 0.7	1.1 ± 0.3	19.3 ± 1.1	9.3 ± 0.7	9.1 ± 0.7	1.0 ± 0.3
5	2161.774	0.278	19.7 ± 1.0	8.5 ± 0.6	10.0 ± 0.7	1.2 ± 0.3	21.1 ± 1.0	8.1 ± 0.6	11.4 ± 0.7	1.6 ± 0.3
6	2162.726	0.668	18.9 ± 0.9	9.5 ± 0.6	8.9 ± 0.7	0.5 ± 0.2	20.3 ± 1.0	9.2 ± 0.6	10.4 ± 0.7	0.7 ± 0.2

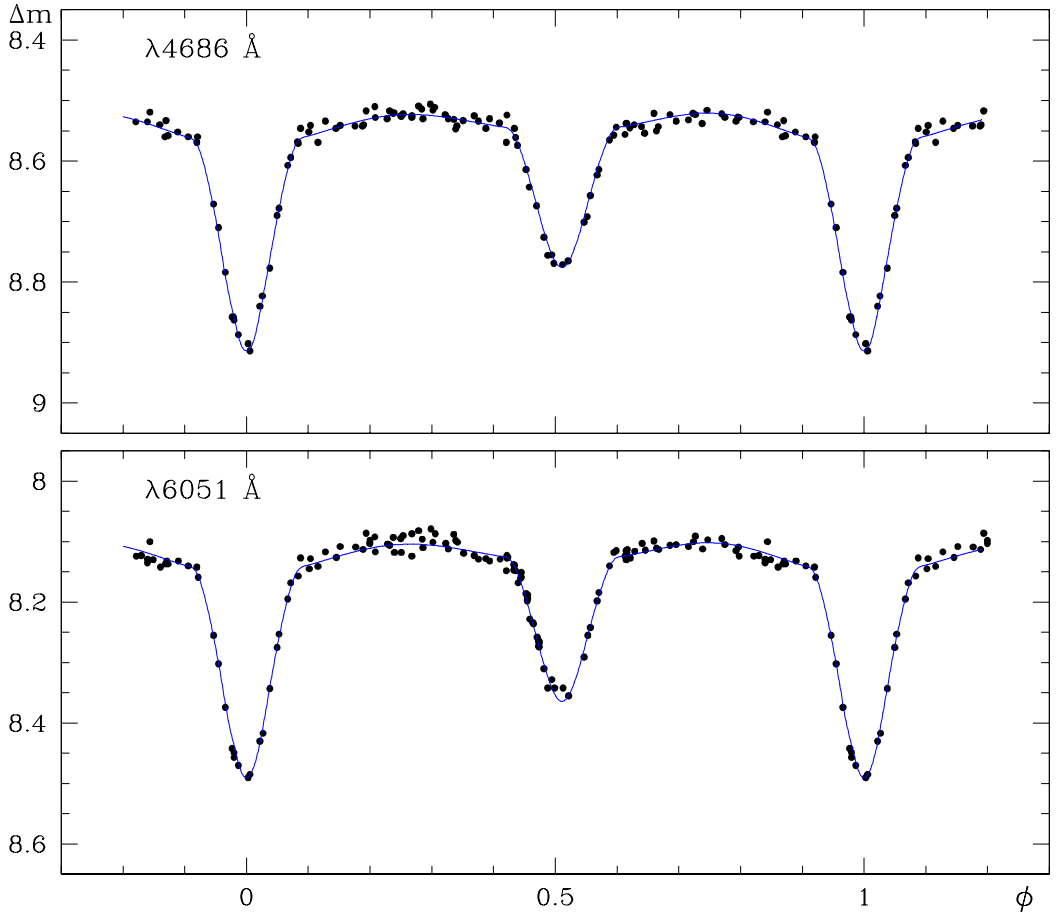

Fig. 2. Observed (dots) and modelled (plain lines) light curves at λ4686 Å and λ6051 Å. The parameters of the adopted model are presented in Table 5. The minimum of the primary eclipse is adopted as phase $\phi = 0.0$ which, according to the ephemeris of Table 1, corresponds to $\psi \approx 0.85$.

3. Optical light curve analysis

Photometric light curves were analysed within the framework of the Roche model for an eccentric orbit, similar to Wilson's (Wilson 1979) model. The algorithm is described in detail by Antokhina (1988, 1996), here we only briefly describe its main features. The computer code allows one to calculate a radial velocity curve, the monochromatic light curves and absorption line profiles of stars simultaneously, either for a circular or an eccentric orbit. Axial rotation of the stars may be non synchronized with the orbital revolution. Following Wilson (1979), we assumed that the shapes of the stars coincide with equipotential

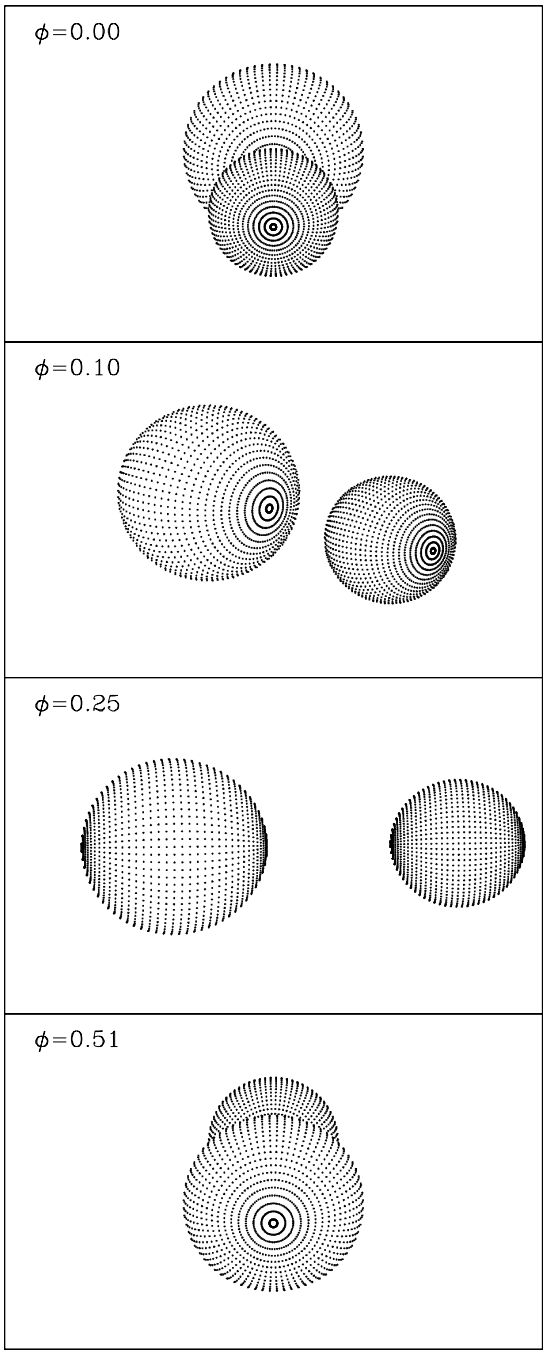

Fig. 3. The model of CPD – 41° 7742 viewed at different orbital phases ϕ. The corresponding phases using the ephemeris of Table 1 are, from top to bottom, ψ = 0.85, 0.95, 0.10 and 0.36.

surfaces in the Roche model at all orbital phases and both stars retain constant volumes during their orbital revolution. The tidally distorted surfaces of the stars are heated by mutual radiation. The intensity of the radiation coming from an elementary area of the stellar surface and its angular dependence are determined by the temperature of the star, gravitational darkening, limb darkening, and heating by radiation from the companion. The input parameters of the model are summarized in Table 4.

Table 4. Input parameters for the program of synthesis of the light curves.

Parameters	Description
$q = M_1/M_2$	Mass ratio
e	Eccentricity
ω	Longitude of periastron of primary star
F_1, F_2	Ratio of surface rotation rate to synchronous rotation rate for both stars
i	Orbital inclination
μ_1, μ_2	Roche lobe filling coefficients, $\mu = R/R^*$, where R and R^* are the polar radii for partial and complete filling of the critical Roche lobe at periastron position ($0 < \mu \leq 1$)
T_1, T_2	Average effective temperatures of the components
β_1, β_2	Gravity darkening coefficients (the temperature of an elementary surface area $T = T_{1,2} \times (\frac{g}{<g>_{1,2}})^{\beta_{1,2}}$, where g and $< g >$ are the local and mean gravity accelerations)
$x_{1,2}, y_{1,2}$	Limb darkening coefficients (see the text)
A_1, A_2	Bolometric albedos (coefficients of reprocessing of the emission of a companion by "reflection")
l_3	Third light
$\Delta\phi$	Phase shift between the times of conjunction t_0 and of periastron passage T_0 (Table 1)
t_0	Time of primary eclipse minimum

For light curve solution, we fixed some parameters whose values were defined in previous investigations of the system or can be assumed from global stellar properties. Namely, we used the known spectroscopic value of mass ratio $q = M_1/M_2 = 1.803$, deduced from the data on He I lines (Paper I). A light curve solution is only sensitive to the temperature ratio between the stars, thus the temperature of one star should be fixed. Usually it is the more reliably determined temperature of the primary star. The spectral types of the stars O9 III (primary) and B1 III (secondary) were derived in Paper I, but we pointed out that adopting a main sequence luminosity class for both components solves much of the inconsistency between the luminosity class III hypothesis and the typical luminosities and radii of giant stars. Our preliminary light curve solution resulted in stellar radii also suggesting the luminosity class V for both stars, thus we fixed the average effective temperature of the primary T_1 = 34 000 K corresponding to an O9 V star (Humphreys & McElroy 1984). This value is also very close to the one given by the new effective temperature scale of O-type dwarfs by Martins et al. (2002).

Gravity-darkening coefficients $\beta_1 = \beta_2 = 0.25$ and albedos $A_1 = A_2 = 1$ were assumed as typical for early type stars. We used the nonlinear 'square-root' limb-darkening law (Diaz-Cordoves & Gimenez 1992; Diaz-Cordoves et al. 1995; van Hamme 1993): $I(\cos\gamma) = I(1)[1 - x(1 - \cos\gamma) - y(1 - \sqrt{\cos\gamma})]$, where γ is the angle between the line of sight and the normal to the surface, $I(1)$ is the intensity for $\gamma = 0$, and x, y are the limb darkening coefficients. As shown by van Hamme (1993), this is

Table 5. CPD – 41° 7742 physical and orbital parameters as obtained from the optical light curve analysis. Two kinds of error estimates are given. The first one defines the confidence intervals inside which the model is still accepted at the 1% significance level (see text). The second one (given in brackets) corresponds to the 1-σ intervals used to define the domain where the true parameter values are expected to lie.

Parameters	λ4686 Å	λ6051 Å	simultaneous solution	Parameter status
$q = M_1/M_2$	1.803	1.803	1.803	adopted
i	77.°35 ± 0.°05 (0.°8)	77.°37 ± 0.°05 (0.°8)	77.°35 ± 0.°05 (0.°8)	adjusted
e	0.020 ± 0.001 (0.006)	0.020 ± 0.001 (0.006)	0.020 ± 0.001 (0.006)	adjusted
ω	33° ± 8° (19°)	33° ± 8° (19°)	33° ± 8° (19°)	adjusted
μ_1	0.782 ± 0.004 (0.037)	0.784 ± 0.004 (0.037)	0.783 ± 0.004 (0.037)	adjusted
μ_2	0.748 ± 0.003 (0.050)	0.751 ± 0.003 (0.050)	0.749 ± 0.003 (0.050)	adjusted
T_1 (K)	34 000	34 000	34 000	adopted
T_2 (K)	26 280 ± 150 (420)	26 230 ± 150 (420)	26 260 ± 150 (420)	adjusted
$L_1/(L_1+L_2)$	0.7380	0.7308	0.7379 | 0.7314	computed
$L_2/(L_1+L_2)$	0.2620	0.2692	0.2621 | 0.2686	computed
F_1	1.0	1.0	1.0	adopted
F_2	1.0	1.0	1.0	adopted
β_1	0.25	0.25	0.25	adopted
β_2	0.25	0.25	0.25	adopted
A_1	1.0	1.0	1.0	adopted
A_2	1.0	1.0	1.0	adopted
l_3	0.0	0.0	0.0	adopted
x_1	−0.213	−0.188	−0.213 | −0.188	adopted
y_1	0.724	0.643	0.724 | 0.643	adopted
x_2	−0.124	−0.112	−0.124 | −0.112	adopted
y_2	0.663	0.559	0.663 | 0.559	adopted
$\Delta\phi$	0.1537 ± 0.0007 (0.0011)	0.1537 ± 0.0007 (0.0011)	0.1537 ± 0.0007 (0.0011)	adjusted
t_0 ($HJD - 2\,450\,000$)	2399.909	2399.909	2399.909	computed
Relative radii (R/a)				
$r_1(pole)$	0.3127 ± 0.0016 (0.0148)	0.3135 ± 0.0016 (0.0148)	0.3131 ± 0.0016 (0.0148)	
$r_1(point)$	0.3351 ± 0.0022 (0.0203)	0.3362 ± 0.0022 (0.0203)	0.3357 ± 0.0022 (0.0203)	
$r_1(side)$	0.3205 ± 0.0018 (0.0164)	0.3214 ± 0.0018 (0.0164)	0.3210 ± 0.0018 (0.0164)	
$r_1(back)$	0.3290 ± 0.0020 (0.0182)	0.3300 ± 0.0020 (0.0182)	0.3295 ± 0.0020 (0.0182)	
$r_2(pole)$	0.2268 ± 0.0009 (0.0152)	0.2277 ± 0.0009 (0.0152)	0.2271 ± 0.0009 (0.0152)	
$r_2(point)$	0.2421 ± 0.0012 (0.0210)	0.2433 ± 0.0012 (0.0210)	0.2425 ± 0.0012 (0.0210)	
$r_2(side)$	0.2306 ± 0.0010 (0.0163)	0.2316 ± 0.0010 (0.0163)	0.2309 ± 0.0010 (0.0163)	
$r_2(back)$	0.2384 ± 0.0011 (0.0189)	0.2395 ± 0.0011 (0.0189)	0.2387 ± 0.0011 (0.0189)	

the most appropriate limb-darkening law at optical wavelengths for $T \geq 10\,000$ K. The rotation of both stars is assumed to be synchronous with the orbital one $F_1 = F_2 = 1$.

The adjustable parameters of the model were the following: the Roche lobe filling coefficients for the primary and secondary μ_1, μ_2 (calculated for the time of periastron passage), the average effective temperature of the secondary star T_2, the orbital inclination i, the eccentricity e, the longitude of periastron of the primary ω. While doing minimization, every model light curve was also shifted along the magnitude axis until the best fit between the model and observed curves was achieved.

Initial phases ψ of observational data points were calculated using the spectroscopic ephemeris of Table 1: $HJD = 2\,452\,400.284 + 2.^{\rm d}44070 \times E$. Since our model assumes an orbital phase ϕ equal to zero at the time of conjunction (the secondary star being in front), the observed light curve was then shifted in phase by $\Delta\phi$, according to $\psi = \phi - \Delta\phi$. The value of $\Delta\phi$ was determined by the minimum of the deviation between the observed and model light curves.

The estimation of adjustable parameters was done with the well-known simplex algorithm (Nelder and Mead's method) (Himmelblau 1971; Kallrath & Linnell 1987). In the vicinity of the minima found, additional calculations were done on a fine grid, in order to explore the details in shape of the deviation surface and to estimate the errors on the parameters. The resulting parameters for the solutions corresponding to λ4686Å, to λ6051Å and to the simultaneous adjustment at both wavelengths are presented in Table 5. Two kinds of confidence intervals have been computed and are also given in Table 5. The first one corresponds to a test of the adequacy of the model. The confidence intervals for the parameters are estimated using an absolute critical value of χ^2 corresponding to a significance level of 1%. This first approach rather defines the zones of variation of the parameters that still lead to an acceptation of the model. The obtained error bars are rather small. The second kind of confidence intervals corresponds to a critical value which is defined relatively to the obtained minimum χ^2 of the fit, increased by a value corresponding to a significance level

Table 6. CPD – 41° 7742 absolute parameters. The errors on the luminosities and the magnitudes were estimated assuming a formal error of 1000 K on the temperatures.

Parameters	Primary	Secondary
$a(R_\odot)$	23.18 ± 0.18	
$R(R_\odot)$	7.45 ± 0.45	5.39 ± 0.43
$M(M_\odot)$	17.97 ± 0.45	9.96 ± 0.22
$T(K)$	34 000	26 260
$\log(L_{\rm bol}/L_\odot)$	4.82 ± 0.07	4.09 ± 0.10
$\log(g)$	3.93 ± 0.48	3.96 ± 0.64
$M_{\rm V}$	−4.00 ± 0.21	−2.98 ± 0.31

of 0.1%. This latter interval corresponds to a 3-σ deviation and it has been transformed to a 1σ-uncertainty in the sake of coherence with the radial velocity adjustment. This approach is reminiscent to a search for the zone where lie the true values of the parameters.

Figure 2 exhibits the observed light curves corresponding to λ4686 Å and to λ6051 Å along with the model predictions of the simultaneous solution. The final model for CPD – 41° 7742 viewed at different orbital phases is presented in Fig. 3.

4. CPD – 41° 7742 orbital and physical parameters

4.1. Period P

Since the time base of our photometric campaign is *only* 28 days long, it provides little constraint on the period. Indeed the width of the associated peak in the periodogram is about 3.6×10^{-2} d^{-1}, yielding an uncertainty of about 2.1×10^{-2} d (corresponding to one tenth of the peak width) on the value of a period determined from the photometric set only. As a consequence, we choose to keep the period fixed at the value determined from the much longer time span of our spectroscopic data set. We thus retain $P = 2.44070$ d for CPD – 41° 7742.

4.2. Eccentricity e

The values of the eccentricity obtained from the analysis of the light curve and of the radial velocity curve are in excellent agreement. From our data, the separation between the two light minima is indeed clearly different from half an orbital cycle and the CPD – 41° 7742 orbit is thus slightly eccentric.

Recently, Sterken & Bouzid (2004) led a photometric campaign searching for new variables in NGC 6231. Using the period from Paper I, they obtained independent light curves for CPD – 41° 7742 in the Strömgren system. Surprisingly, their data set reveals almost perfectly symmetric light curves with the two light minima separated by exactly half a cycle, thus indicating either a non eccentric system or a longitude of periastron very close to 90 or 270°. No detailed analysis of the light curve has been published yet, but the differences between the Sterken & Bouzid observations and ours are quite intriguing.

In our data, the ingress of the secondary eclipse has been observed during three different nights spread over the one month run. It is therefore well defined and clearly indicates a slight eccentricity, except if some systematic biases were present. Our observing run lasted for 28 days and the CPD – 41° 7742 light curves displayed in Fig. 2 show smooth ellipsoidal variations and well behaved eclipses. Spread over at least two years and acquired more recently, the Sterken & Bouzid data set is larger, especially in the *y* and *b* bands, though with some gaps in the phase coverage. Their published light curves display several striking features. First, the primary eclipse seems to vary over the time: it presents different depths over different cycles and shows different ingress and egress shapes. Rapid variations are also observed slightly before the primary eclipse as well as slightly after the secondary one. The right wing of the secondary eclipse displays an inflection point in the *y* and *b* bands, while a strange *bifurcation* is observed in the *u* band. Finally, even outside the eclipses, the behaviour of the system is clearly not as quiet as in our data set (see Fig. 2).

While a change of the period or of the eccentricity with time is hard to explain, a change in the longitude of the periastron could mimic a non-eccentric system. Another hypothesis, also mentioned by Sterken & Bouzid, is that the observed dispersion of their light curves reveal the signature of some kind of activity in CPD – 41° 7742. Under this hypothesis, the system could have remained in a quiet state during the 11-cycle duration of our observations, while Sterken & Bouzid could have observed different activity states during the longer time-span of their campaign.

4.3. Longitude of periastron ω

The two values for the primary longitude of periastron obtained from the spectroscopy ($\omega = 149°$) and from the photometry ($\omega = 33°$) are clearly not consistent. In Paper I, we also computed an orbital solution including all published primary RVs and we obtained an argument $\omega = 27 \pm 31°$ closer to the latter photometric value. In principle, the light curve analysis is a more powerful tool to derive accurate values for ω, again from the separation between the two light minima. In Fig. 2, the separation between the primary and secondary eclipses is slightly larger than half a cycle. This indicates that the longitude of periastron is located between 0° and 90°, thus rejecting the much larger spectroscopic value.

In Paper I, we already noted the large dispersion in the values deduced from data sets associated with different lines, ranging from $\omega = 99°$ to 190°. We tentatively suggested that this was linked to the difficulty to accurately determine the periastron argument in such a slightly eccentric system. From our orbital solution, we however derived a reasonable error bar of 10°. While searching for the origin of the discrepancy between the photometric and spectroscopic solutions, we have investigated this point more deeply. Adopting the orbital parameters of Table 1, we computed a set of orbital solutions, varying the periastron argument from 0° to 360°. The obtained curves are very similar in shape; the main difference is a shift in radial velocity of an amplitude of about 10 km s^{-1} peak-to-peak. Comparing this with the root-mean-square (r.m.s.) residual of 4.8 km s^{-1} of our orbital solution gives us a first impression that the periastron argument is probably loosely constrained by the

radial velocity solution and that the quoted error-bar could be underestimated in this particular case.

In a second approach, we performed Monte-Carlo simulations adopting a Gaussian distribution of the errors on the measured radial velocities (RVs). For the primary, we adopted a standard deviation of 4.8 km s^{-1}, thus equal to the r.m.s. residual of our fit. For the secondary component, we accounted for the obtained ratio between the primary and secondary uncertainties, $s_y/s_x = 2.1$, as quoted in Paper I. Finally, for each observation, we scaled the dispersion according to the relative weighting adopted to compute the orbital solution. For each measured RVs, we randomly drew a series of 10 000 simulated RV points from these distributions, so building an equivalent number of simulated data sets. We then computed the corresponding orbital solutions using the same method as the one described in Paper I. We finally computed the distributions of the resulting orbital elements. This latter approach allows to estimate the errors assuming a random dispersion of the observed points. This evidently does not account for possible systematic errors or outstanding points.

We found that all the orbital parameters follow a Gaussian distribution, centered on the values of Table 1, except the longitude of periastron (and thus the time of periastron passage). The simulated 1-σ dispersions were found to be systematically, but not dramatically, higher than the published uncertainties. The difference is, on average, not larger than 80% but can reach a factor of 3. These new values for the uncertainties are quoted in the right column of Table 1. Concerning the distribution of the periastron argument, Fig. 4 shows that it significantly deviates from a Gaussian distribution. The width of the peak however does approximately correspond to the width of an equivalent Gaussian characterized by an estimated standard deviation equal to the one of the simulated distribution and by an equivalent surface. We thus retain the 1-σ dispersion of the distribution as a good estimator of the typical error on the determined spectroscopic value for ω. As a consequence, while the quoted error on the periastron argument was indeed underestimated in Paper I, this new estimate explains rather well the dispersion observed from time to time but still rules out the photometric value $\omega = 33°$. The origin of the inconsistency between the photometric and spectroscopic values, as well as with the Sterken & Bouzid (2004) data, should be looked for elsewhere.

One could indeed think of a possible physical effect that would modify the observed RV curve compared to the *true* curve of the system. In particular, a modification of the position of the spectral line centroids could produce a different RV value compared to the *true* velocity of the stars. In such a slightly eccentric binary as CPD – 41° 7742, it is also plausible that a small variation in the measured RVs could mimic orbits with quite a different periastron argument. Though the exact nature of the phenomenon is unknown, we tentatively linked it to a possible manifestation of the Barr effect.

The Canadian amateur astronomer, J. Miller Barr noted that the longitudes of periastron of spectroscopic binaries are not uniformly distributed between 0° and 360° (Barr 1908). Out of 30 spectroscopic binaries with elliptical orbits, apparently only four had ω between 180° and 360°, all others had their longitude of periastron in the first two quadrants. Barr advanced

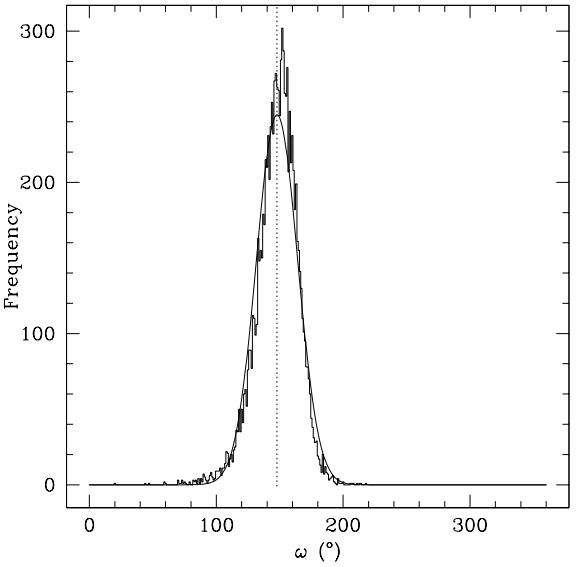

Fig. 4. Distribution of the longitude of periastron ω in a set of 10 000 simulated orbital solutions built using Monte-Carlo techniques (see text). An equivalent Gaussian characterized by the same estimated mean and standard dispersion and with an equivalent surface has been over-plotted.

two possible explanations for this systematic effect: either the pressure or temperature effects in the atmospheres of the stars shift their spectral lines with respect to their genuine orbital motion, or a non-uniform brightness of the components combined with a large rotational velocity causes the spectral lines to become asymmetric. Although Barr included several Cepheid variables in his sample, a similar effect was (re-)discovered by Struve (1948, see also the discussion by Batten 1983, 1988). Struve apparently found an excess of systems with ω in the first quadrant. He suggested that this could be due to streams of gas between the stars which lead to spurious eccentricities and values of ω in the first quadrant. The existence of the Barr effect was confirmed by the studies of Fracastoro (1979) and Howarth (1993). Fracastoro used the data from the VIIth Catalogue of orbital elements of spectroscopic binaries and found a distribution of ω for systems with large eccentricities ($e \geq 0.6$) that shows an excess of systems with $\omega = 0°$ and a flat minimum around $\omega = 250°$. The effect was most prominent in systems with short orbital periods. Howarth (1993) analysed the effect by means of non-parametric statistical tests, restricting his sample to systems with orbital solutions of reasonable quality. He found a statistically significant effect only for systems with orbital periods shorter than 3 days. The distribution of ω peaks at a preferred direction of $\omega \simeq 100°$, corresponding to a shallower, longer rising branch in the radial velocity curve and a steeper, shorter falling branch. Howarth interpreted this effect as the result of a gas stream from the primary towards the secondary, though no simulation of the phenomenon has been performed to check its exact influence on the RV curve.

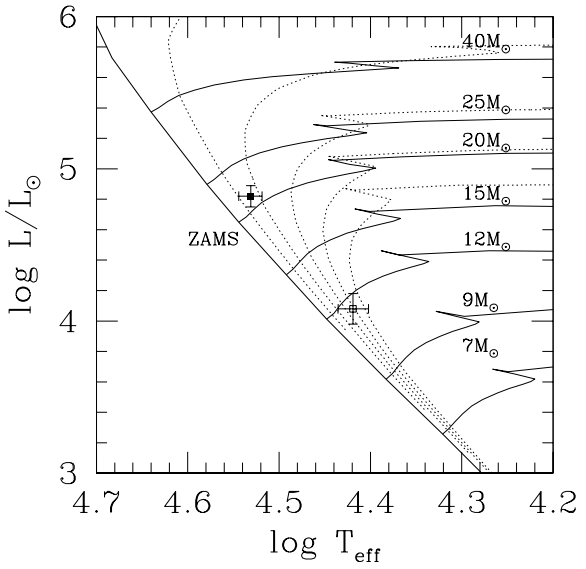

Fig. 5. Position of the primary (filled symbol) and secondary (open symbol) components of CPD – 41° 7742 in the H-R diagram. A formal error of 1000 K has been adopted on the temperatures. Solid lines: evolutionary tracks from Schaller et al. (1992) for different initial masses. Dotted lines: isochrones ranging, from left to right, from 2 to 10 Myr with a step of 2 Myr.

4.4. Time of periastron passage T_0

The difference in the spectroscopically and photometrically determined times of periastron passage directly results from the inconsistency between the values of the periastron argument derived using the two techniques. This problem has already been extensively described in the previous paragraph (Sect. 4.3). We just note here that adopting a periastron argument $\omega = 33°$ yields a value for the time of periastron passage of $T_0 = 2\,452\,399.498$ (HJD).

4.5. CPD – 41° 7742 physical parameters

Thanks to the light curve analysis, the inclination of the system is now very well constrained. Combining this with the spectroscopic information of Table 1, we derived absolute values for the system separation and the star radii and masses. We also derived their luminosity and the surface gravity. The physical parameters of both stars are given in Table 6. With an absolute radius of $R_1 = 7.45 \pm 0.45$ R$_\odot$, the primary component is slightly smaller than typical O9 V stars. Howarth & Prinja (1989), Schmidt-Kaler (1982) and Vacca et al. (1996) respectively listed radii of 8, 9.5 and 8.8 R$_\odot$. The observed radius is however larger than the typical O9.5 V radius of 7 R$_\odot$ given by Howarth & Prinja. Adopting the bolometric correction of Humphreys & McElroy, $BC = -3.3 \pm 0.1$, we derived a visual absolute magnitude $M_{V,1} = -4.00 \pm 0.21$, fainter than the values of −4.5, −4.2, −4.5 and −4.43 respectively reported by Humphreys & McElroy (1984), Howarth & Prinja (1989), Schmidt-Kaler (1982) and Vacca et al. (1996), though again in agreement with the slightly later spectral-type O9.5 V. Comparing the obtained values with those of other eclipsing early-type binaries listed by Gies (2003) clearly indicates that the physical parameters of the primary in CPD – 41° 7742 correspond to the observed range for O9 dwarfs. Vaz et al. (1997) reported a mass of 19 M$_\odot$ for the O9 V component in HD 165921 though with a relatively smaller radius ($R = 6.13$ R$_\odot$). On the other hand, the CPD – 41° 7742 primary is slightly larger and heavier than the O9.5 dwarf components in CPD−59°2603 (Rauw et al. 2001, $M = 14.5$ M$_\odot$, $R = 4.9$ R$_\odot$), HD 193611 (Popper & Hill 1991, $M = 16.6 + 16.3$ M$_\odot$, $R = 7.4 + 7.4$ R$_\odot$) or HD 198846 (Simon et al. 1994; Hill & Holmgren 1995; Burkholder et al. 1997, $M = 17.0 - 17.7$ M$_\odot$, $R = 5.7 - 7.7$ R$_\odot$). The dwarf nature of the primary star is consistent with the derived surface gravity (altough the corresponding error is rather large).

From the effective temperature calibration of Humphreys & McElroy, the secondary temperature corresponds to a spectral sub-type B0.5, in rough agreement with the B1 spectral type obtained from spectroscopy. Its radius and visual magnitude however fall within the expected range for B1-2 stars (Humphreys & McElroy 1984; Schmidt-Kaler 1982). The secondary is also slightly smaller and lighter than the B1 V component in HD 175514 (Bell et al. 1987, $M = 13.5$ M$_\odot$, $R = 5.9$ R$_\odot$). All in all, and accounting for the uncertainties on the spectroscopic data, adopting a B1.5 V spectral sub-type for the secondary in CPD – 41° 7742 yields a better match between its physical parameters and the typical observed and theoretical values expected for such a star.

The locations of the CPD – 41° 7742 components in the H-R diagram are shown in Fig. 5 together with the evolutionary tracks of Schaller et al. (1992). A rough interpolation from these tracks yields initial masses $M_1^{(0)} = 23.7$ M$_\odot$ and $M_2^{(0)} = 11.1$ M$_\odot$ and current ages between 3 and 8 Myr. These ages do well reproduce the range of derived values for the NGC 6231 cluster (see the cluster literature review in Sana et al. 2005a). In such a small time span, the actual masses of the stars remain close to their initial masses and are thus quite larger than the observed masses of about 18 and 10 M$_\odot$ (Table 6). In a binary system, mass exchange between its components, through e.g. Roche lobe overflow, could alter their evolutionary status compared to single star models. From the photometric light curve, CPD – 41° 7742 is actually a well detached system. Due to its young age, it is thus very unlikely that the system could have undergone such a phenomenon (now interrupted) in its past history. New evolutionary tracks that account for the effect of rotation could help to investigate this apparent discrepancy. Finally, comparing the absolute magnitudes obtained in Table 6 with the visual magnitude $V = 8.228$ of CPD – 41° 7742 (Sung et al. 1998), we estimated the distance of the object. We adopted a colour excess $E(B-V) = 0.49$ and $R = 3.3$ as derived by Sung et al. (1998). We finally obtained $DM = 10.92 \pm 0.16$, in excellent agreement with the cluster average distance modulus $DM = 11.07 \pm 0.04$ (Sana et al. 2005a).

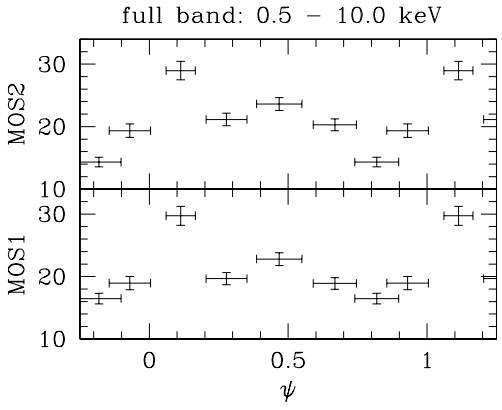

Fig. 6. Net EPIC MOS count rates of CPD – 41° 7742 as a function of orbital phase and averaged over the duration of each pointing (from Sana et al. 2005a). The vertical axes are in units 10^{-3} cnt s^{-1}. The horizontal *error-bars* indicate the extension in phase of the corresponding pointing.

5. X-ray light curves and spectral analysis

The X-ray light curves of CPD – 41° 7742 as seen by the two MOS cameras are shown in Fig. 6. The count-rates, averaged over the duration of each pointing, were taken from the NGC 6231 X-ray source catalogue of Sana et al. (2005a) and were obtained using the SAS task *emldetect*. The count-rates are thus corrected for the effects of exposure, vignetting and finite size of the extraction region. They also account for the background subtraction. It is clear from Fig. 6 that the X-ray emission from CPD – 41° 7742 displays strong signs of variability. A χ^2 test of hypothesis consistently rejects, at the 1% significance level, the null hypothesis of constant rates in the [0.5 - 10.0 keV] band and in the M_X and H_X bands. Fig. 6 also indicates that the phase coverage of the orbital cycle is almost complete with only a small gap slightly before phase $\psi = 0.2$. To increase our time resolution, we also extracted background-corrected light curves with a time binning of 5 ks. Figure 7 shows that the count rate changes by about a factor two over relatively short time scales. These variations are also seen in the different energy ranges (Fig. 8) and are most prominent in the intermediate (M_X) band. As in Fig. 7, they suggest a double-peaked light curve with two broad maxima around phases $\psi \approx 0.1$ and 0.5. From the top panels of Fig. 7, we conclude that the observed modulations are clearly not due to background fluctuations. Note that, in Figs. 7 and 8, no correction for the limited encircled energy fraction has been applied, neither for the vignetting or exposure. This explains the lower count-rates obtained compared to Fig. 6.

One of the main pictures in the X-ray light curve is a sensible decrease of the signal between phase $\psi = 0.27$ and 0.45, which almost exactly corresponds to the time of the secondary minimum in the optical light curve. The observed modulations are probably phase-locked since, for example, the two wings of the *eclipse* have been observed during two different orbital revolutions. However, except near $\psi = 0.85$, the different pointings do not overlap in phase. One can therefore not definitively assert the phase-locked behaviour of the observed X-ray light curves.

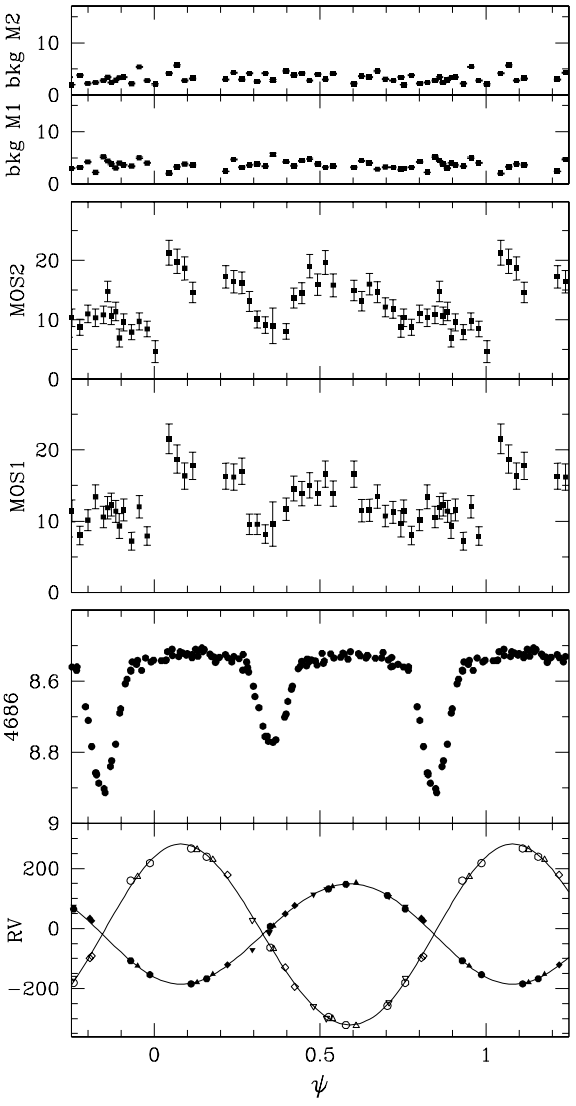

Fig. 7. Top panel: EPIC MOS background count rates in the [0.5-10.0 keV] band. **Middle panel:** CPD – 41° 7742 EPIC MOS background-corrected count rates in the same energy range. The time binning of these two panels is 5 ks. The vertical axes are in units 10^{-3} cnt s^{-1}. No correction for the limited encircled energy fraction has been applied. **Lower panel:** RV curve (in km s^{-1}) and optical light curve (in mag) of CPD – 41° 7742. Note the coincidence of the X-ray drop around $\psi = 0.35$ and the time of conjunction with the primary star being in front, as well as the lack of coincidence of the secondary eclipse with the passage at the systemic velocity.

Figure 7 seems thus to indicate two different emission levels: a higher state between $\psi \approx 0.0$ and 0.5, during which the *eclipse* is observed, and a lower state between $\psi \approx 0.6$ and 1.0, where no counterpart of the primary eclipse can be seen.

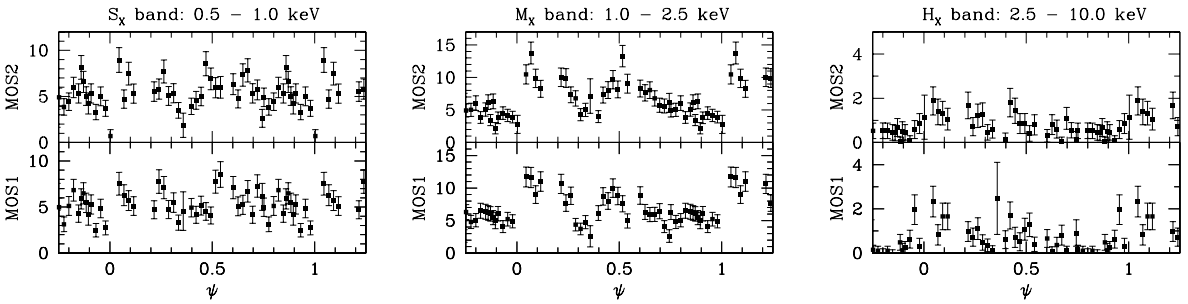

Fig. 8. CPD – 41° 7742 EPIC MOS background-corrected count rates in the three energy bands as a function of orbital phase. The time binning is 5 ks. The vertical axes are in units 10^{-3} cnt s^{-1}. No correction for the limited encircled energy fraction has been applied.

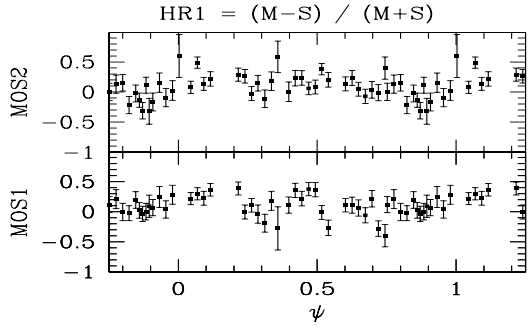

Fig. 9. Hardness ratios vs. phase for the EPIC MOS instruments. The adopted definition for HR_1 is given on top of the panel.

The hardness ratio curves are shown in Fig. 9. Though the error bars are quite large, they seem to indicate that the emission is slightly softer around phase $\psi = 0.3$, so approximately at the time of conjunction, while it is presumably harder at the maximum of the emission.

While the orbit is presumably not circular, the value of the eccentricity is pretty small and it is unlikely that the variation of the distance between the two stars plays a significant role in CPD – 41° 7742. In consequence, the observed modulations of the X-ray emission are more probably due to a modification of the line of sight towards the system while it is revolving around its center of mass. The observed X-ray light curves will be discussed in the framework of a wind interaction model presented in the next section (Sect. 6.3).

As a next step in the analysis, we attempt to constrain the physical properties of the X-ray emission by adjusting a series of models to the obtained spectra for each pointing. We simultaneously fitted the two MOS spectra using the XSPEC software v.11.2.0 (Arnaud 1996). Using the $B - V$ colours quoted by Baume et al. (1999) and Sung et al. (1998), we infer a colour excess of about $E(B - V) = 0.49$ for CPD – 41° 7742. The corresponding ISM neutral hydrogen column density amounts to $N_{\rm H}^{\rm ISM} = 2.8 \times 10^{21}$ cm^{-2}. In the spectral fits, we thus requested a column density larger or equal to $N_{\rm H}^{\rm ISM}$. The best spectral fits are obtained for a two-temperature `mekal` thermal plasma model (Mewe et al. 1985; Kaastra 1992) with two independent absorbing columns. These fits indicate a soft ($kT \sim 0.6$ keV) slightly absorbed plus a harder ($kT \sim 1.0$ keV) and more heavily absorbed component. However, they only provide an upper limit on the absorbing column associated to the soft component. As for HD 152248 (Sana et al. 2004), fixing this additional soft column to zero yields even better fits, characterized by more stable solutions. The best-fit parameters are listed in Table 7 and tend to indicate that the CPD – 41° 7742 X-ray spectrum is significantly harder when the total flux is larger. More accurate information is however difficult to obtain since, as can be deduced from the modulations of the hardness ratios (Fig. 9), the spectral variations are probably averaged out over the 30 ks duration of a pointing. Unfortunately, smaller bin sizes do not allow to obtain spectra of a sufficient quality to derive reliable constraints on the spectral properties.

The combined MOS spectra obtained from the merging of the six XMM-*Newton* observations are shown in Fig. 10 together with the best fit 2-T model. Though the general quality of the fit is relatively good, the model tends to underestimate the fluxes at high energy (> 4 keV). This could indicate the existence of a high energy component as well as the presence of the Fe K line at 6.7 keV. The merged spectra do unfortunately not have a sufficient quality at high energy to constrain this probable additional component.

6. CPD – 41° 7742 X-ray properties

6.1. X-ray emission from the stellar components

The X-ray emission from massive stars presumably comes from shell collisions within the lower layers of their winds, which result from the growing of radiatively-driven wind instabilities (Feldmeier et al. 1997). It is expected that the bulk of the emission is produced in a zone extending to about five times the stellar radius. Within a binary system with an inclination close to 90°, we thus expect only a small fraction of this extended emission zone to be occulted by the motion of one companion in front of the other. In consequence, because of the much larger emission zone, the eclipses in the X-ray domain are probably not as clearly marked as in the optical.

However, the CPD – 41° 7742 X-ray light curve (Fig. 7) shows a clear decrease – around $\psi = 0.35$ – almost perfectly synchronized with the optical secondary eclipse. This suggests a different geometry and, probably, the presence of a localized

Table 7. Results of the simultaneous fits of the MOS1 and MOS2 spectra with XSPEC. The model used is $\texttt{wabs}_{\rm ISM}$ * ($\texttt{wabs}_1$ * $\texttt{mekal}_1$ + $\texttt{wabs}_2$ * $\texttt{mekal}_2$). The term $\texttt{wabs}_{\rm ISM}$ was fixed to the interstellar value ($N_{\rm H,ISM}$ = 0.28 10^{22} cm^{-2}); $\texttt{wabs}_1$ was hold to zero ($N_{\rm H,1}$ = 0 cm^{-2}, see text). The first and second columns give the phase and the observation number. The next six columns (Cols. 3 to 8) provide the best-fit parameters while Col. 9 lists the corresponding reduced chi-square and the associated number of degrees of freedom (d.o.f). $N_{\rm H}$ yields the absorbing column (in units 10^{-22} cm^{-2}), kT is the model temperature (in keV) while *norm* is the normalisation factor (expressed in 10^{-4} cm^{-5}, $norm = \frac{10^{-14}}{4\pi d^2}\int n_{\rm e} n_{\rm H} dV$ with d, the distance to the source – in cm –, $n_{\rm e}$ and $n_{\rm H}$, the electron and hydrogen number densities – in cm^{-3}). Columns 10 to 13 provide the observed fluxes (in 10^{-14} erg cm^{-2} s^{-1}) in the 0.5 - 10.0 keV energy band and in the S_X, M_X and H_X bands respectively. The last line of this table provides the best-fit parameters adjusted on the spectra extracted from the cumulated six pointings.

ψ [1]	Obs. # [2]	$N_{\rm H,1}$ [3]	kT_1 [4]	$norm_1$ [5]	$N_{\rm H,2}$ [6]	kT_2 [7]	$norm_2$ [8]	χ^2_ν (d.o.f.) [9]	$f_{\rm X}$ [10]	$f_{\rm X,S}$ [11]	$f_{\rm X,M}$ [12]	$f_{\rm X,H}$ [13]
0.113	2	0.0	$0.62^{+.06}_{-.08}$	$0.81^{+.15}_{-.13}$	$0.79^{+.33}_{-.28}$	$1.22^{+.26}_{-.17}$	$2.71^{+.74}_{-.70}$	0.63 (59)	21.0	5.6	11.5	3.8
0.278	5	0.0	$0.52^{+.14}_{-.18}$	$0.65^{+.09}_{-.10}$	$0.74^{+.25}_{-.19}$	$0.97^{+.27}_{-.13}$	$1.64^{+.42}_{-.52}$	1.21 (60)	13.0	4.7	7.0	1.3
0.468	3	0.0	$0.52^{+.10}_{-.17}$	$0.66^{+.09}_{-.10}$	$0.76^{+.18}_{-.16}$	$0.95^{+.12}_{-.13}$	$2.28^{+.65}_{-.56}$	0.82 (81)	15.4	4.9	8.7	1.8
0.668	6	0.0	$0.61^{+.05}_{-.14}$	$0.75^{+.14}_{-.28}$	$0.74^{+.41}_{-.36}$	$0.93^{+.36}_{-.35}$	$1.17^{+2.10}_{-.52}$	0.85 (64)	12.7	5.3	6.5	0.9
0.819	1	0.0	$0.40^{+.10}_{-.08}$	$0.76^{+.14}_{-.20}$	$0.52^{+.27}_{-.21}$	$0.81^{+.12}_{-.21}$	$0.94^{+.48}_{-.20}$	1.08 (53)	10.2	5.0	4.7	0.5
0.930	4	0.0	$0.35^{+.19}_{-.09}$	$0.63^{+.30}_{-.23}$	$0.46^{+.19}_{-.16}$	$0.75^{+.14}_{-.08}$	$1.61^{+.49}_{-.48}$	1.22 (46)	11.8	5.2	6.0	0.6
Merged		0.0	$0.59^{+.03}_{-.09}$	$0.74^{+.06}_{-.08}$	$0.73^{+.13}_{-.11}$	$1.05^{+.11}_{-.08}$	$1.39^{+.20}_{-.10}$	1.09 (209)	14.0	5.2	7.3	1.5

emission component, in addition to the intrinsic emission of the two stars. To match the observed light curve, this component should be occulted around ψ = 0.35. It should thus be associated either with the primary inner side, or with the secondary inner or outer sides. The emission level also appears to be lower between ψ = 0.6 and 1.0, thus when the line of sight points both towards the primary inner side or the secondary outer side. The second possibility (i.e. the secondary inner side) therefore seems to best describe the main features of the X-ray light curve, at least qualitatively. In Sect. 6.3, we present a phenomenological model that associates an extra X-ray emission with the secondary inner side.

Using the relations of Berghöfer et al. (1997) and bolometric luminosities from Table 6, we obtained X-ray luminosities of log($L_{\rm X}$) = 31.51 and 30.69 (erg s^{-1}) respectively for the O9 and B1-1.5 components in the band 0.1 – 2.0 keV. Accounting for the distance modulus of the cluster DM = 11.07, this corresponds to unabsorbed fluxes of $f_{\rm X}$ = 9.99 and 1.54×10^{-14} erg cm^{-2} s^{-1}. Though the energy bands considered are slightly different, we can compare these predictions with the values obtained from the X-ray spectral fits (Table 8). It appears that, even at its minimum of emission ($\psi \sim 0.82$), CPD – 41° 7742 is at least twice brighter than expected from the Berghöfer et al. relations. Part of the gap between the observed and predicted values could however be filled by the following considerations. First, the dispersion around the Berghöfer et al. relations is quite large and does not allow an accurate determination of the X-ray luminosities. Second, Massa et al. (1984) reported that the winds from the main sequence B stars in NGC 6231 are particularly strong. The B star in CPD – 41° 7742 could thus have a particularly powerful wind for its spectral type, producing stronger shocks within its lower layers and, subsequently, an enhanced X-ray emission. Sana et al. (2005b) further reported that, in NGC 6231, the B stars seem to follow a brighter $L_{\rm X}/L_{\rm bol}$ relation than predicted from Berghöfer et al. (1997). From this new relation, the B1-1.5 component in CPD – 41° 7742 could be at least three times brighter, yielding a luminosity of a few 10^{31} erg s^{-1}.

Table 8. Unabsorbed fluxes (in 10^{-14} erg cm^{-2} s^{-1}), i.e. fluxes corrected for the interstellar absorption ($N_{\rm H,ISM}$ = 0.28 10^{22} cm^{-2}), according to the best-fit models presented in Table 7. The last column gives the total X-ray luminosity (in erg s^{-1}) assuming a distance modulus DM = 11.07.

ψ [1]	Obs. # [2]	$f_{\rm X}^{\rm unabs}$ [3]	$f_{\rm X,S}^{\rm unabs}$ [4]	$f_{\rm X,M}^{\rm unabs}$ [5]	$f_{\rm X,H}^{\rm unabs}$ [6]	log($L_{\rm X}$) [7]
0.113	2	36.2	16.4	15.8	4.0	32.06
0.278	5	25.4	14.2	9.8	1.4	31.91
0.468	3	28.7	14.8	12.1	1.8	31.96
0.668	6	25.8	15.5	9.3	1.0	31.92
0.819	1	23.8	16.4	6.9	0.5	31.88
0.930	4	25.7	16.4	8.7	0.6	31.92
Merged		27.2	15.4	10.3	1.5	31.95

6.2. CPD – 41° 7742 wind properties

The wind properties of the two components of CPD – 41° 7742 are not known. We however used the newly derived physical parameters of the stars to get an insight into their wind strengths. We estimated their mass-loss rates using the mass-loss recipes from Vink et al. (2000, 2001). We obtained, for the primary, log($\dot{M}_1$) = −7.06 ($M_\odot$yr^{-1}). The temperature of the secondary component however falls within the bi-stability jump region. Using the recommendations from Vink et al., we estimated the position of the bi-stability jump to be located at about 22 800 K for the particular stellar parameters of the secondary. This puts the companion on the hot side of the jump, yielding thus log($\dot{M}_2$) = −8.74 ($M_\odot$yr^{-1}). We estimated the terminal wind velocities by first computing the escape velocities and then adopting the average ratio $v_\infty/v_{\rm esc}$ = 2.6 as appropriate for the winds of the stars on the hot side of the stability jump. We respectively obtained terminal velocities of $v_{\infty,1}$ =

2380 km s^{-1} and $v_{\infty,2}$ = 2150 km s^{-1} for the two components of CPD – 41° 7742. While these values are typical for O-type stars, the secondary terminal velocity seems quite large for a typical B1 dwarf. As stated above, Massa et al. (1984) reported particularly strong winds for the B dwarfs in NGC 6231. For example, they derived, for the single B1 V star CPD–41° 7719, a terminal wind velocity close to 2300 km s^{-1}, thus very near our estimate for the B component in CPD – 41° 7742.

6.3. A wind interaction in CPD – 41° 7742

Using the estimated wind parameters, we computed the position of the ram pressure equilibrium surface that typically indicates the location of a possible wind-wind collision. For this purpose, we adopted a β = 1 velocity law, as appropriate for the hot star winds. Due to its larger mass-loss rate, the primary wind clearly overwhelms the secondary wind and no equilibrium is possible. In consequence, the O-star wind should crush on the B-star surface, preventing the secondary wind to develop towards the primary star. Under the above hypotheses, the primary wind luminosity at the distance of the secondary surface is about $\log(L_{w,1}) = \log(\frac{\dot{M}_1 v_1^2}{2}) \sim 34.7$ (erg s^{-1}). Accounting for the secondary radius and its distance to the primary, a fraction of about 2.7% of the O9 V wind is intercepted by the secondary and we therefore expect the shocked plasma to be heated to temperatures of a few 10^7 K, thus generating a substantial amount of X-rays. According to the formalism of Usov (1992), and using a primary wind pre-shock velocity of 1380 km s^{-1}, the X-ray emission generated by such a wind-photosphere interaction should be about $\log(L_X) \approx 32.8$ (erg s^{-1}) for a purely radiative interaction (Usov's Eq. 80) and $\log(L_X) \approx 30.7$ (erg s^{-1}) in the adiabatic case (Usov's Eq. 79, adopting a solar chemical composition for the wind). Following Stevens et al. (1992), the ratio between the characteristic cooling time and flow time is $\chi = t_{cool}/t_{flow} \approx 5.2$, indicating a mainly adiabatic collision.

However, the interaction region is immersed in the intense UV photon field of the secondary. Inverse Compton cooling (Comptonization) could thus be significant, yielding a higher cooling rate, thus a lower value for the χ parameter. In addition, under the influence of the radiative pressure of the secondary, the acceleration of the primary wind may be slowed down (the so-called *radiative inhibition* effect, Stevens & Pollock 1994). According to the formalism developed by these latter authors, the mass-loss rate on the axis should not be affected by more than 1%. From a crude interpolation of their results, the primary wind velocity at the secondary surface might however be reduced by about one third. In consequence, the wind kinetical energy would be cut down by a factor of about two. Hence, radiative inhibition might significantly affect the value of the χ parameter, which depends on the fourth power of the velocity. Assuming a factor 2/3 on the velocity reached by the primary wind at the distance of the secondary surface, we obtain $\chi \approx 1.0$. Both under the influence of Comptonization and of radiative inhibition, the shock region might thus shift towards the radiative regime.

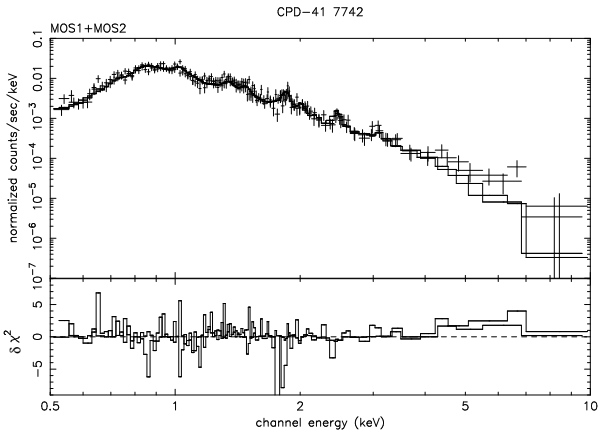

Fig. 10. Least square simultaneous fits of the cumulated MOS1 and MOS2 spectra of CPD – 41° 7742 with absorbed 2-T `mekal` models. The bottom panel shows the contributions of individual bins to the χ^2 of the fit. The contributions are carried over with the sign of the deviation (in the sense data minus model).

Using the formalism of Gayley et al. (1997), we also investigated the possibility to alter the wind-photosphere interaction by sudden radiative braking. In such a phenomenon, the wind of the primary star could be suddenly brought to a stop due to the radiative pressure coming from the companion. The main effect of radiative braking is to modify the position of the dynamical ram pressure equilibrium surface by pushing it further away from the secondary star. In certain cases, radiative braking could be strong enough to prevent the primary star wind to actually crush on the secondary surface, thus yielding a wind-wind interaction structure rather than a wind-photosphere interaction. Adopting the known stellar parameters, we computed the radiative braking coefficient. We then used different values of the CAK parameters (Castor et al. 1975) appropriate for effective temperatures around 30 kK. According to the values of these coefficients as given by different authors (Pauldrach et al. 1986; Shimada et al. 1994; Puls et al. 2000), the radiative braking can, or can not, disrupt the wind-photosphere interaction. It is thus impossible to conclude on this point. However, even when the braking occurs, the interaction is moved only slightly away from the secondary star surface. Though the shock structure would be quite different, the geometry of the emitting region will probably remain rather similar, with an extra emission component mainly located close to the secondary inner surface.

A phenomenological model

To estimate the influence of such a wind interaction on the observed X-ray light curve, we built a simple geometrical model presented in Fig. 11. We adopted a circular orbit, spherically symmetric stars and winds, and a β = 1 acceleration law for the primary wind. Assuming a totally radiative interaction, we considered that, when encountering the secondary star surface, the kinetic energy associated to the normal velocity component of the incident wind flow is totally dissipated into thermal en-

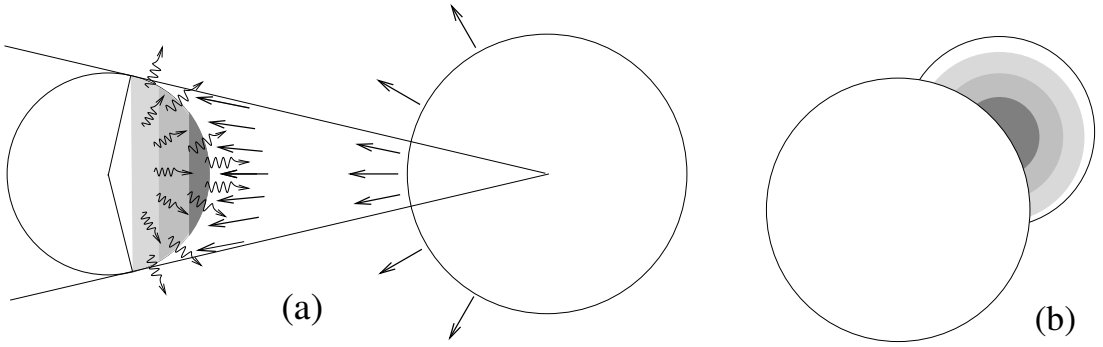

Fig. 11. Schematic view of the geometrical wind-photosphere interaction model in CPD – 41° 7742. **(a)** A view from above the orbital plane: the secondary star intercepts a small fraction of the primary wind, of which part of the kinetic energy is turned into heat. **(b)** A similar view along the line of sight. The different degrees of shading of the secondary surface represent the different X-ray luminosities, these latter being larger closer to the system axis.

ergy. We thus computed the amount of energy re-emitted by each elements of the secondary surface. Then, accounting for the orbital inclination and the possible occultation by the primary star, we computed the interaction contribution to the observed X-ray light curve. We noticed above the possibility of radiative braking to occur within the system. We caution however that it should not alter much this simple model. Indeed, in the case of a wind-wind collision, the interaction region should still be located near the secondary star surface, so that the geometry of the problem would be only slightly modified. The emission from the secondary shock would further be very limited. Indeed, so close to the surface, the radiative acceleration could not have been very efficient yet. The secondary wind velocity is thus probably of the order of the photospheric thermal velocity, therefore close to 20 km s^{-1}. Under these hypotheses, the possible contribution of the secondary shock to the total X-ray emission would thus be about 10^{29}erg s^{-1}, at least one order of magnitude below the other emission components.

The results of this simple model are presented in Fig. 12 (upper panel) and provide an upper limit on the actual contribution of such an interaction. Indeed, as stated above, the interaction is probably not fully radiative, so that only a fraction of the incoming energy is effectively radiated. Radiative inhibition might also reduce the wind velocity, giving rise to a weaker shock, hence to a weaker emission than considered here. In Fig. 12, the occultation of the interaction zone by the primary is clearly seen ($\psi \sim 0.35$), while the interaction does not provide any contribution when the secondary is turning its outer side to the observer ($\psi \sim 0.8 - 0.9$). In this simple form, this phenomenological model indeed predicts the higher emission slightly before and after the secondary eclipse, while the secondary inner side is facing the observer, and the lower emission state half a cycle later, when the interaction zone is hidden by the secondary body. It also reasonably reproduces the width of the observed *eclipse* in the X-ray light curve.

In a second step, we try to provide a moderate tuning to the model, in order to investigate to which degree it can match the observed modulations. According to the model, no emission from the interaction is expected around $\psi = 0.8 - 0.9$, and it should only provide a faint contribution at the time of the secondary minimum. At those particular phases, we thus probably observe the intrinsic emission of the two stars which, as explained above, is only slightly affected by the eclipses because of its wide extension. Correcting the observed light curve for the limited encircled energy fraction, the intrinsic emission from the two stars gives about 14×10^{-3} cnt s^{-1} in the two MOS instruments. From Table 7, this approximately corresponds to an observed flux about 10.2×10^{-14} erg cm^{-2} s^{-1}. We also note that the model provides unabsorbed fluxes while the observed count rates have suffered interstellar absorption. Comparing the values of the absorbed and unabsorbed fluxes (Tables 7 and 8), we estimate the ISM material to absorb about half of the flux at the considered energy.

At this stage, the model predicts an emission rate still much larger than the observed emission. To better match the observations, we had to divide the predicted flux again by a factor of 6, so that the maximum contribution of the interaction zone to the observed flux is now about 10×10^{-14} erg cm^{-2} s^{-1}. This last step finds a relative justification in the fact that, as discussed above, the present purely radiative model only provides an upper limit to the X-ray emission emerging from the interaction zone. In addition, effects that might reduce the shock strength, such as radiative inhibition, are not accounted for. Assuming radiative braking to take place, one might also think that some emission may originate from the trailing arm of the shock cone. In such a configuration, the extra emission from the collision would not drop to zero around $\psi \sim 0.8-0.9$. In the current fully radiative model the plasma immediately cools down after the shock. By nature, it could thus not produce an extra-emission at these particular phases. Such a contribution from the arms of the shock cone would however be less affected by the eclipses in the system and, as a first approximation, one can consider that it has been accounted for in the empirical pedestal adopted in Fig. 12. This latter is indeed higher than expected from the sole Berghöfer et al. (1997) relations for the intrinsic emission of the early-type stars in the system. It is clear that the reality is probably different from this idealized situation. It is not our purpose to over-interpret the present model; our aim was to show that, using reasonable assumptions, an interaction re-

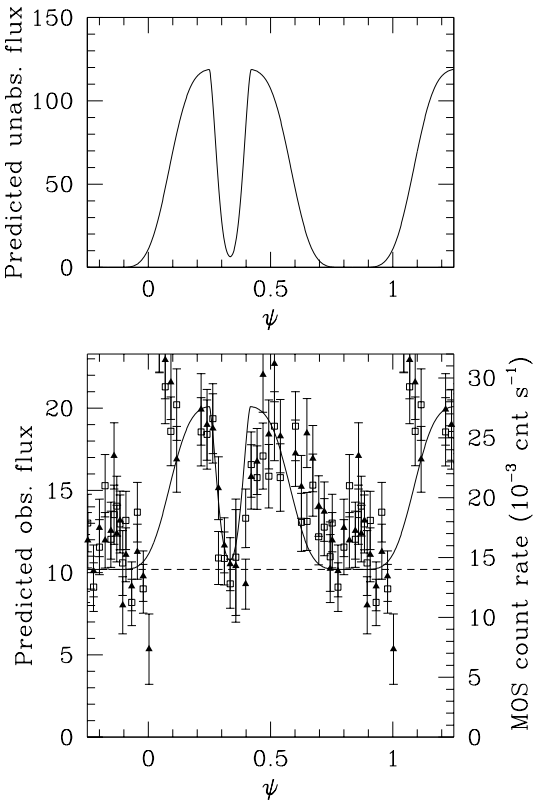

Fig. 12. Upper panel: Predicted unabsorbed flux emitted by a radiative wind-photosphere interaction in CPD – 41° 7742. **Lower panel:** Tuned phenomenological model (thick line) overplotted on the observed X-ray light curves. Filled triangles and open squares respectively show the background-corrected EPIC MOS1 and MOS2 count rates in the 0.5-10.0 keV energy band. These count rates have been corrected for the limited size of the extraction region. Flux axes are in units of 10^{-14} erg cm^{-2} s^{-1} in both panels. The dashed line gives the adopted intrinsic contribution from the two stellar components of CPD – 41° 7742. It acts as a pedestal.

gion located on, or near, the secondary surface can reproduce the main features of the observed X-ray light curve.

From Fig. 12, the time of the beginning of the X-ray eclipse is well reproduced by our model. The right wing of the eclipse is however slightly larger, suggesting that the interaction is more extended on the surface side opposite to the orbital motion. Similarly, the drop in emission around $\psi \approx 0.6$ occurs slightly later than expected from our model, which means that the X-ray emitting region should remain visible slightly longer, a condition which is not encountered by the previous suggestion. Clearly, Fig. 12 shows that the observed modulations in the X-ray light curves is dominated by an extra-emission component associated with the secondary inner surface. However, the details of the phenomenon could be more complicated as suggested by the observed delays in the rising and falling branches near $\psi = 0.4$ and 0.6. Finally, the hardness ratio curves indicate that the hardest emission is observed at the time of the two emission maxima. This is expected if the extra emission is produced in a wind interaction region, which provides typically harder X-rays than the intrinsic emission from the stars.

7. Final remarks and conclusions

In the first part of this paper, we presented optical photometry of CPD – 41° 7742. Adopting the period obtained from Paper I, the analysis of the system light curves indicates that CPD – 41° 7742 is a well detached system with an inclination close to 77°. The obtained curves display two eclipses with a separation slightly different from half an orbital cycle, thus indicating a small eccentricity, in agreement with the results of Paper I. Combining the spectroscopic and photometric analyses, we derived the absolute physical parameters of the stellar components and confirmed that the system is formed by two dwarf early-type stars with masses, sizes and luminosities relatively close to typical values expected both from observational and theoretical works.

The photometric and spectroscopic data sets however provide discrepant values for the longitude of periastron. Independent observations by Sterken & Bouzid (2004) also tend to indicate either a periastron argument close to 90 or 270° or a zero eccentricity. Their light curves, obtained over at least two years, also display intriguing signs of variability. Clearly, further observations are needed to elucidate these apparent discrepancies.

In the second part of the present paper, we focused on recent XMM-*Newton* X-ray observations of the system. The X-ray emission from CPD – 41° 7742 is well described by a two-temperature thermal plasma model with energies close to 0.6 and 1.0 keV, thus slightly harder than typical emission from early-type stars. The X-ray light curve of the system is clearly variable both in the total and in the different energy ranges; the emission level is higher when the primary is in front of the secondary. During the high state, the system shows a drop of its X-ray emission that almost exactly matches the optical secondary eclipse. Assuming that the X-ray light curve is reproductible, we interpreted this as the signature of a wind interaction phenomenon in which the overwhelming primary wind crushes on the secondary star surface. Alternatively, the wind-photosphere interaction could be disrupted by sudden radiative braking, yielding a wind-wind interaction located close to the secondary surface, and displaying thus a similar geometry. We expect this phenomenon to produce a substantial amount of X-rays, which could be the major source for the observed modulations in the EPIC MOS light curves. As a next step, we built a simple phenomenological model that associates an extra X-ray emission component with the inner side of the secondary star surface. Though limited by some simplifying assumptions, this model renders the main properties of the observed variations and lends thus further support to our interpretation of the X-ray light curve.

At this stage, several important questions remain however unanswered. The exact influence of the wind interaction, and of the generated X-ray emission, on the secondary surface properties is very difficult to estimate. We carefully inspected the high resolution high signal to noise spectra from Paper I but could

not find any systematic differences in the secondary spectra obtained when this star is showing either its inner or its outer face to the observer. As a final check, we put a point-like X-ray source at a distance of $1.1 \times R_2$ from the center of the secondary star on the system axis. We assigned to this source a luminosity of 10^{33} erg s^{-1}, which is probably typical of the wind interaction taking place in the system. The additional heating of the secondary star surface elements closest to the X-ray source amounts to a few tens of Kelvin. For comparison, the heating of the same surface elements by the radiation of the primary component, is about 2000-2500 K. This clearly suggests that the heating of the secondary surface by the nearby interaction should be limited.

Formed by an O9 plus a B1-1.5 dwarf, CPD – 41° 7742 *a priori* seemed to be an ordinary, well detached system. We however showed that it probably harbours a wind-wind or wind-photosphere interaction. Such a phenomenon could be quite common among close early-type systems. It is thus of a particular importance to evaluate its possible impact on the determination of the physical parameters obtained using different observational methods. The possible variable activity of CPD – 41° 7742 is an additional motivation to accumulate more data on this particularly interesting early-type binary system.

Finally, the present set of observations provides X-ray light curves that cover almost the full orbital cycle of CPD – 41° 7742 with reasonable signal-to-noise and time resolution. As discussed in Sect. 6.3, different physical phenomena (radiative inhibition, radiative braking, Comptonization, ...) probably affect the shock structure and, hence, the exact amount of X-ray emission generated by the wind interaction. The development of appropriate tools, both theoretical and numerical, to analyse such **high quality** X-ray light curves is probably one of the challenges that the new generation of X-ray stellar scientists will have to face in the coming decade, especially to prepare the ground for the next generation of large X-ray observatories.

Acknowledgements. It is a pleasure to thanks Dr. I.I. Antokhin for fruitful discussions. The one month run at the Bochum telescope has been made possible thanks to a 'crédit aux chercheurs' from the Belgian FNRS. Our Bochum negotiators, H.G. Grothues and R.J. Dettmar, are warmly thanked for their open-minded efficiency. We also acknowledge support from the PRODEX XMM-OM and Integral Projects, as well as contracts P4/05 and P5/36 'Pôle d'Attraction Interuniversitaire' (Belgium). EA acknowledges support from the Russian Foundation for Basic Research (project No 02-02-17524) and the Russian LSS (project No 388.2003.2).

References

Antokhina, E. A. 1988, AZh, 65, 1164
Antokhina, E. A. 1996, Astronomy Reports, 40, 483
Arnaud, K. A. 1996, in ASP Conf. Ser., Vol. 101, Astronomical Data Analysis Software and Systems V, ed. G. Jacoby & J. Barnes, 17
Balona, L. A., & Laney, C. D. 1995, MNRAS, 276, 627
Barr, J. 1908, JRASC, 2, 70
Batten, A. H. 1983, JRASC, 77, 95
Batten, A. H. 1988, PASP, 100, 160
Baume, G., Vázquez, R. A., & Feinstein, A. 1999, A&AS, 137, 233
Bell, S. A., Hilditch, R. W., & Adamson, A. J. 1987, MNRAS, 225, 961
Berghöfer, T. W., & Schmitt, J. H. M. M. 1994, Ap&SS, 221, 309
Berghöfer, T. W., Schmitt, J. H. M. M., Danner, R., & Cassinelli, J. P. 1997, A&A, 322, 167
Bianchi, L., & Garcia, M. 2002, ApJ, 581, 610
Burkholder, V., Massey, P., & Morrell, N. 1997, ApJ, 490, 328
Castor, J. I., Abbott, D. C., & Klein, R. I. 1975, ApJ, 195, 157
Crowther, P. A., Hillier, D. J., Evans, C. J., et al. 2002, ApJ, 579, 774
Diaz-Cordoves, J., & Gimenez, A. 1992, A&A, 259, 227
Diaz-Cordoves, J., Claret, A., & Gimenez, A. 1995, A&AS, 110, 329
Feldmeier, A., Puls, J., & Pauldrach, A. W. A. 1997, A&A, 322, 878
Fracastoro, M. G. 1979, A&A, 78, 112
Gayley, K. G., Owocki, S. P., & Cranmer, S. R. 1997, ApJ, 475, 786
Gies, D. R. 2003, in IAU Symposium, Vol. 212, A Massive Star Odyssey: from main sequence to supernova, ed. K. van der Hucht, A. Herrero, & C. Esteban, 91
Herrero, A. 2003, in IAU Symposium, Vol. 212, A Massive Star Odyssey: from main sequence to supernova, ed. K. van der Hucht, A. Herrero, & C. Esteban, 3
Herrero, A., Kudritzki, R. P., Vilchez, J. M., et al. 1992, A&A, 261, 209
Herrero, A., Puls, J., & Najarro, F. 2002, A&A, 396, 949
Hill, G., & Holmgren, D. E. 1995, A&A, 297, 127
Himmelblau, D. M. 1971, Applied Nonlinear Programming (New-York: McGraw–Hill)
Howarth, I. D. 1993, The Observatory, 113, 75
Howarth, I. D., & Prinja, R. K. 1989, ApJS, 69, 527
Humphreys, R. M., & McElroy, D. B. 1984, ApJ, 284, 565
Jansen, F., Lumb, D., Altieri, B., et al. 2001, A&A, 365, L1
Kaastra, J. 1992, An X-Ray Spectral Code for Optically Thin Plasmas, (Internal SRON-Leiden Report, updated version 2.0)
Kallrath, J., & Linnell, A. P. 1987, ApJ, 313, 346
Manfroid, J. 1993, A&A, 271, 714
Manfroid, J. 1995, A&AS, 113, 587
Manfroid, J., Royer, P., Rauw, G., & Gosset, E. 2001, in ASP Conf. Ser., Vol. 238, Astronomical Data Analysis Software and Systems X, ed. F. Harnden, F. Primini, & H. Payne, 373
Martins, F., Schaerer, D., & Hillier, D. J. 2002, A&A, 382, 999
Massa, D., Savage, B. D., & Cassinelli, J. P. 1984, ApJ, 287, 814
Mewe, R., Gronenschild, E. H. B. M., & van den Oord, G. H. J. 1985, A&AS, 62, 197
Pauldrach, A., Puls, J., & Kudritzki, R. P. 1986, A&A, 164, 86
Popper, D. M., & Hill, G. 1991, AJ, 101, 600
Puls, J., Springmann, U., & Lennon, M. 2000, A&AS, 141, 23
Rauw, G., Sana, H., Antokhin, I. I., et al. 2001, MNRAS, 326, 1149
Royer, P., Vreux, J.-M., & Manfroid, J. 1998, A&AS, 130, 407

Sana, H., Hensberge, H., Rauw, G., & Gosset, E. 2003, A&A, 405, 1063
Sana, H., Stevens, I. R., Gosset, E., Rauw, G., & Vreux, J.-M. 2004, MNRAS, 350, 809
Sana, H., Gosset, E., Rauw, G., Sung, H., & Vreux, J.-M. 2005a, A&A, submitted
Sana, H., Nazé, Y., Gosset, E., et al. 2005b, in Massive Stars in Interacting Binaries, ed. A. Moffat & N. St-Louis, ASP Conf. Ser., 5p., in press
Schaller, G., Schaerer, D., Meynet, G., & Maeder, A. 1992, A&AS, 96, 269
Schmidt-Kaler, T. 1982, Landolt-Börnstein, Numerical Data and Functional Relationships in Science and Technology, New Series, Group VI, Vol. 2b, Physical Parameters of the Stars (Berlin: Springer-Verlag)
Shimada, M. R., Ito, M., Hirata, B., & Horaguchi, T. 1994, in IAU Symp., Vol. 162, Pulsation; Rotation; and Mass Loss in Early-Type Stars, ed. L. Balona, H. Henrichs, & J. Contel, 487
Simon, K. P., Sturm, E., & Fiedler, A. 1994, A&A, 292, 507
Sterken, C., & Bouzid, M. Y. 2004, in Rev. Mex. Astron. Astrofis., Conf. Ser., Vol. 20, Compact Binaries in the Galaxy and Beyond, ed. G. Tovmassian & E. Sion, 79
Stetson, P. B. 1987, PASP, 99, 191
Stevens, I. R., & Pollock, A. M. T. 1994, MNRAS, 269, 226
Stevens, I. R., Blondin, J. M., & Pollock, A. M. T. 1992, ApJ, 386, 265
Struve, O. 1948, PASP, 60, 160
Sung, H., Bessell, M. S., & Lee, S. 1998, AJ, 115, 734
Turner, M. J. L., Abbey, A., Arnaud, M., et al. 2001, A&A, 365, L27
Usov, V. V. 1992, ApJ, 389, 635
Vacca, W. D., Garmany, C. D., & Shull, J. M. 1996, ApJ, 460, 914
van Hamme, W. 1993, AJ, 106, 2096
Vaz, L. P. R., Cunha, N. C. S., Vieira, E. F., & Myrrha, M. L. M. 1997, A&A, 327, 1094
Vink, J. S., de Koter, A., & Lamers, H. J. G. L. M. 2000, A&A, 362, 295
Vink, J. S., de Koter, A., & Lamers, H. J. G. L. M. 2001, A&A, 369, 574
Wilson, R. E. 1979, ApJ, 234, 1054
Zinnecker, H. 2003, in IAU Symposium, Vol. 212, A Massive Star Odyssey: from main sequence to supernova, ed. K. van der Hucht, A. Herrero, & C. Esteban, 80

Chapter 4

The massive binaries in NGC 6231

Wisdom only comes from experience.
Morihei Ueshiba

Knowledge is gained through experiment,
everything else is information only.
Albert Einstein

In addition to the two systems studied in the previous chapter, five other massive binaries lie in the XMM-*Newton* FOV. Thanks to the high quality of the present spectroscopic data set, we have detected the spectral signature of the two components for all these systems and have proposed the first reliable SB2 solution for three of them. Only HD 152218 had an SB2 orbital solution that was reasonably well constrained before our work. The present chapter is thus devoted to the presentation of our investigations on these five O-type binaries.

Three of these systems have a period below 6 days (Sect. 4.1) and their orbital motions have thus been well sampled both by the optical spectroscopic runs and by the 5-day XMM-*Newton* campaign (see Chap. 1). Each of these short period binaries has been the subject of a recently submitted paper that presents their orbital and physical properties. These papers also provide a more complete analysis of the related X-ray data than what was briefly presented in Chap. 2. A brief summary of the main characteristics of these objects is given at the beginning of Sect. 4.1 and is followed by the related papers.

The two longer period systems, HD 152234 and HD 152233, are more loosely constrained because our data acquisition strategy was clearly not optimized for these long period binaries. Both systems are currently monitored with the FEROS instrument. These new data should allow us to constrain their orbital and physical properties with an accuracy never reached so far. A brief overview of our current knowledge of both systems is given in Sect. 4.2.

4.1 The short period binaries ($P < 6$ d)

- **CPD −41°7733** (Sana et al. 2005f, see p. 149) is probably formed by an O8.5 plus a B3 star. The orbital period is close to 5.6815 d and the orbit is circular or has a very small eccentricity. Based on spectroscopic classification criteria, the primary is

expected to be a giant. It is however definitely too faint for such a luminosity class and we prefer to quote it as a main sequence star. The secondary star is about ten times less bright than the primary and its spectrum could only be disentangled near quadrature. Its evolutionary status remains unfortunately largely undefined. No X-ray overluminosity, resulting e.g. from a possible wind interaction phenomenon, is observed and indeed none is expected at our detection level.

- **HD 152219** (Sana et al. 2005b, see p. 163) is an O9.5 III + B1-2 V-III system. The orbital period is close to 4.240 d and the orbit is slightly eccentric ($e = 0.08 \pm 0.01$). The spectral lines of the primary component display clear profile variations that are reminiscent of those expected from non-radial pulsations. Finally, the X-ray flux is most probably variable on a time-scale of days. This could be related to a possible wind interaction, though the present data set does not allow to conclude on this point.

- **HD 152218** (Sana et al. 2005e, see p. 179) is probably an O9 IV + O9.7 V system. With an orbital period of 5.604 d and an eccentricity $e = 0.259 \pm 0.006$, HD 152218 is the system that displays the largest eccentricity among the short period binaries in NGC 6231. The system may further undergo a relatively rapid apsidal motion of the order of a couple of degrees per year. Finally, the X-ray flux from the system presents an increase of about 30% near apastron compared to periastron. This could be the signature of an ongoing wind-wind interaction process occurring within the acceleration region of the winds. We however note that second order effects, such as radiative inhibition, might crucially affect the wind interaction structure in HD 152218.

Astronomy & Astrophysics manuscript no. cpd7733˙v2 May 21, 2005
(DOI: will be inserted by hand later)

The massive binary CPD –41°7733⋆

Optical spectroscopy and X-ray observations

H. Sana⋆⋆, G. Rauw⋆⋆⋆, and E. Gosset⋆⋆⋆

Institut d'Astrophysique et de Géophysique, University of Liège, Allée du 6 Août 17, Bât. B5c, B-4000 Liège, Belgium
e-mail: sana@astro.ulg.ac.be, rauw@astro.ulg.ac.be, gosset@astro.ulg.ac.be

Received September 15, 1996; accepted March 16, 1997

Abstract. We present the results of a high-resolution spectroscopic campaign towards the early-type binary CPD –41°7733 located in the core of the young open cluster NGC 6231 in the Sco OB 1 association. We report the detection of the secondary spectral signature and we derive the first SB2 orbital solution for the system. The orbital period is close to 5.6815 d. The orbit is circular or has a very small eccentricity. CPD –41°7733 is most probably formed by an O8.5 plus a B3 star. We observe discrepant luminosity classifications while using spectroscopic or brightness criteria. Using the typical equivalent widths of O8.5 III (resp. V) stars, we estimate the optical brightness ratio $L_1/(L_1 + L_2)$ to be about 0.87 (resp. 0.74). We deduced minimum masses of 16.9 $M_\odot$ and 6.4 $M_\odot$ for the primary and the secondary components respectively. The primary radius is probably close to 8.5 $R_\odot$ while it ranges from 4 to 8 $R_\odot$ for the secondary. Under these hypotheses, the system should not present eclipses, which is in agreement with the results of our photometric campaign towards the core of the NGC 6231 cluster. We also analyse the X-ray light curves and spectra obtained during the six XMM-*Newton* pointings towards the cluster. We find no significant variability between the different pointings, nor within the individual observations. The CPD –41°7733 X-ray spectrum is well reproduced by a three-temperature thermal `mekal` model with temperatures of 0.3, 0.8 and 2.4 keV. No X-ray overluminosity, resulting e.g. from a possible wind interaction phenomenon, is observed and indeed none is expected at our detection level.

Key words. stars: individual: CPD –41°7733 – stars: binaries: close – stars: binaries: spectroscopic – stars: early-type – X-rays: individuals: CPD –41°7733 – X-rays: star

1. Introduction

Early-type stars of spectral type O, and their evolved descendents, the Wolf-Rayet stars, are amongst the hottest and brightest objects in the Galaxy. Through their large radiative and kinetic energy input, they have an important influence on their surroundings. However our knowledge of the massive star population is still far from complete and many important problems remain largely unsolved. For example, the formation of massive stars still lacks a satisfactory explanation. Indeed the usually accepted accretion rates for the formation of low-mass stars (about 10^{-5} $M_\odot$ yr^{-1}) are definitively to low to form a high mass star in less than 10^6 yr. In addition, it has been suggested that, as soon as the protostar reaches ~ 10 $M_\odot$, the radiation pressure could stop the accretion and thus limit the mass. Proposed alternative models call upon enhanced accretion rates (see e.g. Norberg & Maeder 2000) or suggest preferential accretion through a disk (Yorke & Sonnhalter 2002). Another kind of models is based on collision and merging of protostellar objects in the core of very dense young open clusters. In such a process, one would expect multiple and hierarchical systems to be very common among massive stars because of the many collisions in the cluster core (Bonnell & Bate 2002). Observational multiplicity studies in very young open clusters may then provide an important test for formation scenarios. However, not only the binary frequency may provide useful clues, but their orbital and physical parameters are also of major interest. Indeed, while single stars only conserve one parameter – their mass – as a record of their formation history, binary systems might keep track of their formation by the way of three extra parameters, namely their period, their mass ratio and their eccentricity. Most studies carried out in that context (e.g. Mason et al. 1998) agree on the fact that the multiplicity of OB stars is probably as high, or even higher, than for solar-type field stars. They however fail to converge on the distribution of the physical parameters of the systems. This most probably results from the lack of homogeneity of their samples

Send offprint requests to: H. Sana

⋆ Based on observations collected at the European Southern Observatory (La Silla, Chile) and with the XMM-*Newton* satellite, an ESA science mission with instruments and contributions directly funded by ESA Member States and the USA (NASA).

⋆⋆ Research Fellow FNRS (Belgium)

⋆⋆⋆ Research Associate FNRS (Belgium)

of stars that propagates the effects of different ages, different distances, different origins. In that regard, the studies of binaries in young open stellar clusters provide a more accurate and powerful approach to the above-mentioned problems.

It this context, we have undertaken a long-term monitoring campaign of the massive star population of the young open cluster NGC 6231 in the Sco OB 1 association. In the past years, we mainly concentrated our efforts on the two early-type eclipsing binaries HD 152248 (Sana et al. 2001, 2004) and CPD−41°7742 (Sana et al. 2003, 2005a) whose optical and/or X-ray properties show evidence of wind interaction phenomena. The present paper concerns a quieter early-type binary, CPD −41°7733, located near the cluster core. It is organised as follows. Following a summary of the previous investigations on CPD −41°7733, Sect. 2 presents an overview of our optical and X-ray observations and the details of the data reduction processes. The optical spectroscopic data are fully described in Sect. 3, where we also present the spectral properties, period determination and orbital solution of the system. The most probable physical parameters of the CPD −41°7733 components, their temperatures, radii, brightness ratios and evolutionary status are discussed in Sect. 4. In the next section (Sect. 5), we analyse the X-ray data of the system. We derive the source count rates in different energy bands, its spectrum and its flux. Finally we investigate its X-ray variability on different time scales. The last section (Sect. 6) provides a summary of the main results of this work.

Literature Overview

Located in the core of the young open cluster NGC 6231, CPD −41°7733 — α(J2000.0) = $16^h54^m13\overset{s}{.}21$, δ(J2000.0) = $-41°50'32\overset{''}{.}6$ — is a bright (V = 7.875, Sung et al. 1998) early-type star. It is also known in the literature as CD−41°11037 or Braes 941. The SIMBAD astronomical data base[1] reports its Seggewiss number to be 297. According to Raboud et al. (1997), this number apparently belongs to an extension of the Seggewiss (1968) catalogue – that only listed 295 stars – done by Mermilliod (1988, 1992) in the context of the data base for stars in open clusters (the WEBDA[2] data base). However, the magnitude for the star Se 297 quoted by Raboud et al. (1997) is about 12.5 and does obviously not correspond to CPD −41°7733. From the positions on the CCD, the magnitudes and the spectral types of the objects quoted in their catalogue, we found that the Seggewiss number reported by Raboud et al. (1997) for CPD −41°7733 should rather be Se 323. Such a confusion for extended Seggewiss numbers between 296 and 500 is quite frequent. From our experience, we would thus recommend the greatest caution while using these extended Seggewiss numbers and their associated identifiers quoted in the literature.

Most of the authors classified CPD −41°7733 as O9 III (e.g. Schild et al. 1969; Levato & Malaroda 1980) except Hill et al. (1974) who opted for an O8V spectral type. Referring to a paper in preparation by Perry et al., these authors also quoted the star as displaying magnitude variations larger than $0\overset{m}{.}15$. This result was however not confirmed once the mentioned paper finally appeared as Perry et al. (1990)! From our photometric campaign of the cluster (see Sana et al. 2005a), the root-mean-square of the data set associated to CPD −41°7733 is about $0\overset{m}{.}0125$, slightly larger than the background fluctuations. The peak-to-peak variations over the one month time span of our campaign is 0.05 mag at maximum. No periodicity was found in the data.

CPD −41°7733 was first reported as a spectroscopic binary by Struve (1944) from a single observation. At that time, his diagnostic relied on the large difference between the star velocity (+22.6 km s^{-1}) and the cluster mean velocity (−29.1 km s^{-1}).

[1] http://simbad.u-strasbg.fr

[2] http://obswww.unige.ch/webda

Table 1. Journal of the spectroscopic observations of CPD −41°7733. The first column gives the heliocentric Julian date (HJD−2 450 000) at mid-exposure. The second column provides the orbital phase corresponding to the He I-line SB2 solution of Table 5. The next two columns list the average of the primary and secondary radial velocity (RV) measurements associated with the lines listed in Table 4. These were referred to a zero-systemic velocity frame before averaging. An 'n.' means that no reliable measurement could be performed for the secondary, either because of the low S/N ratio or because of the important blend between primary and secondary lines. The last column indicates the instrumental setting.

HJD	ϕ	$\overline{RV_{1,\lambda} - \gamma_{1,\lambda}}$	$\overline{RV_{2,\lambda} - \gamma_{2,\lambda}}$	Instr.
996.684	0.259	96.8	−262.1	CAT
997.638	0.427	40.3	−107.9	+ CES
998.627	0.601	−55.1	148.8	
999.634	0.778	−89.8	n.	
1000.607	0.950	−28.7	n.	
1299.827	0.615	−62.3	155.9	ESO 1.5m
1300.818	0.790	−90.3	237.5	+ FEROS
1301.825	0.967	−14.6	n.	
1302.827	0.143	74.1	−191.5	
1304.822	0.494	1.0	2.3	
1327.843	0.546	−24.8	82.6	
1668.865	0.570	−39.2	107.9	
1669.867	0.746	−93.6	246.1	
1670.858	0.920	−45.4	119.3	
1671.862	0.097	53.7	−138.3	
1672.851	0.271	92.6	−247.7	
2037.839	0.513	−4.6	−1.7	
2039.826	0.862	−71.9	187.6	
2040.837	0.040	22.4	−55.6	
2335.830	0.962	−17.6	108.7	
2336.809	0.134	71.8	−181.1	
2337.786	0.306	87.4	−233.9	
2338.770	0.479	8.8	n.	
2339.781	0.657	−77.0	203.3	
2381.748	0.044	22.9	−68.3	
2382.714	0.214	91.2	−242.2	
2383.712	0.390	58.9	−160.3	
3130.693	0.865	−70.1	184.4	ESO 2.2m
3131.731	0.048	26.8	−70.3	+ FEROS
3132.765	0.230	93.7	−248.5	
3133.800	0.412	46.7	−128.2	
3134.675	0.566	−38.9	96.8	
3135.718	0.750	−93.9	244.7	

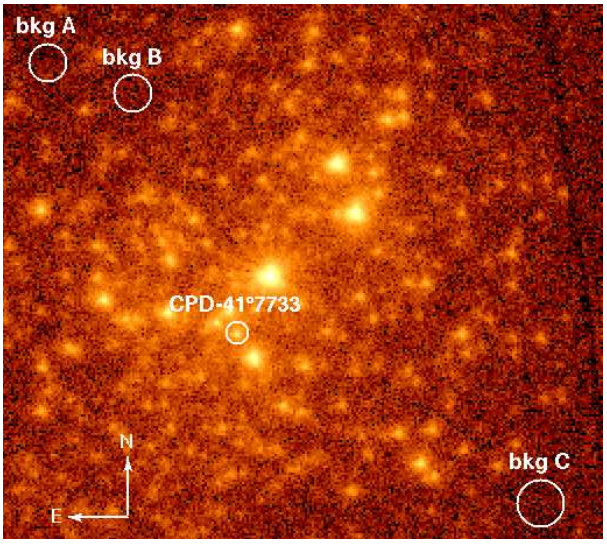

Fig. 1. Combined EPIC MOS image in the range 0.5-10.0 keV. Source and background extraction regions are also shown. North is up, East to the left.

Based on a set of 16 observations spread over 8.1 days plus four observations from Perry et al. (1990) obtained about 800 days earlier, Hill et al. (1974) provided the first SB1 orbital solution with a period $P = 5.64 \pm 0.01$ d, a small eccentricity $e = 0.04 \pm 0.03$ and an amplitude for the primary radial velocity curve of $K_1 = 89.0 \pm 2.7\,\mathrm{km\,s^{-1}}$. With two more observations and including Ca II K-line corrected radial velocities from Struve (1944) and Hill et al. (1974) (but not those of Perry et al. 1990, only published much latter), Levato & Morrell (1983) derived a new orbital solution. They found a larger period $P = 5.74973 \pm 3\,10^{-5}$ d and a moderate eccentricity $e = 0.14 \pm 0.015$ while the amplitude of the radial velocity curve remained mostly unchanged with $K_1 = 84 \pm 2\,\mathrm{km\,s^{-1}}$. Finally CPD –41°7733 was observed once by the IUE observatory. Including this additional radial velocity (RV) point, Stickland & Lloyd (2001) published a slightly modified orbit with $P = 5.749809 \pm 3.0\,10^{-5}$ d, $e = 0.045 \pm 0.021$ and $K_1 = 83.9 \pm 2.1\,\mathrm{km\,s^{-1}}$. While they seemed to confirm Levato & Morrell (1983) solution, they stated that they could not include the data from Perry et al. (1990) in their fitting procedure. They suggested that this could be due to the lower resolution of their spectra and the subsequent high dispersion (ranging from -12 to $-39\,\mathrm{km\,s^{-1}}$) of the K-line velocities corresponding to their four observations. This point will be discussed in Sect. 3.4 while attempting to include the RV measurements from the literature in a combined orbital solution. Finally, we notice that none of the authors mentioned the detection of the companion.

2. Observations and data reduction

2.1. Optical spectroscopic observations

The present work is based on 33 high-resolution spectra of CPD –41°7733 obtained at the European Southern Observatory (ESO, La Silla, Chile). These were acquired during 33 different nights distributed over 7 runs between July 1998 and May 2004. The journal of the observations is presented in Table 1.

In July 1998, five spectra in the range 4460 – 4480 Å (He I λ4471) were obtained at the ESO 1.4m Coudé Auxiliary Telescope (CAT), with the Coudé Echelle Spectrograph (CES) equipped with the Very Long Camera. The detector used was ESO CCD#38, a Loral 2688 × 512 pixel CCD with a pixel size of 15μm × 15μm. The slit width was chosen to achieve a nominal resolving power of 70 000-80 000. The effective resolving power as derived from the $FWHM$ of the lines of the ThAr calibration exposures is 65 000-75 000. Typical exposure times were 40 min and the average S/N ratio is about 100.

Between April 1999 and May 2002, we collected 22 echelle spectra covering the whole optical range (~3750–9200Å) using the Fiber-fed Extended Range Optical Spectrograph (FEROS), an echelle spectrograph mounted at the ESO 1.5m telescope at La Silla. In May 2004, six other FEROS spectra were obtained at the ESO 2.2m telescope at La Silla. The detector was a 2k × 4k EEV CCD with a pixel size of 15μm × 15μm. The spectral resolving power of FEROS is 48 000. Typical exposure times ranged, at the ESO 1.5m telescope, from 20 to 30 min. according to the weather conditions, resulting in typical S/N ratios above 150 (resp. 180) at 4200 Å (resp. 6000 Å). At the ESO 2.2m telescope, thanks to increased instrument performances and to good weather conditions, the S/N ratio is well above 200 for an exposure time of 16 min.

The CES data were reduced in a standard way using the MIDAS package supported by ESO. The spectra were rectified by means of an instrumental response curve built from the observations, obtained under similar conditions, of a metal-poor 'reference' star (HD 203608: F6V). Finally, the spectra were normalised by fitting a low order polynomial to the continuum.

FEROS data were reduced using an improved version of the FEROS context (see details in Sana et al. 2003) working under the MIDAS environment. We mainly used the individual normalised orders. However, in case of doubts on the normalisation, we checked our results with the automatically merged spectrum. In very few cases, we also used a reference star with few metallic lines, observed and reduced under similar conditions, to build an instrumental response curve. This allowed an additional check of the normalisation process.

2.2. XMM-Newton *X-ray observations*

In September 2001, the NGC 6231 open cluster was the target of an X-ray observing campaign with the XMM-*Newton* European observatory (Jansen et al. 2001). The campaign, of a total duration of about 180 ksec, is described in Sana et al. (2005b), together with the data reduction and source identification. We only give here a brief overview of the data. The campaign actually consisted of six separate observations spread over 5 days. All three EPIC instruments (Strüder et al. 2001; Turner et al. 2001) were operated in the Full Frame mode together with the Thick Filter to reject UV/optical light. The field of view (FOV) of the EPIC instruments was centered on the colliding wind binary HD 152248, from which CPD –41°7733 is separated by about 1.′2. It is therefore located

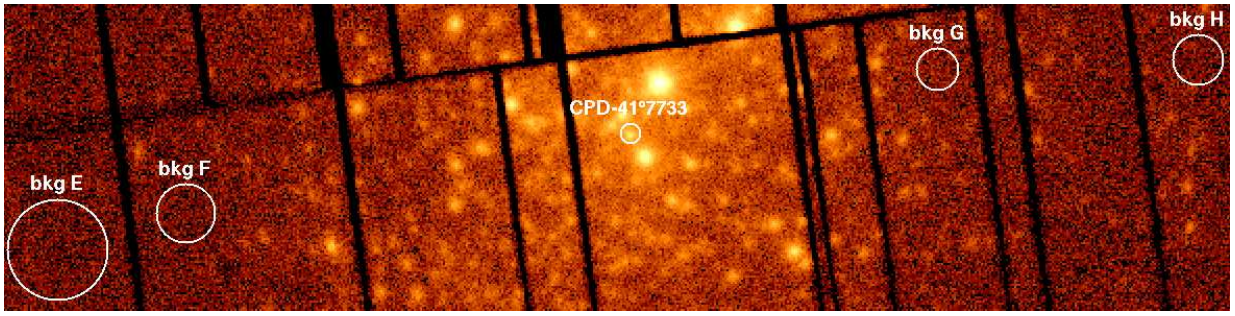

Fig. 2. Combined EPIC pn image in the range 0.5-10.0 keV. Source and background extraction regions are also shown. North is up, East to the left.

Table 2. Journal of the XMM-*Newton* observations of CPD −41°7733. The Julian Date (JD) at mid-exposure is given in Col. 2. Cols. 3 to 5 list the effective exposure times for the EPIC MOS1, MOS2 and EPIC pn instruments while Cols. 6 to 8 report the background-corrected count rates in the different instruments (see text). The last column provides the orbital phase of CPD −41°7733 for each XMM-*Newton* observation at mid-exposure, according to the He I-line ephemeris given in Table 5.

Obs. #	JD	Effective duration (ksec)			Count rates (10^{-3} cnt s^{-1})			Phase ϕ of
	JD−2 450 000	MOS1	MOS2	pn	MOS1	MOS2	pn	CPD −41°7733
1	2158.214	33.1	33.2	30.6	36.0 ± 1.4	10.1 ± 0.7	11.4 ± 0.7	0.530
2	2158.931	19.8	19.8	16.5	40.2 ± 2.1	10.7 ± 1.0	10.4 ± 0.9	0.658
3	2159.796	33.7	33.9	30.1	36.7 ± 1.5	11.0 ± 0.7	9.8 ± 0.7	0.812
4	2160.925	26.0	24.3	11.7	46.0 ± 2.6	12.0 ± 0.9	11.3 ± 0.9	0.013
5	2161.774	30.9	31.0	28.4	38.6 ± 1.5	11.9 ± 0.8	12.5 ± 0.8	0.164
6	2162.726	32.9	32.8	30.3	36.0 ± 1.4	9.8 ± 0.7	10.6 ± 0.7	0.334

in the very center of the field. Figs. 1 and 2 present a view of the XMM-*Newton* X-ray images around CPD −41°7733. Due to the brightness of the cluster objects in the FOV, the Optical Monitor (Mason et al. 2001) was switched off throughout the campaign. Table 2 provides the journal of the X-ray observations of CPD −41°7733.

The raw X-ray data were processed with the Scientific Analysis System (SAS, the dedicated XMM-*Newton* data analysis software) version 5.4.1 implemented on our computers in Liège. The reduction is described in Sana et al. (2005b) and we focus here on the additional elements specific to HD 152248. In addition to the psf fit results given in the X-ray catalogue, we also extracted broad band light curves and spectra using the SAS task *eventselect*. The extraction region was centered on the source position for all the six pointings and for the three EPIC instruments. Due to the presence of three bright X-ray neighbours (HD 152249, HD 326329 and Cl* NGC 6231 SBL 324) the extraction region was limited to a radius of 11.″5. The different backgrounds were estimated from the very few source-free regions. For the two EPIC MOS instruments, the internal background can be considered as uniform on a particular CCD. We thus selected source-free background regions located on the same CCD detector (CCD #1) as CPD −41°7733. Regarding the pn instrument, the internal background is rather considered to depend on the distance to the read-out nodes. We therefore selected source-free regions approximately situated at the same distance from the read-out nodes as our target of interest. The adopted source and background extraction regions for MOS and pn instruments are displayed in Figs. 1 and 2.

We extracted the source spectra for the three EPIC instruments and for the six pointings individually; we also extracted the merged spectra for each instrument, thus combining the six observations of CPD −41°7733. For this purpose, we built the corresponding Ancillary Response Files (the so-called *arf* files) using the SAS task *arfgen*. We adopted the Redistribution Matrix Files (*rmf*) provided by the SOC and adapted to the particular position of CPD −41°7733 on the detectors. The analysis of X-ray data will be presented in Sect. 5.

3. CPD −41°7733 orbital solution

3.1. The optical spectrum

The spectrum of CPD −41°7733 (Fig. 3) is clearly dominated by the H I Balmer, He I and He II absorption lines. Numerous metallic lines (C, N, O, Si and Mg ions) can also be identified. The Balmer lines and all the He I lines in the observed wavelength range present a clear SB2 signature with the primary lines being several times stronger than the associated secondary lines (see e.g. Fig. 4). In the very high S/N ratio spectra, the secondary signature might be seen for a few metallic lines (e.g. O II λ4276, Si III $\lambda\lambda$4552-68-74) but is very close to the detection limit. Two emission lines are detected in the CPD −41°7733 spectrum: S IV λ4486 and C III λ5686. Both are associated with the primary component.

We selected a set of reasonably well isolated lines and we measured their positions and equivalent widths by adjusting Gaussian curves to the studied profiles. Depending on the separation of the double (SB2) lines, one or two Gaussian profiles

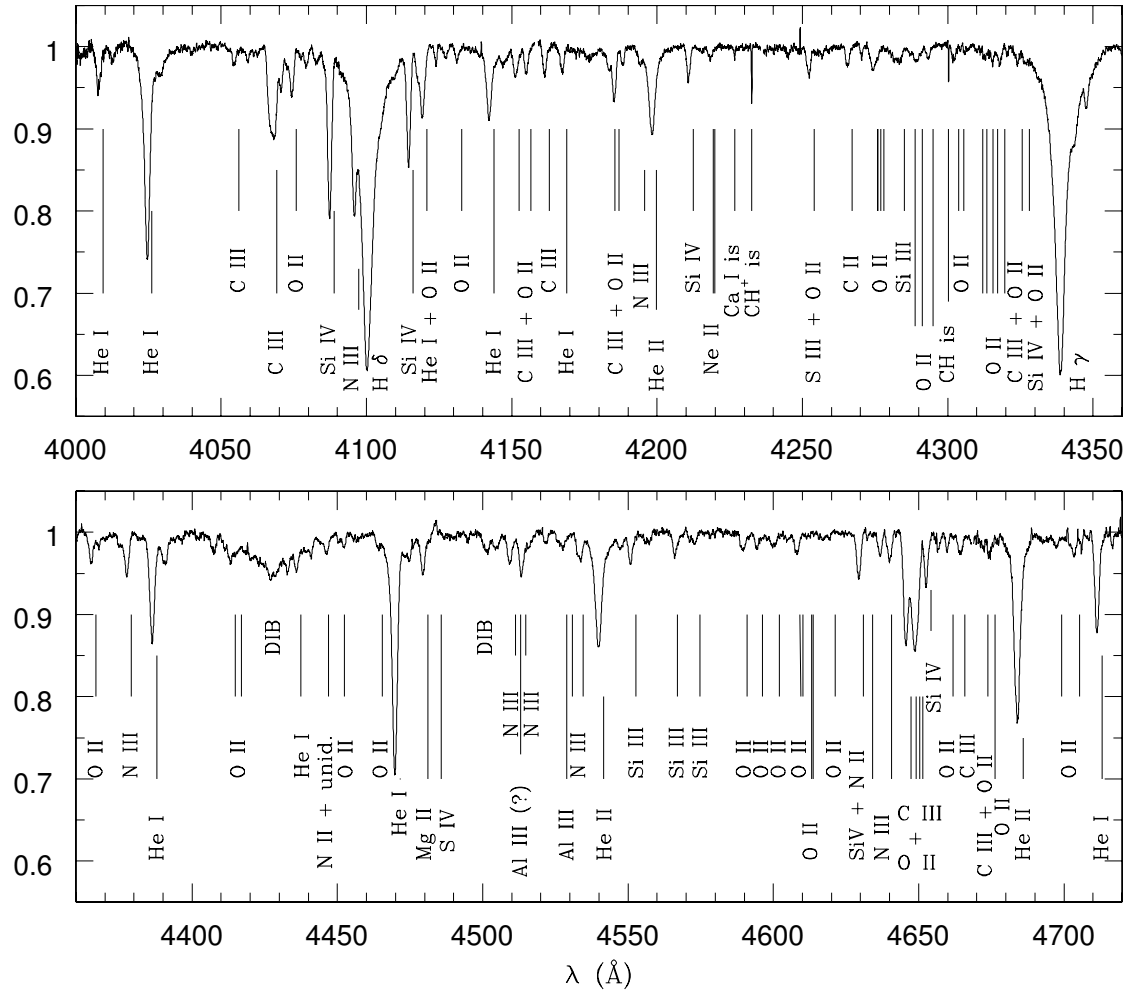

Fig. 3. Blue spectrum of CPD −41°7733 as obtained on HJD = 2 453 135.718 (ϕ = 0.750). The identifications of the main lines have been indicated. The He I lines display a clear SB2 signature, with the blue-shifted primary and the red-shifted secondary components. The identification ticks refer to the rest wavelengths.

were simultaneously adjusted. Due to the presence of numerous metallic lines, some interesting lines are usually blended with neighbouring ones. In those cases where the line profiles are effectively affected by the surrounding lines, we carried out simultaneous multi-Gaussian fittings. To compute the radial velocities (RVs) associated with the measured Doppler shifts, we mostly adopted the effective wavelengths for O-stars from Conti et al. (1977) below 4800 Å and from Underhill (1994) above. For the metallic lines that are not listed in these latter works, we used the rest wavelengths from Moore (1959).

3.2. Period determination

In the search for the orbital period P of the system, we applied both the method of Lafler & Kinman (1965, L&K hereafter) and the Fourier analysis of Heck et al. (1985, HMM hereafter; see also Gosset et al. 2001 for comments). The period search algorithms were applied on the RV data sets associated with the He I λ4471, He II λ4686, O III λ5592 and He I λ5876 lines. The first set is the most extended with 33 observations and offers the largest time base. However, the He I λ4471 lines are often blended with the neighbouring lines O II λ4465 and Mg II λ4481. According to the degree of the blend and to the S/N ratio of the spectrum, the secondary RVs could not be measured at all phases. Primary and secondary lines are also heavily blended near conjunction phases so that we preferred to perform the period search using only the primary RVs. The He II λ4686 and O III λ5592 lines are single lines that are associated with the primary component. While He II λ4686 is brighter, O III λ5592 is better isolated in the spectrum of

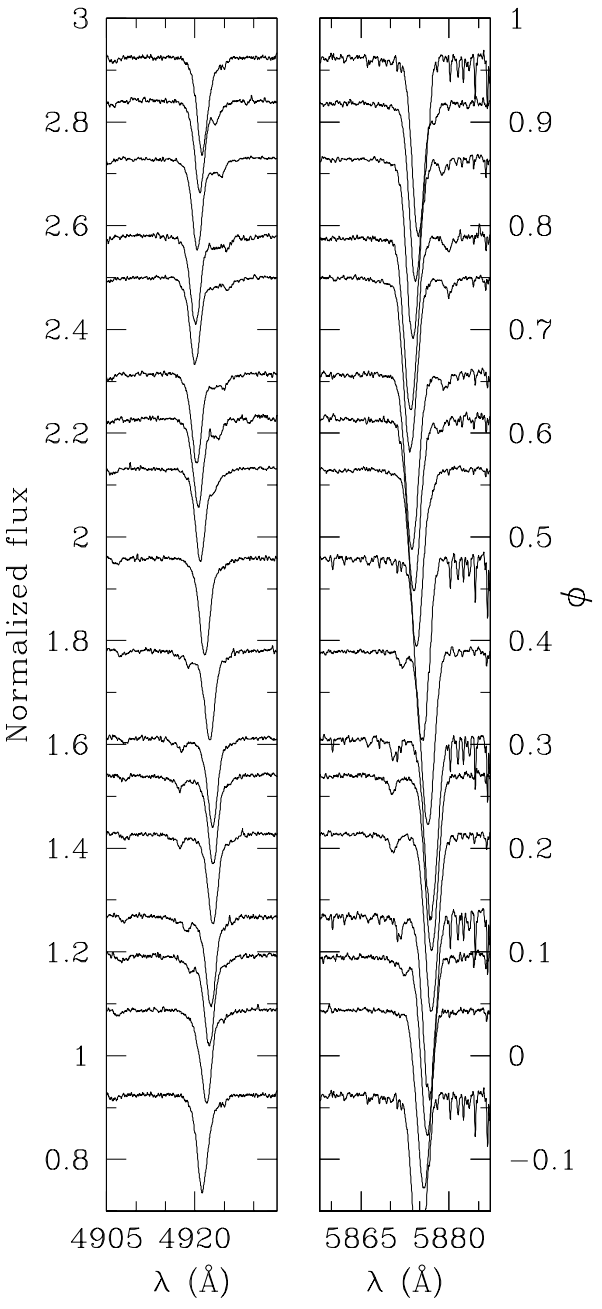

Fig. 4. He I λ4922 (left) and He I λ5876 (right) lines at selected phases. The spectra were shifted along the vertical axis according to the value of their phase (right-hand scale). The secondary spectral signature is clearly identified on most spectra but the blended ones.

CPD −41°7733. Finally the He I λ5876 line shows the signature of the two components. It is strong and well isolated but suffers from blends near conjunction phases. Period values, obtained with the Lafler & Kinman and Fourier analyses, based on different RV sets, are reproduced in Table 3. These are in excellent agreement. The He I λ4471 time base is $T = 2139$ d,

Table 3. Period search carried out with the Lafler & Kinman (L&K) and Fourier (HMM) techniques and based on the RVs associated with different lines. The last column gives the value either of the normalized L&K statistic (Θ_1) or of the Fourier semi-amplitude ($A_{\rm max}$) at the given optimum period.

Data set	Method	Period (d)	Θ_1 / $A_{\rm max}$
He I λ4471: RV_1	L&K	5.6816	0.029
RV_1	HMM	5.6815	88.8
He II λ4686: RV_1	L&K	5.6816	0.040
RV_1	HMM	5.6815	88.3
O III λ5592: RV_1	L&K	5.6814	0.043
RV_1	HMM	5.6815	88.4
He I λ5876: RV_1	L&K	5.6814	0.040
RV_2		5.6816	0.075
RV_1−RV_2		5.6816	0.059
RV_1	HMM	5.6815	86.5
RV_2		5.6818	219.9
RV_1−RV_2		5.6817	306.3

leading to a natural width of the peak in the periodogram of $\Delta\nu = 1/T = 4.68\,10^{-4}\,{\rm d}^{-1}$ and a corresponding resolution on the quoted period value $\Delta P = 0.015$ d. The full width at half maximum in the periodogram gives $\Delta P = 0.014$ d, as expected from the theoretical value. Adopting a final uncertainty of one tenth of the peak width, we obtain $\sigma_P = 1.5\,10^{-3}$ d. Following a similar reasoning, the uncertainty on the period associated with the three other line sets is $1.8\,10^{-3}$ d.

3.3. The CPD −41° 7733 orbital solution

3.3.1. The first SB2 orbital solution

We first computed orbital solutions using RV sets associated with the different absorption lines listed in Table 4. For SB1 lines, we used the algorithm of Wolfe et al. (1967) in its original form. For the sets associated with SB2 lines, we used a modified version of the algorithm, adapted to SB2 systems as explained in Sana et al. (2003). In our derived solutions, we adopted a period value and a relative primary to secondary weight ratio (s_y/s_x) that yield the lowest residuals. The deduced orbital parameters are each other in acceptable agreement. All the computed orbital solutions are characterized by a very low eccentricity. We then computed the averaged RVs of the quoted He I and other primary lines by shifting the individual RVs to a common frame, taking into account the different systemic velocities deduced from the individual orbital solutions. We again obtain an almost circular orbital solution with $e = 0.006 \pm 0.004$ and a root-mean-square (rms) residual of $1.5\,{\rm km\,s^{-1}}$.

As a next step, we also computed circular orbital solutions using a least-square fitting procedure as adapted when the RV equations depend linearly on the adjusted parameters. In addition, for SB2 lines, the equations were symmetrised in a similar way as for the modified Wolfe et al. (1967) algorithm, in order to symmetrically propagate the errors on the parameters associated with each of the components. The circular solutions give very similar rms residuals, not exceeding the eccentric solution ones by more than $0.1\,{\rm km\,s^{-1}}$. In

Table 4. Orbital solutions deduced from different RV data sets. Circular orbits were assumed. The usual notations for the orbital elements have been used. s_y/s_x is the ratio of the uncertainties associated with the secondary and primary RVs respectively. T_0 (in HJD−2 450 000) is the conjunction time, the primary being in front. Quoted uncertainties are the 1-σ error bars.

Lines	P (d)	s_y/s_x	T_0	K_1 (km s^{-1})	K_2 (km s^{-1})	γ_1 (km s^{-1})	γ_2 (km s^{-1})	r.m.s. (km s^{-1})
He I λ4471	5.68151	4.7	3199.634 ± 0.004	94.2 ± 0.5	245.5 ± 1.2	−22.6 ± 0.4	−23.0 ± 0.5	2.0
He I λ4922	5.68149	4.2	3199.627 ± 0.006	94.5 ± 0.8	245.7 ± 2.0	−20.7 ± 0.7	−22.1 ± 0.9	3.2
He I λ5016	5.68153	3.7	3199.640 ± 0.003	93.3 ± 0.4	247.9 ± 1.0	−22.5 ± 0.3	−26.4 ± 0.3	1.9
He I λ5048	5.68150	2.1	3199.639 ± 0.004	92.4 ± 0.7	249.7 ± 1.7	−22.4 ± 0.6	−25.4 ± 0.7	3.2
He I λ5876	5.68148	3.6	3199.630 ± 0.002	93.2 ± 0.3	246.7 ± 0.7	−20.5 ± 0.3	−20.8 ± 0.3	1.3
He I λ7065	5.68147	3.4	3199.641 ± 0.003	94.6 ± 0.4	242.4 ± 1.0	−19.6 ± 0.5	−20.9 ± 0.4	1.8
He II λ4686	5.68154	–	3199.640 ± 0.002	94.6 ± 0.5	–	−16.5 ± 0.2	–	1.5
O III λ5592	5.68150	–	3199.630 ± 0.002	94.7 ± 0.3	–	−24.4 ± 0.2	–	1.1
C III λ5696	5.68155	–	3199.643 ± 0.002	93.8 ± 0.8	–	−34.3 ± 0.2	–	3.1

consequence, we assume in the following that CPD −41°7733 has a circular orbit. Table 4 lists the orbital solutions obtained for the data sets associated with different lines. The orbital solutions obtained using the averaged primary and He I RV measurements are given in Table 5 together with the corresponding physical parameters obtained for the system.

The weighted means of the systemic velocities associated with the primary and secondary components in the different He I-line solutions of Table 4 give respectively $\overline{\gamma_1} = -21.5\,\mathrm{km\,s^{-1}}$ and $\overline{\gamma_2} = -23.1\,\mathrm{km\,s^{-1}}$. These latter values will be adopted as the system apparent systemic velocities. They will be used to compare the average He I-line orbital solution of Table 5 with previously published results.

3.4. Towards a global solution including published and new data

Though at the first-order, the orbital solution derived in the previous section yields orbital parameters of the same order of magnitude than the ones obtained from previous works, a closer inspection reveals fundamental contradictions between the different studies. Our final period $P = 5.681504$ d and the different values in Table 3 do well agree within their respective uncertainties. They are however significantly different from previous determinations. Hill et al. (1974, HCB74 hereafter) indeed found $P = 5.64 \pm 0.01$ d while Levato & Morrell (1983, LM83 hereafter) and Stickland & Lloyd (2001, SL01 hereafter) respectively obtained $P = 5.74973 \pm 3 \times 10^{-5}$ d and $P = 5.749809 \pm 3.0 \times 10^{-5}$ d. From our data set, the orbit of CPD −41°7733 is either circular or has a very low eccentricity ($e < 0.010$). Previous works however reported an eccentricity up to 0.14 ± 0.015 (LM83). Finally, the derived semi-amplitude of the primary RV curve K_1 is systematically higher than the published values, with differences up to 10 km s^{-1} compared to LM83 and SL01.

As a first step, we recomputed the orbital solution using the different RV sets from the literature. HCB74's set is formed by 16 RV data points completed with four additional observations from Perry et al. (1990, PHYB90 hereafter). These latter points are indeed reasonably well positioned on the HCB74 RV curve (their Fig. 4). However the second measurement listed in PHYB90, with $RV = -109\,\mathrm{km\,s^{-1}}$, is clearly not fitted by the HCB74 published solution. Though this observational value corresponds to the same velocity as in the HCB74 paper, it is shifted by about 0.2 in phase compared to what is seen in their plot. This probably results from a typographic error in the corresponding Julian date quoted in PHYB90. A period search performed on this data set is indeed clearly biased while including this particular data point. Rejecting this PHYB90 measurement, we then obtained a period close to 5.681 d, with a strong alias at 5.64 d. As mentioned above, our computations did not account for the uncertain PHYB90 data point while HCB74 apparently had the correct value. It is thus possible that this additional measurement shifts the obtained period value from one alias to the other. This erroneous data point also explains why SL01 could not include PHYB90 observations in their combined solution.

LM83 used Struve (1944) and HCB74 data sets only, completed by their two new measurements. Indeed the PHYB90 data were not yet published. LM83 obtained a period close to 5.75 d, later confirmed by SL01 who did not use the single Struve's data point but added an additional measurement from IUE. We independently re-computed orbital solutions using respectively the same data as these authors. For LM83 data, we find a period of 5.70 d, thus significantly different from the quoted 5.75 d period. Using SL01 data set, we obtained results very similar to the published ones. We also recomputed an orbital solution using the LM83 period value ($P \sim 5.75$ d) but we did not derive an eccentricity as large as theirs. In all the previous computations, the maximum eccentricity that we found was $e = 0.07$, with a null eccentricity well within a 2-σ interval. We thus definitively rule out the large eccentricity quoted by LM83. Finally, we note that the LM83 and SL01 data sets yield a strong ambiguity on the period value with more than ten strong aliases between 5.6 and 5.8 days. All the data sets used by the different authors (except the discrepant point from PHYB90) can be fitted with a period close to the one obtained in the previous paragraph. Our data however can definitively not be adjusted with the period values of HCB74 ($P \approx 5.64$ d) or LM83 and SL01 ($P \approx 5.75$ d).

We finally combined all the available primary RV measurements, still excluding the PHYB90 point with $RV = -109\,\mathrm{km\,s^{-1}}$. For the RVs from the present work, we used the

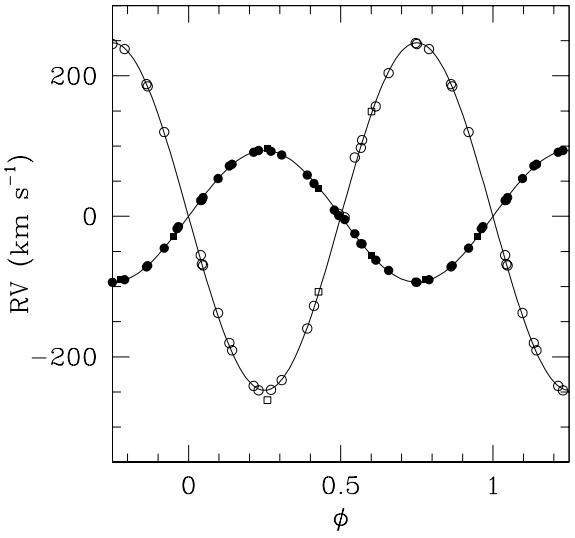

Fig. 5. CPD −41°7733 RV curves corresponding to the non-eccentric He I solution of Table 5. The RV measurements listed in Table 1 are also displayed. Filled and open symbols correspond to the primary and secondary components respectively. The squares give the CES data while the circles indicate the FEROS measurements.

Table 5. Orbital and physical parameters of CPD −41°7733 as deduced from different data sets: our average RVs computed over selected primary SB1 lines (Col. 2) and He I SB2 lines (Col. 3) and a data set extended by primary RVs found in the literature (see Sect. 3.4). The usual notations have been adopted. T_0 is the time of conjunction, the primary being in front; it is adopted as phase $\phi = 0.0$. A 'n.' indicates irrelevant parameters. The two orbital solutions presented in this table correspond to RVs referred to the individual systemic frames.

	Prim.	He I lines	Lit.
P (d)	5.681514	5.681504	5.681534
s_y/s_x	n.	3.3	n.
M_1/M_2	n.	2.640 ± 0.012	n.
T_0 (HJD −2 450 000)	3199.632 ±0.002	3199.635 ± 0.003	3199.640 ± 0.002
K_1 (km s^{-1})	93.6 ± 0.3	93.7 ± 0.3	91.9 ± 0.2
K_2 (km s^{-1})	n.	247.4 ± 0.9	n.
γ_1 (km s^{-1})	−0.3± 0.3	0.0 ± 0.2	−21.7± 0.1
γ_2 (km s^{-1})	n.	−0.3 ± 0.3	n.
$a_1 \sin i$ ($R_\odot$)	10.51 ± 0.06	10.52 ± 0.06	10.31± 0.05
$a_2 \sin i$ ($R_\odot$)	n.	27.76 ± 0.10	n.
$M_1 \sin^3 i$ ($M_\odot$)	n.	16.94 ± 0.15	n.
$M_2 \sin^3 i$ ($M_\odot$)	n.	6.42 ± 0.05	n.
r.m.s. (km s^{-1})	1.4	1.9	5.7

averaged RVs reported to the zero systemic velocity frame and we adopted the primary systemic velocity $\gamma_1 = -21.5\,\mathrm{km\,s^{-1}}$ as obtained by averaging the He I γ-velocities of Table 4. We then performed a period search using both the L&K and Fourier analysis techniques (see Sect. 3.2). Both methods yield values close to 5.6815 d. The time span of the combined 56 RV point sample is ∼ 13 186 d, corresponding to a peak width in the periodogram of $\Delta\nu = 7.6\ 10^{-5}$ d^{-1}. The observed width of the peak is in good agreement with the theoretical value. Adopting a final uncertainty on the period corresponding to one tenth of the peak width, we obtained $\sigma_P = 2.4\ 10^{-4}$ d. Again no significant improvement of the quality of the fit is obtained assuming an eccentric orbit. Fig. 6 shows the values of the fit rms adopting period values between 5.6 and 5.8 d. The different aliases are clearly seen as well as our best period value. The corresponding orbital parameters are listed in Table 5 and the RV curve is displayed in Fig. 7.

4. CPD −41°7733 physical parameters

4.1. Spectral types and luminosity classes

4.1.1. Primary component

The spectral signature of the primary component is easily discernible in the spectrum of CPD −41°7733. We adopted the classification criteria from Conti (1973b) as adapted to late O-stars by Mathys (1988); they are based on the equivalent width (EW) ratio of the He I λ4471 and He II λ4542 lines. He I λ4471 EWs were only measured on spectra obtained at large RV separation phases. We obtain a mean $\log W'(\frac{W_{\lambda4471}}{W_{\lambda4542}}) = 0.22 \pm 0.05$ which corresponds to a spectral type O8.5, with spectral type O8 within $1\,\sigma$.

To determine the luminosity class, we adopted the criterion from Conti & Alschuler (1971) based on the EW ratio of the Si IV λ4089 and He I λ4144 lines. We obtain $\log W''(\frac{W_{\lambda4089}}{W_{\lambda4144}}) = 0.27 \pm 0.04$, which leads to a giant luminosity class. We also measured $\log W''' = \log(W_{\lambda4388}) + \log(W_{\lambda4686}) = 5.23 \pm 0.04$. According to Mathys (1988), this rules out a supergiant class and points towards a giant classification, unless the ratio $l_1 = \frac{L_1}{L_{\rm tot}} < 0.67$. The optical brightness of both components of the system will be discussed in Sect. 4.2.

4.1.2. Secondary component

The main spectral signatures of the secondary star in CPD −41°7733 are the Balmer and He I lines for which we were able to measure the positions and EWs with a good confidence. We also note the absence of He II lines, as well as of the O III λ5592 line, at the positions predicted by the orbital solution. The absence of He II lines definitively excludes an O spectral type and, at our detection threshold, most probably indicates a spectral subtype later than B0.7 (Walborn & Fitzpatrick 1990, WF90 hereafter). To refine our subtype classification, we carefully searched for the presence of secondary metallic lines in our FEROS spectra. This led us to consider low intensity lines, with EWs down to ∼0.01Å. We therefore focused on the FEROS spectra obtained at the ESO 2.2m telescope, that exhibit S/N ratios above 200. Numerous metallic lines associated with the primary (and thus statistically more intense than the relevant secondary lines) render this task even more delicate. The results that we present in Table 6 only con-

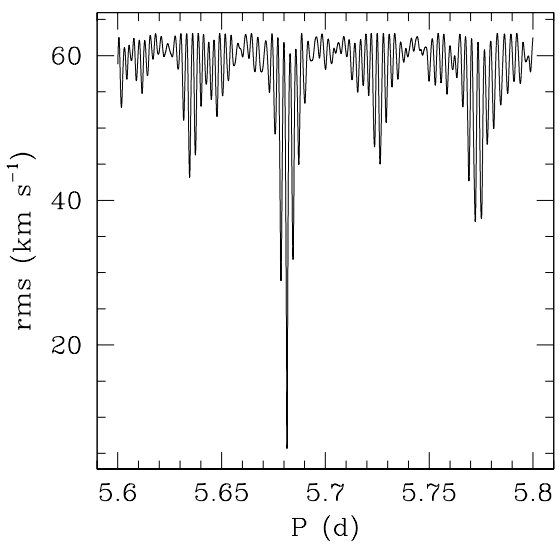

Fig. 6. Root-mean square (rms) residuals of the best circular orbital solutions as a function of the adopted period. The adjustments were performed using the different RV sets presented in Fig. 7, except the point of PHYB90 at $RV = -109\,\mathrm{km\,s^{-1}}$.

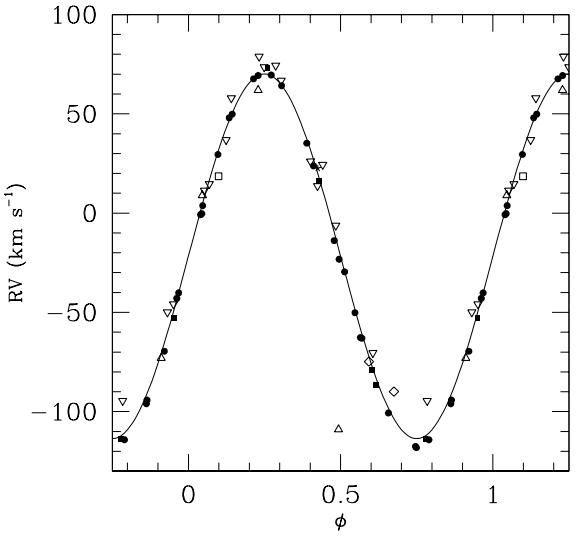

Fig. 7. Combined RV curve computed using literature data together with the measurements of Table 1. Different symbols refer to different data sets. Open symbols are for previous work observations : Struve 1944, asterisk; Perry et al. 1990 (PHYB90), upward triangles; Hill et al. 1974 (HCB74), downward triangles; Levato & Morrell 1983 (LM83), diamonds; Stickland & Lloyd 2001 (SL01), squares. Filled symbols indicate new RV points from this works: CES, squares; FEROS, circles. Note that the PHYB90 point at $RV = -109\,\mathrm{km\,s^{-1}}$, near $\phi \approx 0.5$ was excluded for period search and orbital solution determination.

cern the lines that could unambiguously be associated with the secondary orbital motion and do not pretend to be exhaustive. Some of the secondary lines are clearly deblended from neighbouring lines, and thus securely measured, only on one or two of the six FEROS spectra obtained at the ESO 2.2m telescope.

WF90 suggest to use the Si III λ4552/Si IV λ4089 ratio as a criterion for the spectral type classification of B0-3 stars. However no signature from the Si IV λ4089 could be detected in the secondary spectrum. This, combined with the presence of a comparatively strong C II λ4267 line, clearly indicates a spectral type B2 or later. The usual luminosity criterion in this spectral range is Si III λ4552/He I λ4388. From our measurements, we obtained a ratio of about one to ten; this result definitively excludes a supergiant luminosity class, which is in agreement with the low intensity of the secondary O II spectrum. Similarly, this ratio seems to indicate a main sequence luminosity class rather than a giant class.

The absence of He II λ4686, C III λ4650, N III λ4097 and Si IV $\lambda\lambda$4089, 4116 lines in the secondary spectrum point towards a spectral type later than B2 while the lack of Fe II lines corresponds to a spectral type earlier than B5. As a last check, we compare, in the next paragraph, the secondary EWs (corrected for the expected luminosity ratio) with the typical EWs of B-type stars (Didelon 1982).

4.2. Optical brightness ratio

We roughly estimated the optical brightness ratio based on the dilution of the primary lines in the spectrum of CPD −41°7733. For this purpose, we compared the mean EWs of primary lines with typical (averaged) EWs of O8.5 III stars (Conti & Alschuler 1971; Conti 1973a; Mathys 1988, 1989). Based on the He I $\lambda\lambda$4026, 4388, 4471 and He II $\lambda\lambda$4542, 4686 lines, we respectively obtained a brightness ratio of $l_1 = \frac{L_1}{L_{\rm tot}} = 0.83 \pm 0.36, 0.87 \pm 0.44, 0.79 \pm 0.16, 0.85 \pm 0.25$ and 1.00 ± 0.19. The mean value is then $l_1 = 0.87 \pm 0.10$. Note that He II λ4686 is stronger than in typical O8.5 giants. We compared the secondary intrinsic EWs with typical EWs for B stars (Didelon 1982) using a dilution factor $l_2 = 0.13$. The intensity of the detected lines in the secondary spectra is in rough agreement with a B3 III-V classification but suggests a slightly larger luminosity ratio in favour of the primary component.

Adopting $l_1 = 0.87 \pm 0.10$, Mathys criterion gives $\log W'''_{\rm prim} \approx 5.29 \pm 0.06$, which corresponds to a giant luminosity class for the primary. Assuming a main sequence classification for the primary and comparing the observed EWs with typical EWs for O8.5 V stars, we obtained a luminosity ratio $l_1 = 0.74 \pm 0.08$. This yields $\log W'''_{\rm prim} \approx 5.36 \pm 0.06$ thus in contradiction with the V luminosity class hypothesis.

Typical absolute visual magnitudes for O8.5 stars are $M_{\rm V} = -5.2$ and $M_{\rm V} = -4.5$ or -4.4 for class III and V respectively (Humphreys & McElroy 1984; Howarth & Prinja 1989). The absolute visual magnitudes of B3 stars are $M_{\rm V} = -3.0$ and -1.6 for giants and main-sequence stars respectively (Schmidt-Kaler 1982; Humphreys & McElroy 1984). To compute the visual magnitudes of the CPD −41°7733 components, we adopted the cluster distance modulus $DM = 11.07 \pm 0.04$ as obtained

Table 6. Selected sample of secondary lines and their estimated equivalent width (EW). Typical dispersions are of several mÅ, but some of the lines could only be measured on one or two spectra because of frequent blends with neighbouring lines.

Line	*EW* (mÅ)	Line	*EW* (mÅ)
He I λ4026	86	N II λ4630	7
He I λ4121	21	O II λ4070	9
He I λ4144	92	O II λ4642	<5
He I λ4388	80	Si III λ4553	8
He I λ4471	20	Si III λ4575	7
C II λ4267	11	Mg II λ4481	20

from the average of the different photometric results since the 1990's (Sana et al. 2005a, and references therein) and we used $V = 7.875$, $R = 3.3$ and $(B - V) = 0.158$ from Sung et al. (1998). We first assumed a giant luminosity class for both components and thus adopted $l_1 = 0.87 \pm 0.10$ as derived in the previous paragraph. We obtained $M_V = -4.67 \pm 0.15$ for the total magnitude of the system, and $M_{V,1} = -4.52 \pm 0.20$ and $M_{V,2} = -2.46 \pm 1.12$ for the primary and secondary respectively. Under these hypotheses, the primary magnitude is clearly fainter than typical O8.5 giants. Adopting the effective temperature calibration of Humphreys & McElroy (1984), the spectral types derived above (O8.5 III + B3 III) yield $T_{\rm eff} = 33.6^{+0.9}_{-0.8}$ kK for the primary component and $T_{\rm eff} = 17.1^{+0.9}_{-0.4}$ kK for the secondary. The quoted intervals correspond to the effective temperatures of the neighbouring subtypes in the Humphreys & McElroy (1984) calibration. These values yield $R_1 = 8.8 \pm 1.0$ $R_\odot$ and $R_2 = 6.3 \pm 3.9$ $R_\odot$ for the CPD −41°7733 components. Again, the stars are too small compared to typical giants ($R^{\rm O8.5\ III} \approx 13$ $R_\odot$ and $R^{\rm B3\ III} \approx 9$ $R_\odot$).

Therefore, if we assume that CPD −41°7733 components are indeed main sequence objects, the same reasoning with $l_1 = 0.74 \pm 0.08$ yields $M_{V,1} = -4.31 \pm 0.17$ and $M_{V,2} = -3.18 \pm 0.37$, $\log(\frac{L_1^{\rm bol}}{L_\odot}) = 4.98 \pm 0.08$, $\log(\frac{L_2^{\rm bol}}{L_\odot}) = 3.89 \pm 0.17$ and therefore $R_1 = 8.4 \pm 1.0$ $R_\odot$ and $R_2 = 8.4 \pm 1.9$ $R_\odot$. Corresponding typical radii are, in this case, of 9.0 $R_\odot$ and 4.2 $R_\odot$ for O8.5 and B3 main sequence stars. We now observe a better agreement for the primary, but the secondary parameters are at odds with these of typical B3 dwarfs.

The best agreement between the deduced and typical parameters is obtained assuming that CPD −41°7733 harbours an O8.5 V and a B3 III component. In the latter case, we derived $M_{V,1} = -4.31 \pm 0.17$, $M_{V,2} = -3.18 \pm 0.37$, $R_1 = 8.4 \pm 1.0$ $R_\odot$ and $R_2 = 8.7 \pm 1.7$ $R_\odot$. This option is however rather unlikely. Clearly, the properties of the secondary in CPD −41°7733 are poorly constrained. This probably results from the large brightness ratio between the two components and the subsequent difficulty to constrain the secondary spectral type and luminosity class. Finally, we emphasize that the present discussion relies on the assumption that CPD −41°7733 belongs to the NGC 6231cluster.

In summary, though the spectral criteria rather indicate a giant luminosity class for the primary, the estimated values for its magnitude and radius are more consistent with the primary being a main sequence star. This situation is reminiscent

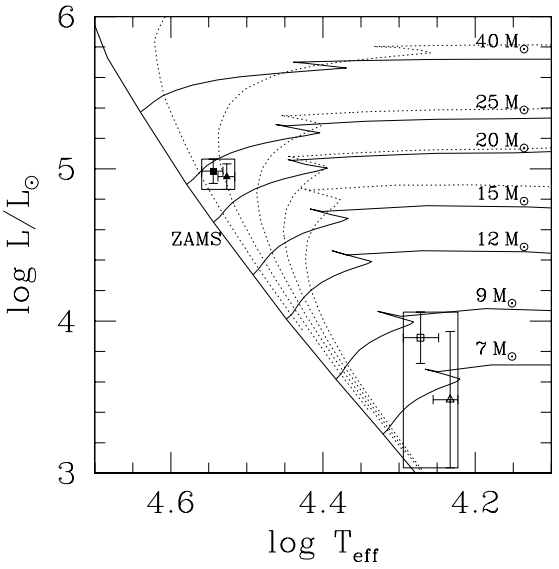

Fig. 8. CPD −41°7733 primary (filled symbols) and secondary (open symbols) location in the H-R diagram. The triangles (resp. squares) indicate an adopted giant (resp. main sequence) luminosity class. The evolutionary tracks from Schaller et al. (1992) are shown (plain lines) as well as the isochrones (dotted lines) computed for ages ranging from 2 to 10 Myr with a step of 2 Myr. The boxes present the ranges of parameter values obtained assuming different luminosity classes for the components.

of CPD−41°7742, an eclipsing SB2 binary in NGC 6231 for which the spectroscopic criteria clearly indicated a giant class. In Sana et al. (2003), we inferred, from the system luminosity, much smaller radii than expected for giants stars. This was confirmed by the analysis of the system light curve (Sana et al. 2005a) and the resulting parameters are in good agreement with the typical values expected for dwarfs of the corresponding spectral types. The locations of the CPD −41°7733 components are plotted in the H-R diagram in Fig. 8 together with the evolutionary tracks of Schaller et al. (1992). The primary indicates an evolutionary age of 3 to 4 Myr, in good agreement with previous age estimates for the cluster. On the other hand, the secondary seems to be much more evolved that the primary, which is rather unexpected. The location of the secondary component is however poorly constrained. As a last check, we also estimated the secondary dilution factor by requiring the secondary EWs to be equal to the typical EWs of B2-B3 stars. This yields slightly lower values for l_2 than previously assumed, thus slightly lower bolometric luminosities. However the secondary location in the H-R remains mostly within the limits of the error box indicated in Fig. 8.

The present discussion brings into light the limits of the individual line fitting method in binary systems with a large brightness difference between the two components. Other techniques, such as spectral disentangling, might be proving more efficient in such cases. By nature, spectral disentangling accounts for most of the lines in the observed spectra. It could

Table 7. Results of the simultaneous fittings of the three EPIC spectra with XSPEC. The model used was $\texttt{wabs}_{\rm ISM}$ * ($\texttt{mekal}_1$ + $\texttt{wabs}_2$ * $\texttt{mekal}_2$). The term $\texttt{wabs}_{\rm ISM}$ was fixed to the interstellar value ($N_{\rm H,ISM} = 0.26 \times 10^{22}$ cm^{-2}). The first and second columns give the phase and the observation number. The next five columns (Cols. 3 to 7) provide the best-fit parameters while Col. 8 lists the corresponding reduced chi-square and the associated number of degrees of freedom (d.o.f). $N_{\rm H}$ yields the absorbing column (in units 10^{22} cm^{-2}). kT is the model temperature (in keV) while *norm* is the normalisation factor (expressed in 10^{-5} cm^{-5}, $norm = \frac{10^{-14}}{4\pi d^2} \int n_{\rm e} n_{\rm H} dV$ with d, the distance to the source – in cm –, $n_{\rm e}$ and $n_{\rm H}$, the electron and hydrogen number densities – in cm^{-3}). The quoted upper and lower values correspond to the limits of the 90% confidence intervals. Columns 9 to 12 provide the observed fluxes (in 10^{-14} erg cm^{-2} s^{-1}) in the 0.5 - 10.0 keV energy band and in the S_X (0.5 - 1.0 keV), M_X (1.0 - 2.5 keV) and H_X (2.5 - 10.0 keV) bands respectively.

ϕ [1]	Obs. # [2]	kT_1 [3]	$norm_1$ [4]	$N_{\rm H,2}$ [5]	kT_2 [6]	$norm_2$ [7]	χ^2_ν (d.o.f.) [8]	$f_{\rm X}$ [9]	$f_{\rm X,S}$ [10]	$f_{\rm X,M}$ [11]	$f_{\rm X,H}$ [12]
0.530	1	$0.26^{0.28}_{0.23}$	$10.2^{11.6}_{8.8}$	$0.54^{0.81}_{0.36}$	$0.73^{0.86}_{0.61}$	$5.8^{7.5}_{4.2}$	1.06 (87)	7.3	4.6	2.4	0.2
0.658	2	$0.19^{0.27}_{0.14}$	$12.4^{21.4}_{8.4}$	$0.26^{0.71}_{0.01}$	$0.50^{0.66}_{0.37}$	$9.5^{19.8}_{5.8}$	0.82 (56)	8.0	5.3	2.7	0.1
0.812	3	$0.28^{0.30}_{0.25}$	$9.6^{11.0}_{8.5}$	$0.58^{0.96}_{0.34}$	$0.74^{0.83}_{0.63}$	$5.6^{8.4}_{3.6}$	0.80 (94)	7.5	4.8	2.5	0.2
0.013	4	$0.25^{0.30}_{0.21}$	$10.8^{12.5}_{8.3}$	$0.80^{1.17}_{0.52}$	$0.67^{2.58}_{0.50}$	$12.3^{23.8}_{3.1}$	1.23 (54)	8.2	4.7	3.2	0.3
0.164	5	$0.26^{0.31}_{0.19}$	$10.4^{11.9}_{8.9}$	$0.47^{0.91}_{0.16}$	$0.63^{1.12}_{0.52}$	$7.1^{10.4}_{2.2}$	1.14 (89)	7.9	5.0	2.7	0.2
0.334	6	$0.28^{0.31}_{0.24}$	$8.6^{9.9}_{7.3}$	$0.41^{0.74}_{0.21}$	$0.71^{0.87}_{0.62}$	$4.8^{6.8}_{3.1}$	1.25 (87)	7.0	4.5	2.4	0.2
Merged	–	$0.28^{0.29}_{0.26}$	$9.9^{10.5}_{9.3}$	$0.54^{0.67}_{0.42}$	$0.80^{1.01}_{0.74}$	$5.1^{6.0}_{4.2}$	1.37 (315)	7.7	4.8	2.6	0.2

also help to derive better constraints on the spectral properties, notably by providing disentangled spectrum of each component. This is however beyond the scope of the present paper.

4.3. Masses and orbital inclination

Typical masses for O8.5 V (resp. III) stars are about 27 (resp. 31) $M_\odot$. Comparing this with the minimal values obtained in Table 5 indicates that the orbital inclination of the system is probably around 55-60°. This corresponds to secondary masses about 10–12 $M_\odot$. Adopting the different estimated values for the radii derived in the previous section, we found that CPD −41°7733 should not display eclipses unless $i \geq 65 - 70°$, which is in agreement with the results of our photometric campaign towards the cluster core (see Sect. 1).

Finally, we note that, while a mass of about 10 to 12 $M_\odot$ indeed correponds to typical values of B3 III stars (see e.g. Schmidt-Kaler 1982), it also corresponds to the mass of B1.5-B2 main sequence stars. Adopting a spectral classification B1.5-B2 V for the secondary, as suggested by its probable mass, would indeed solve much of the discrepancies found in the previous section. Because of the large brightness ratio between the two components, the secondary signature is very diluted and, as show by the present discussion, could be too faint to tightly constrain its spectral classification.

5. X-ray analysis

As mentioned in Section 2.2, we extracted broad band X-ray light curves using the average count rates both during each observation and using a 5 ks time bin. The different energy bands considered are the total band [0.5-10.0 keV], a soft (S_X) band [0.5-1.0 keV], an intermediate (M_X) band [1.0-2.5 keV] and a hard (H_X) band [2.5-10.0 keV]. We found no consistent variations between the three instruments. A χ^2 test of hypothesis performed using the count rates in the different energy bands could not allow to reject the null hypothesis of a constant count rate during all six pointings, except for the pn instrument. Using the individual event lists obtained during each of the six pointings, we performed a time series analysis similar to the one carried out for HD 152248, the central target of the field (Sana et al. 2004). Again no significant variation could be consistently detected for any of the three instruments. This strongly suggests that, at our detection threshold, the X-ray emission from CPD −41°7733 is mostly constant throughout the orbit.

To constrain the physical properties of the emitting plasma, we adjusted a series a optically thin thermal plasma `mekal` models (Mewe et al. 1985; Kaastra 1992) to the spectra obtained during each XMM-*Newton* observation. The EPIC MOS and EPIC pn spectra were adjusted simultaneously using the XSPEC software v.11.2.0 (Arnaud 1996). We adopted an equivalent interstellar column of neutral hydrogen of $N_{\rm H}^{\rm ISM} = 0.26 \times 10^{22}$ cm^{-2}, corresponding to $E(B-V) = 0.447$ obtained from Sung et al. (1998). A single temperature model was insufficient to adequately described the observed spectra. We thus adopted two-temperature (2-T) models allowing for possible local absorption for both `mekal` components. The obtained results are reminiscent of what was observed for HD 152248 (Sana et al. 2004) and CPD−41°7742 (Sana et al. 2005a), two other early-type binaries in the core of the NGC 6231 cluster. The absorption column associated with the lower temperature component tends to be systematically close to zero. Lower residuals and more stable solutions are obtained by fixing this column to zero. Table 7 provides the best parameter values obtained. Finally, for each of the EPIC instrument, we extracted the combined spectrum from the merging of the six X-ray observations. We also used a 2-T `mekal` model to fit the obtained spectra and the best parameters are given in the last line of Table 7. The spectra and the best fit models are presented in Fig. 9.

It is clear from Fig. 9 that an additional, higher energy component is present in the spectrum of CPD −41°7733. We adjusted a three-temperature (3-T) `mekal` model and found that the third component has a best-fit temperature close to 2.4 keV. To investigate the nature of this high energy tail, we also ad-

Table 8. Absorption corrected fluxes ($f^{\rm un.}$, expressed in 10^{-14} erg s^{-1} cm^{-2}) corresponding to the best-fit 2-T models of Table 7 and corrected for the adopted interstellar absorbing column $N_{\rm ISM}$ = 0.26×10^{22} cm^{-2}. The last column gives the X-ray luminosity (in erg s^{-1}) in the 0.5 - 10.0 keV band, assuming DM = 11.07. The last two lines also provide unabsorbed fluxes and luminosities predicted by the 3-T and 2-T+PL models applied to the merged spectra (see text).

ϕ	Obs. #	$f_{\rm X}^{\rm un.}$	$f_{\rm X,S}^{\rm un.}$	$f_{\rm X,M}^{\rm un.}$	$f_{\rm X,H}^{\rm un.}$	log $L_{\rm X}$
2-T models						
0.530	1	21.3	17.6	3.5	0.2	31.83
0.658	2	25.7	21.6	3.9	0.1	31.92
0.812	3	21.0	17.1	3.5	0.2	31.83
0.013	4	23.0	18.3	4.4	0.3	31.87
0.164	5	22.8	18.8	3.9	0.2	31.86
0.334	6	19.6	16.0	3.4	0.2	31.80
Merged	–	21.5	17.5	3.8	0.2	31.84
3-T model						
Merged	–	22.4	18.0	3.8	0.6	31.86
2-T + PL model						
Merged	–	22.4	18.0	3.8	0.6	31.86

justed a 2-T `mekal` + power-law (PL) model. To avoid the fitting procedure of the PL component to be biased by small discrepancies at lower energy, we first adjusted the 2-T model in the 0.5-4.0 keV range. We then hold these parameters fixed to their best fit values while extending the energy domain up to 10.0 keV. Again, both the 3-T and the 2-T+PL models fit the observed spectra with a similar quality. The best-fit photon index of the PL component is about $\Gamma \approx 2.9$, but it is very poorly constrained. A PL component with $\Gamma = 1.5$ fits the spectra equivalently well. The observed X-ray luminosity of CPD −41°7733 is given in Table 8.

From the Berghöfer et al. (1997) relations and adopting either a luminosity class V or III, the expected intrinsic emission from the two stellar components amounts to about $\log(L_{\rm X}) \approx 31.7$ (erg s^{-1}). Though the energy ranges considered are not exactly identical, the observed luminosities from the system are in good agreement with this value. The observed difference can be explained by the intrinsic dispersion around the Berghöfer et al. (1997) relations. Finally, we used the constraints on the physical parameters deduced in the previous section to get more insight into the winds of the CPD −41°7733 components. We assumed an orbital inclination of 60°. Mass-loss rates and terminal velocities were estimated following the mass-loss recipes of Vink et al. (2000, 2001). As expected, the primary wind is overwhelmingly dominant and no ram pressure equilibrium is possible on the system axis. This suggests that the primary wind will crush on the secondary star surface. However, due to the probable separation between the two components, the X-ray emission that could be produced by such an interaction is about 10^{29} erg s^{-1}and is thus two order of magnitude smaller than the intrinsic contribution of the two stellar components. As the CPD −41°7733 orbit is circular, we further do not expect to observe an intrinsic modulation of the emitted flux resulting from a variation of the shock strength. It is thus not surprising

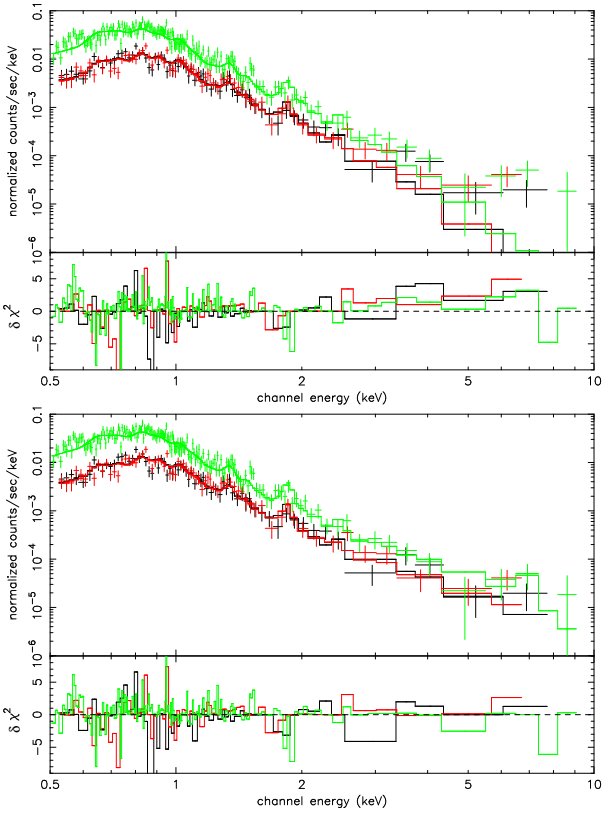

Fig. 9. Merged EPIC MOS1 (black), MOS2 (red) and pn (green) spectra of CPD −41°7733 simultaneously fitted with 2-T (upper panel) and 3-T `mekal` models (lower panel). The bottom window of each panel shows the contributions of individual bins to the χ^2 of the fit. The contributions are carried over with the sign of the deviation (in the sense data minus model). The figures are in colour in the electronic version of this paper.

that the X-ray emission from CPD −41°7733 seems to remain constant over the time.

6. Conclusions

We present the results of a high-resolution spectroscopic campaign towards the early-type binary CPD −41°7733. We report the first detection of the secondary spectral signature that could be unambiguously identified thanks to our high-dispersion high S/N ratio data set. We derive the very first SB2 orbital solution for the system. The orbital period is close to 5.681 d and the orbit is most probably circular or has a very small eccentricity. Our new orbital solution provides orbital elements that are significantly different than the ones obtained in previous works. Using the same data sets as the different authors, we find that their period is ill determined because of strong aliasing that results from the spread of a small amount of observations over a large time span. We combine all the observations available from the literature in a joined orbital solution. The resulting orbital elements are in perfect agreement with those found using our data set alone. We finally report a probable typographic er-

ror in one of the previously published data sets. This data point was discarded throughout the present study.

CPD –41°7733 is most probably formed by an O8.5 star plus a B3 companion, though the luminosity classification is ill defined. We derive minimal masses of respectively 16.9 $M_\odot$ and 6.4 $M_\odot$. Comparing the primary minimal mass with masses typical for O8.5 III-V stars, we find that the orbital inclination of the system should be about 55-60°. Using the typical equivalent widths of O8.5 III (resp. V) stars, we estimate the brightness ratio to be about $l_1 = L_1/(L_1 + L_2) = 0.87$ (resp. 0.74). The primary radius is probably close to 8.5 $R_\odot$ while it ranges from 4 to 8 $R_\odot$ for the secondary. Under these hypotheses, the system should not present eclipses, in agreement with the results of our photometric campaign towards the core of the NGC 6231 cluster.

We also analysed the X-ray light curves and spectra obtained during the six XMM-*Newton* pointings towards the cluster. We find no significant variability between the different pointings, nor within the individual observations. The CPD –41°7733 X-ray spectrum is well reproduced by a two-temperature thermal `mekal` model with $kT_1 \approx 0.3$ keV and $kT_2 \approx 0.8$ keV. The merged spectrum built from the combination of the six pointings shows an additional higher energy component. The latter can be described either by a `mekal` model with an energy close to 2.4 keV or by a power-law component with a photon index Γ close to 3, though very loosely constrained. The obtained X-ray luminosity from the system is in agreement with the predictions of the Berghöfer et al. (1997) *canonical* L_X/L_{bol} relations. No X-ray overluminosity resulting from a possible wind interaction phenomenon is observed and, indeed, none is expected at our detection level.

Acknowledgements. The authors are greatly indebted towards the 'Fonds National de la Recherche Scientifique' (FNRS), Belgium, for multiple supports. Part of this work was also supported by the PRODEX XMM-OM and Integral Projects, contracts P4/05 and P5/36 'Pôle d'Attraction Interuniversitaire' (Belgium). The SIMBAD and WEBDA data bases were consulted for the bibliography.

References

Arnaud, K. A. 1996, in ASP Conf. Ser., Vol. 101, Astronomical Data Analysis Software and Systems V, ed. G. Jacoby & J. Barnes, 17
Berghöfer, T. W., Schmitt, J. H. M. M., Danner, R., & Cassinelli, J. P. 1997, A&A, 322, 167
Bonnell, I. A., & Bate, M. R. 2002, MNRAS, 336, 659
Conti, P. S. 1973a, ApJ, 179, 161
Conti, P. S. 1973b, ApJ, 179, 181
Conti, P. S., & Alschuler, W. R. 1971, ApJ, 170, 325
Conti, P. S., Leep, E. M., & Lorre, J. J. 1977, ApJ, 214, 759
Didelon, P. 1982, A&AS, 50, 199
Gosset, E., Royer, P., Rauw, G., Manfroid, J., & Vreux, J.-M. 2001, MNRAS, 327, 435
Heck, A., Manfroid, J., & Mersch, G. 1985, A&AS, 59, 63
Hill, G., Crawford, D. L., & Barnes, J. V. 1974, AJ, 79, 1271
Howarth, I. D., & Prinja, R. K. 1989, ApJS, 69, 527
Humphreys, R. M., & McElroy, D. B. 1984, ApJ, 284, 565
Jansen, F., Lumb, D., Altieri, B., et al. 2001, A&A, 365, L1
Kaastra, J. 1992, An X-Ray Spectral Code for Optically Thin Plasmas, (Internal SRON-Leiden Report, updated version 2.0)
Lafler, J., & Kinman, T. D. 1965, ApJS, 11, 216
Levato, H., & Malaroda, S. 1980, PASP, 92, 323
Levato, H., & Morrell, N. 1983, Astrophys. Lett., 23, 183
Mason, B. D., Gies, D. R., Hartkopf, W. I., et al. 1998, AJ, 115, 821
Mason, K. O., Breeveld, A., Much, R., et al. 2001, A&A, 365, L36
Mathys, G. 1988, A&AS, 76, 427
Mathys, G. 1989, A&AS, 81, 237
Mermilliod, J.-C. 1988, Bulletin d'Information du Centre de Données Stellaires (CDS), 35, 77
Mermilliod, J.-C. 1992, Bulletin d'Information du Centre de Données Stellaires (CDS), 40, 115
Mewe, R., Gronenschild, E. H. B. M., & van den Oord, G. H. J. 1985, A&AS, 62, 197
Moore, C. E. 1959, A multiplet table of astrophysical interest. Part 1 (NBS Technical Note, Washington: US Department of Commerce, 1959, Rev. edition)
Norberg, P., & Maeder, A. 2000, A&A, 359, 1025
Perry, C. L., Hill, G., Younger, P. F., & Barnes, J. V. 1990, A&AS, 86, 415
Raboud, D., Cramer, N., & Bernasconi, P. A. 1997, A&A, 325, 167
Sana, H., Rauw, G., & Gosset, E. 2001, A&A, 370, 121
Sana, H., Hensberge, H., Rauw, G., & Gosset, E. 2003, A&A, 405, 1063
Sana, H., Stevens, I. R., Gosset, E., Rauw, G., & Vreux, J.-M. 2004, MNRAS, 350, 809
Sana, H., Antokhina, E., Royer, P., et al. 2005a, A&A, in press
Sana, H., Gosset, E., Rauw, G., Sung, H., & Vreux, J.-M. 2005b, A&A, in press
Schaller, G., Schaerer, D., Meynet, G., & Maeder, A. 1992, A&AS, 96, 269
Schild, R. E., Hiltner, W. A., & Sanduleak, N. 1969, ApJ, 156, 609
Schmidt-Kaler, T. 1982, Landolt-Börnstein, Numerical Data and Functional Relationships in Science and Technology, New Series, Group VI, Vol. 2b, Physical Parameters of the Stars (Berlin: Springer-Verlag)
Seggewiss, W. 1968, Veroeffentlichungen des Astronomisches Institute der Universitaet Bonn, 79
Stickland, D. J., & Lloyd, C. 2001, The Observatory, 121, 1
Strüder, L., Briel, U., Dennerl, K., et al. 2001, A&A, 365, L18
Struve, O. 1944, ApJ, 100, 189
Sung, H., Bessell, M. S., & Lee, S. 1998, AJ, 115, 734
Turner, M. J. L., Abbey, A., Arnaud, M., et al. 2001, A&A, 365, L27
Underhill, A. B. 1994, ApJ, 420, 869
Vink, J. S., de Koter, A., & Lamers, H. J. G. L. M. 2000, A&A, 362, 295
Vink, J. S., de Koter, A., & Lamers, H. J. G. L. M. 2001, A&A, 369, 574
Walborn, N. R., & Fitzpatrick, E. L. 1990, PASP, 102, 379
Wolfe, R. H., Horak, H. G., & Storer, N. W. 1967, The machine computation of spectroscopic binary elements, in Modern

astrophysics. A memorial to Otto Struve, Ed. M. Hack (New-York, Gordon Breach), 251
Yorke, H. W., & Sonnhalter, C. 2002, ApJ, 569, 846

Astronomy & Astrophysics manuscript no. hd152219˙v1 May 21, 2005
(DOI: will be inserted by hand later)

The massive binary HD 152219

A pulsating primary component ? ⋆

H. Sana⋆⋆, E. Gosset⋆⋆⋆, and G. Rauw⋆⋆⋆

Institut d'Astrophysique et de Géophysique, University of Liège, Allée du VI Août 17, B-4000 Liège, Belgium
e-mail: sana@astro.ulg.ac.be,gosset@astro.ulg.ac.be,rauw@astro.ulg.ac.be

Received September 15, 1996; accepted March 16, 1997

Abstract. We present the results of an optical spectroscopic campaign on the massive binary HD 152219 located near the core of the NGC 6231 cluster. Though the primary to secondary optical brightness ratio is probably about 10, we clearly detect the secondary spectral signature and we derive the first reliable SB2 orbital solution for the system. The orbital period is close to 4.2403 d and the orbit is slightly eccentric ($e = 0.08 \pm 0.01$). The system is most probably formed by an O9.5 giant and a B1-2 V-III star. We derive minimal masses of 18.6 ± 0.3 and 7.3 ± 0.1 $M_\odot$ for the primary and secondary respectively and we constrain the stellar radius at values about 10 and 5 $R_\odot$. *INTEGRAL*-OMC data reveal that HD 152219 is the third O-type eclipsing binary known in NGC 6231. In the H-R diagram, the primary component lies on the blue edge of the β Cep-type instability strip and its spectral lines display clear profile variations that are reminiscent of those expected from non-radial pulsations. Finally, we report the analysis of XMM-*Newton* observations of the system. The X-ray spectrum is relatively soft and is well reproduced by a two-temperature `mekal` model with $kT_1 = 0.26$ keV and $kT_2 = 0.67$ keV. The X-ray flux is most probably variable on a time-scale of days. The X-ray fluctuations are correlated with a slight increase of its hardness ratio when the emission level is higher, and a slight decrease otherwise. We note that the minimum of the emission arises when the secondary is turning its rear side towards the observer and we tentatively suggest that the observed modulations are linked to a probable additional X-ray component located on, or near, the secondary's front face. Such a component might originate from a probable wind interaction, the primary wind crushing on the secondary star surface.

Key words. binaries: close – binaries: spectroscopic – stars: early-type – stars: individual: HD 152219 – stars: fundamental parameters – X-rays: individual: HD 152219 – X-rays: stars

1. Introduction

Though few in numbers, the O-type stars form a particularly interesting population. They are among the brightest and most massive stellar objects to be found in galaxies. They are the progenitors of the Wolf-Rayet (WR) type stars. They end their life as supernovae, releasing a tremendous amount of energy that considerably influences their surroundings, not to speak of the chemical enrichment of the interstellar medium. Although our comprehension is slowly increasing with the years, many issues are still lacking satisfactory answers. Among the more subtle aspects related to early-type stars, their intrinsic variability is still badly constrained. For example, a large fraction of the O-type stars displays significant line profile variations (Fullerton et al. 1996) that might reflect a variety of underlying phenomena. Corotating structures, winds, magnetic fields and pulsations are probably the most frequently mentioned explanations. It is however particularly difficult to disentangle the specific influence of these effects. Appropriate models, sophisticated enough to allow direct confrontation with the observations, necessitate extended efforts. Clearly cut observational tests are difficult to establish and require a large amount of high quality observations to properly map both the different timescales of the phenomena and the different regions of the parameter space accross the Hertzprung-Russell (H-R) diagram. Finally the possible mutual interactions between these different effects is badly understood, which still increases the complexity of the problem.

An additional problem comes from the intrinsic difficulty to reliably constrain the main physical parameters of these objects. In this regard, binaries have, since long ago, been considered as privileged laboratories. Indeed they potentially offer the possibility to measure stellar masses, radii and in some cases even distances. In this framework, we have carried out an extensive monitoring campaign of the early-type

Send offprint requests to: H. Sana

⋆ Based on observations collected at the European Southern Observatory (La Silla, Chile) and with the XMM-*Newton* satellite, an ESA science mission with instruments and contributions directly funded by ESA Member States and the USA (NASA); also based on data from the OMC Archive at LAEFF, processed by ISDC.

⋆⋆ FNRS Research Fellow

⋆⋆⋆ FNRS Research Associate

Table 1. Journal of the spectroscopic observations of HD 152219. The first column gives the heliocentric Julian date (HJD−2 450 000) at mid-exposure. The second column indicates the corresponding phase according to the He I ephemeris of Table 4. The next two columns provide the mean values of the radial velocity (RV) measurements associated with the lines listed in Table 3. These were referred to a zero-systemic velocity frame before averaging. A 'n.' means that no reliable measurement could be performed for the secondary, either because of a lower S/N ratio or because of the important blend between the primary and secondary lines. The last column indicates the instrumental setting used.

HJD	$\phi_{\rm He\,I}$	$\overline{RV_{1,\lambda}-\gamma_{1,\lambda}}$	$\overline{RV_{2,\lambda}-\gamma_{2,\lambda}}$	Instr.
995.660	0.546	−118.6	n.	CAT
996.591	0.765	−3.6	n.	+ CES
997.608	0.005	92.3	n.	
998.595	0.238	14.8	n.	
999.603	0.476	−120.9	n.	
1000.572	0.704	−32.2	n.	
1299.808	0.836	13.3	n.	ESO 1.5m
1300.802	0.071	−119.1	293.0	+ FEROS
1301.807	0.308	−3.2	n.	
1302.797	0.541	97.5	−248.6	
1304.806	0.015	−111.3	280.2	
1323.872	0.511	91.8	−232.6	
1327.805	0.439	62.5	−216.1	
1668.815	0.860	−18.5	n.	
1668.905	0.881	−38.6	n.	
1669.881	0.111	−113.4	272.4	
1670.872	0.345	14.1	n.	
1671.875	0.581	101.7	−254.9	
1672.800	0.800	20.8	n.	
1672.940	0.832	16.8	n.	
2037.824	0.883	−40.2	n.	
2037.914	0.905	−41.9	n.	
2039.811	0.352	14.7	n.	
2039.925	0.379	27.8	n.	
2040.806	0.587	105.9	−250.1	
2335.774	0.150	−95.7	256.8	
2335.814	0.159	−89.3	250.7	
2336.788	0.389	35.0	n.	
2337.765	0.619	100.7	−250.5	
2338.749	0.851	−3.3	n.	
2339.774	0.093	−117.4	286.4	
2381.671	0.973	−95.0	243.1	
2381.772	0.997	−104.8	267.2	
2382.668	0.209	−61.7	215.1	
2382.815	0.243	−36.0	n.	
2383.674	0.446	69.1	−207.7	
3130.655	0.607	98.7	−261.5	ESO 2.2m
3130.856	0.655	96.0	−246.9	+ FEROS
3131.664	0.845	−0.6	n.	
3131.906	0.902	−40.6	n.	
3132.624	0.072	−122.5	295.6	
3132.897	0.136	−104.7	267.6	
3133.694	0.324	10.3	n.	
3133.902	0.373	29.0	n.	
3134.636	0.546	103.1	−258.4	
3134.890	0.606	102.7	−259.0	
3135.641	0.783	25.5	n.	
3135.882	0.840	7.8	n.	

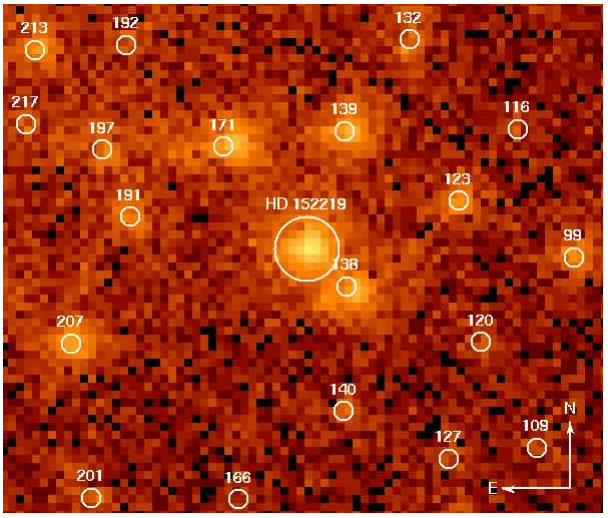

Fig. 1. Cumulated EPIC MOS1 + MOS2 image in the vicinity of HD 152219. The adopted source region is shown. Neighbouring X-ray sources are labelled using the internal numbering scheme of Sana et al. (2005b).

binaries in NGC 6231, a young open cluster regarded as the core of the Sco OB 1 association. NGC 6231 is particularly interesting as it harbours five O-type binaries with a period of less than six days. Three systems have already been analysed. The first two are HD 152248 (Sana et al. 2001, 2004) and CPD −41°7742 (Sana et al. 2003, 2005a), two eclipsing SB2 binaries presenting evidence for wind interaction. The third one, CPD −41°7733, appears much quieter (Sana et al. 2005c). We are currently completing the analysis of the last system, HD 152218, slightly offset from the cluster core. Together with the results of the present work, these papers provide the best set of constraints so far on the orbital and physical parameters of the short-period early-type binary population of NGC 6231.

Following a brief review of the literature related to HD 152219, we present the observational material on which this works relies (Sect. 2). Sect. 3 focuses on the determination of the orbital properties of the system and on a comparison with earlier results. The evolutionary status and the physical parameters of the HD 152219 components are discussed in Sect. 4 and, in Sect. 5, we address the line profile variations in the primary spectrum. Sect. 6 presents the analysis of our X-ray observing campaign. Finally, Sect. 7 provides a summary of the main results of this work.

Literature review

Located at 4.″3 S-W from HD 152248, HD 152219 is one of the bright ($V = 7.56$) early-type binaries belonging to NGC 6231. Quoted spectral classifications range from O9.5 IV (Feinstein & Ferrer 1968) to B0.5IV (Perry et al. 1990, PHYB90 hereafter) whereas Levato & Malaroda (1980) preferred O9.5 III. Projected rotational velocities were measured by Conti & Ebbets (1977) and Levato & Morrell (1983, LM83 hereafter) who respectively reported values of 250 and 160 km s^{-1}. Hill

Table 2. Journal of the XMM-*Newton* observations of HD 152219. The mean Julian Day (JD) is given in Col. 2. Cols. 3 to 5 list the effective exposure times for the EPIC MOS1, MOS2 and EPIC pn instruments while Cols. 6 to 8 report the background-corrected count-rates in the different instruments, as obtained using a 10″ extraction region (see text). No correction for the EEF was applied. The last column provides the HD 152219 orbital phase for each XMM-*Newton* observation at mid-exposure. These were computed according to the He I-line ephemeris given in Table 4. The phase extension of a pointing is about 0.08. Obs. 2 and 4 however suffered from high background events that reduced the useful exposure time by about one third.

Obs. #	Mean JD	Effective duration (ksec)			Count rates (10^{-3} cnt s^{-1})			$\phi_{\rm He\ I}$
	JD−2 450 000	MOS1	MOS2	pn	MOS1	MOS2	pn	
1	2158.214	33.1	33.2	30.6	5.04 ± 0.40	6.01 ± 0.43	16.63 ± 0.75	0.275
2	2158.931	19.8	19.8	16.5	4.16 ± 0.45	4.34 ± 0.46	13.98 ± 0.86	0.444
3	2159.796	33.7	33.9	30.1	5.23 ± 0.40	5.35 ± 0.41	15.82 ± 0.72	0.648
4	2160.925	26.0	24.3	11.7	3.89 ± 0.37	3.12 ± 0.33	6.15 ± 0.47	0.915
5	2161.774	30.9	31.0	28.4	4.92 ± 0.41	6.05 ± 0.45	16.79 ± 0.78	0.115
6	2162.726	32.9	32.8	30.3	4.75 ± 0.39	5.58 ± 0.42	16.15 ± 0.74	0.339

et al. (1974, HCB74 hereafter) obtained 16 radial velocity (RV) measurements over eight days and, including three other measurements later quoted by PHYB90, proposed a first SB1 orbital solution: $P = 4.16 \pm 0.04$ d, $e = 0.10 \pm 0.06$ and $K = 117.4 \pm 3.8$ km s^{-1}. Quoting two papers in preparation, one by Perry et al. (most probably PHYB90) and another by Morris, Hill & Allison (which we could not find in the literature), HCB74 quoted that "this star is a light variable ($\Delta V \sim 0.10$ mag)."

With four additional RV points, and using the HCB74 data, LM83 derived a similar orbital solution with a period $P = 4.16572 \pm 7 \times 10^{-6}$ d, and a slightly larger eccentricity $e = 0.14 \pm 0.04$. More recently, García & Mermilliod (2001, GM01 hereafter) obtained 8 additional spectra of the object and announced to have detected the spectral signature of the companion in three of them. Adopting a slightly longer period $P = 4.069597 \pm 3.4 \times 10^{-5}$ d, they derived an SB2 orbital solution characterized by a much larger eccentricity $e = 0.22 \pm 0.06$. They presented three profiles of the Hγ lines obtained at three different phases (their Fig. 4). Though the primary RV shift is clearly seen, the secondary spectral signature is quite unclear. In addition, according to their RV curves (their Fig. 1a), the observed primary motion does clearly not correspond to the quoted phases. As we already discussed in Sana et al. (2003), these authors reported confusing Julian Dates which biased their period search and orbital solution determination. Finally, focusing on the CCD photometry obtained these last 10 years, we note that the published values for the V magnitude of HD 152219 are in the range 7.55 (Sung et al. 1998) to 7.660 (Balona & Laney 1995). This is similar to the above mentioned work that quoted an 0.10 mag variation.

2. Observations and data reduction

2.1. Optical spectroscopy

The present work is based on 48 high-resolution spectra of HD 152219 obtained at the European Southern Observatory (ESO, La Silla, Chile). These were acquired during 35 different nights distributed over 8 runs between July 1998 and May 2004. The journal of the observations is presented in Table 1.

In July 1998, six spectra in the range 4460 – 4480 Å (He I λ4471) were obtained at the ESO 1.4m Coudé Auxiliary Telescope (CAT), with the Coudé Echelle Spectrograph (CES) equipped with the Very Long Camera. The detector used was ESO CCD#38, a Loral 2688×512 pixel CCD with a pixel size of 15μm × 15μm. The slit width was chosen to achieve a nominal resolving power of 70 000–80 000. The effective resolving power as derived from the $FWHM$ of the lines of the ThAr calibration exposures was rather 65 000–75 000. Typical exposure times were 40 min and the average S/N ratio was about 100.

Between April 1999 and May 2002, we collected 30 echelle spectra covering the whole optical range (~3750–9200Å) using the Fiber-fed Extended Range Optical Spectrograph (FEROS), an echelle spectrograph mounted at the ESO 1.5m telescope at La Silla. In May 2004, twelve other FEROS spectra were obtained at the ESO 2.2m telescope, at La Silla. The detector was a 2k × 4k EEV CCD with a pixel size of 15μm × 15μm. The spectral resolving power of FEROS is 48 000. Typical exposure times ranged at the ESO 1.5m telescope from 10 to 20 min according to the weather conditions, resulting in typical S/N ratios between 150 and 200. At the ESO 2.2m telescope, thanks to increased instrument performances and to good weather conditions, the S/N ratio was above 250 for an exposure time of 15 min.

The CES data were reduced in a standard way using the MIDAS package supported by ESO. The spectra were rectified by means of an instrumental response curve built from the observations, obtained under similar conditions, of a metal-poor 'reference' star (HD 203608: F6V). Finally, the spectra were normalised by fitting a low order polynomial to the continuum.

FEROS data were reduced using an improved version of the FEROS context (see details in Sana et al. 2003) working under the MIDAS environment. We mainly used the normalised individual orders. However, in case of doubts, we checked our results with the automatically merged spectrum.

2.2. X-ray observations

In September 2001, the NGC 6231 open cluster was the target of an X-ray observing campaign with the XMM-*Newton* European observatory (Jansen et al. 2001). The campaign actu-

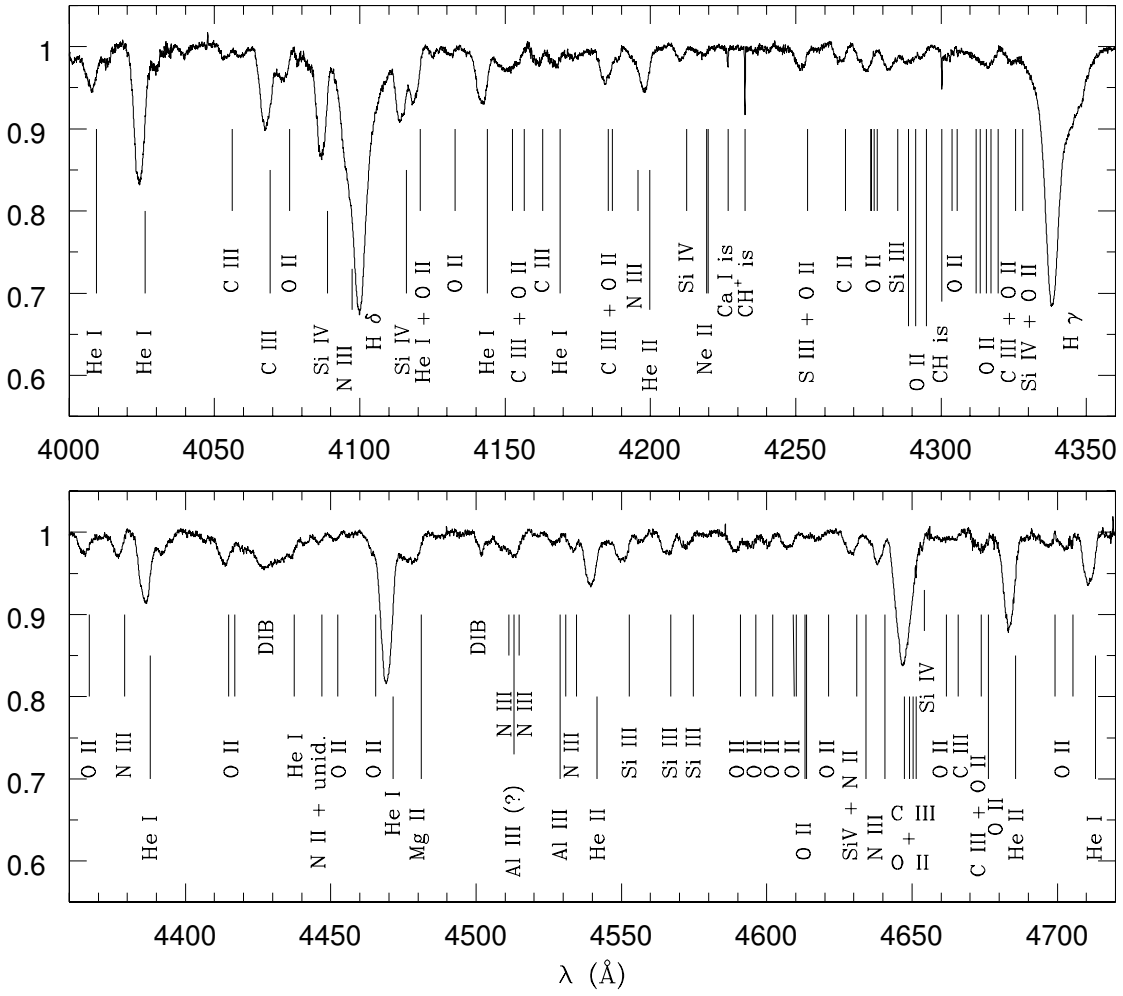

Fig. 2. Blue spectrum of HD 152219 as obtained on HJD = 2 453 132.624 ($\phi_{\overline{\rm HeI}} = 0.072$). The identification of the main lines has been indicated. The He I lines display a clear SB2 signature, with the blue-shifted primary and the red-shifted secondary components. The identification ticks refer to the rest wavelengths.

ally consisted of six separate observations spread over 5 days. All three EPIC instruments (Strüder et al. 2001; Turner et al. 2001) were operated in the Full Frame mode together with the thick filter to reject UV/optical light. The campaign, of a total duration of about 180 ksec, is described in Sana et al. (2005b) together with the data reduction and source identification. We only give here a brief overview, focusing on the additional elements specific to HD 152219. The field of view (FOV) of the EPIC instruments was centered on the colliding wind binary HD 152248, from which the present system is separated by about 4.′3. Due to the brightness of the cluster objects, the Optical Monitor (Mason et al. 2001) was switched off throughout the campaign. Fig. 1 shows a view of the XMM-*Newton* FOV in the vicinity of HD 152219. Table 2 provides the journal of the X-ray observations.

In the pn instrument, HD 152219 falls at less than 13″ from a gap and the X-ray catalogue of the field (Sana et al. 2005b), which relies on a psf fitting method, only considered the EPIC MOS data. Using the Science Analysis System (SAS) task *evselect*, we can however securely extract pn count rates in a circular region with a radius up to 10″. Due to the presence of an X-ray source at about 17″ S-W of HD 152219 (X#138 according to the X-ray numbering defined in Sana et al. 2005b), the extraction of the X-ray light curves and spectra of HD 152219 was first limited to a radius of 8.″5. Because HD 152219 is brighter than X#138, we expect its signal to dominate in a radius of at least 10″. We performed the same analysis with this new radius value, but no difference was found in the results. We thus adopted the largest extraction region. According to the SAS task *calview*, a 10″ radius at the position of HD 152219

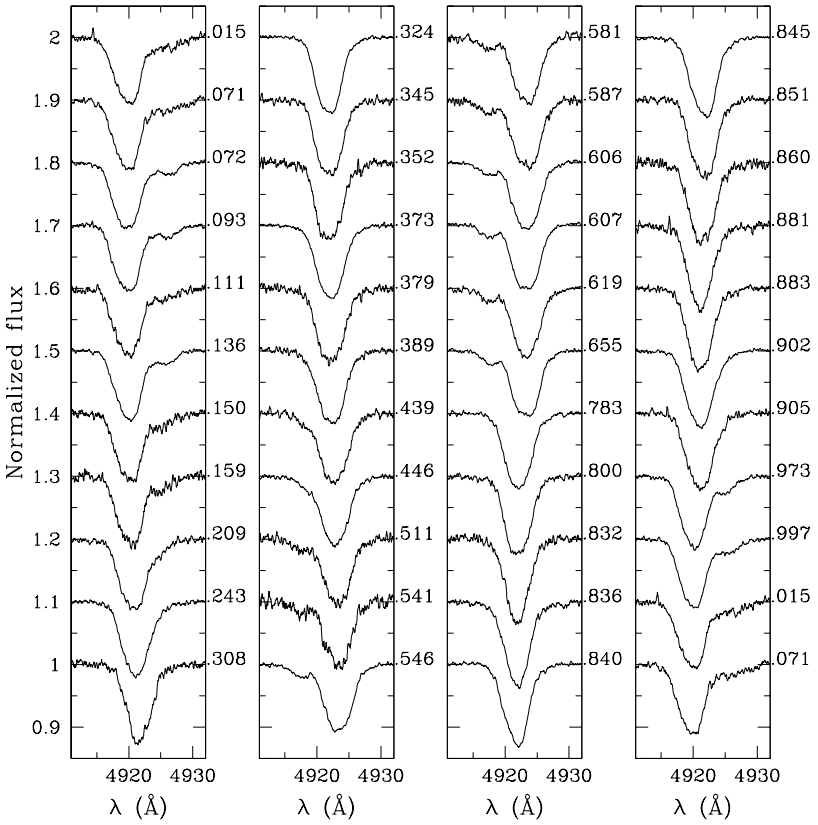

Fig. 3. Evolution of the He I λ4922 line with the phase in our FEROS spectra. Corresponding phases are indicated at right-hand from each panel. The secondary spectral signature is clearly identified on the spectra obtained near quadratures. Note also the variable primary line profile.

corresponds to a psf encircled energy fraction (EEF) of about 54%. The extraction region was centered on the source position for all six pointings and for the three EPIC instruments. The different backgrounds were estimated from the very few source-free regions. The internal background can be considered as uniform on a particular CCD of the MOS instruments. We thus selected source-free background regions located on the same CCD detector (CCD #1) as HD 152219. Concerning the EPIC-pn, the internal background is rather considered to depend on the distance to the CCD nodes. We thus selected source free background regions located approximately at the same distance from the CCD nodes as HD 152219. The adopted source region is shown in Fig. 1. The corresponding background regions are presented in Sana et al. (2005d) together with a description of their positions and sizes.

Adopting these source and background regions, we extracted the HD 152219 count rates in different energy bands (see Sect. 6). Similarly we extracted the source spectra in all EPIC instruments and for the six pointings individually; we also extracted the merged spectrum in each instrument, thus combining the six observations of HD 152219. For this, we built the corresponding Ancillary Response Files (the so-called *arf* files) using the SAS task *arfgen*. We adopted the Redistribution Matrix Files (*rmf*) provided by the SOC and, for the pn, adapted to the particular position of HD 152219 on the detectors. The analysis of the X-ray data is presented in Sect. 6.

3. HD 152219 orbital solution

3.1. The optical spectrum

The optical spectrum of HD 152219 (Fig. 2) is clearly dominated by the H I Balmer, He I and He II absorption lines. The metallic lines (C, N, O, Si and Mg ions) usually seen in O-type spectra can also be identified. All the He I lines and, to a lesser extent, the Balmer lines present a clear SB2 signature. However, because of the broad primary lines and of the large primary to secondary line intensity ratio, the two components are only disentangled at large separation (Fig. 3). The primary lines display variable profiles which, from time to time, broaden and flatten. The C III λ5696 presents mixed absorption and emission that, at first sight, compensate each other. It also presents a variable profile. No other emission lines are seen in the spectrum of HD 152219.

We measured the line positions and equivalent widths (EWs) of a series of selected lines (Table 3) by adjusting Gaussian curves to the observed profiles. Depending on the separation of the double (SB2) lines, one or two Gaussians were simultaneously adjusted. Due to the presence of numerous metallic lines, some interesting lines are usually blended with neighbouring ones. In those cases where the line profiles are effectively affected by the surrounding lines, we carried out simultaneous multi-Gaussian fits. To compute the radial velocities (RVs) associated with the measured Doppler shifts,

Table 3. Orbital solutions deduced from different RV data sets. The usual notations for the orbital elements have been used. s_y/s_x is the adopted ratio of the uncertainties associated with the secondary and primary RVs respectively. Quoted uncertainties are the 1-σ error bars.

Line	P (d)	s_y/s_x	e	ω (°)	K_1 (km s^{-1})	K_2 (km s^{-1})	γ_1 (km s^{-1})	γ_2 (km s^{-1})	r.m.s. (km s^{-1})
He I λ4026	4.24036	3.4	0.068 ± 0.015	157 ± 8	110.3 ± 0.7	283.2 ± 1.7	−23.2± 1.5	−7.6 ± 3.6	4.2
He I λ4388	4.24027	4.3	0.069 ± 0.015	156 ± 7	101.4 ± 0.9	269.9 ± 2.5	−12.7± 1.6	−19.6 ± 3.4	5.0
He I λ4922	4.24043	2.7	0.087 ± 0.009	160 ± 4	109.2 ± 0.4	282.0 ± 1.1	−15.3± 1.0	−33.1 ± 2.3	3.0
He I λ5876	4.24019	3.9	0.090 ± 0.015	152 ± 4	116.7 ± 0.8	288.5 ± 2.0	−22.7± 1.6	−21.1 ± 3.4	4.3
He I λ7065	4.24035	4.0	0.071 ± 0.012	149 ± 9	118.7 ± 1.0	276.2 ± 1.6	−18.8± 1.6	−17.3 ± 3.0	5.0
He I λ4026	4.24029	–	0.102 ± 0.016	139 ± 9	108.4 ± 1.8	–	−22.7± 1.2	–	7.3
Si IV λ4088	4.24029	–	0.110 ± 0.015	138 ± 8	126.6 ± 1.9	–	−20.1± 1.3	–	8.0
He I λ4388	4.24030	–	0.078 ± 0.020	146 ± 14	98.5 ± 1.9	–	−13.3± 1.3	–	8.2
He I λ4471	4.24026	–	0.082 ± 0.014	152 ± 11	110.4 ± 1.7	–	−31.8± 1.1	–	7.7
He II λ4541	4.24033	–	0.127 ± 0.020	137 ± 9	127.9 ± 2.6	–	−11.8± 1.7	–	10.7
He II λ4686	4.24032	–	0.123 ± 0.017	135 ± 7	128.2 ± 2.1	–	−16.9± 1.4	–	8.8
He I λ4921	4.24035	–	0.093 ± 0.014	146 ± 8	107.3 ± 1.5	–	−16.1± 1.0	–	6.2
O III λ5592	4.24034	–	0.142 ± 0.016	140 ± 6	124.7 ± 2.0	–	−17.4± 1.3	–	8.2
He I λ5876	4.24027	–	0.115 ± 0.012	140 ± 6	116.6 ± 1.5	–	−21.7± 1.0	–	6.2
He I λ7065	4.24027	–	0.099 ± 0.014	140 ± 8	117.5 ± 1.6	–	−19.5± 1.1	–	6.8

we mostly adopted the effective wavelengths for O-stars from Conti et al. (1977) below 4800 Å and from Underhill (1994) above. For the metallic lines that are not listed in these latter works, we used the rest wavelengths from Moore (1959).

3.2. Period determination

In the search for the orbital period P of the system, we applied both the method of Lafler & Kinman (1965, L&K hereafter) and the Fourier analysis of Heck et al. (1985, HMM hereafter; see also Gosset et al. 2001 for comments). The period search algorithms were applied on the RV data sets associated with most of the lines listed in Table 3. Because only the primary motion can reliably be followed throughout the orbit, we focused on the primary RVs. We systematically obtained period values in the range 4.24022 - 4.24048 d with an average about 4.2403 days. As a test case, we also used the RV sets formed by the difference between primary and secondary velocities for a few SB2 lines. These sets are about twice less numerous but yielded similar results.

The primary He I λ4471 data set is the most extended with 48 observations. It offers the largest time base $T = 2140$ d, leading to a natural width of the peak in the periodograms of $\Delta\nu = 1/T = 4.67 \times 10^{-4}$ d^{-1}. The corresponding resolution on the quoted period value is $\Delta P = 0.008$ d. The time span of the other data sets is 1836 d, yielding $\Delta P = 0.010$ d. The observed full widths at half maximum in the corresponding periodograms are in good agreement with these theoretical values. Adopting a final uncertainty of one tenth of the peak width, we obtain $\sigma_P = 8 \times 10^{-4}$ d and 10^{-3} d according to the data set considered.

3.3. The SB2 orbital solution

We first computed orbital solutions using the RV sets associated with the different absorption lines listed in Table 3. For SB1 lines, we used the algorithm of Wolfe et al. (1967) in its original form and assigned the same weight to each measurements. For the sets associated with SB2 lines, we used a modified version of the algorithm, adapted to SB2 system as explained in Sana et al. (2003), and we only considered those points for which the two components could be measured. In our derived solutions, we adopted a period value and a relative secondary to primary uncertainty ratio (s_y/s_x) that yield the lowest χ^2. Table 3 gives the best-fit results and the corresponding root-mean-square (r.m.s) residuals.

We also computed the mean RVs of the SB2 He I-lines and of the primary lines quoted in Table 3. For this purpose, we shifted the individual RVs to a common frame before averaging, taking into account the individual systemic velocities. The orbital solutions obtained using the averaged primary and He I RV measurements are given in Table 4 together with the physical parameters of the system. Fig. 4 displays the RV curves corresponding to the averaged SB2 solution.

3.4. HD 152219 orbital parameters

The best period values deduced from the different data sets of Table 3 are in excellent agreement; their mean value is $P = 4.24032 \pm 9 \times 10^{-5}$ and $4.24030 \pm 3 \times 10^{-5}$ d according either to the SB2 He I-lines or to the primary solutions. The standard dispersions are well below the uncertainties obtained from the periodogram peak width. These mean values are further identical to the final values adopted to compute the averaged solutions of Table 4. In the following, we adopt the SB2 solution obtained from the average RVs of the SB2 He I-lines as our final solution. We also adopt the apparent systemic velocities $\overline{\gamma_1} = -17.9$ km s^{-1} and $\overline{\gamma_2} = -22.3$ km s^{-1} for the primary and secondary components. These values were obtained as the weighted means of the systemic velocities associated with the two components in the different He I-line solutions of Table 3. They will be used to compare the average He I-line orbital solution of Table 4 with previously published results.

Table 4. Orbital and physical parameters of HD 152219 as deduced from different data sets: our averaged RVs computed over selected primary lines (Col. 2) and He I SB2 lines (Col. 3) and a data set extended by primary RVs reported in the literature (see Sect. 3.5). The usual notations have been used. T_0 is the time of periastron passage and is adopted as phase zero (i.e. $\phi = 0.0$). Note that the primary and the He I lines solution were computed in the zero systemic velocity frame.

	Prim.	He I lines	Lit.
P (d)	4.24030	4.24032	4.24028
s_y/s_x	n.	3.3	n.
m_1/m_2	n.	2.530 ± 0.023	n.
e	0.108 ± 0.012	0.082 ± 0.011	0.095 ± 0.014
ω (°)	141 ± 6	153 ± 5	136 ± 8
T_0 (HJD	3200.026	3200.165	3199.960
−2 450 000)	±0.073	± 0.090	± 0.002
K_1 (km s^{-1})	116.5 ± 1.4	110.7 ± 0.7	115.0 ± 1.5
K_2 (km s^{-1})	n.	279.9 ± 1.7	n.
γ_1 (km s^{-1})	−0.1 ± 0.9	0.1 ± 1.2	−21.7± 1.0
γ_2 (km s^{-1})	n.	−0.7 ± 2.6	n.
$a_1 \sin i$ (R$_\odot$)	9.70 ± 0.12	9.24 ± 0.06	9.58 ± 0.13
$a_2 \sin i$ (R$_\odot$)	n.	23.36 ± 0.14	n.
$m_1 \sin^3 i$ (M$_\odot$)	n.	18.56 ± 0.27	n.
$m_2 \sin^3 i$ (M$_\odot$)	n.	7.34 ± 0.09	n.
r.m.s. (km s^{-1})	6.0	4.0	9.1

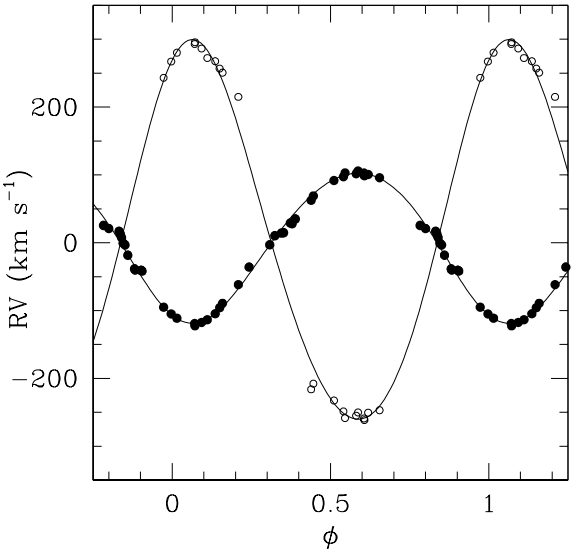

Fig. 4. HD 152219 RV curves corresponding to the He I solution of Table 4. The FEROS RV measurements listed in Table 1 have been overplotted. Filled and open symbols are for the primary and secondary components respectively.

The common orbital parameters (P, e, ω) deduced in Table 3 show a good agreement, though a slight systematic shift between the SB1 and SB2 solutions can be observed. We further derived quite different values for the RV semi-amplitudes and apparent systemic velocities. From Table 4, the final SB1 and SB2 parameters are however in more acceptable agreements. Part of the observed differences might find their origin in the following facts. First, the SB2 solutions were computed using only those points for which the two components are disentangled. As seen from Fig. 4, these are thus located near quadrature only. From Fig. 4, it is also clear that the primary points show some deviations from the RV curve near conjunction phases. Accounting for those points or not might thus lead to slightly different results. The observed dispersion probably originates from the primary line profile variability that seems to affect all the lines in a similar way. This will be discussed into more details in the next section.

3.5. A combined orbital solution

As mentioned in the *Literature Review* of Sect. 1, three SB1 orbital solutions have previously been published: Hill et al. (1974, HCB74), Levato & Morrell (1983, LM83) and García & Mermilliod (2001, GM01). HCB74 and LM83 solutions are in mutual agreement with a period $P \sim 4.16$ d while GM01 rather proposed a shorter value $P \sim 4.07$ d and a quite large eccentricity $e \sim 0.2$ for the system. Using the same data sets and the same period values as HCB74 and LM83, we re-computed their orbital solutions and found them in good agreement with the published values. We could however not reproduce the PHYB90 point at $RV \sim 40$ km s^{-1} as seen in the RV curve of HCB74 (their Fig. 3). We already encountered a similar situation for CPD −41°7733, another massive binary of the cluster (Sana et al. 2005c). We consider that the observed discrepancy comes from an erroneous Julian Date quoted by PHYB90 and we excluded the corresponding point from the RV curve adjustments.

The orbital period derived from our CES and FEROS data sets $P \sim 4.24$ d is slightly but significantly different from the period found by these authors. Again adopting their respective RV sets, we used the period search algorithms mentioned in Sect. 3.2. We found a large number of almost indiscernible aliases corresponding to periods between 4.09 and 4.27 d (9 aliases) for HCB74 and between 4.09 and 4.37 d (> 40 aliases) for LM83. Clearly the orbital periods derived by these authors were ill constrained.

Regarding the GM01 solution, we have already noted in Sana et al. (2003) that part of the GM01 new measurements were associated to erroneous Julian Dates. This clearly biased both their period search and the new orbital solution that they derived. We will thus not consider their solution here, but we will account for their measurements after correcting the quoted Julian Dates. Fig. 5 shows the literature RV points directly overplotted on our newly derived orbital solution. Once the GM01 points are corrected from the erroneous Julian Dates, the agreement for the primary RVs becomes extremely good. The only discordant point is the one from PHYB90 at $RV \sim 40$ km s^{-1} (near $\phi \sim 0.2$). We note that, compared to our new measurements, GM01 have underestimated the secondary RVs and, hence, the amplitude of the RV curve.

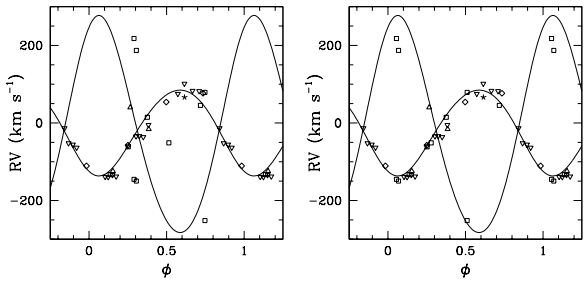

Fig. 5. Literature RV measurements directly overplotted on the SB2 solution of Table 4. Different symbols indicate different data sets: Perry et al. 1990 (PHYB90), upward triangles; Hill et al. 1974 (HCB74), downward triangles; Conti et al. 1977, asterisk; Levato & Morrell 1983 (LM83), diamonds; García & Mermilliod 2001 (GM01), squares. **Left:** *raw* GM01 data. **Right:** corrected GM01 data (see text). Note the PHYB90 point at $RV = 40$ km s^{-1}, near $\phi \approx 0.22$, which significantly deviates from the primary RV curve.

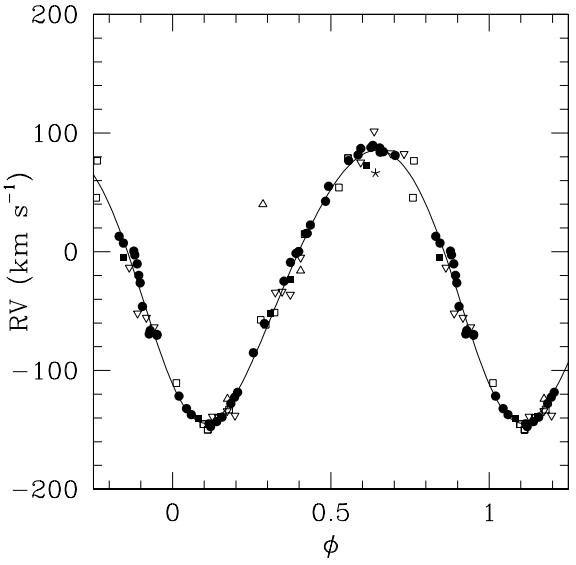

Fig. 6. HD 152219 RV curve computed using literature data together with the measurements of Table 1. Different symbols indicate different data sets. Open symbols are from previous work observations and have the same meaning as in Fig. 5. Filled symbols indicate new RV points from the present work: CES, squares; FEROS, circles. Note that the PHYB90 point at $RV = 40$ km s^{-1}, near $\phi \approx 0.35$, was rejected for period search and orbital solution determination.

Finally we combined all the literature RV measurements with the data from the present work. This yields a total of 79 observations [1] covering a time span of 13 186 d. We performed a new period search and obtained $P \approx 4.24027$ d. The associated uncertainty, corresponding to one tenth of the periodogram peak natural width, amounts to 1.4×10^{-4} d. Using the Wolfe et al. (1967) algorithm, we computed a joined orbital solution. The best-fit parameters are displayed in Table 4 and the corresponding RV curve is shown in Fig. 6. This latter solution is in very good agreement with the other solutions quoted in Table 4.

4. HD 152219 physical parameters

4.1. Spectral types and luminosity classes

4.1.1. Primary component

The spectral signature of the primary component is clearly dominant in the spectrum of HD 152219. We adopted the classification criteria from Conti (1973b) as adapted to late O-stars by Mathys (1988). They are based on the equivalent width (EW) ratio of the He I λ4471 and He II λ4542 lines. Doing this, we only considered the EWs measured on the spectra where the two components are disentangled. We obtained a mean $\log W'(\frac{W_{\lambda 4471}}{W_{\lambda 4542}}) = 0.48 \pm 0.04$ which corresponds to a spectral type O9.5, with spectral type O9 within $1\,\sigma$.

To determine the luminosity class, we adopted the criterion from Conti & Alschuler (1971) based on the EW ratio of the Si IV λ4089 and He I λ4144 lines. We obtained $\log W''(\frac{W_{\lambda 4089}}{W_{\lambda 4144}}) = 0.17 \pm 0.04$, which leads to a giant luminosity class. We also measured $\log W''' = \log(W_{\lambda 4388}) + \log(W_{\lambda 4686}) = 5.31 \pm 0.03$. According to Mathys (1988), this rules out a supergiant class. This also indicates a giant classification, unless $l_1 = \frac{L_1}{L_{\rm tot}} < 0.81$. The optical brightness of both components will be discussed in Sect. 4.2.

[1] These 79 observations include the corrected data from GM01. The discrepant point at 40 km s^{-1} from PHYB90 has however been rejected.

4.1.2. Secondary component

The main spectral signatures of the secondary star are the Balmer and He I lines. For the latter, we have been able to measure the positions and EWs with a good confidence. At our detection level, we clearly note the absence of the He II $\lambda\lambda$4542, 4686 and Mg II λ4481 lines at the positions predicted by the orbital solution (Fig. 7). The lack of He II lines definitively excludes an O spectral type and, at our detection threshold, most probably indicates a spectral subtype later than B0.5 (Walborn & Fitzpatrick 1990, WF90 hereafter). To refine our subtype classification, we carefully searched for the presence of secondary metallic lines in our FEROS spectra. We could not rule out the existence of faint Si IV and Si III lines. If these latter are present, their EWs are probably below 0.02 Å. In the metallic lines, the secondary spectral signature could only be clearly disentangled in the S III+O II λ4254 complex and the C II λ4267 line even on our highest S/N ratio FEROS spectra. These two lines have an EW about 0.01 and 0.02 Å respectively. Clearly neither the S/N ratio nor the spectral resolution of the instrument are the limiting factors here. We rather emphasize the broadness of the lines and the probably large intensity ratio between the primary and secondary lines. Because at our detection level, we do not clearly detect the C III+O II complex at $\lambda\lambda$4650-60, we suppose that the secondary is a main sequence star (however see below). Similarly we adopt a spectral type B1-B2 which, according to Walborn & Fitzpatrick (1990), corresponds to the minimum of the Mg II λ4481 line. Indeed we

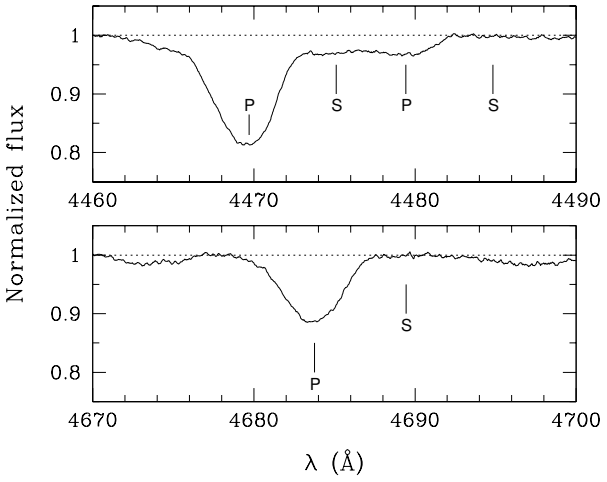

Fig. 7. He I λ4471/Mg II λ4481 and He II λ4686 regions in the HD 152219 spectrum obtained at $HJD \approx 2\,453\,132.897$ ($\phi_{\rm He\,I}$ = 0.136). The tick-marks indicate the expected positions of the primary (P) and secondary (S) lines.

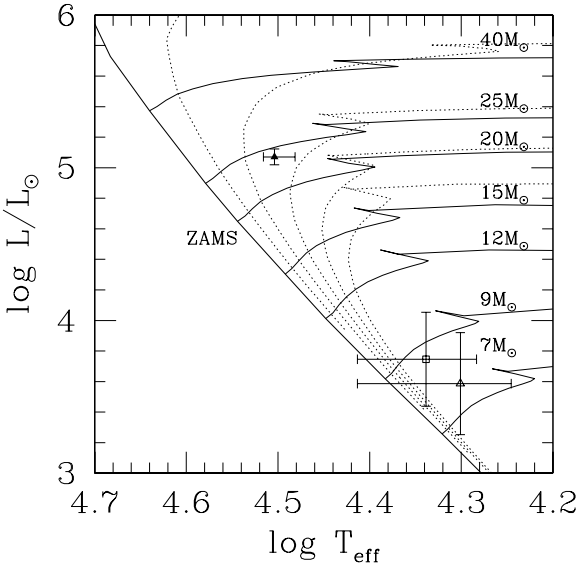

Fig. 8. HD 152219 primary (filled symbol) and secondary (open symbols) locations in the H-R diagram. Triangles (resp. squares) indicate an adopted giant (resp. main sequence) luminosity class. The evolutionary tracks from Schaller et al. (1992) have been overplotted (plain lines) together with isochrones (dotted lines) computed for ages ranging from 2 to 10 Myr with a step of 2 Myr.

would expect to detect the He II λ4686 line if the star were hotter, and the Mg II λ4481 line if it were cooler.

4.2. Optical brightness ratio and evolutionary status

We roughly estimated the optical brightness ratio based on the dilution of the primary and secondary lines in the spectrum of HD 152219. For this purpose, we compared the mean EWs of the primary lines with typical (averaged) EWs of O9.5 stars (Conti & Alschuler 1971; Conti 1973a; Mathys 1988). Based on the He I $\lambda\lambda$4026, 4144, 4388, 4471, He II $\lambda\lambda$4542, 4686 and Si IV λ4088 lines, we obtained an average brightness ratio of $l_1 = 0.86 \pm 0.05$ and 0.99 ± 0.05 assuming respectively a main sequence or a giant class. We also compared the secondary line strengths to the typical EWs reported by Didelon (1982). We focused on the He I $\lambda\lambda$4026, 4144 and 4388 lines. We obtained $l_2 = \frac{L_2}{L_{\rm tot}}$ in the range 0.07-0.10 considering B1-2 V-III stars. We adopt the average value $l_2 \approx 0.09 \pm 0.01$. According to Didelon (1982), this value is in agreement with most of the metallic lines being too diluted for being observed in the HD 152219 spectrum. Let us recall that we rejected the giant classification for the secondary on the basis of the C III+O II $\lambda\lambda$4550-4560 not being observed. With such a value for l_2, it would only be marginally detectable for a giant B1-2 star. The luminosity class of the secondary is thus still uncertain from the sole spectroscopy.

In the following discussion, we adopt a primary to secondary brightness ratio corresponding to $l_1 = 0.91 \pm 0.05$, thus opting for a conservative value for the uncertainty. Sung (2005, private communication) reported $V = 7.560$ and $B - V = 0.165$ for the system. Using $R = 3.3$ (Sung et al. 1998), adopting the absolute colors quoted by Schmidt-Kaler (1982) and a distance modulus $DM = 11.07 \pm 0.04$ (Sana et al. 2005b, and references therein), preliminary computations indicate that the system probably harbours a giant primary star, in agreement with the spectroscopic classification. To estimate the confidence interval of the following results, we considered, for the primary star, the neighbouring sub-spectral type O9 and B0 III. For the secondary, we adopted the central values corresponding to a B1.5 star, and to B0.5 and B2.5 stars as confidence limits. We obtained $M_{\rm V} = -5.03 \pm 0.09$, yielding $M_{\rm V,1} = -4.93 \pm 0.11$ and $M_{\rm V,2} = -2.42 \pm 0.69$. According to Humphreys & McElroy (1984), these values are typical for giant and main sequence stars of the quoted spectral type. For the secondary, this include the giant class at 1-σ. Using the bolometric corrections from Humphreys & McElroy (1984), we obtained $M_{\rm bol,1} = -7.93 \pm 0.13$ and $M_{\rm bol,2} = -4.62 \pm 0.77$, unless the secondary is actually a giant, in which case we have $M_{\rm bol,2} = -4.22 \pm 0.83$.

Finally the Humphreys & McElroy (1984) effective temperature scale indicates $T_{\rm eff}^{\rm O9.5\ III} = 31.9^{32.8}_{30.3}$ kK and $T_{\rm eff}^{\rm B1.5\ V} = 21.8^{25.9}_{19.2}$ kK (resp. $T_{\rm eff}^{\rm B1.5\ III} = 20.0^{25.9}_{17.6}$ kK). We thus obtained primary and secondary stellar radii of $R_1 = 11.2 \pm 1.1$ R$_\odot$ and $R_2 = 5.2 \pm 2.7$ R$_\odot$ (resp. 5.2 ± 3.6 R$_\odot$). These values are again in excellent agreement with typical O9.5 III and B1-2 V parameters. Because of the large errors associated with the secondary, we cannot rule out a B1-2 giant nature. Fig. 8 presents the location of the stars in the H-R diagram and clearly illustrates the uncertain secondary status. The primary evolutionary age is about 5 Myr, which is in agreement with the cluster age determinated from previous photometric studies (Perry et al. 1990; Balona & Laney 1995; Raboud et al. 1997; Baume et al. 1999). From a rough interpolation of the evolutionary tracks, the primary had an initial mass about 24 M$_\odot$, corresponding to

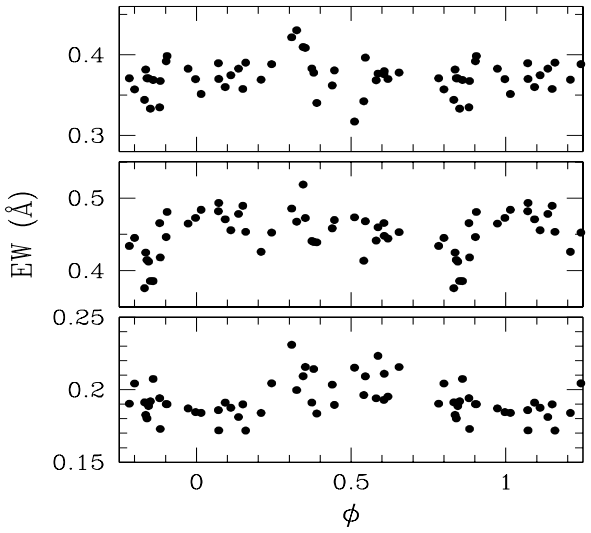

Fig. 9. EWs of the primary Si IV λ4088 (top panel), He II λ4686 (middle panel) and O III λ5592 (lower panel) lines plotted against the phase. Accoding to our He I-line ephemeris (Table 4), the primary and the secondary conjunctions should occur at $\phi \approx 0.83$ and 0.32 respectively.

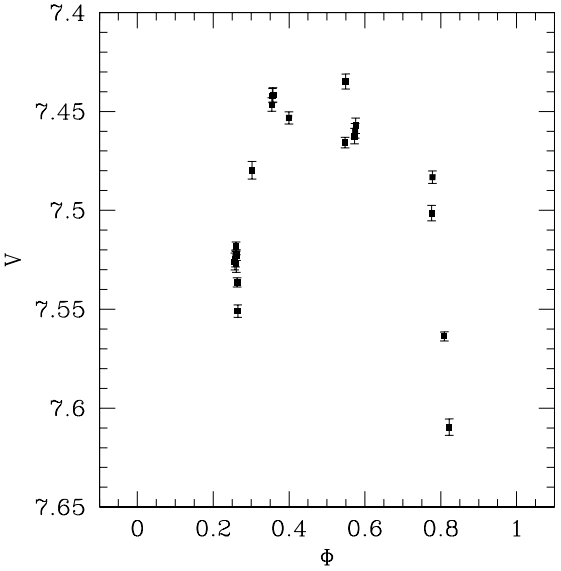

Fig. 10. OMC light curve of HD 152219 folded through our ephemerides. Only data points with a zero offset from the centre of the 5×5 pixels box are plotted.

an actual mass close to 23.3 $M_\odot$, thus slightly lower than typical O9.5 III masses (26 $M_\odot$ according to Howarth & Prinja 1989).

Finally we note that the minimal masses are quite large, suggesting a large orbital inclination. Comparing the values of Table 4 with typical O9.5 III masses, we obtain an inclination i of 63°. The secondary mass should then correspond to 10.3 $M_\odot$, thus agreeing with the adopted spectral type. Using the constraints deduced on the component radii, we find that the limiting inclination above which eclipses may occur in the system lies around 62°. Clearly, HD 152219 is a limiting case. To search for the presence of eclipses, we integrated the profile of the Si IV λ4088, He II λ4686 and O III λ5592 lines. These lines do not show the secondary spectral signature, they are isolated enough and present a clear continuum. The results are displayed in Fig. 9 and suggest that the HD 152219 optical light curve could present some modulations that peak at the conjunctions phases (around $\phi \approx 0.32$ and $\phi \approx 0.83$). Therefore, these are possibly related to eclipses happening in this system. Finally, we used the formula of Eggleton (1983) to estimate the Roche lobe radii. We found that, according to the previous results, the primary and secondary components are filling about 30% and 10% of their Roche lobe volume respectively. Both stars are thus well within their Roche lobe limits.

4.3. An eclipsing binary

To check whether HD 152219 displays photometric eclipses, we have retrieved the V-band photometry of the star from the *INTEGRAL*-OMC archive at LAEFF (Gutiérrez et al. 2004). The Optical Monitoring Camera (OMC, Mas-Hesse et al. 2003) onboard ESA's *INTEGRAL* γ-ray observatory observes the optical emission from the prime target of the main γ-ray instruments as well as from a number of pre-selected optical sources in its field of view. In the course of the survey programme of the Galactic plane, *INTEGRAL* scanned several times the region of NGC 6231 and 129 photometric data points of HD 152219 were obtained (Swings 2005, private communication). When folded with our ephemerides, these data clearly indicate drops in the optical emission ($\sim$ 0.1 – 0.18 mag) at phases near 0.3 and 0.85, i.e. close tto the expected phases of conjunction according to our radial velocity curves. However, the raw OMC light curve also displays a large dispersion ($\sim$ 0.05 mag) at phases outside the expected phases of the photometric eclipses. The OMC photometry is extracted over a 5×5 pixels square window (one pixel corresponding to $17.5'' \times 17.5''$) around the soure. In a crowded field such as NGC 6231, neighbouring sources can introduce a highly structured background thereby considerably reducing the photometric accuracy (Gutiérrez et al. 2004). We have therefore restricted ourselves to the data obtained with a zero offset between the source and the extraction box. In this way, the dispersion is considerably reduced, but at the expense of a significant reduction of the number of data points (21 points remaining). The resulting light curve is shown in Fig. 10. The two eclipses are clearly seen though the data are certainly not of a sufficient quality to perform a more quantitative analysis of the light curve.

5. Line profile variability (LPV) of the primary

As illustrated by Fig. 3, the primary lines display variable profiles with, from time to time, a flattened core and/or asymmetric wings. The phase-locked behaviour is unprobable as a similar profile may be observed near conjunction, thus when the

lines are blended, or quadratures, when they are clearly separated. Similar profile variations appear in all the primary lines. In particular, they are also seen in the Si IV λ4088, Mg II λ4481, He II λ4686, O III λ5596 and C IV λ5812 lines. The latter ones do not show the secondary signature and the variations can therefore not be attributed to the sole blending of the primary and secondary line profiles.

In early-type stars, the Balmer and He lines can harbour an emission component that might influence their observed profile. However the metallic lines should not be affected. HD 152219 is further not a particularly hot O-type star and the emission is expected to remain very faint. An underlying emission component is thus probably not the cause for the observed modulations.

Another explanation could be that the primary component is actually formed by two objects revolving on a closer orbit. In this hypothesis, we attempted to fit two Gaussian components to the primary lines. The resulting profiles much better reproduced the observed profile whenever the lines broaden, but no coherent results from one line to the other could be observed. If the primary is a multiple object, then its components should be of a similar spectral type. The secondary star does not seem to be severely affected, which indicates that the (possibly multiple) primary component is seen by its companion as a point-like mass. If multiple, the system should thus be reasonably hierarchised. Assuming that the separation between the hypothetic A and B components of the primary is at least ten times smaller than for the wider pair, we obtained $(a_A + a_B) \sin i \sim 3.3$ R$_\odot$. According to the expected value for the inclination i (see Sect. 4.2), the total separation should definitively not be larger than 4 R$_\odot$. From our measurements the two components would generally be separated by about 150 km s^{-1}. Assuming a semi-amplitude of the RV curve of $\sim$ 75 km s^{-1}, and a circular orbit, this corresponds to a maximum period around 2 days. However, typical radii of O9.5 stars are about 10 R$_\odot$, and the two components should thus share a common envelope or be at a near merging stage. Such a configuration is highly unprobable. This, in addition to the lack of coherent results for Gaussian fits, leads us to consider that the primary is most probably not a double object.

As a next step, we turn to the analyis of the observed LPV. For this purpose, the He II λ4686 line is probably the most suitable line for a first approach of the phenomenon: it is reasonably strong, well isolated, and unaffected by the secondary spectral signature. As can be deduced from Table 1 and Fig. 3, the line profiles might display heavy changes in two spectra obtained the same night (see e.g. the two spectra obtained the last night of our campaign at $\phi = 0.783$ and 0.840). Our observing strategy is thus clearly not optimized for such a kind of study. The tightest follow up was performed in May 2004 when HD 152219 was observed twice a night for six consecutive nights. As a first step, we thus focus exclusively on the He II λ4686 profiles acquired in May 2004. We used both the Time Variance Spectrum (TVS) analysis of Fullerton et al. (1996) and a 2D Fourier analysis (Rauw et al. 2001). In this latter method, the Heck et al. (1985) Fourier analysis is performed at each wavelength step. It thus provides a 2D Fourier chart (Fig. 11) that allows to identify the different frequencies at work in different part of the studied profile. Prior to the analysis, the He II λ4686 line has been brought to the primary star velocity frame using the primary orbital solution of Table 4 and the He II λ4686 apparent systemic velocity of -16.7 km s^{-1} (Table 3). For comparison, we applied a similar analysis on a line-free wavelength range ($\lambda\lambda$4738–4748 Å) located in the same FEROS echelle ordre as the He II λ4686 line. Fig. 11 also displays the average He II λ4686 profile over the May 2004 run and the results of the TVS analysis. It confirms that the line presents very significant variations.

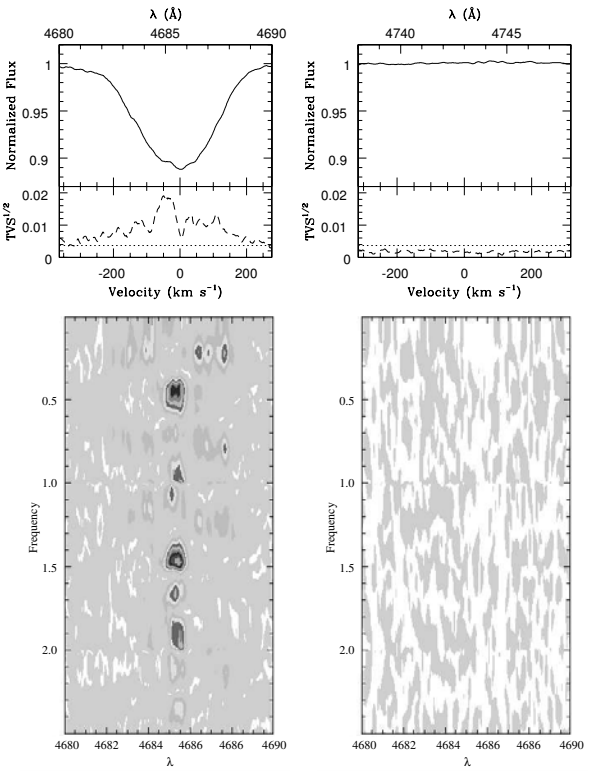

Fig. 11. Upper panels: Mean spectrum (plain lines) and square root of the time variance spectrum (TVS, dashed lines) of the He II λ4686 line profile (left) and a reference continuum domain (right). The dotted lines give the 0.99 significance level. Both the wavelength and radial velocity scales are indicated. The velocities are expressed in the reference frame of the primary. **Lower panels:** Corresponding 2D Fourier charts. The two panels use the same grey-scale levels.

The 2D Fourier chart suggests that different frequencies are probably at work in different part of the lines. To refine our analysis, we focused on narrow wavelength domains where the highest peaks are seen in the Fourier chart. Having identified the corresponding frequencies, we *prewhitened* the data for the variations at these frequencies (see e.g. Rauw et al. 2001). We proceeded recursively until no significant peaks were left in the periodogram. Table 5 summarizes the results of this analysis. Corresponding power spectra and *prewhitened* power spectra are displayed in Fig. 12. We note that it is almost impossible

Table 5. Candidate-frequencies in narrow wavelength domains of the He II λ4686 line profile. The respective aliases of the quoted frequencies are also good candidates.

Domain	ν_1 (d^{-1})	ν_2 (d^{-1})	ν_3 (d^{-1})
$\lambda\lambda$4683.75 – 4684.25	0.2015	0.4660	2.2450
$\lambda\lambda$4685.00 – 4685.80	1.4700	2.4620	
$\lambda\lambda$4687.50 – 4687.80	0.2220	1.6980	0.4150

to distinguish between a frequency-candidate and one of its aliases. These latter are thus (almost) equivalently good candidates.

Although the other observing periods provide a less appropriate coverage and display an lower S/N ratio on average, we also applied a similar analysis. The amplitude of the TVS is much more limited compared to their respective 0.99 significance levels. Briefly, they indicate that the He II λ4686 line is variable during the different runs, though the location of the most prominent variabilities could be quite different from that observed in 2004. For example in 1999 and April 2002, the variability is almost limited to the sole blue wing of the line, while in March 2002, the most prominent variations are to be found in the blue wing. Finally, the 2000 TVS profile is much flatter, indicating an almost equivalent level of variability throughout the line. We note that the observed differences could be due to an uneven sampling of the underlying phenomenon during the different observing runs. Clearly the present data set is inconclusive on that point. Finally, we also note that the He II λ5412 line displays similar results as those of the He II λ4686 line. However the line is partly affected by a neighbouring blend. Results associated with the O III λ5592 line are less conclusive, probably because of the lower S/N ratio for this line. Clearly, extending the present study to other lines in the primary spectrum may help to clarify the nature of the variations. This will however require to *clean* the HD 152219 spectrum from the secondary signature.

The possible reasons for the observed profile variations in the primary spectrum are numerous. Among the most probable, we can mention corotating wind structures (e.g. Rauw et al. 2001). In such hypothesis, we expect the modulations of the profile to be related to the rotation period of the primary. The latter should belong to the interval 0.9–4.2 d. The lower limit is computed from the critical rotational velocity at which the gravity and the centrifugal acceleration compensate each other. The upper limit of the interval was adopted considering both the measured projected equatorial velocities (see Sect. 1) and the possibility of synchronous rotation. The longer period from these two values was then adopted as a conservative upper limit and, in the present case, corresponds to the orbital period of the system. The equivalent interval in the frequency space is 0.24–1.10 d^{-1}. The best periods for the variations located near the core of the profile are apparently quite shorter. If these were confirmed, then a rotational modulation would difficultly render the observed LPV. We also remind that no trace of wind emission was found in the Balmer lines, indicating that

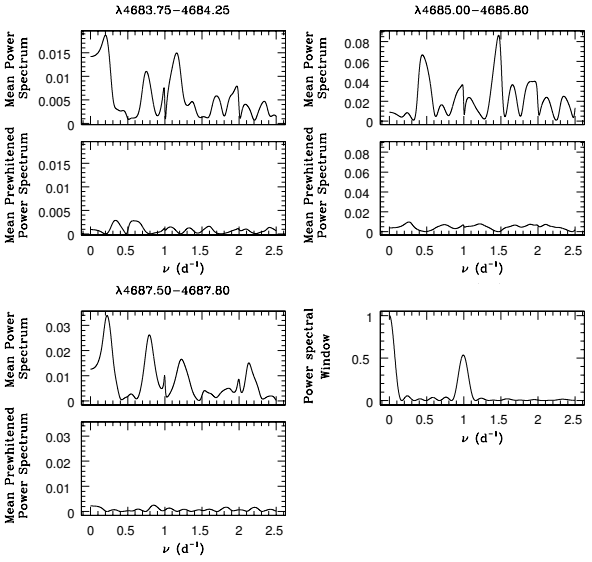

Fig. 12. Mean power spectra and mean *prewhitened* power spectra computed for the three wavelength domains of Table 5. The *prewhitening* was performed using the frequencies quoted in the same table. The bottom panel at righthand gives the power spectral window of the May 2004 observations.

the wind of the primary is rather wide, which is clearly not in favor of a wind-related effect.

Another possible scenario is linked to the magnetic field of the star that can affect the structure of the line formation region (ud-Doula & Owocki 2002), and hence the profile of the line. However, magnetic confinement in late O-type stars is not expected to play a critical role. Finally, we mention the possibility of non-radial pulsations (NRPs). Indeed HD 152219 location in the H-R diagram (Fig. 8) corresponds to the blue edge of the β Cep type pulsational instability strip computed by Kiriakidis et al. (1993, see also Pamyatnykh 1999). Fullerton et al. (1996) performed a survey of the line profile variation of a sample of O-type stars and found a good correlation with these predictions. The observed line profile variations and the subsequent TVS profiles are further reminiscent of those produced by NRPs (e.g. Fullerton et al. 1996). There are at least two other known O9.5 stars that display NRPs (ζ Oph, Kambe et al. 1997; HD 92521, Howarth & Reid 1993), although both of them are main sequence stars. Interestingly enough, their main frequencies corresponds to periods of a couple of hours. Our current time series is however too sparse to address such rapid variations. Therefore, although the main frequency-candidates obtained in Table 5 for the core of the He IIλ4686 line are indeed beyond one cycle per day, these results should be considered as very preliminary.

In regard of these considerations, it is obvious that our present data set will not allow to conclude on the nature of the LPV. Clearly more observations covering time scales of a few tens of minutes to a few days are needed. These, combined with a disentangling technique for removing the secondary signature from the HD 152219 spectrum, thus giving access to a much larger number of lines, should allow to investigate the origin of

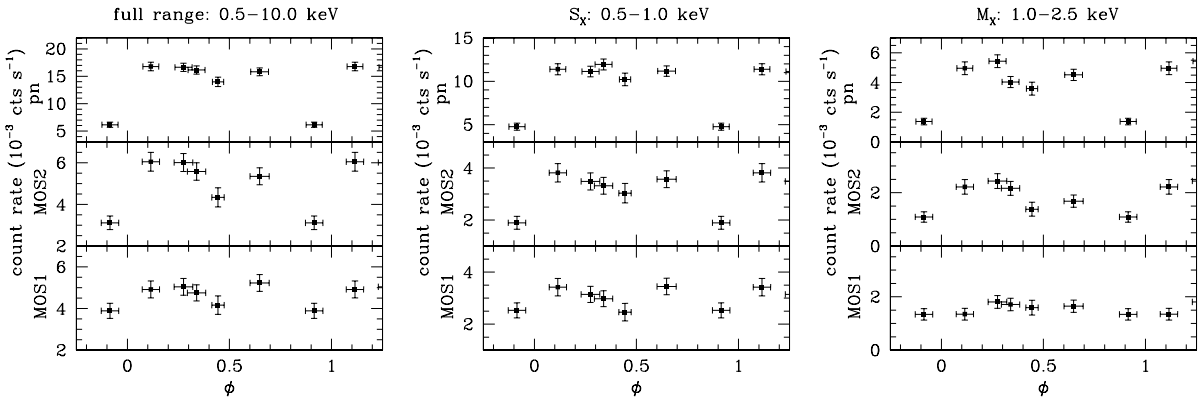

Fig. 13. Broad band X-ray light curves in the three EPIC instruments. The different energy ranges considered are indicated on top of each spectrum. The vertical bars gives the 1-σ uncertainty on the background-corrected count rates. The horizontal bars indicate the duration of each pointings.

the important line profile variations observed. If the NRP hypothesis is confirmed, then comparison with theoretical models could help to probe the inner structure of the O9.5 III component in HD 152219. Indeed the fact that the star belongs to an eclipsing binary system allows a better knowledge of crucial physical quantities (such as the star mass), that greatly facilitates a direct comparison with the models. In this regard, a dedicated follow up of HD 152219 could yield to a better comprehension of the origin of the line profile variations of O-type stars, possibly bringing answers to key questions on the physical properties of these stars.

6. X-ray Observations

As mentioned in Sect. 2.2, HD 152219 is located near a gap in the EPIC pn instrument FOV. In Sana et al. (2005b), we thus restrained the simultaneous psf fit (*emldetect* task) to the two MOS instruments. From the merged event lists of the six observations, we obtained the count rates in the total band [0.5-10.0 keV] and in three smaller ranges: a soft (S_X) band [0.5-1.0 keV], an intermediate (M_X) band [1.0-2.5 keV] and a hard (H_X) band [2.5-10.0 keV]. The hard band only accounts for a few photons and the obtained count rates show large uncertainties. We thus focused on the other energy ranges. In a next step, we performed the psf fit (*emldetect* task) for each pointings and we built broad band light curves in the different energy ranges. Surprisingly, the two instruments yielded rather incoherent results. The obtained light curves presented similar shapes but with a quite different amplitude. Indeed, the MOS1 indicates a slight variability that does however not allow to reject the null hypothesis of constant count rates throughout the six pointings. On the other hand, the MOS2 light curve shows a clear pointing-to-pointing variation, with an amplitude about 2.5 times larger than in the MOS1 instrument. Both curves only marginally agree within errors. To check these results, we re-extracted (using the SAS task *evselect*) X-ray light curves using a circular source region of 10″ radius centered on the source position. As discussed in Sect. 2.2, we included the pn instrument in the analysis. Fig. 13 presents the obtained broad band

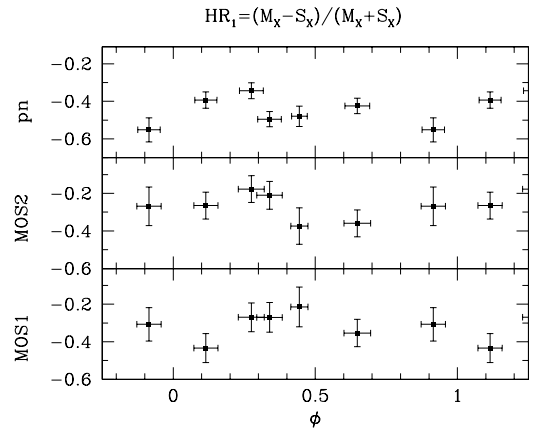

Fig. 14. HD 152219 hardness ratio (defined on top of the panel) plotted versus the phase.

light curves. Clearly the different instruments show different variability amplitudes. We performed different variability tests to detect intrinsic modulations within each pointing duration but none were found at a reasonable significance level.

In a next step, we extracted the HD 152219 X-ray spectra for each pointing and for each instrument, using the same source and background extraction regions as previously adopted for the light curves. The obtained X-ray spectra are relatively soft and peak around 0.8-0.9 keV. To characterize the properties of the emitting plasma, we adjusted optically thin thermal plasma `mekal` models (Mewe et al. 1985; Kaastra 1992). The MOS and pn spectra were adjusted simultaneously using the XSPEC software v.11.2.0 (Arnaud 1996). We adopted an equivalent interstellar column of neutral hydrogen of $N_{\rm H,ISM} = 0.27 \times 10^{22}$ cm^{-2}. A single temperature model was insufficient to adequately describe the observed spectra, except for Obs. 2. We thus adopted a two-temperature (2-T) model allowing for possible local absorption for both `mekal` components. Preliminary results indicate that the absorption column

Table 6. Results of the simultaneous fits of the three EPIC spectra with XSPEC. The model used was $\texttt{wabs}_{\rm ISM}$ * ($\texttt{mekal}_1$ + $\texttt{wabs}_2$ * $\texttt{mekal}_2$). The term $\texttt{wabs}_{\rm ISM}$ was fixed to the interstellar value ($N_{\rm H,ISM} = 0.27\times10^{22}$ cm^{-2}). The first and second columns give the phase and the observation number. The next five columns (Col. 3 to 7) provide the best-fit parameters while Col. 8 lists the corresponding reduced chi-square and the associated number of degrees of freedom (d.o.f). $N_{\rm H}$ yields the absorbing column (in units 10^{-22} cm^{-2}). kT is the model temperature (in keV) while *norm* is the normalisation factor (expressed in 10^{-5} cm^{-5}, $norm = \frac{10^{-14}}{4\pi d^2}\int n_{\rm e} n_{\rm H} dV$ with d, the distance to the source – in cm –, $n_{\rm e}$ and $n_{\rm H}$, the electron and hydrogen number densities – in cm^{-3}). The quoted upper and lower values provide the limits of the 90% confidence interval. Columns 9 to 12 provide the observed fluxes (in 10^{-14} erg cm^{-2} s^{-1}) in the 0.5 - 10.0 keV energy band and in the $S_{\rm X}$ (0.5 - 1.0 keV), $M_{\rm X}$ (1.0 - 2.5 keV) and $H_{\rm X}$ (2.5 - 10.0 keV) bands respectively.

ϕ [1]	Obs. # [2]	kT_1 [3]	$norm_1$ [4]	$N_{\rm H,2}$ [5]	kT_2 [6]	$norm_2$ [7]	χ^2_ν (d.o.f.) [8]	$f_{\rm X}$ [9]	$f_{\rm X,S}$ [10]	$f_{\rm X,M}$ [11]	$f_{\rm X,H}$ [12]
0.275	1	$0.26^{0.29}_{0.21}$	$8.3^{9.9}_{6.7}$	$0.36^{0.56}_{0.20}$	$0.70^{0.77}_{0.57}$	$6.5^{8.9}_{5.1}$	0.82 (74)	7.3	4.3	2.8	0.2
0.444	2	$0.24^{0.34}_{0.15}$	$6.0^{8.7}_{2.9}$	$0.12^{0.45}_{0.00}$	$0.61^{0.77}_{0.50}$	$5.2^{8.7}_{2.4}$	0.78 (38)	6.7	4.3	2.3	0.1
0.648	3	$0.30^{0.33}_{0.19}$	$7.8^{9.5}_{4.9}$	$0.41^{1.01}_{0.01}$	$0.71^{0.78}_{0.56}$	$4.4^{7.6}_{3.2}$	1.06 (72)	6.8	4.3	2.4	0.1
0.915[a]	4	$0.19^{0.39}_{0.08}$	$5.0^{27.1}_{1.4}$	$0.00^{3.18}_{0.00}$	$0.58^{n.}_{0.46}$	$4.2^{6.3}_{1.1}$	1.08 (21)	5.9	3.9	1.9	0.1
0.115	5	$0.22^{0.27}_{0.18}$	$8.0^{11.1}_{5.9}$	$0.00^{0.34}_{0.00}$	$0.69^{0.79}_{0.61}$	$4.8^{6.5}_{3.5}$	1.31 (69)	6.9	4.4	2.4	0.1
0.339	6	$0.28^{0.34}_{0.20}$	$6.3^{8.2}_{3.9}$	$0.25^{0.64}_{0.03}$	$0.62^{0.74}_{0.55}$	$5.5^{7.8}_{3.2}$	0.94 (67)	6.7	4.1	2.4	0.1
Merged	–	$0.26^{0.29}_{0.22}$	$7.5^{8.2}_{6.5}$	$0.22^{0.35}_{0.11}$	$0.67^{0.72}_{0.63}$	$5.0^{5.4}_{4.2}$	1.09 (268)	6.9	4.3	2.4	0.1

a. The simultaneous fit was restrained to the MOS2+pn instruments (see text).

associated with the lower temperature component tends to be systematically close to zero. Lower residuals and more stable solutions are obtained by removing this parameter from the fit. Best-fit results are quoted in Table 6. Except for Obs. 4 at $\phi = 0.915$, the results were quite consistent. A more detailed inspection revealed that the MOS1 spectrum of Obs. 4 presents discrepant channels. We thus rejected the spectrum and simultaneously adjusted the EPIC MOS2 and pn spectra. The results of this latter fit are given in Table 6 instead of the simultaneous EPIC fit. From Table 6 only a slight variation can be seen in the obtained parameters, the HD 152219 X-ray spectrum being somewhat softer when the emissivity is lower. This is also seen in the hardness ratio curves of Fig. 14. Finally, for each of the EPIC instrument, we extracted the combined spectrum from the merging of the six X-ray observations. We also used a 2-T `mekal` model to fit the obtained spectra and the best parameters are given in the last line of Table 6. The spectra and the best fit models are plotted in Fig. 15. From the Berghöfer et al. (1997) relations and adopting either a luminosity class V or III, the expected intrinsic emission from the two stellar components amounts to about $\log(L_{\rm X}) \approx 31.8$ (erg s^{-1}). Though the energy ranges considered are not exactly identical, the observed luminosities from the system are in very good agreement with this value.

Finally, we used the constraints on the physical parameters deduced in the previous section to get more insight into the winds of the HD 152219 components. We assumed an orbital inclination of 63° as suggested by the comparison of the minimal masses of the system with typical masses for stars of similar spectral types and luminosity classes. Mass-loss rates and terminal velocities were estimated following the mass-loss recipes of Vink et al. (2000, 2001). As expected, the primary wind is overwhelmingly dominant and no ram pressure equilibrium is possible along the system axis. This suggests that the primary wind may crush on the secondary star surface. However, due to the probable separation between the two components, the X-ray emission that could be produced by such an interaction is only about a few 10^{30} erg s^{-1} (Usov 1992) and is thus one order of magnitude smaller than the intrinsic contribution of the two stellar components. However, it is of the same order of magnitude than the observed modulations in the HD 152219 X-ray flux. We further note that the minimum of the X-ray emission arises when the secondary is presenting its rear side to the observer ($\phi \sim 0.8 - 0.9$), thus occulting any emission produced on its inner side. We therefore propose that HD 152219 displays a similar wind interaction as CPD –41°7742, an O9 V+B0.5 V massive binary in NGC 6231 (Sana et al. 2005a). Unfortunately, because of the longer period of HD 152219, our X-ray data do not provide a good phase coverage and critical phases are missed. In addition, the HD 152219 eccentricity, tough limited, induce a distance variation of at least 15% between apastron and periastron, which influences the strength of the primary winds at the distance of the secondary surface. Clearly a better phase coverage of the HD 152219 system in the X-rays combined with additional modelling that accounts for the system orientation and for the eccentricity of the orbit are needed to answer this question.

7. Summary

We present the results of an optical spectroscopic monitoring campaign of the early-type binary HD 152219, located near the core of the NGC 6231 open cluster in the Sco OB 1 association. Although the absorption lines are broad in the HD 152219 spectrum, we report the clear detection of the secondary component. We find that previous period determinations suffered from strong aliasing or were biased. The orbital elements deduced from the analysis of different line Doppler shifts are in good agreement. Our final period value, $P \sim 4.2403$ d, further allows to reproduce all the RV observations obtained since the late 1960's. We confirm that the system has a slight eccentricity

Table 7. Unabsorbed fluxes ($f^{\rm un.}$, expressed in 10^{-14} erg cm^{-2} s^{-1}) corresponding to the best-fit 2-T models of Table 6 and corrected using the adopted interstellar absorbing column $N_{\rm H,ISM} = 0.27 \times 10^{22}$ cm^{-2}. The last column gives the X-ray luminosity (in erg s^{-1}) in the 0.5 - 10.0 keV band, assuming $DM = 11.07$.

ϕ	Obs. #	$f_{\rm X}^{\rm un.}$	$f_{\rm X,S}^{\rm un.}$	$f_{\rm X,M}^{\rm un.}$	$f_{\rm X,H}^{\rm un.}$	$\log L_{\rm X}$
0.275	1	20.4	16.2	4.0	0.2	31.82
0.444	2	18.8	15.3	3.5	0.1	31.78
0.648	3	18.8	15.1	3.6	0.1	31.78
0.915	4	17.3	14.4	2.8	0.1	31.74
0.115	5	20.6	17.0	3.5	0.2	31.82
0.339	6	18.1	14.3	3.6	0.1	31.76
Merged	–	19.5	15.8	3.6	0.1	31.80

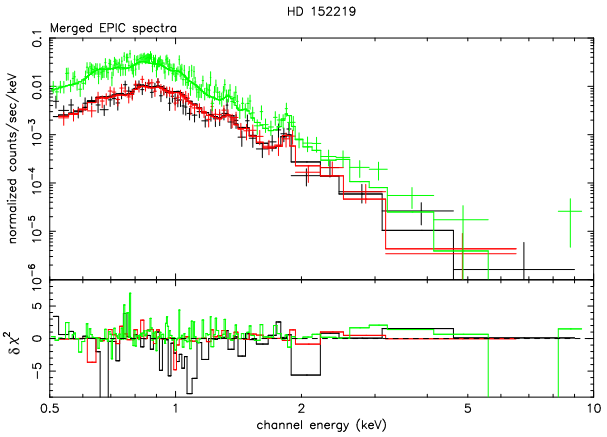

Fig. 15. Combined X-ray spectra of HD 152219. Different colours indicate different instrument: MOS1, black; MOS2, red; pn, green. The best fit model of Table 6 is given by the plain lines. The bottom panel shows the contributions of individual bins to the χ^2 of the fit. The contributions are carried over with the sign of the deviation (in the sense data minus model). This figure appears in colour in the electronic edition of the journal.

$e = 0.08 \pm 0.01$ and we determine a primary to secondary mass ratio of 2.53 ± 0.02. The two components have minimal masses of respectively 18.6 ± 0.3 and 7.3 ± 0.1 M$_\odot$.

Based on spectroscopic criteria, we find that HD 152219 is most probably formed by an O9.5 giant primary and a B1-2 V-III secondary. From the comparison of primary and secondary line EWs with typical line strengths of stars of similar spectral types, we estimate the brightness ratio to correspond to $l_1 = L_1/L_{\rm tot} = 0.91 \pm 0.05$, a value which is rather independent on the assumption on the luminosity classes. We derive absolute magnitudes in good agreement with the typical magnitudes of stars of the corresponding spectral types. The evolutionary status of the primary does well agree with previous estimates of the cluster age. The secondary location in the H-R diagram is very ill constrained. This results from the faintness of the secondary signature in the HD 152219 spectrum and, therefore, from the very few metallic lines reliably detected. These lines are however crucial to accurately determine the spectral type and luminosity class of early B-type stars. We note that, in such situation, spectral disentangling techniques may provide a more powerful tool than our 'line-by-line' approach. We however estimate the component radii to be approximately of 11 and 5 R$_\odot$. Finally, *INTEGRAL*-OMC observations, reveals that HD 152219 is most probably an eclipsing binary systems, though the quality of the data is too limited to provide reliable constraints on the physical and orbital parameters of the systems.

The primary component of HD 152219 shows clear line profile variations that similarly affect most of the lines in its spectrum. In this paper, we restrain our analysis to the He II λ4686 line. We compute the time variance spectrum of the line and perform a 2D Fourier analysis. We suggest that selected regions of the profile could be associated with different frequencies. Data sets from the different campaigns do however not provide converging results, but our coverage of the phenomenon is clearly insufficient to conclude on this point. We note that HD 152219 is located on the blue edge of the β Cep type pulsational instability strip in the H-R diagram (Kiriakidis et al. 1993; Pamyatnykh 1999) and that the observed variations are reminiscent of those produced by non-radial pulsation modes (e.g. Fullerton et al. 1996). Clearly, dedicated observations combining high S/N, high spectral resolution and a tight follow up of the possibly short time-scale variations should help to better constrain the nature of the phenomenon at work in this particularly interesting system.

Finally, we also reported the analysis of the XMM-*Newton* X-ray observations of HD 152219, that were acquired during a 5-day campaign towards the NGC 6231 cluster (Sana et al. 2005b). The three EPIC instruments present somewhat discrepant results, indicating different degrees of variability in the source X-ray flux. Broad band X-ray light curves built from MOS2 and pn data however indicate strong variability on a time-scale of days. The HD 152219 X-ray spectrum is relatively soft and peaks at energies about 0.8-0.9 keV. The averaged spectrum is well described by a 2-T `mekal` model with an unabsorbed lower temperature component ($kT_1 = 0.26$ keV) and a moderately absorbed slightly hotter component ($kT_2 = 0.67$ keV). The mean X-ray luminosity of the source is about $\log(L_{\rm X}) \approx 31.8$ (erg s^{-1}) but presents fluctuations of about 10% around this value. These fluctuations are further correlated with slight changes in the X-ray spectral parameters, the flux being slightly harder when the emission level is higher and slightly softer otherwise. Though the exact nature of the observed variability remains rather uncertain, we tentatively interpret it as the signature of a wind interaction phenomenon. In a binary system such as HD 152219, the overwhelmingly dominant primary wind may crush on the secondary star surface, producing an extra amount of X-rays associated with the side of the secondary facing the primary. We note indeed that the amplitude of the fluctuations that would be produced by such an interaction are of the same order of magnitude as the ones observed in the HD 152219 X-ray flux. The latter reaches its minimum while the secondary is turning its rear side towards the observer, thus occulting the possible X-ray emission associated with its inner surface. Detailed theoretical works and modelling of the phenomenon are however needed to confirm this hypothesis.

Acknowledgements. We are grateful to Jean-Pierre Swings for providing us with the OMC photometry of HD 152219. It is a pleasure to thank M. De Becker as well, for assistance in handling the TVS and 2D Fourier analyses. The authors are greatly indebted towards the 'Fonds de la Recherche Scientifique' (FNRS), Belgium, for multiple supports. Part of this work was also supported by the PRODEX XMM-OM and Integral Projects, contracts P4/05 and P5/36 'Pôle d'Attraction Interuniversitaire' (Belgium).

References

Arnaud, K. A. 1996, in ASP Conf. Ser., Vol. 101, Astronomical Data Analysis Software and Systems V, ed. G. Jacoby & J. Barnes, 17
Balona, L. A., & Laney, C. D. 1995, MNRAS, 276, 627
Baume, G., Vázquez, R. A., & Feinstein, A. 1999, A&AS, 137, 233
Berghöfer, T. W., Schmitt, J. H. M. M., Danner, R., & Cassinelli, J. P. 1997, A&A, 322, 167
Conti, P. S. 1973a, ApJ, 179, 161
Conti, P. S. 1973b, ApJ, 179, 181
Conti, P. S., & Alschuler, W. R. 1971, ApJ, 170, 325
Conti, P. S., & Ebbets, D. 1977, ApJ, 213, 438
Conti, P. S., Leep, E. M., & Lorre, J. J. 1977, ApJ, 214, 759
Didelon, P. 1982, A&AS, 50, 199
Eggleton, P. P. 1983, ApJ, 268, 368
Feinstein, A., & Ferrer, O. E. 1968, PASP, 80, 410
Fullerton, A. W., Gies, D. R., & Bolton, C. T. 1996, ApJS, 103, 475
García, B., & Mermilliod, J. C. 2001, A&A, 368, 122
Gosset, E., Royer, P., Rauw, G., Manfroid, J., & Vreux, J.-M. 2001, MNRAS, 327, 435
Gutiérrez, R., Solano, E., Domingo, A., & García, J. 2004, in ASP Conf. Ser. 314: Astronomical Data Analysis Software and Systems (ADASS) XIII, 153
Heck, A., Manfroid, J., & Mersch, G. 1985, A&AS, 59, 63
Hill, G., Crawford, D. L., & Barnes, J. V. 1974, AJ, 79, 1271
Howarth, I. D., & Prinja, R. K. 1989, ApJS, 69, 527
Howarth, I. D., & Reid, A. H. N. 1993, A&A, 279, 148
Humphreys, R. M., & McElroy, D. B. 1984, ApJ, 284, 565
Jansen, F., Lumb, D., Altieri, B., et al. 2001, A&A, 365, L1
Kaastra, J. 1992, An X-Ray Spectral Code for Optically Thin Plasmas, (Internal SRON-Leiden Report, updated version 2.0)
Kambe, E., Hirata, R., Ando, H., et al. 1997, ApJ, 481, 406
Kiriakidis, M., Fricke, K. J., & Glatzel, W. 1993, MNRAS, 264, 50
Lafler, J., & Kinman, T. D. 1965, ApJS, 11, 216
Levato, H., & Malaroda, S. 1980, PASP, 92, 323
Levato, H., & Morrell, N. 1983, Astrophys. Lett., 23, 183
Mas-Hesse, J. M., Giménez, A., Culhane, J. L., et al. 2003, A&A, 411, L261
Mason, K. O., Breeveld, A., Much, R., et al. 2001, A&A, 365, L36
Mathys, G. 1988, A&AS, 76, 427
Mewe, R., Gronenschild, E. H. B. M., & van den Oord, G. H. J. 1985, A&AS, 62, 197
Moore, C. E. 1959, A multiplet table of astrophysical interest. Part 1 (NBS Technical Note, Washington: US Department of Commerce, 1959, Rev. edition)
Pamyatnykh, A. A. 1999, Acta Astronomica, 49, 119
Perry, C. L., Hill, G., Younger, P. F., & Barnes, J. V. 1990, A&AS, 86, 415
Raboud, D., Cramer, N., & Bernasconi, P. A. 1997, A&A, 325, 167
Rauw, G., Morrison, N. D., Vreux, J.-M., Gosset, E., & Mulliss, C. L. 2001, A&A, 366, 585
Sana, H., Rauw, G., & Gosset, E. 2001, A&A, 370, 121
Sana, H., Hensberge, H., Rauw, G., & Gosset, E. 2003, A&A, 405, 1063
Sana, H., Stevens, I. R., Gosset, E., Rauw, G., & Vreux, J.-M. 2004, MNRAS, 350, 809
Sana, H., Antokhina, E., Royer, P., et al. 2005a, A&A, in press
Sana, H., Gosset, E., Rauw, G., Sung, H., & Vreux, J.-M. 2005b, A&A, submitted
Sana, H., Rauw, G., & Gosset, E. 2005c, A&A, submitted
Sana, H., Rauw, G., Nazé, Y., Gosset, E., & Vreux, J.-M. 2005d, A&A, submitted
Schaller, G., Schaerer, D., Meynet, G., & Maeder, A. 1992, A&AS, 96, 269
Schmidt-Kaler, T. 1982, Landolt-Börnstein, Numerical Data and Functional Relationships in Science and Technology, New Series, Group VI, Vol. 2b, Physical Parameters of the Stars (Berlin: Springer-Verlag)
Strüder, L., Briel, U., Dennerl, K., et al. 2001, A&A, 365, L18
Sung, H., Bessell, M. S., & Lee, S. 1998, AJ, 115, 734
Turner, M. J. L., Abbey, A., Arnaud, M., et al. 2001, A&A, 365, L27
ud-Doula, A., & Owocki, S. P. 2002, ApJ, 576, 413
Underhill, A. B. 1994, ApJ, 420, 869
Usov, V. V. 1992, ApJ, 389, 635
Vink, J. S., de Koter, A., & Lamers, H. J. G. L. M. 2000, A&A, 362, 295
Vink, J. S., de Koter, A., & Lamers, H. J. G. L. M. 2001, A&A, 369, 574
Walborn, N. R., & Fitzpatrick, E. L. 1990, PASP, 102, 379
Wolfe, R. H., Horak, H. G., & Storer, N. W. 1967, The machine computation of spectroscopic binary elements (Modern astrophysics. A memorial to Otto Struve, Ed. M. Hack – New-York, Gordon Breach), 251

Astronomy & Astrophysics manuscript no. hd152218˙v2 May 21, 2005
(DOI: will be inserted by hand later)

The massive binary HD 152218⋆

Optical spectroscopy and X-ray observations

H. Sana[1,⋆⋆], Y. Nazé[1], B. O'Donnell[2,1], G. Rauw[1,⋆⋆⋆,†], and E. Gosset[1,⋆⋆⋆,†]

[1] Institut d'Astrophysique et de Géophysique, Liège University, Allée du 6 Août 17, Bat. B5c, B-4000 Liège, Belgium
e-mail: sana@astro.ulg.ac.be,naze@astro.ulg.ac.be,rauw@astro.ulg.ac.be,gosset@astro.ulg.ac.be
[2] Dept. of Physics & Astronomy, University College London, Gower Street, London WC1E 6BT, UK.
e-mail: zcapy98@ucl.ac.uk

Abstract. This paper is part of a series aiming at the study of the short period ($P < 6$ d) O-type binaries in the young open cluster NGC 6231. It probes the orbital and X-ray properties of the late O-type SB2 binary HD 152218. Thanks to our present set of high-resolution optical spectra, we unveil the existing contradictions between the two latest published works on the subject and we clearly confirm the Stickland et al. (1997) results. Combining the present data set with previous observations, we solve the aliasing on the period and re-derive a value close to 5.604 d. Our eccentricity $e = 0.259 \pm 0.006$ is slightly lower than previously admitted. We show that HD 152218 is probably undergoing a relatively rapid apsidal motion of about 3 yr^{-1} and we confirm the O9IV+O9.7V classification for the two components ofthe system. We derive minimal masses of 15.82 ± 0.26 M$_\odot$ and 12.00 ± 0.19 M$_\odot$ and constrain the radius of the components to $R_1 = 10.3 \pm 1.3$ R$_\odot$ and $R_2 = 7.8 \pm 1.7$ R$_\odot$. These values are in good agreement with previous findings and further indicate that HD 152218 should have an orbital inclination of about 60°. Finally, we report the results of XMM-*Newton* observations monitoring the X-ray emission of HD 152218 throughout its 5.6 d orbital motion. The averaged X-ray spectrum is relatively soft and it is well reproduced by a 2-T optically thin thermal plasma model with component temperatures about 0.3 and 0.7 keV. We show that the system presents an increase of its X-ray flux of about 30% near apastron compared to periastron. We note that this could be the signature of an ongoing wind-wind interaction process occurring within the wind acceleration region. Such a scenario is also supported by the apparent modulation of the hardness ratio, which seems higher when the emission level is stronger. We however note that second order effects, such as radiative inhibition might crucially affect the wind interaction structure and might even govern the flow of colliding wind material in the system.

Key words. stars: individual: HD 152218 – stars: binaries: spectroscopic – stars: early-type – stars: fundamental parameters – X-rays: stars – X-rays: individual: HD 152218

1. Introduction

Early-type stars of spectral type O are characterized by strong stellar winds. Though not as extreme as those of their evolved descendents, the Wolf-Rayet stars, these winds combine terminal velocities of a few thousand km s^{-1} and important mass-loss rates (about $10^{-7} - 10^{-5}$ M$_\odot$ yr^{-1}) that significantly affect both the surroundings of the star and its evolution. In a binary system, it is expected that the winds from the two stars collide, producing a density enhanced region known as the wind interaction zone. The shock-heated plasma within this zone is expected to produce an additional contribution to the X-ray emission from the early-type system and indeed, the early-type binaries are known to be X-ray overluminous compared to single stars of the same spectral type (Chlebowski & Garmany 1991). This extra X-ray emission might display phase-locked modulation, either due to a change of the absorption properties along the line of sight, or to a modulation of the shock strength due e.g. to a varying separation between the components in an eccentric binary. The properties of the shock thus strongly depend both on the geometry of the binary system and on the characteristics of the individual winds. However these properties often cruelly lack accurate constraints. In this framework, our team in Liège is involved in a long-standing effort to study early-type

Send offprint requests to: H. Sana e-mail: sana@astro.ulg.ac.be

⋆ Based on observations collected at the European Southern Observatory (La Silla, Chile), at the Cerro Tololo Inter-American Observatory (Cerro Tololo, Chile) and with XMM-*Newton*, an ESA Science Mission with instruments and contributions directly funded by ESA Member States and the USA (NASA).

⋆⋆ Research Fellow FNRS (Belgium)

⋆⋆⋆ Research Associate FNRS (Belgium)

† Visiting Astronomer, CTIO, National Optical Astronomy Observatories (NOAO). NOAO is operated by the Association of Universities for Research in Astronomy, Inc. under contract with the National Science Foundation.

Table 1. Journal of the spectroscopic observations of HD 152218. Column 1 gives the instrument used and Col. 2 lists the Heliocentric Julian Date (in format HJD−2 450 000) at mid-exposure. The next three columns present the phases (calculated from the He I-line SB2 orbital solution of Table 4) and the averaged primary and secondary radial velocities computed in the respective systemic velocity frames (see Sect. 3.3).

Instrument	HJD (days)	$\phi_{\rm HeI}$	$\overline{RV_{\lambda,1}-\gamma_{\lambda,1}}$ (km s^{-1})	$\overline{RV_{\lambda,2}-\gamma_{\lambda,2}}$ (km s^{-1})
CES +	621.673	0.406	−25.00	−29.31
CAT	622.642	0.579	63.69	−133.73
	622.755	0.599	80.30	−123.20
	623.648	0.759	151.20	−200.79
	623.762	0.779	163.30	−188.40
	624.590	0.927	74.35	−116.83
	624.722	0.950	13.36	9.05
	625.626	0.112	−158.93	209.21
	625.734	0.131	−171.70	233.10
	626.591	0.284	−104.57	166.73
	626.716	0.306	−85.00	141.40
BME +	1328.905	0.609	82.27	−124.90
CTIO 1.5m	1329.855	0.778	147.17	−199.78
	1331.882	0.140	−182.39	213.02
FEROS +	1299.883	0.430	−7.56	−5.01
ESO 1.5m	1300.882	0.608	94.15	−107.22
	1301.883	0.787	152.44	−201.56
	1302.901	0.968	−2.09	0.46
	1304.902	0.325	−82.39	134.85
	1323.853	0.707	132.51	−175.86
	1327.796	0.411	−11.80	−9.25
	1669.812	0.442	−6.42	−3.87
	1670.804	0.619	96.65	−114.87
	1670.918	0.639	108.37	−132.91
	1671.828	0.802	153.10	−200.44
	1672.865	0.987	−12.61	−10.06
	1673.878	0.168	−168.93	211.74
	2037.812	0.110	−172.15	221.33
	2037.903	0.126	−174.37	222.99
	2039.800	0.465	−3.87	−1.32
	2040.859	0.654	111.51	−142.01
	2381.695	0.474	−2.42	0.13
	2382.692	0.652	109.41	−147.06
	2383.691	0.831	149.50	−193.52
FEROS +	2782.709	0.033	−98.31	129.27
ESO 2.2m	2783.748	0.219	−148.99	194.69
	2784.699	0.389	−17.66	−15.11
	3130.843	0.156	−173.97	223.41
	3131.716	0.312	−85.25	133.87
	3132.730	0.493	4.66	3.89
	3133.760	0.677	115.83	−163.34
	3134.723	0.849	141.10	−189.24

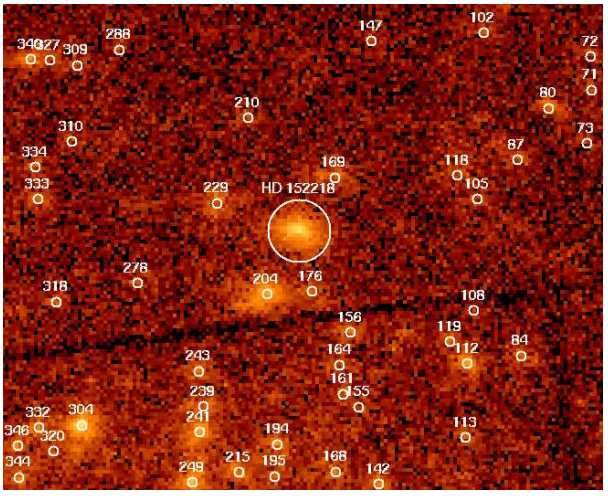

Fig. 1. Combined EPIC MOS1 + MOS2 image in the vicinity of HD 152218. The adopted source extraction region is shown. Neighbouring X-ray sources are labelled using the internal numbering of Sana et al. (2005c).

stars in a number of open clusters. One of our main targets during these last years has been the young open cluster NGC 6231.

Considered as the core of the Sco OB 1 association, NGC 6231 presents a very rich early-type star population (Sana et al. 2005e). It has recently been the target of a deep XMM-*Newton* campaign (Sana et al. 2005c) which has allowed to probe the X-ray properties of its early-type population (Sana et al. 2005e). In parallel to this X-ray campaign, we have been monitoring most of the O-type stars in the XMM-*Newton* field of view using high-resolution optical facilities. In particular, we have focused on the known early-type binaries of the cluster. NGC 6231 indeed presents no less than five O-type systems with orbital periods between 2.4 and 5.8 days. Four of them have already been the subject of previous papers: HD 152248 (Sana et al. 2001, 2004), CPD −41°7742 (Sana et al. 2003, 2005a), CPD −41°7733 (Sana et al. 2005d), HD 152219 (Sana et al. 2005b). The present work focuses on the remaining short period binary, HD 152218. This star is a long known SB2 system (Struve 1944). Previous papers however reported conflicting results and we thus decided to re-appraise the orbital properties of this apparently well-studied system. The aim is to bring its orbital and physical properties on firm ground. As mentioned above, accurate ephemeris and a detailed knowledge of the orbital and physical properties of a system are indeed crucial ingredients for interpreting the X-ray data and, for example, for uncovering the possible signature of a wind interaction.

Together with the previously published papers of this series, the results from the present work will provide one of the best set of observational constraints on the short-period early-type binary population in the open cluster NGC 6231. It will also provide a particularly homogeneous sample (in terms e.g. of distance, age and chemical composition) and aims at providing observational guide-lines for massive binary formation and evolution theories.

The remaining of this paper is organised as follows. The next section describes the observational material and the data reduction processes. In Sect. 3, we derive the orbital solution of the system. In particular, we combine our current data set with previously published observations to probe the orbital period and the possible existence of an apsidal motion. In Sect. 4, we discuss the physical properties and evolutionary status of the

Table 2. Journal of the XMM-*Newton* observations of HD 152218. The Julian Date (JD) at mid-exposure is given in Col. 2. Cols. 3 and 4 list the effective exposure times for the EPIC MOS1 and MOS2 instruments while Cols. 5 and 6 report the background-subtracted, vignetting and exposure-corrected count-rates in the different instruments. The last column provides the orbital phase of HD 152218 for each XMM-*Newton* observation at mid-exposure, according to the He I-line ephemerides given in Table 4. The phase extension of the pointings is about 0.06. Obs. 2 and 4 were however affected by high background events that reduced the nominal exposure time by about one third.

Obs. #	JD	Effective duration (ksec)		Count rates (10^{-3} cnt s^{-1})		Phase $\phi_{\rm HeI}$ of
	JD−2 450 000	MOS1	MOS2	MOS1	MOS2	HD 152218
1	2158.214	33.1	33.2	13.3 ± 0.8	14.7 ± 0.9	0.591
2	2158.931	19.8	19.8	17.5 ± 1.2	12.9 ± 1.0	0.719
3	2159.796	33.7	33.9	13.8 ± 0.8	13.1 ± 0.8	0.873
4	2160.925	26.0	24.3	12.5 ± 0.9	11.6 ± 0.9	0.075
5	2161.774	30.9	31.0	14.4 ± 0.9	13.4 ± 0.9	0.226
6	2162.726	32.9	32.8	15.7 ± 0.9	14.4 ± 0.9	0.396

system. The X-ray observations are analysed in Sect. 5 while Sect. 6 provides a summary of the present work.

Literature review

Located at about 6′.8 N-NW from the NGC 6231 cluster core, HD 152218 is a bright ($V = 7.562$) early-type spectroscopic binary. On the basis of five spectra, Struve (1944) reported the discovery of this SB2 system, noting that the two components have comparable intensities. Later on, Morgan et al. (1953) adopted an O9V spectral classification while Schild et al. (1969) quoted a more evolved O9.5IIIn system. Whereas Walborn (1973) classified the object as O9.5IV(n), Levato & Malaroda (1980) preferred an O9IV type. Using Struve data together with 15 new observations, Hill et al. (1974) proposed the first SB2 orbital solution with a period $P = 5.40 \pm 0.01$ d, an eccentricity $e = 0.26 \pm 0.10$, and primary and secondary radial velocity (RV) curve semi-amplitudes of 161 ± 20 and 202 ± 20 km s^{-1} respectively. In 1983, using a single additional point, Levato & Morrell derived a new orbital solution, obtaining slightly larger period and eccentricity : $P = 5.50090 \pm 3 \times 10^{-5}$ d and $e = 0.29 \pm 0.05$. They also derived a lower semi-amplitude for the secondary RV-curve ($K_2 = 182 \pm 10$ km s^{-1}) while the primary one remains mostly unchanged ($K_1 = 158 \pm 9$ km s^{-1}).

More recently, using IUE observations Penny et al. (1994) and Stickland et al. (1997) probably provided the more comprehensive study of this object so far. On the basis of a tomographic separation of the IUE spectra, Penny et al. found a primary to secondary UV flux ratio of 2.0 and derived an interpolated spectral classification of O9III + O9.8III. Using a cross-correlation technique, Stickland et al. obtained accurate RV measurements throughout the orbital cycle and derived a new orbit. They obtained $P = 5.603979 \pm 0.000026$ d and a still larger eccentricity $e = 0.308 \pm 0.018$, as well as $K_1 = 156.9 \pm 3.6$ km s^{-1} and $K_2 = 210.4 \pm 3.5$ km s^{-1}. They measured rotational velocities $v_{\rm e} \sin i$ of 152 and 133 (± 10) km s^{-1}. Re-addressing the evolutionary status of the two components, these authors found that the luminosity of the object was much more consistent with types O9.5IV+O9.5V. From the comparison of the minimal masses derived ($M_1 \sin^3 i = 14.22$ and $M_2 \sin^3 i = 10.60$ M$_\odot$ respectively), they estimated the inclination i of the system to be about $56^\circ \pm 3^\circ$. Finally, they constrained the radii to values of $R_1 = 10.1 \pm 1.0$ R$_\odot$ and $R_2 = 8.9 \pm 2.0$ R$_\odot$, indicating that the system remains well detached, even near the periastron passage. Later on, García & Mermilliod (2001) obtained seven new observations. Combining their data with previously published measurements, they proposed a quite revised orbital solution characterized with a period of $P = 4.89255 \pm 10^{-5}$ d and a large eccentricity $e = 0.398 \pm 0.005$. To conclude this review of the existing literature on the object, we may also mention the work of Howarth et al. (1997), who obtained projected rotational velocities of 143 and 125 km s^{-1} for the primary and secondary respectively, and a terminal wind velocity of about 2050 km s^{-1}.

2. Observations and data reduction

2.1. Optical spectroscopy

The present work is based on 42 high-resolution spectra of HD 152218 obtained at the European Southern Observatory (ESO, La Silla, Chile) and at the Cerro Tololo Inter-American Observatory (CTIO). These were acquired during 35 different nights distributed over 8 runs between May 1997 and May 2004. The journal of the observations is presented in Table 1.

In May 1997, five (resp. six) high resolution spectra of the He I λ4471 (resp. He II λ4686) line were obtained with ESO's 1.4 m Coudé Auxiliary Telescope (CAT) at La Silla, using the Coudé Echelle Spectrometer (CES) equipped with the Long Camera (LC). The detector used was ESO CCD#38, a Loral 2688×512 pixel CCD with a pixel size of $15 \times 15\,\mu$m. The slit width was chosen to achieve a nominal resolving power of 70000–80000. The effective resolving power as derived from the FWHM of the lines of the ThAr calibration exposures is 65000–75000. Typical exposure times were of the order of 30 minutes and the average S/N ratio is about 140. The observed wavelength domain is centered on the He I λ4471 or He II λ4686 line and is ~ 45 Å wide.

Another set of three echelle spectra over the range 3850 to 5790 Å was obtained with the Bench-Mounted Echelle Spectrograph (BME) attached to the 1.5 m CTIO Ritchey-Chrétien Telescope, during a 5-night run in June 1999. Forty nine orders were observed using the KPGL2 316 lines mm^{-1} grating as a cross-disperser. The detector was a Tek 2048 CCD with 24 μm pixels. The slit width was set to 70 μm corresponding to a resolving power of 45000. Exposure times ranged

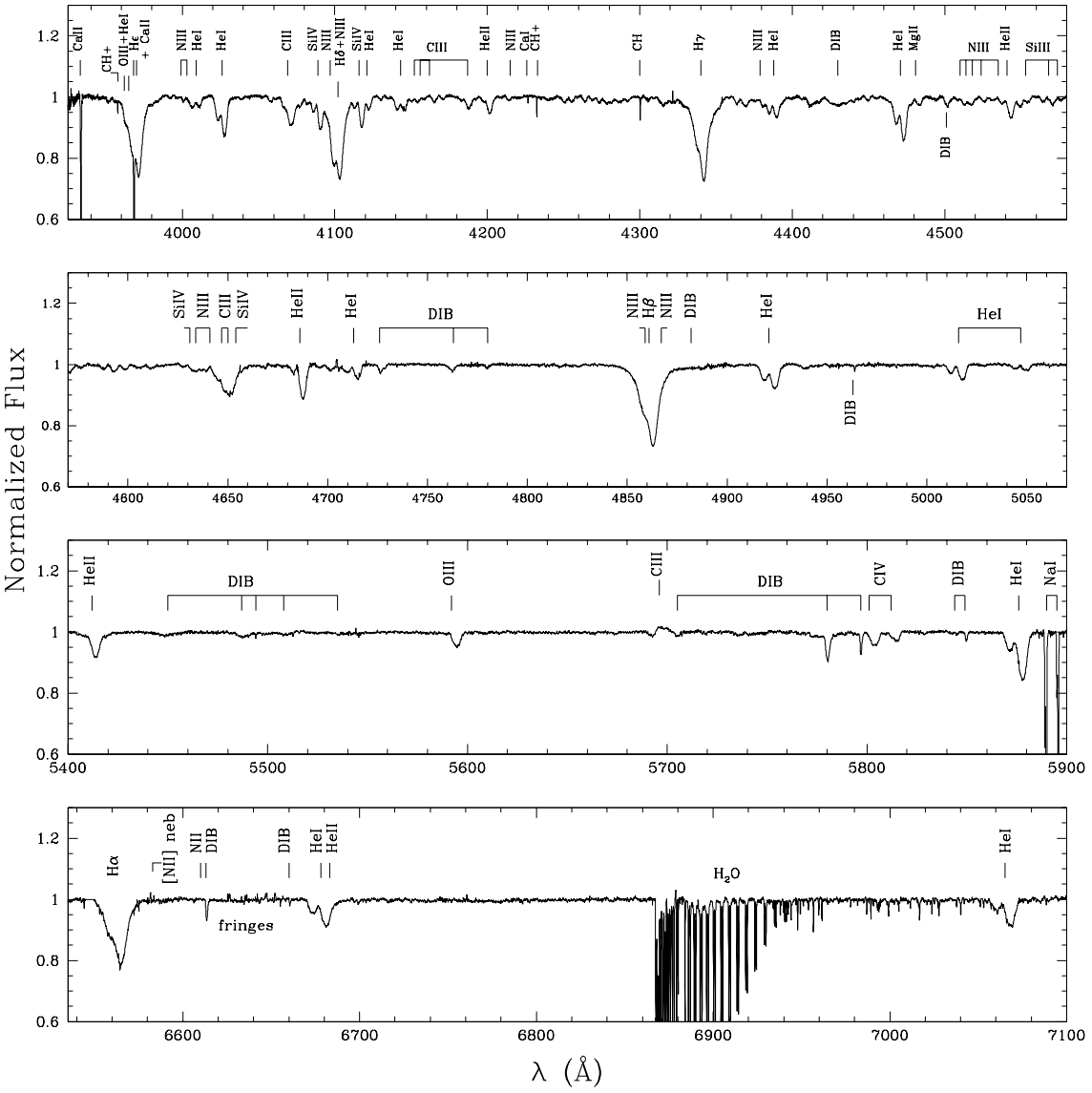

Fig. 2. Spectrum of HD 152218 as observed with the FEROS spectrograph on HJD 2 453 134.723 ($\phi \sim 0.85$). At this orbital phase, the spectrum of the most massive star is shifted towards the red. The most prominent lines are indicated at their rest wavelengths.

from 45 to 60 min, yielding a S/N ratio in the continuum between 40 and 50.

Between April 1999 and May 2002, we collected 20 echelle spectra covering the whole optical range (~3750–9200Å) using the Fiber-fed Extended Range Optical Spectrograph (FEROS), an echelle spectrograph mounted at the ESO 1.5m telescope at La Silla. In May 2003 and May 2004, respectively three and five other FEROS spectra were obtained at the ESO 2.2m telescope, at La Silla too. The detector was a 2k × 4k EEV CCD with a pixel size of 15μm × 15μm. The spectral resolving power of FEROS is 48 000. Typical exposure times ranged, at the ESO 1.5m telescope, from 10 to 20 min according to the weather conditions, resulting in typical S/N ratios around 150. At the ESO 2.2m telescope, the S/N ratio is about 200 in May 2003 and, thanks to increased instrument performances and to good weather conditions, it is above 250 for May 2004. Typical exposure times at the ESO 2.2m were of 13 min.

The CES data were reduced in a standard way using the MIDAS package supported by ESO. The spectra were rectified by means of an instrumental response curve built from the observations, obtained under similar conditions, of a metal-poor 'reference' star (HD 203608: F6V). Finally, the spectra were normalized by fitting a low order polynomial to the continuum.

The BME data were reduced using the IRAF[1] package and following the recommendations of the BME User's Manual. The pixel to pixel variations were removed using flat field exposures taken with a very bright light source and a diffusing screen placed inside the spectrograph (so-called *milky flats*). A first rectification of the extracted echelle orders was carried out with the projector flat exposures. The spectra were then normalized by fitting a low-order polynomial to the continuum.

FEROS data were reduced using an improved version of the FEROS context (see details in Sana et al. 2003) working under the MIDAS environment. We mainly used the normalized individual orders. However, when doubts about the quality of the normalisation arise, we checked our results with the automatically merged spectrum.

2.2. X-ray observations

In September 2001, the NGC 6231 open cluster was the target of an X-ray observing campaign with the XMM-*Newton* European observatory (Jansen et al. 2001). The campaign, of a total duration of about 180 ksec, is described in length in Sana et al. (2005c) together with the data reduction and source identification. We only give a brief overview here, focusing on the additional elements specific to HD 152218.

The campaign actually consisted of six separate observations spread over 5 days. All three EPIC instruments (Strüder et al. 2001; Turner et al. 2001) were operated in the Full Frame mode together with the Thick Filter to reject UV/optical light. The field of view (FOV) of the EPIC instruments was centered on the colliding wind binary HD 152248, from which HD 152218 is separated by about 6.′8. Due to the brightness of the cluster objects in the FOV, the Optical Monitor (Mason et al. 2001) was switched off throughout the campaign. Fig. 1 presents a view of the combined MOS images around HD 152218 while Table 2 provides the journal of the X-ray observations of the system.

HD 152218 unfortunately fell on a gap of the pn instrument and, as in Sana et al. (2005c), we only considered the EPIC MOS data. To obtain the averaged count-rates during the different pointings, we adopted the source positions given in the catalogue of Sana et al. (2005c) and we performed a psf (point spread function) fit using the SAS task *emldetect*. As in the previous works, we restrained our scientific analysis to the 0.5-10.0 keV band and we adopted three energy sub-ranges: a soft (S_X) [0.5:1.0 keV], a medium (M_X) [1.0:2.5 keV] and a hard (H_X) [2.5-10.0 keV] band.

Located slightly offset from the cluster core, HD 152218 is reasonably well isolated in the X-ray images. To extract the source spectra, we used an extraction radius of 20.″2, centered on the source position for all six pointings and for the two EPIC MOS instruments. The different backgrounds were estimated from source-free regions located on the same CCD detector as HD 152218 (CCD #3 and 5 respectively for the MOS1 and MOS2 instruments). The adopted source extraction region is shown in Fig. 1. Displays of the corresponding background ex-

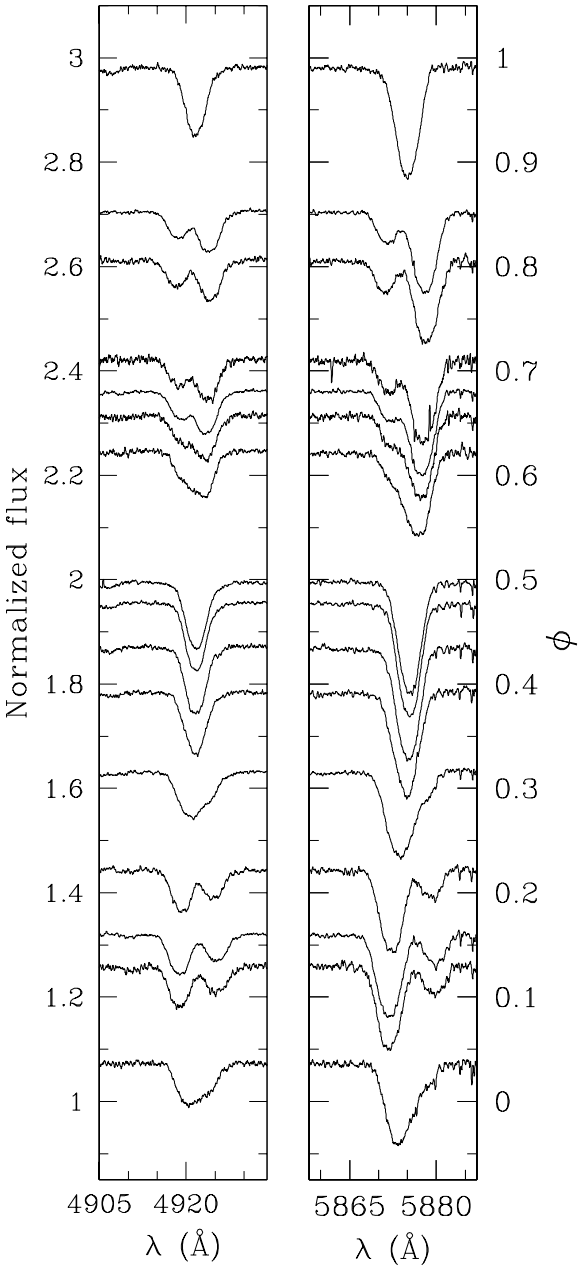

Fig. 3. He I λ4922 (left) and He I λ5875 (right) lines at selected phases. The spectra were shifted along the vertical axis according to the value of their phase (right-hand scale). The secondary spectral signature is clearly identified on most spectra but the blended ones.

[1] IRAF is distributed by the National Optical Astronomy Observatories.

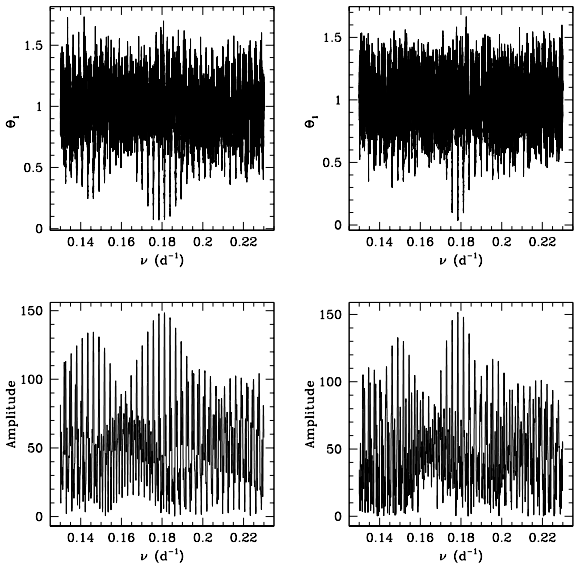

Fig. 4. Left panels: L&K (normalized statistic, top) and HMM (amplitude spectrum, bottom) periodograms associated with the FEROS He I λ4471 primary data set. Periodograms associated with other lines are very similar. **Right panels**: idem, using the CES and BME measurements in addition to the FEROS data. This latter data set favors a period of 5.604 d, corresponding to $\nu \approx 0.1784$ d^{-1}.

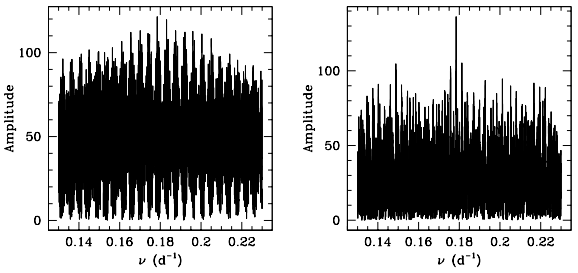

Fig. 5. Left panel: HMM periodogram corresponding to the IUE+optical data sets used by SLP97. **Right panels**: idem, combining our data with published data sets.

traction regions are presented in Sana et al. (2005e) together with their positions and sizes.

Using these regions, we extracted the source spectra from the two MOS instruments and for the six pointings individually. We also extracted the merged spectra in each instrument, thus combining the six observations of HD 152218. For this purpose, we built the corresponding Ancillary Response Files (the so-called *arf* files) using the SAS task *arfgen*. We adopted the Redistribution Matrix Files (*rmf*) provided by the SOC. The spectra were finally binned to reach at least 10 counts per bin. The X-ray data will be discussed in Sect. 5.

3. HD 152218 orbital solution

3.1. The HD 152218 spectrum

The spectrum of HD 152218 is clearly dominated by the usual Balmer, He I and He II lines seen in absorption (Fig. 2). Beside these, the spectrum reveals metallic lines of N III, Si III, Si IV, C IV and O III that are typical of O-type stars. Only the C III λ5696 line is seen in emission. Most of the observed stellar lines are clearly double (see e.g. Fig. 3) and display clear Doppler shifts. The HD 152218 spectrum also reveals a number of diffuse interstellar bands (DIBs), as well as interstellar absorptions due to Na I, Ca I, Ca II, CH and CH^+.

We measured the Doppler shifts by fitting a sum of Gaussians to the different line profiles. Whenever the components get closer to conjunction, the disentangling of their spectral signature was more difficult. To get reliable results we had to constrain the full width at half maximum (FWHM) of the fitted Gaussian profiles. We thus computed the mean FWHMs of the primary and secondary lines according to the measurements performed near quadrature. Considering the properties of the studied lines, we then decided either to fix the line FWHMs to their mean value or to request the primary and secondary lines to have equal FWHMs. The resulting radial velocities (RVs) were assigned a lower weight in the determination of the orbital solution (see Sect. 3.3). In order to get a reliable solution, we considered 11 different lines: He I $\lambda\lambda$4026, 4388, 4471, 4922, 5016, 5876, 7065, He II $\lambda\lambda$ 4542, 4686, 5412 and O III λ5592. Note that the He II $\lambda\lambda$4542 and 5412 lines were only rarely deblended and show only a faint secondary component. For these lines, we thus focused on the primary orbital motion. We also note that the O III λ5592 line is only seen in the primary spectrum. To compute the RVs associated with the measured Doppler shifts, we adopted the effective wavelengths for O-stars from Conti et al. (1977) below 4800 Å and from Underhill (1994) above.

3.2. Period determination

Our period search relies on the method of Lafler & Kinman (1965, L&K) and on the Fourier-analysis technique of Heck et al. (1985, HMM, see also Gosset et al. 2001 for comments) applied on the different data sets of Table 3. Using the L&K algorithm, the obtained periods are in excellent agreement, yielding a mean value of 5.60380 ± 0.00005 d. The results from the Fourier analysis are more conflicting. The He I λ 4471 and He II λ 4686 data sets yield a period of 5.604 days while the other lines indicate 5.519 days. An inspection of the corresponding periodograms revealed that the period determination is strongly affected by a 1-year aliasing, leading to a possible confusion between orbital frequencies of 0.1784 and 0.1812 d^{-1}. These latter values correspond respectively to the two period values quoted here above. From Fig. 4 (left panels), it is clear that the period can not be reliably constrained from the sole FEROS data. The inclusion of the CES and, to a lesser extent, of the BME data clearly improves the situation (Fig. 4, right panels) but still does not allow to draw a firm conclusion.

Our data sets consist of spectra spread over 2500 days for the He I λ4471 and He II λ4686 lines or over 1800 days for the other lines. These observational time bases correspond

Table 3. Orbital solutions for HD 152218 as derived from different lines. The usual notations have been adopted. s_y/s_x gives the adopted secondary to primary ratio of the uncertainties on the measured RVs (see Sect. 3.3). The quoted error-bars are the 1-σ uncertainties.

Lines	P (days)	s_y/s_x	e	ω (°)	K_1 (km s^{-1})	K_2 (km s^{-1})	γ_1 (km s^{-1})	γ_2 (km s^{-1})	rms (km s^{-1})
He I λ4026	5.60400	1.4	0.268 ± 0.007	104.4 ± 1.7	164.4 ± 1.3	209.2 ± 1.6	−16.7 ± 1.4	−17.3 ± 1.6	5.6
He I λ4388	5.60395	1.2	0.253 ± 0.011	99.4 ± 3.3	159.2 ± 2.2	208.1 ± 2.8	−11.4 ± 2.3	−15.5 ± 2.7	9.5
He I λ4471	5.60386	1.7	0.242 ± 0.008	101.7 ± 2.6	160.2 ± 1.6	215.0 ± 2.2	−26.4 ± 1.7	−30.6 ± 2.1	7.7
He II λ4686	5.60391	1.7	0.275 ± 0.008	108.4 ± 1.8	165.8 ± 1.7	207.9 ± 2.2	−15.4 ± 1.7	−16.8 ± 1.9	7.1
He I λ4922	5.60393	1.4	0.261 ± 0.008	103.0 ± 2.1	159.8 ± 1.4	214.4 ± 1.8	−18.0 ± 1.6	−21.8 ± 1.9	6.3
He I λ5016	5.60405	1.6	0.269 ± 0.010	102.6 ± 2.4	167.4 ± 2.0	215.2 ± 2.6	−16.3 ± 2.0	−17.2 ± 2.4	8.3
He I λ5876	5.60410	1.6	0.271 ± 0.006	104.5 ± 1.5	162.4 ± 1.1	221.4 ± 1.5	−21.9 ± 1.2	−21.1 ± 1.5	4.8
He I λ7065	5.60410	1.7	0.255 ± 0.008	101.0 ± 2.2	165.1 ± 1.6	214.0 ± 2.1	−17.1 ± 1.7	−11.7 ± 2.0	6.4
He II λ4542	5.60400	–	0.288 ± 0.014	101.3 ± 2.2	160.9 ± 2.1	–	−21.1 ± 1.2	–	6.5
He II λ5412	5.60419	–	0.302 ± 0.011	104.0 ± 1.6	161.4 ± 1.7	–	−16.5 ± 1.0	–	5.2
O III λ5592	5.60409	–	0.274 ± 0.012	106.1 ± 2.0	162.7 ± 1.9	–	−17.1 ± 1.7	–	6.0

respectively to natural peak widths $\Delta\nu$ of 0.0004 d^{-1} and 0.0006 d^{-1}. The full width at half maximum of the actual peaks in the periodogram is in agreement with these theoretical values. Adopting an uncertainty of one tenth of the peak width, we respectively obtained $\sigma_P = 0.0013$ or 0.0017 d. These values however only account for the uncertainty due to the finite width of the peak, but do not consider the possible confusion between different aliases.

To solve the aliasing problem, we turned to the literature. Hill et al. (1974, hereafter HCB74) and Levato & Morrell (1983, hereafter LM83) derived quite different period values compared to the ones quoted above. We applied our period search methods using their data sets and found a very large number of aliases covering a frequency range corresponding to period values between about 5 and 6.7 days. Their proposed period values were thus very poorly constrained. On the other hand, Stickland et al. (1997, SLP97 hereafter) obtained a period $P \approx 5.604$ d, very similar to one of our aliases and we therefore paid a special attention to their determination. SLP97 proceeded in two steps. First they performed a period search using their IUE data set only and found $P = 5.6038$ d. In a second step, they included the previously published optical data and obtained a final value of $P = 5.603979 \pm 2.6 \times 10^{-5}$ d. We used both the L&K and HMM algorithms on the different data sets considered by SLP97 and we re-derived very similar values, except for the related uncertainties. Adopting a typical error corresponding to one tenth of the periodogram peak width, we obtained values about 6 times larger. The periodogram (Fig. 5, left panel) also indicates a possible confusion with a neighbouring alias at $\nu \approx 0.183$ d^{-1}. The period value is therefore not so clearly established. We however note that this latter alias is not present in our data set. By combining the different data sets, we could thus hope to definitely constrain the period.

As a last step, we therefore combined all the observational data sets. In doing so, we averaged the RV measurements obtained from the different lines quoted in Table 3. We emphasize that, in this approach, we did not correct the individual line RVs from their systemic velocities but we rather performed a direct average. Indeed the systemic velocities should be obtained from RV curve fitting, and thus require an *a priori* rather accurate estimate of the period. Applying the L&K and HMM period searches, we derived values of $P = 5.6039$ and 5.6040 d respectively. The corresponding Fourier periodogram is displayed in Fig. 5 (right panel) and clearly shows that the orbital peak is now well isolated. We thus confirm the period value proposed by SLP97. The time span of the whole observational set is ∼21 915 d, yielding a theoretical periodogram peak width of $\Delta\nu = 4.6 \times 10^{-5}$ d^{-1}. The observed width of the peak agrees with this value and yields $\Delta P = 1.4 \times 10^{-3}$ d. We adopted a final uncertainty corresponding to one tenth of the peak width, i.e. $\sigma_P = 1.4 \times 10^{-4}$ d.

3.3. Orbital elements

Now that the period is reliably constrained, we derive the orbital and physical parameters of the system by fitting the observed RV-curves assuming a Keplerian motion for the two components. We first computed a series of orbital solutions using the RV sets associated with the different absorption lines listed in Table 3. For SB1 lines, we used the algorithm of Wolfe et al. (1967) in its original form and assigned the same weight to each measurement. For the data sets associated with SB2 lines, we used a modified version of the algorithm, adapted to SB2 system as explained in Sana et al. (2003), and we only considered those data points for which the two components could be measured with a reasonable accuracy. We assigned a half weight to those RV points for which the FWHMs had to be constrained (see Sect. 3.1). Because of the lower S/N ratio of the BME data, we gave them a weight of one fourth while computing the orbital solution. In the observed wavelength domain, the BME measurements were further not included for the fainter lines nor for the lines more difficult to disentangle (He I $\lambda\lambda$4388, 5016, He II λ4542, O III λ5592). In our derived solutions, we adopted a period value and a relative primary to secondary weight ratio (s_y/s_x) that yield the lowest χ^2. These best solutions, including a reappraisal of the period, are presented in Table 3 together with the corresponding root-mean-square (r.m.s) residuals of the fit.

Table 4. Orbital and physical parameters of HD 152218 as deduced from different data sets: our averaged RVs computed over selected primary SB1 lines (Col. 2) and He I SB2 lines (Col. 3) and a data set extended by primary RVs found in the literature (see Sect. 3.4). The usual notations have been adopted. T_0 is the time of periastron passage and is adopted as phase zero (i.e. $\phi = 0.0$). Note that the primary and the He I lines solution were computed in the systemic velocity frame.

	Prim.	He I lines
P (d)	5.60404	5.60391
s_y/s_x	n.	1.5
m_1/m_2	n.	1.319 ± 0.014
e	0.275 ± 0.008	0.259 ± 0.006
ω (°)	104.2 ± 1.6	104.0 ± 1.6
T_0 (HJD	3196.493	3197.229
−2 450 000)	±0.024	± 0.025
K_1 (km s^{-1})	162.4 ± 1.1	162.2 ± 1.2
K_2 (km s^{-1})	n.	213.9 ± 1.5
γ_1 (km s^{-1})	0.7 ± 0.9	0.9 ± 1.2
γ_2 (km s^{-1})	n.	−0.6 ± 1.4
$a_1 \sin i$ ($R_\odot$)	17.28 ± 0.13	17.34 ± 0.13
$a_2 \sin i$ ($R_\odot$)	n.	22.87 ± 0.17
$m_1 \sin^3 i$ ($M_\odot$)	n.	15.82 ± 0.26
$m_2 \sin^3 i$ ($M_\odot$)	n.	12.00 ± 0.19
r.m.s. (km s^{-1})	4.1	6.1

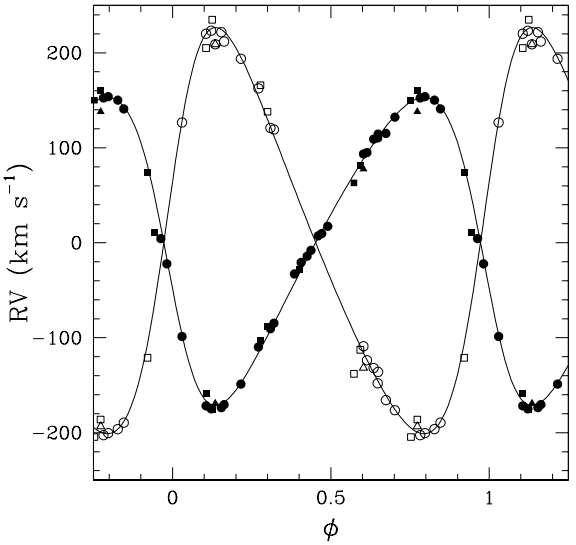

Fig. 6. HD 152218 RV curves corresponding to the He I solution of Table 4. Note that the respective systemic velocities have been subtracted. RV measurements listed in Table 1 have been overplotted. Filled and open symbols are for the primary and secondary components respectively. Different symbols indicate different instruments used: CES, squares; BME, triangles; FEROS, circles.

In a next step, we computed the mean RVs of the SB2 He I-lines quoted in Table 3 as well as of the sole primary lines. For this purpose, we first shifted the individual RVs to a common frame, by subtracting the individual systemic velocities. The resulting mean RVs are listed in Table 1. The orbital solutions computed using the averaged primary (SB1) and the averaged He I-line (SB2) RV measurements are given in Table 4 together with the physical parameters of the system. Fig. 6 displays the RV curves corresponding to the averaged SB2 solution. The latter solution will be adopted throughout the rest of the paper to constrain the physical properties of the HD 152218 components (see Sect. 4). Corresponding primary and secondary apparent systemic velocities, as obtained from a weigthed mean of the values quoted in Table 3, are $\overline{\gamma_1} = -18.7 \pm 0.6$ km s^{-1} and $\overline{\gamma_2} = -19.2 \pm 0.7$ km s^{-1}.

Our final SB2 solution is relatively similar to the solution derived by SLP97 though with a slightly smaller eccentricity and larger RV-curve semi-amplitudes. It is therefore significantly different from the more recent determination by García & Mermilliod (2001, hereafter GM01) who obtained $P \sim 4.9$ d and $e \sim 0.4$. However, it is known that GM01 have associated erroneous Julian Dates to part of their observations (see e.g. Sana et al. 2003). This clearly biased their period search and their determination of the orbital solution.

As mentioned above, our obtained values fall well within 3-σ from the results of SLP97. Only the longitude of the periastron seems to differ significantly: 80.°6 ± 2.°1 for SLP97 versus 104.°2 ± 1.°6 for our solution. This suggests the presence of an apsidal motion of the order of 20° over about 7 yr. This question is addressed in the next section.

3.4. Apsidal motion

As already mentioned, several authors have collected a number of spectroscopic observations of HD 152218 and measured the RVs of its two components. The largest sets are due to Struve (1944), HCB74, SLP97 and GM01 who respectively obtained 5, 15, 22 and 7 spectra. Struve published the observing dates using universal times with day and month. Hill et al. (1974) later presented corresponding Julian dates (JD). We however note that, though quoted otherwise, these dates are not heliocentric Julian dates (HJD) but simply JD. We thus recomputed the appropriate HJD before using the Struve data sets. A word of caution is also required for the GM01 observations. As already mentioned above, GM01 quoted erroneous HJDs for part of their observations[2]. We thus corrected the corresponding values prior to the inclusion of the GM01 observations. We completed these four sets by an additional measurement from Conti et al. (1977) and another one by Levato & Morrell (1983). We finally added the RVs from the present work, obtained as the average of the γ-corrected individual lines measurements; and we adopted the systemic velocities obtained in Sect. 3.3.

In a first approach, Fig. 7 shows the literature measurements plotted over the He I orbital solution of Table 4. The secondary measurements present a larger scatter and we will thus focus on the primary data for the rest of this section. In

[2] In GM01's Table 2, the HJDs around 2 449 910 are probably correct, those around 2 450 590 are overestimated by exactly one day for observations obtained after midnight UT. We could not check the more recent observations obtained by GM01 at HJDs~2 451 360.

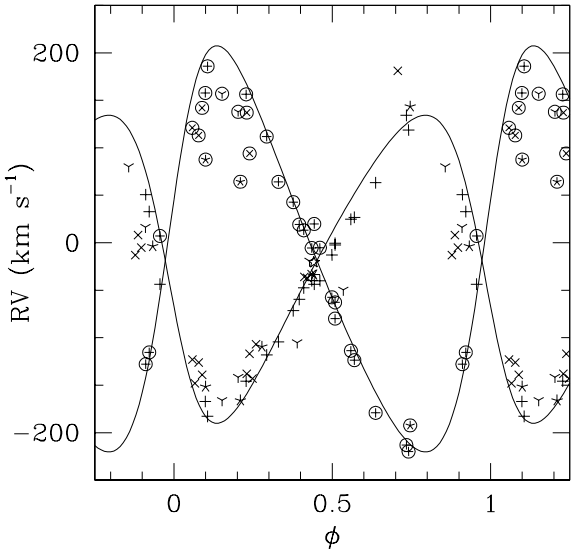

Fig. 7. Literature RV measurements plotted over the He I SB2 RV-curves of Fig. 6, shifted according to their respective apparent systemic velocities. The phases were computed using the He I ephemeris of Table 4. Different symbols indicate different works: (five branch star) Struve (1944); (×) HCB74; (asterisk) LM83; (open five-branch star) Conti et al. (1977); (+) SLP97; (Y) corrected GM01. These symbols inscribed in open circles indicate secondary RV measurements.

Fig. 7, we also observe systematic shifts between the literature measurements and our newly derived orbital solution. As suggested in the previous section, this most probably comes from the presence of an apsidal motion. Fixing the period and the eccentricity at the values quoted in Table 4 for the He I-solution, we adjusted the different data sets of Table 5 and derived, for each epoch, the best-fit longitude of periastron. These values are plotted in Fig. 8. We note that, using the RV sets of HCB74 and Stickland et al. (1997), we rederived the longitude values respectively quoted in their proposed orbital solutions. We also built three subsets of data using the data of GM01, SLP97 and ours. These sets, labelled A, B and C in Table 5, correspond respectively to data obtained before HJD = 2 450 000, in-between HJD = 2 450 000 and HJD = 2 451 800 and after HJD = 2 452 000. These sets are however not independent from the sets labelled 'SLP97' and 'This work' in Table 5 as they are formed by the same observations. We consider our approach to provide a kind of moving average over the time. It can also be seen as a way to give more weight to the more recent data, that probably provide a better accuracy than the older sets of Struve and HCB74. Using a linear regression, we then computed the best-fit linear relation that reproduces the observed values, the slope of which provides the rate of the apsidal motion. We obtained: $\dot{\omega} = 9\overset{\circ}{.}1 \pm 0\overset{\circ}{.}8 \times 10^{-3}$ d^{-1}, corresponding to about $\dot{\omega} = 3\overset{\circ}{.}3 \pm 0\overset{\circ}{.}3$ yr^{-1}. It is worth to note here, that, because of the similar K_1 and K_2, the shape of the RV-curve is little altered by a change of ω of π. By chance, thus, neither the Struve (1944) data nor those of HCB74 could strongly bias the

Table 5. Best fit values for the longitude of the periastron ω at different epochs. The data sets labelled 'A' to 'C' are described in the text.

Data set	$\overline{\text{HJD} - 2\,400\,000}$	ω (°)	rms (km s^{-1})
Struve (1944)	31223.5	−100	5.4
HCB74	40818.9	34	11.7
SLP97 [a]	49627.5	82	7.6
This work	51652.1	102	6.6
A	49333.8	72	19.9
B	50861.8	95	11.8
C	52621.3	106	4.2

a. The first point of the SLP97 set is separated by about 3300 days from the other points of the set and was not included in the fit.

orbital period determination of Sect. 3.2. Indeed similar results are obtained while including or rejecting these two sets from the period search analysis.

A word of caution is however necessary concerning the rate of the apsidal motion. Indeed, we have also performed a similar analysis using our data only. These were grouped into five different subsets according to the different observing epochs. The apsidal motion is again clearly detected, even considering the comparatively smaller time span of our spectroscopic campaign. The obtained rate is however somewhat slower: $\dot{\omega} = 1\overset{\circ}{.}4 \pm 0\overset{\circ}{.}6$ yr^{-1}. Accounting in addition for the SLP97 data, we rather obtain $\dot{\omega} = 3\overset{\circ}{.}0 \pm 0\overset{\circ}{.}6$ yr^{-1}. Although there is little doubt left about the existence of an apsidal motion, the *exact* rate at which the latter occurs might still be uncertain. This probably reflect the difficulty to combine inhomogeneous data sets.

4. HD 152218 physical parameters

4.1. Spectral types and luminosity classes

The dominant spectral signature of the primary component in the spectrum of HD 152218 is characteristic of a late O-type star. We adopted the classification criteria from Conti (1973b) as adapted to late O-stars by Mathys (1988). They are based on the equivalent width (EW) ratio of the He I λ4471 and He II λ4542 lines. Doing this, we only considered the EWs measured on the spectra where the two components are disentangled. For the primary, we obtained a mean $\log W'_1 = \log W_{\lambda 4471} - \log W_{\lambda 4542} = 0.33 \pm 0.06$ which corresponds to a spectral type O9, with spectral type O8.5 within 1 σ. For the secondary, we obtained $\log W'_2 = 0.67 \pm 0.08$. This indicates an O9.7 star, with the O9.5 type at 1-σ.

To determine the luminosity classes, we adopted the criterion from Conti & Alschuler (1971) based on the EW ratio of the Si IV λ4089 and He I λ4144 lines. We respectively obtained $\log W''_1 = \log W_{\lambda 4089} - \log W_{\lambda 4144} = 0.25 \pm 0.05$ and $\log W''_2 = -0.12 \pm 0.13$. These values lead to giant and main sequence luminosity classes for the primary and secondary components respectively. According to Mathys (1988), we also measured $\log W'''_1 = \log W_{\lambda 4388} + \log W_{\lambda 4686} = 5.03 \pm 0.04$. This corresponds to a supergiant if the primary brightness ratio $l_1 = \frac{L_1}{L_{\rm tot}} > 0.76$, to a giant if $0.76 > l_1 > 0.43$ and to a main sequence star otherwise. For the secondary, we

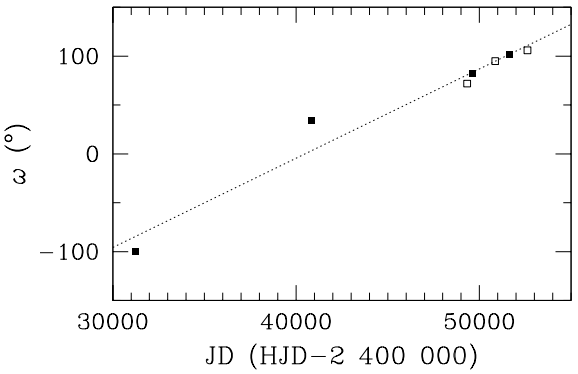

Fig. 8. Values of the argument of periastron ω computed for different epochs. The dotted line gives the best-fit relation, corresponding to an apsidal motion of $9.^{\circ}1 \pm 0.^{\circ}8 \times 10^{-3}$ d^{-1}, or about $3.^{\circ}3 \pm 0.^{\circ}3$ yr^{-1}

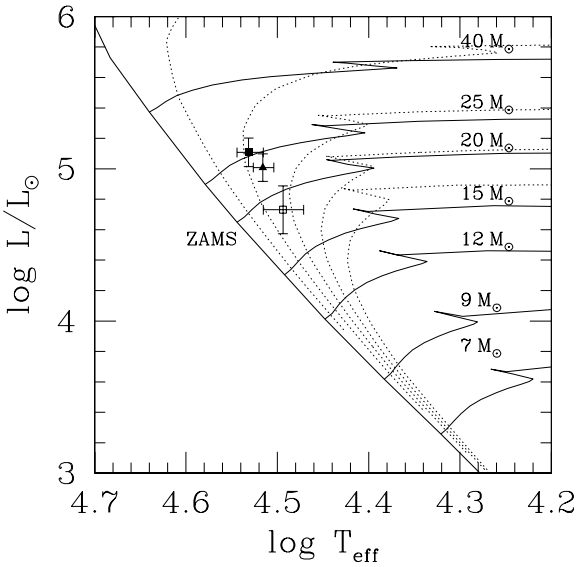

Fig. 9. HD 152218 primary (filled symbols) and secondary (open symbol) location in the H-R diagram. Triangle (resp. square) symbols indicate an adopted giant (resp. main sequence) luminosity class. The evolutionary tracks from Schaller et al. (1992) have been overplotted (plain lines) together with isochrones (dotted lines) computed for ages ranging from 2 to 10 Myr with a step of 2 Myr.

get $\log W_2''' = 4.22 \pm 0.15$. The respective critical values for $l_2 = \frac{L_2}{L_{\rm tot}}$ are this time 0.12 and 0.07. Such a low contribution of the secondary to the total flux is improbable. Mathys criterion thus indicates a supergiant secondary, which is clearly at odds with the result of the Conti & Alschuler (1971) criterion. The optical brightness of both components of the system will be discussed in the next section. Finally, the comparison of our spectra with the atlas of standards (Walborn & Fitzpatrick 1990) seems to favor a giant class for the primary star, but it is very difficult to reject the main sequence option. It also indicates that the secondary is most probably a main sequence star.

4.2. Optical brightness ratio and evolutionary status

We roughly estimated the optical brightness ratio based on the dilution of the primary and secondary lines in the spectrum of HD 152218. For this purpose, we compared the mean EWs of the primary and secondary lines with typical (averaged) EWs of respectively O9 (Conti & Alschuler 1971; Conti 1973a; Mathys 1988, 1989) and O9.7 stars (Mathys 1988, 1989). We first compare the primary line strength with typical O9III EWs. Based on the He I $\lambda\lambda$4026, 4144, 4388, 4471, He II $\lambda\lambda$4542, 4686 and Si IV λ4088 lines, we respectively obtained an averaged brightness ratio of $l_1 = 0.76 \pm 0.05$. Using typical O9V EWs yields a lower value $l_1 = 0.68 \pm 0.11$. We however note that the Si IV λ4088 line is particularly strong in the primary spectrum and is the main cause for the large scatter obtained. Rejecting the Si IV λ4088 line from the comparison with O9V typical EWs, we obtained $l_1 = 0.63 \pm 0.04$.

Turning to the secondary component, we also compared the secondary line strengths to the typical EWs reported by Mathys (1988, 1989), who only considered the He I $\lambda\lambda$4388, 4471 and He II $\lambda\lambda$4542, 4686 lines. We note that the He II λ4686 line provides results that clearly differ from the three other lines, but this is not surprising since the He II λ4686 line is particularly faint in the secondary spectrum. Mean values for the three other lines indicate $l_2 = 0.34 \pm 0.02$ and 0.41 ± 0.05 for dwarf and giant star respectively. The obtained values for the primary and secondary contribution to the observed fluxes are thus in acceptable agreement with each other. They also agree with the results of Penny et al. (1994) who quoted a primary to secondary UV flux ratio of 2.0.

In the following discussion, we adopt a primary to secondary brightness ratio corresponding to $l_1 = 0.67 \pm 0.10$, which reasonably well reproduces the results of the above discussion. Sung (2005, private communication) reported $V = 7.562$ and $B - V = 0.191$ for the system. Using $R = 3.3$ (Sung et al. 1998), adopting the absolute colors quoted by Schmidt-Kaler (1982) and a distance modulus $DM = 11.07 \pm 0.04$ (Sana et al. 2005c, and references therein), preliminary computations indicate that the system is too faint to harbour a giant primary, unless its contribution l_1 to the observed flux brightness were very close to unity. This is clearly not confirmed by the previous discussion and we suggest that the primary in HD 152218 could be a class IV object. Correcting from the reddening and the distance effects, we obtained $M_{\rm V,1} = -4.72 \pm 0.22$ and $M_{\rm V,2} = -3.95 \pm 0.37$. Because the intrinsic colour $(B - V)_0$ of an O-type star does almost not depend on the stellar gravity, we note that these values are free from the hypotheses on the luminosity class. According to Humphreys & McElroy (1984), these values correspond to the primary being a V-IV star and the secondary, a V star. Adopting the Humphreys & McElroy temperature scale and bolometric corrections, we derived $M_{\rm bol,1} = -8.0 \pm 0.2$ (resp. $M_{\rm bol,1} = -7.8 \pm 0.2$) if the primary is a dwarf (resp. giant) star. We obtained $M_{\rm bol,2} = -7.1 \pm 0.4$ for the main sequence secondary. Finally, using tempera-

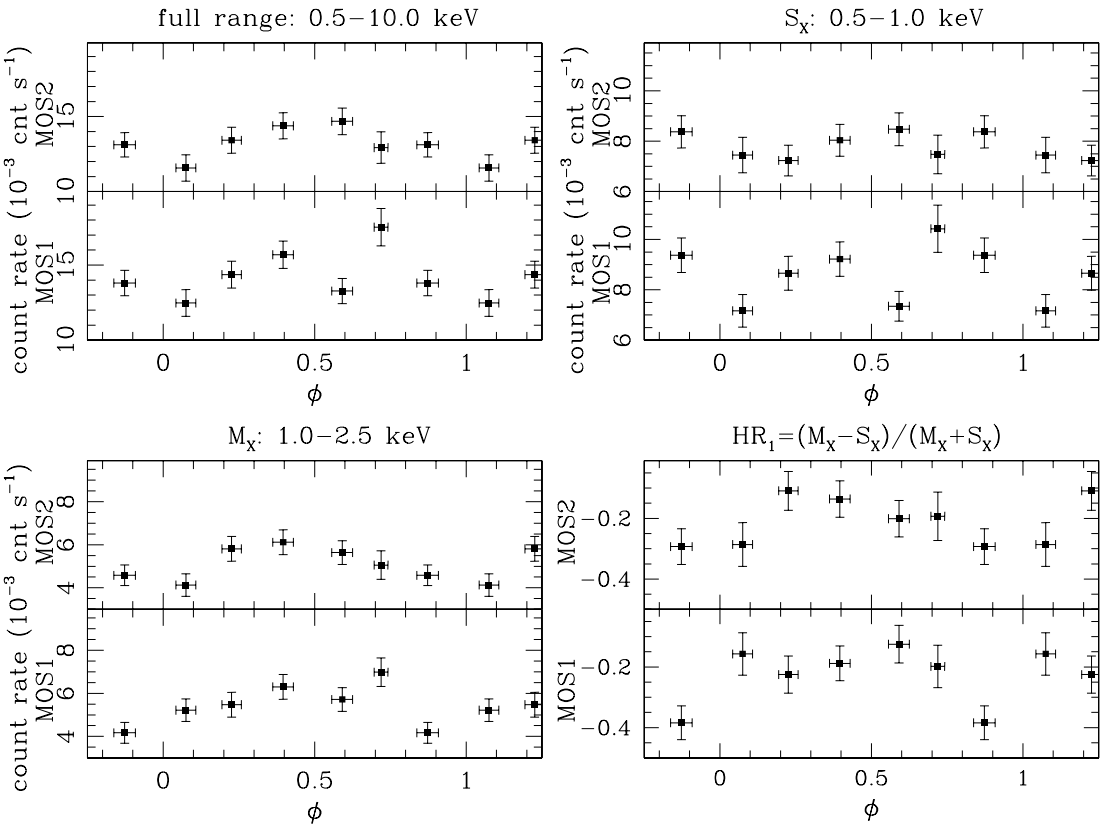

Fig. 10. Broad band X-ray light curves in the two EPIC MOS instruments. The different energy ranges considered are indicated on top of each panel. The vertical bars gives the ±1-σ uncertainty on the background-corrected count rates. The horizontal bars indicate the duration of each pointing. The bottom right panel displays the evolution of the source hardness ratio with the phase, as defined on top of the panel.

tures of $T_{\rm eff}^{\rm O9III} = 32.8^{33.6}_{31.9}$ kK (resp. $T_{\rm eff}^{\rm O9V} = 34.0^{35.0}_{32.8}$ kK), we derived a primary radius of 10.3 ± 1.3 R$_\odot$ (resp. 9.9 ± 1.2 R$_\odot$). For the secondary we interpolated the Humphreys & McElroy temperature scale to obtain values of $T_{\rm eff}^{\rm O9.7V} = 31.2^{32.6}_{29.8}$ kK. This corresponds to $R_2 = 7.9 \pm 1.7$ R$_\odot$. The quoted confidence intervals have been computed by adopting the parameters of the neighbouring spectral sub-types. The obtained values are in excellent agreement with SLP97 results who performed a similar analysis. These authors also conclude that probably neither component is of class III. Our present analysis yields similar results, though some of the spectral classification criteria were pointing towards class III objects. We guess that the particularly strong Si IV λ4088 line in the primary spectra biased the Conti & Alschuler (1971) criterion while the faint He II λ4686 line in the secondary spectrum influences the Mathys (1988) criterion.

Fig. 9 presents the location of the stars in the H-R diagram. The evolutionary age of both components is about 4 to 5 Myr, which is in agreement with previous cluster age determinations from photometric studies (Perry et al. 1990; Balona & Laney 1995; Raboud et al. 1997; Baume et al. 1999). From a rough interpolation of the tracks, the main sequence primary had an initial mass of about 25 M$_\odot$, corresponding to a present mass close to 24.5 M$_\odot$, thus in good agreement with typical O9V masses. Similarly, the secondary initial mass was about 18.5 M$_\odot$. Its present mass should be about 18.2 M$_\odot$.

Comparing the obtained minimal mass of Table 4 with typical O9V masses suggests an orbital inclination i of about 60°. This also corresponds to a secondary mass of 18.5 M$_\odot$. Using the constraints deduced on the components radii, we found that the limiting inclination for which eclipses may or not occur in the system lies around 55-65°. Clearly, HD 152218 is a limiting case. Photometric monitoring is required to search for the signature of eclipses or ellipsoidal deformation in the system light curve. Finally, we used the formula of Eggleton (1983) to estimate the Roche lobe radii. We found that, according to the previous results, both stars should presently fill about 17% of their Roche lobe volume.

5. XMM-*Newton* observations

5.1. Light curves and spectra

With a typical count rate of about 12×10^{-3} cnt s^{-1} in the two MOS instruments, HD 152218 is a relatively bright X-ray source. Using the source position obtained by Sana et al. (2005c), we used the simultaneous psf fit of the *emldetect* task to derive the source count rates for the six pointings and in

Table 6. Best-fitting models and resulting X-ray fluxes at Earth. The 1-T model used was $\texttt{wabs}_{\rm ISM}$ * wabs($N_{\rm H}$) * mekal(kT) while the 2-T model corresponded to $\texttt{wabs}_{\rm ISM}$ * (mekal(kT_1) + wabs($N_{\rm H,2}$) * mekal(kT_2)). The term $\texttt{wabs}_{\rm ISM}$ was fixed to the interstellar value ($N_{\rm H,ISM} = 0.29 \times 10^{22}$ cm^{-2}). The first and second columns give the phase and the observation number. The next three columns (Col. 3 to 5) provide the best-fit parameters while Col. 6 lists the corresponding reduced chi-square and the associated number of degrees of freedom (d.o.f). $N_{\rm H}$ yields the absorbing column (in units 10^{22} cm^{-2}). kT is the model temperature (in keV) while *norm* is the normalisation factor (expressed in cm^{-5}, $norm = \frac{10^{-14}}{4\pi d^2}\int n_{\rm e} n_{\rm H} dV$ with d, the distance to the source – in cm –, $n_{\rm e}$ and $n_{\rm H}$, the electron and hydrogen number densities – in cm^{-3}). The quoted upper and lower values provide the limits of the 90% confidence interval. Columns 7 to 10 provide the observed fluxes (in 10^{-14} erg cm^{-2} s^{-1}) in the 0.5 - 10.0 keV energy band and in the S_X (0.5 - 1.0 keV), M_X (1.0 - 2.5 keV) and H_X (2.5 - 10.0 keV) bands respectively.

$\phi_{\rm HeI}$ [1]	Obs. # [2]	$N_{\rm H}$ [3]	kT [4]	*norm* [5]	χ^2_ν (d.o.f.) [6]	$f_{\rm X}$ [7]	$f_{\rm X,S}$ [8]	$f_{\rm X,M}$ [9]	$f_{\rm X,H}$ [10]
Single-temperature (1-T) model									
0.591	1	$0.10^{0.19}_{0.02}$	$0.53^{0.58}_{0.47}$	$1.16^{1.56}_{0.84} \times 10^{-4}$	1.17 (47)	8.54	4.72	3.68	0.13
0.719	2	$0.11^{0.22}_{0.00}$	$0.53^{0.60}_{0.46}$	$1.27^{1.84}_{0.85} \times 10^{-4}$	0.82 (32)	9.27	5.07	4.05	0.15
0.873	3	$0.00^{0.03}_{0.00}$	$0.61^{0.64}_{0.57}$	$7.63^{8.51}_{7.04} \times 10^{-5}$	1.46 (47)	8.11	4.70	3.25	0.15
0.075	4	$0.38^{0.53}_{0.25}$	$0.24^{0.31}_{0.19}$	$8.40^{0.00}_{29.8} \times 10^{-4}$	0.63 (35)	7.86	4.87	2.98	0.01
0.226	5	$0.40^{0.50}_{0.26}$	$0.25^{0.32}_{0.21}$	$9.20^{0.00}_{23.0} \times 10^{-4}$	1.35 (44)	8.36	5.01	3.33	0.01
0.396	6	$0.38^{0.47}_{0.26}$	$0.24^{0.32}_{0.22}$	$9.23^{0.00}_{17.3} \times 10^{-4}$	1.48 (50)	8.70	5.36	3.32	0.01
–	Merged	$0.01^{0.05}_{0.00}$	$0.58^{0.60}_{0.57}$	$8.62^{8.06}_{9.91} \times 10^{-5}$	1.38 (169)	8.75	5.11	3.49	0.15
Two-temperature (2-T) model									
0.591	1	–	$0.34^{0.54}_{0.24}$	$9.06^{11.3}_{5.59} \times 10^{-5}$					
		$0.57^{1.13}_{0.24}$	$0.68^{0.87}_{0.53}$	$9.97^{16.0}_{5.52} \times 10^{-5}$	0.95 (45)	9.31	5.08	3.96	0.27
0.873	3	–	$0.24^{0.29}_{0.14}$	$1.11^{2.69}_{0.68} \times 10^{-4}$					
		$0.10^{0.36}_{0.00}$	$0.71^{0.83}_{0.61}$	$5.88^{8.61}_{3.88} \times 10^{-5}$	1.07 (45)	9.13	5.75	3.18	0.19
0.226	5	–	$0.32^{0.41}_{0.24}$	$8.98^{11.7}_{5.29} \times 10^{-5}$					
		$0.36^{0.68}_{0.11}$	$0.71^{0.99}_{0.57}$	$7.24^{12.0}_{4.22} \times 10^{-5}$	1.19 (42)	9.12	5.22	3.67	0.24
0.396	6	–	$0.31^{0.38}_{0.26}$	$1.12^{1.36}_{0.88} \times 10^{-4}$					
		$0.63^{1.00}_{0.37}$	$0.71^{0.83}_{0.57}$	$1.06^{1.65}_{0.73} \times 10^{-4}$	0.97 (48)	9.99	5.58	4.08	0.32
–	Merged	–	$0.31^{0.34}_{0.29}$	$9.78^{10.8}_{8.74} \times 10^{-5}$					
		$0.39^{0.50}_{0.28}$	$0.71^{0.76}_{0.65}$	$7.83^{9.20}_{6.56} \times 10^{-5}$	0.89 (164)	9.55	5.47	3.82	0.25

the different energy ranges considered in Sect. 2.2. The count rates in the hard energy band (2.5-10.0keV) are very low and the associated uncertainties are large; we will thus restrain our analysis to the other ranges. Fig. 10 presents the obtained broad band light curves in the total band and in the S_X [0.5-1.0 keV] and M_X [1.0-2.5 keV] bands. Except for Obs. 2 at $\phi \approx 0.7$, the two instruments give very consistent results, indicating a slight modulation with an increase of the X-ray flux of about 30% at apastron compared to periastron.

To constrain the physical properties of the emitting plasma, we adjusted a series of optically thin thermal plasma (mekal) models using the XSPEC software (Arnaud 1996). We simultaneously fitted the two MOS spectra of each pointing, adopting an interstellar column of absorbing matter (neutral hydrogen) of $N_{\rm H,ISM} = 0.29 \times 10^{22}$ cm^{-2}. This value was obtained using $E(B-V) = 0.50$ and the formula of Bohlin et al. (1978). Except for Obs 2 and 4, for which the effective exposure time was reduced by high background events, better results are obtained using two-temperature (2-T) mekal models. Table 6 summarizes the best-fit values obtained while Table 7 gives the corresponding intrinsic fluxes and luminosities. There is no obvious modulation of the spectral parameters. The modulation of the hardness ratios (Fig. 10) however suggests that the observed emission is slightly harder when the flux level is high, and lower otherwise. The merged spectra are well described by 2-T models with kT_1 = 0.31 keV and kT_2 = 0.71 keV. Fig. 11 displays these spectra together with the best-fit 2-T models. It reveals that a hard emission component (> 5 keV) might be present, but clearly the S/N ratio is far insufficient to reliably constrain its properties.

5.2. HD 152218 wind properties

We used the constraints on the physical properties deduced in Sect. 4 together with the mass loss recipes of Vink et al. (2000, 2001) to estimate the properties of the winds in HD 152218. We obtained $v_{\infty,1} = 2280$ km s^{-1}, $v_{\infty,2} = 2340$ km s^{-1}, $\log \dot{M}_1 = -6.59$ ($M_\odot$ yr^{-1}) and $\log \dot{M}_2 = -7.37$ ($M_\odot$ yr^{-1}). The estimated terminal velocities are only slightly larger than the 2050 km s^{-1} value measured by Howarth et al. (1997). Using these parameters with a $\beta = 1$ acceleration law for the winds, we could not establish a ram pressure equilibrium at all phases,

Table 7. ISM-absorption corrected fluxes ($f^{\rm corr.}$, expressed in 10^{-14} erg cm^{-2} s^{-1}) corresponding to the best-fit 1-T and 2-T models of Table 6 and corrected using the adopted interstellar absorbing column $N_{\rm H,ISM} = 0.29\times10^{22}$ cm^{-2}. The last column gives the X-ray luminosity (in erg s^{-1}) in the 0.5 - 10.0 keV band, assuming $DM = 11.07$.

ϕ	Obs. #	$f_{\rm X}^{\rm corr.}$	$f_{\rm X,S}^{\rm corr.}$	$f_{\rm X,M}^{\rm corr.}$	$f_{\rm X,H}^{\rm corr.}$	$\log L_{\rm X}$
Single-temperature (1-T) model						
0.591	1	20.61	14.78	5.69	0.14	31.82
0.719	2	22.20	15.80	6.24	0.16	31.85
0.873	3	19.80	14.63	5.00	0.16	31.80
0.075	4	22.24	17.47	4.75	0.01	31.85
0.226	5	22.90	17.58	5.31	0.01	31.87
0.396	6	24.47	19.15	5.31	0.01	31.89
–	Merged	21.55	16.01	5.39	0.15	31.84
Two-temperature (2-T) model						
0.591	1	24.64	18.42	5.93	0.29	31.90
0.873	3	28.67	23.65	4.82	0.20	31.96
0.226	5	24.84	19.05	5.54	0.25	31.90
0.396	6	27.70	21.29	6.08	0.34	31.95
–	Merged	26.26	20.23	5.77	0.26	31.93

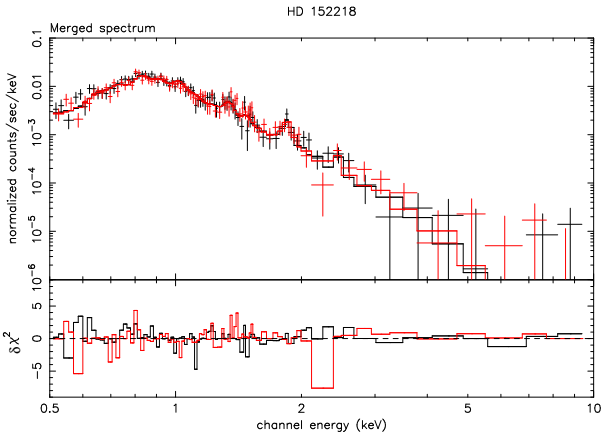

Fig. 11. Top panel: Merged EPIC MOS1 (black) and merged EPIC MOS2 (red) X-ray spectra of HD 152218 and best-fit 2T models. **Lower panel:** Individual contributions of the different energy bins to the χ^2. The contributions are carried over with the sign of the deviation (in the sense data minus model).

indicating that the wind collision structure should be quite unstable. We suspect that the wind velocity law might be affected by radiative inhibition (Stevens & Pollock 1994) which may govern the flux of colliding matter. Clearly, only a detailed modelling could allow to get an insight into the wind collision in this system. This is far beyond the goal of the present paper. We will thus limit ourselves to the observational result that the flux is slightly variable and that the maximum of emission is observed near apastron while the minimum is reached at periastron. As HD 152218 is a close binary, the wind interaction will inevitably take place within the acceleration region of the winds. We thus expect the collision to be stronger at apastron, because of the higher pre-shock velocity reached by the wind at this particular phase. However, we caution that more subtle aspects (such as radiative inhibition) probably affect the strength of the winds, and might thus govern the actual position and shape of the on-going wind interaction.

6. Summary

We have presented the results of a long-term spectroscopic monitoring campaign targeting the massive binary HD 152218 in the young open cluster NGC 6231. The last two investigations on the object were presenting conflicting results. From our analysis, we reject the shorter period and higher eccentricity proposed by García & Mermilliod (2001) and rather confirm the earlier work of Stickland et al. (1997), based on IUE observations. The present data set completed the previous observational sets and allows to definitely overcome the ambiguity on the orbital period of the system, bringing to firm ground the Stickland et al. (1997) period of 5.604 d. Our newly derived orbital solution is characterized by a slightly lower eccentricity than previously accepted: $e = 0.259 \pm 0.006$. The system is most probably formed by an O9 sub-giant and an O9.7 main sequence star. We derived minimal masses of 15.82 ± 0.26 M$_\odot$ and 12.00 ± 0.19 M$_\odot$ and we constrained the component radii to values of $R_1 = 10.1 \pm 1.0$ R$_\odot$ and $R_2 = 8.9 \pm 2.0$ R$_\odot$. These values are in good agreement with previous findings and further indicate that HD 152218 should have an orbital inclination of about 60°. This corresponds to a limiting case in which eclipses or ellipsoidal variations might be observed.

We also report the results of the monitoring of the system in the X-rays thanks to XMM-*Newton* observations of the cluster. The averaged X-ray spectrum is relatively soft. It is well reproduced by a 2-T `mekal` model with component temperatures about 0.3 and 0.7 keV. We showed that the system presents an increase of its X-ray flux of about 30% near apastron compared to periastron. We note that this could be the signature of an ongoing wind-wind interaction process occurring within the wind acceleration region. Such a scenario indeed predicts a stronger shock, and thus a larger X-ray emission from the colliding zone, when the separation between the components is larger, allowing the winds to reach larger pre-shock velocities. This is also supported by the apparent modulation of the hardness ratio, which seems higher when the emission level is stronger. Preliminary computations however indicate that no simple modelling, reproducing the main properties of the interaction, can be obtained. By contrast, the same computations rather point towards second order effects, such as radiative braking, to play a major role in this system. These effects could be strong enough to govern the structure and shape of the interaction. However, only refined modelling, including detailed physics on the wind acceleration and inhibition, could answer these questions, but this is far beyond the scope of the present paper.

The present study completes our observational effort on the known short-period O-type binary systems in the NGC 6231 cluster. Ongoing monitoring of the longer period systems of the cluster should in a near future allows to extend this study towards higher period values. The final aim is to provide a homogeneous sample of observational constraints on the distribution of the physical parameters of the O-type binary population

in the young open cluster NGC 6231. These could then serve as observational guide-lines for the binary formation and evolution theories of massive early-type stars.

Acknowledgements. The authors are greatly indebted towards the 'Fonds de la Recherche Scientifique' (FNRS), Belgium, for multiple supports. Part of this work was also supported by the PRODEX XMM-OM and Integral Projects, as well as contracts P4/05 and P5/36 'Pôle d'Attraction Interuniversitaire' (Belgium).

References

Arnaud, K. A. 1996, in ASP Conf. Ser., Vol. 101, Astronomical Data Analysis Software and Systems V, ed. G. Jacoby & J. Barnes, 17
Balona, L. A., & Laney, C. D. 1995, MNRAS, 276, 627
Baume, G., Vázquez, R. A., & Feinstein, A. 1999, A&AS, 137, 233
Bohlin, R. C., Savage, B. D., & Drake, J. F. 1978, ApJ, 224, 132
Chlebowski, T., & Garmany, C. D. 1991, ApJ, 368, 241
Conti, P. S. 1973a, ApJ, 179, 161
Conti, P. S. 1973b, ApJ, 179, 181
Conti, P. S., & Alschuler, W. R. 1971, ApJ, 170, 325
Conti, P. S., Leep, E. M., & Lorre, J. J. 1977, ApJ, 214, 759
Eggleton, P. P. 1983, ApJ, 268, 368
García, B., & Mermilliod, J. C. 2001, A&A, 368, 122
Gosset, E., Royer, P., Rauw, G., Manfroid, J., & Vreux, J.-M. 2001, MNRAS, 327, 435
Heck, A., Manfroid, J., & Mersch, G. 1985, A&AS, 59, 63
Hill, G., Crawford, D. L., & Barnes, J. V. 1974, AJ, 79, 1271
Howarth, I. D., Siebert, K. W., Hussain, G. A. J., & Prinja, R. K. 1997, MNRAS, 284, 265
Humphreys, R. M., & McElroy, D. B. 1984, ApJ, 284, 565
Jansen, F., Lumb, D., Altieri, B., et al. 2001, A&A, 365, L1
Lafler, J., & Kinman, T. D. 1965, ApJS, 11, 216
Levato, H., & Malaroda, S. 1980, PASP, 92, 323
Levato, H., & Morrell, N. 1983, Astrophys. Lett., 23, 183
Mason, K. O., Breeveld, A., Much, R., et al. 2001, A&A, 365, L36
Mathys, G. 1988, A&AS, 76, 427
Mathys, G. 1989, A&AS, 81, 237
Morgan, W. W., González, G., & González, G. 1953, ApJ, 118, 345
Penny, L. J., Bagnuolo, W. G., & Gies, D. R. 1994, Space Science Reviews, 66, 323
Perry, C. L., Hill, G., Younger, P. F., & Barnes, J. V. 1990, A&AS, 86, 415
Raboud, D., Cramer, N., & Bernasconi, P. A. 1997, A&A, 325, 167
Sana, H., Rauw, G., & Gosset, E. 2001, A&A, 370, 121
Sana, H., Hensberge, H., Rauw, G., & Gosset, E. 2003, A&A, 405, 1063
Sana, H., Stevens, I. R., Gosset, E., Rauw, G., & Vreux, J.-M. 2004, MNRAS, 350, 809
Sana, H., Antokhina, E., Royer, P., et al. 2005a, A&A, in press
Sana, H., Gosset, E., & Rauw, G. 2005b, A&A, submitted
Sana, H., Gosset, E., Rauw, G., Sung, H., & Vreux, J.-M. 2005c, A&A, submitted
Sana, H., Rauw, G., & Gosset, E. 2005d, A&A, submitted
Sana, H., Rauw, G., Nazé, Y., Gosset, E., & Vreux, J.-M. 2005e, A&A, submitted
Schaller, G., Schaerer, D., Meynet, G., & Maeder, A. 1992, A&AS, 96, 269
Schild, R. E., Hiltner, W. A., & Sanduleak, N. 1969, ApJ, 156, 609
Schmidt-Kaler, T. 1982, Landolt-Börnstein, Numerical Data and Functional Relationships in Science and Technology, New Series, Group VI, Vol. 2b, Physical Parameters of the Stars (Berlin: Springer-Verlag)
Stevens, I. R., & Pollock, A. M. T. 1994, MNRAS, 269, 226
Stickland, D. J., Lloyd, C., & Penny, L. R. 1997, The Observatory, 117, 213
Strüder, L., Briel, U., Dennerl, K., et al. 2001, A&A, 365, L18
Struve, O. 1944, ApJ, 100, 189
Sung, H., Bessell, M. S., & Lee, S. 1998, AJ, 115, 734
Turner, M. J. L., Abbey, A., Arnaud, M., et al. 2001, A&A, 365, L27
Underhill, A. B. 1994, ApJ, 420, 869
Vink, J. S., de Koter, A., & Lamers, H. J. G. L. M. 2000, A&A, 362, 295
Vink, J. S., de Koter, A., & Lamers, H. J. G. L. M. 2001, A&A, 369, 574
Walborn, N. R. 1973, AJ, 78, 1067
Walborn, N. R., & Fitzpatrick, E. L. 1990, PASP, 102, 379
Wolfe, R. H., Horak, H. G., & Storer, N. W. 1967, The machine computation of spectroscopic binary elements (Modern astrophysics. A memorial to Otto Struve, Ed. M. Hack – New-York, Gordon Breach), 251

4.2 The long period binaries ($P \sim$ months)

HD 152233 and HD 152234 are among the brightest objects in the cluster core. Due to their longer period, these systems have received less attention in the past and no reliable orbital solution has been so far published in the literature (see below). Even their orbital periods are still almost not constrained. Both systems are currently being monitored throughout ESO period 75 (2005 Apr.-Sept.) using the FEROS spectrograph. Including previous observations, these data will yield accurate SB2 orbital solutions for both systems. This will extend the presently known distributions of physical and orbital parameters (mass ratios, periods, eccentricities, ...) to longer period systems, providing a more complete view of the early-type binary population in NGC 6231. In this section, we provide an overview of our actual knowledge of these two systems. Quoted RVs refer to measurements performed on the He I λ4471 line exclusively. These results are preliminary and should be considered with caution. The present section will probably soon be revised thanks to the ongoing monitoring campaign.

4.2.1 HD 152234

HD 152234 is reported in the literature as a B0Iab radial velocity variable star (Levato & Malaroda 1980). Levato et al. (1988) proposed a very preliminary period of 27.25 days, while García & Mermilliod (2001, GM01 hereafter) claimed to have found the companion signature and proposed a period twice as long ($P = 54.6$ d). Their computed orbital solution (rms = 13.5 km s^{-1}) is slightly eccentric ($e = 0.183 \pm 0.093$) and they estimated $K_1 = 46.5 \pm 2.8$ km s^{-1} and $K_2 = 211.5 \pm 6.1$ km s^{-1}. However we already questioned

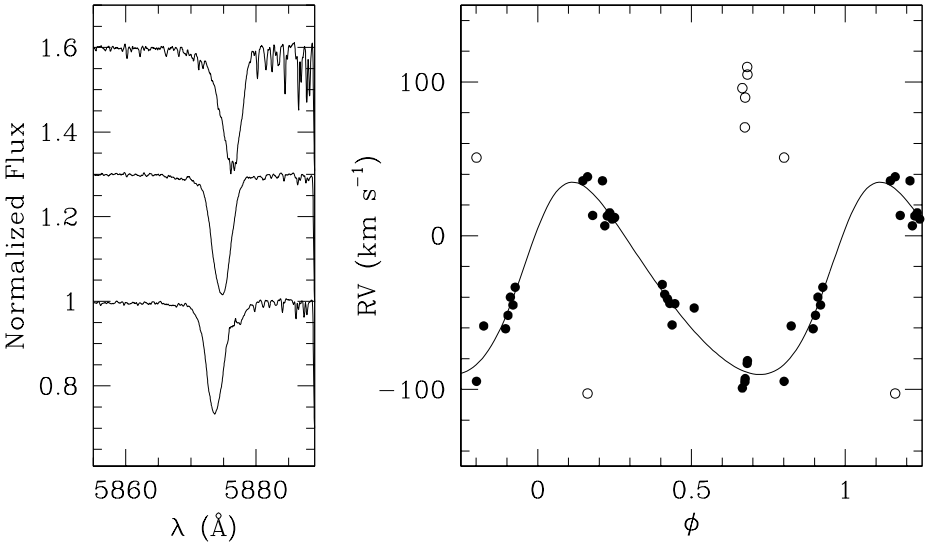

Figure 4.1: **Left:** He I λ5876 line profiles in the spectrum of HD 152234. The orbital shift of the primary is clearly seen. The secondary component is also detected in the blue (resp. red) wing on the top (resp. bottom) spectrum. **Right:** Preliminary RV curve of the system. Filled symbols stand for the primary RVs while open symbols are for the secondary ones. The preliminary adopted period is about 127.0 days and the eccentricity is $e = 0.20 \pm 0.08$.

Table 4.1: Preliminary orbital and physical parameters of HD 152234 as deduced from the He I λ4471 primary RVs (Col. 2) and the former set extended by primary RVs reported in the literature (Col. 3). The usual notations have been used. T_0 is the time of periastron passage and is adopted as phase zero. Values given between square brackets were computed using a mass ratio $M_1/M_2 = 1.51 \pm 0.27$ (see text) as quoted in the table.

	Prim.	Lit.
P (d)	127.01	125.05
s_y/s_x	[1.5]	n.
M_1/M_2	$[1.51 \pm 0.27]$	n.
e	0.201 ± 0.078	0.30 ± 0.04
ω (°)	301 ± 13	220 ± 10
T_0 (HJD	3079.193	3539.360
$-2\,450\,000$)	$\pm$ 4.787	$\pm$ 2.599
K_1 (km s^{-1})	62.6 ± 5.0	51.6 ± 1.8
K_2 (km s^{-1})	$[94.5 \pm 18.5]$	n.
γ_1 (km s^{-1})	-34.2 ± 2.5	-21.9 ± 1.7
γ_2 (km s^{-1})	$[1.8 \pm 24.7]$	n.
$a_1 \sin i$ (R$_\odot$)	153.8 ± 12.6	121.6 ± 4.6
$a_2 \sin i$ (R$_\odot$)	$[232.2 \pm 45.6]$	n.
$M_1 \sin^3 i$ (M$_\odot$)	$[28.9 \pm 18.4]$	n.
$M_2 \sin^3 i$ (M$_\odot$)	$[19.1 \pm 4.3]$	n.
r.m.s. (km s^{-1})	9.4	10.1

the work of GM01 and all the newly derived orbital solutions presented in this work for NGC 6231 objects are in disagreement with their results (see previous objects in this chapter, see also below the case of HD 152233).

Since 1999, we have obtained 24 FEROS spectra (at the ESO1.5 and 2.2m telescopes) and 5 BME spectra (at the CTIO 1.5m telescope). From our observations, HD 152234 most probably consists of an O9.7 supergiant primary and an O8 main sequence secondary. The secondary signature is very faint (Fig. 4.1) and is only detected at very few phases. This partly results from the lower S/N ratio of some of the spectra in our data set. Our preferred orbital period is about 127 days. The corresponding orbital solution is given in Table 4.1 and the RV-curve is plotted in Fig. 4.1. As seen from the latter sketch, the secondary is only disentangled in seven out of our 24 FEROS spectra and only once in the blue wing of the primary. Using an orthogonal regression technique and a secondary to primary uncertainties ratio of $s_y/s_x = 1.5$, we estimated a probable mass ratio of 1.51 ± 0.27. From this information and adopting the physical parameters given by the primary orbital solution, we computed the putative secondary elements and associated error bars. These are also given in Table 4.1. In particular, we derived minimal masses of 28.9 ± 18.4 and 19.1 ± 4.3 M$_\odot$ for the primary and secondary respectively. Comparing with typical masses for the considered spectral types (Howarth & Prinja 1989), the respective components indicate a probable inclination of $73^{90^\circ}_{63^\circ}$ and $62^{70^\circ}_{54^\circ}$. Eclipses are only expected for $i > 85^\circ$, which is thus unlikely to be the case for HD 152234.

We outline that these results are quite putative and still need to be confirmed thanks

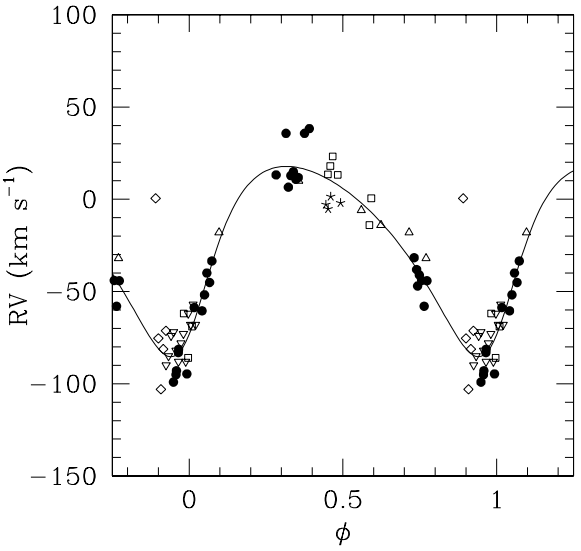

Figure 4.2: **HD 152234:** Primary RV-curve obtained combining data from the literature and from the present work. Open symbols indicate data from the previous works: upward triangles, Campbell & Moore (1938); asterisks, Struve (1944); diamonds, Levato & Morrell (1983); downward triangles, Levato et al. (1988); squares, García & Mermilliod (2001). The filled circles give our FEROS primary RV measurements. The Levato & Morrell (1983) point near $\phi \sim 0.9$ has been rejected for the computation of the best fit RV-curve.

to new observations yielding a good phase coverage on the full orbital cycle. Though the 127 d period is preliminary, we note that a similar period value (P∼125.05 d) fits reasonably well almost all the 37 observations reported in the literature (Fig. 4.2). We could however not reproduce the point of Levato & Morrell (1983) at $RV \approx 0.5$ km s^{-1} near $\phi = 0.9$ (see Fig. 4.2). We thus rejected this point from the period search and from the orbital solution determination. Though the latter disagreement could cast some doubts on our current period estimate, the orbital solution of Table 4.1 is probably the best one can do with the present data set. The new observations will be most welcome.

4.2.2 HD 152233

HD 152233 is known as an O6III(f) star (Walborn 1972; Levato & Malaroda 1980) that displays small RV shifts (e.g. Struve 1944). Based on data from the literature completed by four additional observations, GM01 proposed a very short period of 4.15 d. According to their Table 2, they measured the same RV in two spectra separated by one day. In consequence, they adopted an extremely large eccentricity $e = 0.57$. From our prior data, such a short period was extremely unlikely. In May 2004, we decided to investigate this point more deeply and we observed the system twice a night for six consecutive nights.

From our observations, we only detected a slow trend in the system RVs (Fig. 4.3), definitely ruling out the short period (and high eccentricity) found by GM01. Our May 2003 data reveal for the first time the signature of the secondary component in the blue wing of the He I and He II lines (Fig. 4.4). Unfortunately, the two components could not

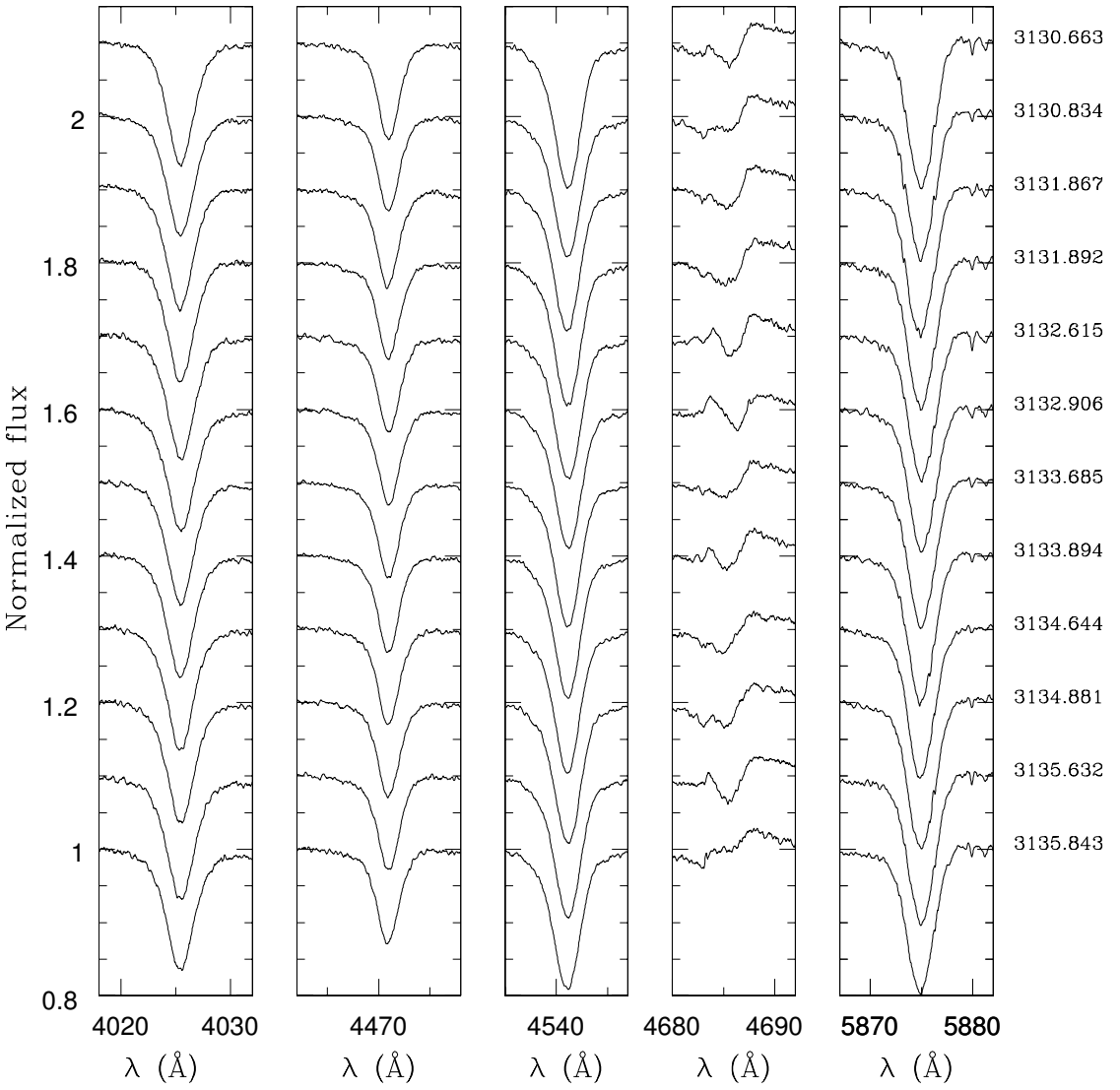

Figure 4.3: **HD 152233:** He I $\lambda\lambda$4026, 4471, He II $\lambda\lambda$4542, 4686 and He I λ5876 lines. The twelve spectra were obtained during a 6-night FEROS run in May 2004. They are ordered chronologically from top to bottom. HJD at mid-exposures are quoted at righthand in the format HJD−2 450 000. No significant difference in the position of the absorption lines is observed from one spectrum to the other, ruling out the 4.15 d period proposed by García & Mermilliod (2001).

be securely disentangled by fitting Gaussians into the observed profiles. This spectrum suggests however that the secondary is probably a late O-type star. In addition, we also detected N III lines that are usually not present in a typical O6III spectrum. As shown in Fig. 4.5, these lines are moving in the opposite direction compared to the primary lines. Clearly this is the signature of the companion, thus probably a less evolved O star of spectral type O8 or later. More disentangled spectra are needed to better constrain the nature of the secondary in HD 152233.

Our best preliminary period is about 41.98 d but this value remains prospective. For

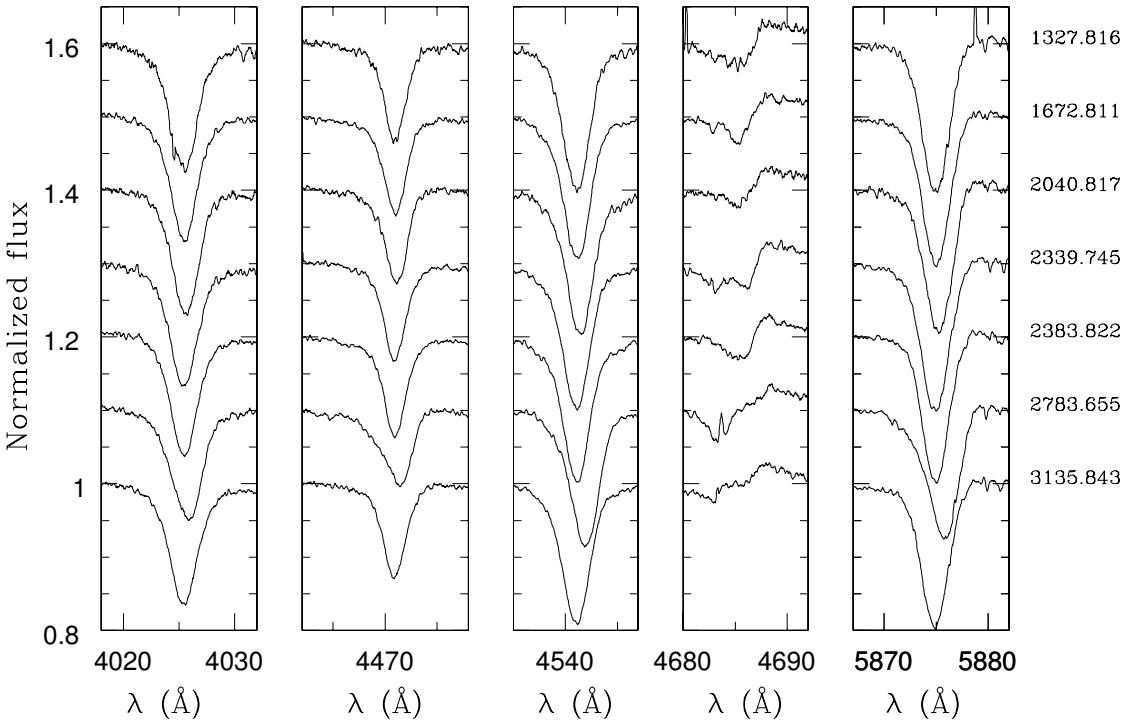

Figure 4.4: **HD 152233:** Same as Fig. 4.3 though obtained during different observing runs from 1999 to 2004. HJD at mid-exposures are quoted at righthand in the format HJD−2 450 000. Clear shifts are seen and the profile asymmetry observed in May 2003 (HJD∼2 452 784) suggests that the secondary is a late O-type star.

example, a period of about 260 d can also fit the observations (Fig. 4.5). From our data, the period can however not be much longer than the latter value. The observed peak-to-peak amplitude of the RV variations is about 60 $\mathrm{km\,s^{-1}}$. The observed secondary velocity during the May 2003 run is about -100 $\mathrm{km\,s^{-1}}$. From our current data set, it would probably be too ambitious to derive further constraints on the orbital properties of HD 152233. The on-going follow up campaign should complete the present data set. We note that the N III λ4379 line, displayed in Fig. 4.5, gives access to the secondary RV at all phases. In consequence, even if the primary and secondary spectra could never be securely disentangled, we will still be able to derive the SB2 properties of the system and, in particular, the mass ratio and the minimal masses of the components.

Finally both HD 152233 and HD 152234 display the He II λ4686 and H α lines with mixed absorption and emission. The situation could be reminiscent of the case of HD 152248 (Sana et al. 2001) and the observed profile variations might reveal an ongoing wind-wind interaction within both systems. However, we first need to constrain the orbital properties in order to distinguish between the individual contribution to the lines and the possible emission originating from the wind-wind collision.

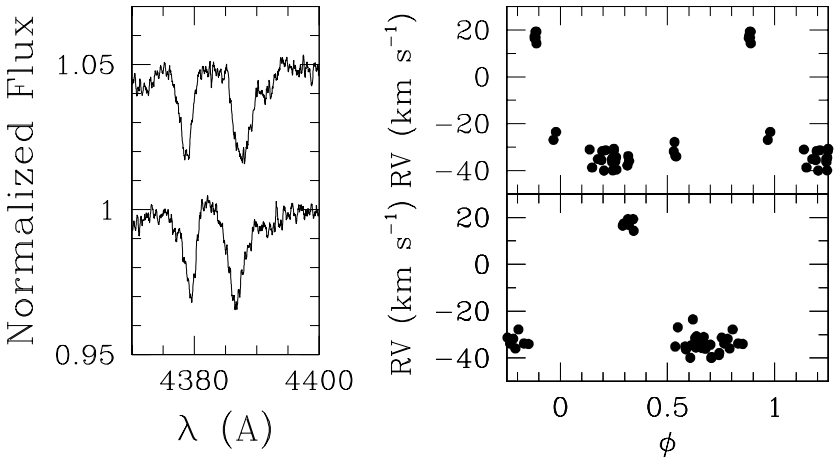

Figure 4.5: **Left:** N III λ4379 and He I λ4388 lines at two different epochs in the spectrum of HD 152233. The lines are clearly seen to move in opposite directions. He I λ4388 belongs to the primary O6 III star. The N III λ4379 line is clearly the signature of the secondary star of the system. **Right:** RVs of the primary component of HD 152233 plotted against the phase for two possible values of the period: $P = 41.976$ d (*lower panel*) and $P = 257.67$ d (*upper panel*). The origin of the phase axis is fully arbitrary.

Chapter 5

Optical spectroscopy of X-ray emitters in NGC 6231

There is nothing like looking, if you want to find something. You certainly usually find something, if you look, but it is not always quite the something you were after.
John R.R. Tolkien

As already mentioned in Chap. 2, the Sco OB 1 association and the NGC 6231 cluster have a particularly rich early type star content. Within the XMM-*Newton* field of view (FOV), we counted 108 OB-type objects plus the Wolf-Rayet system WR 79. About one third of these, among the earliest types, are detected in the X-rays with a reasonable confidence. Their X-ray properties have been presented in Sect. 2.2 and the discussion was largely supported by a reappraisal of the spectral classification of the X-ray emitters, in order, among other things, to derive reliable temperatures, reddening and bolometric corrections for the studied objects. Such parameters indeed play an important role in the accurate estimation of the bolometric magnitudes and, therefore, form the basis on which crucial properties such as the $L_{\rm X}$ vs. $L_{\rm bol}$ relationship rely. The physical properties of most of the O-type binaries have already been presented in the previous chapter. The discussion however was limited to the systems for which our spectroscopic monitoring campaign provided a sufficient data set to reliably constrain the orbital periods of the systems.

In this chapter, we will focus on the remaining objects of the campaign. Some of them, among the brightest ones (e.g. HD 152249, HD 152247), have been regularly monitored since 1999. Other binary candidates, relatively fainter (e.g. HD 152200, HD 152314), received less attention in the earlier years of our spectroscopic campaign. However, thanks to an increase of the FEROS performances since its move to the ESO 2.2m telescope in 2002, we have been able to collect enough data to investigate variability on time scales of a couple of hours till about 5 to 6 days (the typical time span of our observing runs). Finally, the particularly good weather conditions during the May 2004 run allowed us to observe lower priority objects. We obtained snapshot spectra of most of the brightest optical counterparts that were still unobserved. Down to $V < 11$, only three objects could not be observed: CPD $-41°7746$ ($V = 9.193$), a suspected B0.5 V SB 1 system (García & Mermilliod 2001), CPD $-41°7736$ ($V = 10.153$), a B1 V β Cep star (Arentoft et al. 2001) and CPD $-41°7715$ ($V = 10.241$), another β Cep star (Balona 1983; Arentoft et al. 2001). On the basis of a couple of radial velocity (RV) measurements, this B2 IV object was also suspected to be a spectroscopic binary by Raboud (1996).

The current chapter will present the remaining results of our spectroscopic campaign,

thus focusing exclusively on the OB-type objects that have not been discussed in the previous chapter. In the past, RV measurements of some of these objects have mainly been performed by Struve (1944), Hill et al. (1974, HCB74), Levato & Morrell (1983, LM83), Perry et al. (1990, PHYB90), Raboud (1996) and García & Mermilliod (2001, GM01). The most recently published photometric studies are from Perry et al. (1991, PHC91), Balona & Laney (1995, BL95), Raboud et al. (1997, RCB97), Sung et al. (1998, SBL98) and Baume et al. (1999, BVF99). Most of these works however do not cover the whole XMM-*Newton* FOV. As mentioned in Chap. 2, Dr. H. Sung (2005, private communication) recently obtained the UBV(RI)$_C$ photometry (SSB05 catalogue, Sung et al. 2005, in preparation) of the whole FOV down to $V \lesssim 23$. These observations thus provide the most extended and the deepest study of its kind towards the NGC 6231 cluster and its vicinity. For consistency, we thus exclusively used data from the SSB05 catalogue in the following, unless specified otherwise. Cross-identifications were presented in Sect. 2.2. In this chapter, beside the usual HD and CPD identifiers, we also make use of the Se (Seggewiss 1968 , RCB97) and SBL (SBL98) numbering systems.

For each object, we shortly summarize the results of the previous investigations. We then give a brief description of the data obtained (see also Chap. 1). Finally, we focus on the spectral type classification. For O-type stars, we used the criteria of Conti & Alschuler (1971), Conti (1973), Mathys (1988) and Mathys (1989) based on the equivalent widths of specific lines. We adopted the usual notations: $\log W' = \log W(\lambda 4471) - \log W(\lambda 4542)$, $\log W'' = \log W(\lambda 4088) - \log W(\lambda 4144)$ and $\log W''' = \log W(\lambda 4388) + \log W(\lambda 4686)$. With respect to the latter criterion, based on the product of the equivalent widths (expressed in mÅ), we emphasize that the star has to be single, or that the brightness ratio of the two components has to be known for this criterion to be applicable. We also investigate the possible variability of these objects on the different time-scales allowed by our current sample and by the comparison with earlier observations. As a conclusion to this chapter, we will present an atlas of the optical spectra of the early-type stars in our sample. The atlas content is displayed in Appendix A.

5.1 HD 152076

Separated by $\sim 13'$ from and to the N-W of HD 152248, HD 152076 is somewhat offset from the cluster core and has therefore received less attention than the other bright stars. Some confusion seems to exist about its magnitude and indeed, cross-identifiers reported in the SIMBAD data base are clearly erroneous. For example, SIMBAD associated HD 152076 with the star Se 309/SBL 350. HD 152076 however lays outside the field of investigation of these two studies (RCB97; SBL98). It is obvious from comparison with neighbouring objects in DSS images that the $V = 10.85$ magnitude reported in SIMBAD is wrong. We adopt in the following the measurements from SSB05 ($V = 8.471$) which are close to previous determinations of $V = 8.5$ (PHYB90), 8.48 (PHC91), 8.47 (Schild et al. 1969), 8.50 (Feinstein & Ferrer 1968), 8.46 (Bok et al. 1966) or 8.48 (Heske & Wendker 1984). Quoted spectral types are in the range B0 V (Morgan et al. 1953a,b) - B0/1 III (Schild et al. 1969; Houk 1978). A couple of RV measurements were also performed by Struve (1944); Wilson (1953) and PHYB90 who obtained a Ca-K corrected RV of about -25 to -30 km s^{-1}. Balona (1983) reported this object to be constant in the B Johnson filter on a time scale of 5 hours.

As one of the bright stars in NGC 6231 to be detected in the X-ray domain, we acquired a snapshot FEROS spectrum of HD 152076 and we re-derived its spectral classification. Its spectrum reveals relatively narrow lines. The He II signature is faint but clearly

seen, indicating a late O-type star. We obtained $\log W' = 0.515$, $\log W'' = 0.08 - 0.09$ and $\log W''' = 5.3$, respectively corresponding to a spectral type O9.5 and to luminosity classes V and III. $\log W''$ is however very close to the giant limit (located at a value of $\log W'' = 0.10$). With $V = 8.471$ and $B-V = 0.240$, we obtained $M_V = -4.4$, an intermediate value between typical absolute magnitudes of O9.5 dwarfs and giants. HD 152076 is quite offset from the cluster core and may thus not belong to NGC 6231. Instead the star could belong to the Sco OB 1 association, located at the same distance and with a similar age than NGC 6231. Though its luminosity does not perfectly agree with the spectral type deduced from the spectroscopic criteria, HD 152076 is unlikely to be a background object. Because of the narrow lines, suggesting a lower gravity, and the relatively strong metallic spectrum, we opted for an O9.5 III classification. RV measurements performed on the classification lines plus Mg II λ4481 give $\overline{RV} = -30.7 \pm 2.7$ km s^{-1}, in good agreement with previous measurements. We thus consider HD 152076 to most probably be a single star.

5.2 HD 152200

HD 152200 is a late O-type star located about 3.′6 S-SW of HD 152248. It is quoted as variable by Feinstein & Ferrer (1968), with $V \sim 8.35 - 8.42$. Photoelectric measurements reported in other works since the 1960's are all in the range 8.41-8.44, except the measurement from Oja (1986, $V = 8.37$). More recent CCD photometry yielded values between 8.31 (Baume et al. 1999) and 8.42 (BL95). Schild et al. (1969) classified HD 152200 as O9.5 III; Houk (1978) as O9 III, whereas Levato & Malaroda (1980) and PHYB90 respectively preferred O9.5 V(n) and B0 IV classifications. LM83 reported 3 RV measurements on three consecutive nights, which indicate a velocity change of about 70 km s^{-1} from one night to the other. PHYB90 Ca-K corrected velocities show a 30 km s^{-1} range on three measurements spread over 10 days. Finally GM01 claimed to have detected the secondary component signature on 2 out of their 5 spectra. The system should apparently have a period of a few days. The primary and secondary lines are blended one night and separated by $\sim$ 180 km s^{-1} the following night. GM01 showed two profiles of the H β line. One is reported as blended ($RV \sim -27$ km s^{-1}, though with a deep asymmetry in the blue wing); the second is quoted as deblended with $RV_1 \sim +4$ and $RV_2 \sim -110$ km s^{-1}. The observed secondary signature is however much fainter than expected from the first spectrum. This could suggest some normalization problems. There also seems to be some confusion in their plot labels. Indeed, while the graph is entitled Se266 (which does correspond to HD 152200), the caption indicates Se 253, which is CPD $-41°7706$. The quoted Julian dates however correspond to the dates reported in their journal of observations for HD 152200.

From May 1999 till May 2004, we collected 16 FEROS spectra spread over different time scales. The optical spectrum of HD 152200 is characterized by the Balmer, He I and He II lines. The few metallic lines typical of late O-type objects are also clearly seen. The line profiles are variable (Figs. 5.1 and 5.2) but no obvious signature of a companion could be found. We measured the RVs and EWs of 12 lines including the usual He I and He II lines as well as the Ca K, H and Na D_1, D_2 interstellar lines. The observed variations display a peak-to-peak amplitude of 50 km s^{-1} and seem to have a period close to 5 days. The H β line behaviour (Fig. 5.2) is clearly different from what was observed by García & Mermilliod. The maximum night-to-night shift is about 30 km s^{-1}(to be compared with the 70 km s^{-1} shift observed by LM83). From our observations, the central value around

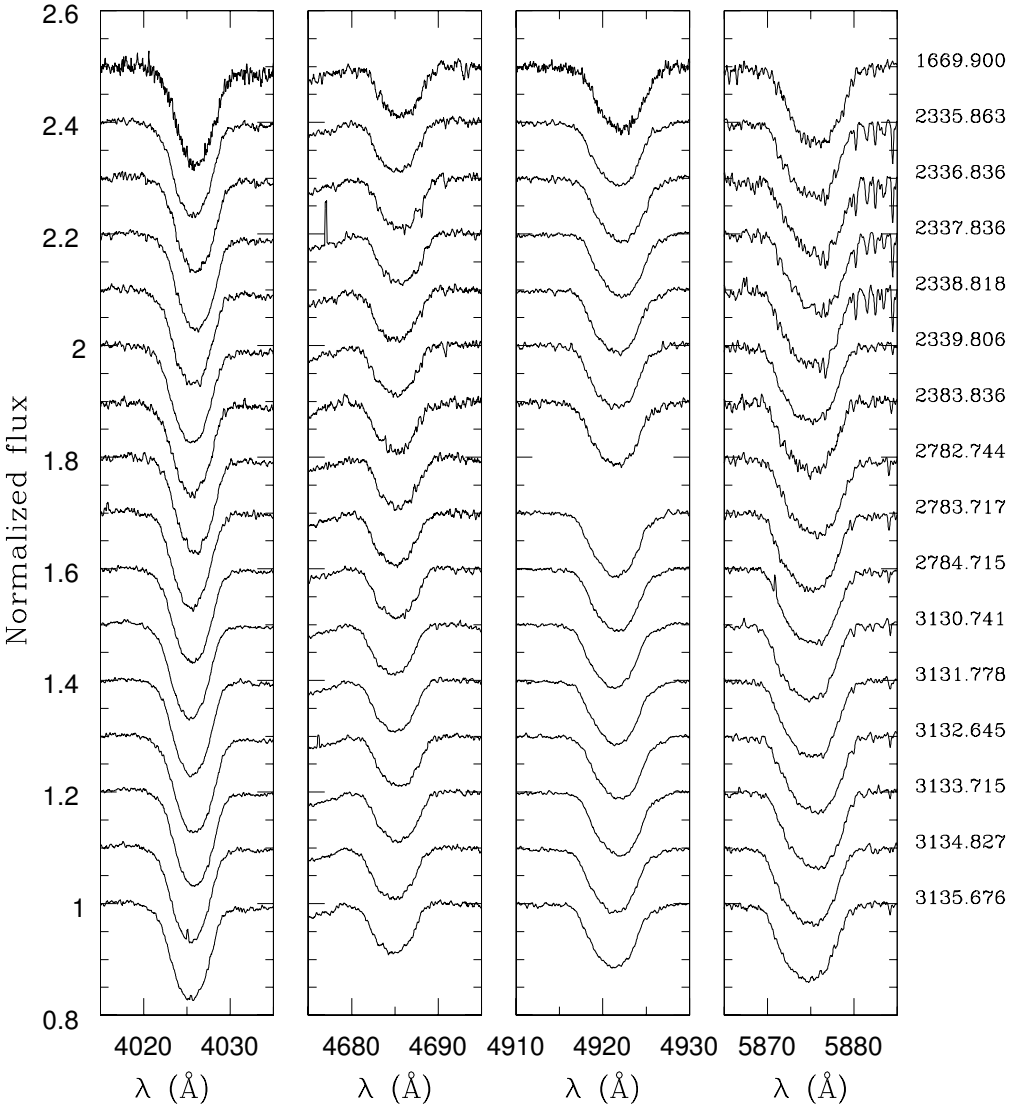

Figure 5.1: **HD 152200:** He I λ4026, He II λ4686 and He I $\lambda\lambda$4921, 5876 lines. HJD at mid-exposures are quoted at righthand in format HJD$-$2 450 000. The He I λ4921 line at HJD = 2 452 782.744 was strongly affected by cosmic rays and is not displayed.

which the variations occur seems to have been shifted by about 10 to 15 km s^{-1} between the years 2002 and 2004. It could however be an apparent effect resulting from a too sparse sampling of the $\sim$ 5-day period. We used the Lafler & Kinman (1965) and the Heck et al. (1985) period search techniques and two aliases were found around $P \sim 4.44$ and 5.56 days. However, both values yielded a large spread of the RV measurements plotted against a hypothetic phase.

From the measured EWs, we obtained $\log W' = 0.689 \pm 0.048$, $\log W'' = 0.162 \pm 0.030$ and $\log W''' = 5.438 \pm 0.022$. This corresponds to an O9.7 star with spectral type O9.5 at 1-σ. Conti's criterion (W'') clearly indicates a giant class while Mathys's criterion (W''') rather points towards class V. From SSB05 data, we computed the absolute visual magnitude to be about $M_V = -4.08$ which is typical of a main sequence O9.7 star. From

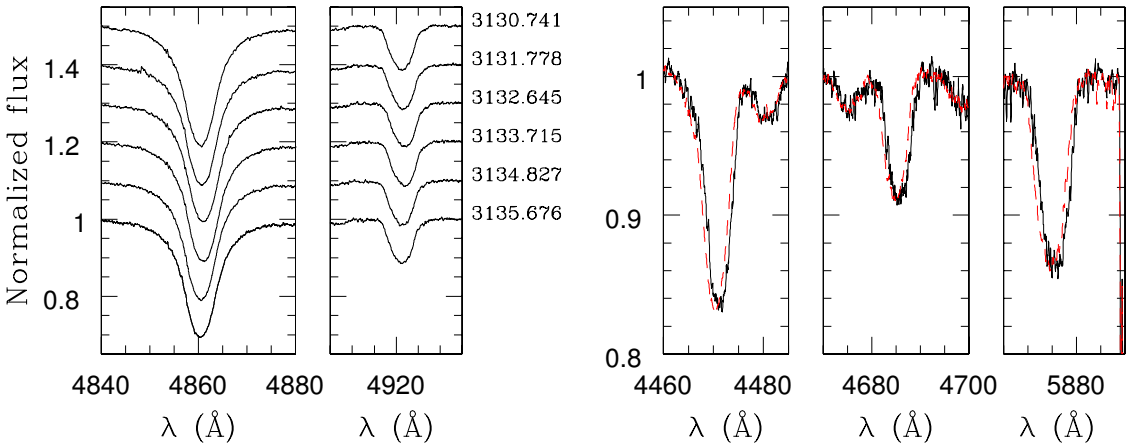

Figure 5.2: **HD 152200:** *Left panel.* Evolution of the H β and He I λ4921 lines during six consecutive nights in May 2004. HJD at mid-exposures are quoted at righthand in format HJD−2 450 000. *Right panel.* He I λ4471, He II λ4686 and He I λ5876 lines obtained at HJD = 2 451 669.900 (plain line) and HJD = 2 453 135.676 (dashed line).

our data and beyond the night-to-night RV variations, we find no direct evidence that HD 152200 is a spectroscopic binary.

5.3 HD 152235

Located at 10′.4 south of the cluster core, HD 152235 is an early-B supergiant that lies in an extremely reddened part of the cluster. First RVs were measured by Struve (1944) who obtained a range of 25 km s^{-1}. More recently Levato et al. (1988) obtained medium-resolution spectra of the star over 13 consecutive nights. They reported that HD 152235 is a B0.7 Ia, nitrogen deficient star, that displays RV variations. Their peak-to-peak amplitude is about 20-30 km s^{-1} for a wide variety of lines, but no periodicity appeared. Different lines may indeed present a different behaviour. Based on the dispersion of the previous observations, PHC91 reported that the star is probably variable both photometrically and spectroscopically. Finally, GM01 obtained two additional RV measurements close to the cluster systemic velocity.

In May 2004, we obtained six spectra of HD 152235 (Fig. 5.3). The main features are the usual Balmer and He I lines, a strong O II spectrum and a faint He II λ4686 line. The spectrum shows very narrow lines, indicating a low surface gravity. The Si III λ4553 line is slightly stronger than Si IV λ4089, with an intensity ratio about 1.25. Si III λ4553 is also about 15% stronger than He I λ4388. According to Walborn & Fitzpatrick (1990) this clearly indicates a B1 Ia type. We also compared the measured EWs with typical B-stars EWs (Didelon 1982) and we obtained an almost perfect agreement with the adopted classification. We observed slight RV changes from one night to the other, with a maximum amplitude of $\sim$ 20 km s^{-1}. These are reminiscent of the shifts observed by Levato et al. (1988) and are probably due to slight profile variations that, in the He I lines, can come from a faint emission component in the line. The H α line shows a variable P-Cyg profile (Fig. 5.3) whose intensity and morphology change on a time scale of days. With $V = 6.319$ and $B - V = 0.528$, we obtained $M_V = -7.1$, thus quite similar to the typical

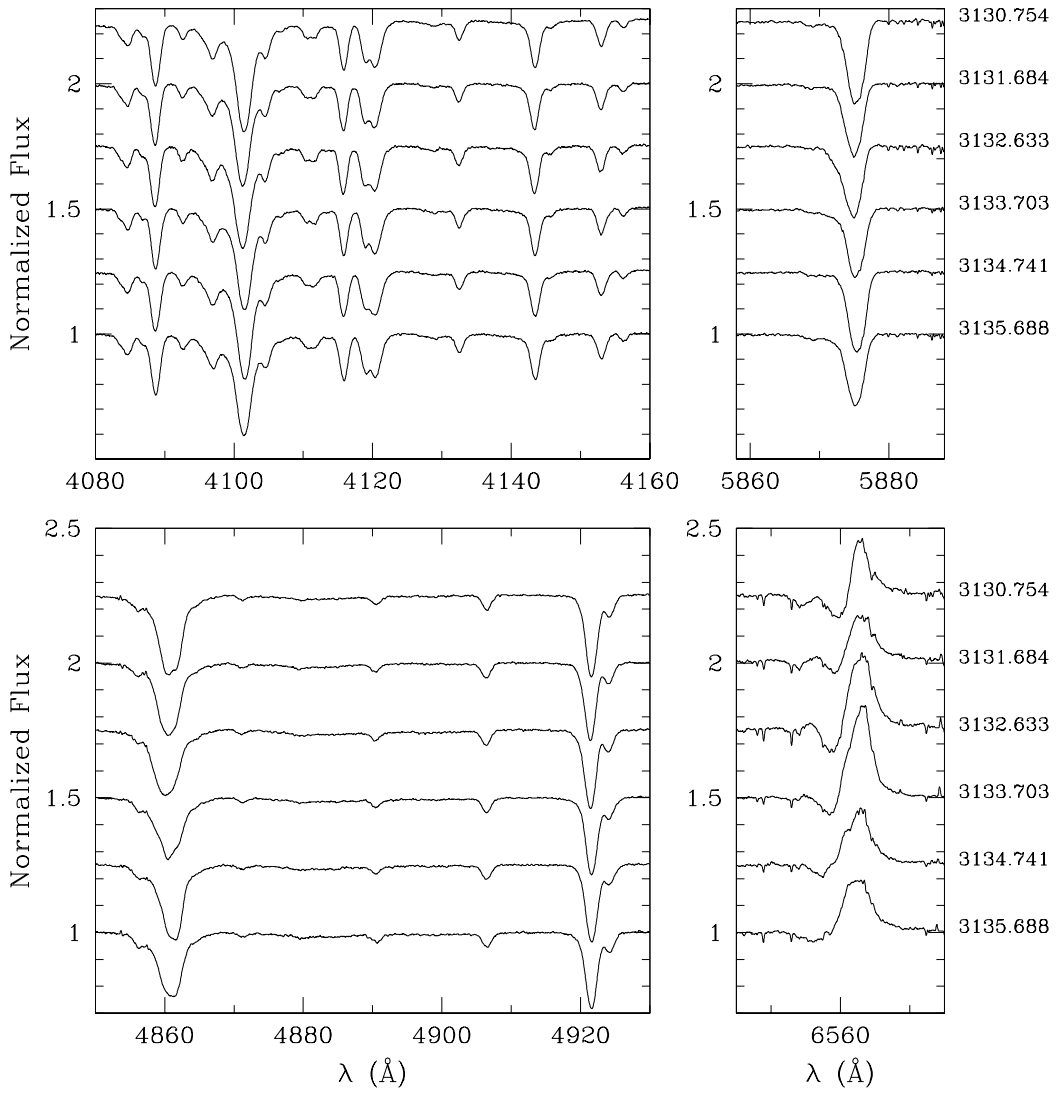

Figure 5.3: **HD 152235:** Different wavelength ranges. The heliocentric Julian Dates (HJD−2 450 000) are quoted on the righthand sides. The six spectra were obtained during six consecutive nights in May 2004. The different panels use the same scales. Note the strong variation of the H α profile compared to the other lines.

B1 Ia magnitude. The star is presumably single

5.4 HD 152247

At 11′ N of HD 152248, HD 152247 is a bright O-type star. Probably because of its larger distance from the cluster core, it has clearly suffered from a lack of attention in the literature. Mostly classified as O9.5 III (Houck 1956; Feinstein & Ferrer 1968; Mathys 1988; Penny et al. 1996), the star seems to be constant in the V band (Balona 1983) with a dispersion in the published values smaller than 0.05 mag. Owing to the absence of the star in the usual reference works on the cluster, we adopted the value of Diplas

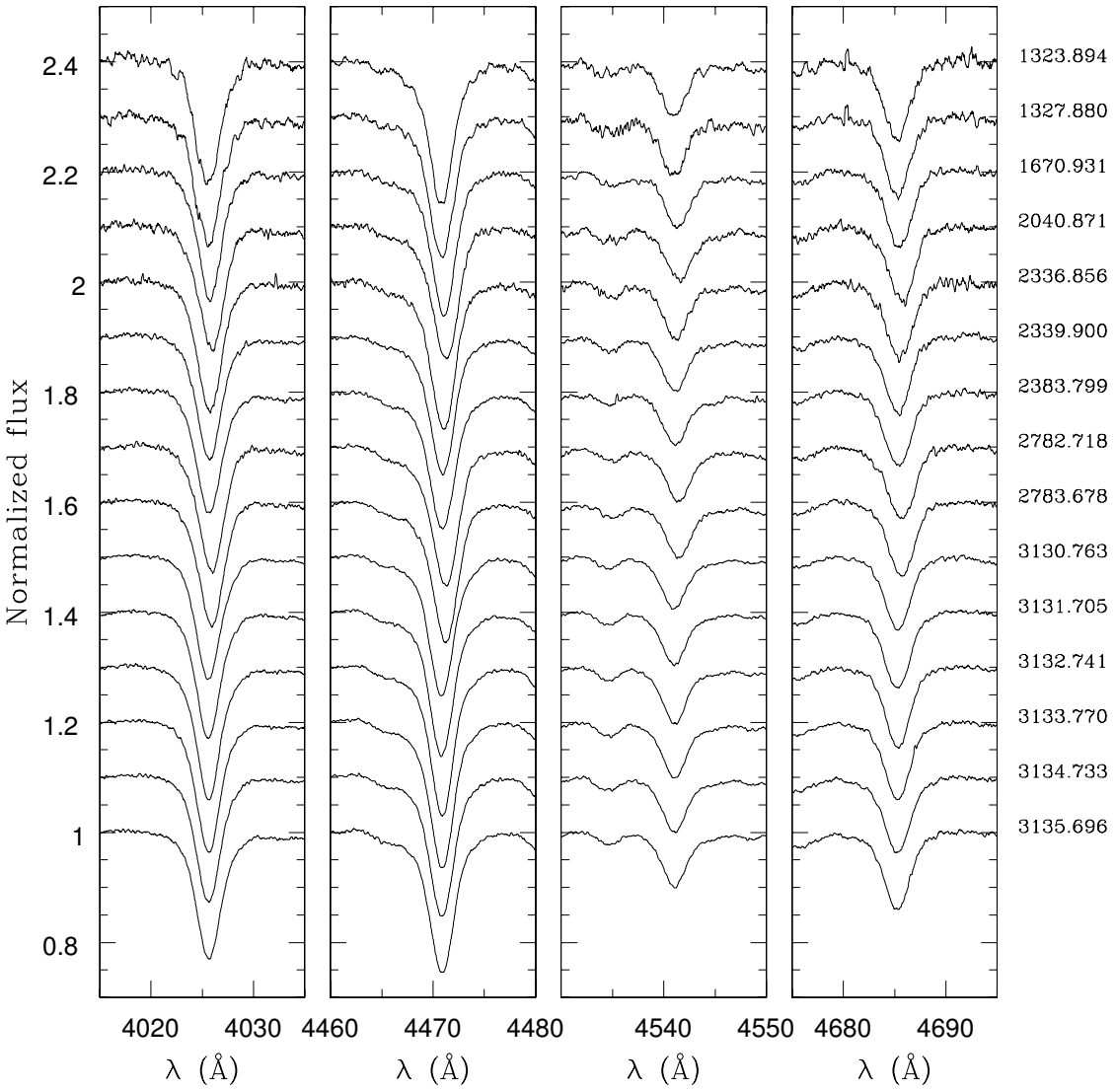

Figure 5.4: **HD 152247:** He I $\lambda\lambda$4026, 4471 and He II $\lambda\lambda$4542, 4686 lines. Spectra are ordered chronologically from top to bottom. Clear shifts are seen throughout the years. HJD at mid-exposures are quoted at righthand in format HJD−2 450 000.

& Savage (1994): $V = 7.18$. Penny (1996) obtained a projected rotational velocity of 120 km s^{-1} while Howarth et al. (1997) derived 112 km s^{-1} and a terminal wind velocity of 2295 km s^{-1}. The first RVs were obtained by Struve (1944) who quoted values around -14 km s^{-1}. No other measurements were obtained until Raboud (1996) suggested the star was displaying RV shifts. He indeed reported 5 measurements spread over two observing periods (WEBDA database). The first set was acquired over three consecutive nights and indicated values around +20 km s^{-1}. The next two measurements were obtained about two years later, again on two consecutive nights, and yielded values close to -23 km s^{-1}. More recently Stickland & Lloyd (2001) reported two additional IUE observations obtained about 10 years before Raboud (1996) and indicating $RV \sim -39$ km s^{-1}. The star thus presents clear RV variations. However the time scale at which the latter occur is very poorly constrained. We regularly attempted to acquire FEROS spectra of this target

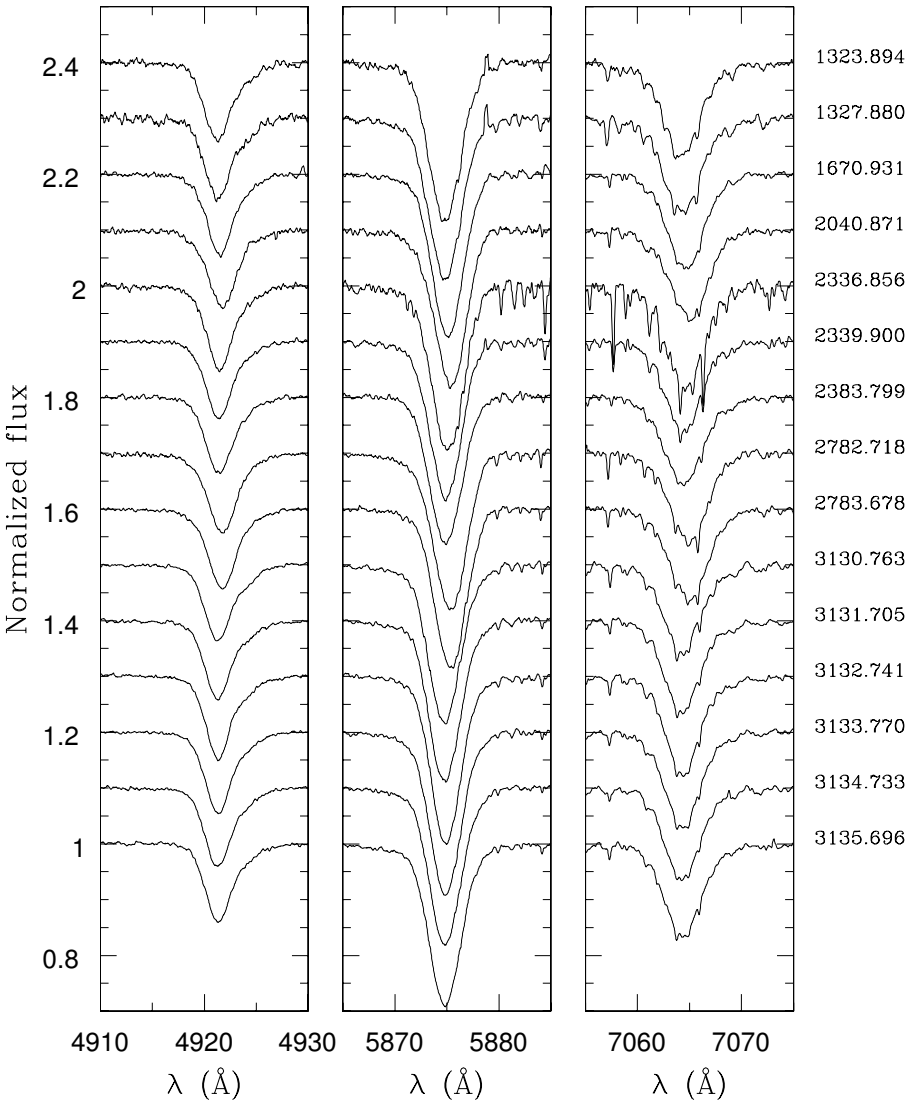

Figure 5.5: **HD 152247:** He I $\lambda\lambda$4920, 5876 and 7065 lines. Spectra are ordered chronologically from top to bottom. Clear shifts are seen throughout the years. HJD at mid-exposures are quoted at righthand in format HJD−2 450 000.

since 1999 but, until 2004, we could not observe it as frequently as it would have deserved because of the frequent bad weather conditions.

From our observations, clear RV shifts are seen from year-to-year (Figs. 5.4 and 5.5). The two extreme RV values in our set are approximately −40 (1999, 2004) and −10 km s^{-1} (2000, 2003). In May 2004, we obtained six spectra over six consecutive nights but the HD 152247 spectrum remains almost unchanged. Similarly no significant shift is observed between the 2002 March and April data. We obtained $\log W' = 0.39 \pm 0.03$ and $\log W'' = 0.29 \pm 0.03$, which corresponds to an O9 III type. The luminosity criterion is however very close to the border line with the supergiant class. With $V = 7.18$ and $B - V = 0.22$ (Diplas & Savage 1994), we obtained $M_V = -5.6$, thus too faint for a supergiant. Finally, comparing with the Walborn & Fitzpatrick (1990) atlas, we confirm the O9 III classification for the (possibly composite) spectrum of HD 152247.

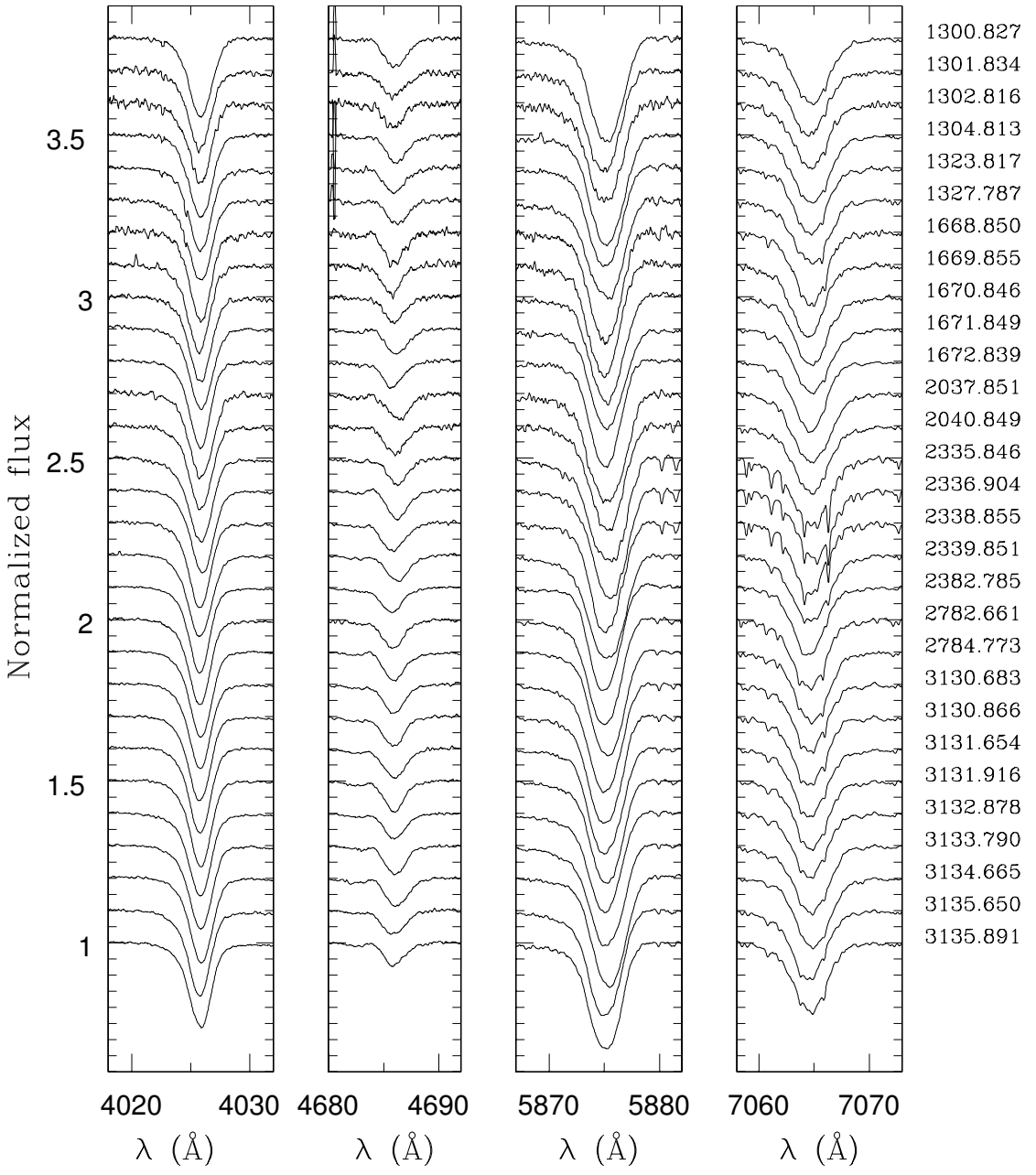

Figure 5.6: **HD 152249:** He I λ4026, He II λ4686, He I λ5876, H α and He I λ7065 lines. Spectra are ordered chronologically from top to bottom. Small line profile variations can be seen. HJD at mid-exposures are quoted at righthand in format HJD−2 450 000.

5.5 HD 152249

HD 152249 is one of the brightest members of the cluster. Its visual magnitude, as quoted since the 1960's, is in the range 6.43-6.51, with the notable exception of Feinstein & Ferrer (1968) who reported the star as variable with $V = 6.34 - 6.50$. Quoted spectral types are

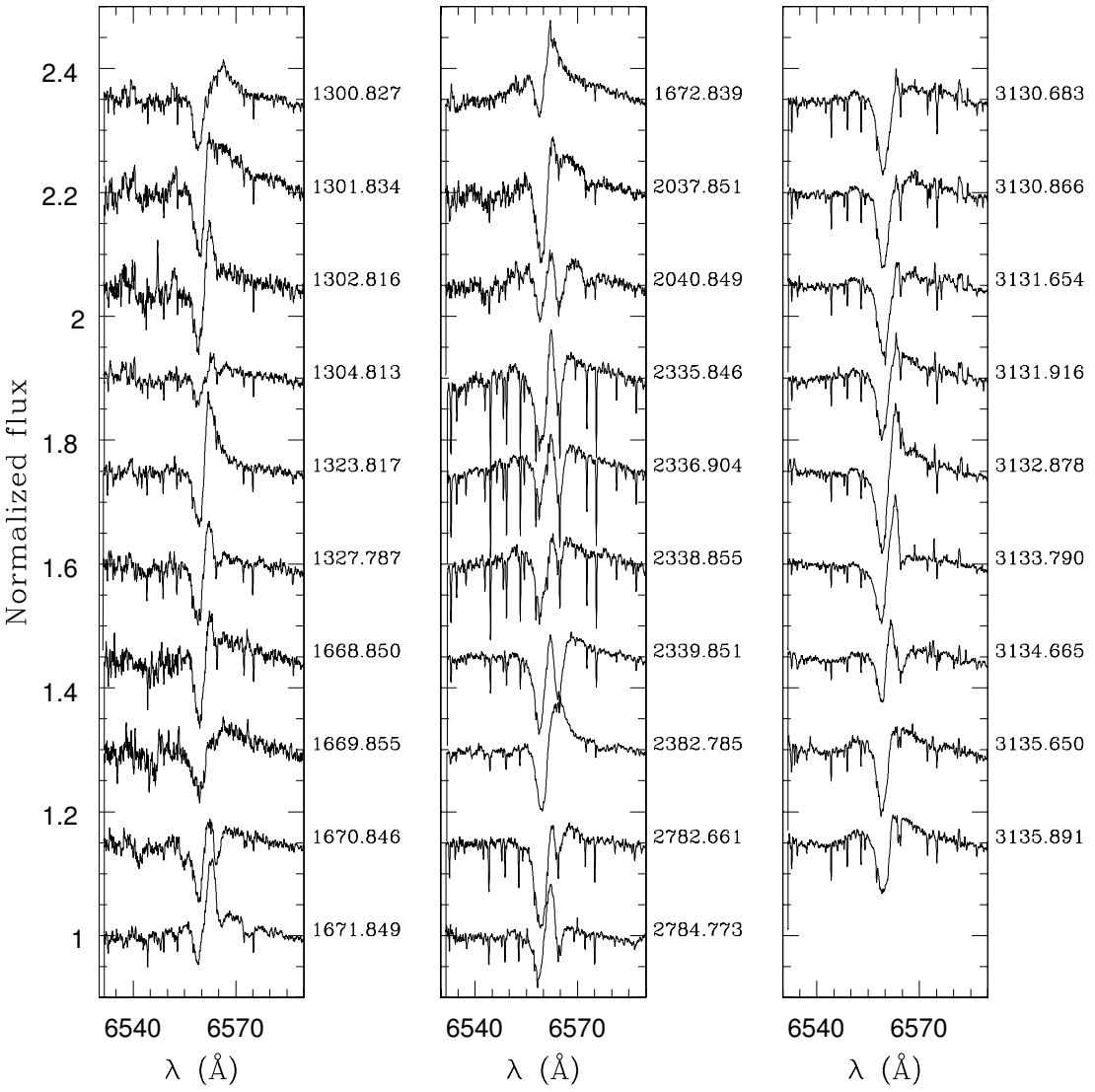

Figure 5.7: **HD 152249:** Evolution of the H α line. Spectra are ordered chronologically from top to bottom and from left to right. HJD at mid-exposures are quoted at righthand of each panel in format HJD−2 450 000.

O9-B0 Ia/b/ab, with the exception of RCB97 who listed O7-O9V! HD 152249 is adopted by Walborn & Fitzpatrick (1990) as an OC9.5Iab standard. Several authors indicated RV variations. Neubauer (1930) obtained a ΔRV range of 46 km s^{-1} on 3 plates and classified it as a spectroscopic binary. Struve (1944) and Perry et al. (1990) respectively obtained 15 and 13 measurements on a time-span of 16 and 75 days. Both data sets display a similar range as the one obtained by Neubauer (1930). However these do not present the smooth variations that could be expected for a binary with a period larger than a couple of days. Later on, Garmany et al. (1980) and Levato et al. (1988) obtained new measurements. These do not indicate night-to-night variability but, separated by about 5 years, they differ by 20 km s^{-1}.

Sine HD 152249 is one of the brightest stars of the cluster, we regularly monitored it. Since 1999, we collected 34 spectra. The peak-to-peak dispersion over the 6 years is

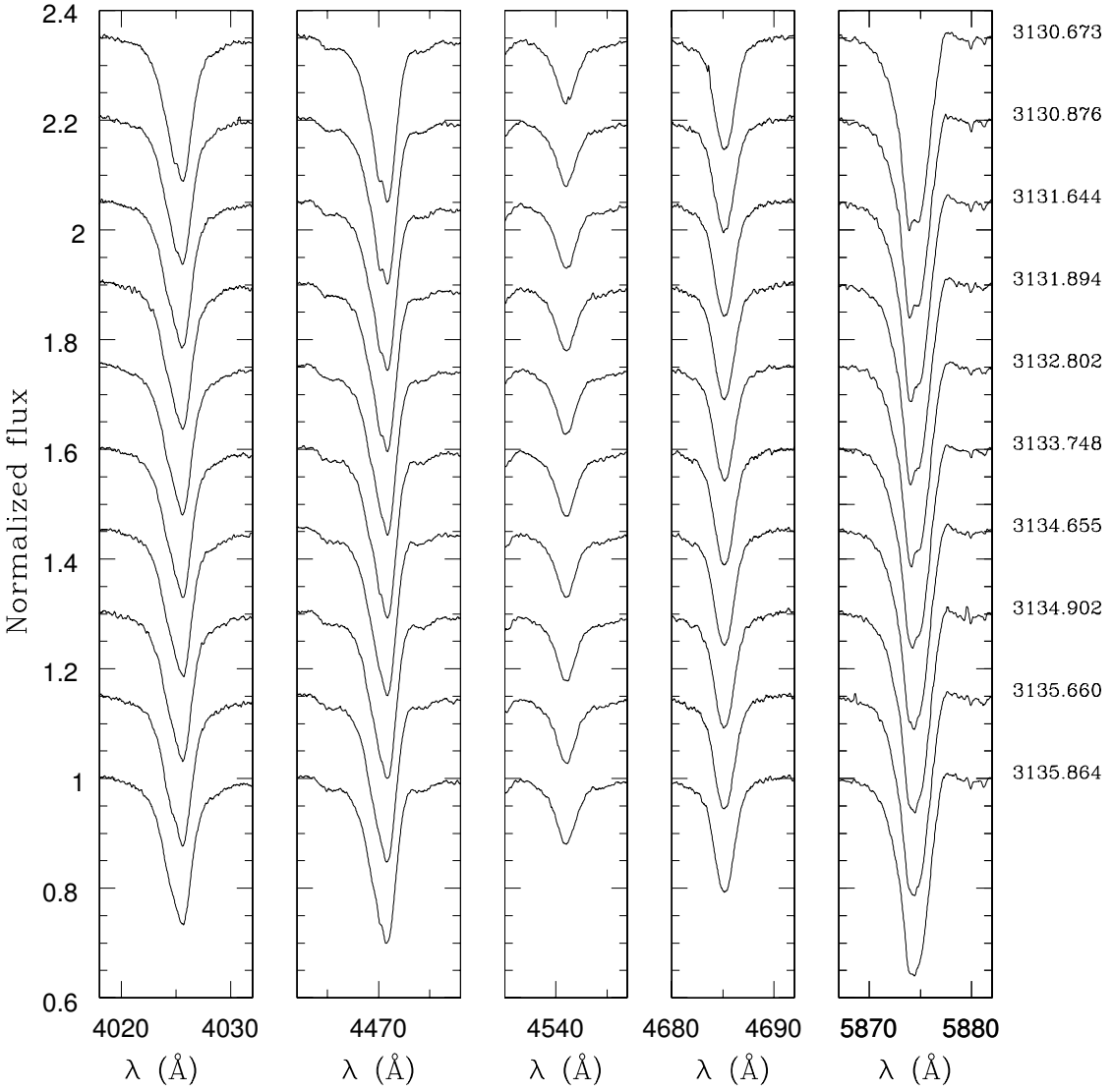

Figure 5.8: **HD 152314:** He I $\lambda\lambda$4026, 4471, He II $\lambda\lambda$4542, 4686 and He I λ5876 lines obtained on six consecutive nights. The spectra are ordered chronologically from top to bottom. HJD at mid-exposures are quoted at righthand in format HJD−2 450 000. These data do not reveal any variability on a time-scale of days.

20 km s^{-1} and the night-to-night variability has an amplitude of $\sim$ 10 km s^{-1} (Fig. 5.6). We consider the star to present slight RV changes but clearly, we cannot associate these with a binary nature. The H α line presents mixed absorption and emission and undergoes strong line profile variations from night to night as well as from one period to the other (Fig. 5.7). We measured $\log W' = 0.39 \pm 0.02$, $\log W'' = 0.554 \pm 0.004$ and $\log W''' = 4.73 \pm 0.06$. This unambiguously leads to an O9 I star, thus slightly different from Walborn & Fitzpatrick (1990) classification. With $V = 6.437$ and $B - V = 0.193$, we obtained $M_V = -6.1$, quite typical of Ib supergiants rather than Iab (Lang 1992). With the presence of the N III $\lambda\lambda$4634-4641 lines in weak emission, we finally adopt an O9 Ib ((f)) classification.

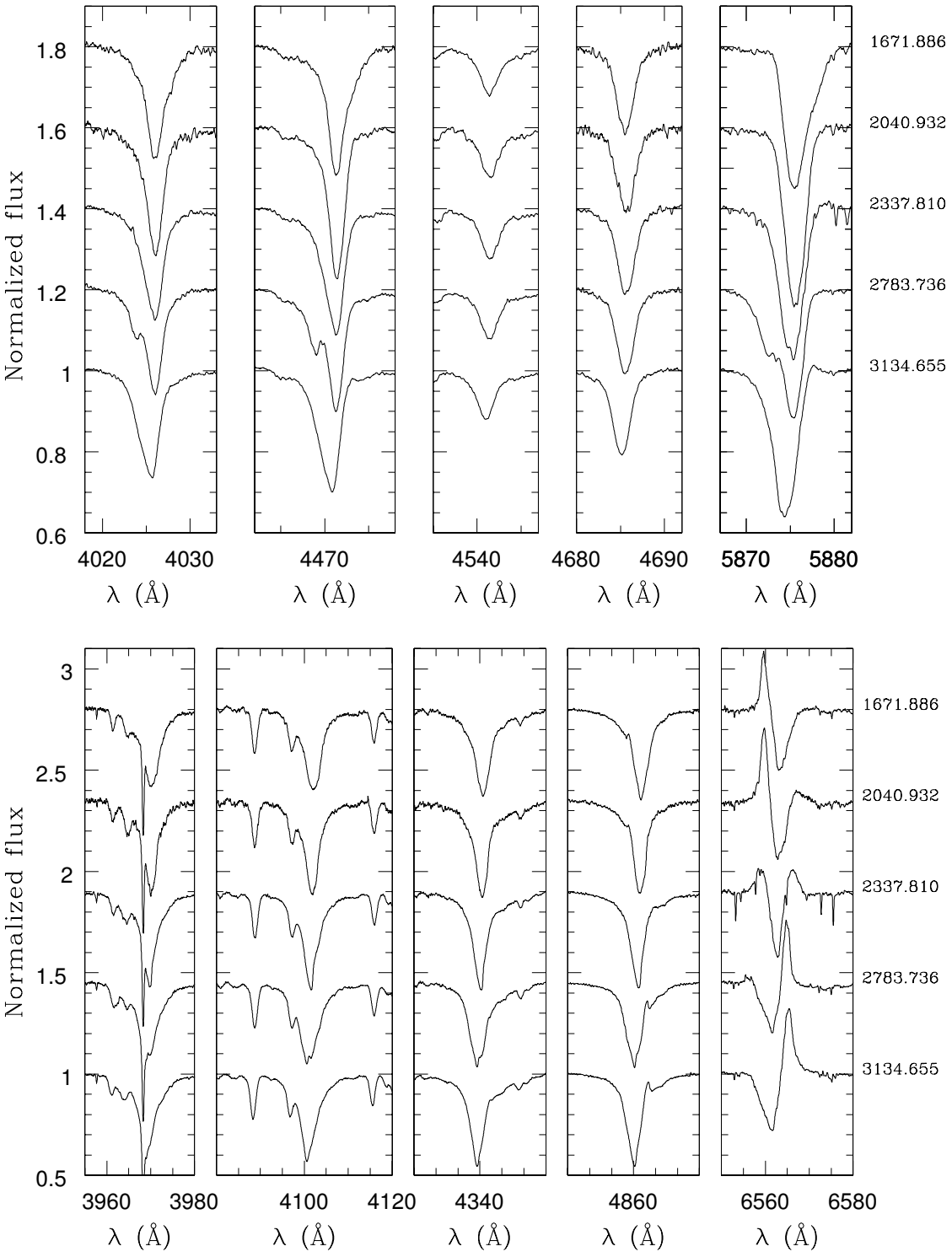

Figure 5.9: **HD 152314:** He I λλ4026, 4471 He II λλ4542, 4686, He I λ5876 (*upper panel*) and Balmer (*lower panel*) lines acquired in five different observing runs. Spectra are ordered chronologically from top to bottom. HJD at mid-exposures are quoted at righthand of each panel in format HJD−2 450 000. The spectral signature of the companion is clearly seen in the May 2003 spectrum (at HJD∼2 452 784).

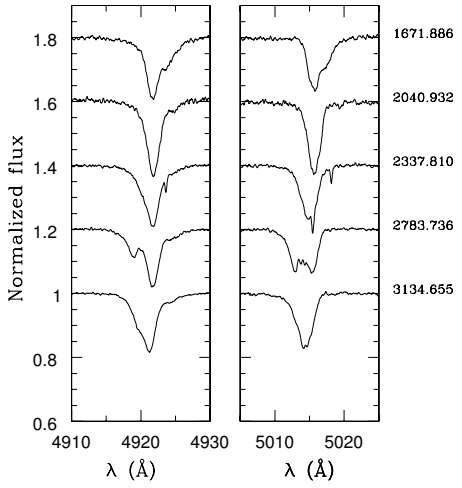

Figure 5.10: **HD 152314:** He I $\lambda\lambda$4920 and 5025 lines acquired in five different observing runs. HJD at mid-exposures are quoted at righthand in format HJD−2 450 000. Spectra are ordered chronologically from top to bottom and suggest the presence of an additional, narrow line, component.

5.6 HD 152314

At 4′.2 E-NE of the cluster core, HD 152314 is a late O-type object. With $V = 7.92 - 8.12$, Feinstein & Ferrer (1968) reported it to display photometric variability. RCB97 found long-term variability on a time-scale of $\sim$ 18 years. These variations display a different amplitude in the different bands of the Geneva system. The star is becoming bluer when it brightens. RCB97 also suggested a shorter time-scale variability of the order of 1.5 month. RV measurements by Struve (1944), PHYB90 and LM83 do not present any particular variation and the latter authors reported the star as RV constant. More recently, GM01 obtained three additional spectra, two of which separated by 4 days, while the other one was acquired about two years later. Though with some uncertainty on the RV measurements, they indicated to have detected the signature of a blue-shifted secondary component on the first spectrum of their series, thus suggesting variability on a time-scale of days. The spectral types quoted in the literature are O8.5 III (Levato & Malaroda 1980), O9 III (Schild et al. 1969; Perry et al. 1990) or O9 V (Morgan et al. 1953a). The remark by RCB97 that the object's colour is changing with time could also indicate a slight change of its spectral type. Finally, we note that no companion was found by the Mason et al. (1998) speckle observation campaign.

We have sparsely acquired a few FEROS spectra of HD 152314 since May 2000. In May 2004, the weather conditions (finally) allowed us to spend more time on lower priority objects. Among them was HD 152314 and we acquired 9 spectra over the 6-night run. The night-to-night variability is very limited (Fig. 5.8) but we observed important changes from one year to the other (Fig. 5.9). In May 2003, we detected the presence of a secondary companion in most of the He I and Balmer lines. However profiles from different lines often show striking differences. The comparison of the year-to-year profile variations further seems to indicate that the system might actually host more than two components. The H α profile presents mixed absorption and emission and evolves from an inverse P-Cygni profile to a normal P-Cygni through the years (Fig. 5.9). It suggests an absorption component moving on top of a slightly broader emission. It is plausible

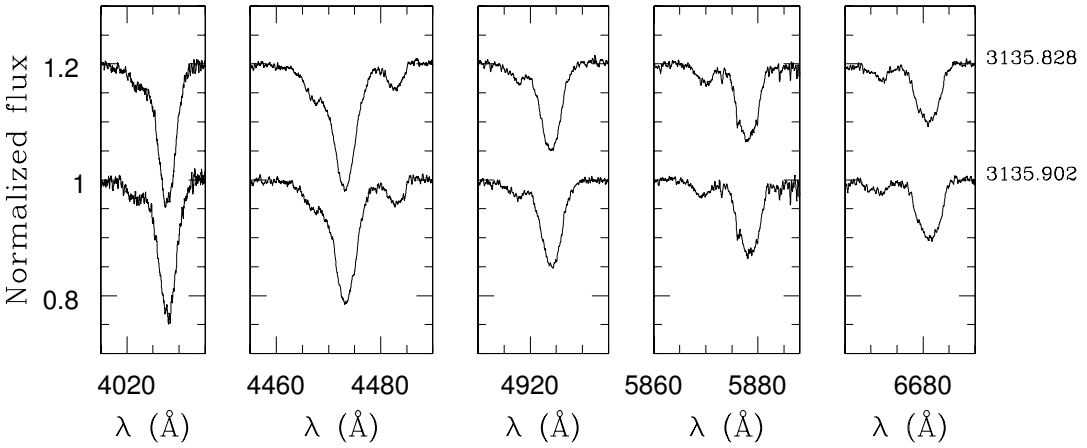

Figure 5.11: **HD 326320:** He I λλ4026, 4471, 4921, 5876 and 6678 lines. HJD at mid-exposures are quoted at righthand in format HJD−2 450 000. The two components are clearly separated.

that the two components could be associated with different objects. Our data set does unfortunately not allow to investigate variability on time scales of several weeks to a few months. The spectral type changes from O9 to O8.5 between 2000 and 2004, but this could be due to an effect of line blending. The best spectral type estimation is probably obtained in 2003 and indicates an O8.5 III primary. The He II line seems to belong to the sole primary, the secondary component probably being a B-type star. However, we could not detect its signature in the metallic lines, which renders very difficult the spectral classification. Because of the strong secondary signature in the He I lines, it could be located around the He I maximum, thus at B1-3. This classification is however very putative. Finally with $V = 7.749$ and $B - V = 0.525$, we obtained $M_V = -4.95$ for the system, much fainter thus than a typical O8.5 III. This situation is reminiscent to the one observed for other O-type binaries in the cluster. We thus assumed that the primary is rather a dwarf and we adopt, as our best classification, O8.5 V + B1-3? + ... This possibly multiple object definitively needs a follow up covering time scales from weeks to years.

5.7 HD 152437

This late B-type object in the periphery of the cluster was reported as a non-member by PHC91 and RCB97. The latter authors assigned it a B9 V type while Houk (1978) had adopted a B9 III/IV classification. All published photometric studies give $V = 9.13 - 9.16$. We obtained one snapshot FEROS spectrum in May 2004 which gives $RV \sim +15.5\,\mathrm{km\,s^{-1}}$, quite different from the cluster systemic velocity. Though clearly not used to classify late B-type stars, we would assign a A0 III type to the star. HD 152437 is probably a foreground object. With $V = 9.145$ and $B - V = 0.15$, we obtained $m_V \approx 8.6$, indicating that the star is probably located at about 500 pc from the Sun.

5.8 HD 326320

HD 326320 is a suspected variable star located in the periphery of the cluster, at about 11′ N of HD 152248. PHC91 classified it as a variable B1 V member of NGC 6231 and reported $V = 9.91$. RCB97 also assigned it as a member of the cluster and quoted $V = 10.08$. More recently GM01 obtained one spectrum of this object. They measured $RV \sim +61\,\mathrm{km\,s^{-1}}$, assigned it a B1 V classification and mentioned that, if the star were a member of the cluster, it should be a binary.

In May 2004, we obtained two FEROS spectra of HD 326320 separated by about two hours. We clearly detected the signature of the two components on both of our spectra (Fig. 5.11). We measured RVs of about +120 and −280 for the primary and secondary lines respectively. We emphasize the rapidity of the variations between our two spectra, with $\Delta RV \sim 10\,\mathrm{km\,s^{-1}}$ for the primary and $\Delta RV \sim 20\,\mathrm{km\,s^{-1}}$ for the secondary components. The two components are clearly B-type stars. With the Si III λ4552 line slightly more intense than Si IV4088, but largely overwhelmed by He I λ4088, the primary is most probably a main sequence B0.5 star. No signature of Si IV λ4088 is found in the secondary spectrum, which indicates a spectral type B2 or later. No sign of the secondary Mg II λ4481 line is observed in the blue wing of the primary He I λ4471 line, which indicates that this line should be relatively faint in the secondary spectrum. This, in addition to the extremely faint Si III λ4552 line ($EW \sim 0.01$mÅ), yields a probable classification B2.5 V for the secondary.

5.9 HD 326329 ≡ CPD −41°7735

HD 326329 is located in the core of the cluster. With $V \sim 8.8$, it is relatively bright and has thus been observed for a long time. Derived spectral classifications oscillate between O9 and B0 and agree on the main sequence luminosity class. A relatively large scatter in the reported visual magnitudes led some authors to consider this object as variable. Focusing on CCD data published since the 1990's, we observed V in the range 8.71 (RCB97) – 8.81 (BL95). LM83 and PHYB90 respectively obtained 3 and 2 spectra of HD 326329 and found consistent values (respectively $\overline{RV} = -29$ and -33 km s^{-1}). GM01 obtained three additional spectra spread over 6 days. They derived RVs from −34 to −60 km s^{-1}, thus largely scattered and quite different from the cluster systemic velocity. They however did not comment on these facts.

We obtained two FEROS spectra in May 2000 and six additional spectra in May 2004. Within our data set, HD 326329 does not present any significant RV change. For example, we obtained $\overline{RV} = -20.3 \pm 1.5$ km s^{-1} for the He I λ4388 line, $\overline{RV} = -18.0 \pm 1.9$ km s^{-1} for the He I λ5876 line and $\overline{RV} = -16.5 \pm 2.2$ km s^{-1} for the He I λ7065 line. The HD 326329 spectrum displays the clear signature of an O-type star. We thus used Conti's and Mathys criteria to determine the spectral type and luminosity class. We obtained $\log W' = 0.49 \pm 0.04$, $\log W'' = 0.03 \pm 0.03$ and $\log W'''' = 5.43 \pm 0.02$ which correspond to an O9.5 V type, while the O9 type lies at 1-σ. Though no signature of a companion can be seen in the HD 326329 spectrum, we note the differences in the average RVs reported by different authors. This could suggest a long period modulation but only a long term monitoring of this object could bring an answer to this question. Finally, we checked the luminosity of the star. With $V = 8.756$ and $B - V = 0.165$, we obtained $M_V = -3.8$, which is slightly too faint for an O9.5 star at the cluster distance. Until proven otherwise, we consider HD 326329 as being single.

5.10 HD 326331 ≡ CPD −41°7744

With $V \sim 7.5$ (SBL98), HD 326331 is an O-type star located at 3′ East of the cluster center. Together with CPD −41°7744B ($V \sim 10$), it forms a visual pair separated by 7.3″. If physically related, their revolution period should be over 200 000 years (Mason et al. 1998). Quoted spectral types range from O7 III (Levato & Malaroda 1980; Levato & Morrell 1983) to O9 III (HCB74), but only give the composite classification. The system is reported as light variable by PHC91 and HCB74 mentioned an amplitude of 0.3 mag. If we except the value $V = 7.71$ from Feinstein & Ferrer (1968), all the published data since the 1960's indicate a maximum amplitude of 0.15, with an average value of 7.52 ± 0.08. RV measurements were obtained by Struve (1944), PHYB90, HCB74 and LM83. HCB74 data consisted of 13 spectra obtained over 7 consecutive nights. Based only on the O II λ4069 and Si IV λ4089 lines, they reported smooth velocity variations between +94 and −124 km s^{-1} and then up again. They thus suggested that the star is a binary with a period $P \gtrsim 7$ d. They however quoted that "the spectrum is very difficult to measure as the lines are weak". Finally, with an additional measurement obtained about 7 years later, LM83 published a first SB1 orbital solution with $P = 6.24208 \pm 0.00015$, $e = 0.12 \pm 0.09$ and $K_1 = 75 \pm 8$ km s^{-1}. The obtained residuals (∼17 km s^{-1}) are however very large compared to other orbital solutions published in the same paper.

We have sparsely observed HD 326331 since 1998. We obtained 4 spectra of the He I λ4471 region with the CES in May 1998, which revealed very broad lines (> 10Å) that were indeed difficult to normalize because of the narrowness of the wavelength domain (∼ 20Å) of the VLC camera. We then successively acquired FEROS spectra in May 1999 (5), in April 2002 (2) and in May 2004 (6). These were usually separated by one night to map the proposed 6.4-day orbital period. The HD 3262331 spectrum presents the clear signature of the usual Balmer, He I and He II lines. Both He II λ4686 and H α profiles show mixed absorption and emission. A slight emission component could also be present in the red wing of He I λ5876. The lines present a flat bottom and their profiles are therefore clearly not Gaussian (Fig. 5.12). As a first attempt, we adjusted a single Gaussian to the last third of the line to estimate the position of the profile centroid. Though we observed a dispersion of about 30 km s^{-1} in our measurements, we never obtained such highly positive RVs as the ones reported by HCB74. There are obvious profile changes as illustrated by Fig. 5.12. We tried to adjust two Gaussians in the observed profiles but we obtained mitigated results and an important spread in the measured RVs. The line profile variability seen in Fig. 5.12 most probably reflects intrinsic variability of a single star, either due to non radial pulsations or a variable wind emission component blended with the absorption line.

To estimate the spectral type, we measured the EWs of the usual classification lines. For this peculiar object, we integrated the different line profiles rather than adopting the EWs of the fitted Gaussians. We obtained $\log W' = 0.14 \pm 0.03$ and $\log W'' = 0.53 \pm 0.10$ which clearly points towards an O8 I star. However, with the He II λ4686 and H α lines showing mixed absorption and emission, with N III λλ4634-41 weakly in emission and with the clearly marked He I λ4388, the observed spectrum is not that of a supergiant. Furthermore, the broad absorption lines suggest a rather rapid rotation, which is not likely for a supergiant. We thus prefer the III((f)) classification. With $V = 7.497$ and $B - V = 0.181$, the visual magnitude of the object is about $M_V = -5.2$, which clearly rules out a supergiant classification. According to Howarth & Prinja (1989) and (Humphreys & McElroy

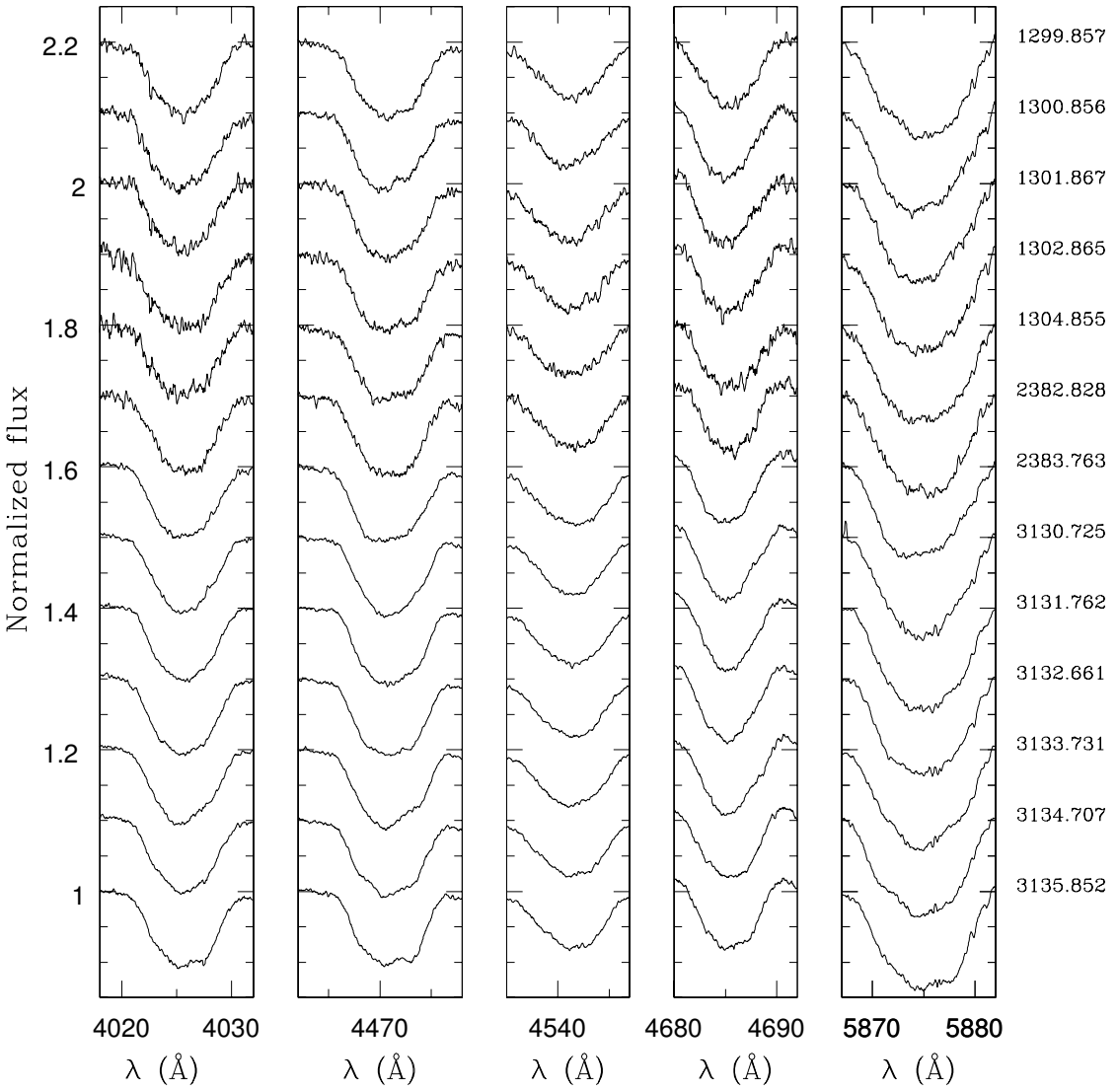

Figure 5.12: **HD 326331:** He I $\lambda\lambda$4026, 4471, He II $\lambda\lambda$4542, 4686 and He I λ5876 lines obtained on six consecutive nights. The spectra are ordered chronologically from top to bottom. HJD at mid-exposures are quoted at righthand in format HJD−2 450 000.

1984), this value is typical for giant stars. Clearly we need more follow up observations of this strange object. We can however rule out the 6 or 7 day period previously obtained by LM83 and, until proven to be otherwise, we consider the star as single, though displaying clear profile variations.

5.11 HD 326343

HD 326343 is a $V \sim 10.6$ (SSB05) star located about 10.′7 S-W of HD 152248. It has been classified as B3 in the HDE catalogue and B1V by PHC91. These authors also reported $RV = -33$ km s^{-1}, close to the average cluster velocity. PHC91 classified the object as a cluster member while RCB97 indicate a probable membership, but added an uncertainty

flag.

We obtained one snapshot spectrum displaying a strong set of metallic lines but no He II signature. The average RV is around -15 km s^{-1}. We assigned a B3 III classification. With $V = 10.598$ and $B - V = 0.416$, we obtained $M_V = -2.6$, too faint for the adopted classification. HD 326343 is however definitely brighter than a B3 V star and a better agreement can be obtained adopting a subgiant class.

5.12 CPD $-41°7706$

CPD $-41°7706$ is located near HD 152219, at about $4'$ S-W from HD 152248. Reported as a B1 V + B1 V binary by Levato & Malaroda (1980), these authors mentioned that "all lines are very wide and $\lambda\lambda$4471, 4387 and 4026 are double. The core of H γ is also double." LM83 confirmed the binary status and reported primary RVs changing from -35 to $+73$ km s^{-1} on two consecutive nights. PHYB90 reported three measurements spread over three months, with primary RVs down to -65 km s^{-1}. Finally GM01 measured the primary and secondary RVs on their sole CPD $-41°7706$ spectrum. They obtained -109 and $+165$ km s^{-1} respectively. They presented a figure of the He I $\lambda\lambda$4009-4026 lines with a low S/N ratio and an approximative normalisation to illustrate the secondary spectral signature. CPD $-41°7706$ is also a known β Cep variable (Balona 1983; Balona & Shobbrook 1983). This was recently confirmed by Arentoft et al. (2001) who measured three frequencies in the light curve but stated that the latter "do not describe the light curves completely".

We obtained one FEROS snapshot spectrum in May 2004. The blue part of the spectrum shows the usual Balmer and He I lines. These are apparently single and indicate RVs close to the systemic velocity of the cluster. Our observation thus probably corresponds to a phase where the two binary components are blended. We observed no sign of He II lines. Together with the weakness of Si IV λ4089, this indicates a spectral type B1 or later. On the other hand, the presence of the C III-O II complex near λ4070 and λ4650 favors types earlier than B2. The line ratios He I λ4144–He I λ4121, Si III λ4553–He I λ4144 as well as the low intensity of the O II spectrum clearly indicate a main sequence luminosity class. We thus classify the composite spectrum of CPD $-41°7706$ as B1 V, in agreement with the first indications of Levato & Malaroda (1980). Looking further to the red, the H α and all the He I lines from λ4920 to λ7100 display mixed absorption plus emission. All these lines have the same profile with a narrow absorption superimposed on a broader emission which results in line profiles reminiscent of the Be spectral signature. Because the component signatures are blended, it is not possible to decide whether both components or just one of them is actually a B1 Ve star.

5.13 CPD $-41°7712$

CPD $-41°7712$ is a 9th mag member of NGC 6231 (Perry et al. 1991; Raboud et al. 1997; Baume et al. 1999) located near HD 152219, at about $3\farcm7$ S-W of HD 152248. First reported as a B0 IV by Schild et al. (1969), Levato & Malaroda (1980) assigned to it a B1 V type. Balona (1983) found it to be constant in the V band for 7 consecutive hours. Recent CCD photometric studies reported V in the range 9.08-9.19. A few RV measurements have been published by PHYB90 and GM01 but indicated no significant variations.

We obtained one snapshot spectrum in May 2004. The average velocity is $-26.0\,\mathrm{km\,s^{-1}}$. No He II λ4542 is present but we detect He II λ4686, thus indicating an early B-type star. We assigned a spectral type B0.5 V in agreement with previous determinations. With $V = 9.146$ and $B - V = 0.183$, we obtained $M_V = -3.4$, thus in fair agreement with the adopted classification.

5.14 CPD −41°7721

CPD −41°7721 is a visual double star with components, labelled p and s respectively, separated by ∼5.″8 and corresponding to SBL 350 and 351 or BVF 12 and 27. These authors reported similar visual magnitudes $V = 8.72 + 9.90$. Two spectra were obtained by PHYB90 indicating $RV = -23$ and $-28\,\mathrm{km\,s^{-1}}$. These were probably composite spectra of the 2 components. GM01 also acquired two spectra of the p component and quoted $RV = -26.8$ and $-33.0\ \mathrm{km\,s^{-1}}$. They assigned it a spectral type O9.5 V.

We obtained one FEROS snapshot spectrum of each of the CPD −41°7721 components in May 2004; the stars are apparently single. For the bright (p) component, we measured $\log W' = 0.43$, corresponding to an O9 type. Both luminosity criteria W'' and W''' point to a main sequence object. The measured RV is, on average, $-25.5\ \mathrm{km\,s^{-1}}$, but we observed a large scatter (from −36 to $-13\ \mathrm{km\,s^{-1}}$ according to the various lines measured). With no He II λ4542 line and a faint He II λ4686 line, the s component of CPD −41°7721 is clearly an early B-type star. The strengths of the Si III λ4552 and Si IV λ4089 lines are very similar. Comparing with the spectral atlas of Walborn & Fitzpatrick (1990), we finally adopt a B1 V class. The X-ray source X#251 is clearly associated with the O-type component. A larger residual is seen at the position of SBL 358 ($V = 15.89$), but there seems to be no detected X-ray emission associated with CPD −41°7721s. With $V_\mathrm{p} = 8.709$ (resp. $V_\mathrm{s} = 9.892$) and $(B - V)_\mathrm{p} = 0.168$ (resp. $(B - V)_\mathrm{s} = 0.178$), the visual magnitude of the object is about $M_{V,\mathrm{p}} = -5.2$ (resp. $M_{V,\mathrm{p}} = -2.6$). Both stars are a few tenths of mag too faint if located in the cluster core. Alternatively, slightly later spectral types would yield a much better agreement.

5.15 CPD −41°7737

CPD −41°7737 is a B-type star in the cluster core. Garrison & Schild (1979) assigned it a B1.5 V spectral type and PHYB90, B1 V. The latter authors also obtained two RV measurements separated by ∼6 days. Once the RVs are corrected for the Ca-K velocity, no variation is found. More recently, Arentoft et al. (2001) reported CPD −41°7737 as a possible slowly pulsating B-star. They indeed observed variations of 0.015-0.020 mag in the *b* band on a time scale of a couple of days. Previous CCD photometry (Balona & Laney 1995; Sung et al. 1998; Baume et al. 1999) are all in the range $V = 10.74 - 10.76$, with the notable exception of RCB97 who quoted $V = 10.38$.

We have obtained 2 FEROS spectra separated by one night in May 2004 which show no RV difference. The average RV, as measured on He I lines is $-29.1\ \mathrm{km\,s^{-1}}$, is in agreement with the cluster systemic velocity. No trace of He II $\lambda\lambda$4542-4686 is found in CPD −41°7737. Comparing the line EWs with typical values from Didelon (1982), we adopt a spectral classification of B2 V which corresponds to the maximum He I line strength. Finally, we mention that CPD −41°7737 has a close visual companion (SBL 459 – V=11.84 – or BVF 73 – V=11.82) separated by about 4″ and situated to the N-W. The

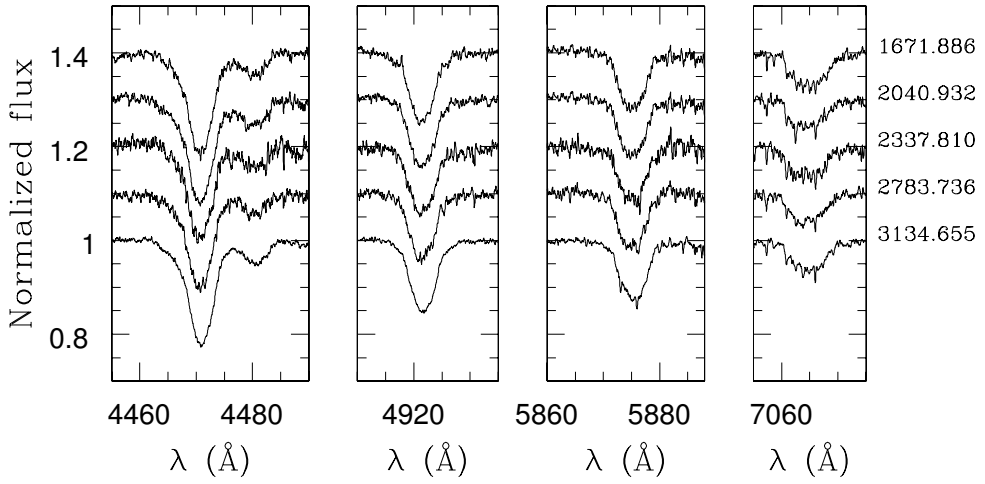

Figure 5.13: **CPD −41°7744B:** He I λ4471, 4921, 5876 and 7065 lines. The figure presents our five FEROS spectra chronologically sorted from top to bottom. The first four spectra were obtained in May 1999 while the last spectrum was acquired in May 2005.

X-ray emission is perfectly centered on CPD −41°7737.

5.16 CPD −41°7744B

Distant by about 7″, CPD −41°7744B is the visual companion of the O-type star HD 326331. These two objects were first resolved by Shapley & Sawyer (1927) but have been forgotten for a long time. We obtained four FEROS spectra in May 1999 and one additional spectrum in May 2004 (Fig. 5.13). We observed no night-to-night RV variability in the 1999 run but the 2004 spectrum is clearly shifted by about 15 km s^{-1}. For example we obtained $\overline{RV}^{1999}_{\lambda 5876} = -25.6 \pm 1.8$ while $RV^{2004}_{\lambda 5876} = -15.0$ km s^{-1}. No signature of a companion is found. Our snapshot data suggest the possibility of a low level line profile variability which could reflect the effect of non-radial pulsations. Clearly, we need to monitor this system for further information. No He II signature is seen while Si IV λ4088 is slightly fainter than Si III λ4552. We thus adopt a B1 V type for the possibly composite spectrum. At our detection level, no X-ray emission seems to be associated with CPD −41°7744B. We obtained $M_V = -2.7$, thus in a better agreement with a spectral type B1.5V.

5.17 CPD −41°7753

At 6′.4 S-W of HD 152248, CPD −41°7753 is a known β Cep star (Balona 1983; Arentoft et al. 2001) in NGC 6231. Schild et al. (1971) assigned it a B1 V type. PHYB90 obtained 3 RV measurements that, once corrected for the Ca-K RV, do not show significant difference. More recently GM01 claimed to have detected the spectral signature of a companion on one of their two spectra separated by two days. They reported RVs of −26.1 and −170.1 km s^{-1}. They presented the two H β profiles but the reader can hardly see a difference. On another plot, they showed the same H β region with a different scale, to outline the presence of the companion. However, they do not show the second spectrum

for comparison. What is more puzzling is that, in their two plots, they quoted HJD = 50 595.694 for the spectrum on which they detected the companion signature. However none of the CPD −41°7753 observations corresponds to that period. According to their observation journal, another star, Se 28, was observed on HJD = 50595.694. Se 28 is a suspected binary for which they detected (at least they said so) a companion signature in the blue wing. If the companion signature can, even slightly, be seen in the H β profile, then the separation should be very clearly marked in any of the He I lines. It is thus further surprising that García & Mermilliod focused on H β though this is clearly not the most appropriate profile for the present purpose.

Although the star was not associated with an X-ray source, we decided to obtain a snapshot spectrum in May 2004. The object is obviously a B main sequence star. We probably detect the signature of a secondary companion in the blue wing of He I $\lambda\lambda$4388, 5876 and 7065. Adjusting two Gaussians, we obtained RVs of −47.4 and +148.8 km s^{-1}, thus a separation similar to the one obtained by GM01. The H β profile however remains almost perfectly symmetric. Clearly we need to monitor CPD −41°7753 to confirm its probable binary status. We adopted a B0.5 V classification for the (possibly composite) spectrum.

5.18 CPD −41°7755

CPD −41°7755 is a 10th mag member of NGC 6231 (Perry et al. 1991; Raboud et al. 1997; Baume et al. 1999), located at about 7′ S-E of the cluster core. Balona (1983) reported it to be constant in the V band during 7 consecutive hours. PHYB90 obtained three RV measurements which, once corrected for the Ca-K RV, have a range of 22 km s^{-1} over three days. Such a dispersion is however not much larger than the typical dispersion of the PHYB90 data. The only spectral type reported in the literature is B1 V (Schild et al. 1971).

In May 2004, we obtained a single FEROS spectrum. The average RV is −23.0 km s^{-1}. No He II λ4542 is seen while He II λ4686 is faintly detected. Si IV λ4088 is also clearly present. We thus confirm the B1 V class of CPD −41°7755 and consider the star as most probably single.

5.19 CPD −41°7760

CPD −41°7760 was reported by Laval (1972) to be a B0 III star. With V = 9.51 (Perry et al. 1991; Raboud et al. 1997), these authors respectively found it to be a probable member, and a member of the cluster. The latter authors assigned it a B1-2 III class. GM01 reported two RV measurements obtained on two consecutive nights that yielded $RV \sim -31$ km s^{-1} and preferred a main sequence B2 classification. In May 2004, we pointed the ESO 2.2m telescope towards CPD −41°7760. We clearly resolved two components on the guiding camera. We obtained intermediate S/N spectra of both components and we adopted spectral classifications B0.5 III and B1 V for these two objects. The RVs of the giant and main sequence components of the pair are −23.5 and −36.0 km s^{-1} respectively.

5.20 Se 209 ≡ SBL 394

Member of NGC 6231 (Perry et al. 1991; Raboud et al. 1997; Baume et al. 1999), Se 209 lies in the cluster core, at 1.′7 North of HD 152248. Garrison & Schild (1979) classified it as B2 V-IV while RCB97 quoted B2-3 V-III. On the basis of two independent measurements, Raboud (1996) detected significant RV variations (from -38.2 to -23.1 km s^{-1}) and suggested that it could be a binary system. More recently, Arentoft et al. (2001) observed slow modulations of a peak-to-peak amplitude about 0.020 mag in the b band and suggested it could be a slowly pulsating B-star.

We obtained a snapshot FEROS spectrum of the object in May 2004. We measured RVs close to -30 km s^{-1}, in agreement with previous measurements. No trace of He II is observed in this spectrum and we adopted a spectral type B2 V. From our data, this star is apparently single. We would thus rather support the Arentoft et al. (2001) hypothesis of a slowly pulsating B-star rather than a possible binary.

5.21 Se 259 ≡ SBL 317

At 2.′6 S-SW of HD 152248, Se 259 is an 11th mag star near the cluster core. All the published values for V are in the range 10.91-10.93 except a value $V = 10.79$ obtained by Baume et al. (1999). On the basis of this difference, the latter authors suggested that the star could be variable. Using a cross-correlation technique with synthetic spectra, Raboud (1996) found the star to be most probably single. PHC91, RCB97 and Raboud (1996) retained it as a cluster member while, again, Baume et al. (1999) rejected it. The only quoted spectral type in the literature is from Garrison & Schild (1979). These authors adopted a B3 type but cautioned that their determination was very uncertain.

We obtained an intermediate S/N single snapshot spectrum in May 2004. Usual Balmer and He I lines are clearly identified and are quite broad compared to other B-stars of the cluster. Adjusting single Gaussians in a set of bright lines, we obtained a large range of RVs which we first assigned to the broadness of the lines that renders accurate measurements difficult. However at a second glance, a few line profiles (e.g. He I $\lambda\lambda$4120-5016) seem to indicate the presence of two stars. We tried to adjust two Gaussians and, though the S/N is clearly a limitation that prevents a firm conclusion, these nicely reproduced the observed profiles. The obtained RVs are about -90 (primary?) and $+130$ km s^{-1} (secondary?). We assigned a B2-2.5 V type to the composite spectrum. Clearly, more numerous and higher S/N spectra are required to clarify the nature of Se 259.

5.22 An optical spectral atlas

As mentioned in the introduction, we present here the optical spectral atlas of the early-type stars observed during our spectroscopic campaigns. The atlas is included at the end of this dissertation, in Appendix A. Both the early-type binaries discussed in the previous chapters and the objects presented in this chapter have been included. Most of the displayed spectra thus belong to optical counterparts of X-ray sources detected in the XMM-*Newton* FOV.

In the atlas, the objects are ordered following their luminosity class and spectral type. Their name and spectral classification are clearly mentioned in the different panels. Because of the large wavelength domain observed with the FEROS spectrograph ($\lambda\lambda$3950-

7150), the spectral range has been divided into four contiguous sub-domains ($\lambda\lambda$3950-4750, $\lambda\lambda$4750-5550, $\lambda\lambda$5550-6350 and $\lambda\lambda$6350-7150), each of which being 800 Å wide. Except for the HD 152248 and CPD $-41°7742$ binaries, the displayed spectra were all acquired in May 2004 at the ESO 2.2m telescope.

Chapter 6

The O-type star population in NGC 6231: observational constraints

What is learned without effort is worthless and will not remain.
René Barjavel

In the previous three chapters, we have separately investigated the characteristics of the individual O-type objects in NGC 6231. On the basis of the derived constraints, the present chapter will now probe the properties of the NGC 6231 O-type star population as a whole. The O-type star X-ray emission has already been studied at length in Chap. 2 and will not be investigated further. The present chapter will rather focus on the spatial distribution (Sect. 6.1), on the binary fraction (Sect. 6.2), on the distribution of the orbital parameters (Sect. 6.3) and on the location, in the H-R diagram (Sect. 6.4), of the O-type stars in the cluster .

6.1 Spatial distribution

In Chap. 2.1, we studied the spatial distribution of the X-ray sources in the XMM-*Newton* FOV and we concluded that most of the detected sources are probably physically linked to the NGC 6231 cluster or to the wider Sco OB 1 association. Probing the source density profile by means of King profile fittings, we found a probable cluster core radius $d_c = 3\farcm1$. This value compares very well with the value of $2\farcm7$ obtained from the reasonably bright ($V < 17$) stars of the SSB05 catalogue (Sung et al. 2005, in preparation).

As illustrated by Fig. 6.1, ten out of the 16 O-type stars of the present sample are located within the cluster core radius of $3\farcm1$, and 13 of them within $1.5 \times d_c$. The binaries HD 152218 and HD 152247 are to be found at respectively more than $2 \times d_c$ and $3 \times d_c$ while the single star HD 152076 lies even further away from the cluster core. These last three objects may in fact belong to the Sco OB 1 association. However, as NGC 6231 is embedded in the Sco OB 1 association, the exact limit between the two aggregates is rather an abstract notion.

In Chap. 2.1, we also showed that the distribution of the X-ray sources was displaying a slight N-S elongation. Fig. 6.1 reveals a quite different pattern for O-type stars. Their distribution rather seems to be oriented almost perpendicularly to the one of the PMS X-ray emitters, with an obvious lack of O-type stars in the S-E part of the field. It is however difficult to draw any general conclusion. Indeed, on one hand we are dealing here

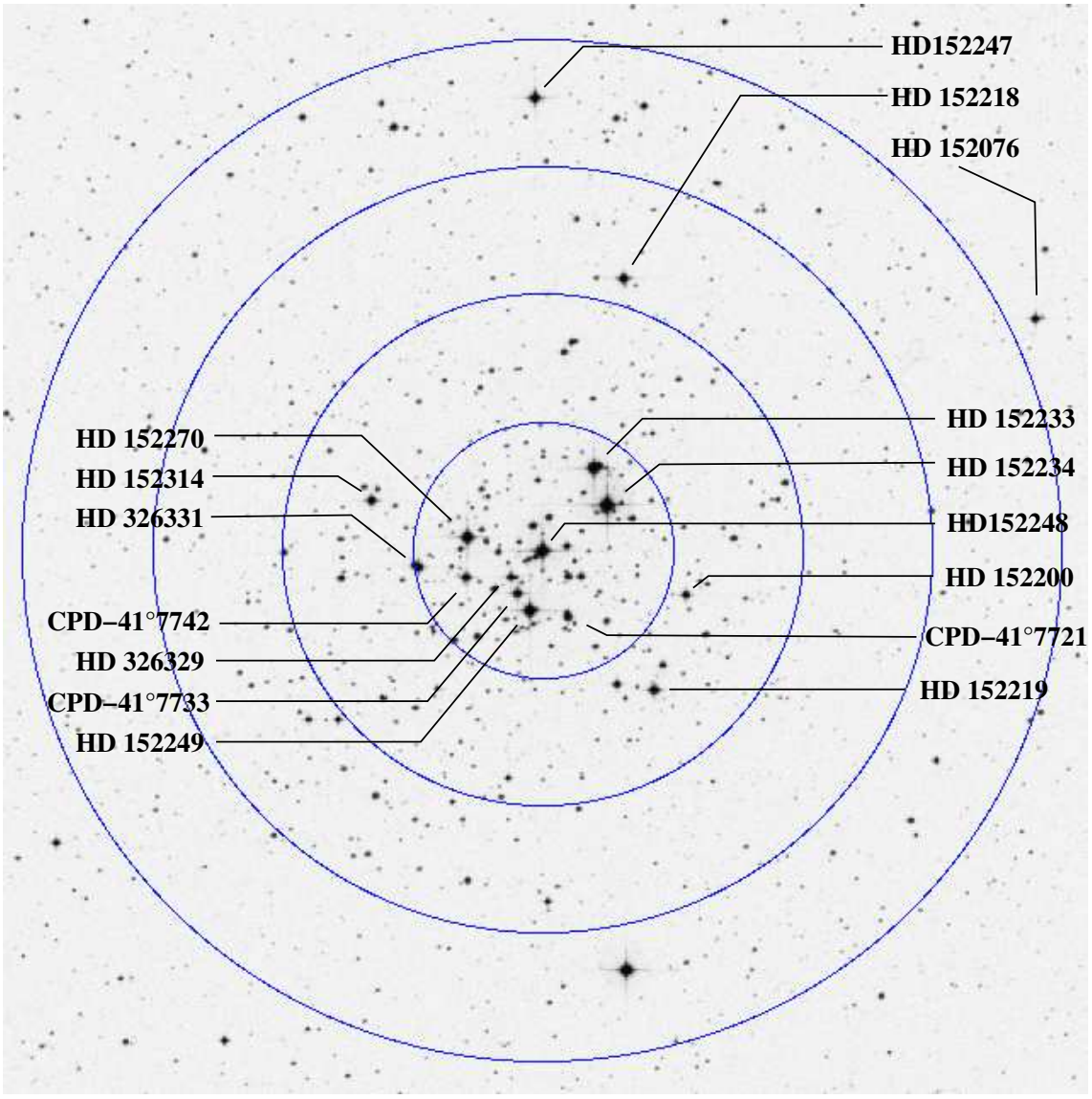

Figure 6.1: O-type objects in the XMM-*Newton* FOV. The large circles are centered on the location of HD 152248 and have a respective radius of 1×, 2×, 3× and 4× the cluster core radius $d_c = 3.1'$. North is up, East to the left.

with a small number of objects and a better statistics is probably required to provide firm constraints. On the other hand, even a slight proper motion could have significantly altered the position of the stars since their birth. For example, over a 3 Myr time-span, a proper motion as low as 1 $\mathrm{km\,s^{-1}}$ in a direction perpendicular to the line of sight would, at the distance of NGC 6231, correspond to an angular motion of about 6 $'$, thus twice larger than the estimated cluster core radius.

6.2 The binary fraction

For a given population of stars, the binary fraction is *a priori* one of the easiest properties to probe, and probably requires less observations than to investigate the distribution of other orbital parameters. However, accurately constraining the binary fraction is far from being a trivial task. It mainly relies on a diagnostic of the multiplicity of the studied objects. Those for which no evidence of multiplicity is found are then considered as presumably single. Indeed it is particularly difficult to prove that a star is definitively single. Even if no RV shift is observed, it could still turn out to be a binary system seen under a very low inclination. It could also be a particularly long period binary, perhaps with a large eccentricity, in which case an object can present no significant RV change over a long period of time. As a consequence, the derived binary fraction should often be considered as a lower limit on the actual value.

It is important to keep in mind the possible observational biases induced by the sampling, either due to its uneven nature or, more fundamentally, resulting from its finite time-base. As most of those working in this field of research probably experienced, it is particularly difficult to have access to a sufficient amount of telescope/satellite time in order to probe the different variability scales and an in-depth review of the literature can, in this regard, reveal precious information on much longer time bases. However, the homogeneity of the set is then difficult to preserve.

6.2.1 An overview of the techniques

Several different methods have been and are still used to probe the binarity of selected samples of stars. These methods are complementary and allow to investigate different regions of the parameter space. We provide here a brief overview of the most frequent methods, emphasizing on their respective limitations.

From the position of the stars in the **colour-magnitude diagram**, one can detect abnormally bright stars for their spectral types. This however requires a relatively good knowledge of the distance to the studied object. For O-type stars, this is thus mostly applied in clusters or associations for which the distance can be estimated from different tools, such as the study of the less massive stellar population or of eclipsing binaries belonging to the same aggregate. This method remains however relatively crude and should only be considered as a possible indicator. It is further biased towards systems with components of similar magnitude, as faint companions give a modest extra luminosity and are thus hardly seen.

From the **photometric monitoring**, binarity can be unveiled by the transit of one component in front of the other in an eclipsing binary system. This method is of course limited to the detection of systems with relatively large orbital inclinations, a condition which becomes tighter when the period (thus the separation) of the system increases. In addition,

the eclipse duration is relatively limited in phase and the chance to identify eclipses thanks to snapshot surveys (as those dedicated to investigate the stellar population of a field) are quite limited. The chance to detect long period systems clearly decreases with increasing period values, both because of the longer observational time base required, of the more strict constraints on the orbital inclination for eclipses to occur, and of the comparatively narrower eclipses (thus the comparatively shorter time at which the binarity signature is seen). Though few in number, these eclipsing binary systems are particularly important because the combined analysis of their light- and RV-curves allows a direct measurement of the masses and sizes of the binary components. A reasonably accurate distance might further be obtained, so that these systems might also provide distance yardsticks for clusters or associations.

Another proven method for binary detection is the search for **Doppler shifts** in spectroscopic time-series. The amplitude of the shifts will however decrease with the orbital inclination and, though the constraints are much looser than for eclipsing binaries, it remains one of the major limitations of the method. This limitation is of course coupled with the usual sampling limitation, especially for long period, eccentric binaries.

In addition, not all the observed RV shifts reflect the signature of an orbital motion. In particular, line profile deformations might mimic orbital shifts and, especially in lower-resolution spectra, are hardly identified as such. These line profile variations can originate from a variety of phenomena. They might be related to non-radial pulsations, co-rotating and/or magnetically confined structures as well as partial and possibly variable emission filling-in of some absorption lines. If a velocity stratification is present between the different line forming regions, one may further artificially induce a bias by including or comparing RV values (or RV mean values) obtained from different lines, resulting in an apparent shift that does not reflect any Keplerian motion. All these effects might thus lead to overestimate the binary fraction, by selecting RV-variable objects whose variations are in fact not induced by an orbital motion.

Finally, binary detection based on Doppler shift monitoring clearly favours the detection of systems with similar components. This method thus presents clear observational biases in terms of mass, luminosity ratio, orbital period and inclination.

Long period systems may actually display a separation large enough for the different components of the system to be resolved. The projection of the true positions of the objects on the sky plane can then be followed **astrometrically** and an orbit can be inferred. Biases in terms of period (for the motion to be detectable) and of distance of the object from the observer are obvious. Indeed if the revolution of the objects around their mass centre cannot be followed during a reasonable fraction of the period, one cannot exclude the possibility of non physically related visual pairs.

Adaptive optics, speckle interferometry or longer base-line interferometry are alternative methods allowing to increase the resolution with which one can probe the surroundings of a star. Unfortunately these methods are subject to similar limitations as the old-fashioned astrometric detection. Indeed massive stars are often found in distant clusters. As an example, at the distance of NGC 6231, $1''$ of separation between two components corresponds to a projected distance of about 1600 AU (corresponding thus to 3.5×10^5 $R_\odot$ or 2.4×10^{16} cm). Although the interferometry is particularly dedicated for longer period systems, it is to be hoped that, in a near future, it will allow to fill the observed gap between the detection of short period (SB or EB systems) and long period (astrometric systems) binaries (see e.g. Mason et al. 1998). At their best, these methods

offer an alternate option to probe systems which are possibly seen under a low inclination (thus presenting only limited RV shifts, if any). Only the combination of these different methods used on the different variability time-scales expected for binaries could thus allow to cover the range of parameter space where binary detection is awaited.

Beyond these 'classical methods', evidence for binarity of an early-type star can also be unveiled from other wavelength domains. An indirect diagnostic may, for example, rely on the detection of the characteristic signature of a wind-wind collision occurring between the stellar winds of the two components. In particular, such a collision should generate an extra amount of X-ray emission that could be modulated according to the system geometry. From Chap. 2, we know that the intrinsic variation of the X-ray emission from a single star is very limited. The sole mechanism that is expected to produce a significant amount of variation comes from a wind-interaction. In wider pairs (> 100 $R_\star$), non-thermal radio emission produced in the wind interaction can also be observed (Dougherty et al. 2003). Though some of these points can still be considered as controversial and not fully established, we just outline here that the detection of these probable wind-wind collision signatures is a good indication of a star being multiple.

Accurate measurements of the binary fraction in a selected star sample is thus not as trivial as one could have first thought. Particularly, campaigns relying only on snapshot RV-measurements can be ambiguous. First, they might not provide a sufficient sampling of the different orbital period ranges, though the bias can be more or less inferred through statistic and probabilistic considerations, assuming an underlying distribution of the periods. In addition, the observed RV differences might not be related to an orbital motion. It is however very difficult on the basis of a few, sparsely acquired observations, to provide a reliable diagnostic. Though it can be considered as a too conservative approach, we think that a firmly established binary nature should, beyond the detection of RV or photometric variability, or of a visual companion, provide a follow-up of the object to probe its period and its orbital motion. Only when the latter are reasonably constrained can we assert that a system is *definitely* multiple.

6.2.2 Binarity in NGC 6231

As mentioned earlier in this work, we observed 16 stars or multiple systems containing at least one O-type star (including WR 79). As shown in Figs. 6.1 and 6.2, these stars are unevenly spread across the field of view. Most of the objects are located in the vicinity of HD 152248. Indeed ten of them lie within $3'$ of HD 152248, while 13 of them are to be found within $4\farcm5$. Among these 16 objects, five are close SB2 binaries with periods of less than 6 days and the WR+O system has a period of 8.9 days. The orbital properties of these six systems are tightly constrained and no doubt remains about their multiple nature. In addition, we presented in Sect. 4.2 strong evidence than HD 152233 and HD 152234 are SB2 binaries with orbital periods of a few months and a preliminary orbital period for HD 152234 has been proposed. In Chap. 5, we also reported our suspicion about HD 152247 (Sect. 5.4) and HD 152314 (Sect. 5.6) being multiple O-type systems too. Again in Chap. 5, we note that HD 152200 (Sect. 5.2), HD 152249 (Sect. 5.5) and HD 326331 (Sect. 5.10) were all displaying clear line-profile variations. HD 326331 and HD 152200 were previously reported as SB systems. From our work however, these conclusions could not be firmly established and we could not assign the observed RV-variations to an orbital motion. We rather suggested non-radial pulsations or wind-structures as more

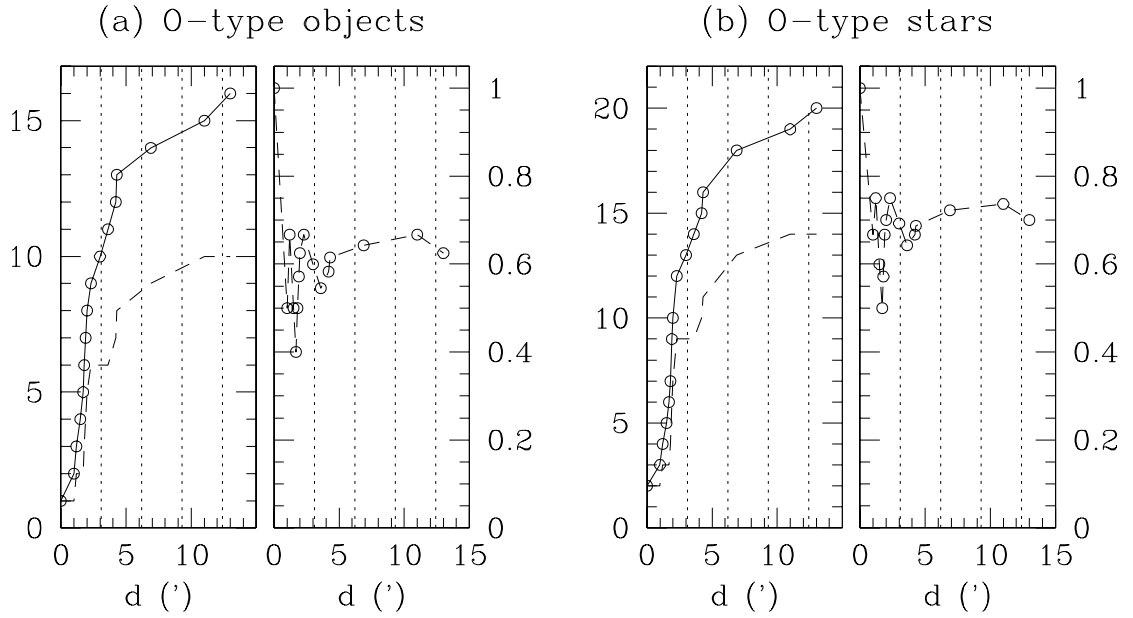

Figure 6.2: **(a) O-type objects:** *(Left panel)* Cumulative distribution of the number (N) of O-type objects (plain lines) and O-type binaries (dashed line) as a function of the distance d from HD 152248. *(Right panel)* Evolution of the binary fraction in a circle with a radius equal to the distance d from HD 152248. **(b) O-type stars:** *idem* considering the individual O-type stars, be them single or bound in a binary system.

probable explanations. The remaining three stars, HD 152076 (Sect. 5.1), HD 326329 (Sect. 5.9) and CPD −41°7721p (Sect. 5.14) do not present any indication of binarity and are thus considered as single stars.

The speckle interferometric campaign of Mason et al. (1998) included the brightest objects ($V < 8$) of the cluster. Their results indicate that HD 152233, HD 152234 and HD 152248, in addition of being SB2 systems, have several visual companions. These authors estimated minimal periods of 190 000, 4900 and 150 yr for the putative revolution of the closest visual companion for the three systems. They also reported visual companions for HD 152270 and for HD 326331, separated by 4.″3 and 7.″3 respectively, and corresponding to periods larger than 60 000 and 200 000 yr. Finally, Mason et al. stated that HD 152249 could have a binary companion at a separation of 0.″06, but asked for confirmation. If verified, this would correspond to a period of the order of 150 yr too. Other stars of our sample (HD 152218, HD 152219, HD 152247, CPD −41°7733 and HD 152314) were also observed but no companion was found. HD 152076, HD 152200, HD 326329, CPD −41°7721 and CPD −41°7742 were not included in the Mason et al. (1998) study.

Beside the speckle interferometric campaign of Mason et al. (1998), direct imaging (e.g. Sung et al. 1998, 2005, in preparation), one can further note that CPD −41°7721s is located at 5.″8 from CPD −41°7721p which, if physically related, would yield a period of several ten thousand years at least. HD 326329 also has a visual companion at 7.″3; HD 152076 is not isolated by more than 8″ from two other stars. Only HD 152200 remains seemingly alone in a 20″ radius. So far, it is however almost impossible to state whether these visual pairs are physically linked or arise by coincidence in such a crowded FOV.

In brief, NGC 6231 displays six SB2 systems with periods shorter than 9 days, and two other SB2 systems with periods of several months. This yields a minimal binary fraction of 50%. Among the 8 clearly confirmed binaries, four can further belong to hierarchical systems with the wider pairs having periods from 100 yr to several 10^5 yr. Two other systems, HD 152247 and HD 152314, are further probable SBs with periods around a year, which yields a percentage of 62.5%. The six remaining objects should be considered more cautiously. From speckle interferometry and other observations, five of the six remaining objects have a visual companion separated by less than $10''$. If physically related, these systems would have periods ranging from a few hundred yr to several 10^5 yr. However, because of the long periods of time considered, there is no clue so far of the possible existence of a physical link between these objects.

In conclusion, among O-type objects and accounting for systems with a period shorter than a human life time, 10 out of the 16 objects are binaries. This gives a binary frequency of 0.63. From our data set and over the considered time-scale, only HD 152314 is suspected to host more than two stars, but this requires confirmation. This would yield a fraction of triple systems of 0.06 but, indeed, it is based on small numbers.

Adopting a different point of view, one can count the O-type stellar components, be them single or bound in a multiple system. 20 O-type stars are found in the present FOV. From the above considerations, 14 of them belong to a binary/multiple system. As a consequence, 70% of the O-type stars in NGC 6231 are found in multiple systems. Finally, we have investigated the possibility of a variation of the binary fraction with the distance to the cluster centre. Our results are summarized by Fig. 6.2. Beyond the statistical fluctuations, we could not distinguish any trend in its radial distribution. The binary fraction of NGC 6231 clearly oscillates at values about 0.60.

6.3 Distribution of the orbital parameters

Table 6.1 summarizes the orbital parameters of the six O-type binaries investigated in Chaps. 3 and 4. The orbital solution of HD 152248 slightly differs from the one presented in Sana et al. (2001). The solution quoted in Table 6.1 was actually recomputed using the RV-curve fitting technique described in Sana et al. (2003), which allows a symmetric propagation of the errors on the primary and secondary components. This avoids the large differences observed in Sana et al. (2001) which, in such a symmetric system as HD 152248, was clearly an artefact of the method rather than reflecting any intrinsic difficulty to accurately measure the secondary RVs. Beyond these six systems quoted in Table 6.1, the orbital solution of the Wolf-Rayet system WR 79(≡HD 152270) was taken from Luehrs (1997). We emphasize that NGC 6231 naturally provides a binary sample which is homogeneous in terms of age, distance and metallicity.

Fig. 6.3 focuses on the interrelation between three fundamental parameters of a binary system: its period, its eccentricity and its mass ratio. In Fig. 6.3, we have considered the mass ratio (q) as being the ratio of the mass of the heaviest component over the mass of the lightest component (thus $q \geq 1$). All the studied binaries in NGC 6231 (see e.g. Table 6.1) have an eccentricity below 0.3, while five out of seven have $e < 0.15$. The present eccentricities are significantly reduced compared to the previous work of García & Mermilliod (2001). Reasons for these discrepancies have already been given at length in the previous chapters. We however outline the case of the very short period CPD $-41°7742$

Table 6.1: Orbital and physical parameters of the O+O and O+B binaries with computed orbits in NGC 6231. The usual notations have been used. For eccentric systems, T_0 is the time of periastron passage while, for the non-eccentric system CPD −41°7733, it is the time of conjunction, the primary being in front.

Object	CPD −41°7742	HD 152219	HD 152218	CPD −41°7733	HD 152248	HD 152234
Spectral Type	O9V+B1.5V	O9.5III+B1-2III/V	O9IV+O9.7V	O8.5V+B3	O7.5III(f)+O7III(f)	O9.7Ia+O8V
P (d)	2.44070	4.24032	5.60391	5.681504	5.816002	127.01
s_y/s_x	2.1	3.3	1.5	3.3	1.1	[1.5]
m_1/m_2	1.803 ± 0.015	2.530 ± 0.023	1.319 ± 0.014	2.640 ± 0.012	0.988 ± 0.011	[1.51 ± 0.27]
e	0.027 ± 0.006	0.082 ± 0.011	0.259 ± 0.006	n.	0.133 ± 0.005	0.201 ± 0.078
ω (°)	149 ± 10	153 ± 5	104.0 ± 1.6	n.	82.9 ± 3.3	301 ± 13
T_0 (HJD	2400.284	3200.165	3197.229	3199.635	2003.844	3079.193
−2 450 000)	± 0.067	± 0.090	± 0.025	± 0.003	± 0.057	± 4.787
K_1 (km s^{-1})	167.1 ± 0.9	110.7 ± 0.7	162.2 ± 1.2	93.7 ± 0.3	217.7 ± 1.5	62.6 ± 5.0
K_2 (km s^{-1})	301.3 ± 1.8	279.9 ± 1.7	213.9 ± 1.5	247.4 ± 0.9	214.2 ± 1.5	[94.5 ± 18.5]
γ_1 (km s^{-1})	−15.3 ± 0.5	−17.9± 0.6	−18.7 ± 0.6	−21.5 ± 0.2	−26.4 ± 0.9	−34.2 ± 2.5
γ_2 (km s^{-1})	−26.3 ± 0.7	−22.3± 1.3	−19.2 ± 0.7	−23.1 ± 0.2	−24.6 ± 0.9	[1.8 ± 24.7]
$a_1 \sin i$ ($R_\odot$)	8.05 ± 0.05	9.24 ± 0.06	17.34 ± 0.13	10.52 ± 0.06	24.67 ± 0.18	153.8 ± 12.6
$a_2 \sin i$ ($R_\odot$)	14.52 ± 0.09	23.36 ± 0.14	22.87 ± 0.17	27.76 ± 0.10	24.38 ± 0.17	[232.2 ± 45.6]
$m_1 \sin^3 i$ ($M_\odot$)	16.69 ± 0.25	18.56 ± 0.27	15.82 ± 0.26	16.94 ± 0.15	23.31 ± 0.35	[28.9 ± 13.4]
$m_2 \sin^3 i$ ($M_\odot$)	9.25 ± 0.12	7.34 ± 0.09	12.00 ± 0.19	6.42 ± 0.05	23.58 ± 0.35	[19.1 ± 6.2]
r.m.s. (km s^{-1})	4.8	4.0	6.1	1.9	8.0	9.4

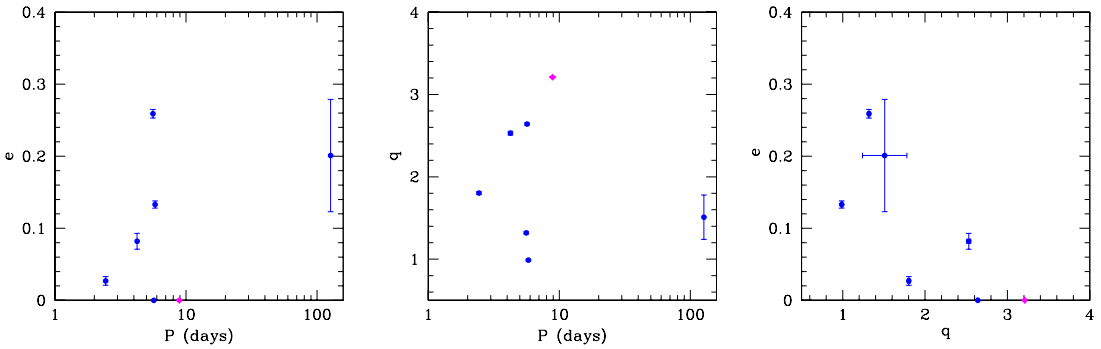

Figure 6.3: Distribution of various orbital and physical parameters (period, eccentricity, mass ratio) of the O-type binaries in NGC 6231. The diamond indicates the WR system HD 152270.

system which now displays an eccentricity of 0.027 ± 0.006 compared to the previously established value of 0.205 ± 0.053. This new value is in better agreement with the fact that short period systems tend to circularise their orbit faster than longer period systems.

Plotting the mass ratio versus the period, no obvious pattern seems to emerge. On can however note that the maximum mass ratio in our sample is below 3. This could reflect the difficulty to detect the spectral signature of a faint, low mass component in a combined spectrum. It is generally admitted that the luminosity of a high-mass star scales with its mass as $L \sim M^{2.5}$ (e.g. Figueiredo et al. 1991). A mass ratio about 2.5–3 roughly corresponds to a limiting brightness ratio about 10–15 (assuming that both stars have the same luminosity class). Indeed as illustrated by the analysis of HD 152219 ($q = 2.53 \pm 0.02$) and CPD $-41°7733$ ($q = 2.64 \pm 0.01$), the secondary spectral signature is very faint in these two systems.

Finally, we have plotted the eccentricity versus mass-ratio. While there are only 7 points in this diagram, it suggests that only systems with similar components display a large eccentricity. As our sample of binaries is mostly uniform in term of age, this suggests that circularisation processes tend to be more efficient in systems displaying a larger mass ratio, thus that tidal dissipation may be more efficient in such a configuration.

6.4 Early-type stars in the H-R diagram

Using the constraints derived throughout this work, we have plotted the location of the O-type stars in the Hertzsprung-Russell diagram (see Fig. 6.4). For binaries, we used the luminosity ratios derived by the previous analyses (see Chaps. 3 and 4) to estimate the luminosities of the individual components. HD 152314 is not plotted in the diagram because of its relatively uncertain nature (Sect. 5.6). Similarly the Wolf-Rayet system was not accounted for neither. As in Chap. 2, the V-band magnitudes were taken from the catalogue of SSB05 (Sung et al. 2005, in preparation). The reddening was estimated by comparing the $B - V$ index from the latter catalogue with intrinsic colours quoted by Schmidt-Kaler (1982) and adopting $R = 3.3$ (Sung et al. 1998). The cluster distance was assumed to correspond to $DM = 11.07 \pm 04$. The temperature and bolometric correction scales were taken from Schmidt-Kaler (1982). In Fig. 6.4, the quoted error-bars on the

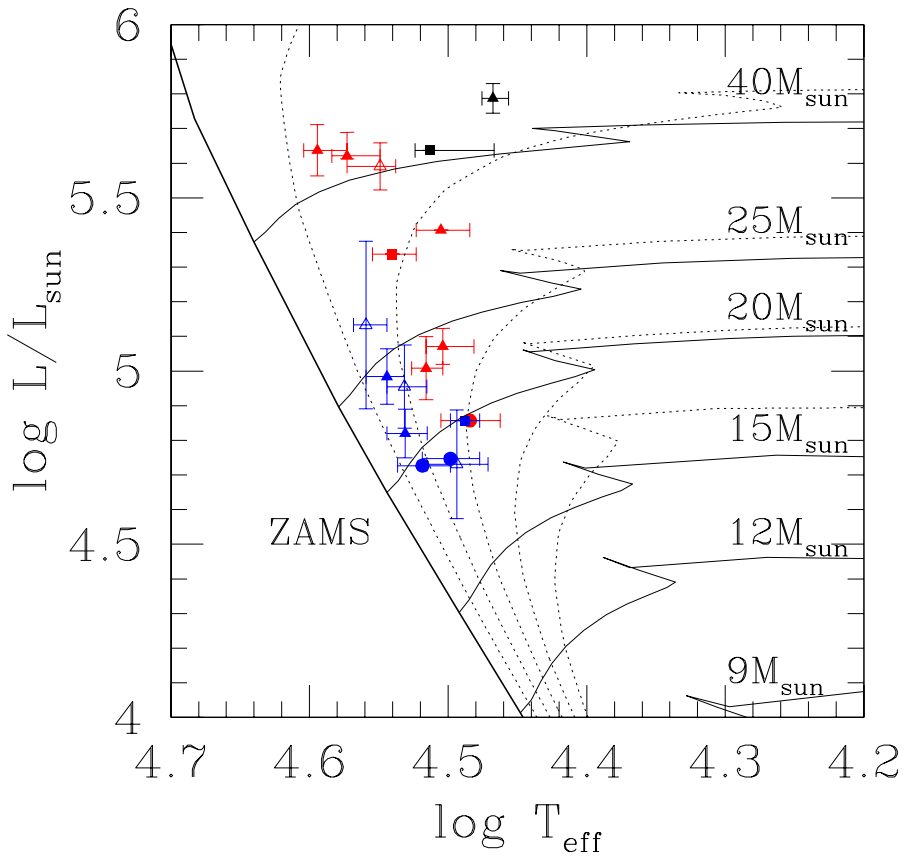

Figure 6.4: Locations of the NGC 6231 O-type stars in the H-R diagram. Symbol shapes and colours provide different indications on the object nature: black, supergiant; red, giant; blue, main sequence; triangle, belong to a binary system (filled triangles indicate the heaviest star of the system while open triangles stand for the less massive companion); square, RV-shift; circle, presumably single, constant-RV star. The evolutionary tracks from Schaller et al. (1992) have been plotted (plain lines) together with isochrones (dotted lines) computed for ages ranging from 2 to 10 Myr with a step of 2 Myr. The figure appears in colour in the electronic version of this work.

effective temperatures ($T_{\rm eff}$) correspond to half a sub-type on each side. For binaries, the main uncertainty on the luminosity comes from the relatively limited precision on the determination of the brightness ratio between the two components. From the superposition of the evolutionary tracks of Schaller et al. (1992), one notices that evolutionary ages of all the objects are between 2 and 6 Myr, while the average age is probably around 3 to 4 Myr. This epoch coincides with the peak of formation of low mass objects in NGC 6231 (see Chap. 2) and clearly suggests that the formation of both categories of objects could be interrelated. Finally, Fig. 6.4 indicates that the formation period of the early-type stars in NGC 6231 may display a significant extension in time. This is somewhat confirmed by the presence in the FOV of HD 152235, a B1 supergiant with an evolutionary age about 5 Myr. We note however that, in binary systems, the evolution of the stellar component could be significantly altered compared to single star evolution. For example, mass transfer through Roche lobe overflow (RLOF) can rejuvenate the accreting component, thus extending its main-sequence life-time. No sign of such phenomenon was however observed in the

spectra of the NGC 6231 binaries. Their young ages as well as their eccentricities are further arguments indicating that RLOF has not yet occured in the past evolution of these systems.

6.5 Discussion

The present study probably provides the most accurate set of constraints on the properties of the O-type star population in NGC 6231 so far. We have shown that the minimal binary fraction in NGC 6231 was about 0.6 and is mainly composed of short period ($P < 10$ d) systems (six out of ten). From the location of the O-type stars in the H-R diagram, it may be deduced that these stars were formed about 4 Myr ago, but their formation could have extended over about 1 Myr around this date. Clearly formation and evolution theories of early-type stars should account for a significant fraction of binaries, among which a significant fraction of close binaries. The distribution of the period and eccentricity in NGC 6231 indicates that the systems with the shortest periods tend to display a smaller eccentricity. Similarly, we suggested a possible relationship between the eccentricity and the mass ratio. Though this aspect should be investigated further, it may provide an additional observational constraint on tidal dissipation and circularisation processes.

The present fraction of binaries in NGC 6231 (around 60%) is significantly reduced compared to the value of 79% obtained by García & Mermilliod (2001). We have actually revised the status of two binaries in our FOV, namely HD 152200 and HD 326331 which were previously reported as binaries. These objects have already been presented at length and their status discussed in previous sections. The revision of the binary fraction of NGC 6231 puts the cluster in a less extreme position compared to other rich (in terms of the number of O-type stars) open clusters. IC 1805 was also reported by García & Mermilliod (2001) as presenting a very large fraction of binaries: 80%, thus quite similar to what was found for NGC 6231. A recent work by De Becker et al. (2005) yields a quite different picture. Among the O-type stars of the cluster, two are definitely binaries and another one could also be a binary. For three other objects, they could not find any evidence of binarity and, in consequence, quoted them as presumably single. These authors did not observe the remaining 6 objects but, clearly, literature data are not convincing. It appears thus that the binary fraction in IC 1805 presumably lies between 0.2 (or 0.3) and 0.7. Together with the above figures for NGC 6231, a quite different sketch emerges. Both IC 1805 and NGC 6231 could display a much lower binary fraction compared to the very high value of ∼80% previously assumed. These two studies clearly illustrate the limitations of previous estimates of the binary fraction that, sometimes, did not rely on a sufficient observational sample. It also outlines the need of extensive studies to accurately constrain this important property among various stellar populations and, particularly, among early-type stars whose formation and evolution are still not firmly understood.

To bring the observational constraints derived in this work in a larger frame, we finally selected the O-type binaries (but not the WR systems) listed in the 9th Catalogue of Spectroscopic Binary Orbits (Pourbaix et al. 2004). Orbital solutions already quoted in the 8th catalogue (Batten et al. 1989) are accompanied by a quality flag ranging from 1 (bad quality) to 5 (good quality) and we restricted our analysis to orbits with quality flags equal 4 or 5. For newly incorporated orbits, no quality flag is provided anymore and we considered them all. Several orbits, published by different authors, could be associated with the same object. In such a case, we adopted only one orbit, usually the more recently published. We come up with a list of 71 SBs, among which 31 SB2. The corresponding e vs. P, q vs. P and e vs. q diagrams are presented in Fig. 6.5. The mass ratios were com-

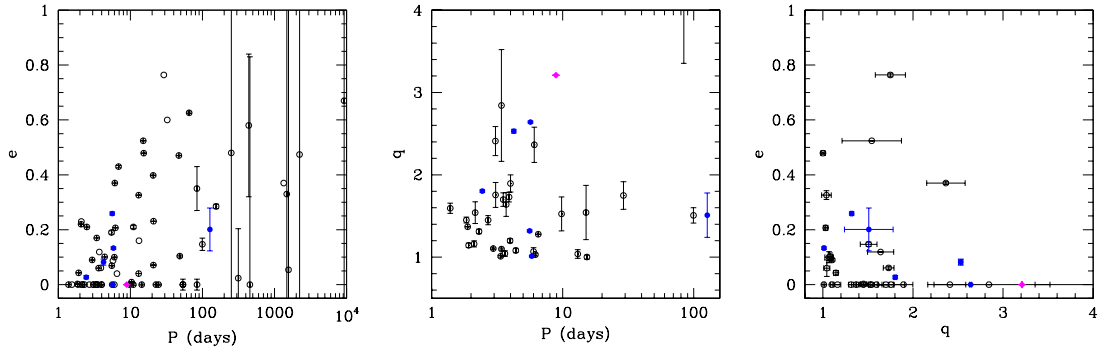

Figure 6.5: Distribution of various orbital and physical parameters (period, eccentricity, mass ratio) of the binaries in the 9th catalogue of spectroscopic orbits (open circles) and in NGC 6231 (filled circles). The filled diamond indicates the WR system HD 152270.

puted using the ratio of the quoted semi-amplitude of the primary and secondary RV-curve for the SB2 systems. The error on the mass-ratio was obtained from the theory of error propagation when uncertainties on the semi-amplitudes were provided in the catalogue. All three panels of Fig. 6.5 confirm the pattern obtained from the sole NGC 6231 binaries (Fig. 6.3). From the period-eccentricity diagram, one indeed notices the obvious lack of highly eccentric very short period systems. The q vs. P diagram does not seem to provide further constraints, beyond the intrinsic difficulty to detect SB2 systems with large q. Our latter remark on the possible relation between q and e seems to be confirmed by the e vs. q diagram of Fig. 6.5. Interestingly enough, as can be guessed from the first panel, all SB2 systems with $e > 0.4$ have actually periods larger than 10 d. This again suggests that, at least for early-type stars, the period, the eccentricity and the mass-ratio are all important parameters to constrain the binary evolution. For shorter period systems, displaying $e < 0.4$, only HD 93250 has a relatively large mass ratio ($q \approx 2.4$) and high eccentricity ($e \approx 0.35$).

To conclude this chapter, we emphasize that the present approach, using the 9th Catalog of Spectroscopic Orbits, may actually only provide a first, rough, approximation. On the one hand, a significant fraction of the orbits are not accompanied by appropriate error estimates, so that one can hardly guess the accuracy of a point in the above diagrams. Furthermore, as the quality of the orbit could not be estimated, we have checked several orbits individually and noted that some of them were only computed from very few points (sometimes less than 10). As a consequence, even if the quoted uncertainties on the orbital parameters are relatively small, the period may be ill-defined. This could dramatically alter the position of all other orbital parameters. Finally a series of recently computed orbital solutions have not been included in the 9th catalog yet. As only 30 SB2 systems are quoted in the catalogue, these newly derived orbital solutions are statistically significant and should be taken into account in future works. It would thus be necessary to check one by one the various orbital solutions proposed in the 9th catalogue, and to complete it. Though the number of systems is of a few tens only, this work remains beyond our present purpose. We will nevertheless address this aspect in a near future.

Summary and conclusions

The true traveller does not have an established plan and does not intend to arrive.
Lao Tseu

In sciences, the path is more important than the goal. Sciences have no ending.
Erwin Chargaff

Throughout this work, we have presented the results of an observational multi-wavelength study (in the optical and X-ray domains) of the massive star population of the young open cluster NGC 6231. Located at a distance of about 1.6 kpc from Earth and considered as the core of the Sco OB 1 association, NGC 6231 hosts a rich early-type star population of different sub-spectral types and luminosity classes. Our study of this cluster and of its surroundings has been limited to a radius of about $15'$ around the cluster core. In this area, one finds 15 O-type stars and a Wolf-Rayet binary as well as about one hundred B-type stars. We have mainly focused on the O-type star population of the cluster.

As an observational work, this dissertation is based on a large set of observational material that combines intermediate- and high-resolution optical spectroscopy, narrow-band optical photometry and XMM-*Newton* X-ray observations. Collected between 1996 and 2004, this extensive set of data has allowed to probe the characteristics of the O-type star population in NGC 6231 and the distribution of its physical parameters.

In the $15'$ radius of the EPIC instrument field of view (FOV) onboard XMM-*Newton*, our deep X-ray campaign reveals more than 600 sources, mostly point-like, that cluster on the NGC 6231 core. The contamination by foreground and background objects should not be much larger than $\sim 6\%$, so that most of the detected sources are probably physically related to NGC 6231 or to the wider Sco OB 1 association. The source density distribution presents a slight North–South elongation. Its radial distribution remains however well described by a King profile with a core radius of $3\farcm1$. A similar value is obtained from the distribution of the optical sources in the FOV.

All the O-type stars are detected in the X-rays and display a strong but soft X-ray emission. In the 0.5-10.0 keV band, their X-ray emission scales with their bolometric luminosities as

$$\log L_{\rm X} - \log L_{\rm bol} = -6.91 \pm 0.15 \ ({\rm erg\ s^{-1}})$$

The dispersion around this *canonical* relation is much more limited that previously thought, which may partly result from the homogeneity of the present sample in terms of distance, age and chemical composition. It is worth noting however, that the present sample is formed both by single stars and by binaries ranging from the sub-spectral types O5.5/O6 to O9.7, and belonging to different luminosity classes. The dispersion seems slightly larger among the late O9.5–O9.7 dwarfs. The more significant deviations are however observed

for two binaries that display a prominent wind-interaction signature. Within our sample of stars, X-ray emission from wind interaction is also the sole mechanism that, at our detection threshold, seems to produce a significant modulation of the X-ray flux from O-type stars.

Beside the O-type population, about one quarter of the B-type stars could be associated with an X-ray source. This fraction seems approximately constant throughout the different sub-spectral types. Its seems slightly higher for giants compared to dwarfs but this statistics relies on small numbers only. Their spectral properties and flaring behaviours suggest that most of the detected X-ray emission should rather be attributed to a pre-main sequence companion, either in a binary system or on the line of sight. However we still detect a significant correlation between the bolometric luminosities of the B-type stars and the associated X-ray flux. The exact origin of this relation remains uncertain and could result from an observational bias.

Most of the remaining X-ray sources are probably pre-main sequence objects. From the comparison of their optical properties with theoretical tracks in the Hertzsprung-Russell diagram, we have proposed the following history for star formation. The star formation in NGC 6231 could have started more than 10 Myr ago at a relatively slow rate. The latter has then increased, culminating in a star-burst like event about 3 to 4 Myr ago, an epoch during which massive stars have formed too. The star formation finally came to an abrupt end about 1 Myr ago.

As mentioned above, two early-type stars in NGC 6231 are displaying a large X-ray emission excess compared to what is expected from the *canonical* $L_{\rm X}$ vs. $L_{\rm bol}$ relation. In a second part of this work, we focused on the study of these two systems and showed that HD 152248 (O7.5III(f)+O7III(f)) and CPD -41°7742 (O9V+B1.5V) were harbouring a prominent wind interaction, though of a probably different nature each. Both systems are eclipsing SB2 binaries. Prior to the analysis of the wind interaction, we have first computed their orbital solutions in order to provide the accurate ephemeris needed to correctly interpret the X-ray data. In particular, we have derived the very first SB2 orbital solution for CPD -41°7742. We have also performed the first analysis of its optical light curve and, combining the obtained constraints the the results of the spectroscopic analysis, we have derived the absolute values of the component masses, radii and luminosities. We found that, according to our analysis, the system should be located at a distance corresponding to $DM = 10.92 \pm 0.16$, in excellent agreement with the cluster average distance.

HD 152248 is almost located at the cluster centre and is the brightest X-ray source in the FOV. Concentrating on its optical spectrum, we have first uncovered the ongoing wind-wind interaction thanks to the analysis of the line profile variability of the He IIλ4686 and H$\,\alpha$ lines. In the X-ray domain, the system presents a clear increase of its flux at apastron compared to periastron. We interpret this feature as the modulation of the X-ray emission from the wind-wind interaction in this close, slightly eccentric system. Indeed, in HD 152248, the interaction happens within the wind acceleration regions. At apastron compared to periastron, the winds can thus reach larger pre-shock velocities, yielding stronger shocks and, hence, a larger X-ray emission. The present behaviour is clearly opposite to the usually admitted $1/D$ modulation (where D is the separation between the two components) of the X-ray flux produced in a wind-wind interaction. The latter sketch remains valid in slightly wider pairs, such as HD 93403 ($P \approx 15.9$ d, Rauw et al.

2000), in which the winds collide at velocities close to their terminal velocities. HD 93403 indeed presents an increase of its X-ray flux at periastron (Rauw et al. 2002), attributed to a stronger shock resulting from the lower dilution of the wind material that enters the collision. As demonstrated by the present results the latter scenario breaks down for shorter-period binaries. As a last step in the analysis, we have also performed hydrodynamical simulations reproducing as closely as possible the physical and orbital configuration of HD 152248 at the time of the different XMM-*Newton* observations. The predictions of the hydrodynamical model reproduce the observed modulations to the first order and thus provide a strong support to the colliding-wind origin of the X-ray extra-emission and subsequent variations in HD 152248.

The second colliding-wind binary studied in detail in this work is CPD −41°7742, an O9V+B1.5V system. The XMM-*Newton* observations of the cluster almost fully covered the 2.4 d orbital period of the system. The resulting X-ray light curves are of an unprecedented quality and present clear signs of variability. We interpreted their main features as the signature of a particular kind of wind interaction in which the dominant primary wind crushes on the secondary surface. We also provided a geometrical model that associates an extra X-ray luminosity component to the secondary inner side (i.e. the surface side that is facing the primary component). This simple model reproduced rather well the main features of the X-ray light curve, yielding further support to our interpretation.

In a third part of this work, we concentrated on the remaining O-type binaries in the FOV. Three of them (CPD −41°7733, HD 152218, HD 152219) have a period below 6 days and have thus been well covered by the spectroscopic and XMM-*Newton* campaigns. The spectral signature of the two binary components could be disentangled for all three objects thanks to the quality of our high-resolution spectroscopic observations in the optical. We derived the very first SB2 orbital solutions for CPD −41°7733 and HD 152219 and we improved the orbit of HD 152218. The latter system probably undergoes a relatively rapid apsidal motion while the primary of HD 152219 displays strong line profile variations that are reminiscent of those produced by non-radial pulsations.

Though these data are of a poorer quality than those of HD 152248 and CPD −41°7742, we also reported the analysis of the XMM-*Newton* observations of these three systems. HD 152219 (O9.5III+B1-2V/III) and HD 152218 (O9IV+O9.7V) show a slightly variable X-ray emission that could be related to a possible wind-interaction. On the other hand, CPD −41°7733 (O8.5V+B3V) seems to present a constant X-ray flux and, at our detection threshold, one indeed does not expect to detect significant variations resulting from a possible wind interaction in this system.

We also showed that both HD 152233 and HD 152234 were SB2 systems with periods of the order of months and we proposed a preliminary orbital solution for HD 152234. These systems are currently being monitored on the appropriate time scales using the FEROS spectrograph. These forthcoming data should provide unprecedented constraints on the orbital and physical properties of both systems.

In the following part of this work, we briefly analysed the optical spectrum of most of the early-type X-ray emitters in the FOV. In this task, we mainly concentrated on the spectral classification and on the search for variability, possibly indicating a multiple nature. Limiting the present summary to O-type objects, we uncovered two long period (probably of the order of a year) O-type systems and we found significant line profile variability for three other O-type stars. Such a variability is unlikely to result from a

Keplerian motion in a binary system and we rather pointed out non-radial pulsations or wind structures as more likely explanations. Our data set was unfortunately too sparse to better constrain the nature of these variations.

Finally, we used the observational constraints deduced throughout this work to probe the properties of the O-type star population in NGC 6231. We obtained a binary fraction of 0.63, among which 60% are short period ($P < 10$ d), slightly eccentric ($e < 0.3$) systems. Though our binary sample contains only seven objects, we note that the shorter period systems tend to have a lower eccentricity. Similarly, we note that systems with a larger mass ratio usually display a lower eccentricity compared to systems with two similar components. This result is somewhat confirmed by the distribution, in the eccentricity vs. mass ratio diagram, of the objects listed in the 9th Catalogue of Spectroscopic Binary Orbits. However, we noted that a more careful work should be undertaken to properly investigate this relation. Finally, the comparison of the location of the O-type stars in the Hertzsprung-Russell diagram with evolutionary tracks indicates that these stars have been formed, on average, about 4 Myr ago, although the formation epoch could have lasted for at least 1 Myr.

The present work has provided a tight set of observational constraints on a limited but homogeneous sample of O-type stars. Most of these stars were poorly known before our study and, thanks to the high-quality of our X-ray and optical data sets, we could perform a detailed analysis. Still many things remain to be done on NGC 6231 and its surroundings. First, one has to extend this study to longer period objects located in or near the cluster core. A monitoring campaign is currently on-going for two of these systems while the two other suspected long period binaries have been the topic of an observing time proposal for the next ESO period (P76). On the other hand, many objects display line profile variations on different time scales. These could be related to different phenomena such as non-radial pulsations (NRPs) or wind structures. Dedicated observing campaigns should be designed to investigate their properties. In particular, we have shown that HD 152219 is actually an eclipsing binary system whose primary component was probably displaying NRPs. This system may prove to be particularly interesting as its masses and size can potentially be determined thanks to the analysis of its light curve. Finally, it would be very interesting to extend the present study towards B-type stars in NGC 6231. Most of these objects are indeed very poorly known.

Regarding the colliding wind phenomenon, our work has outlined the need to develop appropriate tools that account both for 3-D effects (such as the orientation of the line of sight, but also the deflection induced by the orbital motion) and detailed physics. Concerning the latter, appropriate 2D wind acceleration laws (radial and azimuthal), computed in regard of the effects of the radiation field of both stars, should definitively be considered. On the observational point of view, this work also illustrates the need to provide as good a phase coverage as possible. This statement remains true even in the X-ray domain, where indeed observing time is often sparsely attributed because of its cost and of the high pressure factor on the facilities. Indeed, many of the results obtained in this work would have never been uncovered with only a fraction of the 180 ks duration of the present XMM-*Newton* campaign.

Finally, it is interesting to note that, while some people are gazing at the edge of the Universe, a large fraction of our galactic neighbourhood is still poorly studied. Significantly

enough, all the O-type stars studied in this work are brighter than $V = 9$ while one third has a magnitude $V < 6.5$! The large majority of the B-star population in the studied FOV has $V < 12$ as well. Definitely, in the optical at least, the observational facilities required to properly study these objects are rather modest and the techniques well mastered. Regarding the importance of the massive stars and the number of crucial issues still left open (see e.g. a brief overview in the Introduction), significant scientific gains may, and should, thus be reached, at comparatively low costs, thanks to small- to medium-scale observing facilities.

Appendix A

An optical spectral atlas of early-type stars in NGC 6231

As mentioned in Chap. 5, we present here an atlas of the optical spectra of the early-type stars observed during our spectroscopic campaign. Both the early-type binaries discussed in the Chaps. 3 and 4 as well as the objects of Chap. 5 are included. Most of the displayed spectra belong thus to optical counterparts of X-ray sources detected in the XMM-*Newton* FOV.

In the atlas, the objects are ordered following their luminosity class and spectral type. Their name and spectral classification are clearly mentioned in the different panels. Because of the large wavelength domain observed with the FEROS spectrograph ($\lambda\lambda$3950-7150), the spectral range has been divided into four contiguous sub-domains ($\lambda\lambda$3950-4750, $\lambda\lambda$4750-5550, $\lambda\lambda$5550-6350 and $\lambda\lambda$6350-7150), each of which are 800 Å wide. Except for the HD 152248 and CPD $-41°7742$ binaries, the displayed spectra were all acquired in May 2004 at the ESO 2.2m telescope.

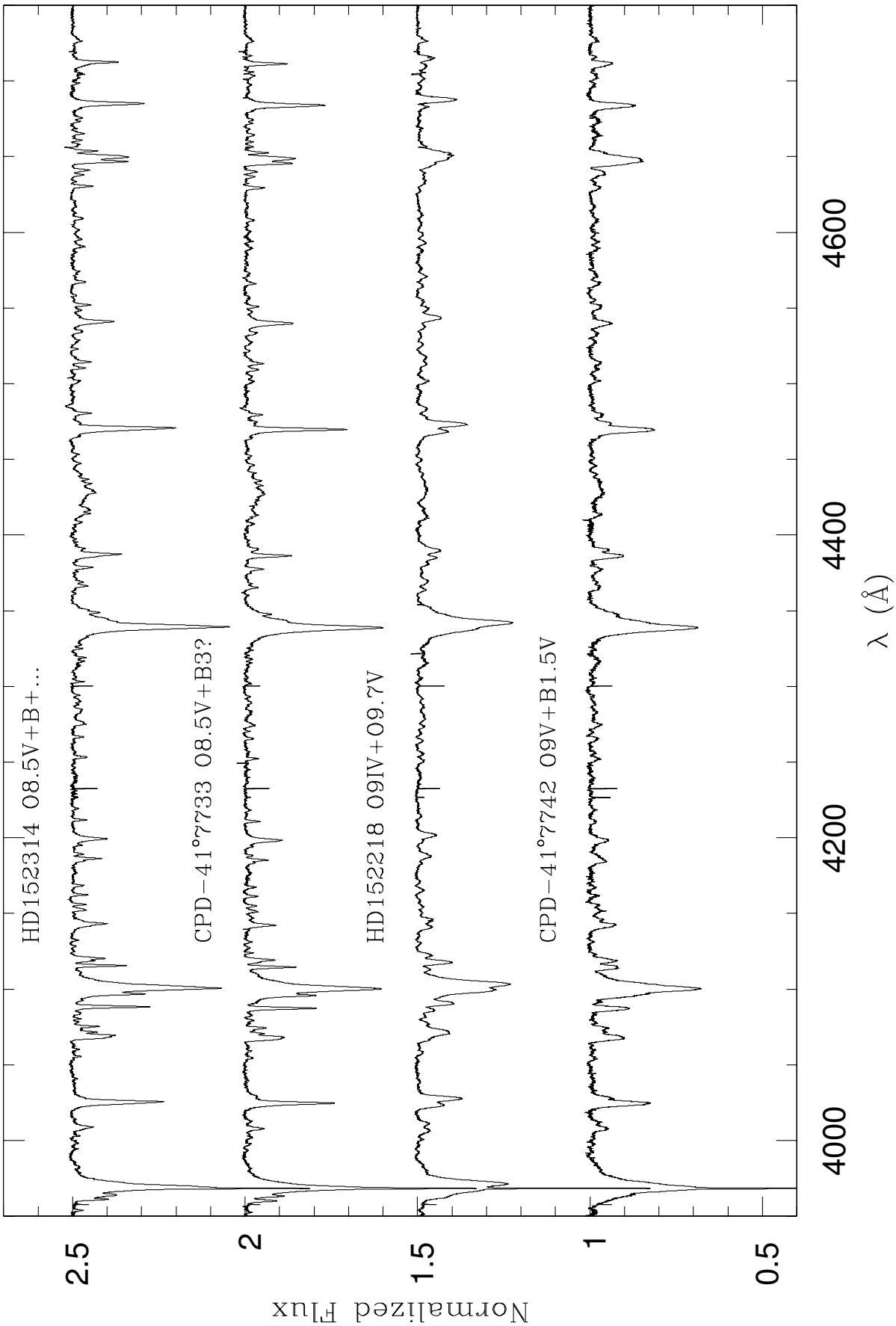
HD152314 O8.5V+B+...
CPD−41°7733 O8.5V+B3?
HD152218 O9IV+O9.7V
CPD−41°7742 O9V+B1.5V
Normalized Flux
λ (Å)
0.5
1
1.5
2
2.5
4000
4200
4400
4600

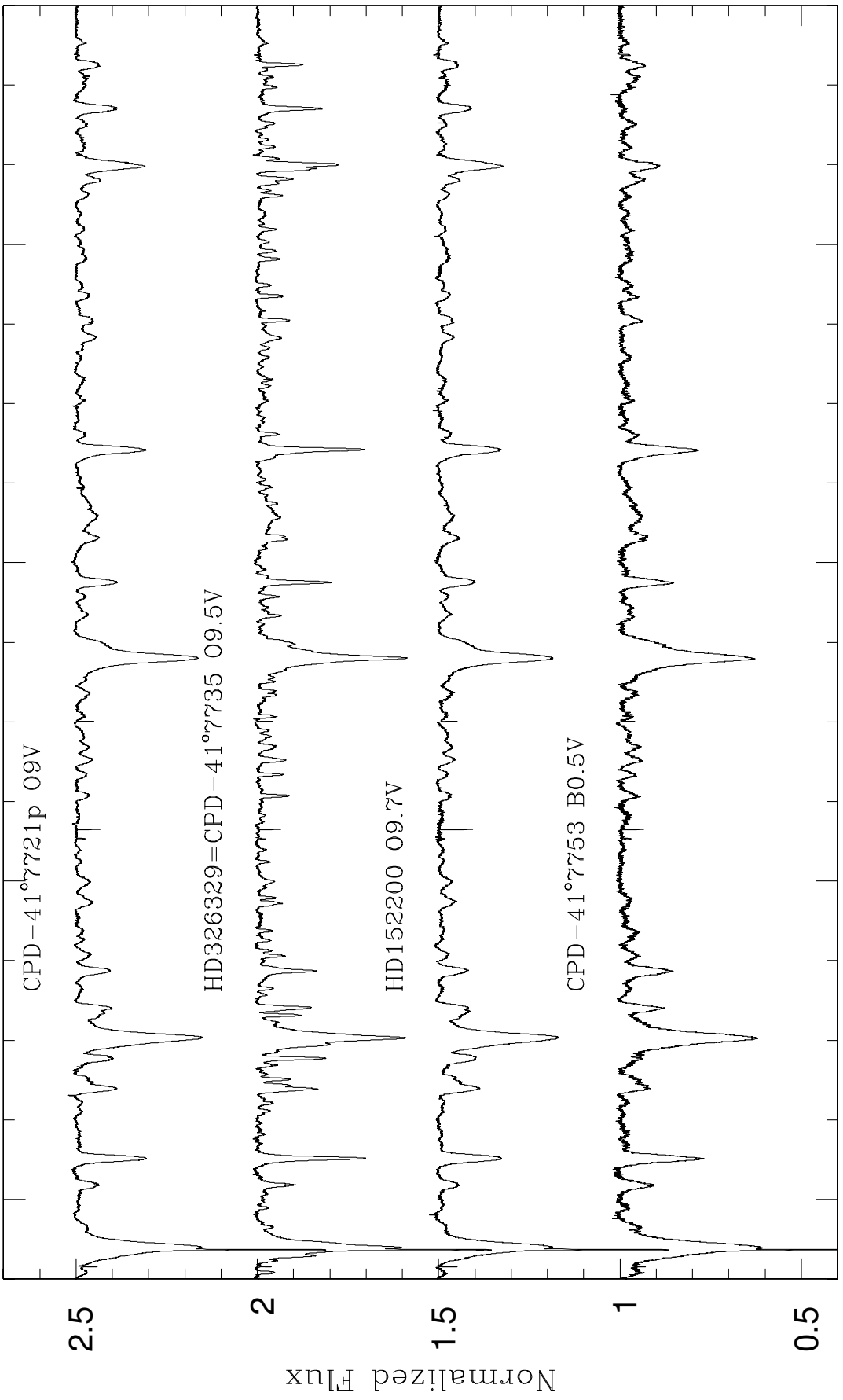
CPD−41°7721p O9V
HD326329=CPD−41°7735 O9.5V
HD152200 O9.7V
CPD−41°7753 B0.5V
Normalized Flux
λ (Å)
0.5
1
1.5
2
2.5
4000
4200
4400
4600

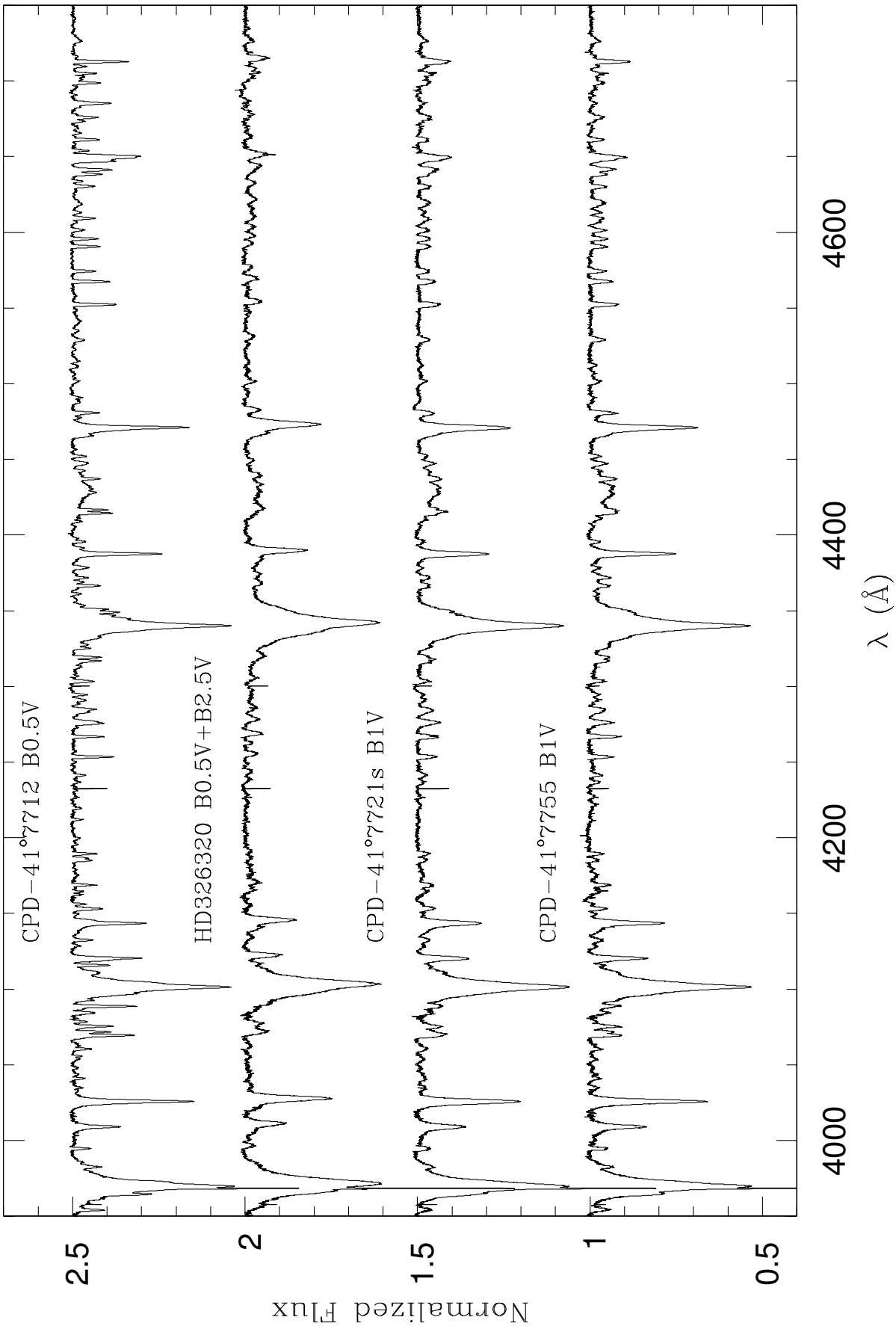
CPD−41°7712 B0.5V
HD326320 B0.5V+B2.5V
CPD−41°7721s B1V
CPD−41°7755 B1V
Normalized Flux
λ (Å)
0.5
1
1.5
2
2.5
4000
4200
4400
4600

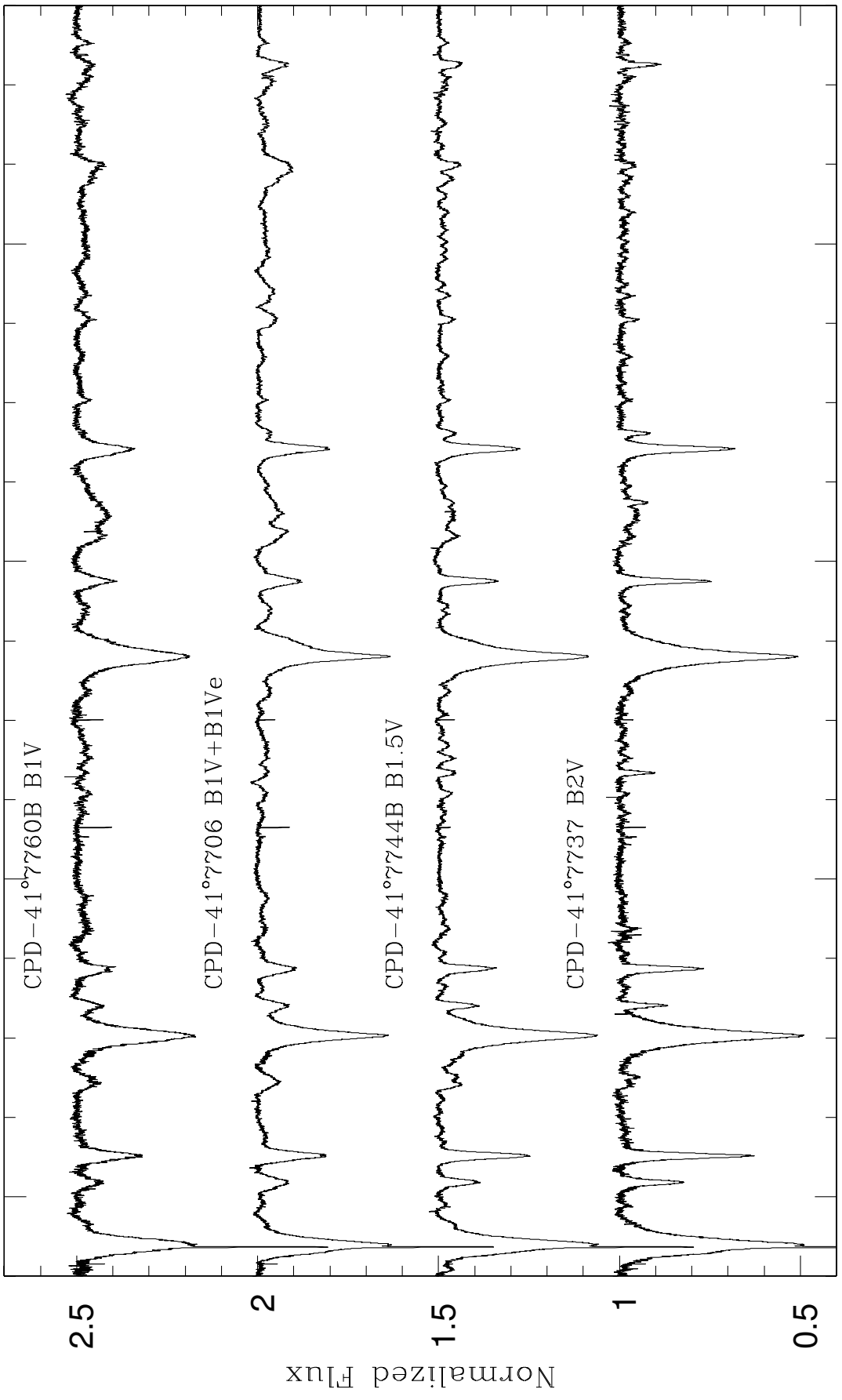
CPD−41°7760B B1V
CPD−41°7706 B1V+B1Ve
CPD−41°7744B B1.5V
CPD−41°7737 B2V
Normalized Flux
λ (Å)
0.5
1
1.5
2
2.5
4000
4200
4400
4600

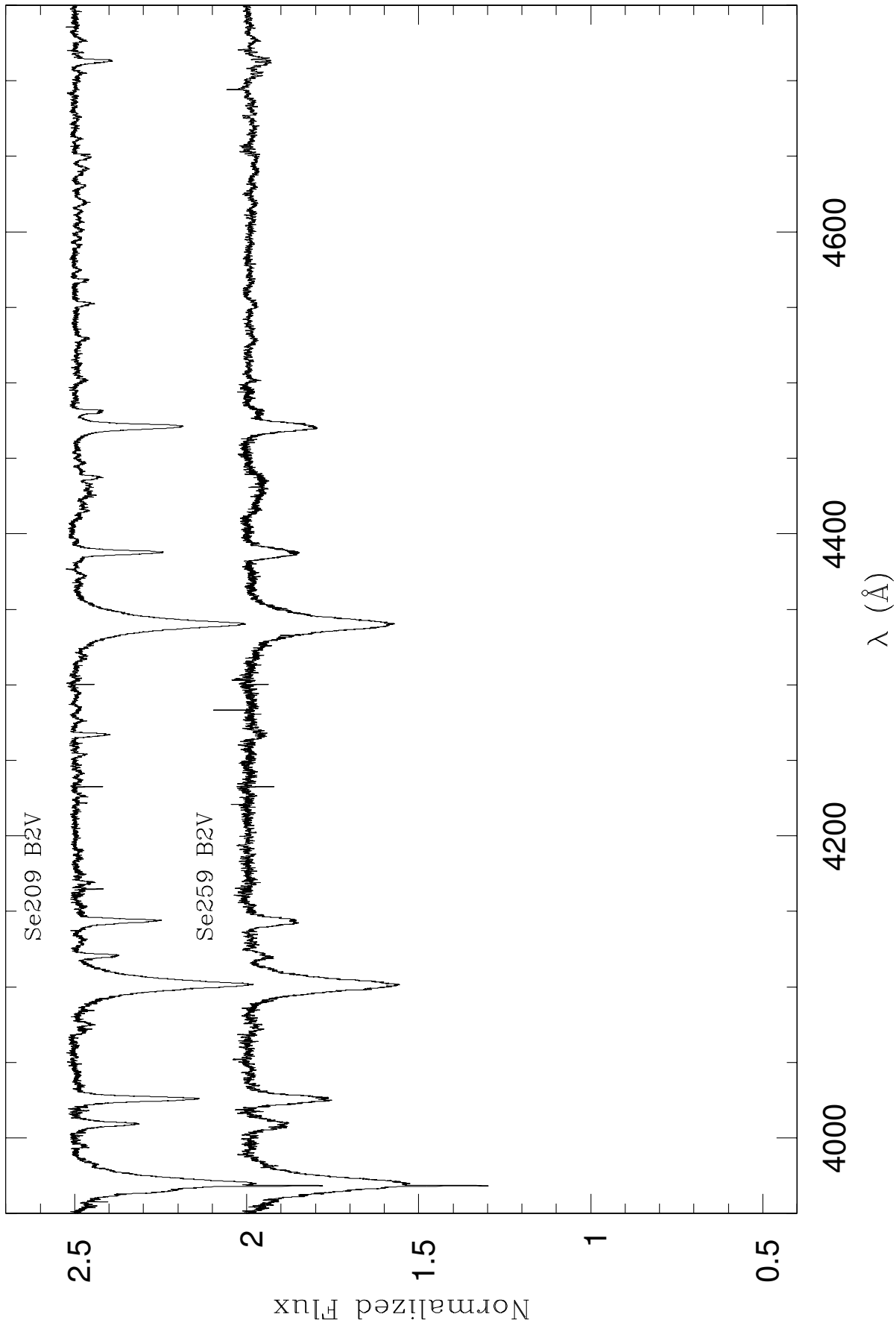
Se209 B2V
Se259 B2V
Normalized Flux
λ (Å)
0.5
1
1.5
2
2.5
4000
4200
4400
4600

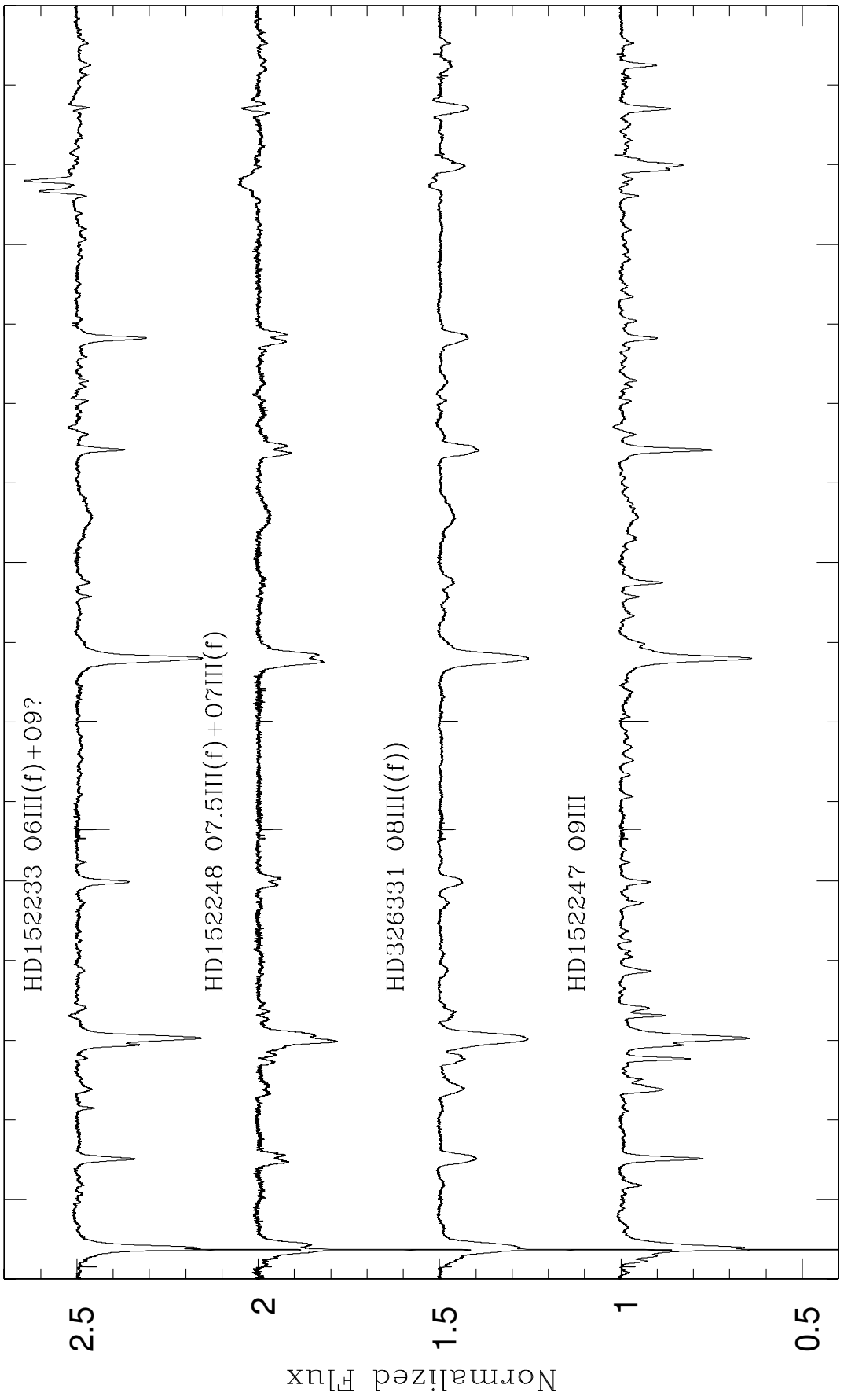
HD152233 O6III(f)+O9?
HD152248 O7.5III(f)+O7III(f)
HD326331 O8III((f))
HD152247 O9III
Normalized Flux
λ (Å)
0.5
1
1.5
2
2.5
4000
4200
4400
4600

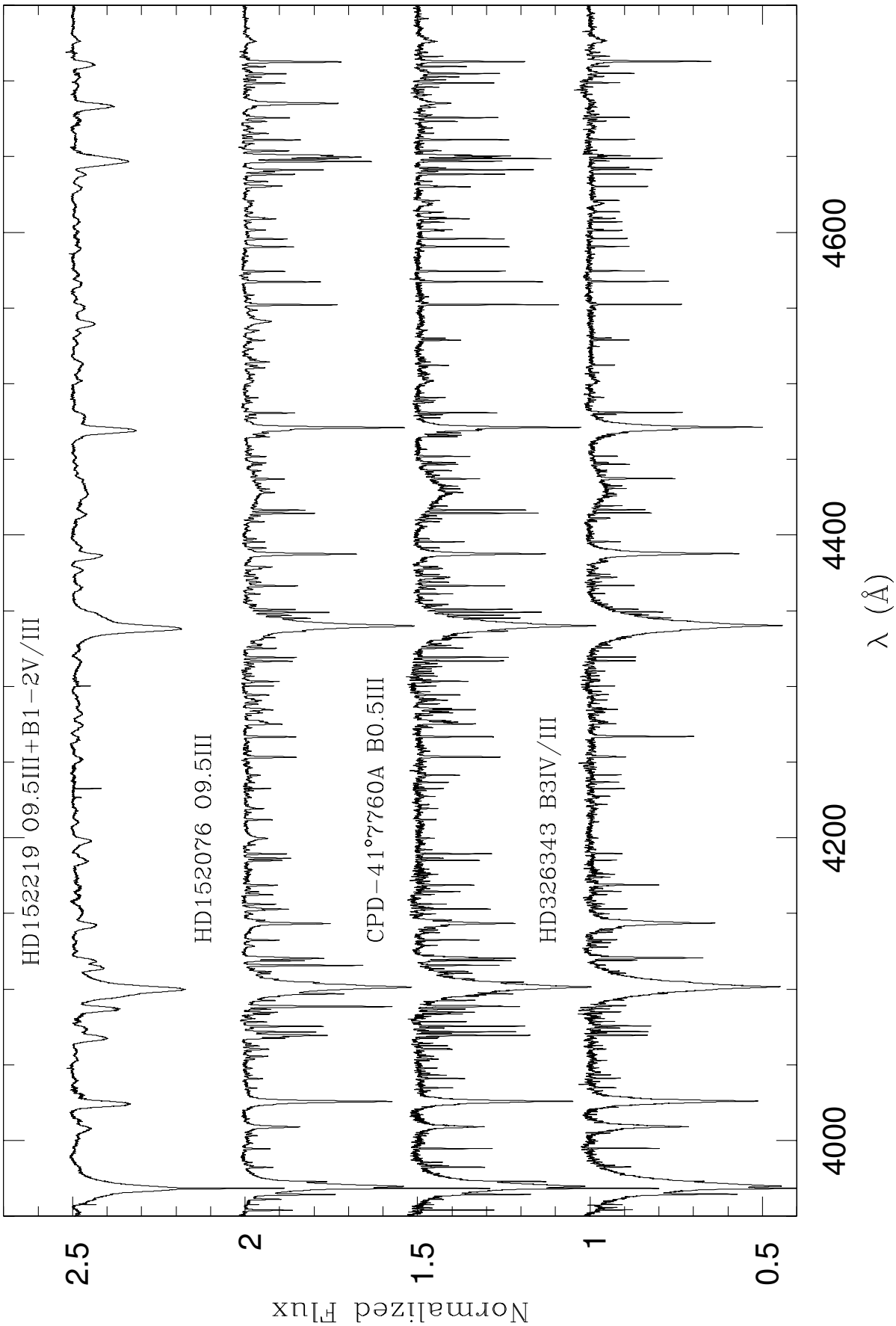
HD152219 O9.5III+B1−2V/III
HD152076 O9.5III
CPD−41°7760A B0.5III
HD326343 B3IV/III
Normalized Flux
λ (Å)
0.5
1
1.5
2
2.5
4000
4200
4400
4600

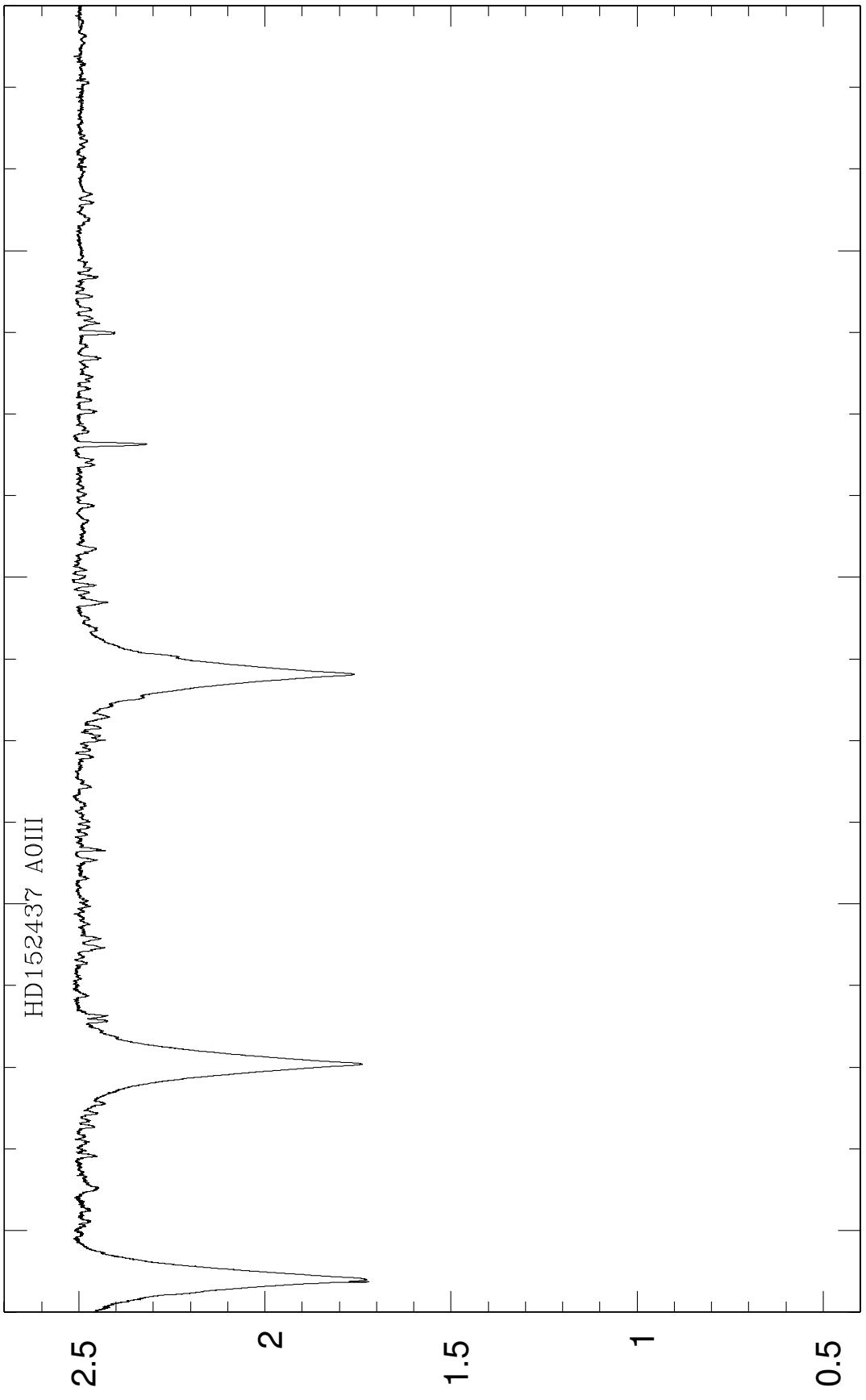
HD152437 A0III
2.5
2
1.5
1
0.5
4000
4200
4400
4600

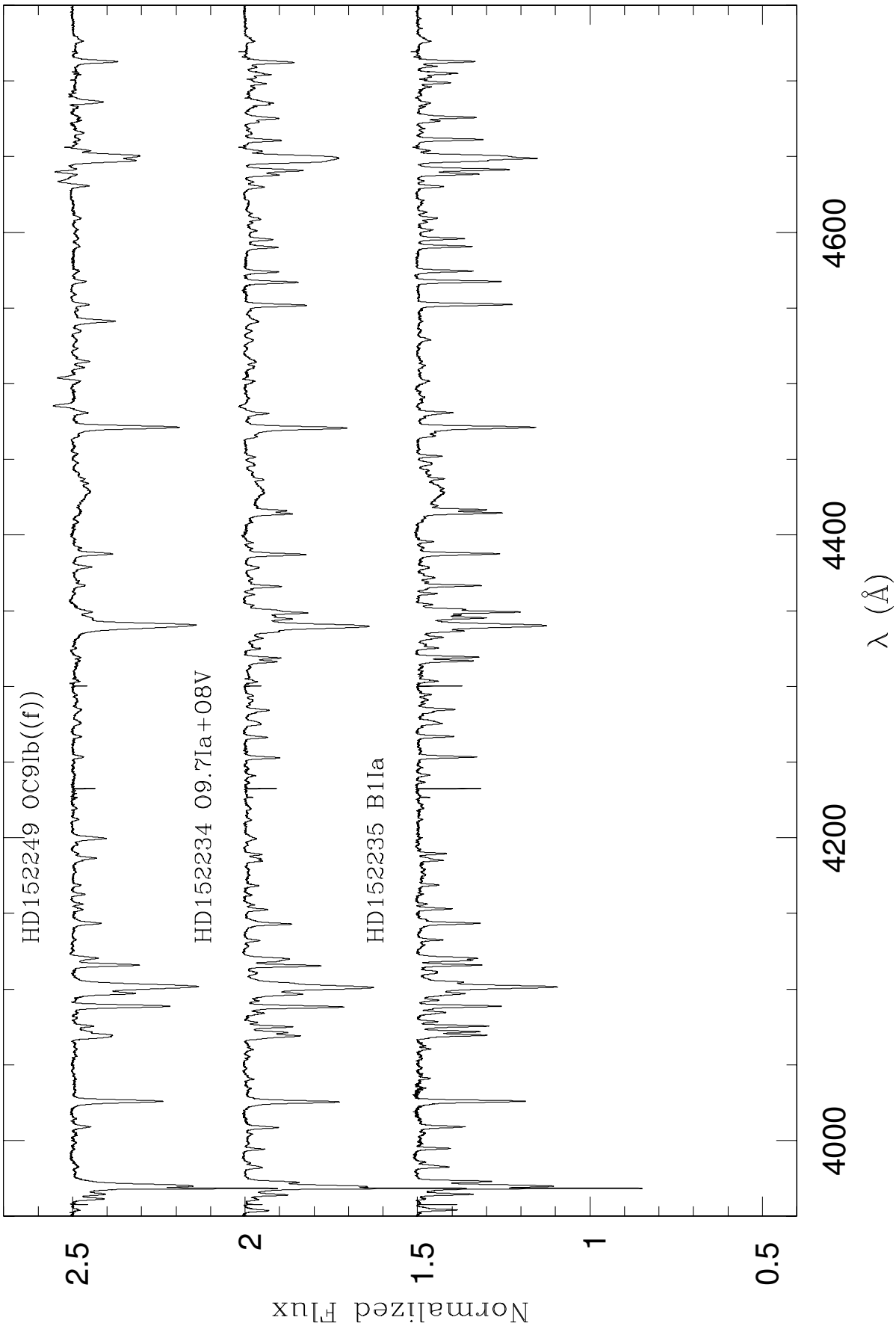
HD152249 OC9Ib((f))
HD152234 O9.7Ia+O8V
HD152235 B1Ia
Normalized Flux
λ (Å)
2.5
2
1.5
1
0.5
4000
4200
4400
4600

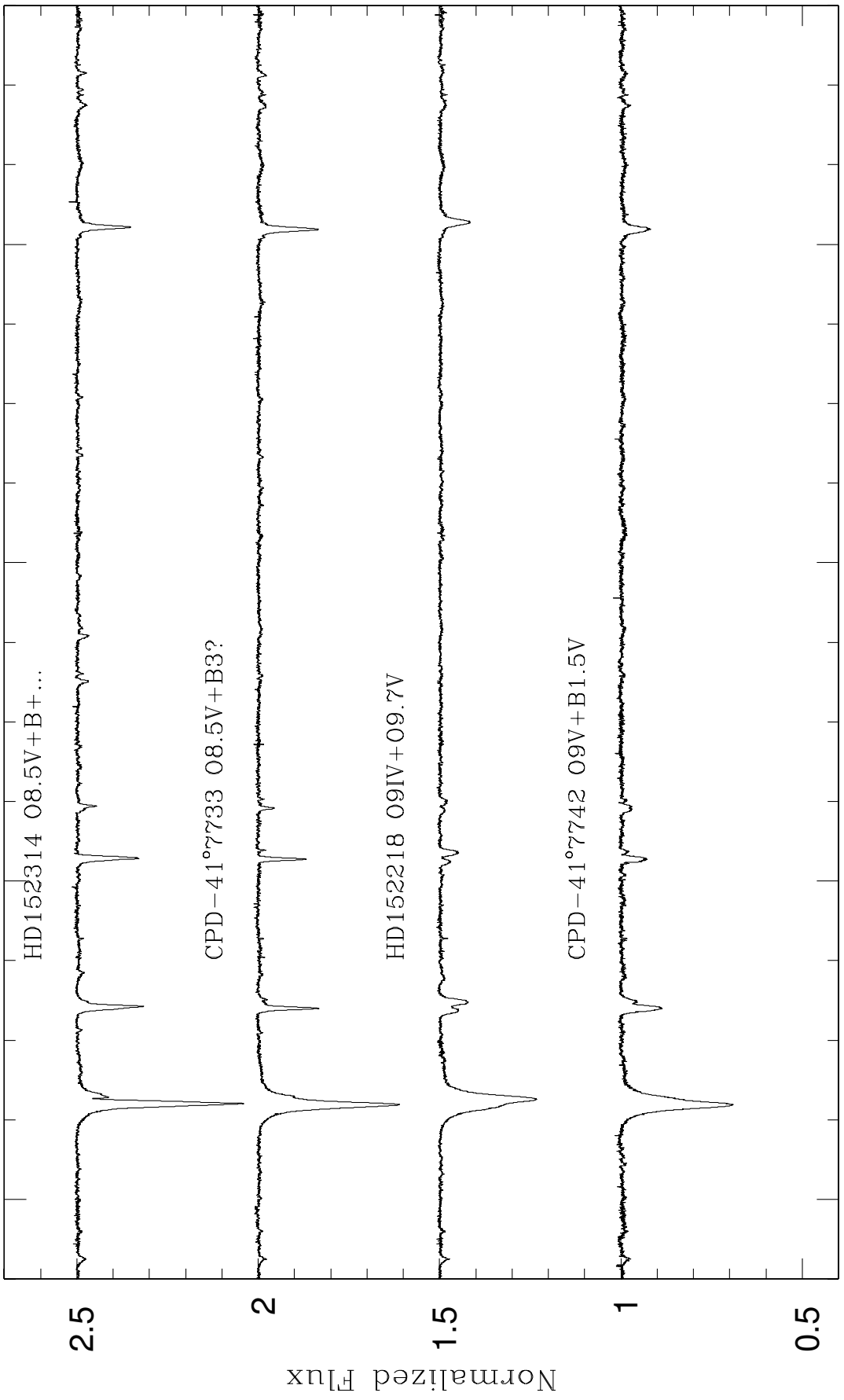
HD152314 O8.5V+B+...
CPD−41°7733 O8.5V+B3?
HD152218 O9IV+O9.7V
CPD−41°7742 O9V+B1.5V
Normalized Flux
λ (Å)
0.5
1
1.5
2
2.5
4800
5000
5200
5400

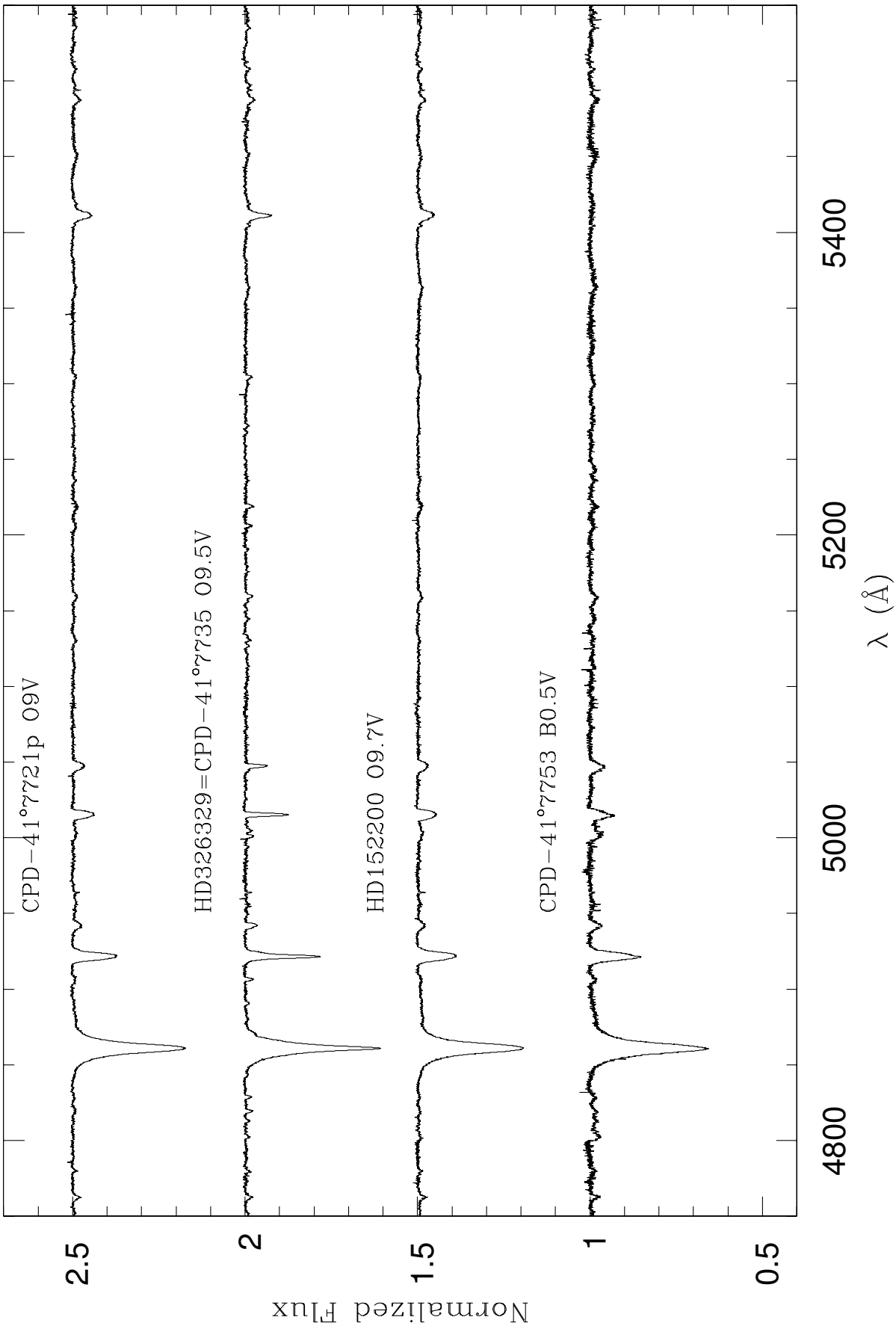
CPD−41°7721p O9V
HD326329=CPD−41°7735 O9.5V
HD152200 O9.7V
CPD−41°7753 B0.5V
Normalized Flux
λ (Å)
0.5
1
1.5
2
2.5
4800
5000
5200
5400

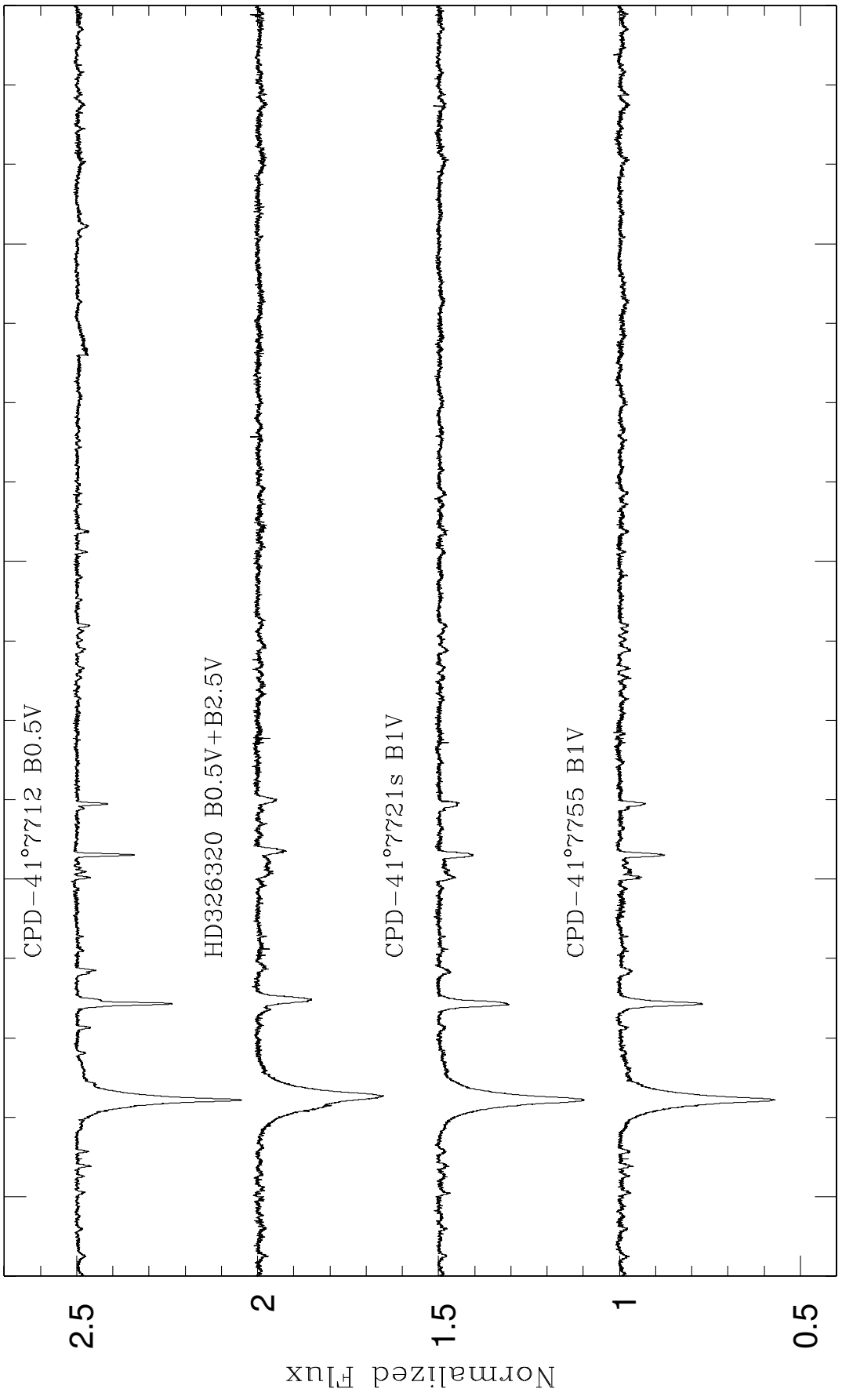
CPD−41°7712 B0.5V
HD326320 B0.5V+B2.5V
CPD−41°7721s B1V
CPD−41°7755 B1V
Normalized Flux
λ (Å)
0.5
1
1.5
2
2.5
4800
5000
5200
5400

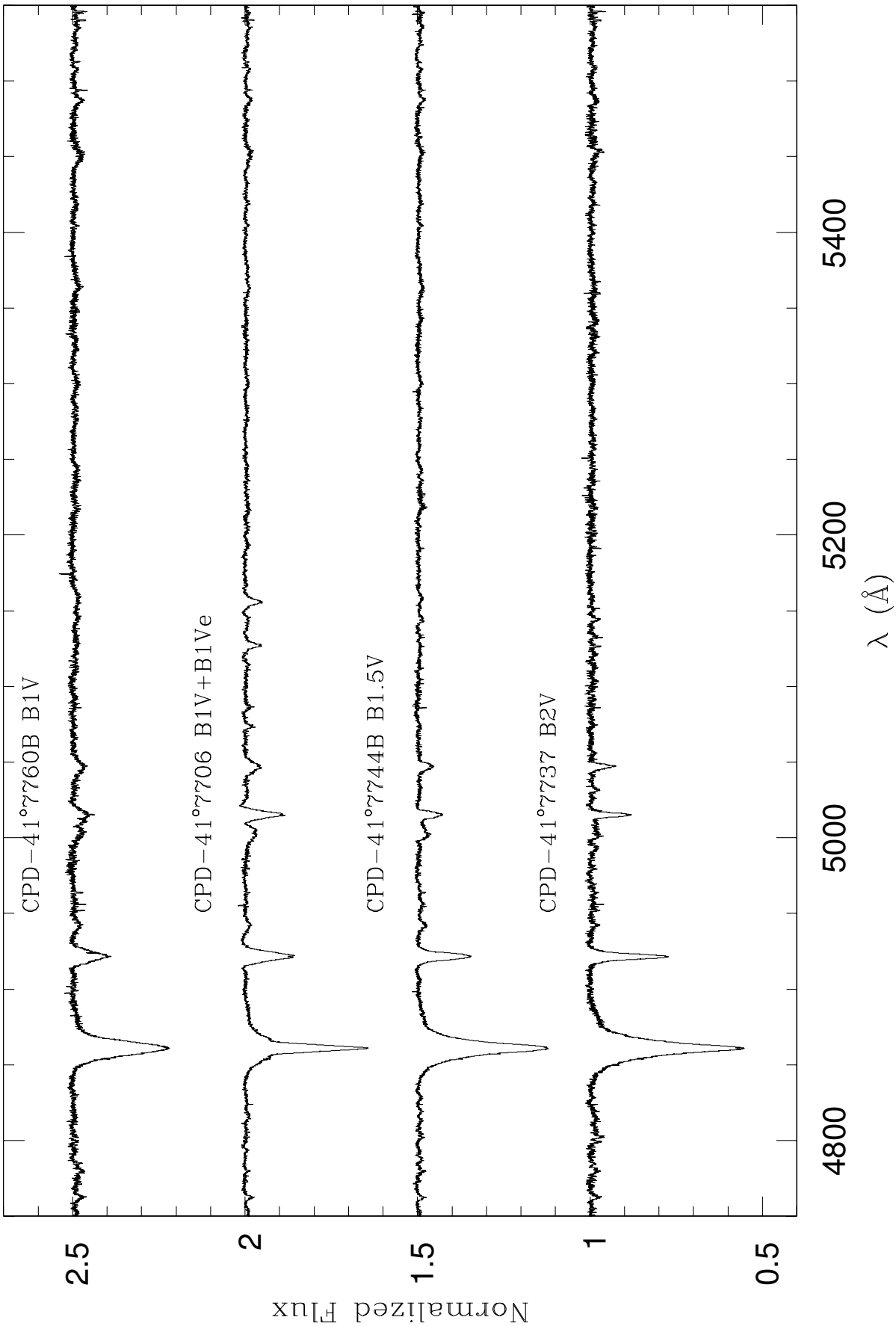
CPD−41°7760B B1V
CPD−41°7706 B1V+B1Ve
CPD−41°7744B B1.5V
CPD−41°7737 B2V
Normalized Flux
λ (Å)
0.5
1
1.5
2
2.5
4800
5000
5200
5400

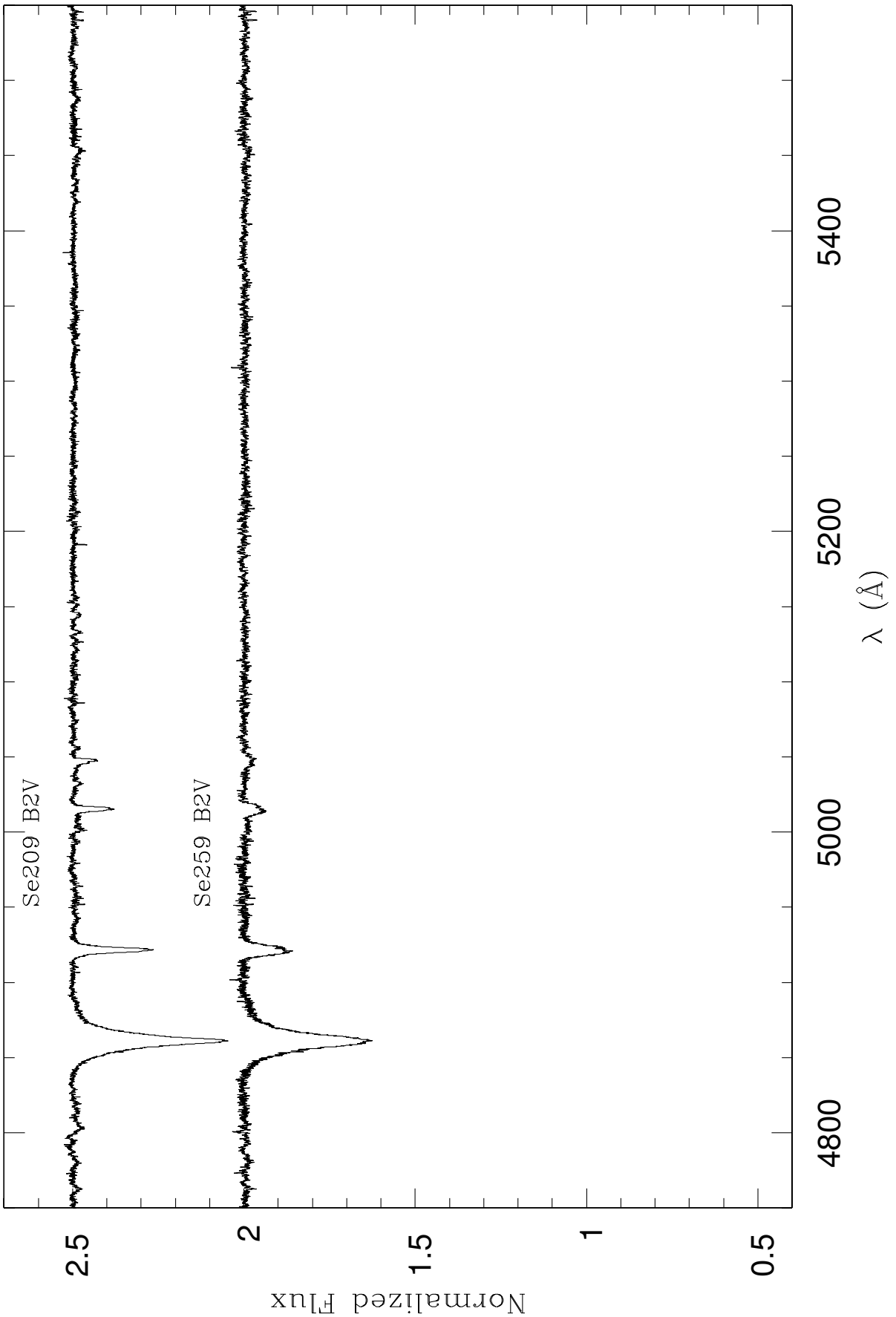
Se209 B2V
Se259 B2V
Normalized Flux
λ (Å)
0.5
1
1.5
2
2.5
4800
5000
5200
5400

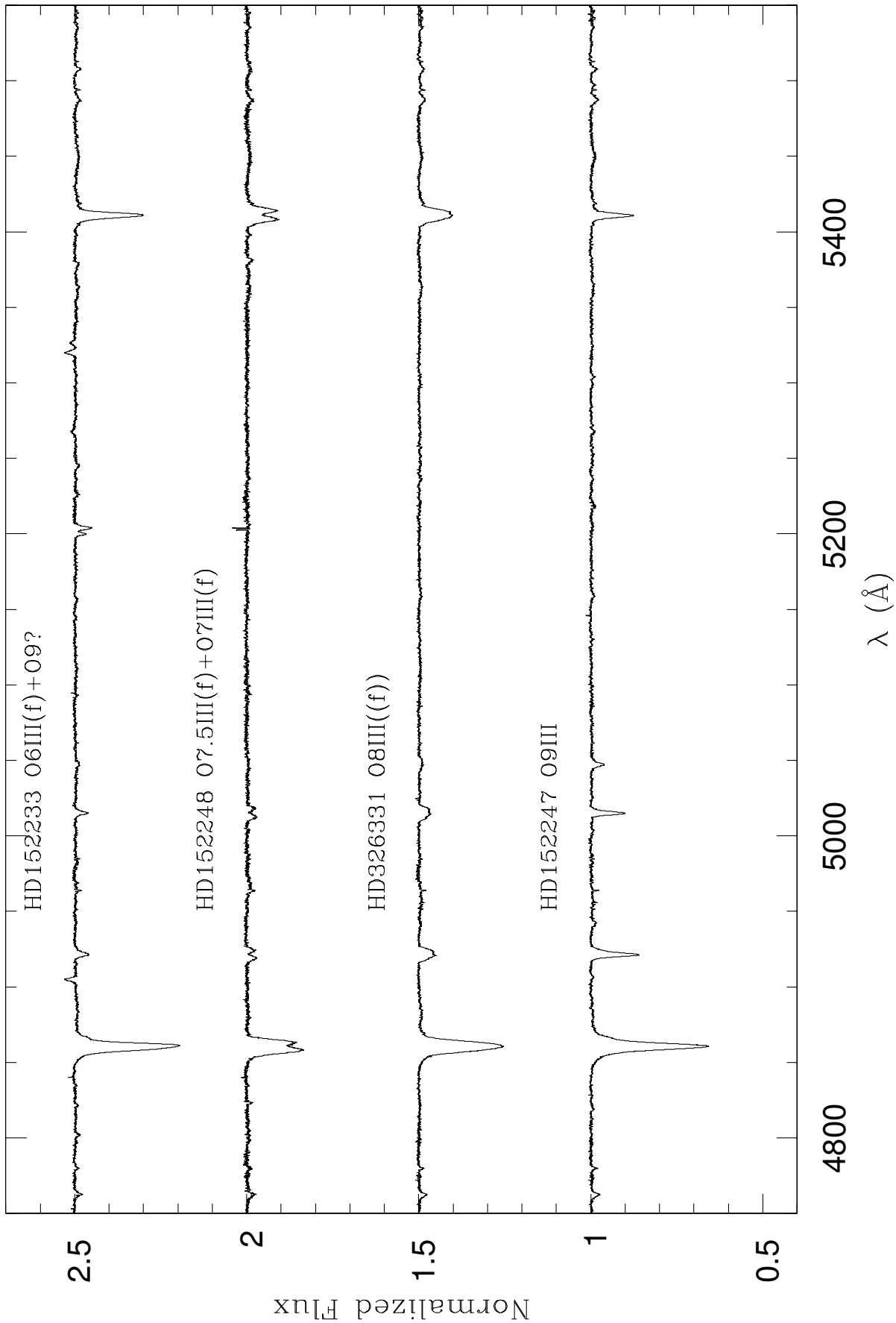
HD152233 O6III(f)+O9?
HD152248 O7.5III(f)+O7III(f)
HD326331 O8III((f))
HD152247 O9III
Normalized Flux
λ (Å)
0.5
1
1.5
2
2.5
4800
5000
5200
5400

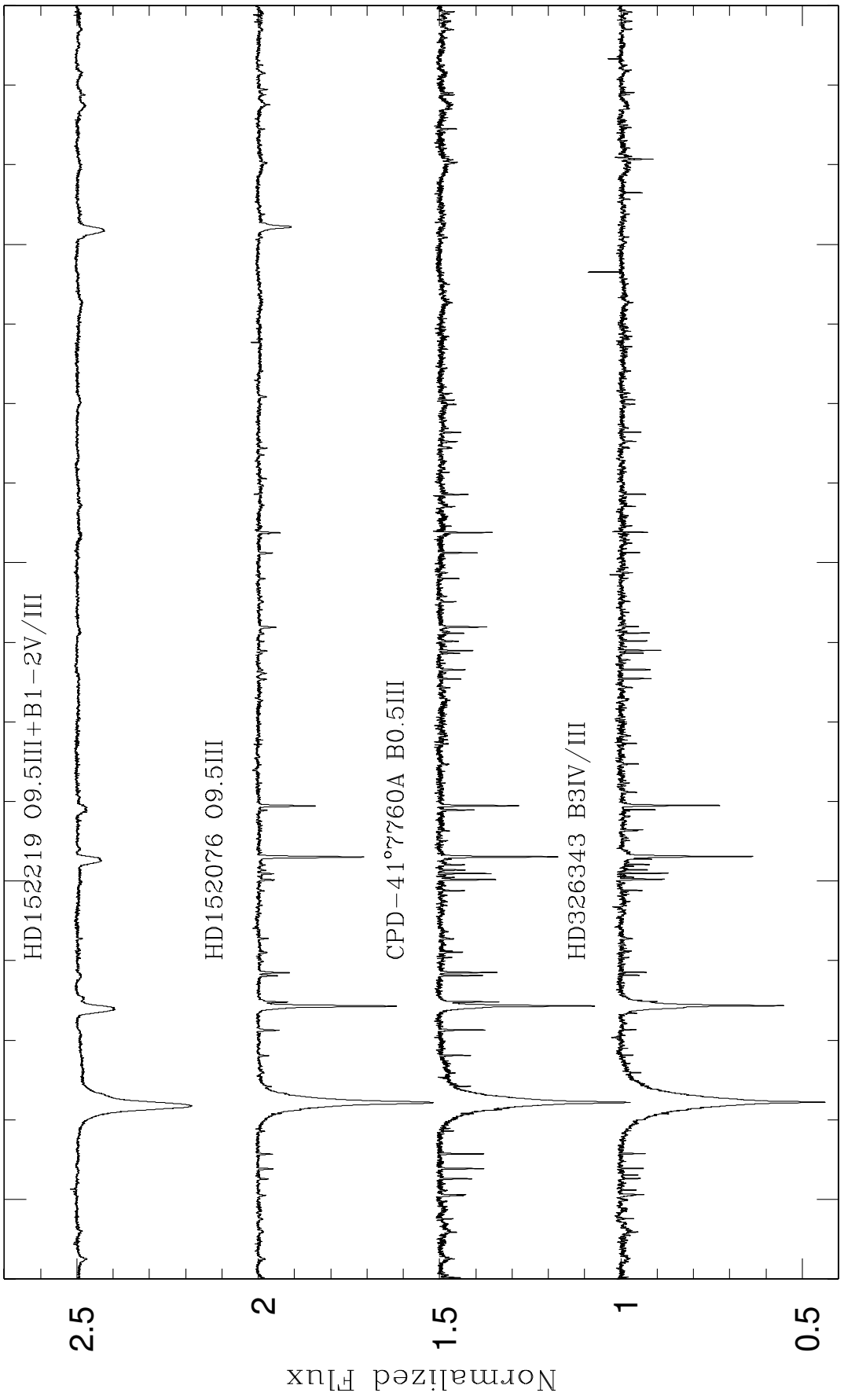
HD152219 O9.5III+B1−2V/III
HD152076 O9.5III
CPD−41°7760A B0.5III
HD326343 B3IV/III
Normalized Flux
λ (Å)
2.5
2
1.5
1
0.5
4800
5000
5200
5400

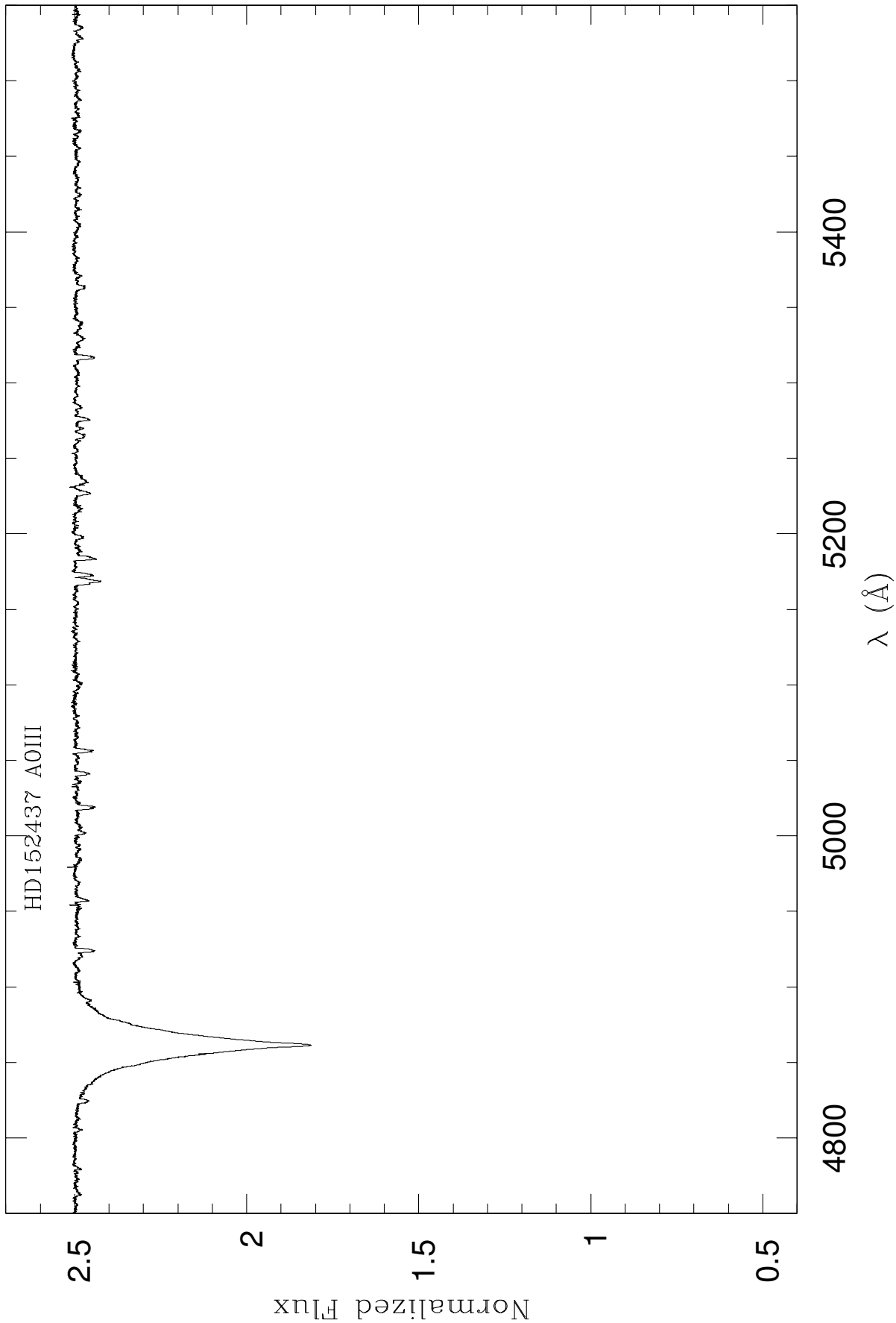
HD152437 A0III
Normalized Flux
2.5
2
1.5
1
0.5
4800
5000
5200
5400
λ (Å)

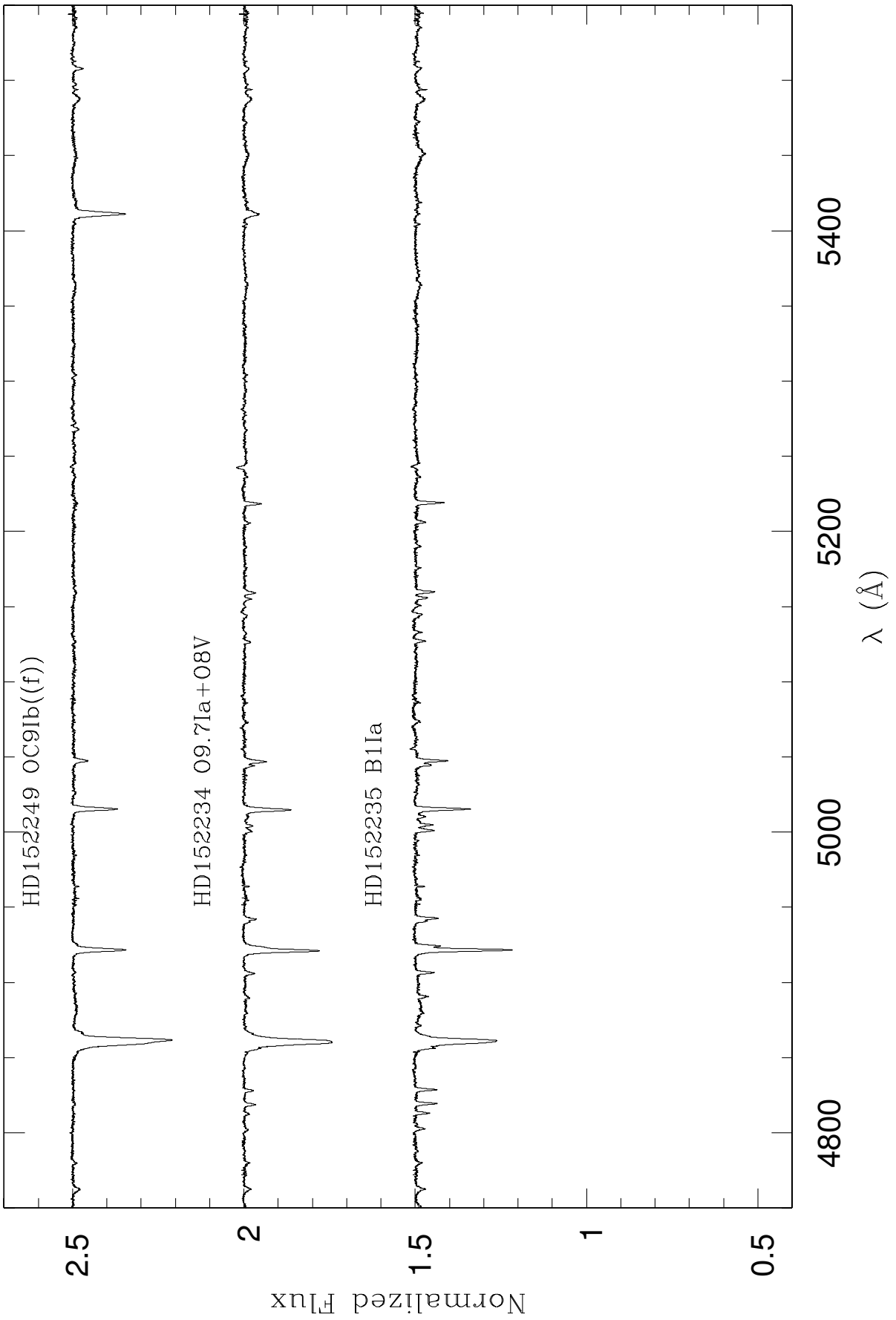
HD152249 OC9Ib((f))
HD152234 O9.7Ia+O8V
HD152235 B1Ia
Normalized Flux
λ (Å)
0.5
1
1.5
2
2.5
4800
5000
5200
5400

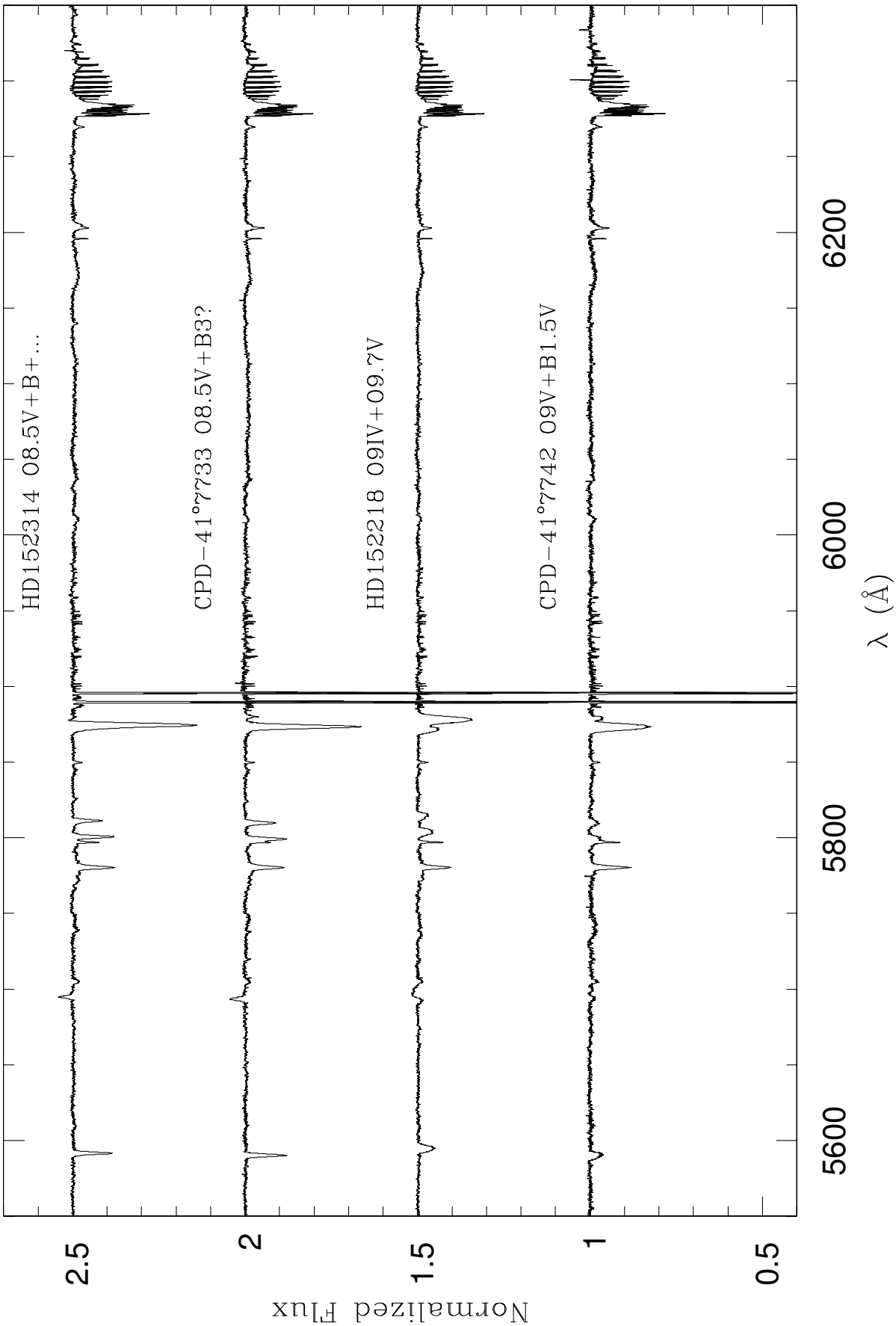
HD152314 O8.5V+B+...
CPD−41°7733 O8.5V+B3?
HD152218 O9IV+O9.7V
CPD−41°7742 O9V+B1.5V
Normalized Flux
λ (Å)
2.5
2
1.5
1
0.5
5600
5800
6000
6200

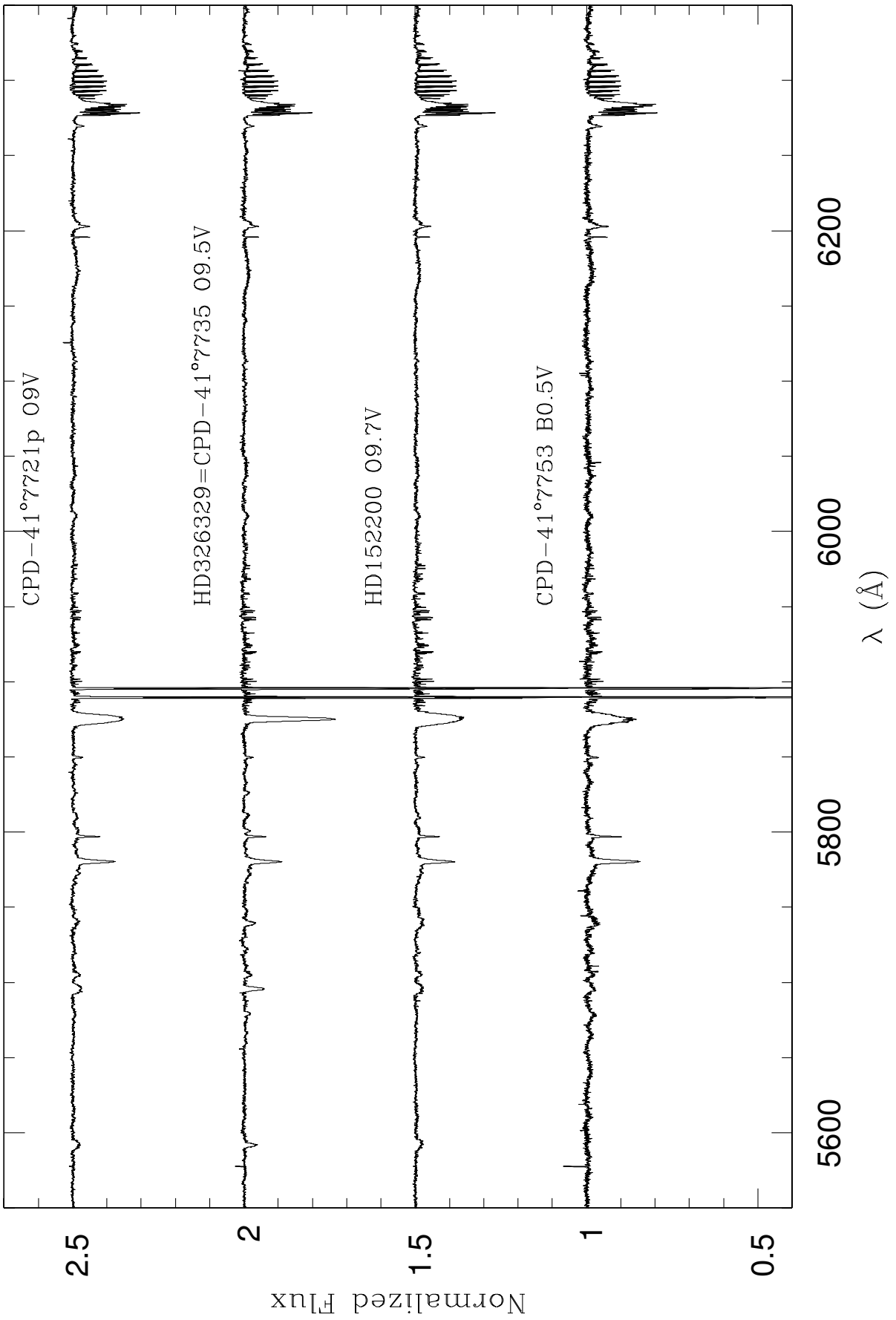
CPD−41°7721p O9V
HD326329=CPD−41°7735 O9.5V
HD152200 O9.7V
CPD−41°7753 B0.5V
Normalized Flux
λ (Å)
0.5
1
1.5
2
2.5
5600
5800
6000
6200

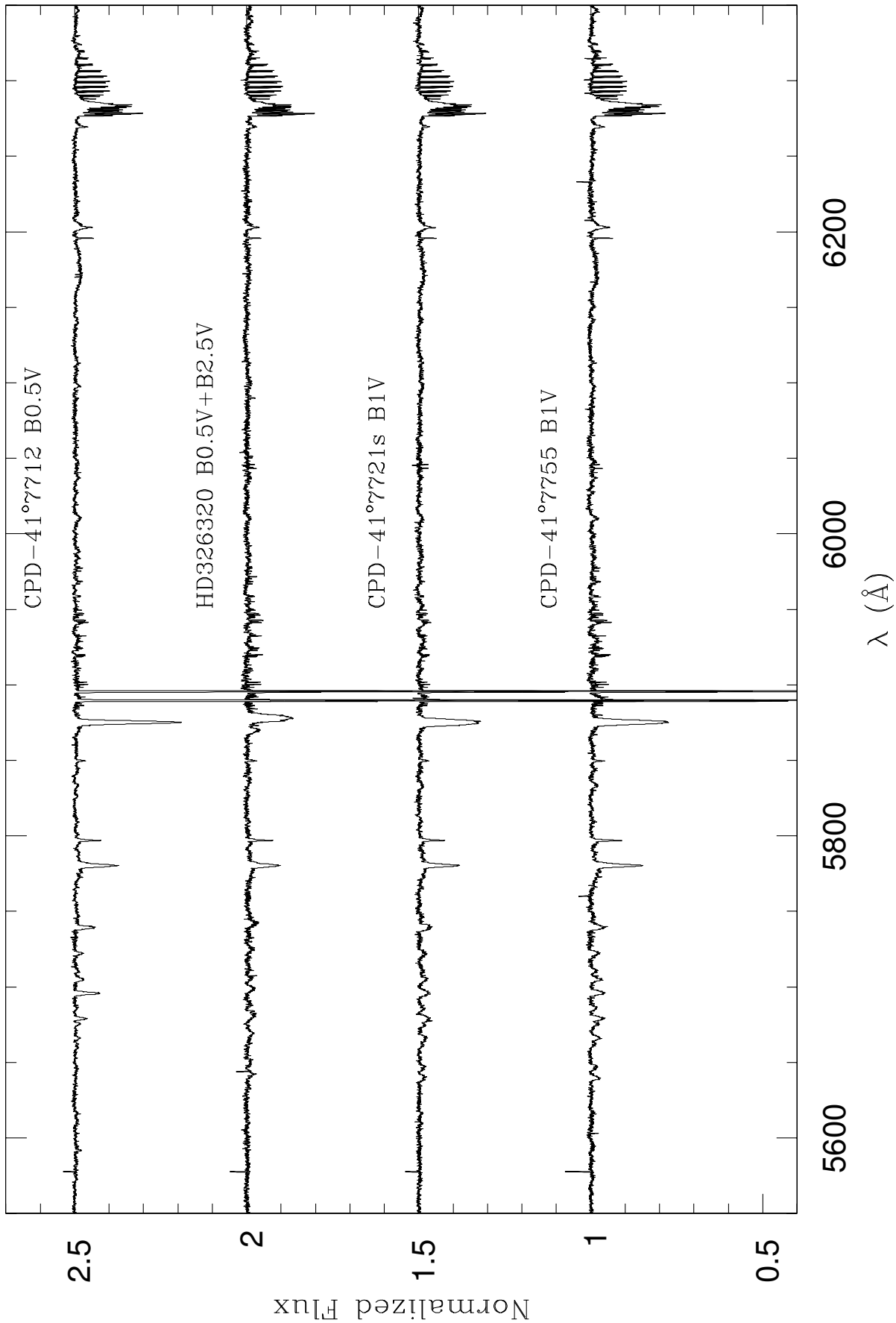
CPD−41°7712 B0.5V
HD326320 B0.5V+B2.5V
CPD−41°7721s B1V
CPD−41°7755 B1V
Normalized Flux
λ (Å)
2.5
2
1.5
1
0.5
5600
5800
6000
6200

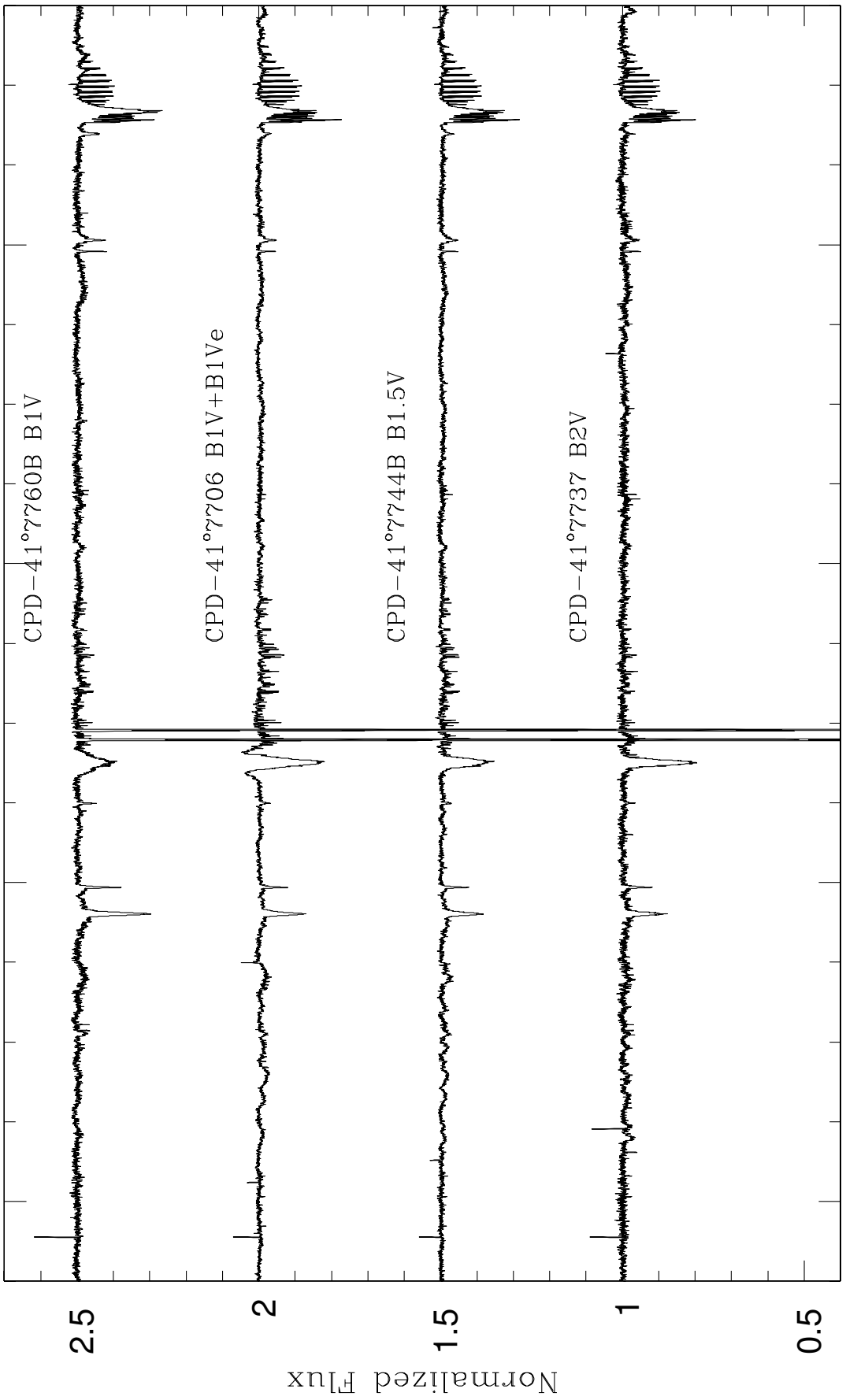
CPD−41°7760B B1V
CPD−41°7706 B1V+B1Ve
CPD−41°7744B B1.5V
CPD−41°7737 B2V
Normalized Flux
λ (Å)
0.5
1
1.5
2
2.5
5600
5800
6000
6200

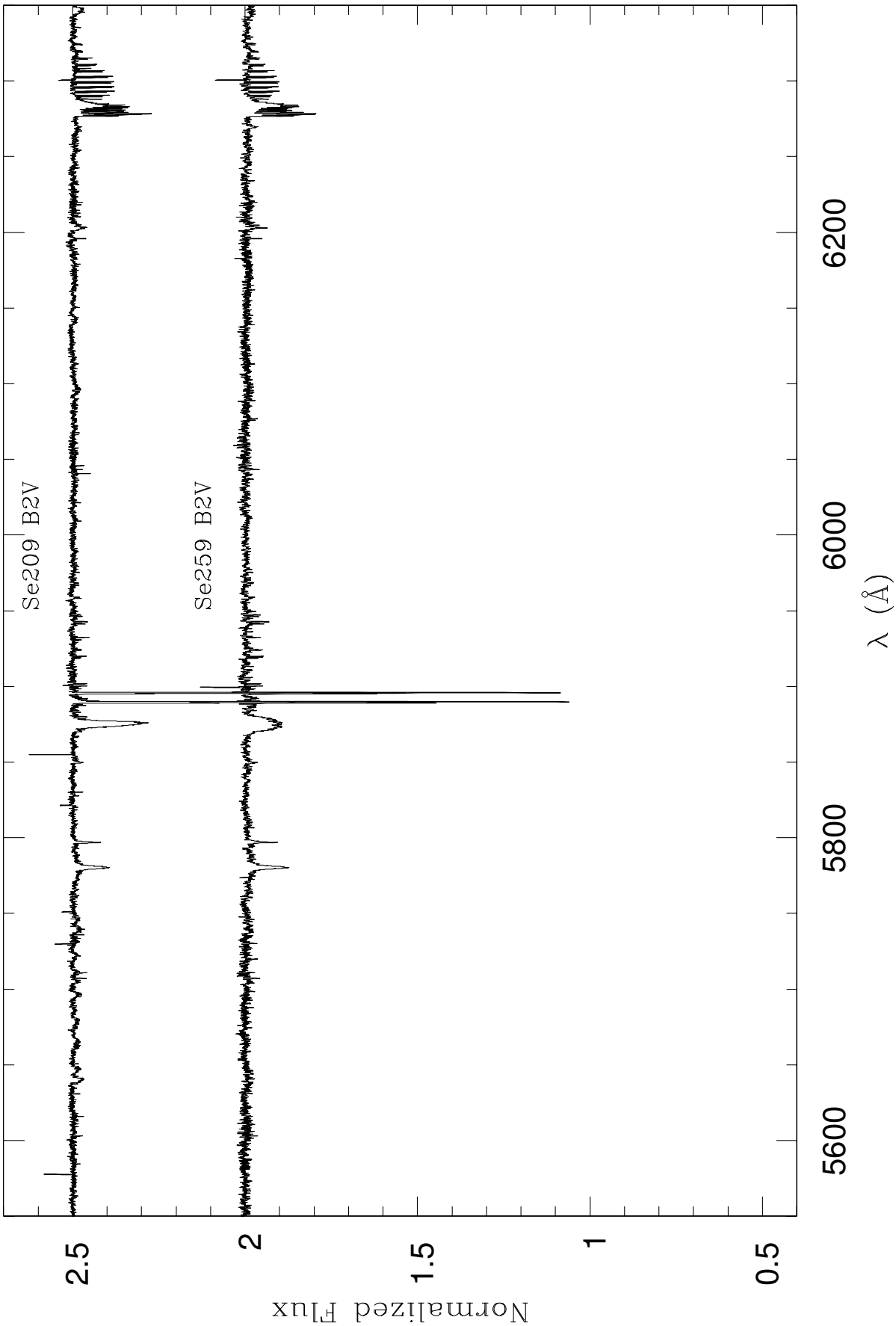
Se209 B2V
Se259 B2V
Normalized Flux
λ (Å)
2.5
2
1.5
1
0.5
5600
5800
6000
6200

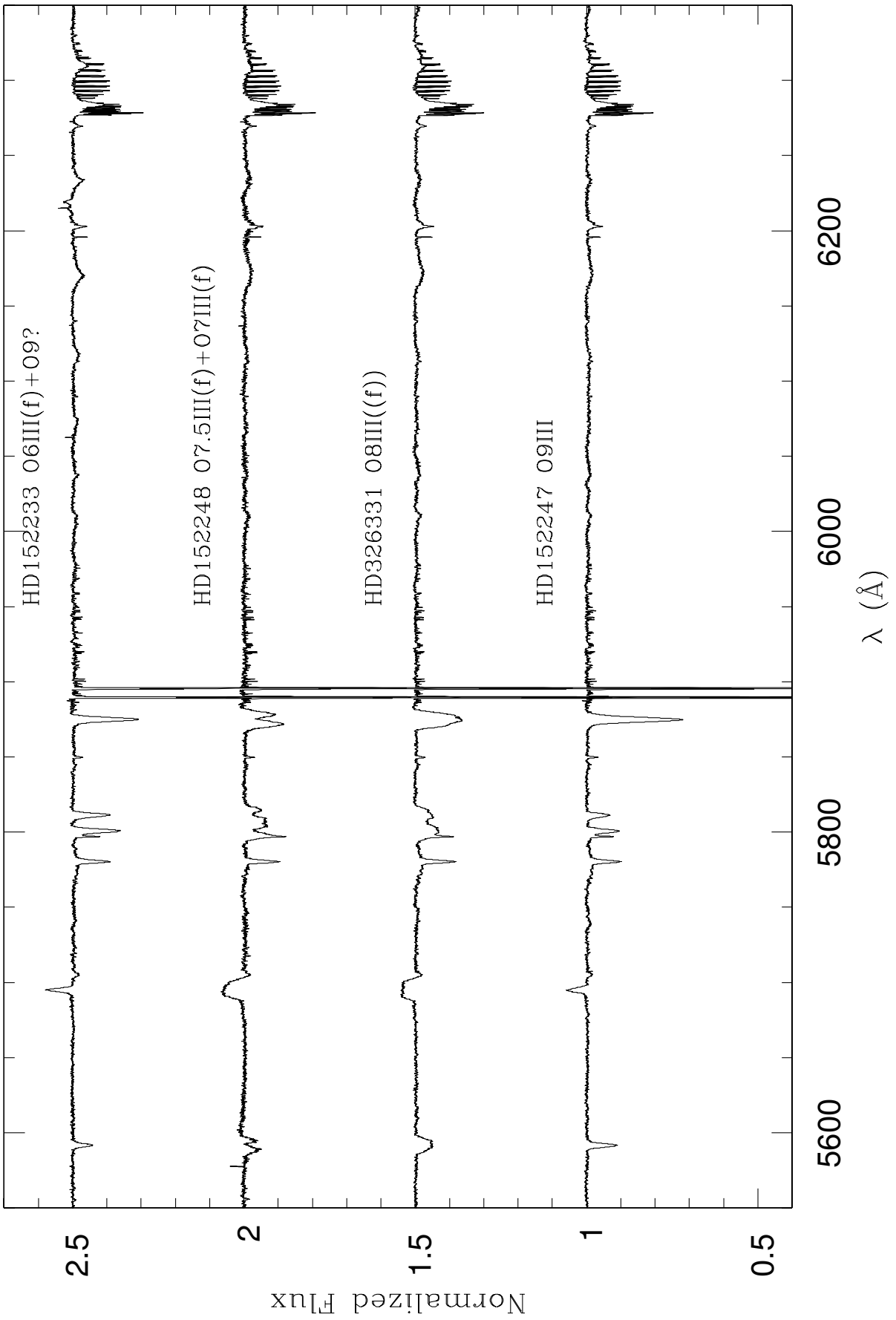
HD152233 O6III(f)+O9?
HD152248 O7.5III(f)+O7III(f)
HD326331 O8III((f))
HD152247 O9III
Normalized Flux
λ (Å)
2.5
2
1.5
1
0.5
5600
5800
6000
6200

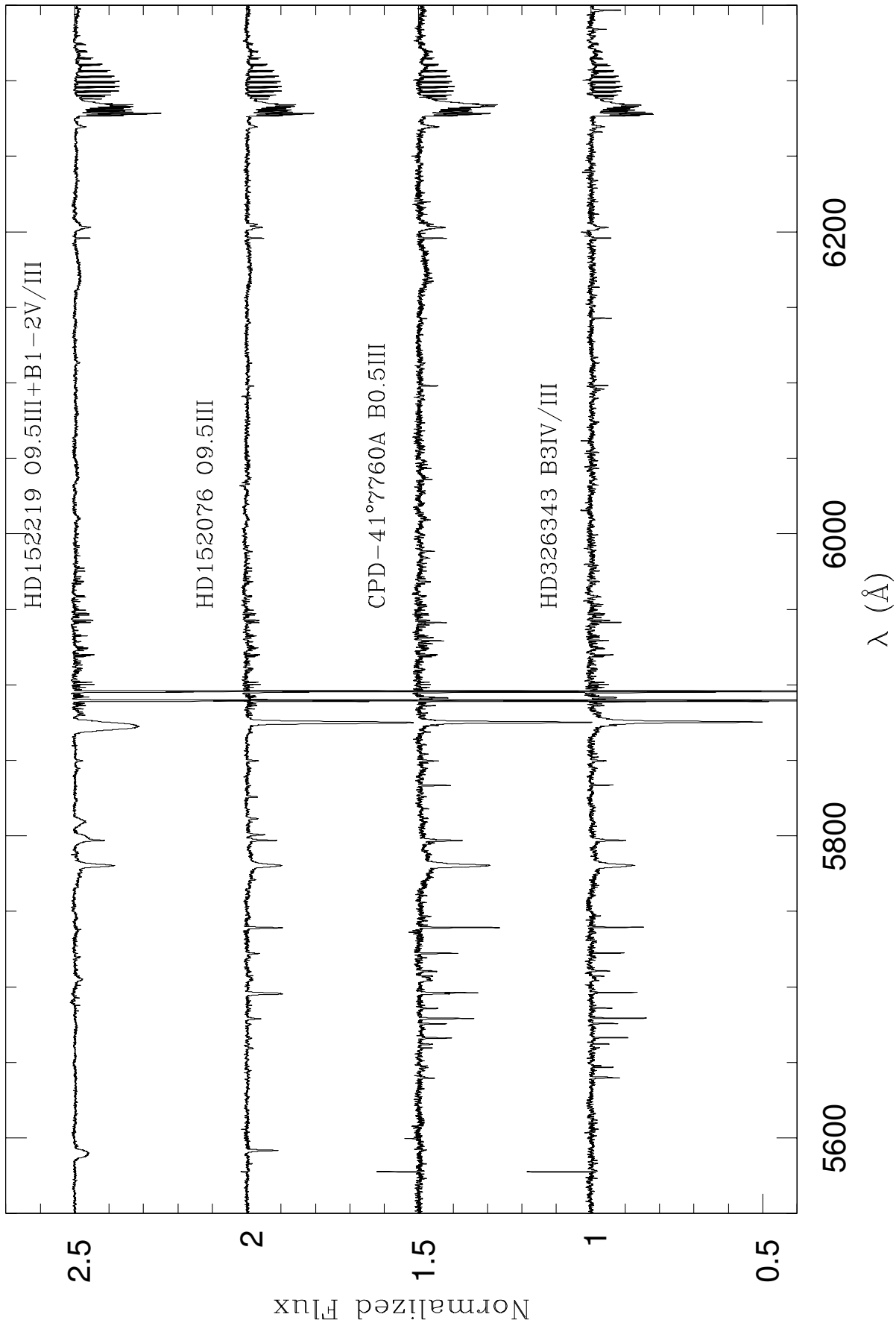
HD152219 O9.5III+B1−2V/III
HD152076 O9.5III
CPD−41°7760A B0.5III
HD326343 B3IV/III
Normalized Flux
λ (Å)
2.5
2
1.5
1
0.5
5600
5800
6000
6200

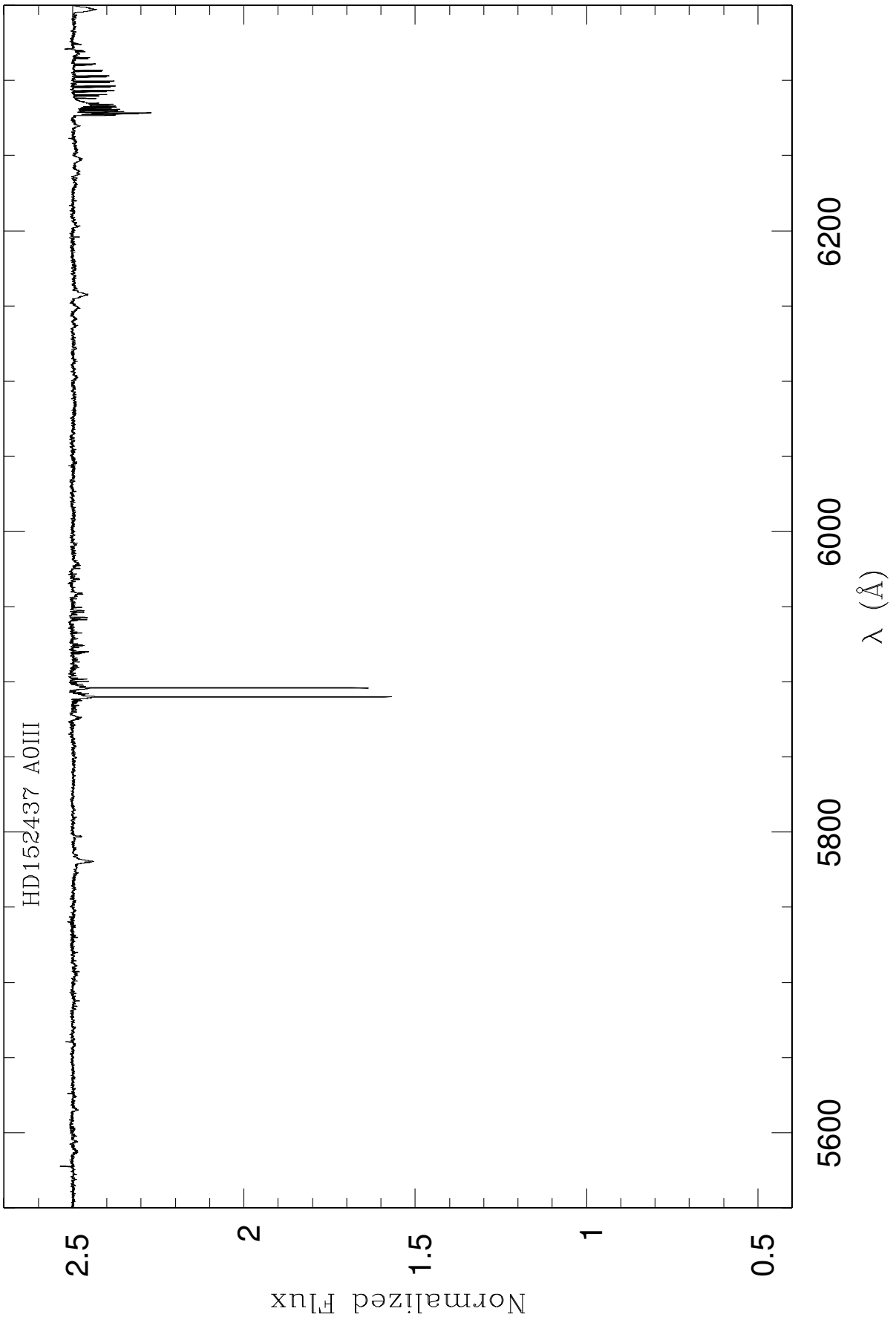
HD152437 A0III
Normalized Flux
2.5
2
1.5
1
0.5
5600
5800
6000
6200
λ (Å)

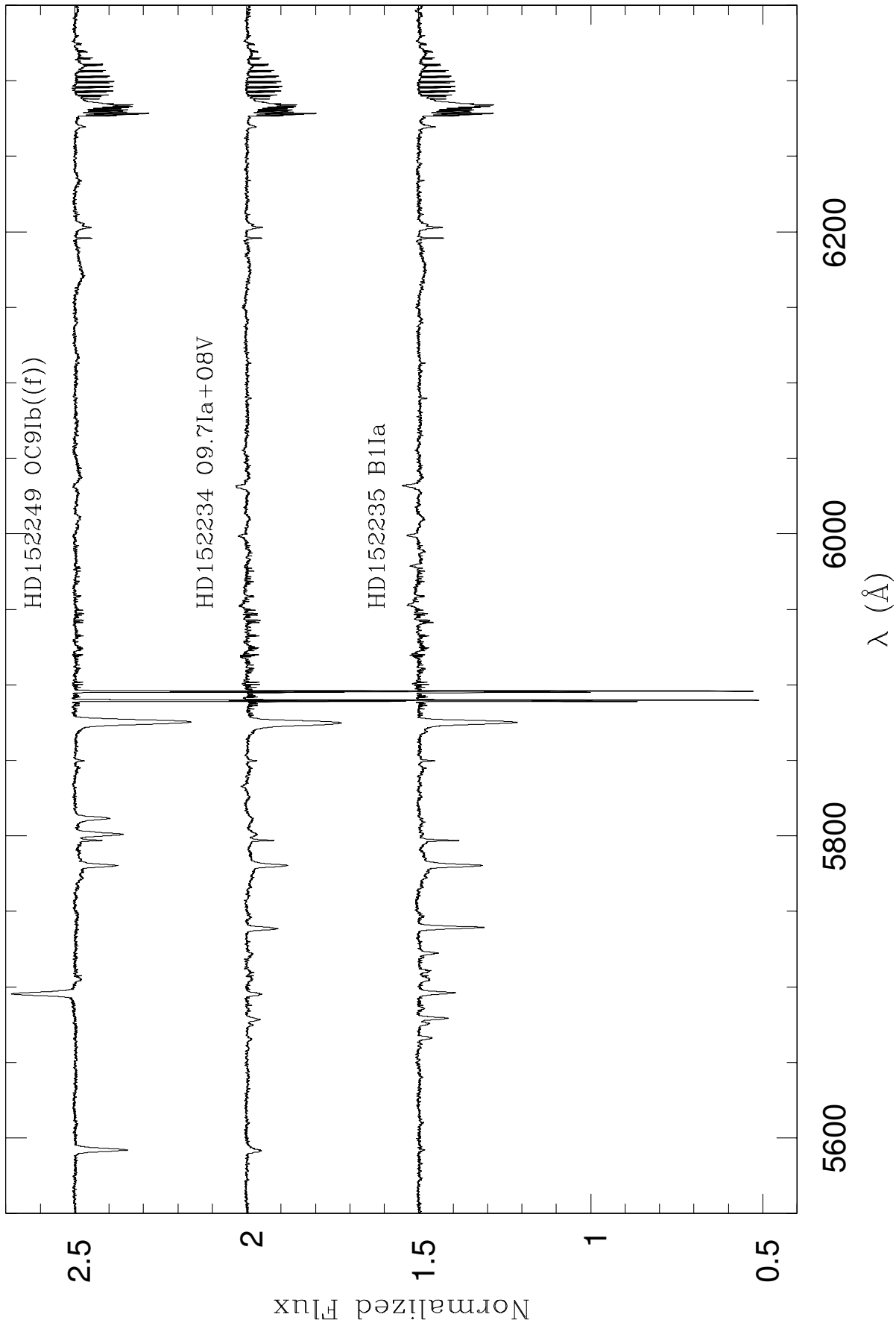
HD152249 OC9Ib((f))
HD152234 O9.7Ia+O8V
HD152235 B1Ia
Normalized Flux
λ (Å)
2.5
2
1.5
1
0.5
5600
5800
6000
6200

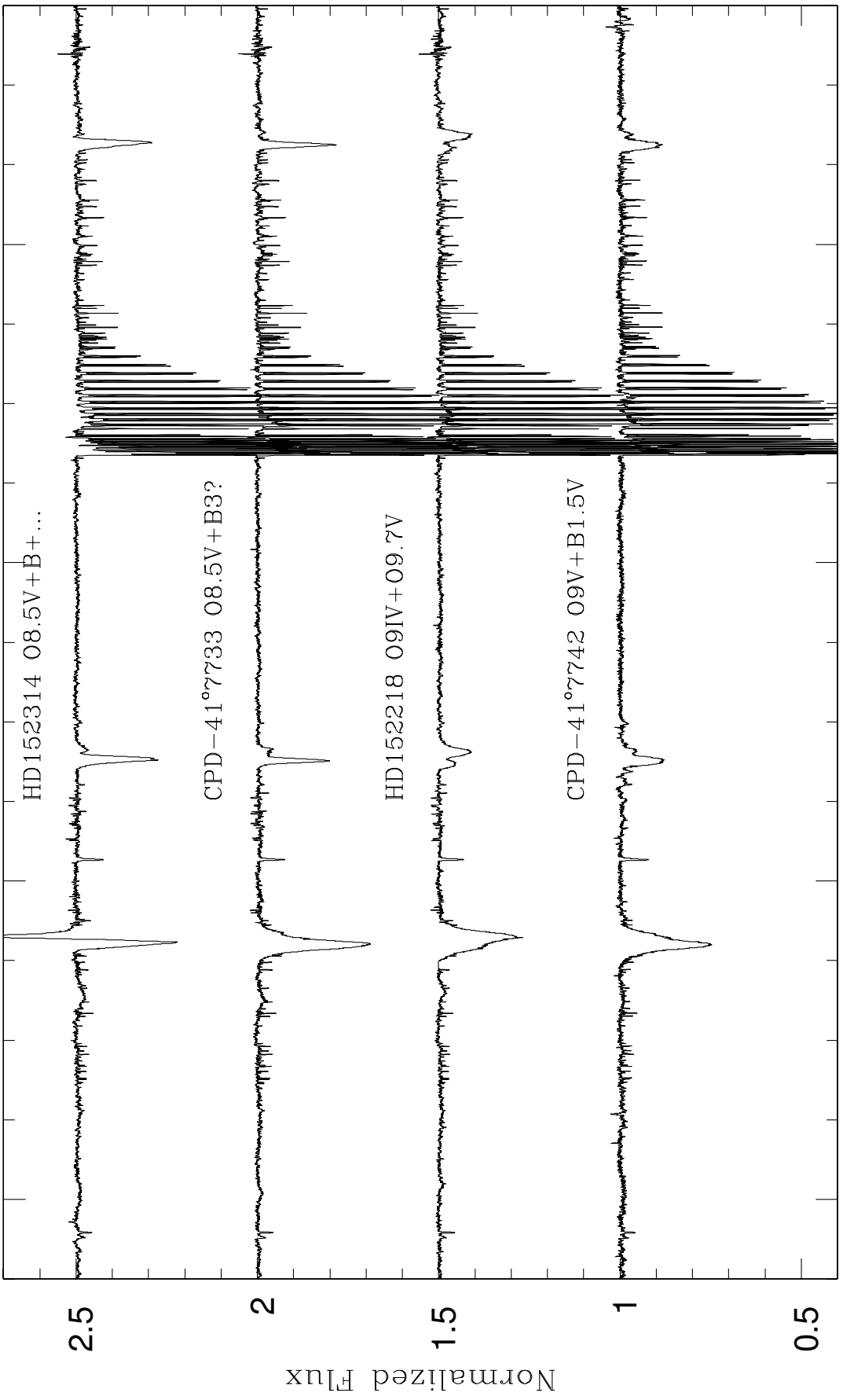
HD152314 O8.5V+B+...
CPD−41°7733 O8.5V+B3?
HD152218 O9IV+O9.7V
CPD−41°7742 O9V+B1.5V
Normalized Flux
λ (Å)
2.5
2
1.5
1
0.5
6400
6600
6800
7000

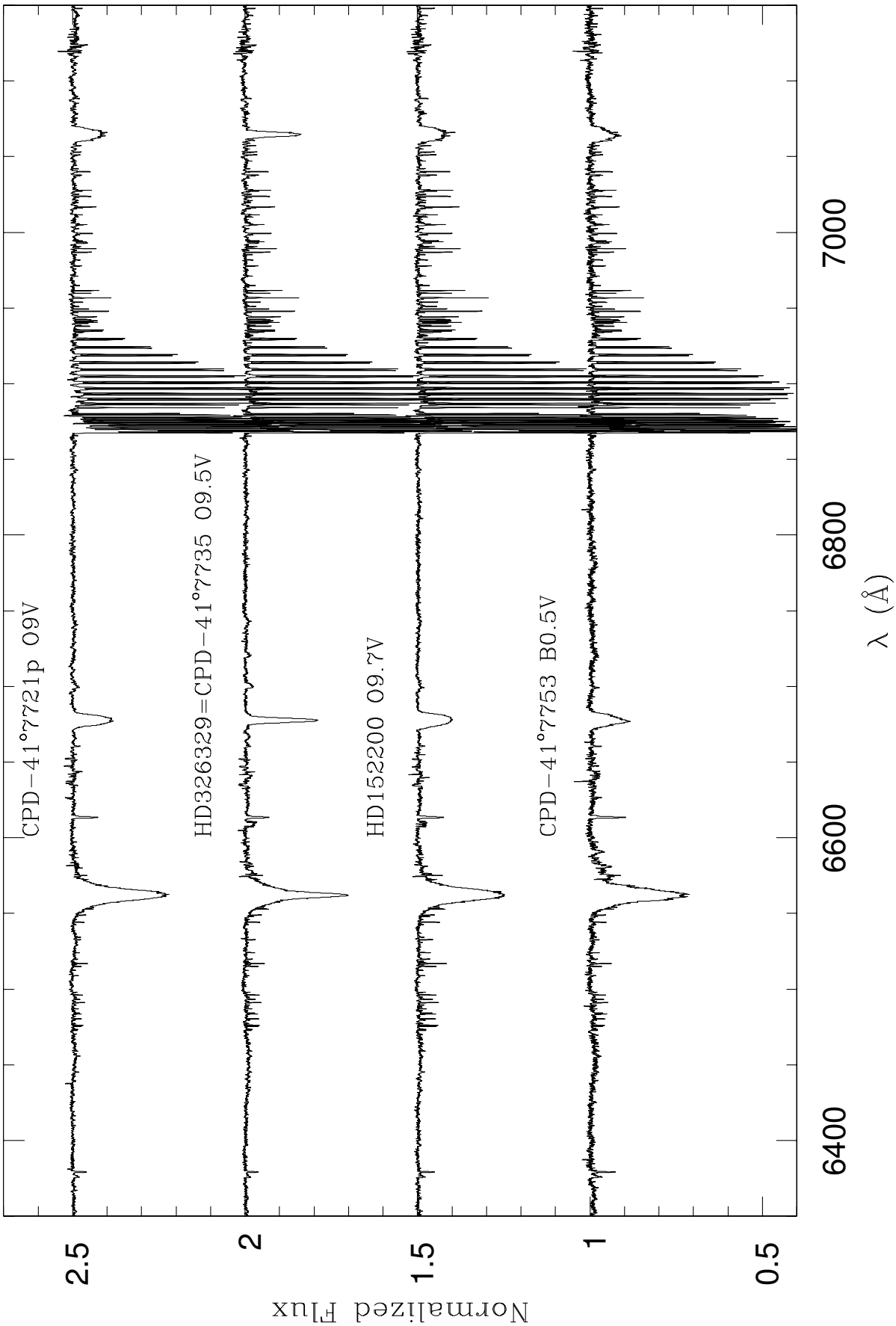
CPD−41°7721p O9V
HD326329=CPD−41°7735 O9.5V
HD152200 O9.7V
CPD−41°7753 B0.5V
Normalized Flux
λ (Å)
0.5
1
1.5
2
2.5
6400
6600
6800
7000

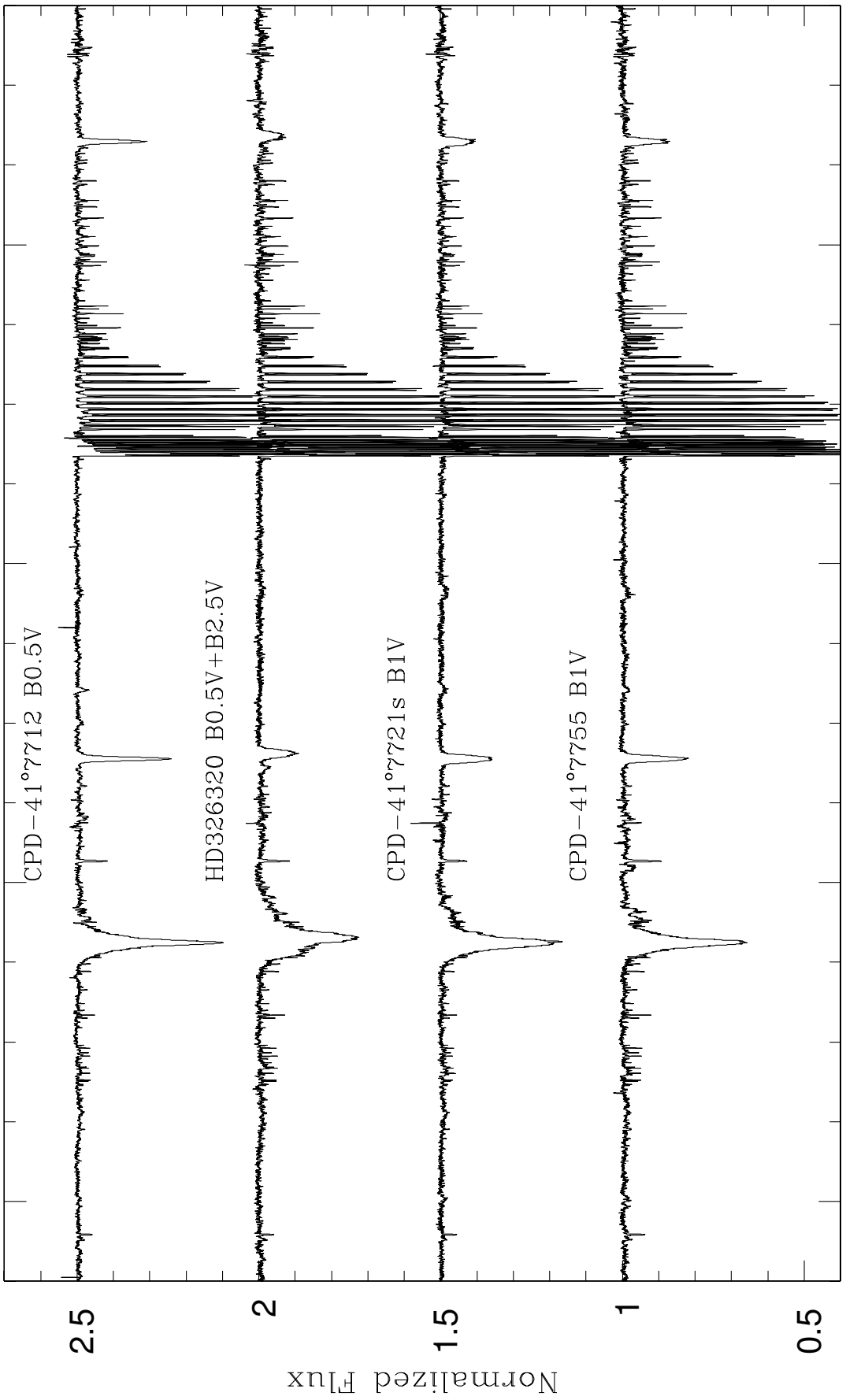
CPD−41°7712 B0.5V
HD326320 B0.5V+B2.5V
CPD−41°7721s B1V
CPD−41°7755 B1V
Normalized Flux
λ (Å)
0.5
1
1.5
2
2.5
6400
6600
6800
7000

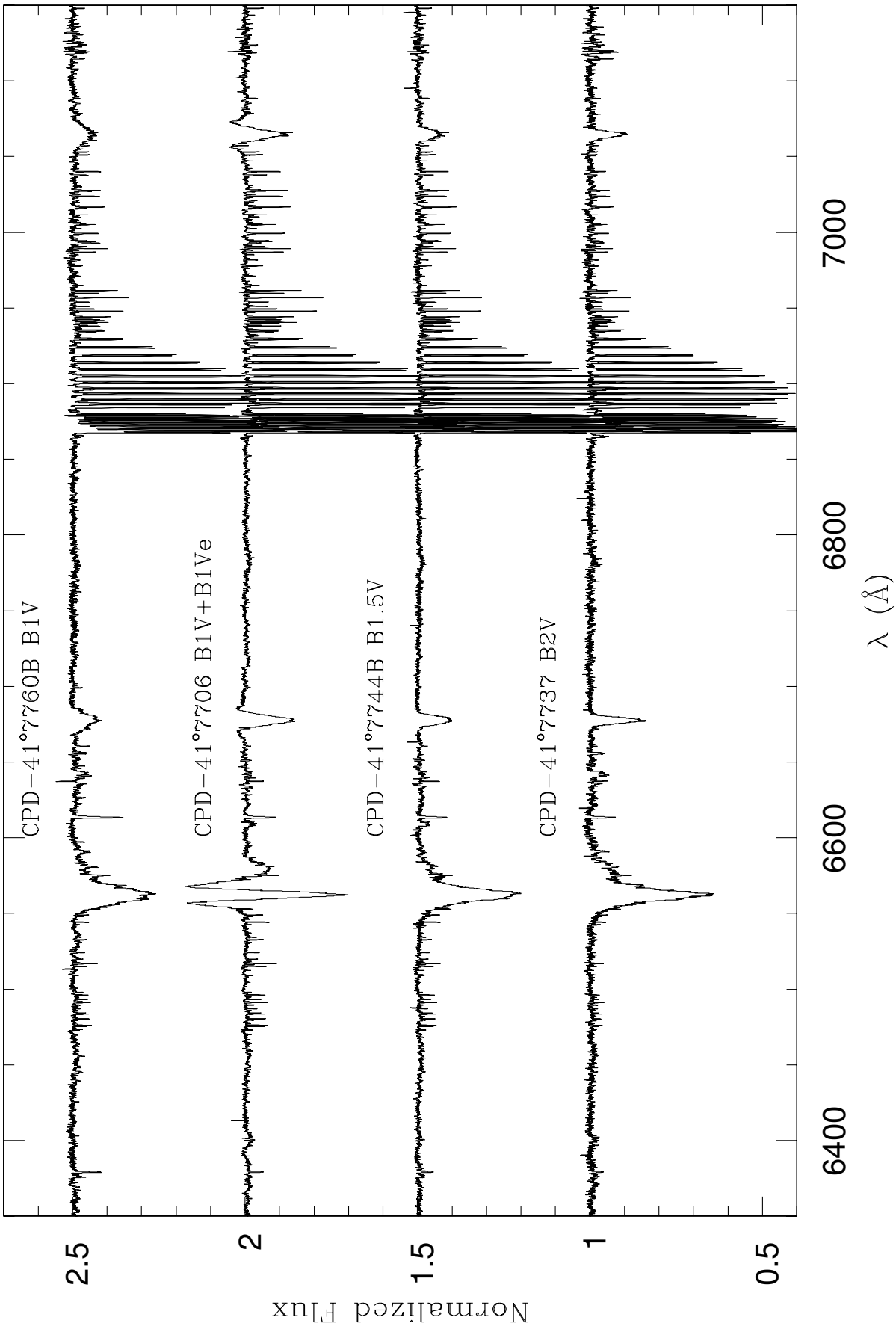
CPD−41°7760B B1V
CPD−41°7706 B1V+B1Ve
CPD−41°7744B B1.5V
CPD−41°7737 B2V
Normalized Flux
λ (Å)
2.5
2
1.5
1
0.5
6400
6600
6800
7000

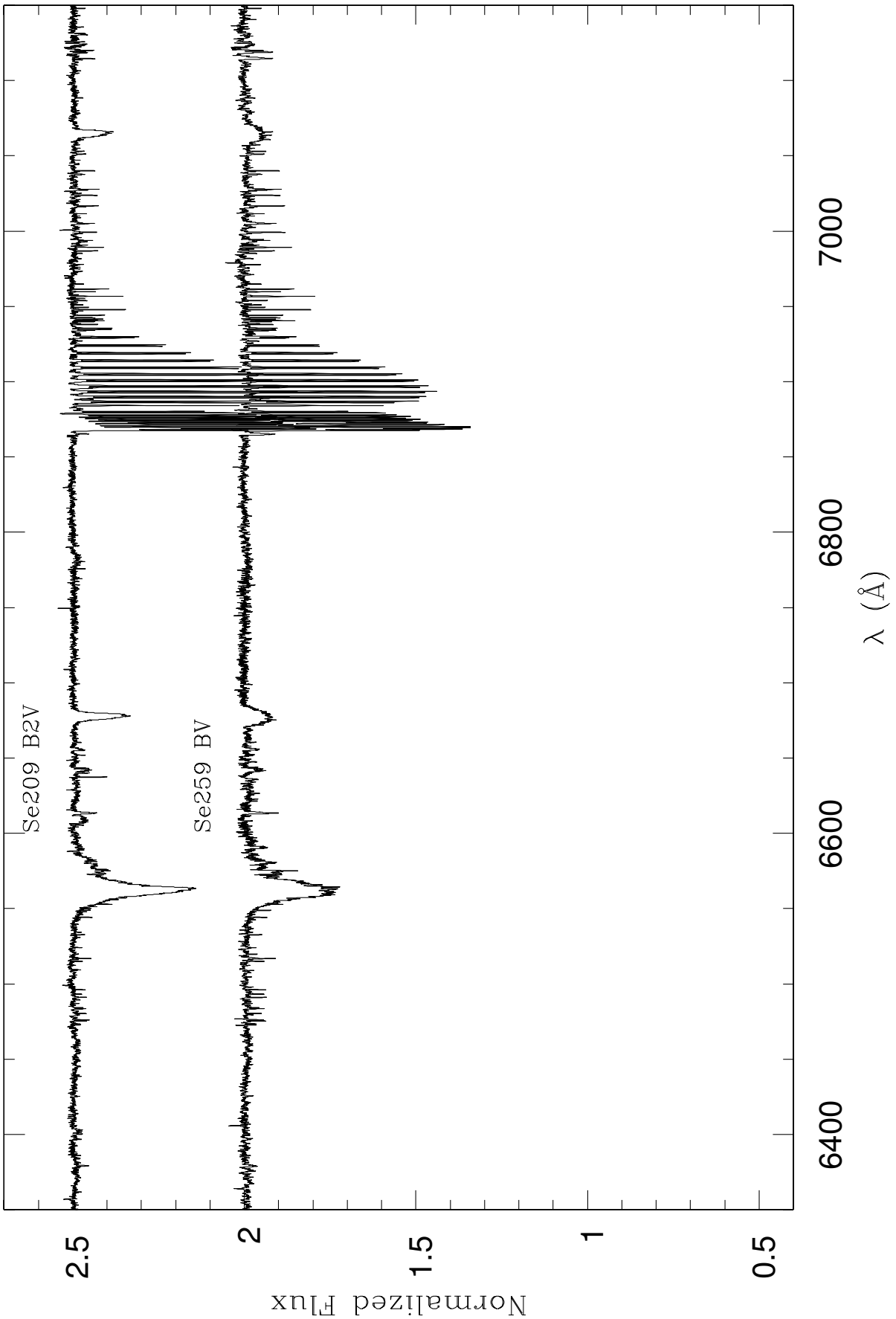
Se209 B2V
Se259 BV
Normalized Flux
λ (Å)
0.5
1
1.5
2
2.5
6400
6600
6800
7000

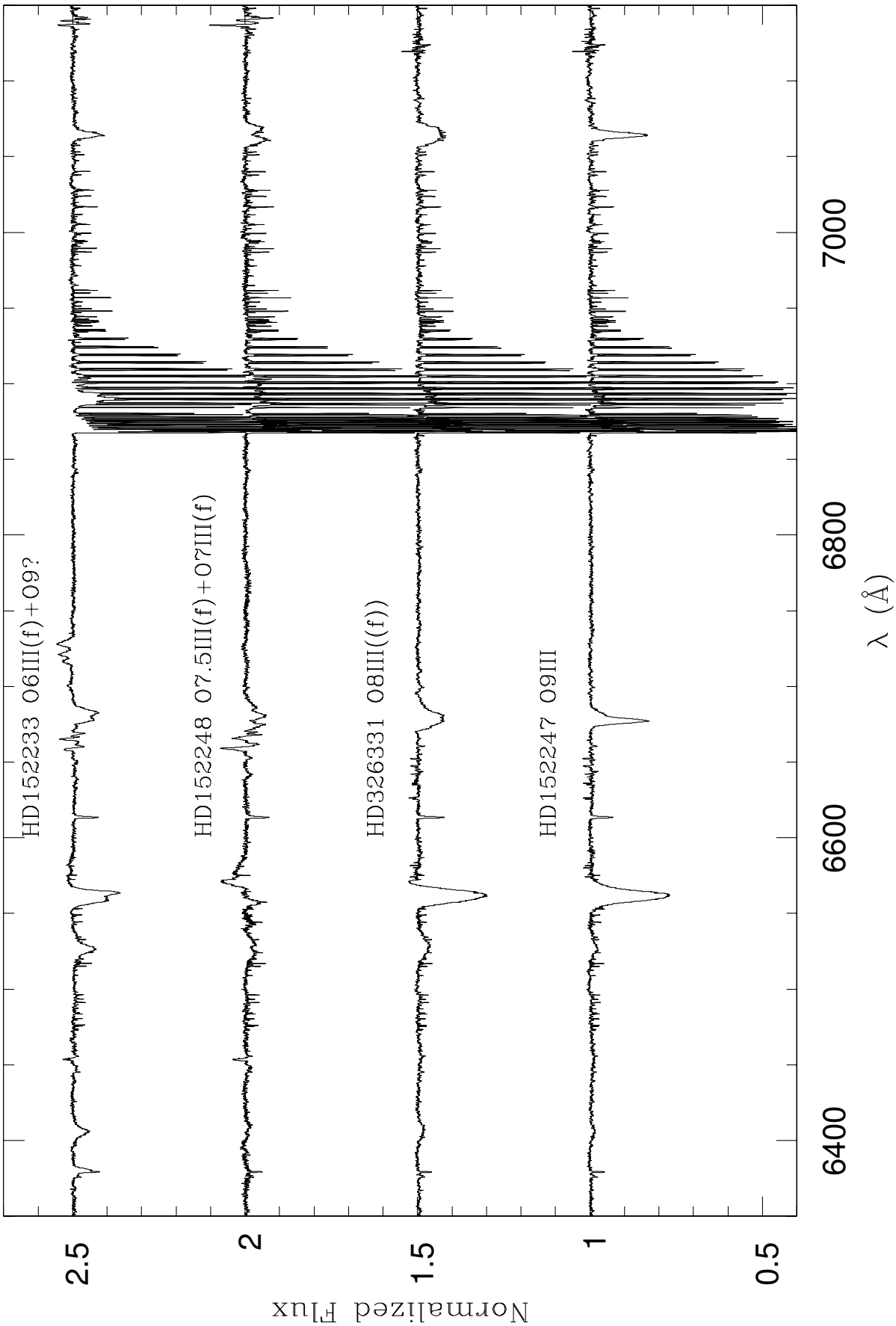
HD152233 O6III(f)+O9?
HD152248 O7.5III(f)+O7III(f)
HD326331 O8III((f))
HD152247 O9III
Normalized Flux
λ (Å)
2.5
2
1.5
1
0.5
6400
6600
6800
7000

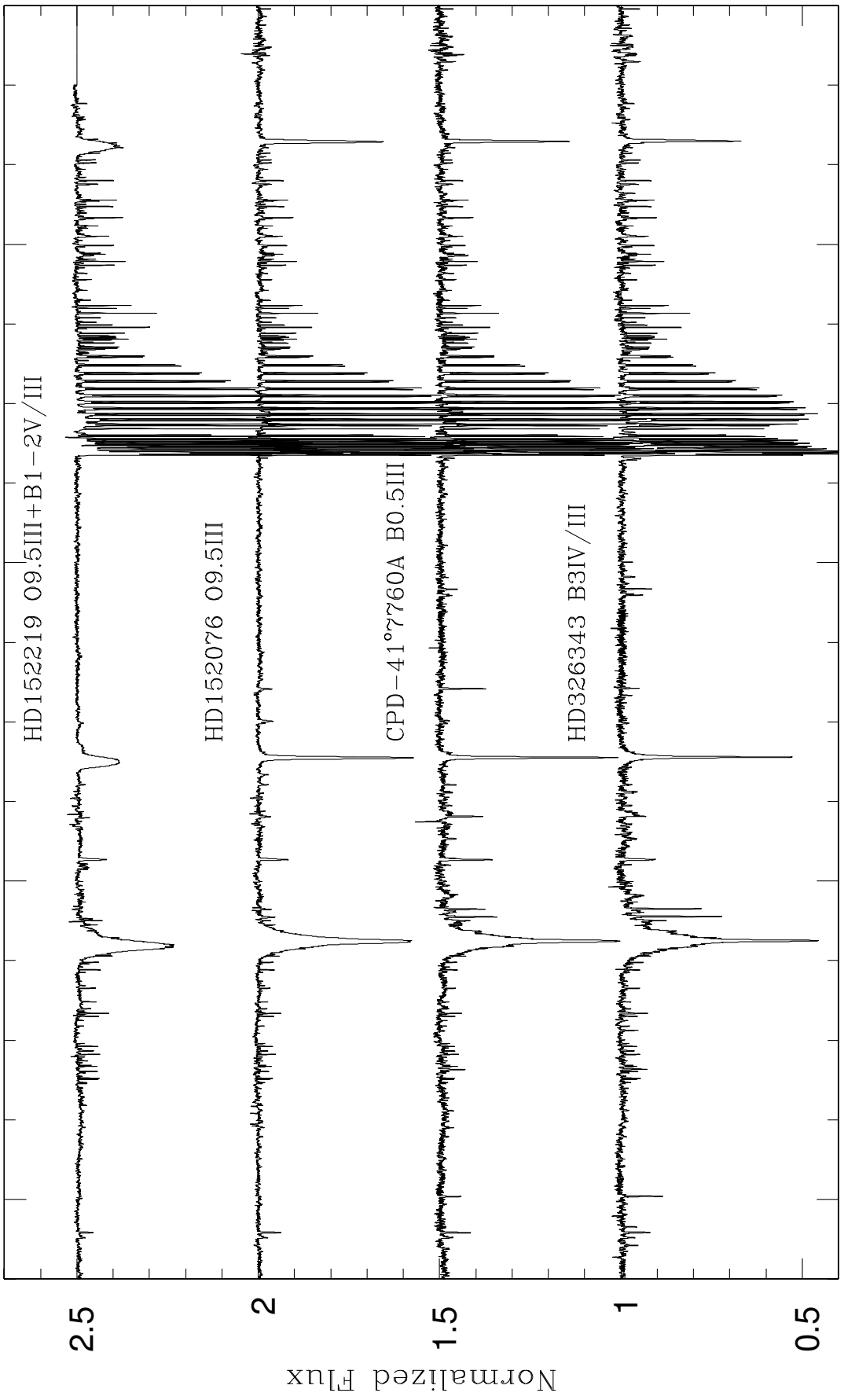
HD152219 O9.5III+B1−2V/III
HD152076 O9.5III
CPD−41°7760A B0.5III
HD326343 B3IV/III
Normalized Flux
λ (Å)
0.5
1
1.5
2
2.5
6400
6600
6800
7000

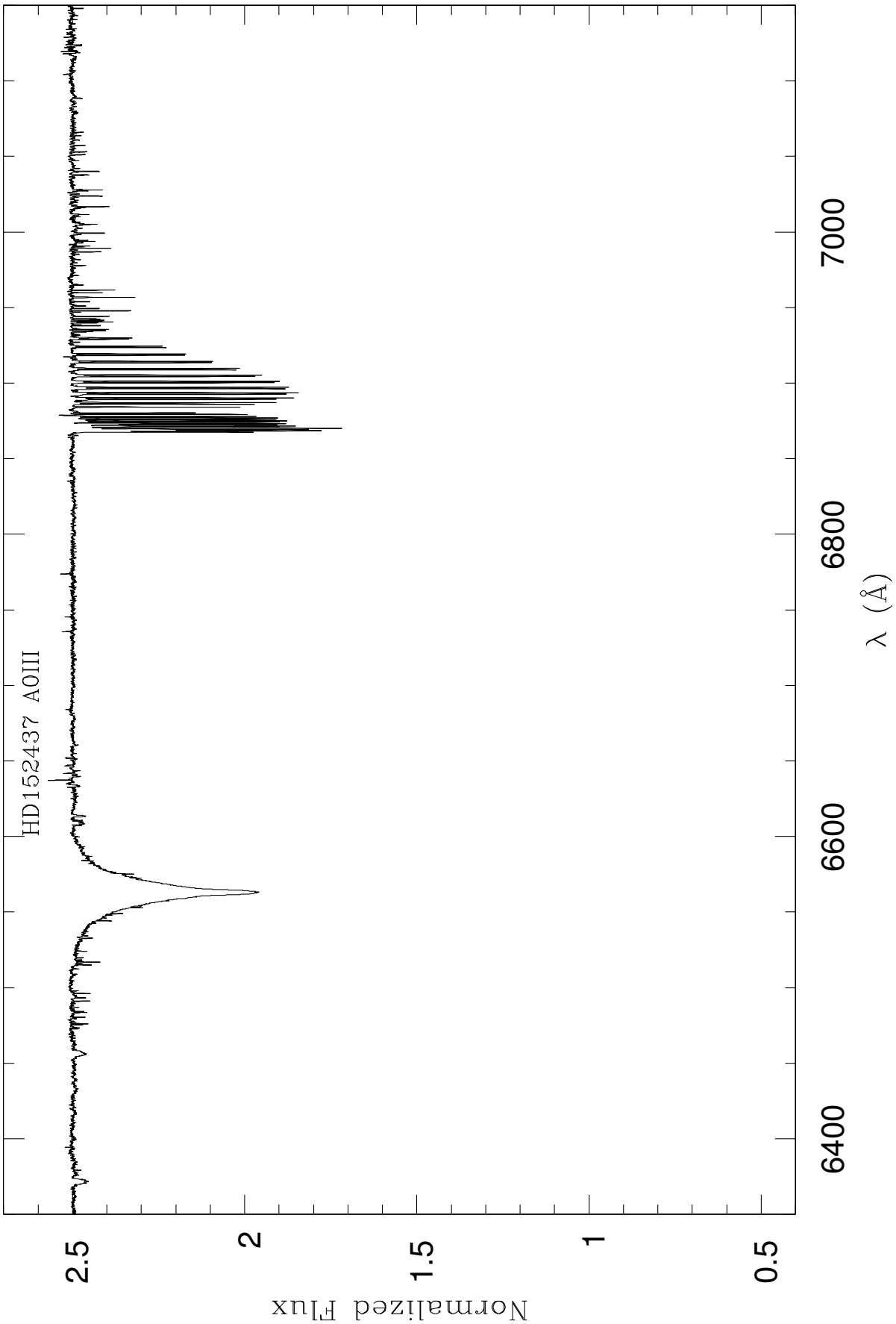
HD152437 A0III
Normalized Flux
2.5
2
1.5
1
0.5
6400
6600
6800
7000
λ (Å)

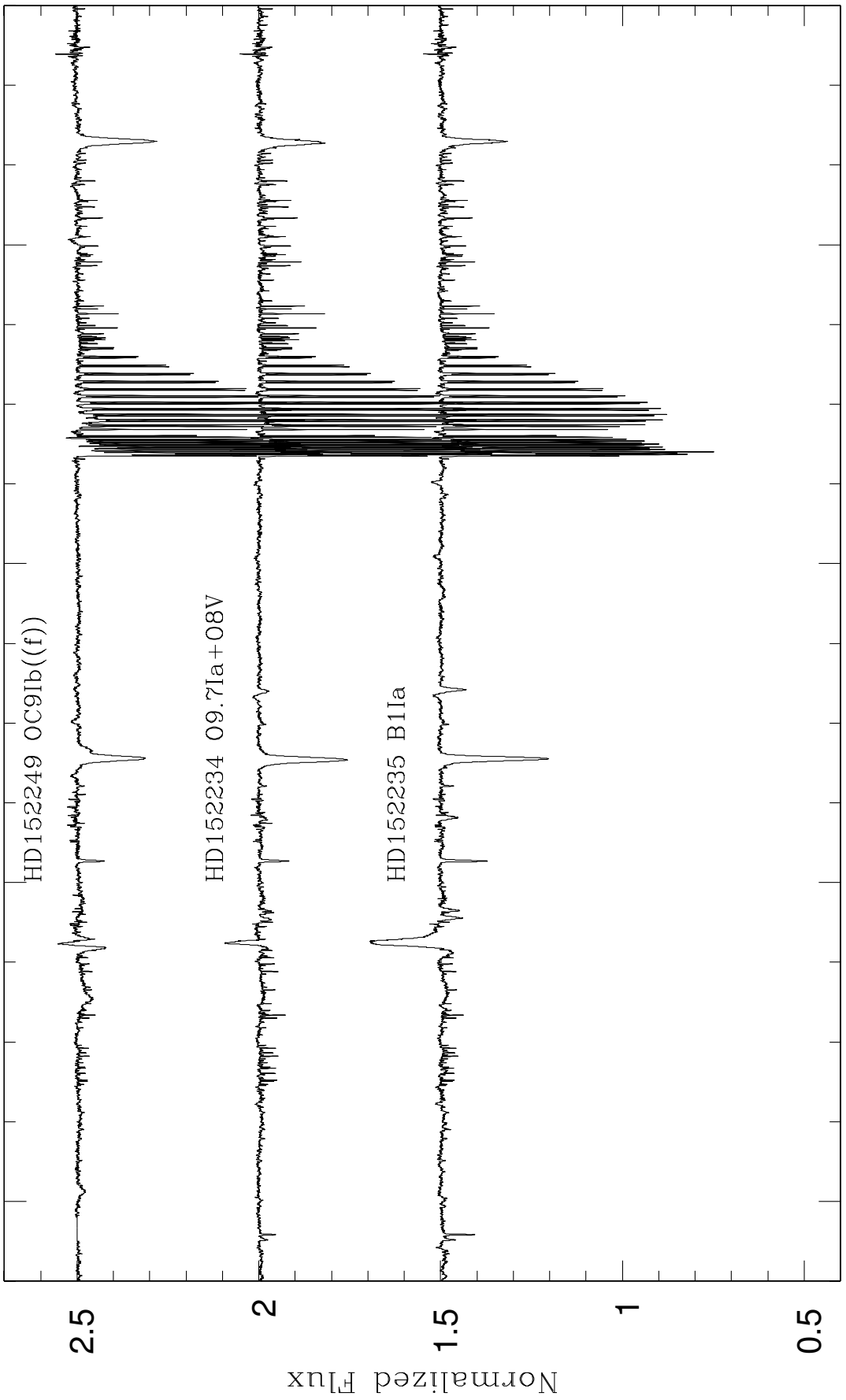
HD152249 OC9Ib((f))
HD152234 O9.7Ia+O8V
HD152235 B1Ia
Normalized Flux
λ (Å)
0.5
1
1.5
2
2.5
6400
6600
6800
7000

Appendix B

An X-ray view of the young open cluster NGC 6231: *online material*

This appendix provides the complementary tables and figures related to the paper entitled *An XMM-Newton view of the young open cluster NGC 6231 II. The early-type star population* (Sana et al. 2005g) presented in Chap. 2. This *online material* has been proposed for electronic publication only. We first present a summary of the performed census of the early-type stars in the XMM-*Newton* FOV (Table 2, p. 280). In Figs. 2 to 6 (p. 282 to 288), we then provide the EPIC spectra of the different early-type X-ray emitters as described in Sana et al. (2005g, see p. 43)

Table 2. Census of the early-type stars in the XMM-*Newton* FOV. The first seven columns give various identifiers. Among these, Col. 6 indicates the associated X-ray source, if any, using the numbering scheme of Paper I. A 'r.' means that large residuals were observed in the EPIC image at the position of the early-type star. The '+' and '*' symbols joined to the X-ray source number indicate respectively that the X-ray source position is probably biased or that the distance d_{cc} to the associated optical source is between 3″ and 3.″6 (see Sect. 3). Col. 8 provides the adopted positions while Cols. 9 and 10 list the V magnitudes and $B-V$ colours obtained from the SSB05 catalogue. The adopted visual (M_V) and bolometric (M_{bol}) absolute magnitudes are provided in Cols. 11 and 12. The adopted spectral types and the corresponding references are given in Cols. 13 and 14 while the last column provides miscellaneous notes about the objects, together with the related references. The meaning of the abbreviations used is given at the bottom of the table.

Object IDs.							α δ (J2000.0)	V	$B-V$	M_V	M_{bol}	Sp. Type	Ref. [a]	Comments [a,b]
HD	CPD−41°	Se68	SBL98	BVF99	X#	SSB05	hh mm ss.s ±dd am as.s							
[1]	[2]	[3]	[4]	[5]	[6]	[7]	[8]	[9]	[10]	[11]	[12]	[13]	[14]	[15]
–	–	724	–	–	r.	1107	16 53 06.06 −41 53 18.5	11.075	0.428	−2.40	−5.56	B0V/IV	GM01	
152076	7684	–	–	–	006	1147	16 53 07.31 −41 43 45.4	8.471	0.240	−4.38	−7.39	O9.5III	San05	
–	–	723	–	–	–	1150	16 53 07.39 −41 53 31.0	11.424	0.455	−1.81	−3.75	B3V	GM01	nm? (GM01)
–	–	726	–	–	–	1176	16 53 08.18 −41 47 11.9	10.833	0.366	−2.30	−5.00	B1V	GM01	
326343	7688	616	019	–	022	1500	16 53 19.40 −41 54 29.8	10.598	0.416	−2.51	−4.11	B3III	San05	
326326	7689	518	020	–	–	1520	16 53 20.33 −41 48 26.6	10.914	0.325	−2.02	−4.37	B2V	Lav72	
326327	7697	28	113	–	–	2088	16 53 39.07 −41 47 47.6	9.719	0.279	−3.08	−5.62	B1.5IVe+shell	LM80	βCep? (BaE85) SB1?(GM01)
–	–	30	134	–	–	2171	16 53 41.96 −41 48 20.5	11.601	0.349	−1.05	−2.07	B7V	SIMBAD	
–	–	41	149	–	078	2236	16 53 44.04 −41 50 36.7	12.413	0.307	−0.28	−1.98	B4V	SIMBAD	
326328	7700	34	157	–	–	2292	16 53 45.59 −41 49 09.4	10.196	0.213	−2.44	−5.14	B1V	PHYB90	SB1? (GM01)
–	–	33	164	–	–	2325	16 53 46.99 −41 48 54.7	12.363	0.288	−0.09	−1.11	B7V	SIMBAD	
–	–	54	171	–	–	2353	16 53 47.98 −41 55 04.4	12.639	0.365	−0.13	−1.26	B6III/IV	SIMBAD	
–	–	14	175	–	–	2365	16 53 48.47 −41 45 21.5	11.724	0.313	−0.99	−2.69	B4IV	SIMBAD	
–	–	300	190	074	–	2428	16 53 49.83 −41 50 12.4	11.915	0.265	−0.33	−0.98	B8.5V?	SIMBAD	nm (BVF99)
–	–	265	200	109	121	2487	16 53 51.22 −41 50 53.7	12.608	0.295	0.27	−0.39	B8.5V	SIMBAD	nm (BVF99)
152200	7702	266	206	010	126	2506	16 53 51.68 −41 50 32.6	8.380	0.147	−4.17	−7.38	O9.7V	San05	
–	7706	253	226	020	139	2637	16 53 54.54 −41 52 14.9	9.569	0.179	−2.95	−5.65	B1V+B1Ve	San05, GM01	βCep (Bal83) SB2 (LM80)
152219	7707	254	234	007	149	2674	16 53 55.62 −41 52 51.5	7.560	0.165	−5.03	−7.98	O9.5III+B1-2III/V	SGR05	SB2O (SGR05)
–	–	24	236+	069	–	2692	16 53 56.03 −41 46 38.8	13.957	0.000	2.28	0.58	B4V	SIMBAD	SB (Rab96)
–	–	283	241	076	–	2702	16 53 56.19 −41 48 15.5	11.867	0.276	−0.77	−2.71	B3V	SIMBAD	
326320	7710	745	–	–	167	2759	16 53 57.59 −41 38 41.6	9.803	0.182	−2.73	−5.21	B0.5V+B2.5V	San05	SB2 (San05)
–	–	255	262	124	–	2770	16 53 57.80 −41 52 47.0	12.830	0.328	0.18	−1.03	B6V	SIMBAD	
–	7711	282	268	026	–	2800	16 53 58.62 −41 48 41.6	9.757	0.196	−2.75	−5.10	B2V+B2V	LM80	βCep (Bal83; ASK01)
152235	7709	501	–	–	179+	2810	16 53 58.87 −41 59 39.2	6.319	0.528	−7.12	−8.99	B1Ia	San05	
–	–	284	272	096	–	2813	16 53 58.95 −41 47 20.2	12.332	0.470	−0.88	−2.46	B4.5V	SIMBAD	nm (BVF99)
–	–	249	275	–	–	2828	16 53 59.33 −41 53 04.1	11.870	0.251	−0.61	−2.19	B4.5V	SIMBAD	
152218	7713	2	853	–	185	2861	16 53 59.98 −41 42 52.6	7.562	0.191	−5.15	−8.22	O9IV+O9.7V	SNoD05	SB2O (SLP97, SNoD05)
–	7712	248	288	014	191*	2882	16 54 00.41 −41 52 43.6	9.146	0.183	−3.45	−6.38	B0.5V	San05	
–	7717	749	–	–	–	2918	16 54 01.13 −41 38 59.8	10.192	0.206	−2.38	−4.91	B1.5V	GM01	
–	–	276	301	138	199*	2934	16 54 01.56 −41 49 25.1	12.832	0.312	0.37	−0.43	B8Vp	GaS79	strong SiII (GaS79)
–	7715	261	303	037	203	2949	16 54 01.80 −41 51 11.8	10.241	0.219	−2.34	−4.69	B2IV	PHYB90	SB (Rab96) β Cep (Bal83, ASK01)
152234	7716	290	855	001	202	2951	16 54 01.83 −41 48 22.6	5.426	0.188	−7.08	−9.89	O9.7Ia+O8V	San05	SB2 (San05)
–	–	259	317	041	213	3016	16 54 03.18 −41 51 49.3	10.896	0.255	−1.81	−4.16	B2V	San05	Vvar? (BVF99) SB2? (San05)
–	–	1	321	–	–	3028	16 54 03.49 −41 42 51.8	11.932	0.292	−0.71	−2.41	B4V	SIMBAD	
152233	7718	306	858	004	216	3034	16 54 03.60 −41 47 29.6	6.547	0.155	−6.08	−9.55	O6III(f)+O9?	San05	SB2 (San05)
–	–	194	323	057	–	3042	16 54 03.81 −41 45 48.2	11.441	0.301	−1.26	−3.08	B3.5V	SIMBAD	
–	7719	272	334	019	r.	3089	16 54 05.11 −41 50 07.0	9.452	0.151	−2.97	−5.67	B1V	LM80	RVvar (PHYB90, LM80) Vvar (RuB83)
–	–	274	340	072	–	3119	16 54 05.96 −41 49 44.7	11.726	0.243	−0.81	−2.75	B3V	GaS79	nm var? (BVF99)
–	7722	312	346	032	–	3141	16 54 06.58 −41 44 26.2	10.003	0.201	−2.59	−5.29	B1V	PHYB90	SB1 (GM01)
–	7723	295	349	018	–	3150	16 54 06.73 −41 50 07.2	9.414	0.145	−2.99	−5.69	B1V	LM80	SB1 (LM83)
–	7721p	309	350	012	251	3153	16 54 06.76 −41 51 07.0	8.709	0.168	−3.94	−7.07	O9V	San05	
–	7721s	309	351	027	–	3156	16 54 06.87 −41 51 01.3	9.892	0.178	−2.62	−5.32	B1V	San05	
–	7724	289	353	021	–	3161	16 54 06.97 −41 49 23.3	9.503	0.163	−3.03	−5.96	B0.5V	LM80	SB1 (LM83) SB1O (GM01) βCep? (LE85)
–	7725	6	364	029	–	3194	16 54 07.52 −41 44 40.4	9.872	0.208	−2.87	−6.03	B0V	PHYB90	SB? (GM01) B0.5V (LM80)
326340	7726	70	374	–	–	3246	16 54 09.02 −41 58 00.8	9.911	0.269	−2.97	−5.90	B0.5V	PHYB90	SB1? (GM01)
–	–	273	376	131	–	3252	16 54 09.18 −41 50 13.0	12.769	0.303	0.47	−0.04	B9IVp	GaS79	He weak (GaS79) SB (Rab96)
–	7727	286	378	017	–	3258	16 54 09.29 −41 48 41.1	9.410	0.174	−3.16	−6.09	B0.5V	LM80	SB2 (GM01)
152248	7728	291	856	002	279	3287	16 54 10.05 −41 49 30.0	6.088	0.138	−6.49	−10.02	O7.5III(f)+O7III(f)	SRG01	SB2O (SRG01) EB (MHL01)
–	–	209	394	039	282	3315	16 54 10.74 −41 47 47.3	10.591	0.240	−2.00	−4.14	B2.5V	San05	B2V/IV (GaS79) SB (Rab96) SPB? (ASK01)
–	–	374	400	–	-?-	3331	16 54 10.98 −41 49 39.2	10.151	0.227	−2.46	−4.81	B2V	SIMBAD	
–	7730	287	403	016	–	3339	16 54 11.33 −41 48 54.0	9.311	0.173	−3.19	−5.89	B1V	LM80	SB1 (GM01)
152247	7732	321?	–	–	291	–	16 54 11.52 −41 38 31.0	7.180	0.220	−5.64	−8.77	O9III	San05	SB? (San05)
152249	7731	293	857	003	292	3354	16 54 11.62 −41 50 57.1	6.437	0.193	−6.16	−9.34	O9Ib((f))	San05	

Table 2. Continued.

Object IDs.							α δ (J2000.0)	V	$B-V$	M_V	M_{bol}	Sp.T.	Ref. [a]	Comments [a,b]
HD	CPD−41°	Se68	SBL98	BVF99	X#	SSB05	hh mm ss.s ±dd am as.s							
[1]	[2]	[3]	[4]	[5]	[6]	[7]	[8]	[9]	[10]	[11]	[12]	[13]	[14]	[15]
–	–	243	410	105	–	3373	16 54 12.30 −41 52 38.0	12.473	0.390	−0.18	−0.84	B8.5V	SIMBAD	
–	–	75	422	–	–	3402	16 54 13.08 −41 56 31.4	12.745	0.378	0.13	−0.52	B8.5V	SIMBAD	
–	7733	323	862	009	306	3410	16 54 13.27 −41 50 32.7	7.849	0.170	−4.64	−7.84	O8.5V+B3?	SRG05	SB2O (SRG05)
326329	7735	292	434	013	313	3450	16 54 14.14 −41 50 08.8	8.756	0.165	−3.87	−7.11	O9.5V	San05	
–	7734	80	437	038	–	3461	16 54 14.27 −41 55 01.6	10.320	0.336	−2.85	−6.01	B0Vn	PHYB90	var, β Cep? (BaE85)
–	–	236	443	051	r.	3484	16 54 14.78 −41 51 11.0	11.373	0.238	−1.21	−3.35	B2.5V	GaS79	
–	–	78	447+	–	–	3496	16 54 15.11 −41 55 29.5	11.595	0.364	−0.97	−1.74	B8.5III	SIMBAD	
–	–	235	452	166	328*	3517	16 54 15.59 −41 50 54.9	13.265	0.373	0.67	0.01	B8.5V	GaS79	
–	7736	330?	456	036	330+	3525	16 54 15.78 −41 49 32.6	10.153	0.260	−2.63	−5.33	B1Vn	SNW71	β Cep (ASK01)
–	7737	294	461	040	337	3552	16 54 16.35 −41 50 27.1	10.725	0.238	−1.92	−4.27	B2V	San05	SPB (ASK01)
–	–	189	464	056	–	3570	16 54 16.81 −41 45 08.5	11.557	0.318	−0.86	−1.51	B8.5V	SIMBAD	nm (BVF99)
–	–	234	476	127	–	3595	16 54 17.44 −41 51 03.0	12.810	0.336	0.27	−0.53	B8Vn	GaS79	
–	–	213	480	044	–	3614	16 54 17.95 −41 48 01.6	11.063	0.210	−1.49	−3.84	B2IVn	GaS79	
–	–	225	482	148	r.	3624	16 54 18.17 −41 50 16.9	13.065	0.370	0.54	0.03	B9V	GaS79	nm (Rab96)
326330	7738	238	486	022	–	3630	16 54 18.29 −41 51 35.2	9.597	0.181	−2.93	−5.63	B1V(n)	LM80	β Cep (BaE85)
326339	7739	73	497	–	–	3669	16 54 19.34 −41 57 31.0	10.113	0.400	−3.18	−5.84	B0.5III	PHYB90	nm? (PHC91)
152270	7741	220	854	005	371	3686	16 54 19.69 −41 49 11.2	6.597	0.186	−4.88	−9.10	WC7+O6	Lue97, NuL00	WR 79
–	7742	224	505	011	372	3691	16 54 19.81 −41 50 10.1	8.225	0.166	−4.36	−7.49	O9V+B1.5V	SAR05	SB2O (SHR03) EB (SAR05)
–	–	227	513	110	–	3715	16 54 20.34 −41 50 49.3	12.480	0.321	−0.08	−1.10	B7Vn	GaS79	SB (Rab96)
–	–	334	515	049	–	3725	16 54 20.60 −41 49 29.2	11.183	0.254	−1.58	−4.28	B1Vn	SNW71	
–	7743	232	521	25+	–	3747	16 54 21.28 −41 51 41.4	9.720	0.214	−2.95	−5.88	B0.5V	LM80	SB1 (LM83) EB (BE85)
–	–	89	522	–	386*	3748	16 54 21.33 −41 55 36.8	11.176	0.325	−1.69	−3.50	B2.5III	SIMBAD	SB? (Rab96)
–	–	223	528	066	–	3764	16 54 21.67 −41 49 55.0	11.679	0.298	−0.87	−2.08	B6Vn	GaS79	member? (BVF99)
–	–	217	529	091	–	3769	16 54 21.99 −41 48 47.7	12.229	0.304	−0.34	−1.55	B6Vn	GaS79	
–	–	186	539	054	–	3814	16 54 22.85 −41 45 23.6	11.494	0.283	−1.24	−3.38	B2.5V	SIMBAD	
–	–	108	547	052	–	3846	16 54 23.45 −41 52 51.1	11.420	0.298	−1.43	−3.78	B2V	GaS79	
–	–	165	570	103	–	3949	16 54 25.97 −41 47 07.3	12.438	0.299	−0.02	−0.93	B7.5V	SIMBAD	nm (BVF99)
326331	7744	338	571	006	422	3950	16 54 25.97 −41 49 55.5	7.497	0.181	−5.19	−8.58	O8III((f))	San05	
–	–	184	572	077	–	3953	16 54 26.06 −41 45 54.5	11.959	0.347	−0.55	−1.21	B8.5V	SIMBAD	nm (BVF99)
–	7744B	–	578	031	–	3974	16 54 26.46 −41 49 51.8	9.931	0.223	−2.70	−5.23	B1.5V	San05	SB? (San05)
–	–	222	587	071	–	4023	16 54 27.95 −41 50 14.5	11.826	0.282	−0.79	−2.49	B4Vn	GaS79	
–	–	160	593	070	440	4057	16 54 28.96 −41 48 26.3	11.822	0.298	−0.89	−2.49	B3III	SIMBAD	
–	7746	769	–	–	448	4076	16 54 29.51 −41 39 15.1	9.193	0.212	−3.50	−6.43	B0.5V	GM01	SB1 (GM01)
152314	7749	161	615	008	468	4180	16 54 32.01 −41 48 18.6	7.749	0.225	−5.05	−8.54	O8.5V+B+...	San05	SB2+? (San05)
–	–	96	617	–	r.	4186	16 54 32.15 −41 56 53.5	11.036	0.349	−2.01	−4.54	B1.5V	SIMBAD	
–	–	115	643	058	–	4311	16 54 35.31 −41 54 49.9	11.461	0.282	−1.20	−3.14	B3V	SIMBAD	SB (Rab96)
–	–	152	648	100	r.	4330	16 54 35.70 −41 49 42.8	12.338	0.307	−0.31	−1.77	B5V	SIMBAD	
326332	7752	343	651	024	r.	4335	16 54 35.79 −41 50 12.4	9.654	0.241	−3.07	−5.50	B1III*	LM80	
–	7753	110	653	028	–	4346	16 54 36.06 −41 53 38.2	9.806	0.241	−2.98	−5.91	B0.5V	San05	SB? (GM01, San05)
	7755	112	684	034	521	4474	16 54 39.89 −41 53 38.5	10.063	0.214	−2.57	−5.27	B1V	San05	
326317	7756	774	–	–	–	4530	16 54 41.23 −41 39 02.0	10.129	0.196	−2.38	−4.40	B2III	Lav72	
–	–	173	702	–	–	4576	16 54 42.32 −41 45 58.1	12.905	0.343	0.47	−0.04	B9V	SIMBAD	
326333	7757	150	712?	023	–	4622	16 54 43.15 −41 49 35.5	9.584	0.193	−2.98	−5.68	B1V(n)	LM83	β Cep (BaS83) SB1? (GM01)
–	–	123	717	094	–	4655	16 54 44.20 −41 55 08.7	12.282	0.310	−0.27	−1.39	B6.5V	SIMBAD	
–	–	121	718	–	542*	4657	16 54 44.23 −41 56 27.3	11.219	0.265	−1.19	−2.30	B6.5V	SIMBAD	
–	–	172	721	–	545*	4664	16 54 44.37 −41 46 42.6	12.823	0.345	0.38	−0.13	B9V	SIMBAD	
–	–	175	726	–	–	4697	16 54 44.91 −41 44 59.3	13.244	0.359	0.76	0.25	B9V	SIMBAD	
–	–	127	746	–	557	4776	16 54 47.28 −41 52 49.7	12.021	0.384	−0.68	−1.50	B8III-IV	SIMBAD	
–	–	142	748	085	559	4793	16 54 47.73 −41 50 47.6	12.143	0.311	−0.56	−2.26	B4V	SIMBAD	
–	7760B	810b	–	–	566	4881	16 54 50.35 −42 01 27.6	10.452	0.449	−2.96	−5.66	B1V	San05	
–	7760	810	–	–	566	4885	16 54 50.38 −42 01 25.6	10.113	0.403	−3.19	−5.85	B0.5III	San05	
326334	7762	169	769	–	–	4997	16 54 53.41 −41 47 07.3	10.722	0.210	−1.70	−3.64	B3V	Bra67	SB? (Rab96)
–	–	147	773	–	–	5006	16 54 53.69 −41 49 12.4	12.313	0.381	−0.16	−0.57	B9.5V	SIMBAD	
–	–	146	790	–	–	5151	16 54 58.24 −41 49 17.5	11.294	0.253	−1.27	−3.21	B3V	SIMBAD	SB? (Rab96)
152437	7766	798	–	–	602	5601	16 55 12.12 −41 56 40.3	9.145	0.150	−2.52	−2.94	A0III	San05	nm (PHC91,RCB97) B9III/IV (Hou78)

a. Bra67: Braes (1967); SNW71: Schild et al. (1971); Lav72: Laval (1972); Hou78: Houk (1978); GaS79: Garrison & Schild (1979); LM80: Levato & Malaroda (1980); RuB82: Rufener & Bartholdi (1982); LM83: Levato & Morrell (1983); Bal83: Balona (1983); BaS83: Balona & Shobbrook (1983); BaE85: Balona & Engelbrecht (1985); PHYB90: Perry et al. (1990); PHC91: Perry et al. (1991); Rab96: Raboud (1996); Lue97: Luehrs (1997); RCB97: Raboud et al. (1997); SLP97: Stickland et al. (1997); BVF99: Baume et al. (1999); NuL00: Nugis & Lamers (2000); ASK01: Arentoft et al. (2001); GM01: García & Mermilliod (2001); MHL01: Mayer et al. (2001); SRG01: Sana et al. (2001); SHR03: Sana et al. (2003); San05: Sana (2005); SAR05: Sana et al. (2005a); SGR05: Sana et al. (2005b); SNoD05: Sana et al. (2005e); SRG05: Sana et al. (2005f)

b. EB: eclipsing binary; nm: non member; SB(O): spectroscopic binary (with computed orbit); RVvar: radial velocity variable; SPB: slowly pulsating B star; Vvar: photometric variable.

H. Sana et al.: An XMM-*Newton* view of NGC 6231. II, *Online Material p 4*

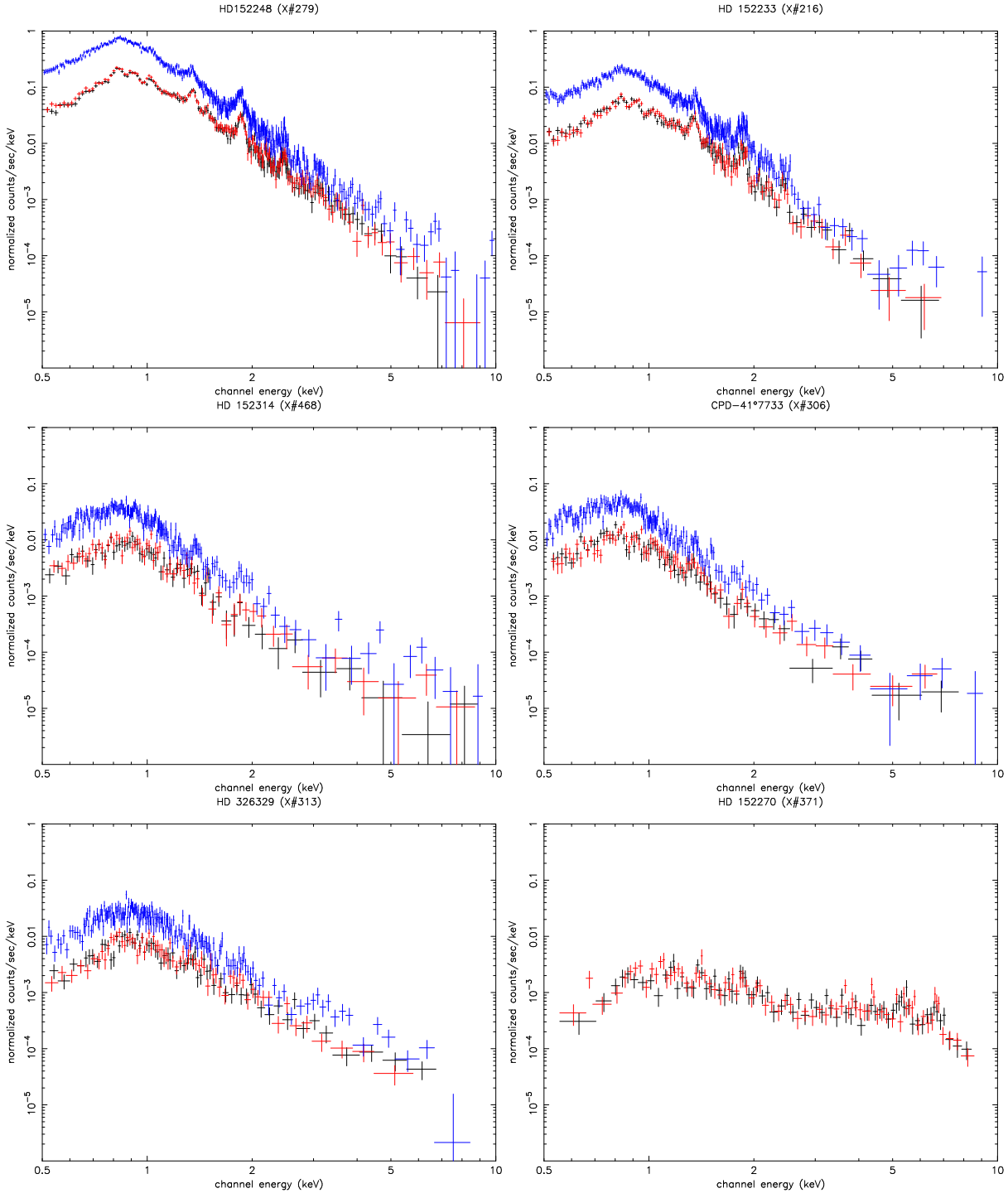

Fig. 2. O-type star EPIC spectra that have required a 3-T MEKAL model fit (see Table 6). The source name is given on top of each panel. Different colours refer to the different EPIC instruments: MOS1, black; MOS2, red; pn, blue. The source are ordered by decreasing $L_{\rm bol}$ (see Table 3). The last spectrum belongs to the WR-type binary HD 152270 (WR 79).

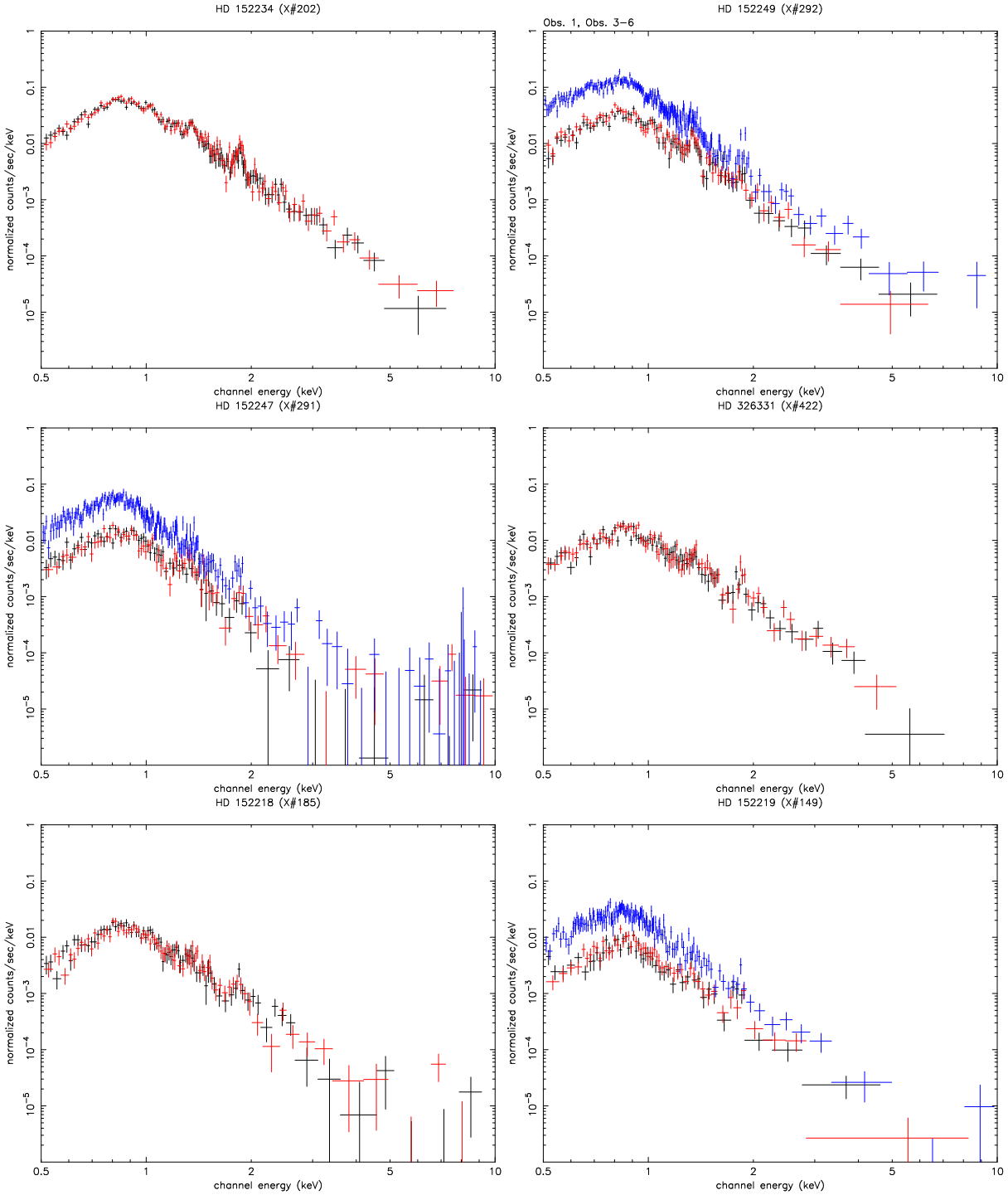

Fig. 3. Same as Fig. 2 for the O-type star spectra that have required a 2-T MEKAL model fit (see Table 5).

H. Sana et al.: An XMM-*Newton* view of NGC 6231. II, *Online Material p 6*

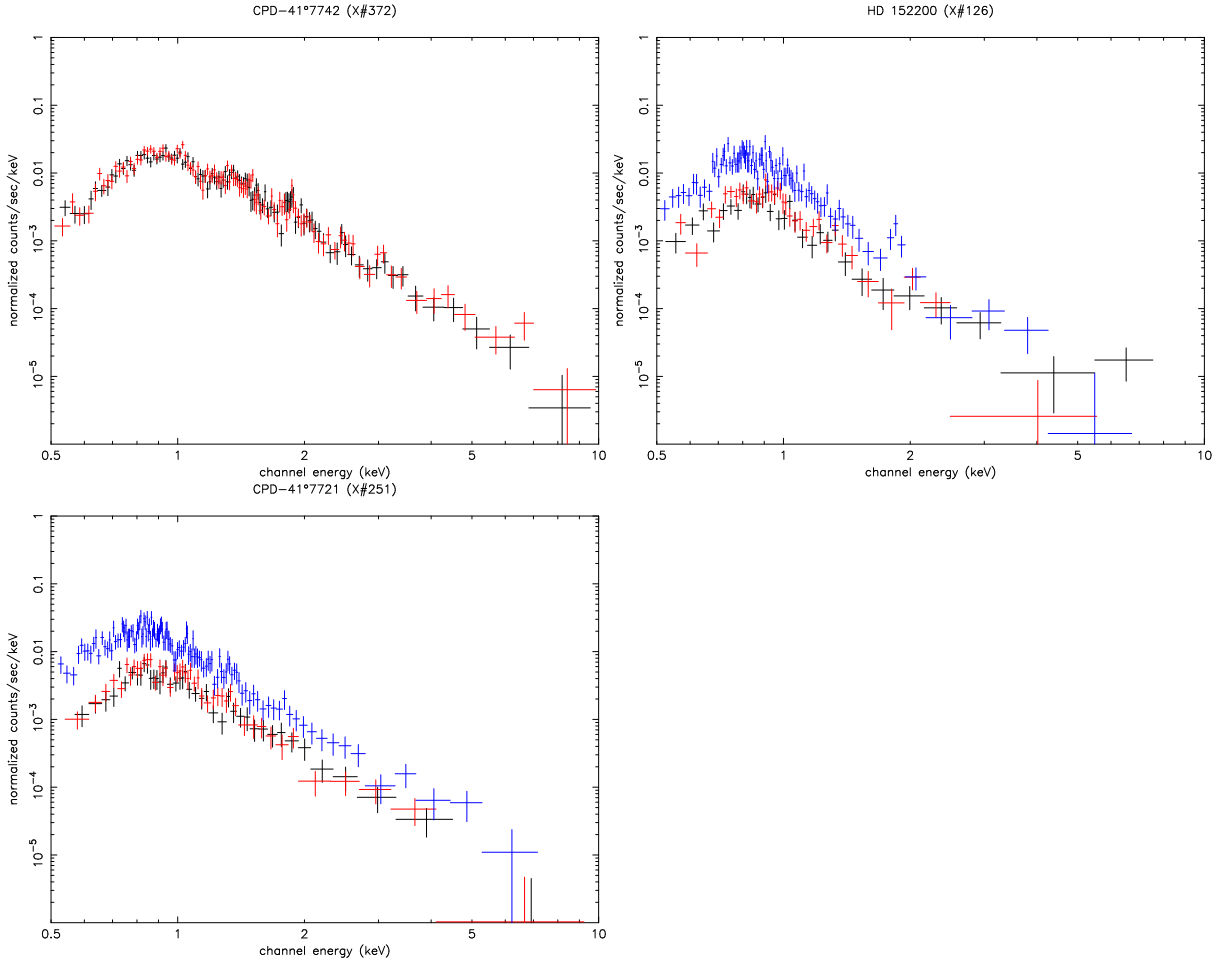

Fig. 3. Continued.

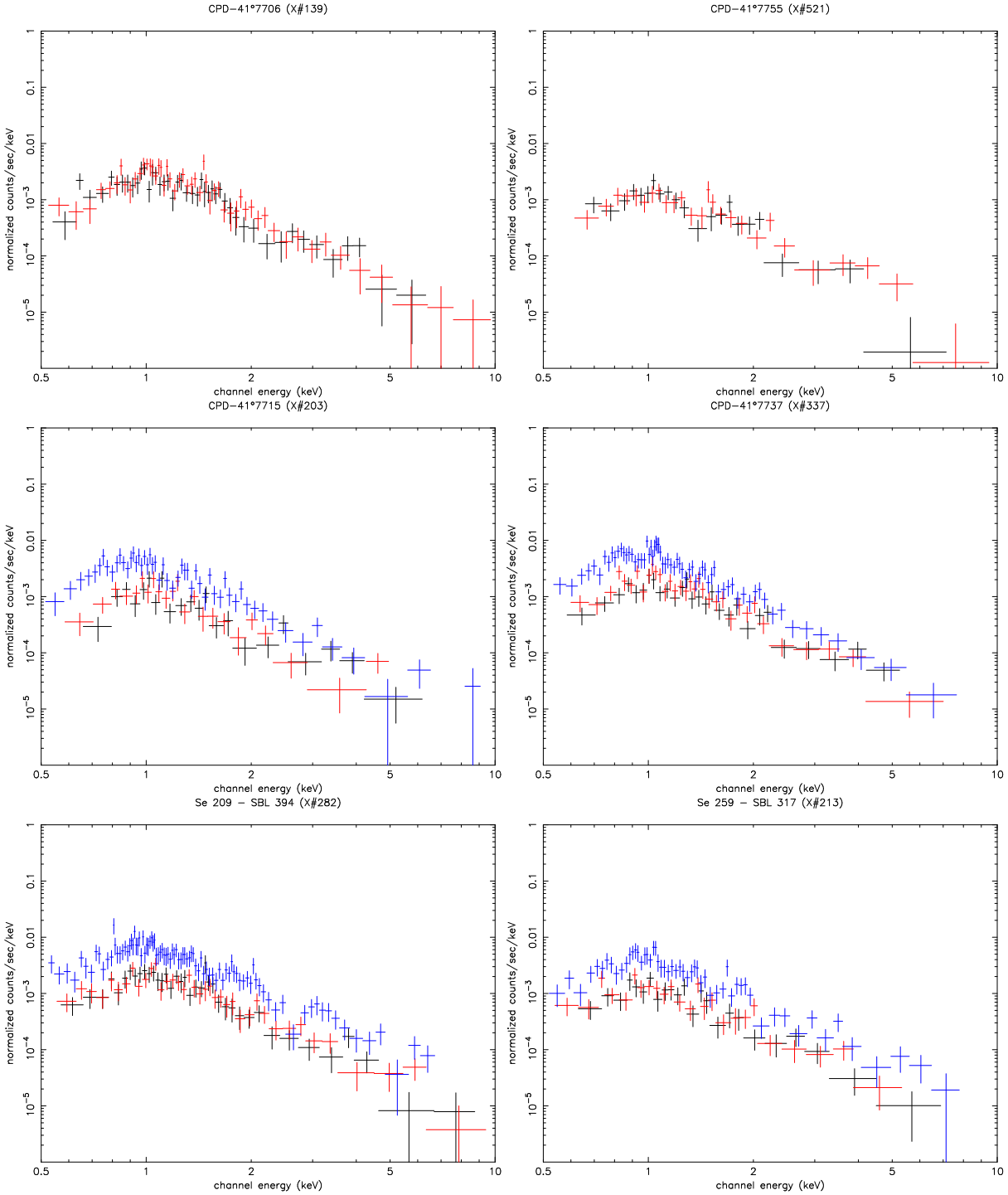

Fig. 4. Same as Fig. 2 for the B-type star spectra that have required a 2-T MEKAL model fit (see Table 5).

H. Sana et al.: An XMM-*Newton* view of NGC 6231. II, *Online Material p 8*

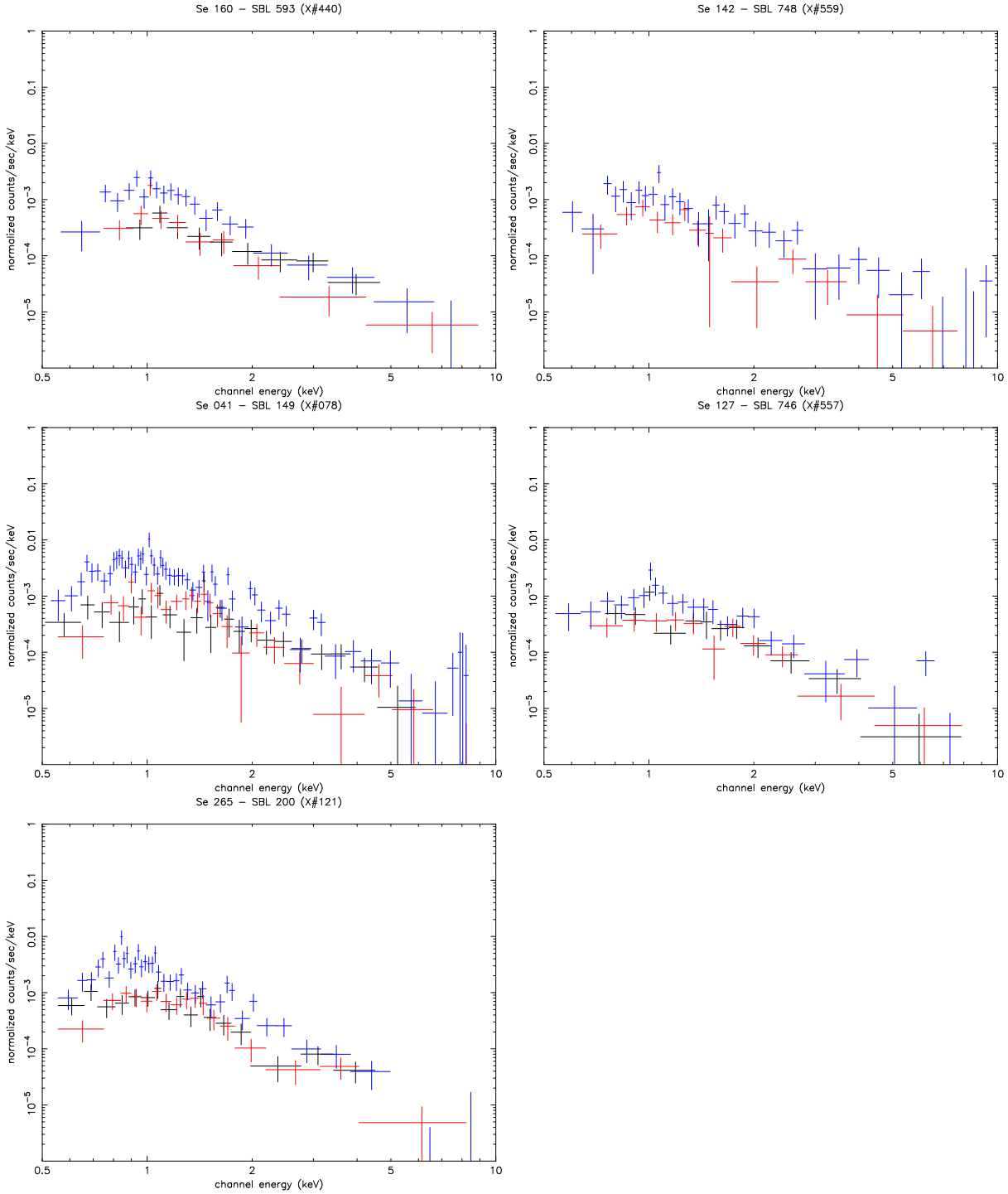

Fig. 4. Continued.

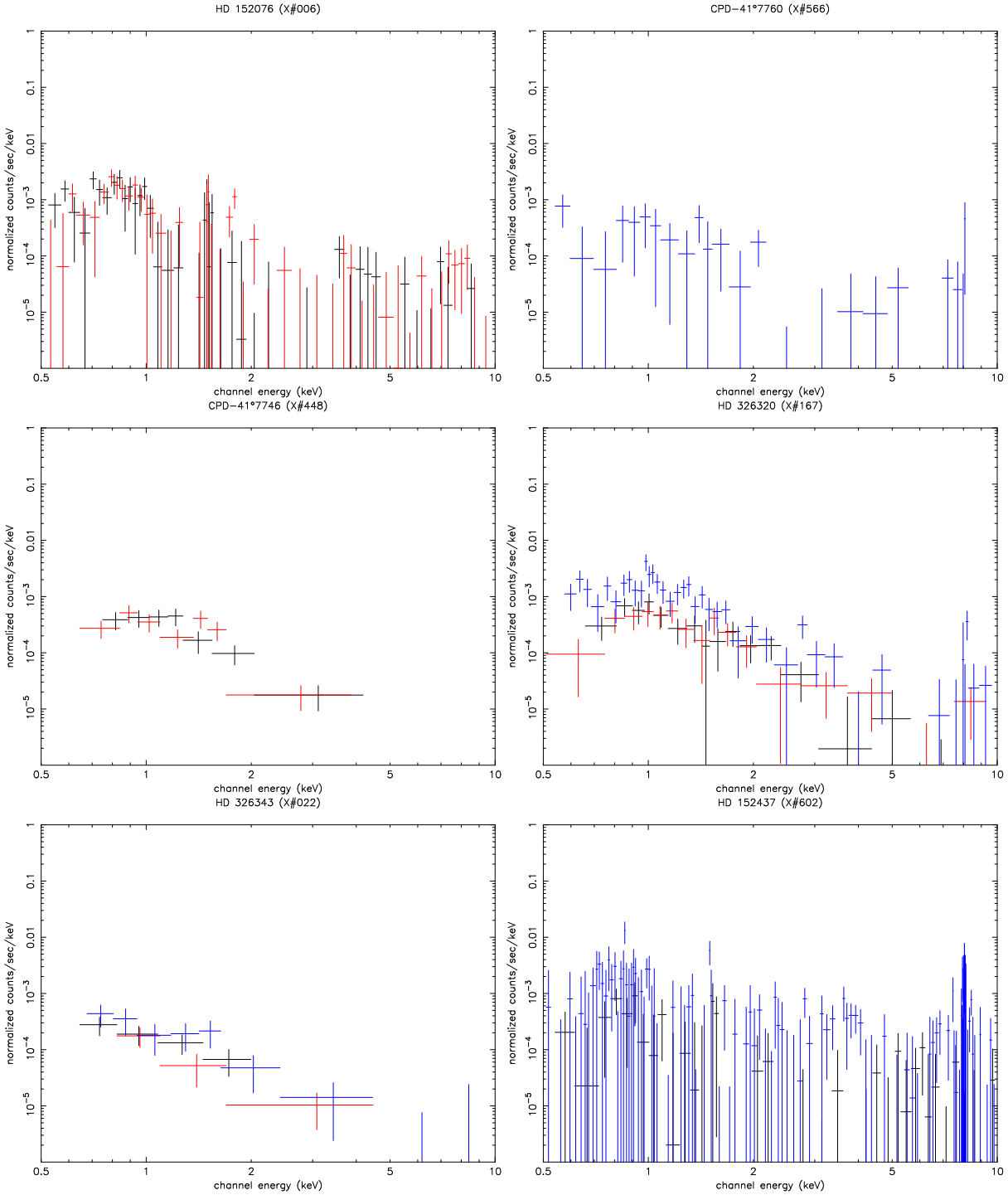

Fig. 5. Same as Fig. 2 for the source spectra that have required a single temperature MEKAL model fit (see Table 4).

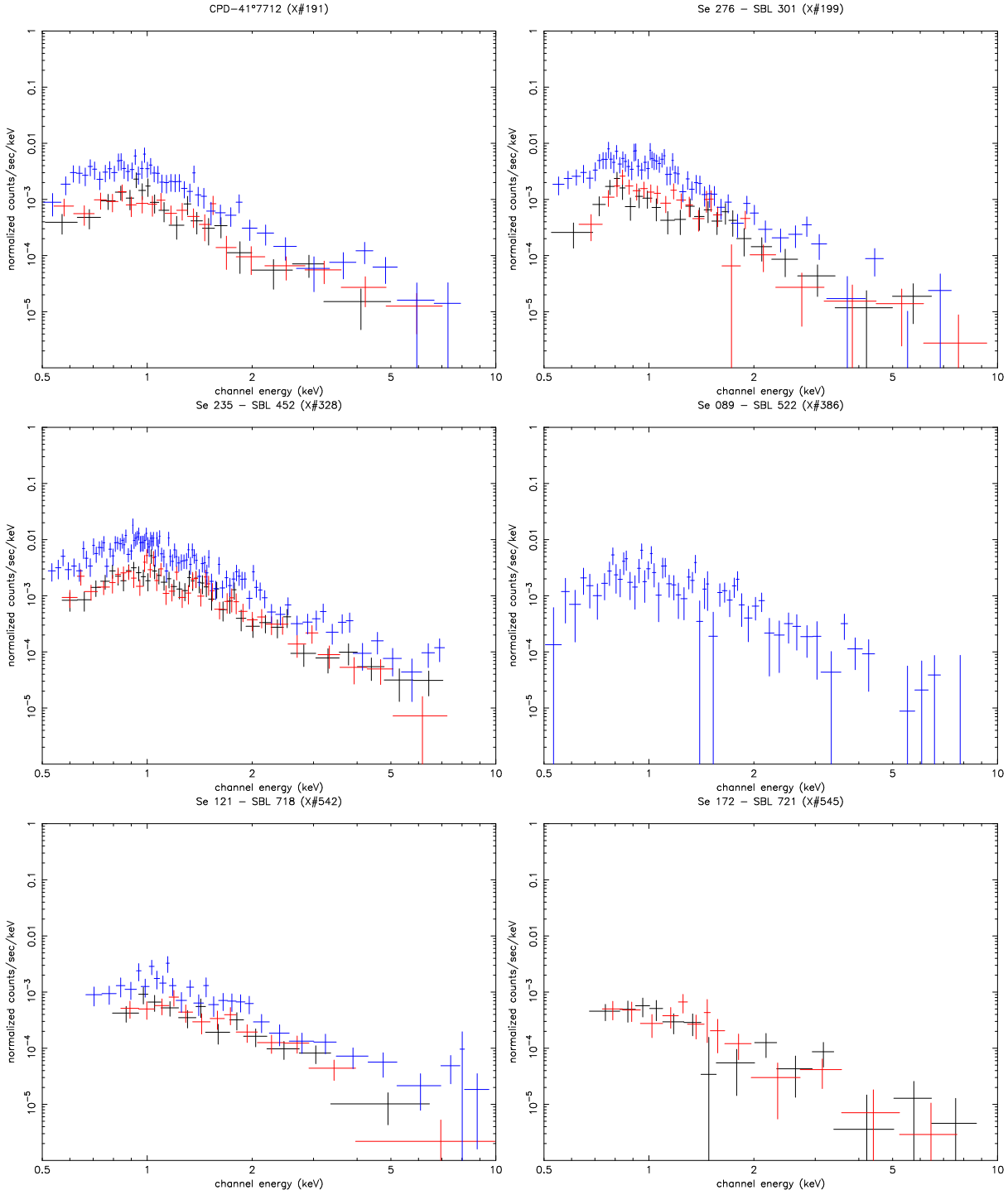

Fig. 6. Same as Fig. 4 for the sources with $3.0'' < d_{cc} < 3.6''$ (see Table 7).

Appendix C

List of the publications related to this work

Publications with a peer review

HD 152248: Evidence for a colliding wind interaction,
Sana, H., Rauw, G., & Gosset, E. 2001,
A&A, **370**, 121–135 (see p. 81 in this dissertation)

The massive binary CPD −41°7742 I. High-resolution optical spectroscopy,
Sana, H., Hensberge, H., Rauw, G., & Gosset, E. 2003,
A&A, **405**, 1063–1074 (see p. 117 in this dissertation)

A phase-resolved XMM-Newton campaign on the colliding-wind binary HD 152248
Sana, H., Stevens, I. R., Gosset, E., Rauw, G., & Vreux, J.-M. 2004,
MNRAS, **350**, 809–828 (see p. 97 in this dissertation)

The massive binary CPD −41°7742 II. Optical light curve, X-ray observations,
Sana, H., Antokhina, E., Royer, P., Manfroid, J., Gosset, E., Rauw, G., & Vreux, J.-M. 2005a,
A&A, 18p., in press (see p. 129 in this dissertation)

The massive binary HD 152219: A pulsating primary component?,
Sana, H., Gosset, E., & Rauw, G. 2005b,
A&A, 16p., submitted (see p. 163 in this dissertation)

An XMM-Newton view of the young open cluster NGC 6231 I. The catalogue,
Sana, H., Gosset, E., Rauw, G., Sung, H., & Vreux, J.-M. 2005c,
A&A, 20p., accepted (see p. 23 in this dissertation)

The massive binary HD 152218,
Sana, H., Nazé, Y., O'Donnell, B., Rauw, G., & Gosset, E. 2005e,
A&A, 14p., submitted (see p. 179 in this dissertation)

CPD −41°7733: Optical Spectroscopy, XMM-Newton Observations,
Sana, H., Rauw, G., & Gosset, E. 2005f,
A&A, 14p., submitted (see p. 149 in this dissertation)

An XMM-Newton view of the young open cluster NGC 6231 II. The early-type star population,
Sana, H., Rauw, G., Nazé, Y., Gosset, E., & Vreux, J.-M. 2005g,
A&A, 23p., submitted (see p. 43 in this dissertation)

An XMM-Newton view of the young open cluster NGC 6231 III. The optically faint sources,
Sana, H., Rauw, G., Sung, H., Gosset, E., & Vreux, J.-M. 2005h,
A&A, 12p., in preparation, (see p. 67 in this dissertation)

Publications without a peer review

NGC 6231: X-ray properties of the early-type star population,
Sana, H., Rauw, G., Gosset, E., & Vreux, J.-M.. 2002,
in ASP Conf. Ser., Vol. 260, Interacting Winds from Massive Stars, eds. A. Moffat & N. St-Louis, 431–438

Colliding Wind Binaries: an insight into O-star physics.,
Sana, H., & Rauw, G. 2003,
Rev. Quest. Scient., **174**, 40–48

NGC 6231: X-ray properties of the early-type star population,
Sana, H., Nazé, Y., Gosset, E., Rauw, G., Sung, H., & Vreux, J.-M. 2005d,
in Massive Stars in Interacting Binaries, eds. A. Moffat & N. St-Louis, ASP Conf. Ser., 5p., in press

Bibliography

Albacete Colombo, J. F., Méndez, M., & Morrell, N. I. 2003, MNRAS, 346, 704

Arentoft, T., Sterken, C., Knudsen, M. R., et al. 2001, A&A, 380, 599

Balona, L. A. 1983, MNRAS, 203, 1041

Balona, L. A., & Laney, C. D. 1995, MNRAS, 276, 627

Balona, L. A., & Shobbrook, R. R. 1983, MNRAS, 205, 309

Batten, A. H., Fletcher, J. M., & MacCarthy, D. G. 1989, Publications of the Dominion Astrophysical Observatory Victoria, 17, 1

Baume, G., Vázquez, R. A., & Feinstein, A. 1999, A&AS, 137, 233

Bok, B. J., Bok, P. F., & Graham, J. A. 1966, MNRAS, 131, 247

Bonnell, I. 2005, in Massive Stars in Interacting Binaries, eds. A. Moffat & N. St-Louis, ASP Conf. Ser., 8 p., in press

Bonnell, I. A., Bate, M. R., & Zinnecker, H. 1998, MNRAS, 298, 93

Bonnell, I. A., Vine, S. G., & Bate, M. R. 2004, MNRAS, 349, 735

Campbell, W., & Moore, J. 1938, Publ. Lick Obs., 16, 1

Cassinelli, J. P., Mathis, J. S., & Savage, B. D. 1981, Science, 212, 1497

Castor, J. I., Abbott, D. C., & Klein, R. I. 1975, ApJ, 195, 157

Cherepashchuk, A. M. 1976, Soviet Astronomy Letters, 2, 138

Chlebowski, T., & Garmany, C. D. 1991, ApJ, 368, 241

Conti, P. S. 1973, ApJ, 179, 181

Conti, P. S., & Alschuler, W. R. 1971, ApJ, 170, 325

Crowther, P. A., Hillier, D. J., Evans, C. J., et al. 2002, ApJ, 579, 774

De Becker, M., Rauw, G., & Eenens, P. 2005, A&A, submitted

de Wit, W. J., Testi, L., Palla, F., Vanzi, L., & Zinnecker, H. 2005, A&A, in press

Didelon, P. 1982, A&AS, 50, 199

Diplas, A., & Savage, B. D. 1994, ApJS, 93, 211

Dougherty, S. M., Pittard, J. M., Kasian, L., et al. 2003, A&A, 409, 217

Dougherty, S. M., Beasley, A. J., Claussen, M. J., Zauderer, B. A., & Bolingbroke, N. J. 2005, ApJ, 623, 447

Feinstein, A., & Ferrer, O. E. 1968, PASP, 80, 410

Figer, D. F. 2005, Nature, 434, 192

Figueiredo, J., de Greve, J. P., & de Loore, C. 1991, A&A, 252, 155

García, B., & Mermilliod, J. C. 2001, A&A, 368, 122

Garmany, C. D., Conti, P. S., & Massey, P. 1980, ApJ, 242, 1063

Garrison, R. F., & Schild, R. E. 1979, AJ, 84, 1020

Gayley, K. G., Owocki, S. P., & Cranmer, S. R. 1997, ApJ, 475, 786

Gies, D. R. 2003, in IAU Symposium, Vol. 212, A Massive Star Odyssey: from main sequence to supernova, eds. K. van der Hucht, A. Herrero, & C. Esteban, 91

Heck, A., Manfroid, J., & Mersch, G. 1985, A&AS, 59, 63

Hensberge, H. 2002, 2002, *Evaluation of* FEROS *Pipeline*, http://www.ls.eso.org/lasilla/Telescopes/2p2T/E1p5M/FEROS/Reports/index.html, Tech. rep., Royal Obs. of Belgium

Herrero, A., Kudritzki, R. P., Vilchez, J. M., et al. 1992, A&A, 261, 209

Herrero, A., Puls, J., & Najarro, F. 2002, A&A, 396, 949

Heske, A., & Wendker, H. J. 1984, A&AS, 57, 205

Heydari-Malayeri, M. 1996, in The Interplay Between Massive Star Formation, the ISM and Galaxy Evolution, 51

Hill, G., Crawford, D. L., & Barnes, J. V. 1974, AJ, 79, 1271

Houck, T. E. 1956, Ph.D. Thesis

Houk, N. 1978, Michigan catalogue of two-dimensional spectral types for the HD stars (Ann Arbor : Dept. of Astronomy, University of Michigan : distributed by University Microfilms International, 1978-)

Howarth, I. D., & Prinja, R. K. 1989, ApJS, 69, 527

Howarth, I. D., Siebert, K. W., Hussain, G. A. J., & Prinja, R. K. 1997, MNRAS, 284, 265

Humphreys, R. M., & McElroy, D. B. 1984, ApJ, 284, 565

Lafler, J., & Kinman, T. D. 1965, ApJS, 11, 216

Lamers, H. J. G. L. M., & Cassinelli, J. P. 1999, Introduction to stellar winds, cambridge university press edn. (Introduction to stellar winds / Henny J.G.L.M. Lamers and Joseph P. Cassinelli. Cambridge ; New York : Cambridge University Press, 1999. ISBN 0521593980)

Lang. 1992, Astrophysical data: planets and stars

Laval, A. 1972, A&A, 21, 271

Levato, H., & Malaroda, S. 1980, PASP, 92, 323

Levato, H., & Morrell, N. 1983, Astrophys. Lett., 23, 183

Levato, H., Morrell, N., Garcia, B., & Malaroda, S. 1988, ApJS, 68, 319

Luehrs, S. 1997, PASP, 109, 504

Luo, D., McCray, R., & Mac Low, M. 1990, ApJ, 362, 267

Maeder, A., & Behrend, R. 2002, in ASP Conf. Ser. 267: Hot Star Workshop III: The Earliest Phases of Massive Star Birth, 179

Manfroid, J. 1993, A&A, 271, 714

Martins, F., Schaerer, D., & Hillier, D. J. 2002, A&A, 382, 999

Martins, F., Schaerer, D., & Hillier, D. 2005, A&A, in press

Mason, B. D., Gies, D. R., Hartkopf, W. I., et al. 1998, AJ, 115, 821

Mathys, G. 1988, A&AS, 76, 427

Mathys, G. 1989, A&AS, 81, 237

Mayer, P., Harmanec, P., Lorenz, R., et al. 2001, in ASSL Vol. 264: The Influence of Binaries on Stellar Population Studies, 567

McKee, C. F., & Tan, J. C. 2003, ApJ, 585, 850

Morgan, W. W., González, G., & González, G. 1953a, ApJ, 118, 345

Morgan, W. W., Whitford, A. E., & Code, A. D. 1953b, ApJ, 118, 318

Neubauer, F. J. 1930, PASP, 42, 235

Norberg, P., & Maeder, A. 2000, A&A, 359, 1025

Oey, M. S., & Clarke, C. J. 2005, ApJ, 620, L43

Oja, T. 1986, A&AS, 65, 405

Owocki, S. 2004, in EAS Publications Series, 163

Penny, L. R. 1996, ApJ, 463, 737

Penny, L. R., Gies, D. R., & Bagnuolo, W. G. 1996, ApJ, 460, 906

Perry, C. L., Hill, G., Younger, P. F., & Barnes, J. V. 1990, A&AS, 86, 415

Perry, C. L., Hill, G., & Christodoulou, D. M. 1991, A&AS, 90, 195

Pittard, J. M., & Stevens, I. R. 1997, MNRAS, 292, 298

Pourbaix, D., Tokovinin, A. A., Batten, A. H., et al. 2004, A&A, 424, 727

Prilutsky, O. F., & Usov, V. V. 1976, NASA STI/Recon Technical Report N, 77, 10994

Raboud, D. 1996, A&A, 315, 384

Raboud, D., Cramer, N., & Bernasconi, P. A. 1997, A&A, 325, 167

Rauw, G., Sana, H., Gosset, E., et al. 2000, A&A, 360, 1003

Rauw, G., Vreux, J.-M., Stevens, I. R., et al. 2002, A&A, 388, 552

Rauw, G., Crowther, P. A., de Becker, M., et al. 2005, A&A, 432, 985

Royer, P. 2001, PhD thesis, University of Liège

Royer, P., Vreux, J.-M., & Manfroid, J. 1998, A&AS, 130, 407

Sana, H., & Rauw, G. 2003, Rev. Quest. Scient., 174, 40

Sana, H., Rauw, G., & Gosset, E. 2001, A&A, 370, 121

Sana, H., Rauw, G., Gosset, E., & Vreux, J.-M. 2002, in ASP Conf. Ser., Vol. 260, Interacting Winds from Massive Stars, eds. A. Moffat & N. St-Louis, 431

Sana, H., Hensberge, H., Rauw, G., & Gosset, E. 2003, A&A, 405, 1063

Sana, H., Stevens, I. R., Gosset, E., Rauw, G., & Vreux, J.-M. 2004, MNRAS, 350, 809

Sana, H., Antokhina, E., Royer, P., et al. 2005a, A&A, in press

Sana, H., Gosset, E., & Rauw, G. 2005b, A&A, submitted

Sana, H., Gosset, E., Rauw, G., Sung, H., & Vreux, J.-M. 2005c, A&A, accepted

Sana, H., Nazé, Y., Gosset, E., et al. 2005d, in Massive Stars in Interacting Binaries, eds. A. Moffat & N. St-Louis, ASP Conf. Ser., 5p., in press

Sana, H., Nazé, Y., O'Donnell, B., Rauw, G., & Gosset, E. 2005e, A&A, submitted

Sana, H., Rauw, G., & Gosset, E. 2005f, A&A, submitted

Sana, H., Rauw, G., Nazé, Y., Gosset, E., & Vreux, J.-M. 2005g, A&A, submitted

Sana, H., Rauw, G., Sung, H., Gosset, E., & Vreux, J.-M. 2005h, A&A, in preparation

Schaller, G., Schaerer, D., Meynet, G., & Maeder, A. 1992, A&AS, 96, 269

Schild, R. E., Hiltner, W. A., & Sanduleak, N. 1969, ApJ, 156, 609

Schild, R. E., Neugebauer, G., & Westphal, J. A. 1971, AJ, 76, 237

Schmidt-Kaler, T. 1982, Landolt-Börnstein, Numerical Data and Functional Relationships in Science and Technology, New Series, Group VI, Vol. 2b, Physical Parameters of the Stars (Berlin: Springer-Verlag)

Seggewiss, W. 1968, Veroeffentlichungen des Astronomisches Institute der Universitaet Bonn, 79

Shapley, H., & Sawyer, H. B. 1927, Harvard College Observatory Bulletin, 846, 1

Sobolev, V. V. 1960, Moving envelopes of stars (Cambridge: Harvard University Press, 1960)

Stetson, P. B. 1987, PASP, 99, 191

Stevens, I. R., Blondin, J. M., & Pollock, A. M. T. 1992, ApJ, 386, 265

Stevens, I. R., & Pollock, A. M. T. 1994, MNRAS, 269, 226

Stickland, D. J., & Lloyd, C. 2001, The Observatory, 121, 1

Struve, O. 1944, ApJ, 100, 189

Sung, H., Bessell, M. S., & Lee, S. 1998, AJ, 115, 734

Usov, V. V. 1992, ApJ, 389, 635

Vink, J. S., de Koter, A., & Lamers, H. J. G. L. M. 1999, A&A, 350, 181

Vink, J. S., de Koter, A., & Lamers, H. J. G. L. M. 2000, A&A, 362, 295

Vink, J. S., de Koter, A., & Lamers, H. J. G. L. M. 2001, A&A, 369, 574

Walborn, N. R. 1972, AJ, 77, 312

Walborn, N. R., & Fitzpatrick, E. L. 1990, PASP, 102, 379

Walder, R., & Folini, D. 2003, in IAU Symposium, 139

Wilson, R. 1953, Carnegie Institution of Washington Publ., Vol. 601, General Catalogue of Stellar Radial Velocity (Washington D.C.)

Yorke, H. W., & Sonnhalter, C. 2002, ApJ, 569, 846

Zinnecker, H. 2003, in IAU Symposium, Vol. 212, A Massive Star Odyssey: from main sequence to supernova, ed. K. van der Hucht, A. Herrero, & C. Esteban, 80